

LITHOGEOCHEMISTRY OF THE SEDIMENTARY STRATIGRAPHY  
AND METOSOMATIC ALTERATION IN THE MUSSELWHITE GOLD  
DEPOSIT, NORTH CARIBOU LAKE BELT, SUPERIOR PROVINCE,  
CANADA: IMPLICATIONS FOR DEPOSITION AND  
MINERALIZATION

By

Patrick C. Moran

Thesis  
submitted in partial fulfillment of the  
requirements for the Degree of  
Masters of Science in Geology



Lakehead University

July, 2008

© Copyright by Patrick C. Moran, 2008

# Lakehead

UNIVERSITY

OFFICE OF GRADUATE STUDIES

---

NAME OF STUDENT:

DEGREE AWARDED:

ACADEMIC UNIT:

TITLE OF THESIS:

This thesis has been prepared  
under my supervision  
and the candidate has complied  
with the Master's regulations.

---

Signature of Supervisor

---

Date

## **LICENSE TO THE UNIVERSITY**

In the interests of facilitating research by others at this Institution and elsewhere, and in consideration of my being accepted for enrolment as a graduate student at this Institution, I hereby grant license to Lakehead University to make copies of any original thesis or dissertation or substantial parts thereof, the copyright in which may vest in me, which I may submit to this Institution in the future, provided that this License is subject to the following conditions:

- Only single copies shall be made or authorized to be made at any one time, and only in response to a written request from the library of any university or similar institutions on its own behalf or on behalf of one of its users.
- This License shall continue for the full term of the copyright, or for so long as may be legally permitted.
- The University Copyright Notice shall appear on all copies made under the authority of this License.
- This License does not permit the sale of authorized copies at a profit, but does permit the collection by the institution or institutions concerned of charges covering actual costs.
- All copies made under the authority of this License shall bear a statement to the effect that the copy in question "is being made available in this form by the authority of the copyright owner solely for the purpose of private study and research and may not be copied or reproduced except as permitted by the copyright laws, without written authority from the copyright owner".
- The foregoing shall in no way preclude the granting by the author of a license to the National Library of Canada to reproduce the thesis or dissertation and to lend or to sell copies of the same. For this purpose it shall also be permissible for Lakehead University to submit the above mentioned thesis or dissertation to the National Library of Canada.

---

Signature of Student

Date

---

Signature of Witness

Date

## Acknowledgements

*This thesis, and all the work involved, is dedicated to my parents.*

An immense deal of gratitude is extended to Dr. Philip Fralick who, as head supervisor, watched over this thesis from start to finish and provided invaluable insight into both Archean and modern geological processes. Dr. Mary Louise Hill is deeply thanked for making available her deep and prophetic insight into structural and metamorphic processes, as well as providing support and strong encouragement to complete this thesis. Dr. Peter Hollings is thanked for his constructive criticism regarding geochemistry and tectonic setting.

Musselwhite Gold Mine and Goldcorp Ltd. are thanked for supporting this thesis financially, providing unconstrained access to the mine-site, and employing me over the past two summers. Above all I thank Chief Geologist Andrew Cheatle as well as senior exploration geologists John Biczok and Jim Edwards. Further thanks are forwarded to the entire geology/exploration department including Billy, Rohan, Shauna, Ruslan, Serena, Elizabeth, and Damian for providing me with their knowledge, guidance, and genuine support and interest with this project. If I become half the geologist these people are, I'll consider myself very fortunate. Also deserving thanks are Musselwhite employees Jason, Mark, Dwayne, Absalom, Nathan and Morris for helping me with finding, and moving, core at the core farm.

Anne Hammond deserves a great deal of recognition for dedicating countless hours processing thin-sections and geochemistry samples. I also thank her for training me on thin-section preparation, always lending a friendly ear, and providing plenty of tea and snacks whenever I stopped by. Dr. Patricia Gillies deserves a show appreciation for always offering thoughtful, friendly, and insightful advice.

Last but not least, I want to thank my parents, brother and sister for their constant support. I also want to thank my friends back in N.S. as well as those made during my time in Thunder Bay. I would never have been able to complete this thesis without Serena, Dan, Vicky, Christine, Ling Hong, and Tina, thank you all.



## Abstract

The Musselwhite gold deposit, 100% owned and operated by Goldcorp Inc., has cumulatively produced in excess of 2 million ounces since opening in 1997 and has a projected mine life through 2013. It is situated in the North Caribou Lake metavolcanic/metasedimentary belt in the central northwestern portion of Superior Province, approximately 430 km northwest of Thunder Bay, Ontario, Canada. The belt occurs along the contact between the North Caribou Terrane and the Island Lake Domain, with a large, crustal-scale deformation zone forming its eastern margin. The Musselwhite gold deposit is hosted by amphibolite facies metamorphic rocks dominated by banded iron formation (BIF). This study primarily focuses on the Northern Iron Formation (NIF) metasedimentary assemblage, host to the majority of gold mineralization at Musselwhite.

Stratigraphic and geochemical analyses suggest that the lithologies of the NIF assemblage were deposited on Mesoarchean mafic to ultramafic volcanic rocks forming the ocean floor. The NIF assemblage and another iron formation lower in the stratigraphy, the Southern Iron Formation (SIF), record hydrothermal regimes associated with, and interrupted by, eruptive volcanic activity. The stratigraphically lowest lithologies in the NIF assemblage, meta-argillite, quartz-grunerite BIF, and magnetite-dominant BIF, were deposited in deep, calm water, in association with venting hydrothermal fluids. These ancient chemical sediments are analogous in geochemistry to modern day deposits in places such as the Red Sea and the East Pacific Rise. Differing Eu contents between chert and magnetite layers indicate that rhythmically changing temperature variations drove the hydrothermal system, imparting the banded nature. The chemically pure chert and magnetite layers of the lower portion of the NIF assemblage contrast with silicate-dominant banded iron formation; the silicate-dominant BIF increases in frequency up stratigraphically. It represents a decreasing hydrothermal system and/or an increase in the rate of clastic sedimentation. Hornblende-garnet and biotite-garnet schists were formed by metamorphism of mudstones composed of eroded material. The sediment that formed the hornblende-garnet schist is the same sediment that comprises the siliciclastic component of the silicate-dominant NIF. Similarly the biotite-garnet schist represents a mudstone, but unlike the hornblende-garnet schist, it is primarily derived from intermediate to felsic volcanic rocks. Lastly the garnet-bearing quartzite represents metamorphosed sandstone eroded from the same intermediate to felsic igneous source rocks as the biotite-garnet schist. Just as there is an overall increase in clastic content upwards through the approximately 30 m thick sedimentary succession, there is also a change from more mafic-sourced debris to a more intermediate/felsic source.

The majority of samples collected from Musselwhite did not experience significant remobilization of typically immobile elements. This is indicated by the relatively linear geochemical ratios between the immobile elements ( $\text{Al}_2\text{O}_3$ ,  $\text{TiO}_2$ , Zr, U, Th, etc.). Even elements that are commonly more mobile ( $\text{K}_2\text{O}$ ,  $\text{Na}_2\text{O}$ , etc.) appear to have remained relatively immobile at Musselwhite. The only samples that show significant geochemical change are from shear zones. The gold mineralization is primarily associated with shear zones within the siliciclastic-rich, upper NIF assemblage, where pyrrhotite (possibly originally pyrite) replaced iron oxides and iron silicates. This indicates that the control on areas of gold mineralization was a combination of: 1) the presence of structural zones allowing gold-bearing fluids to move through the NIF, which could act as a geochemical trap for gold; and 2) structural conditions in the siliciclastic-rich NIF that favoured hydrothermal fluid involvement with this unit.

## Table of Contents

	Page
Title Page.....	i
Graduate Studies Permit of Completion.....	ii
License to the University.....	iii
Acknowledgements.....	iv
Abstract.....	v
Table of Contents.....	vi
List of Tables.....	x
List of Plates.....	xi
List of Figures.....	xii
List of Abbreviations.....	xvii
<b>Chapter 1: Introduction</b>	
1.1 Introduction.....	1
1.2 Purpose of the Study.....	6
1.3 Location and Access.....	6
1.4 Exploration History.....	7
1.5 Geologic Setting.....	9
1.6 Regional Geology.....	9
1.6.1 Agutua Arm Metavolcanic Assemblage.....	10
1.6.2 Keeyask Lake Metasedimentary Assemblage.....	11
1.6.3 Keeyask Lake Metavolcanic Assemblage.....	11
1.6.4 South Rim Metavolcanic Assemblage.....	12
1.6.5 North Rim Metavolcanic Assemblage.....	14
1.6.6 Eyapamikama Lake Metasedimentary Assemblage.....	18
1.6.7 Opapimiskan Lake Metavolcanic Assemblage.....	19
1.6.8 Forrester Lake Metavolcanic Assemblage.....	22
1.7 Metamorphism.....	23
1.8 Structural Geology.....	24
1.9 Local Geology.....	27
1.9.1 Lower Basalts.....	28
1.9.2 Southern Iron Formation Assemblage.....	28
1.9.3 Basement Volcanic Unit.....	28
1.9.4 Meta-Argillite Unit.....	32
1.9.5 Quartz-Gruenerite BIF.....	32
1.9.6 Northern Iron Formation Assemblage Oxide-Dominant BIF.....	33
1.9.7 Silicate-Dominant BIF.....	33
1.9.8 Hornblende-Garnet Schist.....	34
1.9.9 Biotite-Garnet Schist.....	35
1.9.10 Garnet-bearing quartzite.....	36
1.9.11 Bvol Mafic Meta-Volcanic Unit.....	37
1.9.12 Avol Felsic Meta-Volcanic Unit.....	37
1.10 Previous Research.....	38
1.11 Methods.....	39

<b>Chapter 2: Field Relations, unit definitions, and Stratigraphic Succession</b>	
2.1 Introduction.....	44
2.2 Detailed Stratigraphy of the NIF Assemblage.....	45
2.2.1 Lithologic Association One.....	47
2.2.2 Lithologic Association Two.....	52
2.2.3 Lithologic Association Three.....	52
2.2.4 Lithologic Association Four.....	57
2.2.5 Lithologic Association Five.....	58
2.3 Chapter Summary.....	61
 <b>Chapter 3: Physical Characteristics of the Lithologies</b>	
3.1 Introduction.....	63
3.2 SIF Assemblage Oxide-Dominant BIF.....	63
3.2.1 Macroscopic Character.....	63
3.2.2 Petrographic Character.....	66
3.2.3 Mineral Composition.....	69
3.2.4. Geochemical Composition.....	73
3.3 NIF Assemblage Meta-Argillite.....	76
3.3.1 Macroscopic Character.....	76
3.3.2 Petrographic Character.....	79
3.3.3 Mineral Composition.....	82
3.3.4. Geochemical Composition.....	86
3.4 NIF Assemblage Quartz-Grunerite BIF.....	89
3.4.1 Macroscopic Character.....	89
3.4.2 Petrographic Character.....	91
3.4.3. Geochemical Composition.....	97
3.5 NIF Assemblage Oxide-Dominant BIF.....	100
3.5.1 Macroscopic Character.....	100
3.5.2 Petrographic Character.....	103
3.5.3 Mineral Composition.....	107
3.5.4. Geochemical Composition.....	110
3.6 NIF Assemblage Silicate-Dominant BIF.....	115
3.6.1 Macroscopic Character.....	115
3.6.2 Petrographic Character.....	119
3.6.3 Mineral Composition.....	123
3.6.4. Geochemical Composition.....	127
3.7 Hornblende-Garnet Schist.....	132
3.7.1 Macroscopic Character.....	132
3.7.2 Petrographic Character.....	135
3.7.3 Mineral Composition.....	139
3.7.4. Geochemical Composition.....	143
3.8 Biotite-Garnet Schist.....	145
3.8.1 Macroscopic Character.....	145
3.8.2 Petrographic Character.....	148

	viii
3.8.3 Mineral Composition.....	151
3.8.4. Geochemical Composition.....	155
3.9 Garnet-bearing quartzite.....	157
3.9.1 Macroscopic Character.....	157
3.9.2 Petrographic Character.....	160
3.9.4. Geochemical Composition.....	163
3.10 Minor Lithologies.....	166
3.10.1 Introduction.....	166
3.10.2 Macroscopic Character.....	166
3.10.3 Petrographic Character.....	170
3.10.4. Geochemical Composition.....	175
<b>Chapter 4: Whole Rock Lithochemistry</b>	
4.1 Introduction.....	179
4.2 Element Mobility and Relationships.....	181
4.3 Chemical Versus Siliciclastic Detrital Protoliths: Geochemical trends.....	186
4.4 Tectonic Setting.....	209
4.5 Major Elements: General Characteristics.....	229
4.6 Rare Earth Elements: General Characteristics.....	236
4.7 Metasomatic Alteration.....	256
4.8 Alteration Dendrograms.....	264
<b>Chapter 5: Discussion</b>	
5.1 Introduction.....	269
5.2 Type of Iron Formation: Implications for Conditions of Deposition.....	269
5.3 Mine Lithology Protoliths and Stratigraphic Succession.....	285
5.4 Vectors to Mineralization.....	303
5.5 Comparison to Other BIF Hosted Orogenic Gold Deposits.....	321
5.5.1 Lupin Gold Mine.....	321
5.5.2 Meadowbank Gold Deposit.....	325
5.5.3 Ajjanahalli Gold Mine.....	326
5.5.4 Musselwhite Geochemistry Relative to Lupin, Meadowbank, and Ajjanahalli.....	328
<b>Chapter 6: Conclusions</b>	
Conclusions.....	337
<b>Appendices</b>	
A: Sample Descriptions and General Information.....	
B: Thin-Section List and Descriptions.....	
C: CIPW Normative Mineralogy (SEM-EDS Data).....	
D: Whole Rock Lithochemistry Data.....	



## List of Tables

ix

Table Number	Title	Page
1.1	Summary of Samples and Sample Information.....	42
1.2	Detection Limits.....	43
3.1	SIF Assemblage Oxide-Dominant BIF Mineral Chemistry.....	71
3.2	SIF Assemblage Oxide-Dominant Lithogeochemistry.....	74
3.3	NIF Assemblage Meta-Argillite Mineral Chemistry.....	85
3.4	NIF Assemblage Meta-Argillite Lithogeochemistry.....	88
3.5	NIF Assemblage Quartz-Grunerite BIF Lithogeochemistry.....	99
3.6	NIF Assemblage Oxide-Dominant BIF Mineral Chemistry.....	109
3.7	NIF Assemblage Oxide-Dominant Lithogeochemistry (Mag) .....	111
3.8	NIF Assemblage Oxide-Dominant Lithogeochemistry (Qtz).....	112
3.9	Silicate-Dominant BIF Mineral Chemistry.....	126
3.10	Silicate-Dominant BIF Lithogeochemistry.....	128
3.11	Hornblende-Garnet Schist Mineral Chemistry.....	142
3.12	Hornblende-Garnet Lithogeochemistry.....	144
3.13	Biotite-Garnet Schist Mineral Chemistry.....	154
3.14	Biotite-Garnet Schist Lithogeochemistry.....	156
3.15	Garnet-Bearing Quartzite Lithogeochemistry.....	165
3.16	Miscellaneous Lithologies Lithogeochemistry.....	176
4.1	Sample Groupings for Statistical Analysis.....	182
4.2	N-MORB normalizing values for Figure 4.10.....	226
4.3	C1 chondrite normalizing values from Taylor and McLennan (1985)...	237

**List of Plates**

x  
Page

Plate Number	Title	Page
1.1	Photographs of Musselwhite mine from past to present.....	8
1.2	Photographs of deformation features in the NRMV.....	16
2.1	Photographs of various lithologies from the NIF Assemblage.....	56
2.2	Photographs of various lithologies from the NIF Assemblage.....	60
3.1	Photographs of SIF Assemblage oxide-dominant BIF.....	65
3.2	Photomicrographs of SIF Assemblage oxide-dominant BIF.....	67
3.3	SEM backscatter electron micrographs of oxide-dominant BIF.....	70
3.4	Photographs of NIF Assemblage meta-argillite.....	77
3.5	Photomicrographs of NIF Assemblage meta-argillite.....	80
3.6	SEM backscatter electron micrographs of meta-argillite.....	84
3.7	Photographs of NIF Assemblage quartz-grunerite BIF.....	90
3.8	Photomicrographs of NIF Assemblage quartz-grunerite BIF.....	92
3.9	Photomicrographs of NIF Assemblage quartz-grunerite BIF.....	93
3.10	Photographs of NIF Assemblage oxide-dominant BIF.....	101
3.11	Photomicrographs of NIF Assemblage oxide-dominant BIF.....	104
3.12	SEM backscatter electron micrographs of oxide-dominant BIF.....	108
3.13	Photographs of silicate-dominant BIF.....	116
3.14	Photomicrographs of silicate-dominant BIF.....	120
3.15	SEM backscatter electron micrographs of silicate-dominant BIF.....	125
3.16	Photographs of hornblende-garnet schist.....	133
3.17	Photomicrographs of hornblende-garnet schist.....	137
3.18	Photomicrographs of hornblende-garnet schist.....	140
3.19	SEM backscatter electron micrographs of hornblende-garnet schist.....	141
3.20	Photographs of biotite-garnet schist.....	146
3.21	Photomicrographs of biotite-garnet schist.....	149
3.22	SEM backscatter electron micrographs of biotite-garnet schist.....	153
3.23	Photographs of garnet-bearing quartzite.....	158
3.24	Photomicrographs of garnet-bearing quartzite.....	161
3.25	Photographs of miscellaneous lithologies.....	167
3.26	Photomicrographs of miscellaneous lithologies.....	171

## List of Figures

Figure Number	Title	Page
1.1	Map of the Superior province.....	2
1.2	Map of the North Caribou Superterrane.....	3
1.3	Simplified geologic map of the NCLB.....	4
1.4	Map of the Musselwhite Mine site.....	5
1.5	Metamorphic isogrades of the northern NCLB.....	13
1.6	Structure of the NCLB.....	15
1.7	Total magnetic field intensity map of the NCLB.....	21
1.8	Map of trench 4 and 5 sample locations.....	25
1.9	Generalized stratigraphy of the Musselwhite Gold Deposit.....	29
1.10	Generalized stratigraphy of the Northern Iron Formation.....	30
1.11	Simplified cross section of mine stratigraphy.....	31
2.1	Detailed log of hole 04-ESN-010.....	46
2.2	Detailed log of hole 05-PQE-012.....	48
	Detailed log of hole 05-PQE-012 continued.....	49
2.3	Detailed log of hole 05-PQE-013.....	50
	Detailed log of hole 05-PQE-013 continued.....	51
2.4	Detailed log of hole 06-S2E-002.....	53
	Detailed log of hole 06-S2E-002 continued.....	54
4.1	Dendrograms For Samples From The Current Study.....	180
4.2	Comparison dendrogram from Peter (2003).....	183
4.3a/b	Ternary diagrams showing hydrothermal and non-hydrothermal.....	187/
	sediment fields (Boström, 1973) (exhalite/siliciclastic respectively)	188
4.4	Exhalative versus siliciclastic detrital sediments diagram (Boström, 1973).....	193
4.5 a	Average MnO values for the various lithologies.....	197
4.5 b	Average Zr values for the various lithologies.....	197
4.6 a	Average Fe <sub>2</sub> O <sub>3</sub> <sup>T</sup> (wt.%) values for the various lithologies.....	199
4.6b	Average MnO/Fe <sub>2</sub> O <sub>3</sub> <sup>T</sup> values for the various lithologies.....	199
4.7a/b	Al <sub>2</sub> O <sub>3</sub> vs. Zr plot for exhalite and siliciclastic dominated lithologies, respectively.....	201
4.7c/d	Al <sub>2</sub> O <sub>3</sub> vs. TiO <sub>2</sub> plot for exhalite and siliciclastic dominated lithologies, respectively.....	201
4.7e/f	U vs. Th plot for exhalite and siliciclastic dominated lithologies, respectively.....	201
4.8a/b	Ternary discrimination diagram based on relative molecular proportions of Al <sub>2</sub> O <sub>3</sub> -Na <sub>2</sub> O+CaO-K <sub>2</sub> O, for exhalite and siliciclastic dominated lithologies, respectively.....	207
4.9a/b	Log Nb/Y vs. Log Zr/(TiO <sub>2</sub> *0.001) for exhalite and siliciclastic dominated lithologies respectively, .....	212
4.9c/d	Log Zr/(TiO <sub>2</sub> *0.001) vs. SiO <sub>2</sub> for exhalite and siliciclastic dominated Lithologies, respectively.....	212

4.9e/f	Y vs. Zr for exhalite and siliciclastic dominated lithologies, respectively.....	212
4.9g/h	SiO <sub>2</sub> vs. Na <sub>2</sub> O+K <sub>2</sub> O for exhalite and siliciclastic dominated lithologies, respectively.....	212
4.10a/b	(K <sub>2</sub> O/(K <sub>2</sub> O+Na <sub>2</sub> O)) *100 vs. K <sub>2</sub> O+Na <sub>2</sub> O for exhalite and siliciclastic dominated lithologies respectively, modified after .....	215
4.10c/d	Zr vs. Ti for exhalite and siliciclastic dominated lithologies, respectively.....	215
4.10e/f	Log Zr vs. Log Zr/Y for exhalite and siliciclastic dominated Lithologies, respectively.....	215
4.10g/h	Ti/1000 vs. V for exhalite and siliciclastic dominated lithologies, respectively.....	215
4.11a/b	La-Th-Sc ternary discrimination diagrams for exhalite- and siliciclastic-dominated lithologies, respectively.....	218
4.11c/d	Th-Co-Zr/10 ternary discrimination diagrams for exhalite and siliciclastic dominated lithologies, respectively.....	218
4.11e/f	Th-Sc-Zr/10 ternary discrimination diagrams for exhalite and siliciclastic dominated lithologies, respectively.....	218
4.12a/b	Binary plot of V/Zr versus Ni/Al <sub>2</sub> O <sub>3</sub> modified for exhalite and siliciclastic dominated lithologies, respectively.....	221
4.13a/b	Binary plot of Th/Sc versus Zr/Sc for exhalite and siliciclastic dominated lithologies, respectively.....	223
4.14a/b	Th-Hf-Co ternary diagram, for exhalite and siliciclastic dominated lithologies, respectively.....	225
4.14c/d	Ti/Zr vs. La/Sc plot, for exhalite and siliciclastic dominated lithologies, respectively.....	225
4.14e/f	K <sub>2</sub> O vs. Rb diagram, for exhalite and siliciclastic dominated lithologies, respectively.....	225
4.15a/b	Incompatible-element spider diagrams, a) Average normalized mafic and intermediate volcanic rock values plotted against Island Arc Tholeiitic Basalt, b) Average normalized mafic and intermediate volcanic rock values plotted against Continental Arc Calc-Alkaline.....	227
4.15c/d	Incompatible-element spider diagrams, c) Average normalized mafic and intermediate volcanic rock values plotted against Island Arc high K calc-alkaline basalt, d) Average normalized mafic and intermediate volcanic rock values plotted against within plate basalt.....	227
4.15e/f	Incompatible-element spider diagrams, e) Average normalized metasediment rock values plotted against island arc tholeiitic basalt, f) Average normalized metasediment rock values plotted against continental arc calc-alkaline basalt.....	227
4.15g/h	Incompatible-element spider diagrams, g) Average normalized metasediment rock values plotted against island arc high K calc-alkaline basalt, h) Average normalized metasediment rock values plotted against within plate basalt.....	227
4.16a/b	Fe <sub>2</sub> O <sub>3</sub> vs. SiO <sub>2</sub> for exhalite and siliciclastic dominated lithologies respectively.....	230

4.16c/d	FeO/Fe <sub>2</sub> O <sub>3</sub> vs. Fe <sub>2</sub> O <sub>3</sub> for exhalite and siliciclastic dominated lithologies, respectively.....	230
4.16e/f	MnO vs. Zr for exhalite and siliciclastic dominated lithologies, respectively.....	230
4.17a/b	U vs. Zr for exhalite and siliciclastic dominated lithologies, respectively.....	235
4.17c/d	Total REE vs. Zr for exhalite and siliciclastic dominated lithologies, respectively.....	235
4.17e/f	Total REE vs. Al <sub>2</sub> O <sub>3</sub> for exhalite and siliciclastic dominated lithologies, respectively.....	235
4.18a/b	C1 normalized REE spider diagrams: magnetite and quartz samples (respectively) from the SIF assemblage oxide-dominant BIF.....	238
4.18c/d	C1 normalized REE spider diagrams: metargillite samples and quartz-grunerite BIF samples respectively.....	238
4.18e/f	C1 normalized REE spider diagrams: magnetite and quartz samples from the NIF assemblage oxide-predominant BIF, respectively.....	238
4.18g/h	C1 normalized REE spider diagrams: magnetite and quartz samples from the NIF assemblage oxide-predominant BIF from trenches.....	238
4.19a/b	C1 normalized REE spider diagrams: Metasomatic SIF assemblage oxide-dominant BIF (trenches) and silicate-dominant BIF samples, respectively.....	243
4.19c/d	C1 normalized REE spider diagrams: biotite-garnet schist plotted with mafic metavolcanic samples and hornblende-garnet schist samples, respectively.....	243
4.19e/f	C1 normalized REE spider diagrams; e) garnet-bearing quartzite and felsic metavolcanic samples (drill core); f) biotite-garnet schist and biotite-garnet alteration samples plotted together (drill core).....	243
4.19g/h	C1 normalized REE spider diagrams: chlorite-schist samples and ultramafic metavolcanic sample, respectively.....	243
4.20a/b	Binary diagrams of Eu anomaly (y-axis) vs. Ce anomaly (x-axis): magnetite and quartz samples (respectively) from the SIF assemblage oxide-dominant BIF.....	247
4.20c/d	Binary diagrams of Eu anomaly (y-axis) vs. Ce anomaly (x-axis): metargillite samples and quartz-grunerite BIF samples, respectively.....	247
4.20e/f	Binary diagrams of Eu anomaly (y-axis) vs. Ce anomaly (x-axis): magnetite and quartz samples from the NIF assemblage oxide-predominant BIF, respectively.....	247
4.20g/h	Binary diagrams of Eu anomaly (y-axis) vs. Ce anomaly (x-axis):	

	magnetite and quartz samples from the SIF assemblage oxide-predominant BIF from trenches.....	247
4.21a/b	Binary diagrams of Eu anomaly (y-axis) vs. Ce anomaly (x-axis): Metasomatic NIF assemblage oxide-dominant BIF (trenches) and silicate-dominant BIF samples, respectively.....	248
4.21c/d	Binary diagrams of Eu anomaly (y-axis) vs. Ce anomaly (x-axis): Biotite-garnet schist plotted with mafic metavolcanic samples and Hornblende-garnet schist samples, respectively.....	248
4.21e/f	Binary diagrams of Eu anomaly (y-axis) vs. Ce anomaly (x-axis): garnet-bearing quartzite and felsic metavolcanic samples (drill core), f) biotite-garnet schist and biotite-garnet alteration samples plotted together (drill core).....	248
4.21g/h	Binary diagrams of Eu anomaly (y-axis) vs. Ce anomaly (x-axis): Chlorite-schist samples and ultramafic metavolcanic sample, respectively.....	248
4.22a/b	Ce/Ce* (Ce anomaly) vs. Pr/Pr* (Pr anomaly) for exhalite and siliciclastic dominated lithologies, respectively.....	253
4.22c/d	Fe <sub>2</sub> O <sub>3</sub> <sup>T</sup> vs. Eu/Eu* (Eu anomaly) for exhalite and siliciclastic dominated lithologies, respectively.....	254
4.22e/f	FeO vs. Eu/Eu* (Eu anomaly) for exhalite and siliciclastic dominated lithologies, respectively.....	254
4.22g/h	Fe <sub>2</sub> O <sub>3</sub> vs. Eu/Eu* (Eu anomaly) for exhalite and siliciclastic dominated lithologies, respectively.....	254
4.23a/b	Zn vs. Eu/Eu* (Eu anomaly) for exhalite and siliciclastic dominated lithologies, respectively.....	255
4.23c/d	C1 normalized La vs. Eu/Eu* (Eu anomaly) for exhalite and siliciclastic dominated lithologies, respectively.....	255
4.23e/f	Fe/Ti vs. Eu/Eu* (Eu anomaly) for exhalite and siliciclastic dominated lithologies, respectively.....	255
4.24a/b	Histograms displaying the ((Cs+Rb)/Th) <sub>N</sub> values for individual samples, a) Exhalite dominant lithologies, b) siliciclastic dominant lithologies.....	259
4.25a/b	((Cs+Rb)/Th) <sub>N</sub> vs. Se for exhalite and siliciclastic dominated lithologies, respectively.....	261
4.25c/d	((Cs+Rb)/Th) <sub>N</sub> vs. K <sub>2</sub> O for exhalite and siliciclastic dominated lithologies, respectively.....	261
4.25e/f	((Cs+Rb)/Th) <sub>N</sub> vs. As for exhalite and siliciclastic dominated lithologies, respectively.....	261
4.25g/h	((Cs+Rb)/Th) <sub>N</sub> vs. Au for exhalite and siliciclastic dominated lithologies, respectively.....	261

4.26a/b	Cs vs. K <sub>2</sub> O for exhalite and siliciclastic dominated lithologies, respectively.....	263
4.26c/d	Cs vs. Rb for exhalite and siliciclastic dominated lithologies, respectively.....	263
4.26e/f	Na <sub>2</sub> O vs. Cs for exhalite and siliciclastic dominated lithologies, respectively.....	263
4.26g/h	Cs vs. CaO for exhalite and siliciclastic dominated lithologies, respectively.....	263
4.27	Dendrogram showing the relationship of all samples with Au value.....	265
4.28	Dendrogram showing the relationship of all samples.....	268
5.1a/b	FeO/Fe <sub>2</sub> O <sub>3</sub> vs. Fe <sub>2</sub> O <sub>3</sub> (total) for exhalite and siliciclastic dominated lithologies, respectively.....	271/ 272
5.2	Schematic Diagram of Different Types of BIF and the Environments they form in.....	273
5.3	Detailed stratigraphic log of drill hole 05-PQE-012.....	275
5.4a/b	Log Nb/Y vs. Log Zr/(TiO <sub>2</sub> *0.001) for volcanic samples.....	276
5.4c/d	Ti/1000 vs. V for volcanic samples.....	276
5.4e/f	Binary plot of Th/Sc versus Zr/Sc for exhalite- and siliciclastic-dominant lithologies, respectively.....	276
5.5	Schematic diagram of the formation of Algoma-type iron formation.....	278
5.6a	REE curves for modern seawater, mound and metalliferous sediment, as well as black and white smoker hydrothermal fluids.....	280
5.6b	REE curves for Brunswick belt iron formation.....	280
5.6c	REE curves for Windy Craggy deposit iron formation.....	280
5.6d	REE curves for NIF assemblage oxide-dominant BIF (magnetite) samples.....	280
5.6e	North American shale composite (NASC) REE curve.....	280
5.6f	Meta-argillite REE curves .....	280
5.6g	Silicate-dominant REE curves.....	280
5.6h	Biotite-garnet schist REE curves.....	280
5.7	Schematic diagram of zoned IF.....	281
5.8a/b	Exhalative Versus Siliciclastic detrital sediments diagram.....	283
5.9	Ternary discrimination diagram based on relative molecular proportions of Al <sub>2</sub> O <sub>3</sub> -Na <sub>2</sub> O+CaO-K <sub>2</sub> O for exhalite and siliciclastic dominated lithologies respectively.....	284
5.10	Schematic representation of the evolution of the Musselwhite stratigraphy showing the SIF and NIF assemblages.....	284
5.11a/b	Schematic diagrams related to the formation of Algoma-type iron formation.....	288
5.12a-h	C1 normalized REE spider diagrams.....	293
5.13a/b	Log Nb/Y vs. Log Zr/(TiO <sub>2</sub> *0.001) for volcanic and siliciclastic samples, respectively.....	296
5.13c/d	Log Zr/(TiO <sub>2</sub> *0.001) vs. SiO <sub>2</sub> for volcanic and siliciclastic samples, respectively.....	296
5.13e/f	Y vs. Zr for for volcanic and siliciclastic samples, respectively.....	296

5.13g/h	V/Zr vs. Ni/Al <sub>2</sub> O <sub>3</sub> for volcanic and siliciclastic samples, respectively.....	296
5.14	Detailed stratigraphic log of drill hole 04-ESN-010.....	298
5.15a	Al <sub>2</sub> O <sub>3</sub> vs. Zr plot, siliciclastic dominated lithologies.....	302
5.15b	Al <sub>2</sub> O <sub>3</sub> vs. TiO <sub>2</sub> plot, siliciclastic dominated lithologies.....	302
5.15c	Zr vs. TiO <sub>2</sub> plot, siliciclastic dominated lithologies.....	302
5.15d	U vs. Th plot, siliciclastic dominated lithologies.....	302
5.16	Histograms displaying the ((Cs+Rb)/Th) <sub>N</sub> values for individual samples; a) exhalite-dominant samples, b) siliciclastic dominant samples, c) mafic volcanic samples.....	304
5.17a-d	Binary plots displaying ((Cs+Rb)/Th) <sub>N</sub> as the x-variant versus various elements associated with gold mineralization (as the y-variant).....	307
5.18a-d	Binary plots of Cs vs. various elements associated with metasomatic alteration.....	310
5.19a-b	Dendrograms For Samples From the current study.....	312
5.20	Dendrogram showing the relationship of all samples with Au value.....	314
5.21	Dendrogram showing the relationship of all samples.....	318
5.22a-b	Al-Fe-Mn diagrams comparing Musselwhite samples to Meadowbank and Ajjanahalli samples.....	329
5.23a-b	Exhalative versus siliciclastic detrital sediments diagram comparing Musselwhite samples to Meadowbank and Ajjanahalli samples.....	332
5.24a-b	C1 normalized REE spider diagrams for; a) Meadowbank samples, b) Ajjanahalli samples.....	333
5.25a-c	Histograms displaying the ((Cs+Rb)/Th) <sub>N</sub> values for Musselwhite samples compared to Meadowbank and Ajjanahalli samples.....	334
5.26a-h	Binary plots displaying ((Cs+Rb)/Th) <sub>N</sub> as the x-variant versus various elements associated with gold mineralization (as the y-variant).....	335
5.27a-h	Binary plots of Cs versus various elements associated with metasomatic alteration.....	336



## Abbreviations

### **Regional Geology**

NCLB	North Caribou Lake Metavolcanic / Metasedimentary Belt
AAMV	Agutua Arm Metavolcanic Assemblage
AAMS	Agutua Arm Metasedimentary Assemblage
KLMV	Keeyask Lake Metavolcanic Assemblage
KLMS	Keeyask Lake Metasedimentary Assemblage
NRMV	North Rim Metavolcanic Assemblage
SRMV	South Rim Metavolcanic Assemblage
OLMV	Opapimiskan Lake Metavolcanic Assemblage
FLMV	Forrester Lake Metavolcanic Assemblage
LLMV	Lundmark Lake Metavolcanic Assemblage
ELMS	Eyapamikama Lake Metasedimentary Assemblage
TTG	Tonalite-Trondjemite-Granodiorite

### **Mine-Scale Geology**

NIF	Northern Iron Formation
SIF	Southern Iron Formation
4h	Meta-Argillite (mine terminology)
4a	(mine terminology) Quartz-Grunerite Banded Iron Formation
4b	(mine terminology) Oxide-Dominant Banded Iron Formation
4ea	(mine terminology) Silicate-Dominant Banded Iron Formation
4e	(mine terminology) Hornblende-Garnet Schist
4f	(mine terminology) Biotite-Garnet Schist
6	(mine terminology) Garnet-bearing quartzite
2	(mine terminology) Mafic Metavolcanic
2t	(mine terminology) Intermediate Metavolcanic

### **Analytical Terms**

SEM	Scanning Electron Microscope
ICP-MS	Inductively Coupled Plasma-Mass Spectroscopy
PPM	Parts Per Million
PPB	Parts Per Billion
PM05-	Samples Collected in Fall 2005
PM06-	Samples Collected in March 2006
07-20-0	Samples Collected Over the Summer 2007
°C	Degree Celsius
%	Per Cent
<	Less Than
>	Greater Than
δ	Delta
σ	Sigma
µm	Micrometer

**Analytical Terms Continued...**

C1	C1 Chondrite Normalizing value
cm	Centimeter
g	Gram
Kbars	Kilobars
kg	Kilogram
Km	Kilometer
m	Meter
Ma	Million Years
mm	Millimeter
N	North
NASC	North American Shale Composite
n	Normalized
OGS	Ontario Geological Survey
Ppl	Plain Polarized Light
REE	Rare Earth Element
S1,2,3	Different Foliation Events
UG	Underground Sample
vs.	Versus
Xpl	Crossed Polarized Light

**Minerals**

Po	Pyrrhotite		
Qtz	Quartz	Ccp	Chalcopyrite
Bt	Biotite	Chl	Chlorite
Garn	Garnet (Almandine)	Cpx	Clinopyroxene
Gru	Grunerite	Fe-Dol	Iron-rich Dolomite
Hbl	Hornblende	Fe-Cal	Iron-rich Calcite
Cord	Cordierite	Ilm	Ilmenite
Staur	Staurolite	Kfs	Potassium-Feldspar
Silm	Sillimanite	Mag	Magnetite
Cal	Calcite	Ms	Muscovite
Ser	Sericite	Pl	Plagioclase
Fgr	Fine-grained		
Mgr	Medium-grained	Cgr	Coarse-grained

# Chapter 1

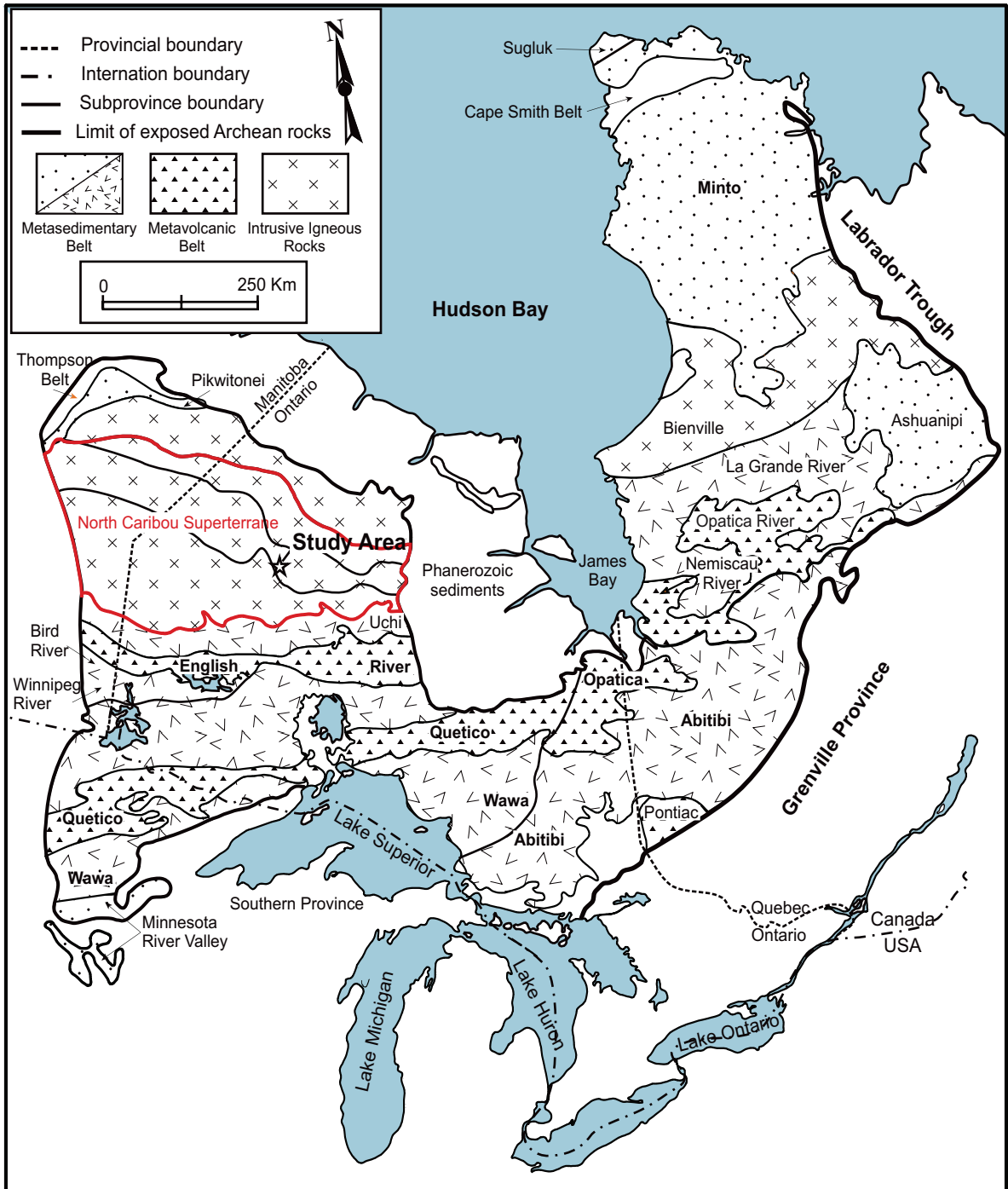
## Introduction

### 1.1 Introduction

The Musselwhite gold deposit, first described by Hall and Rigg (1986), is located roughly one hundred and twenty kilometres northwest of the town of Pickle Lake, in Ontario, Canada. Geologically, Musselwhite is situated in the North Caribou Lake metavolcanic metasedimentary belt (NCLB) in the central northwest portion of the Superior Province (Fig. 1.1). The NCLB occurs along the contact between the North Caribou Terrane and the Island Lake Domain, the two components which comprise the North Caribou Superterrane (Rayner and Stott, 2005) (Fig. 1.2).

The reader should note that the study area falls within the bounds of the North Caribou Lake Metasedimentary/Metavolcanic Belt (Fig. 1.3). The Musselwhite gold deposit is hosted by silicate- and oxide-dominant iron formations which were metamorphosed to amphibolite facies during an orogenic event. Therefore, previous workers (Otto, 2002; Hill *et al.*, 2006) interpret Musselwhite to be a BIF- hosted orogenic gold deposit.

Extensive interpretation of mine-scale stratigraphy has been carried out by the Musselwhite exploration and geology departments, as well as by a number of contracted scientists, resulting in information on lithologies, structures, and occurrence of gold (Hall and Rigg, 1986; Klipfel, 2002a and b). Gold is primarily associated with pyrrhotite-almandine-chlorite-quartz and is disseminated in nature. In the main orebody mineralization is confined to several narrow sub-vertical shear zones (Andrew Cheatle, personal communication, 2007) (Fig. 1.4). In the West Anticline area mineralization patterns are more variable (Fig. 1.4). A relatively small amount of academic study has been completed on the Musselwhite gold deposit and its surrounding geology (Hollings and Kerrich, 1999; Otto, 2002; Hill *et al.*, 2006).



**Figure 1.1.** Map of the Superior Province, modified after Card and Ciesielski (1986) as well as Rayner and Stott (2005), showing terrane subdivisions. Notice location of study area, denoted by the white-star, in roughly the middle of the North Caribou Superterrane (Fig. 1.2).







## 1.2 Purpose of the study

The objectives of this study were to:

1. Describe both major and minor lithologies in the Northern and Southern Iron Formation assemblages (macroscopic appearance, geochemistry, petrography, and mineral chemistry).
2. Establish sedimentary facies changes using the geochemistry and stratigraphic logs.
3. Develop a depositional model for the sedimentary succession at Musselwhite gold mine.
4. Quantify the geochemistry of the metasedimentary units, developing a model for the development of the geochemistry of the sedimentary strata from deposition through to their present day composition including the metasomatic alteration history, using petrography, SEM examination of mineral chemistry, and litho-geochemistry.
5. Investigate the environment of deposition (i.e. tectonic setting) by tying together the regional geology of the NCLB and the results of objectives one and two
6. Investigate the similarities between the Musselwhite gold deposit and other well known banded iron formation hosted gold deposits.
7. If possible, identify vectors for gold mineralization based on whole rock geochemistry.

## 1.3 Location and access

The Musselwhite gold deposit is located at 52° 35' N and 90° 22' W, approximately 430 kilometres northwest of the city of Thunder Bay, and 120 kilometres north of the town of Pickle Lake, in Ontario Canada. Nearby First Nations communities include Kingfisher Lake (Shibogama First Nations), Round Lake (Windigo First Nations), Wunnumin Lake (Shibogama First Nations), Mishkeegogamang (Independent), and Cat Lake (Windigo First Nations) (Blower and Kiernan, 2003). The gold deposit is located in the Patricia mining district (NTS 53B/9). Road access, from Thunder Bay is by highway 17 (Trans-

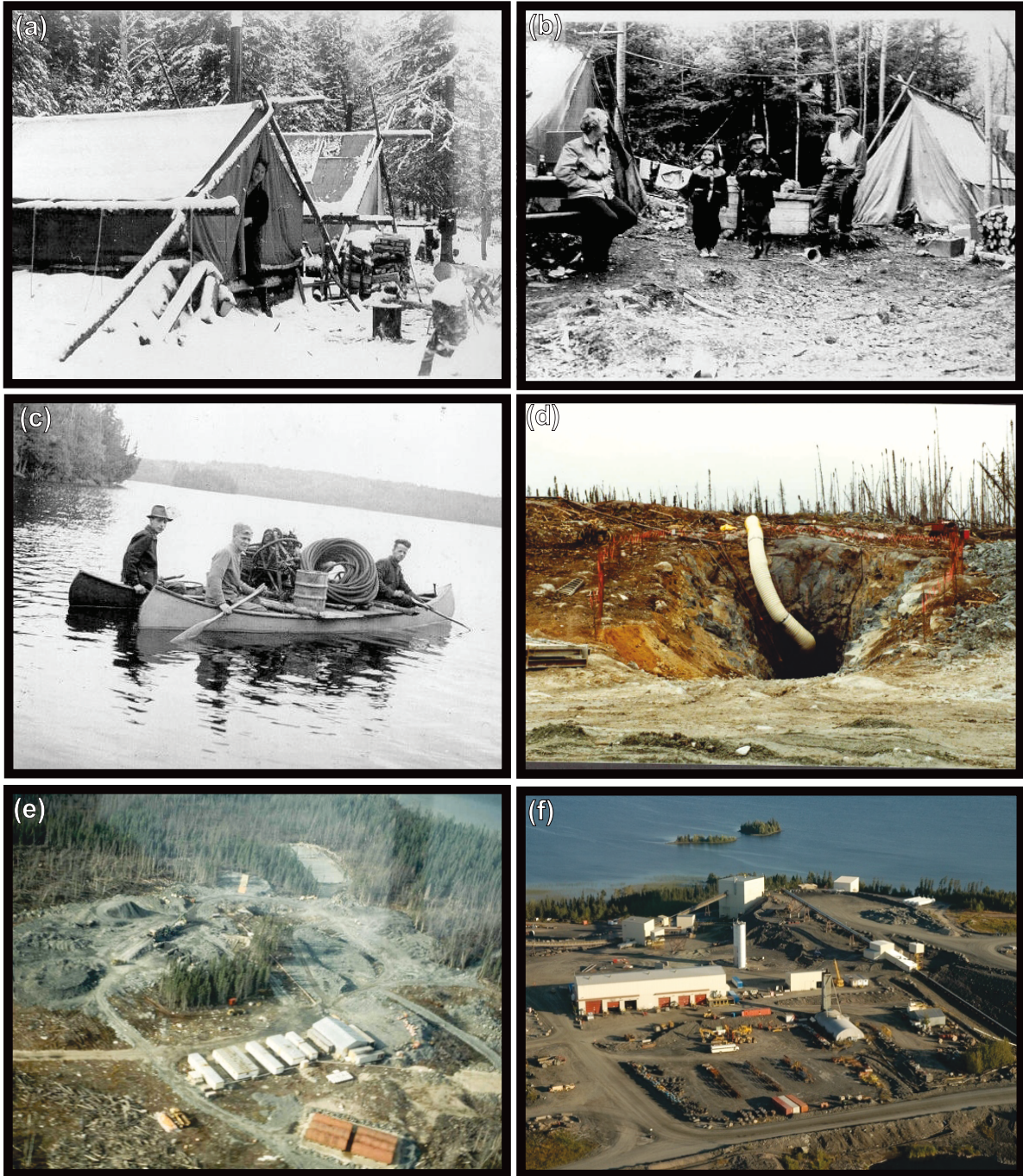


Canada) to Ignace, Highway 599 from Ignace to Pickle Lake, and highway 808 from Pickle Lake to the Musselwhite Mine-site. There is a 1500 m gravel airstrip at the mine and transportation of personnel to and from the site is primarily by air.

#### 1.4 Exploration history

The Musselwhite gold deposit was discovered in the early 1960s (Plate 1.1a, b). The original discovery was made in 1962 by Kenpat Mines Ltd. operated by Harold and Alan Musselwhite (Fig 1.4, 'Kenpat rectangle' on north shore of Opapimiskan Lake). It consisted of visible gold found in a quartz vein (Kenpat vein). The Musselwhite brothers (Plate 1.1c) discovered gold through panning regolith on the south shore of Opapimiskan Lake, near an outcrop of iron formation. The brothers did much of the early work on the property, such as extensive drilling in the West Anticline area (Fig. 1.4) (Blower and Kiernan, 2003). They then optioned the property to a syndicate of mining companies.

In 1973 the ten companies involved with the property consolidated to form the Musselwhite Grubstake and from 1973 to 1984 executed a series of exploration projects with the intention of identifying the source of the anomalous gold in the area. In the fall of 1983 a winter road connecting Opapimiskan Lake to highway 808 was constructed in order to allow underground bulk sampling of the West Anticline Zone (Fig. 1.4; Plate 1.1d). This bulk sampling was completed in 1989 with results indicating it was not economically feasible to build a mine in that location. This disappointing development was offset by drilling, over 1986-1987, which identified gold mineralization in the T-antiform Zone of the East Bay area of Opapimiskan Lake several kilometres away from the initial discovery (Plate 1.1e). In 1994 underground exploration of the T-Antiform commenced and surface diamond drilling began delineating the PQ zone (Fig. 1.4). Between 1994 and 1995 the winter road was converted to an all weather road, an exploration shaft was sunk, and excavation of the portal began. In 1996, upon completion of a feasibility study, the Musselwhite Joint Venture put the property into production beginning with open pit mining of the OP Zone and underground development of the T-Antiform Zone. On March 10<sup>th</sup> 1997 the first gold bar was poured. On April 1<sup>st</sup> 1997 the mine officially entered commercial production.



**Plate 1.1. Various photographs showing Musselwhite from past to present times.** (a) Early exploration camp on the Musselwhite property (photo courtesy of Musselwhite mine), (b) Early exploration camp on the Musselwhite property (photo courtesy of Musselwhite mine), (c) Musselwhite brothers in canoe loaded with equipment (photo courtesy of Musselwhite mine), (d) Original underground exploration portal for bulk sampling in the West Anticline area (photo courtesy of Musselwhite mine), (e) Photo of the exploration camp in the East Bay area, 1980s (photo courtesy of Musselwhite mine), (f) Photograph, from above, of the current workings at Musselwhite mine taken by the author.

Musselwhite gold mine (Plate 1.1f) is primarily an underground operation 100% owned and operated by Goldcorp Inc. Mine life is projected through 2013 based on presently delineated mineral reserves ([www.goldcorp.com/operations/Musselwhite](http://www.goldcorp.com/operations/Musselwhite) [June 2008]). In 2006 exploration on the mine property branched out with a 2,430 metre mother hole and two daughter holes on the North Shore of Opapimiskan Lake ([www.goldcorp.com/operations/Musselwhite](http://www.goldcorp.com/operations/Musselwhite) [June 2008]). Exploration is focused on drilling off the PQ Deeps resources and converting the existing inferred mineral resources to mineral reserves. In 2007 the West Anticline area was under renewed focus of the exploration department for possible open pit development. Presently cumulative mine production exceeds two million ounces of gold ([www.goldcorp.com/operations/Musselwhite](http://www.goldcorp.com/operations/Musselwhite) [June 2008]).

### 1.5 Geological setting

The North Caribou Lake metavolcanic-metasedimentary belt is located along the contact between the North Caribou Terrane and the Island Lake Domain, which together comprise the North Caribou Superterrane of the Superior Province of Canada (Fig. 1.2; Rayner and Stott, 2005). The North Caribou Superterrane and its components were formerly known as the Sachigo Subprovince (Card and Ciesielski, 1986; Rayner and Stott, 2005). Subdivision of the North Caribou Superterrane into tectonic domains and terranes was brought about through recent LITHOPROBE and Natmap studies (Rayner and Stott, 2005). Additional Sm-Nd isotopic analysis and U/Pb zircon dating (deKemp, 1987; Davis and Stott, 2001) completed along the Ontario-Manitoba border has further enabled authors to subdivide the far northern portion of the North Caribou Superterrane (Stone, 2005).

### 1.6 Regional geology

The NCLB was first mapped by Satterly (1941) at a scale of one inch to one mile. Subsequently the belt was mapped at reconnaissance scale by Emslie (1962), Thurston *et al.* (1979), Andrew *et al.* (1981), and Breaks *et al.* (2001). The Ontario Department of

Mines, predecessor to the Ontario Geological Survey, completed an airborne magnetic survey over the belt at one inch to one mile in 1960.

The ~3 Ga belt is composed of metavolcanic and metasedimentary lithotectonic assemblages (Fig. 1.1) juxtaposed against extensive gneissic and plutonic rocks (Breaks *et al.*, 2001). This belt, along with several others, comprise the core of the North Caribou Superterrane, which is interpreted by Thurston *et al.* (1991) to have formed the core of the Superior Province with accretion of other terranes occurring both from the north and the south. Other significant belts in the North Caribou Superterrane include parts of the Red Lake and Uchi greenstone belts. The NCLB was fully amalgamated by 2.87 Ga, based on U/Pb age dates of the surrounding rocks (Schade Lake gneissic complex and intrusive igneous rocks; Breaks *et al.*, 2001).

The North Caribou Lake metavolcanic-metasedimentary belt is comprised of eight lithotectonic supracrustal assemblages formed over two periods of volcanism and sedimentation between  $2981 \pm 1.8$  and  $2932 \pm 3$  Ma (deKemp, 1987). However, there is still debate over the validity of these subdivisions. The basement to the North Caribou Lake metavolcanic-metasedimentary belt is not known; however, due to the presence of the Weagamow batholith (U/Pb zircon  $2990 \pm 2$  Ma; deKemp 1987), which is tonalitic in nature, and the Schade Lake Gneissic Complex, the basement is possibly sialic in nature. The eight assemblages of the greenstone belt are described below.

#### *1.6.1 Agutua Arm Metavolcanic Assemblage*

The Agutua Arm Metavolcanic Assemblage (AAMV) (Fig. 1.1) is interpreted by Breaks *et al.* (2001) as the stratigraphically lowest assemblage in the NCLB and therefore the oldest volcanic assemblage in the belt. This is supported by deKemp's (1987) U/Pb zircon age determination of  $2981 \pm 2$  Ma for a felsic flow in the AAMV. The rocks of this assemblage likely acted as a substrate for the successive assemblages within the belt. The Round Lake and Weagamow batholiths (tonalite-granodiorite) are in intrusive contact with the Agutua Arm metavolcanic assemblage. The Weagamow batholith ( $2990 \pm 1$  Ma) slightly predates the felsic metavolcanic rocks in the AAMV assemblage. Breaks

*et al.* (2001) propose that the AAMV and the Weagamow batholith are close enough in age to assume they are the same igneous event.

The AAMV assemblage consists of different mafic tholeiitic and felsic metavolcanic flows unconformably overlain by the Keeyask Lake metasedimentary assemblage (KLMS). The relative relationship of the South Rim (SRMV) and North Rim (NRMV) metavolcanic assemblages to the AAMV are unknown, as the SRMV is in faulted contact with the AAMV and the NRMV is spatially separated from the AAMV.

### *1.6.2 Keeyask Lake Metasedimentary Assemblage*

The Keeyask Lake Metasedimentary Assemblage (KLMS) is roughly 20 m thick and has a strike length of 3.5 km. It is predominantly composed of metamorphosed mudstone, quartz-arenite, and banded iron formation (Breaks *et al.*, 2001). Additional, but minor, lithologies include plagioclase arkosic arenite, quartz wacke and chert. This assemblage together with the Agutua Arm Metavolcanic Assemblage was interpreted as being deposited on a stable shelf platform as a volcano-sedimentary mound (Groves and Batt, 1984). Breccias of thickly laminated dolomitic meta-sedimentary rock are found at the top of the sedimentary succession and lie directly below the komatiitic metavolcanic rocks of the Keeyask Lake Metavolcanic Assemblage. The breccia is interpreted to have formed due to seismic activity associated with the beginning of rifting that led to the formation of the Keeyask Lake Metavolcanic Assemblage (Breaks *et al.*, 2001).

### *1.6.3 Keeyask Lake Metavolcanic Assemblage*

Overlying the Keeyask Lake Metasedimentary Assemblage is the Keeyask Lake Metavolcanic Assemblage (KLMV), which is a metavolcanic succession ranging from 50 to 1700 metres in thickness. Spinifex-textured ultramafic flows dominate the lowermost units (Breaks *et al.*, 2001). The upper units of the KLMV assemblage contain intercalated pillowed basaltic komatiite with minor peridotitic, komatiitic rocks. Massive basaltic komatiite flows characterise the top of the assemblage (Breaks *et al.*, 2001). Thurston (1991) indicates that the overlying North Rim and South Rim Metavolcanic Assemblages are in depositional contact with the KLMV. The relationship between these three assemblages was also correlated by deKemp's (1987) radiometric dating.

The Keeyask Lake Metavolcanic Assemblage is significant to the overall evolution of the NCLB as it contains a progression from ultramafic to mafic metavolcanic rocks. Therefore this assemblage possibly records the transition from stable platform supracrustal development of the older assemblages (AAMV and KLMS) to formation of the younger assemblages associated with rifting activity (Keeyask Lake Metavolcanic assemblage, North Rim Metavolcanic Assemblage, South Rim Metavolcanic Assemblage, Opapimiskan Lake Metavolcanic Assemblage, Forrester Lake Metavolcanic Assemblage, Lundmark Lake Metavolcanic Assemblage, Eyapamikama Lake Metasedimentary Assemblage) (Groves and Batt, 1984).

#### *1.6.4 South Rim Meta-Volcanic Assemblage*

The South Rim Metavolcanic Assemblage (SRMV) defines the western edge of the NCLB (Fig. 1.3). To the west the SRMV is intruded by the  $2869 \pm 4$  Ma (U/Pb zircon age date, deKemp, 1987) North Caribou Lake Batholith and, to the east, is stratigraphically overlain by the Eyapamikama Lake Metasedimentary Assemblage (Breaks *et al.*, 2001). The SRMV is interpreted to be older than the batholith due to the presence of mafic metavolcanic xenoliths in the batholith and an inferred contact aureole along the edge of the otherwise low grade SRMV (Fig. 1.5) (Breaks *et al.*, 2001).

The SRMV is characterized by low metamorphic grade (greenschist facies), tholeiitic to magnesium-tholeiitic, pillowed and massive mafic flows (Breaks *et al.*, 2001). Pillowed flows are widespread, on the order of metres to tens of metres in thickness, and are intercalated with less abundant massive flows. Rarer intermediate and felsic flows, pyroclastic units, and the hypabyssal equivalents to the aforementioned lithologies represent less than five percent of the SRMV (Breaks *et al.*, 2001). The largest felsic unit (200 by 600 m) in the SRMV, composed of heterolithic tuff breccia, intermediate tuff, lapilli tuff, and rare felsic flows, is located along the western shore of Opapimiskan Lake (Breaks *et al.*, 2001). The senior exploration geologists at Musselwhite correlate this unit with felsic volcanic rocks seen in drill core from the top of the Musselwhite Mine stratigraphy (John Biczok, personal communication, 2007). Occasional rare banded iron formation is found in the SRMV (Breaks *et al.*, 2001), the most extensive of which is the



Eyapamikama Lake BIF far to the north of Musselwhite gold mine (Figs. 1.3, 1.6).

The SRMV assemblage is increasingly deformed and metamorphosed toward the south as indicated by progressively more penetrative foliations and a greater number of distinct shear zones (Fig. 1.5; Breaks *et al.*, 2001). This is clearly seen in outcrop on the western shore of Opapimiskan Lake where length-width ratios of pillows range between 20 and 35 (Breaks *et al.*, 2001).

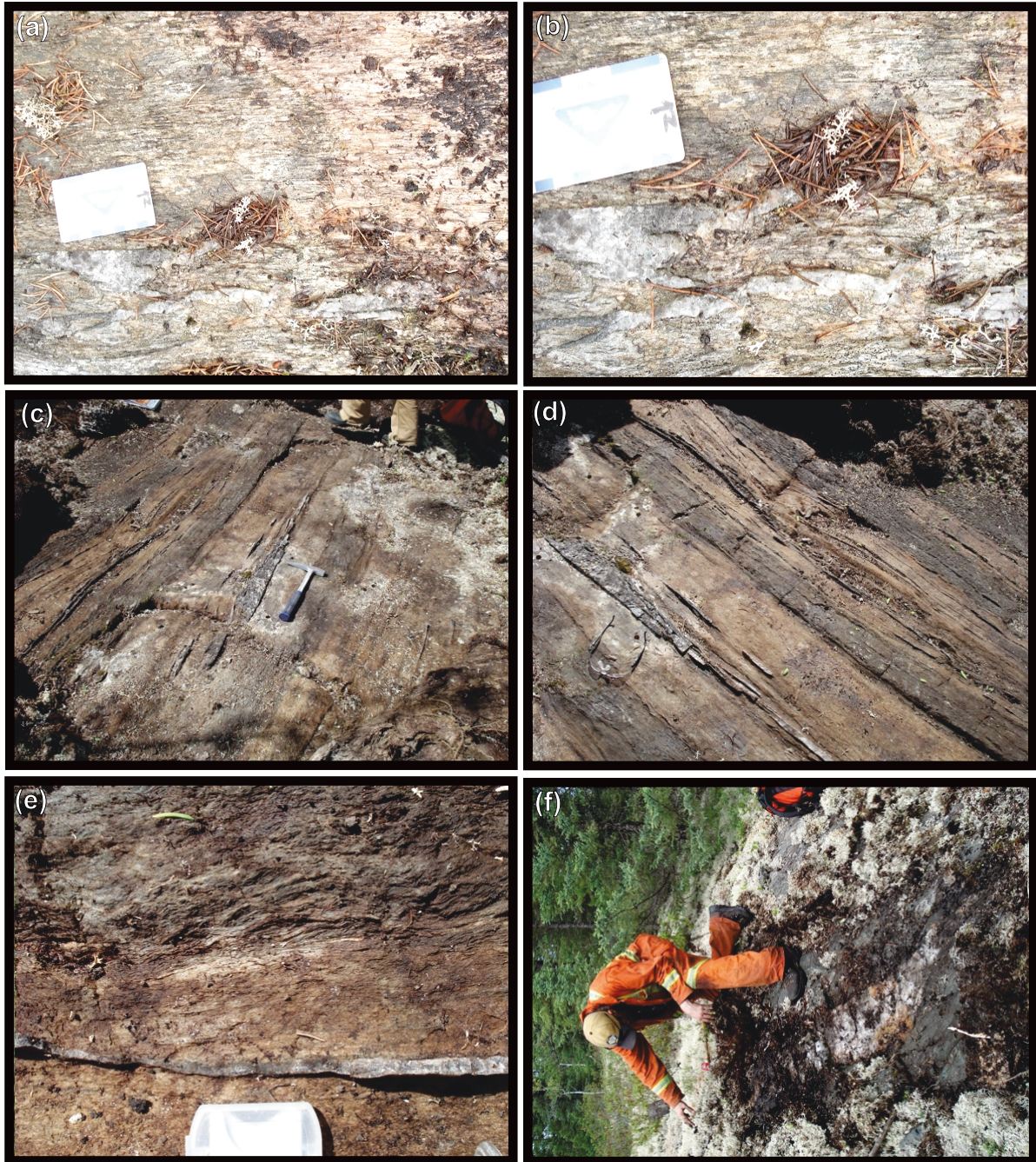
### *North Rim Metavolcanic Assemblage*

The North Rim Metavolcanic Assemblage (NRMV) ranges from 400 to 2600 metres in thickness and forms the eastern margin of the NCLB (Fig. 1.3). To the north the NRMV assemblage is bordered by the Schade Lake gneissic complex and to the east it is intruded by tonalitic rock. Enclaves of the NRMV assemblage are found in the tonalite intrusive bodies indicating the NRMV assemblage predates them (Thurston, Williams *et al.*, 1991). These tonalite rocks commonly have a protomylonitic fabric (Plate 1.2a, b) which suggests a continuous deformation zone (Breaks *et al.*, 2001).

The NRMV is dominated by mafic metavolcanic rocks (Breaks *et al.*, 2001). The North Rim Metavolcanic Assemblage is in contact with the Eyapamikama Lake Metasedimentary assemblage for most of its extent (Fig. 1.3). This contact appears to be gradational over a width of up to 100 meters with sedimentary layers gradually appearing as decimetre to metre scale intercalated beds in the NRMV. The NRMV has a U/Pb zircon age date of 2932 Ma (Davis, unpublished data referenced in Thurston, Williams *et al.*, 1991). The NRMV assemblage gradually becomes thinner from north to south and does not outcrop south of Opapimiskan Lake (Fig. 1.3). Due to the lake's location, directly on top and in the middle of the intersection of the three limbs of the NCLB (Fig. 1.3), it is difficult to decipher the relationship between the various assemblages at this critical location. Possible geologic scenarios include truncation of the belt by major shear zones or attenuation of the assemblage from north to south. Understanding the geology in this location is critical as it is the location of the only mine, to date, in the belt.







**Plate 1.2. Various photographs, taken just north of Musselwhite Mine (refer to Fig. 1.1 for exact location), showing deformation features in the North Rim metavolcanic assemblage and surrounding intrusive igneous rocks. a) protomylonitic fabric in tonalitic rock, b) close up of plate 1.2a showing deformed syntectonic quartz-vein in tonalitic protomylonite, c) deformed amphibolite containing dismembered quartz-veins, d) photograph of same outcrop showing the banded nature imparted on the amphibolite through shearing, (e) crenulation in amphibolite, same outcrop as 1.1c and 1.1d, f) photograph of different outcrop showing large quartz vein cross-cutting amphibolite in the NRMV assemblage.**

The NRMV assemblage is dominated by mafic metavolcanic rocks of tholeiitic composition (Breaks *et al.*, 2001). Intermediate and felsic rocks are scarce in the NRMV assemblage. The mafic metavolcanic rocks of the NRMV assemblage exhibit intense ductile deformation features (Plate 1.2c, d, e, and f), as well as medium grade (greenschist to amphibolite facies) metamorphism. Preservation of original features and structures is rare due to intense penetrative foliation and lineation. Rarely preserved structures include pillows containing >10% amygdales (Breaks *et al.*, 2001). Fine- to coarse-grained, hornblende-porphyrific mafic metavolcanic rocks are common in the NRMV. These rocks are associated with areas of severe tectonic deformation and high grade metamorphism associated with a large crustal scale shear zone along the eastern side of the belt (Fig. 1.3; Rayner and Stott, 2005). The author of the current study observed the mafic meta-volcanic rocks of the NRMV assemblage in contact with mylonitic plutonic rocks (Plate 1.2a-f).

Minor lithologies in the NRMV assemblage include dolomitic metasedimentary and rare cordierite-cummingtonite siliciclastic metasedimentary rocks. Several thinly-banded iron formation and chert units are found scattered throughout the NRMV assemblage, although they typically occur in close proximity to the contact between the NRMV assemblage and the Eyapamikama Lake Metasedimentary Assemblage. Five different localities in and around the McGruer-Castor lakes area (Figs.1.3, 1.6), as verified in the field or inferred from aeromagnetic data (Ontario Department of Mines–Geological Survey of Canada 1960, Maps 909G and 919G), contain banded iron formation. One weak aeromagnetic anomaly (maximum relief <1000 gammas) at Caster Lake corresponds to a quartz-grunerite banded iron formation (Breaks *et al.*, 2001). McLearty (1985) reports a BIF containing several intercalated fine- to medium-grained <60cm thick meta-pelitic interbeds 200 m south of the east end of Pollux Lake. An 8 meter thick quartz-grunerite banded iron formation is found in contact with laminated feldspathic arenite and garnetiferous mafic mineral-rich metasedimentary rocks at the south-western end of Castor Lake (Breaks *et al.*, 2001). Accessory garnet and tourmaline is found in the grunerite layers.

### *1.6.6 Eyapamikama Lake Metasedimentary Assemblage*

The Eyapamikama Lake Metasedimentary Assemblage (ELMS) is one of the most widespread components in the North Caribou Lake Metavolcanic / Metasedimentary belt. The ELMS assemblage is located in the centre of the belt and spans nearly its entire 20 km length (Fig. 1.3). It is bordered to the west and to the east by the SRMV and NRMV assemblages, respectively (Fig. 1.3). The ELMS is composed of metamorphosed siliciclastic sedimentary rocks, the youngest supracrustal rocks in the belt. This assemblage is only crosscut by meta-gabbro dykes and fluorite-bearing peraluminous granitoid dykes. The ELMS assemblage is characterized by a fining-upward sequence with fan delta conglomeratic and basal alluvial rocks grading into finer grained metasedimentary rocks (Breaks *et al.*, 2001).

Conglomerates are found primarily at the base of the ELMS assemblage and were probably deposited during one phase of deposition (Breaks *et al.*, 2001). Orthoconglomerates with arkosic- and subarkosic-wacke as the supporting matrix predominate. These conglomerates contain clasts from the main lithologies of the underlying assemblages including banded iron formation and quartz-arenites from the KLMS assemblage, ultramafic and variolitic mafic metavolcanic rocks from the KLMV assemblage, and felsic metavolcanic rocks of the AAMV assemblage. The majority of trondhjemite-tonalite-diorite clasts found in the conglomerates have similar modal mineral percentages to those seen in the Weagamow batholith (Breaks *et al.*, 2001). All of the clast types occur throughout the Eyapamikama Metasedimentary Assemblage although their presence in the southern portion may be obscured by the high degree of deformation.

Metasedimentary rocks derived from fine-grained sediment compose the bulk of the ELMS assemblage. Graywackes are found primarily as massive beds ranging in thickness from ~0.01m to 2.00m. Rare primary structures and textures observed in these beds include large-scale trough cross stratification and graded bedding (Breaks *et al.*, 2001). Gradation is more commonly seen in beds <5cm thick and found in association with mudstone. Breaks *et al.* (2001) interpret these rhythmically alternating metasedimentary

rocks as turbidites formed in a distal to medial fan environment. Quartz-arenites are not widespread in the ELMS assemblage and are primarily found as thin interbeds within graywacke-mudstone sequences.

Siltstones, phyllites, and slates are predominantly confined to the central region of the ELMS assemblage. Preserved features, including rip-up clasts and ball and pillow structures, can be identified due to alternating light and dark brown laminations. Chlorite-bearing siltstones and slates are found in the southwest of the ELMS assemblage, whereas slates containing biotite are found north of Eyapamikama Lake where the metamorphic grade is higher (Breaks *et al.*, 2001).

#### *1.6.7 Opapimiskan Lake Metavolcanic Assemblage*

Currently the Opapimiskan Lake Metavolcanic Assemblage (OLMV) is the most economically important assemblage in the NCLB, because it hosts the only viable gold deposit in the belt to date. The OLMV assemblage is located within a bifurcated, roughly U-shaped, portion of the North Caribou Lake Greenstone Belt (Fig. 1.3). This assemblage is between 100 and 1500 metres thick. The metavolcanic rocks composing the OLMV assemblage range from ultramafic to mafic in composition with possible minor intermediate to felsic components (Hollings and Kerrich, 1999). Oxide- and silicate-facies banded iron formations are common and useful stratigraphic markers. They are also the hosts to mineralization of the Musselwhite gold deposit.

The OLMV assemblage is bounded to the south and southwest by intrusive granitoid rocks. To the northwest the OLMV assemblage shares a complexly folded contact, of uncertain nature, and primarily inferred from aeromagnetic data, with the SRMV assemblage (Breaks *et al.*, 2001). It is likely that this contact is observable in Musselwhite drill core.

The defining feature of the OLMV assemblage is the abundance of komatiitic meta-volcanic rocks. Roughly 90% of the rocks collected and analyzed by Breaks *et al.* (2001) plotted in the komatiite field (MgO versus Al<sub>2</sub>O<sub>3</sub>). The remaining rocks fall within the

tholeiite field. Metavolcanic rocks of the Lundmark Lake, Forrester Lake, and Keeyask Lake Assemblages share similar ultramafic to mafic compositions. Preserved primary volcanic structures include pillows, varioles, and pillow breccia indicating subaqueous deposition. The metamorphosed ultramafic rocks are composed principally of serpentine and minor talc (John Biczok, personal communication, 2007). It is common for the ultramafic rocks of the OLMV assemblage to be strongly deformed. Near Opapimiskan Lake, rocks of the OLMV are intensely sheared and overprinted by a strong tectonic fabric (Breaks *et al.*, 2001). Shearing is focused along, or close to, contacts with the ELMS assemblage and/or sub parallel to axial planes. In these cases komatiites can be distorted into units, which appear to be primarily bedded actinolite-rich units (Breaks *et al.*, 2001).

Stratigraphically the OLMV may correlate to the Lundmark Lake, Forester Lake, or the Keeyask Lake Metavolcanic Assemblages based on similar geochemistry, abundant komatiitic metavolcanic rocks, and significant silicate- and oxide-facies banded iron formations (Breaks *et al.*, 2001). Correlation of these assemblages is difficult due to their physical separation. Breaks *et al.* (2001) suggest that if the KLMV and the OLMV assemblages were deposited at the same time this could signify rift volcanism. However, Hollings and Kerrich (1999) did not find geologic or geochemical indicators of rift type volcanism associated with the OLMV. Instead they propose plume magmatism impinging on the margin of a proto-cratonic Superior margin.

Iron formation commonly forms significant units within the OLMV. In general these BIF are intercalated with komatiitic metavolcanic units (Breaks *et al.*, 2001). Silicate- and oxide-facies iron formations are present and can be associated with siliciclastic, pelitic meta-sedimentary rocks. Undeniably the most significant BIF in the OLMV is the Opapimiskan banded iron formation. It is the largest at 30 km long as well as having the highest magnetic relief at 6500 nanoTeslas (Fig. 1.7). It is also significant as it is the host to the Musselwhite orebody. This unit has a complex structure due to the interference of three different folding episodes. Hall and Rigg (1986) describe this unit in detail with respect to gold mineralization.



Interpreting the relationship of the Opapimiskan Lake Metavolcanic Assemblage to the SRMV, ELMS, and NRMV assemblages is difficult. The SRMV and NRMV assemblages become progressively thinner towards Opapimiskan Lake and do not crop out south of the lake. Instead the Opapimiskan Lake Metavolcanic assemblage (OLMV) is present on the southern side.

### *1.6.8 Forester Lake Metavolcanic Assemblage*

The Forester Lake Metavolcanic Assemblage (FLMV) is found at the southern end of the belt (Fig. 1.3) and consists of ultramafic and mafic metavolcanic rocks. On its southern side the FLMV assemblage shares an irregular contact with surrounding granitoid rocks. Within the NCLB the FLMV assemblage is overlain by the clastic metasedimentary rocks of the 'ELMS assemblage' (bracketed because the true ELMS probably does not extend south of Opapimiskan Lake).

The FLMV is dominated by massive, pillowed, and amygdaloidal ultramafic and mafic metavolcanic rocks. Rocks of komatiitic affinity are more common than tholeiitic rocks (Breaks *et al.*, 2001). Two felsic units are found intercalated with deformed mafic metavolcanic rocks close to the southernmost contact with plutonic rocks external to the belt (Breaks *et al.*, 2001).

Iron formation is rarely exposed in outcrop and its presence is therefore mostly inferred from aeromagnetic surveys. Magnetic relief ranges from 1300 to 2100 nanoTeslas (Ontario Geological Survey, 1985). The magnetic anomalies show patterns, which indicate many of the iron formations are faulted and complexly folded. The most notable iron formations include a 15m thick, thinly bedded to laminated, quartz-magnetite BIF with minor layers of garnet-actinolite-chlorite metasedimentary rocks which Breaks *et al.* (2001) indicate resemble rocks at Musselwhite Mine. This formation is located roughly 1 km northwest of Forester Lake. Just north of Sage Lake, there is an outcrop of quartz-magnetite-grunerite iron formation, roughly 12m in thickness and having an exposed strike length of 100m. This iron formation is found within hornblende-porphyroblastic mafic and ultramafic volcanic rocks.



## 1.7 Metamorphism

Chlorite zone rocks dominate the west of the belt and include the majority of the AAMV and ELMS assemblages (Fig. 1.5; Breaks *et al.*, 2001). Metamorphic grade increases from low- to medium-grade, beginning at roughly the centre of the belt, increasing towards the east. Medium-grade metasedimentary rocks in the belt contain grunerite, cordierite, staurolite, garnet, and less commonly sillimanite (Breaks *et al.*, 2001).

Another pattern of regional metamorphism occurs in the NCLB. It is found at Eyapamikama Lake (Fig. 1.5). Here there is a local increase from low- to medium-grade metamorphism toward the north (Breaks *et al.*, 2001). The mineral isograds display a convex nature from north to northeast and are parallel to the strike of the greenstone belt.

Breaks *et al.*, (2001) concluded, based on earlier petrographic work (Breaks *et al.*, 1985; Breaks *et al.*, 1991), that the NCLB is characterized by low- to medium-grade prograde metamorphic zones. This style of metamorphism is similar to what is seen in other greenstone belts of the Superior Province (Pirie and Mackasey 1978; Thurston and Breaks, 1978; Breaks, 1989). Staurolite and andalusite are found throughout the belt whereas kyanite is relatively rare, being found in only two locations. Grunerite is another medium-grade metamorphic mineral that is commonly seen in banded iron formations throughout the belt (NRMV, LLMV, OLMV, and FLMV).

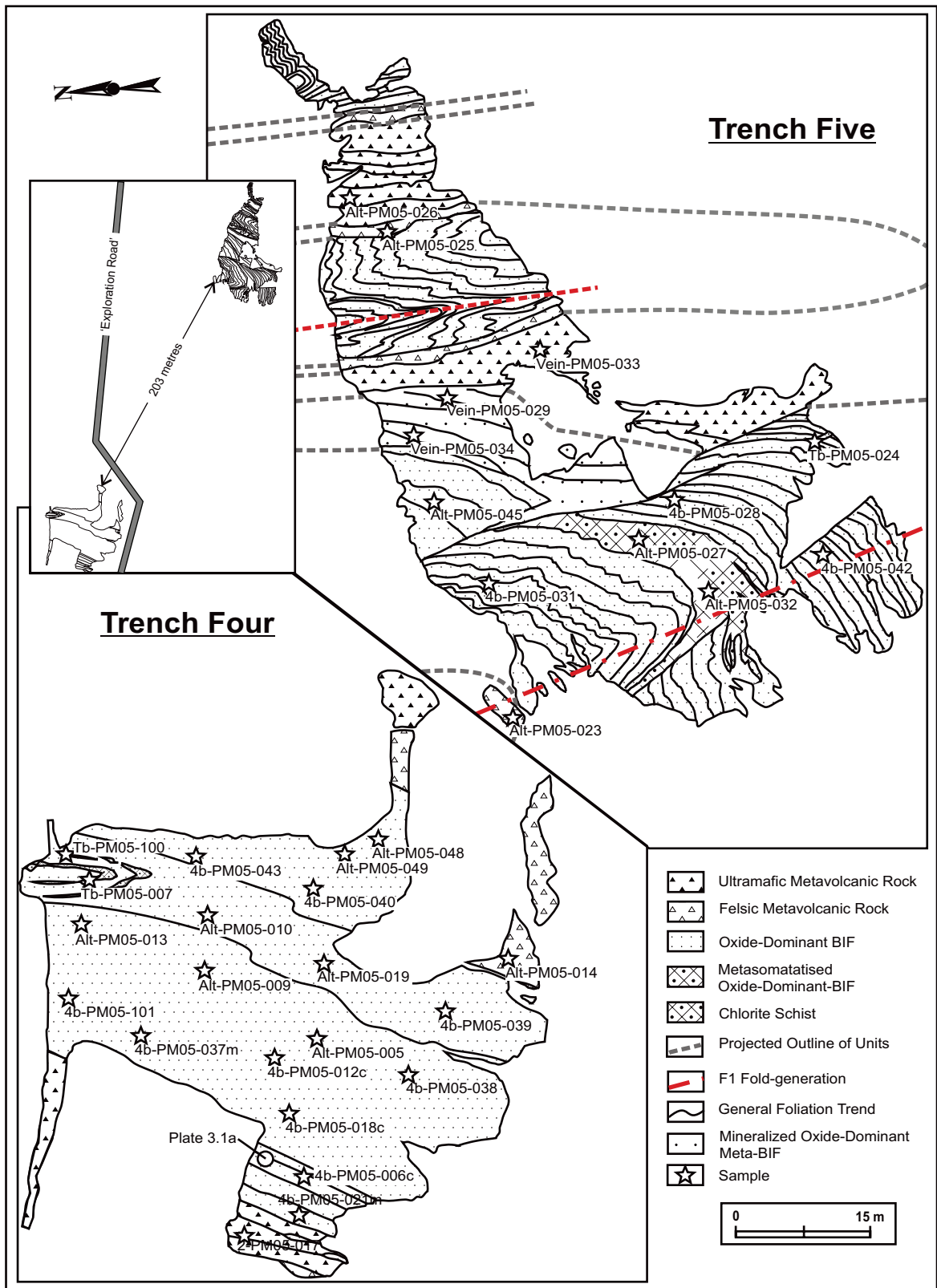
Breaks *et al.*, (2001) arrived at probable metamorphic conditions by analyzing mineral data from medium-grade staurolite-bearing zones in the NCLB. These conditions were constrained using the staurolite-in isograds of Froese and Gasparinni (1975) and staurolite-out isograd of Hoschek (1969). Based on the mineral assemblages, they postulate  $\leq 3$  kilobars pressure and temperature range from 400 °C to 500 °C, placing the rocks in the andalusite field of stability. Temperature estimates by Breaks *et al.*, (2001) are slightly lower than the 500 °C to 550 °C estimate of Hall and Rigg (1986) who used arsenopyrite-iron sulphide and garnet-biotite geothermometry on the garnet-biotite schist at Musselwhite Mine. Otto (2002) concluded peak metamorphic conditions of 540 °C to 600°C and 5 to 7 kilobars, based on garnet-biotite geothermometry of rocks from the Musselwhite Mine.

## 1.8 Structural Geology

Three deformation events, D<sub>1</sub>, D<sub>2</sub>, and D<sub>3</sub> (Fig. 1.6), were originally interpreted by R. Hall (geologist, Esso Minerals Limited, 1984) and D. Rigg (geologist, Dome Explorations Limited, 1985) in the vicinity of Opapimiskan Lake. The authors base their conclusions on folds, lineations, and tectonite fabrics in the supracrustal rocks of the NCLB. Breaks *et al.* (2001) suggest these three deformation events affected the rest of the NCLB as well.

The oldest observed deformation event in the NCLB is D<sub>1</sub>. It is affected by both later D<sub>2</sub> and D<sub>3</sub> deformation events. D<sub>1</sub> is only documented as superimposed folds in banded iron formation and as such folds generated by D<sub>1</sub> are usually asymmetrical and isoclinal in nature (Breaks *et al.*, 2001). Axial plane attitudes vary among the D<sub>1</sub> generation but are commonly horizontal. However, it is difficult to discern the original orientation and nature of F<sub>1</sub> folds as they have been modified by later deformation events. In trenches (Fig. 1.8) excavated on the Musselwhite Mine property, it is possible to see refolded F<sub>1</sub> folds along the limbs and crests of F<sub>2</sub> folds. F<sub>1</sub> and F<sub>2</sub> hinges are roughly co-axial. Rootless intrafolial folded quartz veins are surrounded by penetrative S<sub>2</sub> foliations possibly belonging to the F<sub>1</sub> fold generation (Hall and Rigg, 1986). Similarly outcrop of the SRMV along the western edge of Opapimiskan Lake contains F<sub>2</sub> folds and penetrative S<sub>2</sub> foliation, which has overprinted S<sub>1</sub> foliation and is related to the antiform on the Musselwhite Mine property (Fig. 1.7; Hall and Rigg, 1986). S<sub>1</sub> foliation is commonly preserved in metamorphic minerals like helicitic garnet at Musselwhite, as well as andalusite, staurolite, and cordierite in other regions of the belt (Breaks *et al.*, 1985). In general S<sub>1</sub> foliation is at high angles to later S<sub>2</sub> foliation (Hall and Rigg, 1986). Outside of the mine property this metamorphic feature is best preserved at Akow Lake (Breaks *et al.*, 1985).

The D<sub>2</sub> event was the highest energy and most pervasive deformation event affecting the North Caribou Lake Metavolcanic-Metasedimentary belt (Breaks *et al.*, 2001). The most



**Figure 1.8.** Map of trenches four and five: showing sample locations, lithologies and structure. Refer to Figure 1.4 for the location of these trenches on the mine site. Note Fig. 1.8 is modified after a map generated by the Musselwhite exploration department. Additionally Plate 3.1a is located near the western margin of trench four.

widespread physical manifestation of this event is asymmetric open to closed  $F_2$  folds. Other common features include boudinage and moderately- to strongly-developed  $S_2$  planar fabric.  $F_2$  folds are observable in the trenches at Musselwhite (Fig. 1.8). Unlike  $F_1$  folds,  $F_2$  fold axial planes are roughly vertical with interlimb angles ranging between  $070^\circ$  and  $100^\circ$ . Typically  $F_2$  are cylindrical and disharmonic with amplitudes ranging from 0.3 to 3.0 m. Syntectonic  $D_2$  shearing is focused along  $F_2$  axial planar cleavage. In outcrop these shear zones are manifested as grunerite-rich, rust-stained zones and can be found near Graf Lake, Sage Lake, and east of Lundmark Lake (Breaks *et al.*, 2001). Increase in grunerite content in the iron formation is associated with shear zones up to 3m wide and parallel to banding. These deformation zones are parallel to  $F_2$  fold axial planes.

Breaks (2001) interprets  $D_3$  as the third deformation event affecting the NCLB. This event is characterized by heterogeneous strain. In general structures created by this event are on a smaller scale than  $D_1$  and  $D_2$ .  $D_3$  deformation is manifested as asymmetric and gentle  $F_3$  warping and chevron crenulation of  $F_1$  and  $F_2$  folds. Fold amplitude is on the order of 1 cm to 5 cm with folds commonly cylindrical in nature and Z-shaped (Breaks *et al.*, 2001). Axial planes are upright and commonly parallel to the boundaries of the belt. The  $D_3$  deformation event was powerful enough to produce local well developed crenulation cleavage overprinting  $D_2$  cleavage in grunerite-rich, banded iron formation. These features were observed in the underground workings of the West Anticline Zone by Hall and Rigg (1986, p.129). R. Hall (geologist, Esso Minerals Canada, 1987), through personal communication with Breaks, indicated that mineralization in the West Anticline Zone is locally associated with the  $D_3$  event. There are likely large-scale  $F_3$  folds in the NCLB based on abrupt reversals in  $D_2$  lineations in several areas of the belt brought about by broad  $F_3$  folds (Breaks *et al.*, 2001).

Breaks *et al.* (2001) identified several new brittle-ductile shear zones within the NCLB. These shear zones coincide with mid- to late- $D_2$  deformation and affect all assemblages in the belt. They are focused along areas of competency contrast such as lithologic contacts.  $D_2$  shear zone fabric is overprinted by  $D_3$  deformation. Shear zones are abundant in the SRMV along the western side of Opapimiskan Lake, in the AAV, and in

the Agutua Arm area (Breaks *et al.*, 1985; Piroshco, 1986; Breaks *et al.*, 1991). The most significant shear zone in the NCLB is a large crustal-scale structure that runs along the eastern edge of the belt (Rayner and Stott, 2005).

D<sub>4</sub> is the latest deformation event in the NCLB. It is brittle in nature. This event is characterized by pseudotachylyte and cohesive fault breccia (Hall and Rigg, 1986).

### 1.9 Local Geology

The Musselwhite property (Fig. 1.3) is dominated by metavolcanic lithologies, specifically ultramafic and mafic rocks of the Opapimiskan Metavolcanic Assemblage and tholeiitic basalts and minor felsic flows of the South Rim Metavolcanic Assemblage.

The stratigraphy of the mine is well defined; it was established over several decades by early workers, and thoroughly delineated by the Musselwhite exploration department after 1997. It consists of metamorphosed mafic/ultramafic rocks at depth, iron formations, and an upper felsic unit (Fig. 1.9). Ultramafic content increases in abundance with depth (Hall and Rigg, 1986), whereas metasedimentary rocks dominate the upper part of the stratigraphy. Metasedimentary units include both chemical and siliciclastic lithologies. Lithologies maintain relatively consistent stratigraphic relationships. Unfortunately, way-up indicators are rarely observed due to the high metamorphic grade and strong deformation of the rocks. The generalized stratigraphy of the Musselwhite property is summarized in Figure 1.10. It should be noted that this stratigraphy has been folded into a large synform. A simplified and schematic cross section of the mine-stratigraphy is depicted in Figure. 1.11.

Two principle 'iron formations', inferred from an aeromagnetic survey (Fig. 1.7) and drill core, exist on the property. Both iron formations produce distinct magnetic highs and generally strike in an east-west direction (Hall and Rigg, 1986). They are referred to in this study as the Northern and Southern Iron Formation Assemblages. The names are derived from the surface relationship the two iron formations have to one another with

the Northern Iron Formation (NIF) Assemblage being located further north of the Southern Iron Formation (SIF) Assemblage. The iron formation at Musselwhite is part of the larger Opapimiskan Metavolcanic Assemblage. The NIF Assemblage is composed of a complex sequence of oxide- and silicate-dominated banded iron formation as well as several siliciclastic units (Hall and Rigg, 1986). The NIF Assemblage hosts considerably more gold, and is substantially thicker, than the SIF Assemblage. Note that the SIF does host several small gold zones. The basic stratigraphy of the NIF Assemblage is summarized in Figure 1.10. The SIF assemblage is primarily oxide-dominant BIF. Unit names are mine terminology. Please refer to Chapter Two for a more detailed characterization of the mine stratigraphy.

### 1.9.1 Lower Basalt Unit

The stratigraphically lowest unit normally encountered in drill core is called the Lower Basalts. The Lower Basalt unit forms the footwall to the deposit (Otto, 2002). This unit consists of undifferentiated massive and pillowed flows of high-iron/high-magnesium basalt with tholeiitic geochemical affinity (Hall and Rigg, 1986). Sample UG-PM05-064, an ultramafic rock, is from this unit. These flows are overlain by the Southern Iron Formation Assemblage (Zang, 1997).

### 1.9.2 Southern Iron Formation Assemblage

The Southern Iron Formation assemblage primarily consists of two thinly banded oxide-dominant iron formations which are between 5 and 30 m thick. The SIF assemblage can contain a minor discontinuous basal meta-argillite unit (sample 4H-07-20-071). The argillite contains  $\leq 30\%$  semi-massive to massive pyrrhotite with minor chalcopyrite and pyrite. The Southern Iron Formation assemblage rarely contains gold mineralization. The few mineralized zones known are associated with quartz veins.

### 1.9.3 Basement Basalt Unit

The ‘Basement Basalt’ unit is located above the Southern Iron Formation Assemblage and physically separates it from the Northern Iron Formation Assemblage. The NIF assemblage is host to the gold mineralization at Musselwhite. Therefore, the Basement Volcanic rock forms the footwall of this deposit.









The rocks of this unit are known at Musselwhite as '2vol' and the unit has been labelled the 'Basement Basalt' by Wells (1995a) and the Footwall Mafic-Ultramafic rocks by Hall and Rigg (1986). This unit consists of undifferentiated iron-rich basalt flows of tholeiitic affinity (Wells, 1995a). On the macroscopic scale they are fine-grained and generally massive. Pillow structures are occasionally observed. This unit also contains a persistent andesite unit (John Biczok, personal communication, 2007) in addition to an ultramafic component (Hall and Rigg, 1986; Wells, 1995a). The ultramafic component is particularly abundant in the West Anticline area. Mineralogically these ultramafic rocks are composed of tremolite-serpentine-calcite with minor talc-phlogopite-biotite (Hall and Rigg, 1986).

#### 1.9.4 Meta-Argillite Unit

The basal unit of the Northern Iron Formation Assemblage is a discontinuous meta-argillite (4h, mine terminology). It is pyrrhotite-rich and similar to the meta-argillite intermittently found at the base of the Southern Iron Formation Assemblage. This unit contains weakly magnetic quartz-bands, which represent metamorphosed chert. This unit is commonly strongly deformed. Deformation at mine-scale is typically focused along these lithologic contacts. This unit ranges from 0.5 to <2 metres thick and it is typically overlain and/or intercalated with a thinly laminated quartz-grunerite iron formation. Both units are discontinuous, but are normally found together. The meta-argillite is commonly found overlying ultramafic metavolcanic rock more so than mafic metavolcanic rocks. The meta-argillite is unmineralized with respect to gold (John Biczok, personal communication, 2007).

#### 1.9.5 Quartz-Grunerite Banded Iron Formation

The quartz-grunerite banded iron formation (4a, mine terminology) is a minor discontinuous unit within the Northern Iron Formation Assemblage. As mentioned in section 1.9.4., this lithology is normally found in association with the meta-argillite. The quartz-grunerite BIF consists of roughly 60% to 80% quartz bands and 20% to 40% diffuse fine-grained grunerite bands. Typically it is <1 to 2 metres thick but can range up to 10-20m thick in the PQ Deeps A Block on the east side of the Esker fold (John Biczok, personal communication, 2007). It is occasionally well preserved because of its high

quartz content. In its deformed state this unit is composed mostly of fine-grained grunerite and has a beige appearance. The quartz-grunerite iron formation occurs in gradational contact with the overlying thickly banded oxide facies iron formation. This unit is typically unmineralized with respect to gold.

#### 1.9.6 NIF Assemblage Oxide-Dominant Banded Iron Formation

The oxide-dominant banded iron formation (4b, mine terminology) typically consists of ~1cm thick alternating bands of quartz and magnetite and represents a classic banded iron formation. This unit is the most extensive component of the Northern Iron Formation Assemblage. It ranges from 10 to 20 metres thick in fold limbs but is considerably thicker, ranging between 75-150 m, in fold keels and crests (John Biczok, personal communication, 2007). Commonly the oxide-dominant BIF is in direct contact with the metavolcanic rock of the basement metavolcanic unit. The oxide-dominant BIF is located stratigraphically below, grading upward into, the silicate-dominant BIF. It is common for the oxide-dominant BIF to contain variable amounts of biotite and garnet at the expense of magnetite. Locally the oxide-dominant BIF grades into silicate-dominant BIF and to a lesser extent biotite-garnet schist. Macroscopically the oxide-facies BIF is variable and can be subdivided into three distinct subunits: 1) at the bottom of the oxide-dominant BIF is a discontinuous thinly laminated (0.1-0.3cm thick laminations) oxide-dominant BIF, 2) the bulk of the unit is composed of a thickly banded quartz-magnetite-grunerite BIF, and 3) at the top of the oxide-dominant BIF, the transition between oxide- and silicate-dominant BIF is normally marked by a coherent lithology composed of alternating quartz and hornblende-garnet schist bands,  $\pm$  magnetite bands ('clastic 4B', mine terminology).

On average the oxide-dominant BIF is thicker than the silicate-dominant BIF. The present thickness does not represent the original thickness of the units because of the deformation the rocks have undergone since deposition; however, its *relative* thickness is greater. Both units are laterally continuous.

#### 1.9.7 Silicate-Dominant Banded Iron Formation

The silicate-dominant banded iron formation (4ea, mine terminology) is located stratigraphically above the oxide-dominant banded iron formation and below the

hornblende-garnet schist. It should be noted that the silicate- and oxide-dominant banded iron formations share a gradational contact. Together these two banded iron formations make up the majority of the NIF assemblage. Refer to section 1.9.6 for a more detailed description.

This unit ranges in thickness from <10m to 30m and typically consists of a hornblende-amphibole-garnet-magnetite-quartz,  $\pm$  pyrrhotite and chlorite, mineral assemblage. Quartz-bands are separated by bands composed of hornblende-garnet, grunerite-garnet, and grunerite-amphibole-garnet. Magnetite and when present pyrrhotite and chlorite are disseminated in nature. These bands, on average, are roughly 1cm thick. In hand sample, the silicate-dominant BIF ranges from beige to green in appearance. Colour is dependent on the dominant compositional band in the sample. For example, samples containing abundant hornblende are green and those containing abundant grunerite are beige. Metamorphosed chert bands are recognizable and are typically boudinaged.

The silicate-dominant BIF is the host to the ore at Musselwhite and represents greater than 90% of the material targeted for mining. The major ore zones are the PQ Deeps (A1, A2, B and C Blocks), the S1 and S2, and the WA, T and C zones. All of these zones are in sheared silicate-dominant BIF. The silicate-dominant BIF ranges from broadly folded to strongly sheared. The major ore zones in this unit are associated with sub-vertical shear zones and, in one area, a sheath fold of at least 400m in length (Andrew Cheatle, personal communication, 2007). The exact relationship between the sheath fold and gold mineralization is currently not well understood.

Similar to the oxide-dominant BIF the silicate-dominant BIF contains local intercalated biotite-garnet schist and hornblende-garnet schist. The silicate-dominant BIF is in gradational contact with the overlying biotite-garnet schist unit. Unlike the oxide-dominant BIF the silicate-dominant BIF is not commonly exposed in outcrop except for the area immediately north of the PQ shallows open pit (Fig. 1.4).

### 1.9.8 Hornblende-Garnet Schist

The hornblende-garnet schist (4e, mine terminology) is a discontinuous unit located above the silicate-dominant BIF. This unit ranges from <1m to 3m in thickness. It is typically found intercalated with the biotite-garnet schist and more rarely as a homogeneous unit. The hornblende-garnet schist is commonly but erratically mineralized with respect to gold. Layers of hornblende-garnet schist also occur at the transition between oxide- and silicate-dominant BIF (described in Chapter Two). This transitional BIF consists of metamorphosed chert bands intercalated with hornblende-garnet as well as magnetite bands. Hornblende-garnet schist layers also appear to make up a minor part of the silicate-dominant BIF. This lithology is found as centimetre- to decimetre-scale bands and can make up a significant portion of the silicate-dominant BIF.

Typically the hornblende-garnet schist is non-magnetic to weakly magnetic and composed of 80-90% hornblende-rich matrix in which sit 10-20% 1mm to 2cm anhedral to subhedral elongated pink almandine garnet porphyroblasts. Garnet size is relatively consistent in individual samples. Aside from what is typically seen, the ratio of garnet porphyroblasts to hornblende dominated matrix can be variable in this lithology. This ratio influences the rock's general appearance, which can be dark-green when composed of >95% hornblende and few to no garnets to having a brownish-pink appearance when garnet content is in excess of 60%. An example of this brown-pink colour is sample 4E-07-20-022 (photograph on page VIII of Appendix A), an atypical version of the amphibole-garnet schist.

### 1.9.9 Biotite-Garnet Schist

The biotite-garnet schist (4f, mine terminology) occurs between the silicate-dominant BIF and either the overlying "Bvol" mafic metavolcanics or garnet quartzite. It is therefore an important marker bed in the stratigraphy of the mine workings. It should be noted, biotite-garnet schist is more widespread and forms thicker sequences in the West Anticline area (Hall and Rigg, 1986) relative to the active mine workings of the T-Antiform (John Biczok, personal communication 2007). Refer to Figures 1.4 and 1.8 for the location of the West Anticline and its relative location to the mine-workings respectively. This unit commonly contains intercalated meta-chert bands, silicate-

dominant BIF, hornblende-garnet schist and garnet-quartzite layers and bands. As this unit overlies the silicate-dominant BIF, the host to gold mineralization, it delineates the 'hanging wall' of the main orebody. Locally this unit may be absent from the stratigraphy and this is believed to be the result of shearing (John Biczok, personal communication 2007).

Some of the mine geologists speculate that deformation is focused along this lithology because of its high biotite content (John Biczok, personal communication, 2007). The biotite-garnet schist is also found as an 'intraformational' unit within the overlying mafic metavolcanic succession. The intraformational biotite-garnet schist contains abundant staurolite (up to 30%) compared to the biotite-garnet schist in the NIF Assemblage. Ar-Ar dating of biotite from this unit gives an age of  $2485 \pm 12$  Ma (Spell, 2002, in Klipfel, 2002b).

All samples of the biotite-garnet schist are ferruginous ( $>21$  wt %  $\text{Fe}_2\text{O}_3^T$ ). The biotite-garnet schist is variable in thickness commonly ranging from ~1 to 15 metres thick. This unit is significantly thicker in the West Anticline ranging from tens to hundreds of metres thick in this area. There is minor local gold enrichment associated with quartz-pyrrhotite veins in the biotite-garnet schist.

#### 1.9.10 Garnet-Quartzite

The garnet-quartzite is a relatively thin, discontinuous, and unmineralized unit found in association with the biotite-garnet schist at the top of the NIF assemblage. It typically occurs as intercalations in gradational contact with the biotite-garnet schist and overlying it. On average this unit is between 1 and 2 metres thick at the top of NIF assemblage, but ranges from a few centimetres to ~10m thick. This unit is commonly intercalated with the biotite-garnet schist. This unit caps the NIF assemblage and as such is an important marker bed as it delineates the end of the NIF assemblage's stratigraphic succession.

At some locations, individual beds in this unit show no garnet in their lower half with a gradual increase in garnet in their upper half culminating in biotite-garnet schist. This

appears to originally have been graded bedding and gives an up direction toward the overlying felsic volcanic rocks.

#### 1.9.11 Bvol Intermediate to Mafic Metavolcanic Unit

The 'Bvol' intermediate to mafic metavolcanic unit shares a gradational to sharp upper contact with overlying rocks of the 'Avol' unit. This unit consists of medium- to dark-green, schistose, fine-grained andesitic to basaltic metavolcanic rocks of transitional to tholeiitic affinity (Wells, 1995b).

In terms of mineralogy these rocks are composed of hornblende-plagioclase-actinolite,  $\pm$  biotite. Rock from this unit is known as 'Bvol' (basic volcanic) (Klipfel, 2002a). This unit has a zircon age date of  $2920 \pm 4.7$  Ma (Heaman, 2002; in Klipfel, 2002b). However, this age date remains suspect because only two zircons were dated (John Biczok, personal communication 2007).

There are approximately four one- to four-metre thick intraformational hornblende-garnet schist layers in this unit. These are typically composed of hornblende-garnet schist intercalated with metamorphosed chert bands. Like the hornblende-garnet schist at the top of the NIF assemblage these intraformational layers can be locally, but erratically, well mineralized.

#### 1.9.12 AVOL Felsic Metavolcanic Unit

The Avol unit is predominantly composed of felsic metavolcanic rocks (dacite to rhyolite in composition). This unit has a zircon age date of  $2973.7 \pm 2.2$  Ma (Heaman, 2002, in Klipfel, 2002b). Klipfel (2002b) suggests this date may be erroneous, possibly due to a Grenvillian aged Pb disturbance and miscalculations in constructing a 'reference line.'

Structurally the Avol is the uppermost unit encountered in the mine stratigraphy. It is roughly 50 m thick and likely in depositional contact with the underlying rocks (John Biczok, personal communication 2007). Rocks in this unit have calc-alkaline to tholeiitic geochemical signatures (Hall and Rigg, 1986; Hollings and Kerrich, 1999). Wells

(1995a) interprets this unit to be reworked felsic tuff. Rocks of this unit are typically light-grey, fine-grained, and composed of plagioclase-muscovite-quartz-calcite with minor apatite and pyrite (Wells, 1995a).

The eastern margin of the 'Avol' felsic metavolcanic unit appears to be stratigraphically conformable with metavolcanic units to the east (SRMV assemblage). This contact is laterally extensive and does not appear to be tectonic but stratigraphic (Klipfel *et al.*, 2002a).

### 1.10 Previous Research

Hollings and Kerrich (1999) concluded that the komatiites and basalts in the Opapimiskan Lake metavolcanic assemblage, host to the Musselwhite orebody, were contaminated by early crustal material. They are enriched in light REE and have negative Ti and Nb anomalies. The authors concluded that contamination of a primary Munro-type Al-undepleted ultramafic melt by tonalitic-trondhjemitic-granodioritic (TTG) felsic material would result in the observed geochemical anomalies. The SRMV assemblage is composed of Mg- to Fe-tholeiites and overlies the OLMV, possibly in stratigraphic contact. The rocks of the SRMV are uncontaminated and are characterized by a flat trace element pattern. They are comparable to a modern day oceanic plateau (Hollings and Kerrich, 1999). Together these units are interpreted to have resulted from volcanism driven by a mantle plume. This mantle plume mixed with tholeiitic melts in the upper mantle before passing through the Archean crust at ~3 Ga. The conclusions of Hollings and Kerrich (1999) offer important supporting evidence on the tectonic setting of formation of the NIF Assemblage.

Otto (2002) completed a Master's thesis on the Musselwhite deposit titled, "Ore forming process in the BIF-hosted gold deposit Musselwhite Mine, Ontario, Canada". He characterized the chemistry of the metavolcanic and metasedimentary units and concluded that the mafic metavolcanic rocks are basalts with tholeiitic affinity and the felsic metavolcanic rocks are dacites/rhyolites with calc-alkaline geochemical signatures.



He established an increasing clastic component stratigraphically upward in the Northern Iron formation assemblage; from pure exhalative to clastic. Otto also concluded that  $\delta^{34}\text{S}$  values of quartz veins (12.1‰ to 13.4‰) indicated a metamorphic fluid source, whereas the range of  $\delta^{34}\text{S}$  values for whole rock samples indicate a magmatic source of sulphur. He concluded that gold is mainly found along the fractures in garnets in the silicate facies iron formation. Chlorite geothermometry modeled after Walshe (1986) indicated temperatures between 210 °C and 250 °C at reduced conditions (Otto, 2002).

Liferovich authored several internal reports, which focused on a unique and minor quartz-pyrrhotite vein, for Musselwhite in 2006. He concluded that gold is associated with PbTe-minerals in this vein (Petzite  $\text{Ag}_3\text{AuTe}_2$ , Calaverite  $\text{AuTe}_2$ ; R. Liferovich personal communication, 2006), pyrrhotite, and chlorite.

## 1.11 Methods

Field work, at the Musselwhite Mine site, including the collection of samples and detailed logging of core was completed over several trips through 2005-2007. During these trips digital data such as maps, references, and images were also collected. Careful notes were taken to record such aspects as lithology and the relationships between lithologies. In total roughly two-hundred and fifty rock samples were collected. Of these, one-hundred and twenty-five samples were sent for whole rock lithochemical analysis at the Ontario Geologic Survey (OGS) lab in Sudbury, Ontario, Canada. A breakdown of samples by lithology can be found in Table 1.1, as well as in Appendix A. Table 1.1 contains information on sample location, whether or not a thin-section was made, and geochemistry status. Appendix A contains detailed descriptions of each sample sent for analysis.

Forty-four samples were collected from trenches four and five (Fig. 1.8). The trenches are located several hundred metres away from the ore zones (refer to Fig. 1.4 for location of trenches on the mine property). Lithologies collected from the trenches include oxide-dominant banded iron formation, mafic and intermediate/felsic metavolcanic lithologies,

and metasomatically altered lithologies. Lithologies found in the trenches but lacking analogues in the mine include fine-grained felsic intrusive igneous rock, certain types of highly grunerite-altered rocks, and chlorite schist. These samples were collected as background standards. The reasoning was that these samples should provide more insight into the original geochemistry of the lithologies, as opposed to rock closer to the ore zones which, in theory, may exhibit more geochemical change.

Seventy-three samples were collected from drill core. These samples came from closer to or within the ore bodies. Several lithologies are only found in core and do not have surface analogues including the southern iron formation oxide-dominant BIF, meta-argillite, thinly-laminated quartz-grunerite banded iron formation, oxide/silicate banded iron formation, silicate banded iron formation, hornblende-garnet schist, biotite-garnet schist, and garnet-quartzite.

Sample preparation was as follows: samples were carefully cut so that no quartz or carbonate veins were included with the final sample. Samples were then washed to remove any residual material. Sample preparation was labour intensive, particularly for banded iron formation as it was necessary to separate the magnetite and quartz bands. Quartz and magnetite bands were separated by cutting them apart with a rock saw. These separated bands were crushed by hand, using a tungsten-carbide mallet, to <3 mm diameter chips. In the case of thinly laminated samples (mainly SIF), where cutting apart magnetite and quartz bands was not practical, the rock was crushed to <3mm diameter and magnetite was separated from quartz using a powerful hand-held magnet. These chips were then pulverized in an agate mill until ~0.1mm powder was achieved. The resulting powders were put in sterile containers and mailed to the OGS labs for analysis.

Chemical analysis, as reported by the OGS, was completed using CT4 T4 closed beaker digestion. The rare earth elements (REE), large lithophile elements (LILE), and high field strength elements (HFSE) were analysed by using inductively coupled plasma-mass spectroscopy (ICP-MS). Major and trace elements were analysed by using wavelength dispersive x-ray fluorescence (WD-XRF). FeO was measured by titration. For detection limits, standards, and errors refer to Table 1.2 and Appendix D.

Polished thin-sections, in disk form, were analysed by a JEOL 5000 Scanning Electron Microscope. In total one-hundred and three SEM disks were prepared. Refer to Appendix A to see samples that SEM disks were prepared from. The author made SEM disks by cutting the desired samples into square chips roughly 2cm x 2cm, which than had their corners rounded off. Chips were polished using 0.440 silicon-carbide grit and a grinding wheel. Next, chips were placed on a hotplate at 100°C to dry. Once dry, epoxy was applied and left to harden for ½ hour. Chips were further finished by using 0.220 grit on a glass plate. Sample surfaces were examined for scratches using reflected light microscope at 40x magnification. If no scratches were found, chips were epoxied to glass disk and left to dry for 1 hour. Once epoxy solidified and cooled the chips were cut off the glass disk leaving behind approximately 1mm of rock. The disk was then transferred to a grinding wheel where the remaining rock was ground down to 0.5µm. Final grinding of disk was done by hand using 0.220 grit on a glass plate. In the final step the SEM disks were put in a polishing machine, using diamond polishing grit, for 15 minutes.

Once the polished SEM disks were made they were examined by the author using an Olympus BX2M microscope in both transmitted and reflected light settings. The author selected several SEM disks from each lithology (n=30), based on the previously mentioned microscopy, for further examination using the JEOL JSM-5900 Scanning Electron Microscope (SEM) at Lakehead University Centre for Analytical Research (LUCAS). This SEM is equipped with a Super ATW Element Detector (133 eVFwHm MnK). Analysis of mineral chemistry was completed through Quantitative Energy-Dispersion X-ray Spectrometry (EDXA) with raw data being processed by LinkISIS 300 computer software. Individual data points (EDS spectra) were acquired with count times ranging from 40 to 60 seconds. A beam current of 0.475 nA was used, standardized on Ni, with an accelerating voltage of 20kV. The acquired spectra were analyzed using the quantitative LINK ISIS-SMQUANT software program incorporating full ZAF corrections. Both mineral and synthetic standards were used and are listed in the following order: corundum (Al), fluorapatite BM 1926-665 (P, Ca), ilmenite (Fe), jadeite BM 1913-451 (Na), Mn-fayalite (Mn), orthoclase (K), and pyroxene DJ-35 (Si).

**Table 1.1.** Table listing samples, their locations, geochemistry (complete/not measured), and thin-sections (complete/not made). Please refer to Figure 1.8 for location of samples from trenches. The information presented in this table is expanded upon in Appendices A-D.

Samples (n=125)									
Lithology	Sample Number	Location	Geochem	T.S.	Lithology	Sample Number	Location	Geochem	T.S.
SIF Oxide BIF	PM05-063	500 Level	Yes	Yes	Hornblende-Garnet Schist	07-20-018	03-PQU-090, 6m	Yes	Yes
"	07-20-060c	03-RDW-003, 295.6m	Yes	Yes	"	07-20-019	03-CMP-057, 26.8m	Yes	Yes
"	07-20-060m	03-RDW-003, 295.6m	Yes	Yes	"	07-20-022	03-PQU-162, 84.6m	Yes	Yes
"	07-20-062m	03-RDW-035, 241.9m	Yes	No	"	07-20-023	03-PQU-066, 22m	Yes	No
"	07-20-063c	04-ESS-026, 157.6m	Yes	Yes	"	07-20-034a	03-PQU-058, 54m	Yes	Yes
"	07-20-063m	04-ESS-026, 157.6m	Yes	Yes	"	07-20-034b	03-PQU-068, 59.2m	Yes	Yes
"	07-20-071m	05-KAZ-005, 39m	Yes	No	"	07-20-047	04-ISL-010, 130.4m	Yes	Yes
"	07-20-072m	05-KAZ-048, 11m	Yes	Yes	"	07-20-048	04-PQU-022, 216.6m	Yes	No
8 5					8 6				
Metargillite	4H-07-20-042	04-ESN-012, 98.2m	Yes	No	Garnet-Quartzite	07-20-024	03-PQU-066, 25.3m	Yes	Yes
"	4H-07-20-043	04-ESN-012, 97.8	Yes	No	"	07-20-025	03-PQU-056, 39.8m	Yes	No
"	4H-07-20-046	04-ESS-009, 149.3m	Yes	No	"	07-20-033	03-PQU-059, 34m	Yes	Yes
"	4H-07-20-051	04-PQD-001, 26.9m	Yes	No	"	07-20-038	03-PQU-006, 50.9m	Yes	No
"	4H-0720-053a	04-PQD-006, 1023.8m	Yes	Yes	"	07-20-058b	06-PQE-086, 32.9m	Yes	Yes
"	4H-0720-053b	04-PQD-006, 1024.2m	Yes	Yes	5 3				
"	4H-07-20-056	04-PQU-135, 34m	Yes	Yes	Biotite-Garnet Bands	07-20-001	06-PQE-072, 43.1m	Yes	Yes
"	4H-07-20-057	04-PQU-135, 32.9m	Yes	Yes	"	07-20-007	06-PQU-008, 151m	Yes	Yes
"	4H-07-20-070	05-KAZ-002, 141m	Yes	Yes	"	07-20-017	03-PQD-044, 1053.2m	Yes	No
"	4H-07-20-071	05-KAZ-005, 39m	Yes	Yes	"	07-20-020	03-PQU-144, 119.8m	Yes	Yes
10 6					6 4				
Quartz-Grunerite BIF	07-20-012	06-PQU-019, 30.5m	Yes	No	Quartz-Bands from BIF	PM05-006	Trench 4	Yes	Yes
"	07-20-028	03-CMP-053, 27.9m	Yes	No	"	PM05-012	Trench 4	Yes	Yes
"	07-20-039	04-ESS-002, 148.7m	Yes	No	"	PM05-018	Trench 4	Yes	Yes
"	07-20-041	04-ESN-012, 96.8m	Yes	No	"	PM05-028c	Trench 4	Yes	Yes
"	07-20-044	04-ESS-009, 148.6m	Yes	Yes	"	PM05-031c	Trench 5	Yes	Yes
"	07-20-054c	04-PQU-135, 28.3m	Yes	Yes	"	PM05-038c	Trench 4	Yes	Yes
"	07-20-054m	04-PQU-135, 28.3m	Yes	Yes	"	PM05-040c	Trench 4	Yes	Yes
7 4					8 8				
Quartz-Bands Oxide-BIF	07-20-053c	04-PQU-130, 71m	Yes	Yes	Magnetite-Bands from BIF	PM05-021	Trench 4	Yes	Yes
"	07-20-005c	06-PQE-073, 126m	Yes	No	"	PM05-028m	Trench 5	Yes	Yes
"	PM05-065c	05-PQE-006, 141m	Yes	No	"	PM05-031m	Trench 5	Yes	Yes
"	PM05-067c	05-PQE-016, 99.25m	Yes	No	"	PM05-037	Trench 4	Yes	No
"	PM06-028c	05-PQE-013, 147.43m	Yes	No	"	PM05-038m	Trench 4	Yes	Yes
5 1					9 6				
Magnetite-Bands Oxide-BIF	07-20-004m	06-PQE-071, 101.6m	Yes	Yes	"	PM05-039	Trench 4	Yes	No
"	07-20-040m	04-PQU-062, 325.5m	Yes	Yes	"	PM05-040m	Trench 4	Yes	Yes
"	07-20-053b	04-PQU-130, 71m	Yes	Yes	"	PM05-042	Trench 4	Yes	Yes
"	PM05-067m	05-PQE-016, 99.25m	Yes	No	"	PM05-101	Trench 4	Yes	No
"	PM05-050	500 Level	Yes	Yes	9 6				
"	PM06-028m	05-PQE-013, 147.43m	Yes	No	Altered Oxide BIF	PM05-005	Trench 4	Yes	Yes
Silicate/Oxide BIF	07-20-056	04-PQU-153, 145.7m	Yes	Yes	"	PM05-009	Trench 4	Yes	Yes
Laminated BIF	07-20-055m	04-PQD-006, 1270.1m	Yes	Yes	"	PM05-010	Trench 4	Yes	Yes
8 6					10 9				
Silicate BIF	07-20-044	04-ESS-009, 148.6	Yes	Yes	Felsic Porphyry	PM05-014	Trench 4	Yes	Yes
"	07-20-061	03-PQU-141, 42m	Yes	Yes	"	PM05-023	Trench 5	Yes	Yes
"	07-20-065	04-ESS-016, 225.8m	Yes	Yes	"	PM05-025	Trench 5	Yes	Yes
"	07-20-067	04-ISL-010, 131.3m	Yes	Yes	3 3				
"	07-20-068	04-PQU-028, 204.3m	Yes	No	Chlorite Schist	PM05-007	Trench 4	Yes	Yes
"	07-20-069	04-PQD-001, 1081.7m	Yes	Yes	"	PM05-024	Trench 5	Yes	Yes
"	08-30-001	06-PQE-073, 77.5m	Yes	Yes	"	PM05-100	Trench 4	Yes	No
"	08-30-002	06-PQE-098, 74.2m	Yes	Yes	3 3				
"	08-30-004	05-PQE-073, 84.85m	Yes	Yes	Felsic Volcanic	PM05-053	500 level	Yes	Yes
"	PM05-057	500L, near S2 Limb	Yes	Yes	"	PM05-054	500 level	Yes	Yes
"	PM05-066	05-PQU-077, 659.4m	Yes	No	2 2				
"	PM06-002	05-PQE-013, 51.1m	Yes	Yes	Mafic Volcanic	PM05-017	Trench 4	Yes	Yes
"	PM06-007	05-PQE-013, 63.33m	Yes	Yes	"	PM05-026	Trench 5	Yes	Yes
"	PM06-018	05-PQE-013, 112.97m	Yes	Yes	"	PM05-052	PQ hanging wall, 500L	Yes	Yes
"	PM06-043	05-PQE-012, 18.38m	Yes	Yes	"	PM05-055	500 level	Yes	Yes
"	4EA-0620-UG04	620L, T-antiform limb	Yes	Yes	"	PM06-065	05-PQE-012, 72m	Yes	Yes
16 14					5 5				
Biotite-Garnet Schist	07-20-001	06-PQE-097, 18.1m	Yes	No	Quartz Vein	PM05-029	Trench 5	Yes	Yes
"	07-20-002	06-PQE-072, 42.2m	Yes	Yes	"	PM05-033	Trench 5	Yes	Yes
"	07-20-008	06-S2E-002, 0.30m	Yes	Yes	"	PM05-034	Trench 5	Yes	Yes
"	07-20-009	06-S2E-002, 0.50m	Yes	Yes	5 5				
"	07-20-011	06-PQE-098, 40.5m	Yes	No	Ultramafic	PM05-064	500 level	Yes	Yes
"	07-20-027a	03-PQU-082, 65.4m	Yes	Yes	7 5				
"	PM05-050	PQ hanging wall, 500L	Yes	Yes	7 5				

**Table 1.2.** Detection limits for the various analysis completed by the OGS Geoscience Laboratories in Sudbury. Abbreviations are as follows: WD-XRF: Wavelength dispersive x-ray fluorescence, and ICP-MS: Inductively coupled plasma-mass spectroscopy.

Detection Limits							
Element	WD-XRF	ICP-MS	Titrimetry	Element	WD-XRF	ICP-MS	Titrimetry
SiO <sub>2</sub>	0.01 wt. %	-	-	Er	0.008 ppm	-	-
TiO <sub>2</sub>	0.01 wt. %	-	-	Tm	0.003 ppm	-	-
Al <sub>2</sub> O <sub>3</sub>	0.01 wt. %	-	-	Yb	0.01 ppm	-	-
Fe <sub>2</sub> O <sub>3</sub>	0.01 wt. %	-	-	Lu	0.003 ppm	-	-
FeO	-	-	0.06 wt. %	Th	0.06 ppm	4 ppm	-
MnO	0.01 wt. %	-	-	U	0.007 ppm	4 ppm	-
MgO	0.01 wt. %	-	-	Na	-	40 ppm	-
CaO	0.01 wt. %	-	-	P	-	10 ppm	-
Na <sub>2</sub> O	0.01 wt. %	-	-	K	-	10 ppm	-
K <sub>2</sub> O	0.01 wt. %	-	-	Sc	-	6 ppm	-
P <sub>2</sub> O <sub>5</sub>	0.01 wt. %	-	-	Ti	-	10 ppm	-
LOI	0.05 wt. %	-	-	V	-	4 ppm	-
Rb	0.05 ppm	2 ppm	-	Cr	-	4 ppm	-
Sr	0.5 ppm	2 ppm	-	Mn	-	10 ppm	-
Y	0.02 ppm	1 ppm	-	Co	-	10 ppm	-
Zr	4 ppm	3 ppm	-	Ni	-	2 ppm	-
Nb	0.2 ppm	2 ppm	-	Cu	-	1 ppm	-
Cs	0.007 ppm	7 ppm	-	Zn	-	3 ppm	-
La	0.02 ppm	-	-	Ga	-	2 ppm	-
Hf	0.1 ppm	-	-	As	-	1 ppm	-
Ta	0.2 ppm	10 ppm	-	Se	-	2 ppm	-
Ce	0.07 ppm	-	-	Mo	-	2 ppm	-
Pr	0.006 ppm	-	-	Ag	-	5 ppm	-
Nd	0.003 ppm	-	-	Sn	-	5 ppm	-
Sm	0.01 ppm	-	-	Sb	-	5 ppm	-
Eu	0.005 ppm	-	-	Ba	-	20 ppm	-
Gd	0.009 ppm	-	-	W	-	10 ppm	-
Tb	0.003 ppm	-	-	Pb	-	5 ppm	-
Dy	0.008 ppm	-	-	Bi	-	5 ppm	-
Ho	0.003 ppm	-	-				

## **Chapter 2**

### **Stratigraphic Succession of the NIF Assemblage**

#### **2.1 Introduction**

Current interpretations of the stratigraphy were developed, over the last decade, by geologists working in the exploration and geology departments at Musselwhite Mine. Their work is based on drill core collected and preserved at the mine site. Newer drill-core, dating back roughly a decade, is stored on site in a core-library, drill logs from holes prior to 1997 are preserved on paper and stored in a fire-proof vault at the administrative building. In some cases earlier core logs have been digitized and incorporated into the three-dimensional mine model created by the geologists. Please refer to Section 1.9 (p. 26) in Chapter One for a description of the idealized Musselwhite Mine stratigraphy (Figs. 1.8, 1.9, and 1.10). The reader will find comprehensive petrologic descriptions of the lithologies in Chapter Three.

Chapter Two investigates the spatio-temporal evolution of the various lithologies present in the NIF assemblage and their basic affiliation with gold mineralization. It should be noted that the stratigraphy of the Mesoarchaen NIF assemblage is more complex than the idealized version presented in Chapter One. However, the general trends of increasing siliciclastic and decreasing exhalite material stratigraphically upward in the NIF assemblage hold true. The stratigraphic relationships become increasingly complicated in the upper region relative to the lower region of the NIF assemblage. The complexity of the lithologic relationships is likely a product of original depositional features compounded by later structural deformation.

The objectives of Chapter Two are to: 1) produce four detailed stratigraphic logs which show the stratigraphic variability of the NIF assemblage, and 2) relate gold mineralization to the different lithologies in a basic way. The following holes were logged: 04-ESN-010 (Fig. 2.1), 05-PQE-012 (Fig. 2.2), 05-PQE-013 (Fig. 2.3), and 06-S2E-002 (Fig. 2.4). It should be noted that out of the four holes logged, hole 04-ESN-010

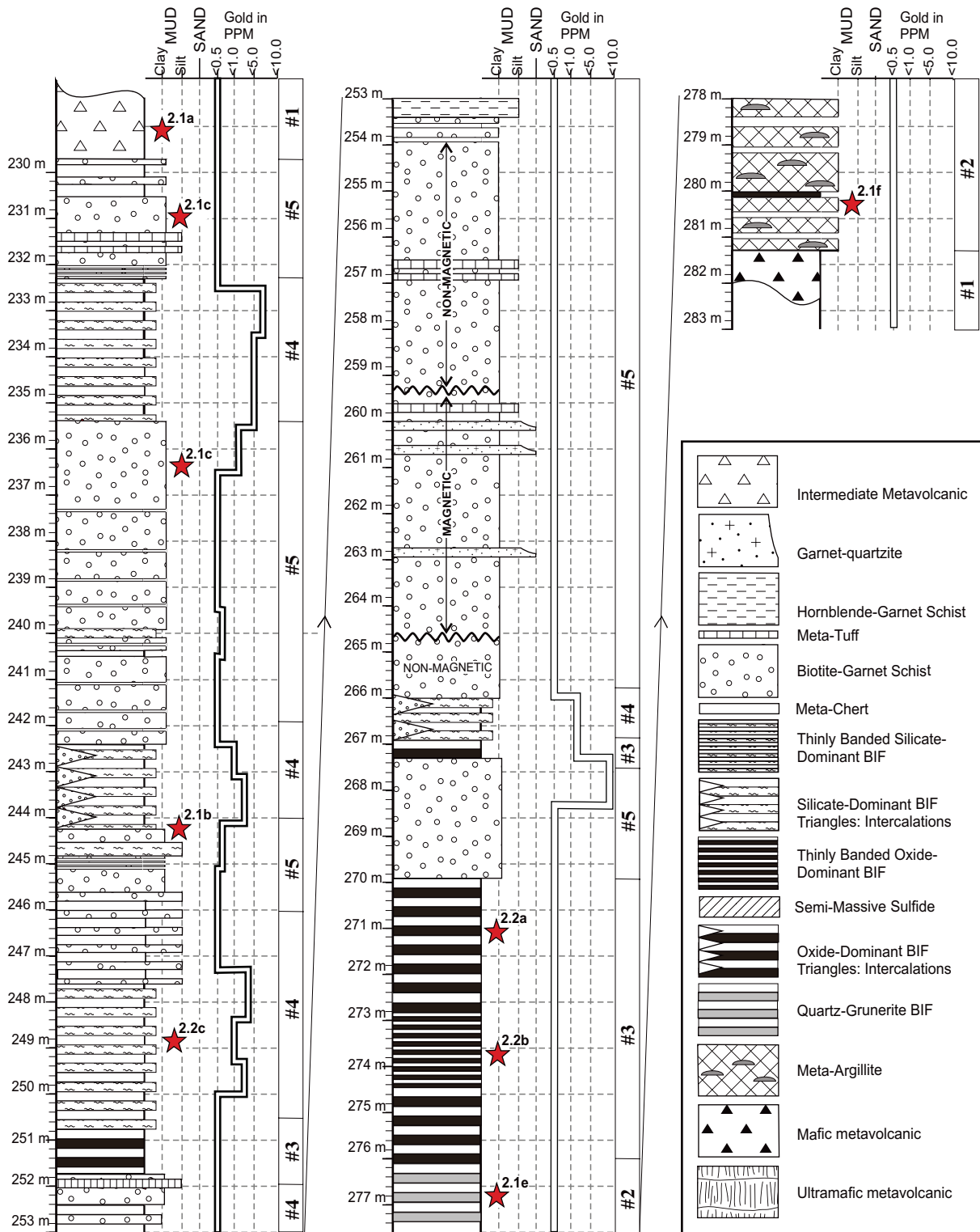
(Fig. 2.1) contains all five lithologic associations and exhibits the best correlations between increased gold values and silicate-dominant BIF.

Re-logging of these drill cores was carried out by the author over several trips to the mine during 2006. Detailed logging was undertaken with the intention of observing preserved primary lithologic features, normally not considered by core loggers, in order to glean information on original depositional environment such as: the changing conditions contributing to the deposition of the NIF assemblage as well as the relationships between the lithologies.

## 2.2. Detailed Stratigraphy of NIF

Few strictly original sedimentary depositional features are preserved at Musselwhite Mine due to the grade of metamorphism and the transposed nature of the rocks. However, in addition to original geochemical gradients, relatively resilient sedimentary structures, such as metamorphosed chert bands, are abundant. Graded bedding, in the biotite-garnet schist and the garnet-bearing quartzite, which can be interpreted as a type of geochemical gradient, is a commonly preserved feature. It is indicated by varying concentration of garnet and can be used as a way-up indicator.

Assessment of the four detailed stratigraphic logs reveals that the lithologies in the NIF assemblage can be roughly grouped into five dominant lithologic associations. These groupings are based on criteria such as mineralogy and relict sedimentary structures. The most basic criterion for grouping the lithologies into lithologic associations are whether the rocks are volcanic, volcanoclastic or sedimentary in origin. The sedimentary rocks can be broadly divided into; 1) oxide-dominant, 2) siliciclastic-dominant, and 3) transitional oxide- to siliciclastic-dominant. The following subsections describe the lithologic associations observed in the Northern Iron Formation Assemblage. Descriptions focus on the observable primary features and omit later features such as veining and deformation. Also, the prefix 'meta' is dropped from the lithologies.



**Figure 2.1. Detailed stratigraphic log of drill hole 04-ESN-010.** White lines represent Au values. Stars represent location of photographs shown in plates 2.1 and 2.2. Note the lithologic associations to the right of each stratigraphic column, these lithologic associations are described in the text. Top of log is on the upper left.



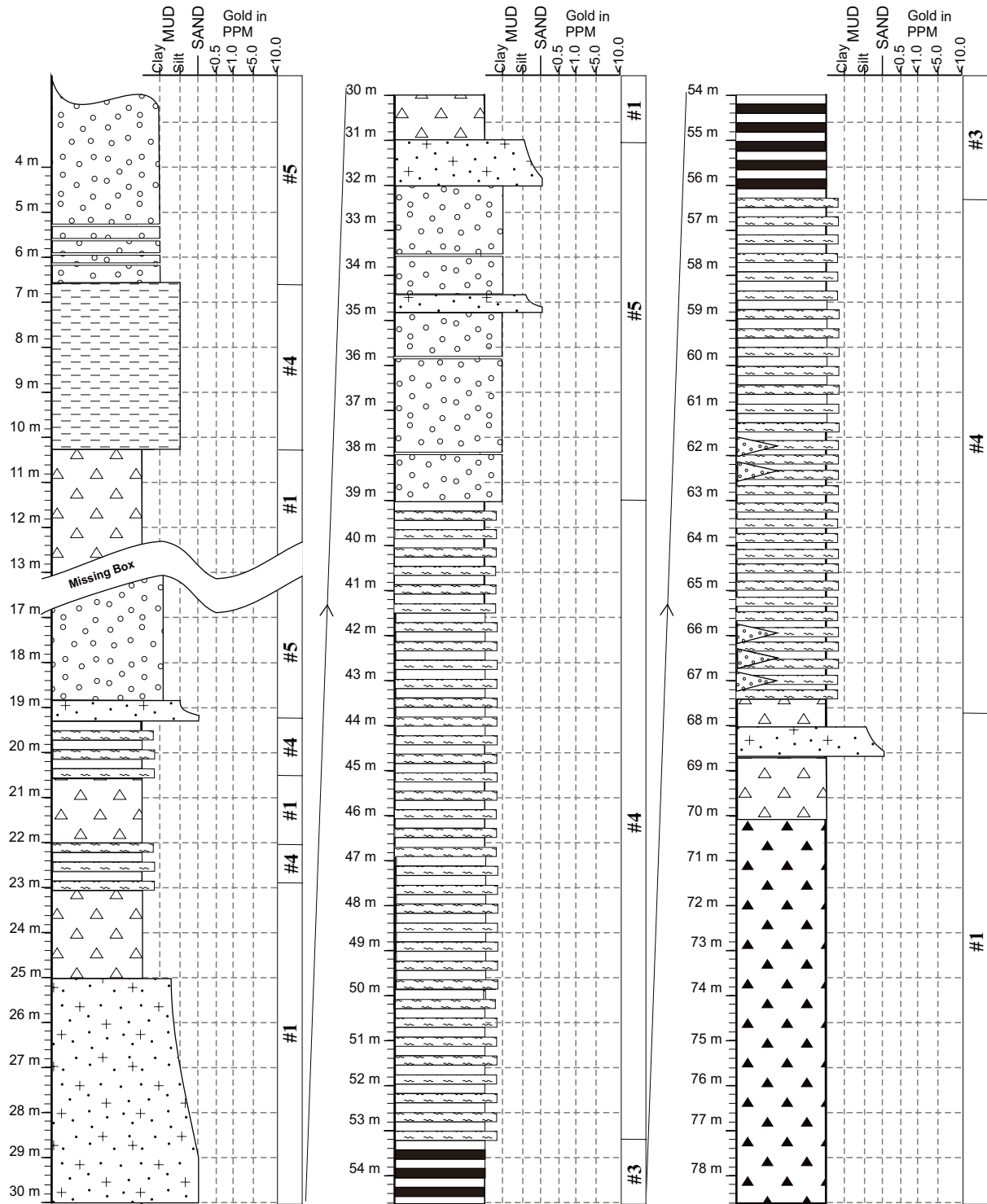
### *2.2.1 Volcanic-Volcaniclastic: Lithologic Association One*

The volcanic-volcaniclastic group of lithologies are found both underlying and overlying the Northern Iron Formation Assemblage. This lithologic assemblage consists of undifferentiated mafic- to intermediate-volcaniclastic flows intercalated with non-volcaniclastic rocks. Metavolcanic material, containing medium-grained biotite-porphyroblasts (Plate. 2.1a), was classified as volcaniclastic material whereas massive mafic-metavolcanic rocks were classified as true volcanic eruptive flows and, in some instances, dykes.

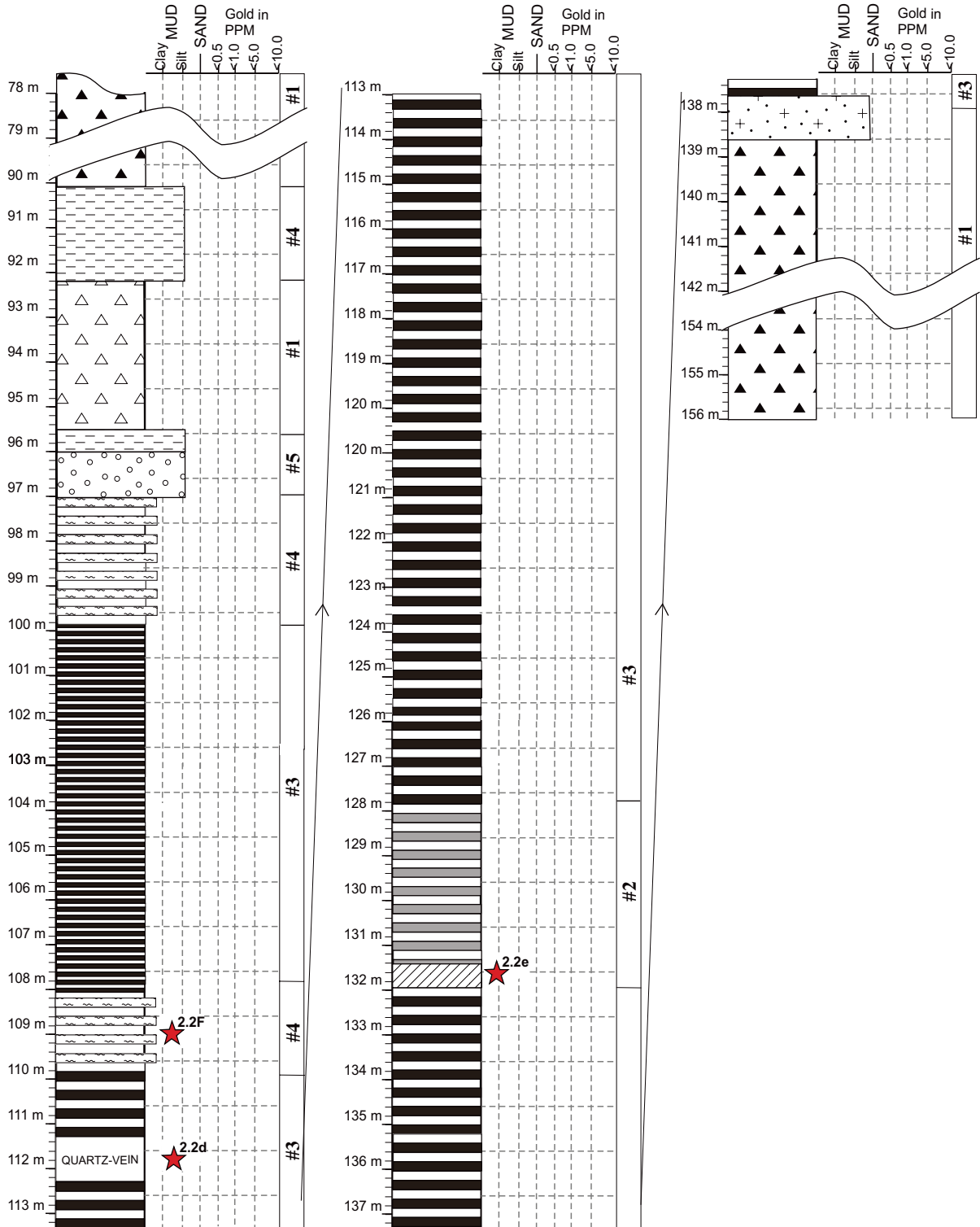
The volcanic-volcaniclastic lithologic grouping occurs in association with the silicate-dominant BIF, the hornblende-garnet schist (Plate 2.1b), and the biotite-garnet schist (Plate 2.1c). There does not appear to be a particular sequence to the stratigraphy as a number of combinations of these lithologies occur. However, the garnet-bearing quartzite (Plate 2.1d) does occasionally occur as an independent unit within the volcanic-volcaniclastic lithologic association.

The connection between garnet-bearing quartzite (Plate 2.1d) and the volcanic-volcaniclastic lithologies is seen in 05-PQE-012 where a package of garnet-bearing quartzite is contained between metavolcanic flows in the following intervals: 25-32m, 67-69m, and 138-139m (see Fig. 2.2). This relationship is again observed in hole 05-PQE-013 in the following intervals: 28-31m (see Fig. 2.3).

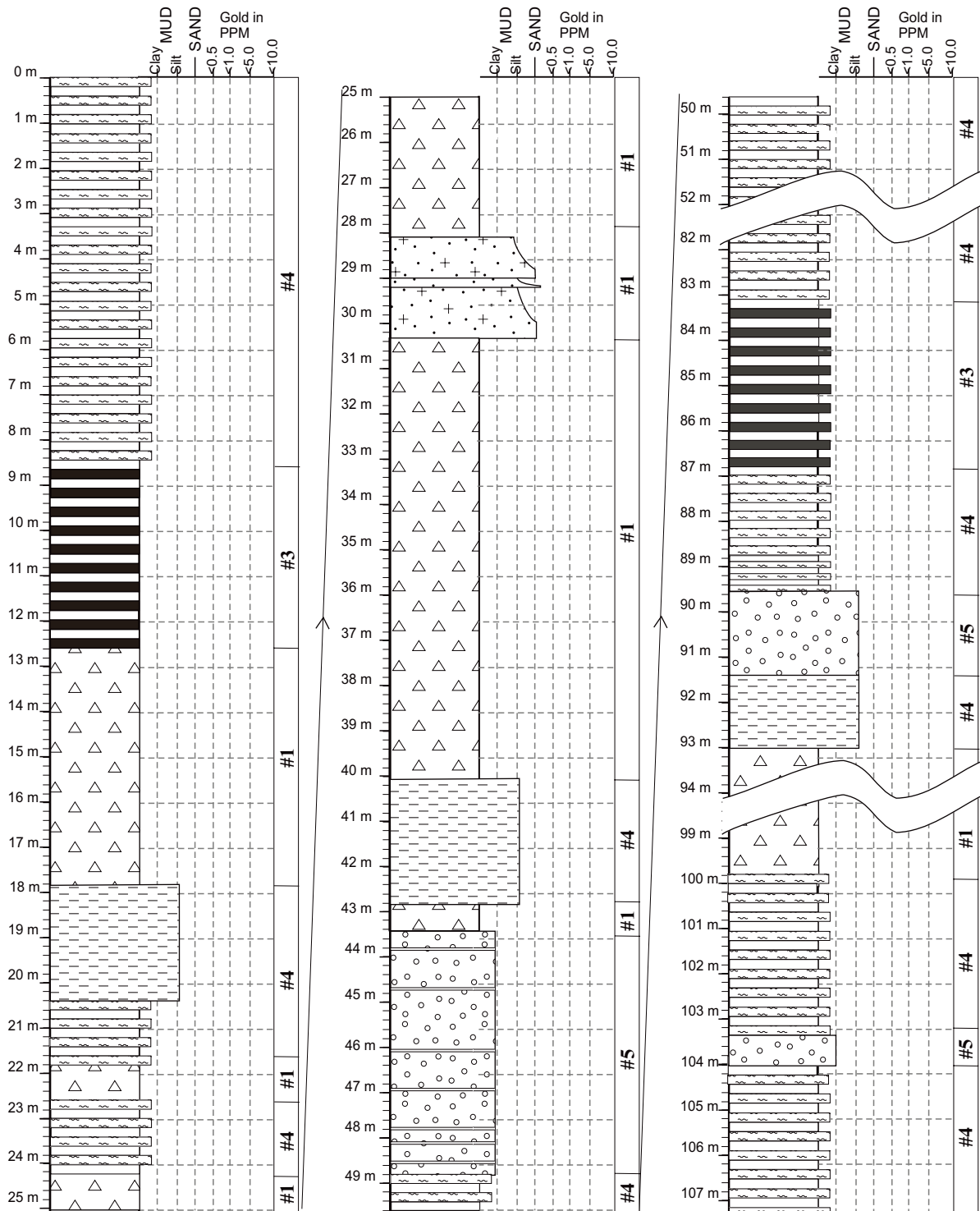
Minor ultramafic rocks are observed in the Northern Iron Formation assemblage and these are grouped into the volcanic-volcaniclastic lithologic association for simplicity. However, these rocks actually represent an ultramafic dyke. Ultramafic rocks from this dyke were observed in hole 06-S2E-002 between 113-114.1m (Fig. 2.4). It should be noted that ultramafic flows are principally present in the lower portion of, as well as below, the NIF assemblage. Ultramafic volcanic lithologies increase in volume, and therefore importance, stratigraphically below the NIF assemblage. This is the opposite trend to the mafic- and intermediate-volcanic flows discussed above.



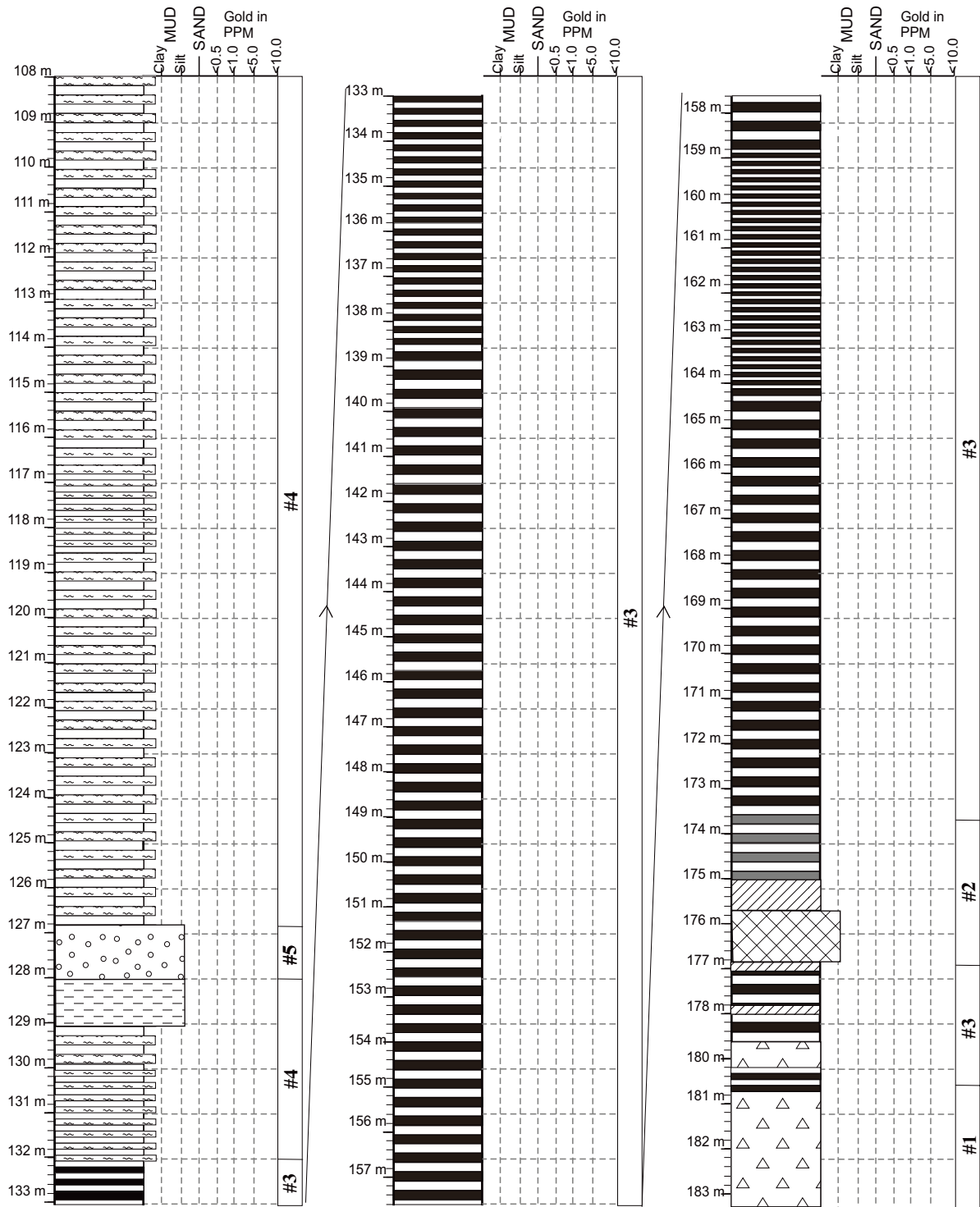
**Figure 2.2. Detailed stratigraphic log of drill hole 05-PQE-012 (refer to Fig. 2.1 for legend).** Note the lithologic associations to the right of each stratigraphic column, these lithologic associations are described in the text. Also the interval between 13-17m was not logged due to a missing box of core. Top of log is on the upper left. Note that mafic volcanic rocks are present between 79-108m in 05-PQE-012.



**Figure 2.2 continued. Detailed stratigraphic log of drill hole 05-PQE-012 (refer to Fig. 2.1 for legend).** Note the lithologic associations to the right of each stratigraphic column, these lithologic associations are described in the text. Stars represent location of photographs shown in Plates 2.1 and 2.2. Also the interval between 78-108m was not logged because it consists of undifferentiated mafic volcanic rock. Top of log is on the upper left.



**Figure 2.3. Detailed stratigraphic log of drill hole 05-PQE-013 (refer to Fig. 2.1 for legend).** Note the lithologic associations to the right of each stratigraphic column, these lithologic associations are described in the text. Also the interval between 74-108m was not logged because it consists of undifferentiated mafic-volcanic rock. Top of log is on the upper left. Note that silicate-dominant BIF exists between 75-108m.



**Figure 2.3. Detailed stratigraphic log of drill hole 05-PQE-013 (refer to Fig. 2.1 for legend).** Note the lithologic associations to the right of each stratigraphic column, these lithologic associations are described in the text. Also the interval between 74-108m was not logged because it consists of undifferentiated mafic volcanic rock. Top of log is on the upper left.

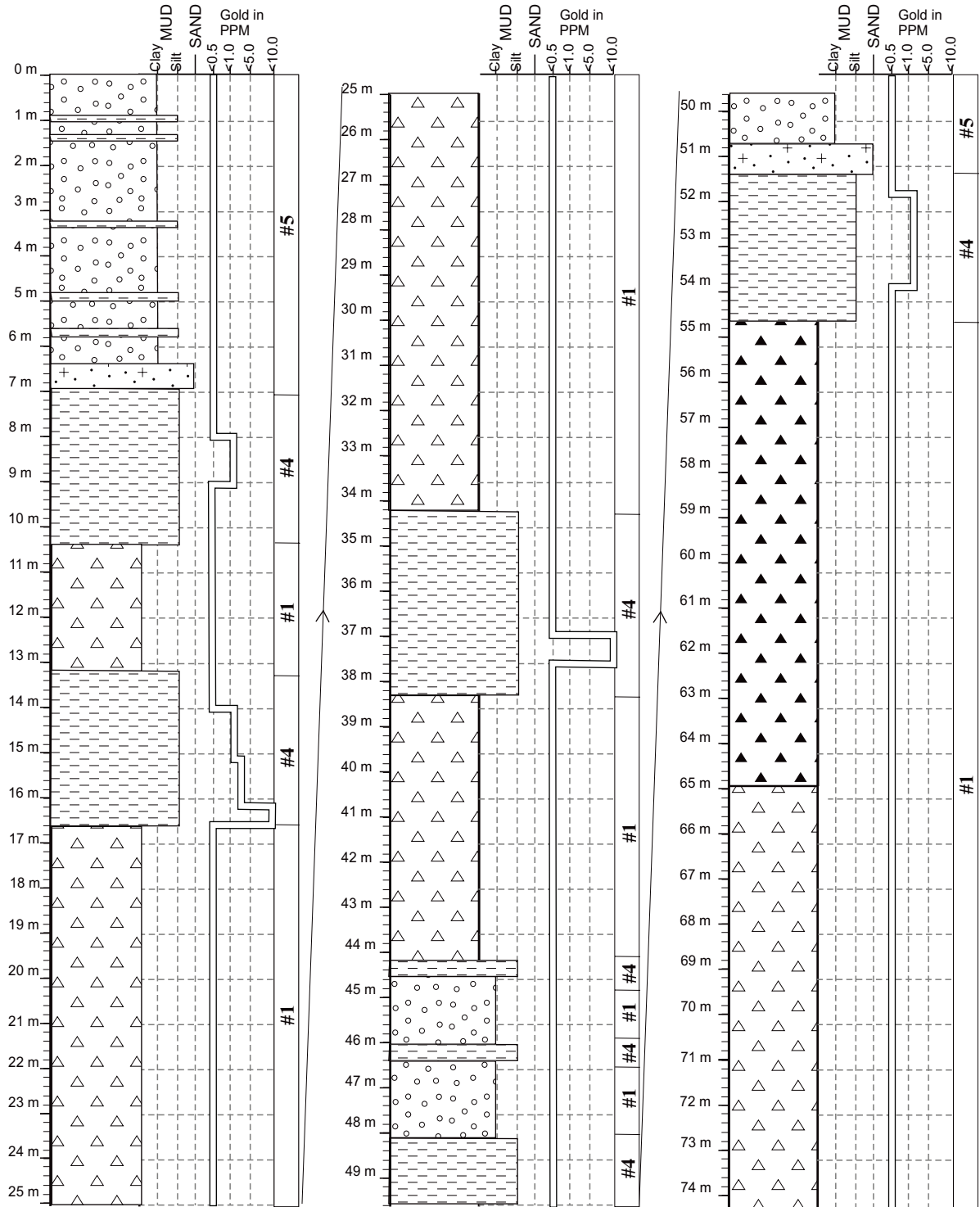
### *2.2.2 Meta-Argillite and Quartz-Grunerite BIF: Lithologic Association Two*

The quartz-grunerite BIF (Plate 2.1e) and meta-argillite (Plate 2.1f) comprise a group of exhalite-dominant lithologies, which form a discontinuous zone basal to the Northern Iron Formation assemblage. This lithologic association consists of sulfide-rich meta-argillite overlain, and intercalated with, quartz-grunerite BIF. The exhalite-dominant lithologies, of lithologic association two, are seen in hole 04-ESN-010 where a package of meta-argillite is overlain by quartz-grunerite BIF in the following interval: 276.4-281.4m (see Fig. 2.2). Lithologic association two is always found in this stratigraphic location, at the bottom of the NIF assemblage, sitting directly on top of volcanic rocks.

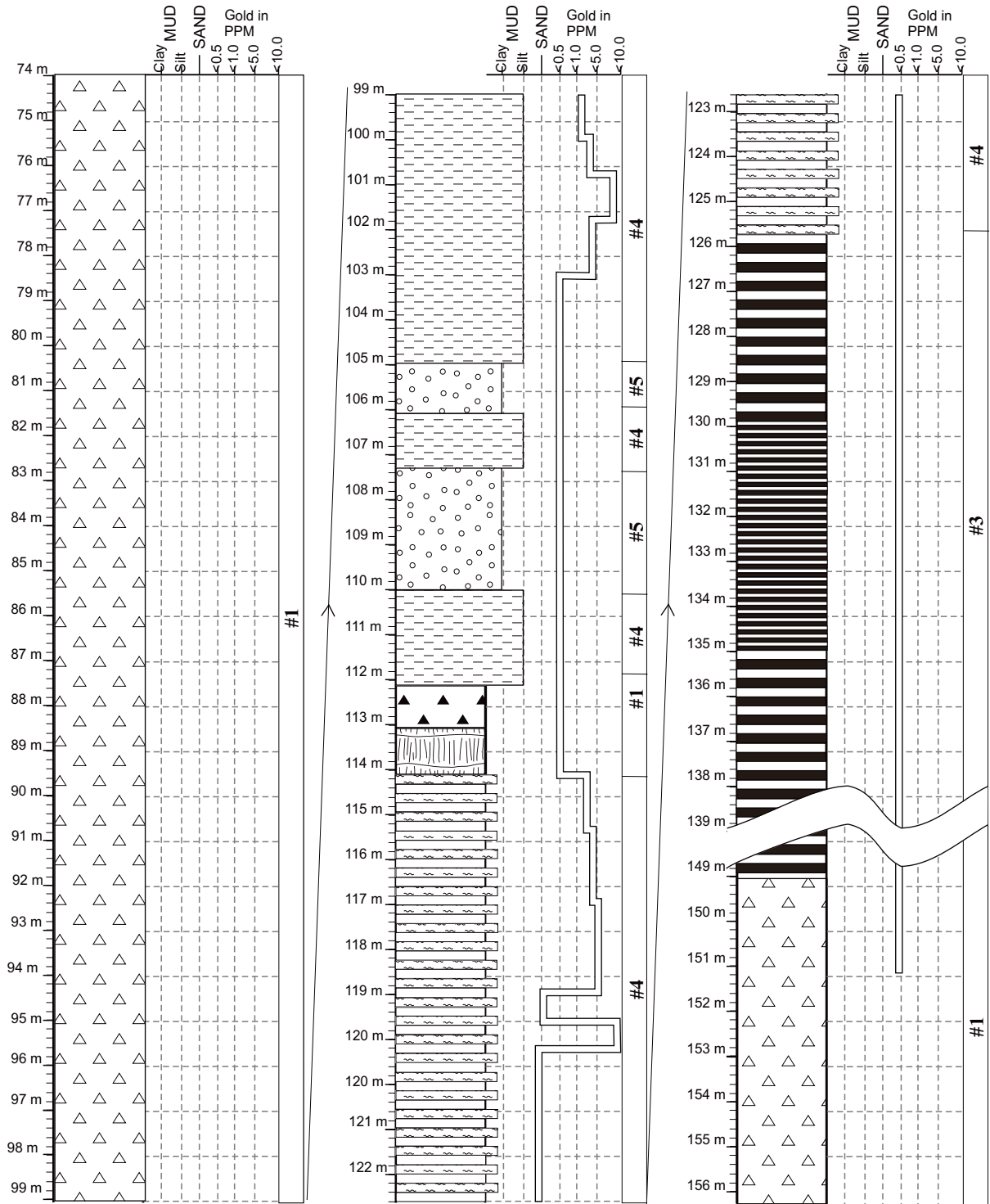
The meta-argillite contains both a high sulfide-content and high degree of siliciclastic material. These two mineralogical, and geochemical, characteristics provide important information on the conditions of formation of this lithology and by extension the establishment of the NIF assemblage. The quartz-grunerite BIF also provides important information on the conditions of deposition. At this point, it should also be noted that the discontinuous nature of this lithologic association communicates important information on the initiation of formation of the NIF assemblage. This will all be discussed in Chapter Five.

### *2.2.3 Thinly- to Thickly-Laminated Oxide-Dominant BIF: Lithologic Association Three*

This lithologic association is the main exhalite component, by volume, of both the NIF and SIF assemblages (John Biczok, personal communication, 2007). Lithologic association three consists of oxide-dominant BIF (Plate 2.2a and 2.2b) composed of alternating bands of quartz and magnetite. The magnetite and quartz bands can be considered independent lithologies that together form banded iron formation. The banded nature should be noted as it is the result of changing environmental conditions during the deposition of this lithology. These environmental conditions are discussed in detail in Chapter Five.



**Figure 2.4. Detailed stratigraphic log of drill hole 06-S2E-002 (refer to Fig. 2.1 for legend). White lines represent Au values. Note the lithologic associations to the right of each stratigraphic column; these lithologic associations are described in the text. Top of log is on the upper left.**



**Figure 2.4. Detailed stratigraphic log of drill hole 06-S2E-002 (refer to Fig. 2.1 for legend). White lines represent Au values. Note the lithologic associations to the right of each stratigraphic column; these lithologic associations are described in the text. Interval 139-149m is shortened to conserve space. Top of log is on the upper left.**



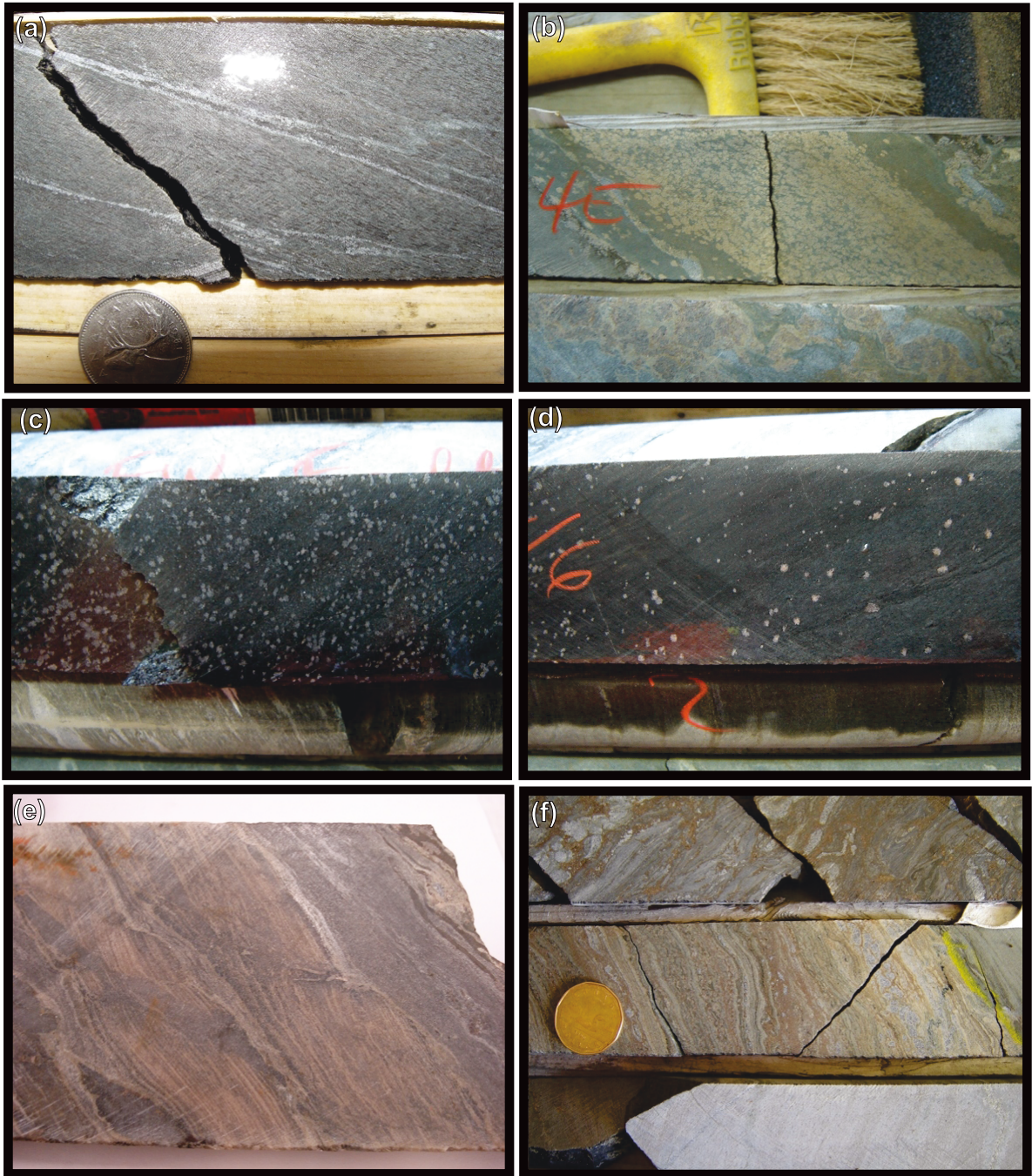
Commonly observed variations, in lithologic association three, involve different forms of the oxide-dominant BIF, namely variable thickness of the quartz and magnetite bands composing this lithology. The thickly-banded version (Plate 2.2a) predominates over the thinly-banded version of oxide-dominant BIF (Plate 2.2b). In general the thinly-banded variety is found halfway up the horizon and gradually becomes more clastic rich with increasing height (John Biczok, personal communication, 2007).

The intercalation of thinly-laminated and thickly-laminated, oxide-dominant BIF is seen in 04-ESN-010 where a package of thinly-laminated BIF is contained between thicker-laminated BIF in the following interval: 276-276.4m (see Fig. 2.1). This relationship is again observed in hole 05-PQE-012 in the following interval: 103-137m (see Fig. 2.3), as well as in hole 06-S2E-002 between 126-149m (Fig. 2.4).

Minor intercalations of siliciclastic-dominant BIF are observed in the oxide-dominant BIF. This relationship can be seen in hole 05-PQE-012 between 108-111m (Fig. 2.2). The opposite relationship is also seen, where intercalations of oxide-dominant BIF are contained in thicker sequences of silicate-dominant BIF. This relationship is seen in hole 04-ESN-010 between 250-252m and 266-268m (Fig. 2.1). The presence of intercalated silicate-dominant BIF (Plate 2.2c), in the oxide-dominant BIF, may be an indication of changes in the redox conditions. This topic will be discussed in detail in Chapter Five.

Like most lithologies in the NIF assemblage, the oxide-dominant BIF of lithologic association three, contains later epigenetic quartz-veins, some of which contain visible gold (Plate 2.2d).

Brecciated, semi-massive sulfide veins containing pyrrhotite  $\pm$  arsenopyrite (Plate 2.2e) are unique to lithologic association three. Examples of brecciated semi-massive sulfide bands in the oxide-dominant BIF of lithologic association three are seen in hole 05-PQE-012 between 131-133m (Fig. 2.2) and hole 05-PQE-013 between 175-179m (Fig. 2.3). The semi-massive sulfide veins occur in the lower-portion of the oxide-dominant BIF and may represent remobilized sulfide from the meta-argillite of lithologic association two.



**Plate 2.1. Photographs of various lithologies from the Northern Iron Formation Assemblage of the Musselwhite gold deposit. The diameter of the core is 4.5cm. a) Intermediate metavolcanic (note biotite porphyroblasts), b) Hornblende-garnet schist, c) Biotite-garnet schist, d) Garnet-Quartzite, e) Quartz-grunerite banded iron formation, f) Meta-argillite.**

#### *2.2.4 Oxide/Silicate-BIF and Silicate-Dominant BIF: Lithologic Association Four*

The silicate-dominant BIF (Plate 2.2c) and the underlying and comparatively minor discontinuous oxide/silicate-transitional BIF (Plate 2.2f) compose a group of lithologies containing both a siliciclastic and exhalite component (Otto, 2002). Collectively these lithologies make up lithologic association four.

The silicate-dominant BIF is usually composed of grunerite and garnet-rich bands ( $\pm$  hornblende, biotite) alternating with quartz-bands, whereas the oxide/silicate-transitional BIF consists of thinly-banded quartz and magnetite bands intercalated with hornblende-garnet schist. This transitional BIF is in gradational contact with both the oxide- and silicate-dominant BIFs with amphibole-garnet layers becoming more numerous stratigraphically upward in this lithology. Please refer to Chapter Three for more detailed petrologic descriptions of these lithologies.

The transitional exhalite/siliciclastic lithologies, of lithologic association four, are usually observed in drill-core. In drill core lithologic association four can occur as a small package within the biotite-garnet schist. This relationship is seen in hole 04-ESN-010, between 230-268m (Fig. 2.1), where several small units of silicate-dominant BIF are intercalated in a larger biotite-garnet schist unit. A similar affiliation is seen in hole 05-PQE-012 between 4-10m (Fig. 2.2).

Note that, although not shown in the stratigraphic logs of Chapter Two, lithologic association four can also occur within the volcanic/volcaniclastic units above the NIF assemblage. It occurs as roughly four small hornblende-garnet schist ( $\pm$  silicate-dominant BIF) units intercalated within the volcanic-volcaniclastic lithologic association stratigraphically overlying the NIF assemblage.

However, it is more common to find lithologic association four as a thick and relatively homogeneous package in gradational contact with the lithologies of assemblage three. This relationship is seen in hole 05-PQE-012, between 48-62m (Fig. 2.2), where two large units of silicate-dominant BIF encompass a smaller oxide-dominant BIF unit. A

similar affiliation, except with silicate-dominant BIF overlying oxide-dominant BIF, is seen in hole 05-PQE-013 between 0-13m and 49-180m (Fig. 2.3), as well as hole 06-S2E-002 between 114-149m (Fig. 2.4).

Lithologic association four records an increase in the amount of siliciclastic sedimentation taking place in the Northern Iron Formation during this time. Therefore lithologic association four records the shift from one facies to another. Again this is elaborated on in Chapter Five.

#### *2.2.5 Hornblende-Garnet Schist, Biotite-Garnet Schist, and Garnet-bearing quartzite: Lithologic Association Five*

The hornblende-garnet schist (Plate 2.1b) and biotite-garnet schist (Fig. 2.1c) form a group of lithologies composed mainly of a siliciclastic constituent, whereas the garnet-bearing quartzite (Fig. 2.1d) is composed of volcanoclastic material. These lithologies lack a banded nature and have a massive, porphyroblastic, appearance. Collectively the lithologies make up lithologic association five. The siliciclastic lithologies of lithologic association five are relatively iron-rich compared to normal, purely siliciclastic, sedimentary. These lithologies are confined to the stratigraphically uppermost portion of the Northern Iron Formation assemblage. Please refer to Chapter Three for a more detailed petrologic description of each lithology and Chapter Four for their geochemical relationships.

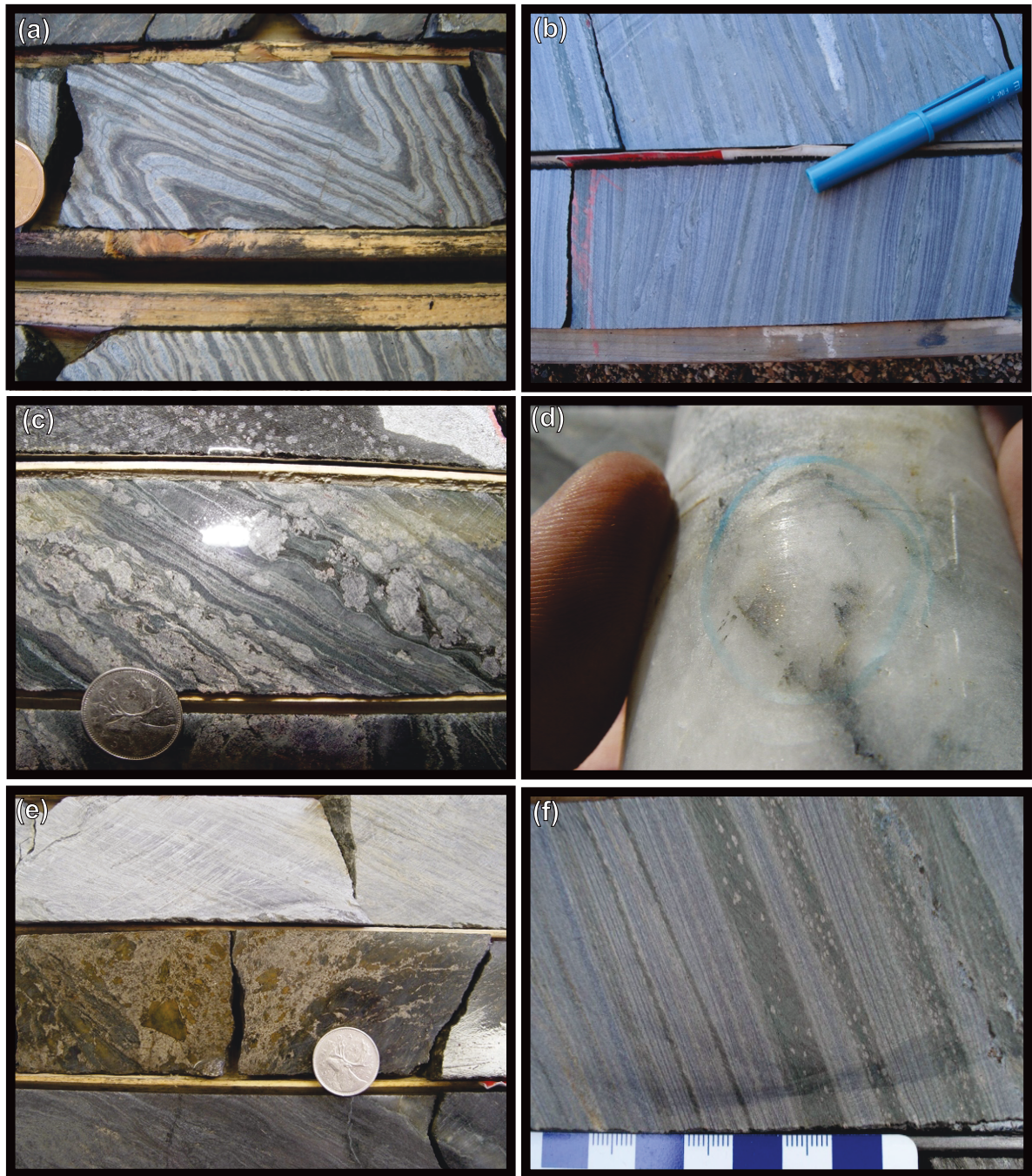
By volume the biotite-garnet schist is the dominant lithology in lithologic association five with the other two lithologies typically occurring as centimetre to decimetre-scale intercalated bands. Varying garnet content in the biotite-garnet schist possibly indicates variations in the original clay content and may provide a way-up indicator. It is important to note that the biotite-garnet schist ranges from magnetic to non-magnetic (see hole 04-ESN-010, interval 245-264m) as this has implications for the conditions during its deposition. These conditions of deposition and the varying garnet content are discussed, in more detail, in Chapter Five.

Lithologic association five displays the most diverse nature out of the various lithologic associations. In addition to the three lithologies that compose this lithologic association, it also contains intercalated units of the following non-associated lithologies: volcanic, oxide- and silicate-dominant BIF, as well as quartz-rich bands and tuffaceous bands. The diverse nature of lithologic association five is displayed pre-eminently in drill-holes 04-ESN-010 and 05-PQE-012.

In hole 04-ESN-010, between 230-270m (Fig. 2.1), multiple intercalated units, not associated with lithologic association five, occur in a broader package of biotite-garnet schist. These include several units of oxide- and silicate-dominant BIF, as well as disperse quartz and tuffaceous bands. A similar, but much simpler, situation occurs in hole 05-PQE-012, between 4-39m (Fig. 2.2), several intercalated units, not associated with lithologic association five, occur in a broader package of biotite-garnet schist. These include several units of silicate-dominant BIF, mafic and felsic volcanic rocks.

Additional minor, but important, lithologies occur in association five. Disperse quartz-rich bands, representing meta-chert, are present. Examples of quartz-rich meta-chert bands in siliciclastic-dominant lithologies are seen in hole 04-ESN-010 between 236-242m. Minor tuffaceous bands, based their quartz-rich nature, also occur in the biotite-garnet schist. These tuffaceous bands only occur in lithologic grouping five. Examples of tuffaceous bands in siliciclastic-dominant lithologies are seen in hole 04-ESN-010 between 231-232m and 256-260m.

It should be noted that the garnet-bearing quartzite also occurs as a unit within the biotite-garnet schist. These two lithologies commonly exhibit graded-contacts and likely represent a continuum from one respective lithology to the other. Note that the garnet-bearing quartzite is quartz-rich, whereas the biotite-garnet schist is mica-rich. This mineralogical difference has important implications for formation of the original sediment, as well as relationships between lithologic associations one and two, and is discussed in more detail in Chapter Five.



**Plate 2.2. Photographs of various lithologies from the Northern Iron Formation Assemblage of the Musselwhite gold deposit. The diameter of the core is 4.5cm. a) Thickly-banded oxide-dominant banded iron formation, b) Thinly-banded oxide-dominant banded iron formation, c) Silicate-dominant banded iron formation, d) Quartz-vein containing gold, collected from within oxide-dominant BIF unit, e) Late stage sulfide-rich breccia, f) Transitional oxide/silicate-dominant BIF .**

Additionally, centimetre- to decimetre-scale tuffaceous bands occur in association with the garnet-bearing quartzite in the biotite-garnet schist. These bands are typically centimetre- to decimetre-scale and are therefore too thin to break out as a separate lithologic grouping. However, their presence in the stratigraphy is important, and is elaborated on in Chapter Five.

The connection between garnet-bearing quartzite (Plate 2.1d), the biotite-garnet schist (Fig. 2.1c), and the tuffaceous lithologies is seen in 04-ESN-010, between 260-265m, where several small units of garnet-bearing quartzite and tuff are contained in a thicker biotite-garnet schist unit. This relationship is also observed in hole 05-PQE-012 between 31-40m.

### 2.3 Chapter Summary

The lithologic associations described above likely represent different sedimentary facies. These facies are the product of shifting environmental and depositional conditions. The changing environmental and depositional conditions controlled which types of lithologies could physically and chemically be deposited. Please refer to Chapter Five for a more detailed and in-depth discussion on the topic of facies change as it relates to the stratigraphy of the Northern Iron Formation Assemblage.

The lithologic associations observed are not confined to a strict stratigraphic order especially in the upper reaches of the NIF assemblage. It is clear from observing the drill core that one lithology, or lithologic association, may predominate but can be broken up by the presence of an unrelated lithology or group of lithologies. However, some general trends are noticeable.

Lithologic association two, when present, is always at the base of the NIF assemblage (John Biczok, personal communication, 2007). Lithologic association three is always present in the lower portion of the NIF assemblage. This is observable in Figures. 2.1 to 2.4. However, lithologic association three can also occur as a minor package

stratigraphically higher up in the NIF assemblage as seen in 04-ESN-010 at 251m and 267m. Similarly, lithologic association four is always observed in gradational contact with lithologic association three. This is observable in Figures 2.2 to 2.4 with a particularly superior example seen in hole 05-PQE-013 between 49-178m. Lithologic association four, more so than lithologic association three, can occur as a minor package stratigraphically higher in the NIF assemblage as seen in 04-ESN-010 between 231-270m. Lithologic association five is always observed at the top of the Northern Iron Formation Assemblage. It is the most complex lithologic grouping as it commonly contains intercalated lithologies which are not restricted to this particular lithologic association.

Gold mineralization, at Musselwhite, predominantly occurs in the silicate-dominant BIF (Andrew Cheatle, personal communication, 2007). As mentioned in Section 2.2.4 the silicate-dominant BIF is part of lithologic association four. In the current study, the most convincing relationship between the silicate-dominant BIF of lithologic association four and gold mineralization is observed in hole 04-ESN-010 (Fig 2.1). In this hole gold values decrease rapidly away from the silicate-dominant BIF regardless of surrounding lithologies. This relationship is seen in multiple intervals between 230m and 270m with gold values being minor in the biotite-garnet schist, but displaying excellent correlation with intervals of silicate-dominant BIF (Fig. 2.1).

Another excellent example of the correlation between increased gold-values and the silicate-dominant BIF, of lithologic association four, is observed in hole 06-S2E-002 between the interval 114m to 149m. Gold values are particularly high in the stratigraphically upper portion of the silicate-dominant BIF, but are minor in both the immediately overlying and underlying lithologic units.



## **Chapter 3**

### **Petrologic Characteristics of the Lithologies**

#### **3.1 Introduction**

Chapter Three presents macroscopic, petrographic, mineral and whole rock geochemical data for the metasedimentary lithologies collected from the Musselwhite gold deposit. This chapter is subdivided by lithology with the lithologies presented from stratigraphically lowest to highest. For a detailed description of the Northern Iron Formation Assemblage stratigraphic succession please refer to Chapter Two.

Petrologic observations are based on the study of 123 hand samples, 123 whole rock geochemical analysis, and 91 thin-sections. In addition 24 thin-sections from Hollings and Kerrich (1999) were looked at, for reference, but not described. Please refer to Appendix A for sample descriptions, Appendix B for thin-section descriptions, Appendix C for scanning electron microscope-energy dispersive spectrometer (SEM-EDS) data, and Appendix D for geochemical data.

The objectives of Chapter Three revolve around detailed characterization of the intrinsic qualities of the individual lithologies. The information presented in this chapter will be built upon and analysed in the proceeding chapters.

#### **3.2 ‘Southern Iron Formation’ Assemblage Oxide-Dominant BIF**

##### **3.2.1 Macroscopic Characteristics**

The SIF assemblage oxide-dominant BIF is a magnetite-rich oxide-dominant BIF (Plate 3.1). It is a strongly magnetic unit. The SIF assemblage oxide-dominant BIF is visually distinct due to its thinly-layered nature. This lithology is typically well layered with distinct contacts between magnetite- and quartz-layers. It consists of alternating layers, on the order of 0.1-0.5cm thick, of dark grey magnetite and cream to white meta-chert which impart a distinct black and white striped appearance to the unit (mine terminology

‘zebra striped’); (Plate 3.1a-f). The SIF assemblage oxide-dominant BIF can also be thickly-layered, but this may be due to structural deformation. Open to tight folding (Plate 3.1c, d) and slightly sheared fabric (Plate 3.1e) is observed in several samples. The SIF assemblage oxide-dominant BIF is observed underground in one drift and a single sample was collected from this locality (SIF-PM05-063; Plate 3.1f). The rest of the samples were collected from drill-core.

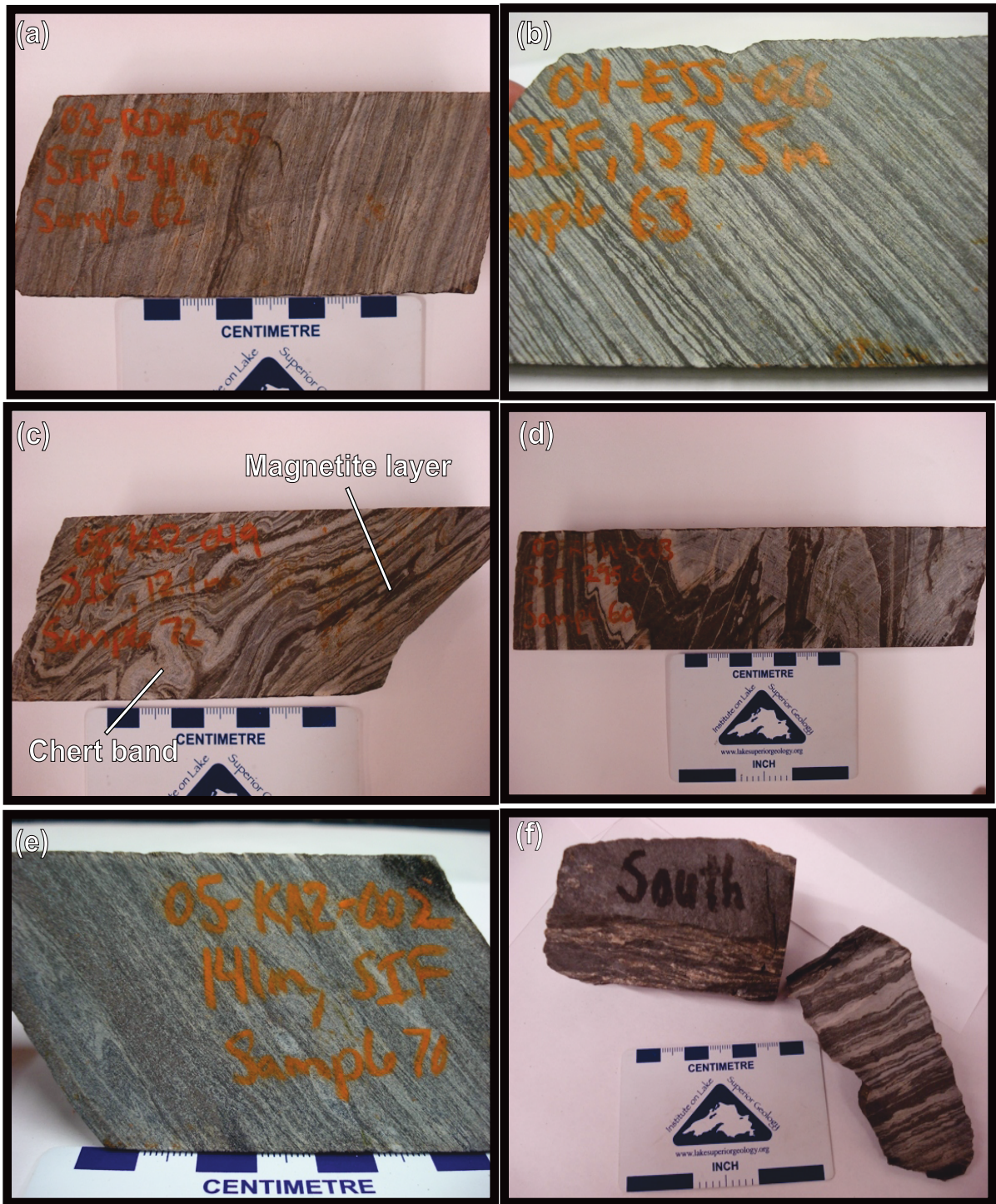
This lithology on average consists of 40% quartz layers and 60% magnetite layers. The Southern Iron Formation, in terms of mineralogy, is simple as it is dominated by magnetite and quartz, but also contains Fe-carbonate, minor garnet and feldspar. Previous workers (Klipfel, 2002b) indicated that the carbonate content increases in the lower part of the SIF assemblage oxide-dominant BIF. Compositional layering is well developed in the SIF assemblage oxide-dominant BIF with defined contacts between the various layers. Layers can be divided into; 1) magnetite dominated layers, 2) quartz dominated layers (meta-chert), and 3) iron-silicate reaction layers occurring between quartz- and magnetite-dominant layers.

#### *Magnetite layers*

Depending on the degree of deformation, magnetite compositional layers range from weakly to strongly defined in the SIF assemblage oxide-dominant BIF. Primary disseminated pyrrhotite is confined to the magnetite-layers, whereas secondary pyrrhotite occurs in fractures crosscutting both magnetite- and quartz-layers.

#### *Quartz Layers*

Depending on the degree of deformation, quartz-layers range from weakly to strongly defined in the SIF assemblage oxide-dominant BIF. Quartz-layers in the SIF oxide-dominant BIF are non-translucent cream coloured, have a rather sugary-texture, and are commonly boudinaged. The quartz-layers contain disseminated carbonate as the layers effervesce when acid is applied. These layers also contain disseminated magnetite as they weakly attract a handheld magnet. ns (Plate 3.2e).



**Plate 3.1. Photographs of Southern Iron Formation oxide-dominant BIF collected from Musselwhite mine.** a) magnetite-rich, thinly laminated and slightly deformed Southern Iron Formation oxide-dominant BIF (sample SIF-07-20-062), b) Characteristic black and white ‘zebra striped’ pattern (sample SIF-07-20-063), c) Open folds in Southern Iron Formation oxide-dominant BIF (sample SIF-07-20-072), d) Open folds in Southern Iron Formation oxide dominant BIF (sample SIF-07-20-060), e) Sample showing strong deformation of Southern Iron Formation oxide-dominant BIF (sample SIF-07-20-070), f) Southern Iron Formation oxide-dominant BIF collected from underground workings (sample SIF-PM05-063).

### *Grunerite Layers*

Grunerite-layers are found between the magnetite- and quartz-layers. They typically have a tan-yellow appearance and range between 0.1cm to 0.4cm in thickness (approximately half as thick as average quartz- and magnetite- layers). These layers consist of fine- to medium-grained grunerite grains with lesser amounts of carbonate.

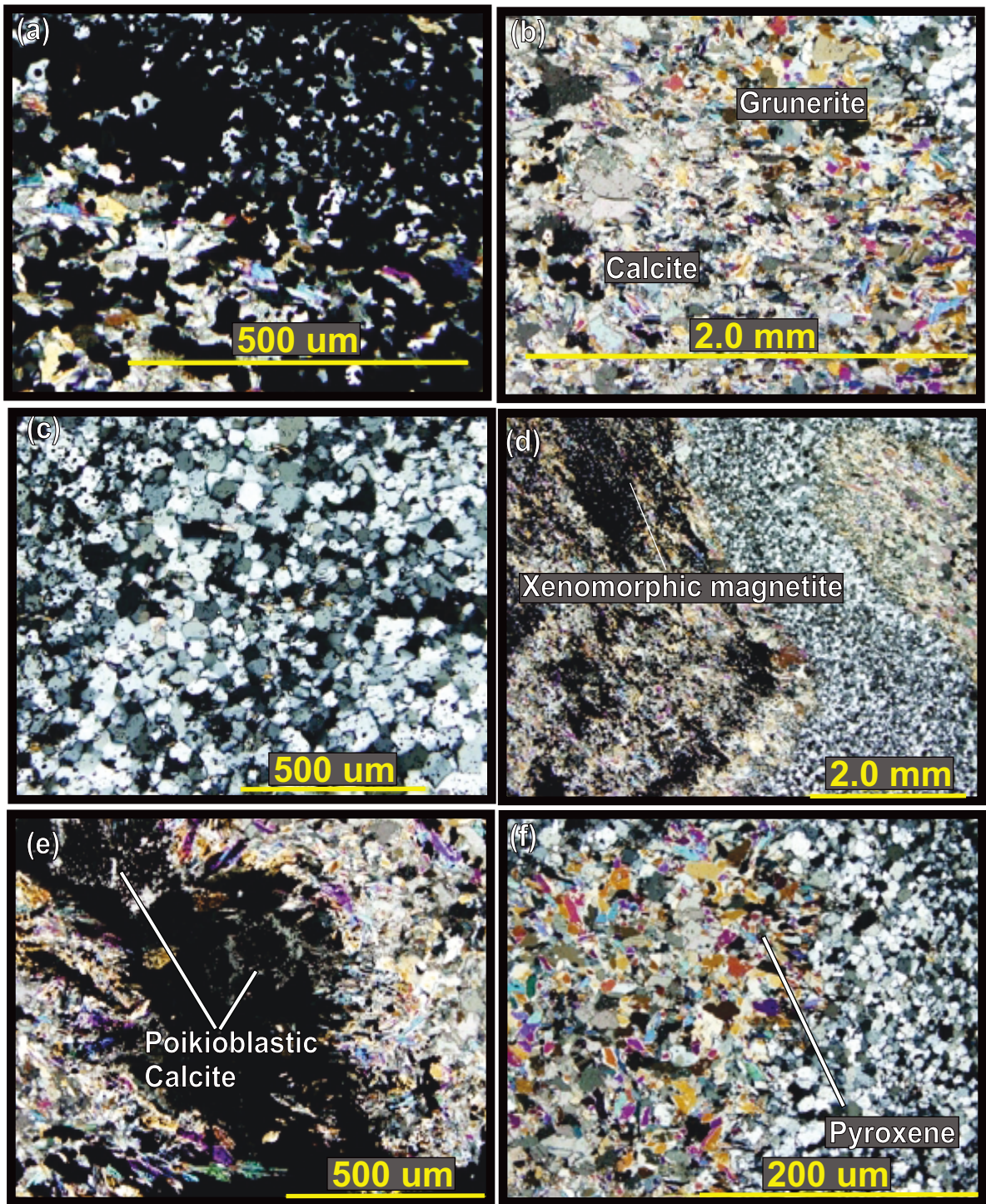
### 3.2.2 Petrographic Characteristics

Petrographic observations are based on four thin-sections of the SIF assemblage oxide-dominant BIF. Thin-sections were only made from samples sent for geochemical analysis. Representative samples, exhibiting a range of commonly observed features such as layering, folding, and shear fabrics, were specifically selected. Please refer to Appendix B for the individual thin-section descriptions.

On a microscopic level samples of the SIF oxide-dominant BIF are a reflection of the macroscopic appearance of the lithology. They consist of 60% magnetite and 40% quartz and Fe-silicate minerals. In thin-section this lithology is compositionally layered with three types of layers prevailing; 1) magnetite-dominated (Plate 3.2a), 2) grunerite-pyroxene- carbonate-dominated (Plate 3.2 b), and 3) quartz-dominated (meta-chert) (Plate 3.2c).

### *Magnetite layers*

Magnetite layers are typically zoned, consisting of a relatively intact core of fine-grained magnetite and quartz grains surrounded by a rim of xenomorphic magnetite, quartz, and grunerite grains (Plate 3.2d). The rim assemblage is transitional to the grunerite-pyroxene-carbonate layers (described below). On average the magnetite layers are between 0.5-1.0cm thick and contain 80% to 90% magnetite grains, 10% to 20% quartz grains and <5% grunerite and carbonate grains. Carbonate minerals are often found as single poikiloblastic-grains containing euhedral magnetite grains (Plate 3.2e).



**Plate 3.2. Photomicrographs of Southern Iron Formation oxide-dominant BIF, sample SIF-07-20-072, collected from Musselwhite mine.** a) Magnetite-rich layer from Southern Iron Formation showing magnetite, quartz, and grunerite grains (xpl), b) Reaction layer found between quartz and magnetite layers showing calcite and grunerite grains (xpl), c) Quartz layer showing relatively undeformed quartz grains with well developed triple point junctions as well as very fine-grained and disseminated magnetite, grunerite, and calcite (xpl), d) Fine-grained xenomorphic magnetite grains (xpl), e) Poikiloblasts of calcite found within magnetite layers (xpl), (f) Grains of orthopyroxene found in the fold nose of a reaction layer (xpl).

### *Quartz layers*

Quartz layers, like the magnetite layers, are typically zoned. These layers consist of fine-grained quartz with minor disseminated magnetite, grunerite, and carbonate grains (Plate 3.2c). On average the quartz layers are between 0.2-1.0cm thick and contain >95% quartz grains with <5% magnetite, grunerite, and carbonate grains. Quartz grains are fine-grained in the centre of the layer and coarser grained nearer the margins of the layer. Grains range between 0.03-0.05mm in diameter, display moderately developed triple point junctions, and are characterized by planar grain boundaries.

Very fine-grained magnetite, grunerite, and carbonate grains are disseminated throughout the quartz layers. Grains of these minerals are much finer grained than the quartz grains and are found along grain boundaries rather than as inclusions. Grunerite grains are needle-like to euhedral diamond-shaped (Plate 3.2c), whereas magnetite and carbonate grains are subhedral, equidimensional grains.

Thin quartz-veins perpendicularly crosscut the quartz layers. These veins are distinguished from quartz layers by their coarser grain size and linear nature. Pyrrhotite is mainly associated with these crosscutting quartz veins, as well as fractures in the SIF assemblage oxide-dominant BIF. Minor chalcopyrite and pyrite are associated with the pyrrhotite as annealed grains.

### *Grunerite-pyroxene-carbonate layers*

These layers (Plate 3.2b) are principally composed of iron-rich silicate minerals, primarily grunerite with lesser amounts of pyroxene, as well as carbonate,  $\pm$  hornblende, plagioclase, and potassium feldspar. Sporadic plagioclase (<1%) is also observed. The layers are generally 0.1-0.4cm thick which is less than half the width of the above described quartz and magnetite layers. The grunerite-pyroxene-carbonate layers always occur between quartz and magnetite layers and the grains in these layers are coarser grained than the grains in the quartz and magnetite layers.

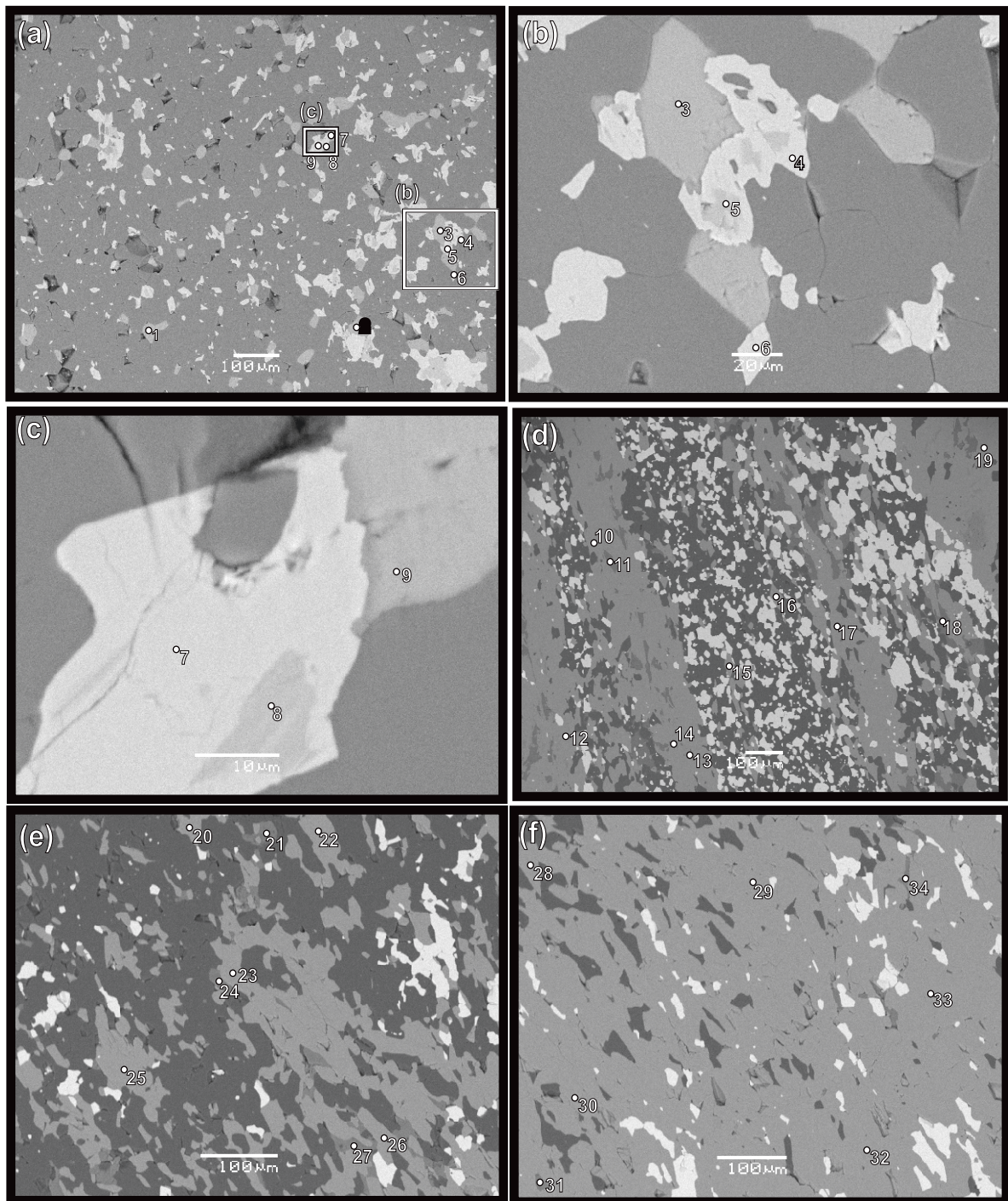
Fine- to medium-grained grunerite grains occur as both laths and typical euhedral amphibole ‘diamond’ shapes. These grains have 54/126° cleavage, well developed twinning, and high birefringence characteristic of grunerite. Grunerite laths, sometimes in ‘fan’ shaped aggregates, are commonly found at the edges of the grunerite-pyroxene-carbonate layers radiating into the quartz layers. Fine- to medium-grained, anhedral to subhedral, orthopyroxene grains compose a minor percentage of the grunerite-pyroxene-carbonate layers. In the SIF assemblage oxide-dominant BIF orthopyroxene grains are first- to second-order yellow-orange in colour, exhibit well developed cleavage, and have parallel extinction. This mineral’s occurrence is primarily confined to ‘fold noses’ of deformed grunerite-pyroxene-carbonate layers (Plate 3.2f).

Carbonate grains are, on average, the coarsest-grained mineral in the SIF. Carbonate grains are confined to the centre of the layers and exhibit characteristic well-developed calcite twinning with high-birefringence. This mineral is a significant component, composing up to  $\leq 40\%$ , of the grunerite-pyroxene-carbonate layers.

### 3.2.3 Mineral Composition

As mentioned in Section 3.2.2, the SIF assemblage oxide-dominant BIF is composed primarily of quartz and magnetite with lesser amounts of grunerite, carbonate, pyroxene, hornblende, and pyrrhotite. Grunerite, carbonate, pyroxene, and hornblende were analysed with the SEM for mineral chemistry. However, quartz, magnetite, and pyrrhotite were not analysed because their chemistry is uniform and consequently the amount of information gained from them is negligible. Plate 3.3 shows SEM backscatter electron images of the SIF assemblage oxide-dominant BIF. Numbered points on Plate 3.3 correspond to mineral analysis results summarized in Table 3.1.

Grunerite is the third most abundant mineral, after quartz and magnetite, in the SIF assemblage oxide-dominant BIF. Grunerite grains in the SIF assemblage oxide-dominant BIF typically consist of 9.0-13.0 wt.% MgO, 50.5-53.5 wt.% SiO<sub>2</sub>, 30-37 wt.% FeO, and have a mean total ranging between 96-98 wt.%. There are some differences in grunerite chemistry, based on which layer it is found in.



**Plate 3.3. Backscatter electron images (BSE) of Southern Iron Formation oxide-dominant BIF collected from Musselwhite mine. Note that the numbered points correspond to the point analysis in Table 3.1. a) Quartz-dominated layer containing fine-grained disseminated grunerite and carbonate, inset rectangles are enlarged in Figures b and c, b) Enlarged area from Figure 1a, showing hornblende (5) surrounded by grunerite that is associated with carbonate (3), also notice euhedral grunerite crystal in lower middle of photograph, c) Enlarged area from Figure 1a showing grunerite (7) surrounding hornblende (8), d) Alternating layers of carbonate and quartz+magnetite, e) Contact between quartz and grunerite dominated layers, f) Grunerite-dominated layer containing minor magnetite and carbonate.**





Grunerite grains found in the quartz layers contain ~13 wt.% MgO, ~30 wt.% FeO, and ~53 wt.% SiO<sub>2</sub>. Grunerite found in the magnetite layers contains ~9 wt.% MgO, ~36 wt.% FeO, and ~51 wt.% SiO<sub>2</sub>. Therefore, grunerite in the magnetite layers has higher FeO than the grunerite in the quartz layers, and the grunerite in the quartz layers has higher MgO than its magnetite layer counterpart. The SiO<sub>2</sub> content of grunerite is consistent across compositional layers. Grunerite in the grunerite-pyroxene-carbonate layers is compositionally similar to grunerite in the magnetite layers.

The presence of hornblende in the SIF assemblage oxide-dominant BIF was not recognised prior to examination of the lithology with the scanning electron microscope. Hornblende is much less common than grunerite as it is difficult to observe in thin-section, and when present, hornblende grains are found at the core of grunerite grains (Plate 3.2b) and occasionally exhibit intergrowth textures with grunerite (Plate 3.2c). Hornblende is primarily found in quartz layers as opposed to magnetite layers. In the SIF assemblage oxide-dominant BIF hornblende consists of ~14.50 wt.% MgO, ~55 wt.% SiO<sub>2</sub>, ~12.20 wt.% CaO, and ~17 wt.% FeO.

Carbonate is found predominantly in the grunerite-pyroxene-carbonate layers with lesser amounts found disseminated in the quartz and magnetite layers. Carbonate mineral chemistry was not known prior to examination of the SIF assemblage oxide-dominant BIF with the SEM. The most abundant carbonate mineral in this lithology is iron-rich calcite (Fe-calcite). Iron-rich calcite, in this lithology, contains on average ~50 wt.% CaO and ~2 wt.% FeO with a total of ~53-54 wt.% (low total due to inability of EDS to detect CO<sub>2</sub>). A less abundant, but still significant, carbonate mineral in this lithology is iron-rich dolomite (ferroan-dolomite). The ferroan-dolomite contains between ~7 wt.% MgO, ~1 wt.% MnO, ~20 wt.% FeO, and ~30wt.% CaO. Ferroan-dolomite appears to be only associated with the grunerite-pyroxene-carbonate layers (Plate 3.3e and f).

### 3.2.4 Geochemical Composition

The geochemistry of this lithology, summarized in Table 3.2, is variable. Differences in chemistry are primarily attributed to different combinations of the two end-member components which comprise this lithology. These end-member lithologies are: 1) magnetite-dominated (n=6) and 2) quartz-dominated layers (n=2). The geochemistry of this lithology can therefore be discussed in terms of magnetite-dominated layers and quartz-dominated layers. It should be noted that compositional layers in the SIF oxide-dominant BIF represent a spectrum from magnetite-dominant to quartz-dominant end-members.

Magnetite-dominant layers exhibit the following ranges of major elements in their geochemical composition: 20-40 wt.% Fe<sub>2</sub>O<sub>3</sub>, 25-30 wt.% FeO, 19-46 wt.% SiO<sub>2</sub>, 2-4 wt.% MgO, 1-4 wt.% CaO, 0.01-0.02 wt.% TiO<sub>2</sub>, 0.05-0.20 wt.% Al<sub>2</sub>O<sub>3</sub>, 0.06-0.6 wt.% MnO, 0.04-0.07 wt.% Na<sub>2</sub>O, 0-0.06 wt.% K<sub>2</sub>O, and 0.05-0.26 wt.% P<sub>2</sub>O<sub>5</sub>. Relative to the quartz-dominant layers, concentrations of minor and trace elements such as P, Zn, and Cu are highest in the magnetite layers.

Of the eight SIF assemblage oxide-dominant BIF samples sent for analysis, sample SIF-07-20-071m represents the most magnetite-dominant layer end-member. Categorizing this sample as the magnetite-dominant layer end member is based on the fact that it has the highest Fe<sub>2</sub>O<sub>3</sub>, FeO, Cr, Cu, Ni, Zn, and lowest SiO<sub>2</sub>, content of all the samples. The exact concentration of these elements are as follows: 34 wt.% Fe<sub>2</sub>O<sub>3</sub>, 24 wt.% FeO, 0.22 wt.% P<sub>2</sub>O<sub>5</sub>, 63 ppm Cr, 187 ppm Cu, 44 ppm Ni, 6 ppm Sb, 12 ppm Sn, and 75 ppm Zn. Sample SIF-07-20-071m contains the lowest value of the following element at 19 wt.% SiO<sub>2</sub>.

In addition to SIF-07-20-071m, samples SIF-07-20-060m, SIF-07-20-062m, SIF-07-20-063m, and SIF-07-20-073m are magnetite-dominant layer samples. Again, this is based on the samples high Fe<sub>2</sub>O<sub>3</sub>, FeO, P<sub>2</sub>O<sub>5</sub>, and low SiO<sub>2</sub> content. Sample SIF-07-20-060m exhibits very similar Fe<sub>2</sub>O<sub>3</sub> and FeO values to SIF-07-20-017. Sample SIF-07-20-063m is

**Table 3. 2. Whole-rock geochemical data for the Southern Iron Formation oxide-dominant BIF.**

	Quartz-Dominant Bands			Magnetite-Dominant Bands					
Sample ID	SIF-PM05-63c	SIF-0720-060c	SIF-0720-063c	SIF-0720-060M	SIF-0720-071m	SIF-0720-062m	SIF-0720-072m	SIF-0720-063m	
units	wt%	wt%	wt%	wt%	wt%	wt%	wt%	wt%	
MAJOR Elements	SiO <sub>2</sub>	45.63	78.82	66.93	23.81	19.09	39.79	35.34	33.5
	Al <sub>2</sub> O <sub>3</sub>	0.08	0.05	0.11	0.05	0.09	0.20	0.11	0.09
	TiO <sub>2</sub>	0.01	0.02	0.03	0.01	0.01	0.02	0.01	0.01
	Fe <sub>2</sub> O <sub>3</sub>	0.59	N.D.	0.59	39.82	33.63	20.07	31.58	20.97
	FeO	17.46	10.15	17.46	29.71	24.65	28.73	24.75	26.02
	MnO	0.15	0.25	1.11	0.24	0.38	0.55	0.06	0.51
	MgO	4.28	2.14	5.73	2.74	2.43	3.16	2.50	2.60
	CaO	1.14	5.03	4.59	1.57	3.41	3.83	4.34	2.77
	Na <sub>2</sub> O	0.04	0.01	0.02	0.07	0.06	0.05	0.05	0.05
	K <sub>2</sub> O	N.D.	0.01	0.02	0.01	0.01	0.06	0.01	0.01
	P <sub>2</sub> O <sub>5</sub>	0.19	0.17	0.20	0.05	0.22	0.18	0.20	0.26
	LOI	N.D.	2.6	2.55	0.05	0.05	0.05	0.05	0.05
	TOTAL	100.15	100.36	101.26	99.91	99.91	99.19	100.84	99.97
units	ppm	ppm	ppm	ppm	ppm	ppm	ppm	ppm	
REE, LILE, HFSE	Ce	6.32	6.51	12.91	8.66	9.38	11.19	3.99	13.73
	Cs	0.126	0.029	0.235	0.035	0.091	0.827	0.128	0.209
	Dy	1.37	1.222	2.151	1.512	1.708	2.187	1.12	2.263
	Er	1.09	0.909	1.536	1.137	1.224	1.448	0.876	1.581
	Eu	0.689	0.843	1.218	0.68	0.901	1.188	0.249	1.271
	Gd	1.19	1.12	1.905	1.334	1.55	1.954	0.961	2.005
	Hf	N.D.	0.2	N.D.	N.D.	N.D.	N.D.	N.D.	N.D.
	Ho	0.336	0.295	0.503	0.367	0.406	0.483	0.279	0.513
	La	3.49	3.58	6.52	4.98	4.99	5.08	2.23	6.92
	Lu	0.169	0.137	0.264	0.174	0.175	0.225	0.128	0.241
	Nb	N.D.	N.D.	N.D.	N.D.	N.D.	0.2	N.D.	N.D.
	Nd	3.36	3.28	6.31	4.09	4.72	5.89	2.3	6.54
	Pr	0.771	0.781	1.575	0.981	1.102	1.404	0.492	1.653
	Rb	0.24	0.39	0.68	0.51	0.34	2.95	0.42	0.99
	Sm	0.79	0.76	1.45	0.92	1.06	1.49	0.55	1.52
	Sr	9.3	57.1	16.1	15.3	22.2	24.3	12.3	11.4
	Tb	0.197	0.178	0.311	0.213	0.247	0.323	0.153	0.327
	Th	N.D.	N.D.	N.D.	N.D.	N.D.	N.D.	N.D.	N.D.
	Tm	0.158	0.131	0.236	0.168	0.176	0.218	0.125	0.233
	U	0.013	0.013	0.018	0.011	0.025	0.052	0.011	0.019
Y	12.80	9.71	14.16	12.36	13.35	13.64	10.21	14.92	
Yb	1.05	0.89	1.59	1.08	1.11	1.46	0.81	1.58	
Zr	N.D.	8.5	N.D.	N.D.	4	4.9	N.D.	N.D.	
units	ppm	ppm	ppm	ppm	ppm	ppm	ppm	ppm	
TRACE	Ag	N.D.	N.D.	N.D.	N.D.	N.D.	5	N.D.	
	As	1	7	9	8	1	9	1	
	Ba	N.D.	N.D.	N.D.	N.D.	40	31	N.D.	
	Co	46	N.D.	N.D.	N.D.	N.D.	N.D.	N.D.	
	Cr	30	5	7	N.D.	63	5	N.D.	
	Cs	7	N.D.	N.D.	N.D.	N.D.	N.D.	N.D.	
	Cu	18	14	13	20	187	29	19	
	Ga	2	N.D.	N.D.	N.D.	N.D.	N.D.	N.D.	
	K	N.D.	65	111	34	26	598	28	
	Mn	1693	1994	8689	2173	3711	4607	550	
	Na	N.D.	78	63	59	46	125	62	
	Nb	2	N.D.	N.D.	N.D.	N.D.	N.D.	2	
	Ni	14	5	10	18	44	19	16	
	P	1188	890	1052	602	1431	1152	1393	
	Pb	N.D.	14	N.D.	8	6	8	5	
	Rb	N.D.	N.D.	N.D.	N.D.	2	3	N.D.	
	Sb	N.D.	N.D.	N.D.	N.D.	6	N.D.	N.D.	
	Sc	13	N.D.	N.D.	N.D.	N.D.	6	6	
	Sn	5	N.D.	N.D.	N.D.	12	N.D.	8	
	Sr	9	55	16	17	26	25	14	
	Ta	N.D.	N.D.	N.D.	N.D.	N.D.	N.D.	10	
	Th	N.D.	N.D.	4	4	4	6	N.D.	
	Ti	20	N.D.	N.D.	N.D.	N.D.	40	N.D.	
	V	N.D.	N.D.	4	6	8	9	7	
	W	26	55	46	61	28	36	50	
	Y	15	10	16	16	18	17	12	
	Zn	34	34	38	58	75	57	15	
	Zr	N.D.	4	3	3	3	6	3	

Note that REE, LILE, and HFSE values are the result of ICP-MS analysis whereas other trace element values and major elements are the result of XRF analysis. In the case of duplicate element values, i.e. Y and Zr, ICP-MS values are used. N.D.= not detected i.e. below detection limit (detection limits are presented in Table 1.2).

anomalous because it contains the highest concentrations of REE, LILE, HFSE, and P<sub>2</sub>O<sub>5</sub> of any SIF sample. Concentrations of these elements are as follows: 0.26 wt.% P<sub>2</sub>O<sub>5</sub>, 13.7 ppm Ce, 2.26 ppm Dy, 1.58 ppm Er, 1.27 ppm Eu, 2.01 ppm Gd, 0.51 ppm Ho, 6.92 ppm Lu, 6.54 ppm Nd, 1.65 ppm Pr, 1.52 ppm Sm, 0.33 ppm Tb, and 14.9 ppm Y. The high REE values coinciding with high P<sub>2</sub>O<sub>5</sub> values are likely the result of high apatite content in this sample. It is assumed the REE are incorporated in phosphate minerals such as apatite.

Quartz-dominant layers exhibit the following ranges, of major elements, in their geochemical composition: 0.3-0.6 wt.% Fe<sub>2</sub>O<sub>3</sub>, 10-18 wt.% FeO, 67-79 wt.% SiO<sub>2</sub>, 2-6 wt.% MgO, ~5 wt.% CaO, 0.02-0.03 wt.% TiO<sub>2</sub>, 0.05-0.11 wt.% Al<sub>2</sub>O<sub>3</sub>, 0.25-1.0 wt.% MnO, 0.01-0.02 wt.% Na<sub>2</sub>O, 0.01-0.02 wt.% K<sub>2</sub>O, and 0.17-0.20 wt.% P<sub>2</sub>O<sub>5</sub>.

Relative to the magnetite-dominant layers, concentrations of CaO are highest in the quartz-dominant layers. Additionally, the ratio between FeO and Fe<sub>2</sub>O<sub>3</sub> is much higher in the quartz-dominant layers, suggesting Fe is primarily found in Fe-silicate minerals as opposed to magnetite. These geochemical features correlate to what is observed in thin-section, with grunerite and calcite observable in the quartz-dominant layers.

Of the eight SIF assemblage oxide-dominant BIF samples sent for analysis, sample SIF-07-20-060c represents the quartz-dominant layer end-member. Categorizing this sample as the quartz-dominant layer end member is based on the fact that it has the highest SiO<sub>2</sub> and lowest Fe<sub>2</sub>O<sub>3</sub> content. The exact concentrations of these elements are as follows: 78.82 wt.% SiO<sub>2</sub>, 5.03 wt.% CaO, 57.1 ppm Sr, 8.5 ppm Zr, 55 ppm Sr, and 14 ppm Pb. Sample SIF-07-20-060c contains the lowest values of the following elements at 11.26 wt.%, Fe<sub>2</sub>O<sub>3</sub>, 10.15 wt.% FeO, 2.14 wt.% MgO, 0.05wt.% Al<sub>2</sub>O<sub>3</sub>, 0.01wt.% Na<sub>2</sub>O, 5 ppm Cr, 14 ppm Cu, 5 ppm Ni, and 10 ppm Y.

In addition to SIF-07-20-060c, samples SIF-PM05-063c and SIF-07-20-060c are quartz-dominant layers. Again this is based on their high SiO<sub>2</sub> and low Fe<sub>2</sub>O<sub>3</sub> content. Sample SIF-07-20-063c contains the highest MgO (6 wt.%) and MnO (~1 wt.%) concentrations

of all SIF samples. These elements are contained primarily in grunerite and carbonate minerals.

Aside from  $\text{Fe}_2\text{O}_3$ ,  $\text{FeO}$ ,  $\text{SiO}_2$ ,  $\text{MnO}$ ,  $\text{MgO}$ , and  $\text{CaO}$  concentrations, the geochemical makeup of the magnetite- and quartz-dominant layers does not differ dramatically. Values of  $\text{Al}_2\text{O}_3$ ,  $\text{TiO}_2$ ,  $\text{K}_2\text{O}$ ,  $\text{Na}_2\text{O}$ ,  $\text{P}_2\text{O}_5$ , and Y are comparable between magnetite- and quartz-dominant layers. Elemental ranges, in both the magnetite- and quartz-dominant layers, are as follows: 0.05-0.20 wt.%  $\text{Al}_2\text{O}_3$ , 0.01-0.03 wt.%, 0.0-0.06 wt.%  $\text{K}_2\text{O}$ , 0.01-0.07 wt.%  $\text{Na}_2\text{O}$ , 0.05-0.26 wt.%  $\text{P}_2\text{O}_5$ , and 10-15 ppm Y.

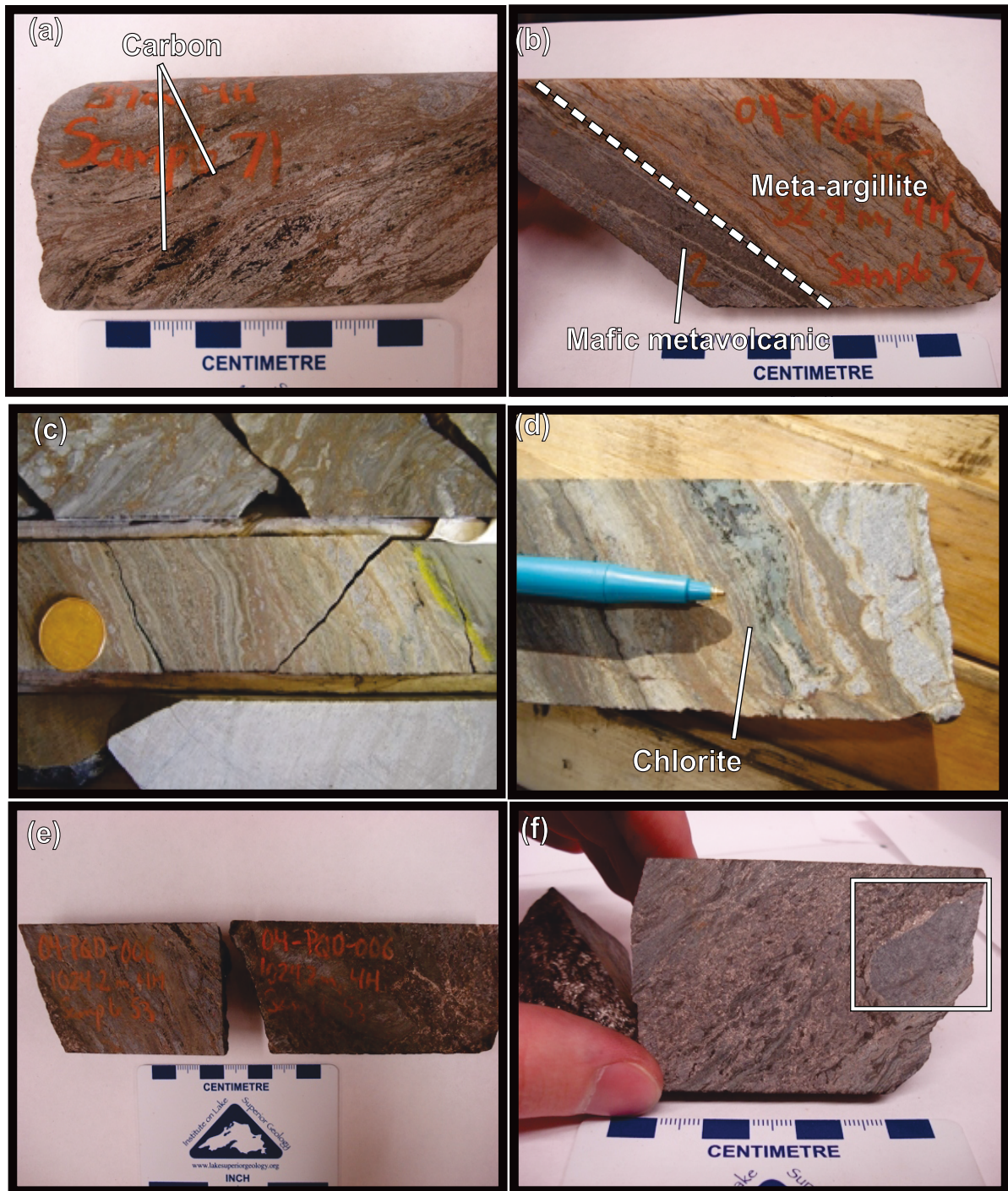
Ce values appear random and range between 4.9 and 13.8 ppm. Cs values range between 0.03 and 0.83 ppm. SIF-07-20-062 m has an anomalous value of 0.83 ppm Cs and also has an anomalous Rb value of 3.0 ppm, where as other samples range between 0.2 and 1.0 ppm.

Hf, Nb, and Th, were not detected in greater than 90 percent of the SIF magnetite- and quartz-dominated layer samples. Ho, Lu, Rb, Tb, Tm, and U, all have values less than 1ppm and, again, no significant variation between concentrations in quartz and magnetite layers.

### 3.3 Meta-Argillite

#### 3.3.1 Macroscopic Character

Ten samples of meta-argillite, all from drill core, were collected for the current study. One sample was collected from the SIF assemblage and nine samples were collected from the NIF assemblage. Since there is only one SIF assemblage meta-argillite sample (Plate 3.4a), which is very similar to the NIF assemblage meta-argillite samples (Plate 3.4b, c, d, e, f), both types of argillite are discussed as one lithology in this section. For detailed hand sample descriptions please refer to Appendix A.



**Plate 3.4. Photographs of meta-argillite in core samples collected from Musselwhite mine.** a) Photograph, of SIF assemblage meta-argillite, showing tan-brown colour of the meta-argillite as well as carbon-rich material (sample 4h-07-20-071), b) Photograph showing contact between meta-argillite and mafic metavolcanic rock (sample 4h-07-20-057), c) Photograph showing layered nature (hole 04-ESN-010, not sampled), d) Photograph showing light blue-green chlorite layer in unit (hole 04-ESN-010, not sampled), e) Photograph showing dark colour of lithology as well as semi-massive pyrrhotite (sample 4h-07-20-053a/b respectively), f) Photograph showing sample containing roughly 10% pyrrhotite. Notice concentration of pyrrhotite along edge of chert 'clast' at the right end of the sample (inset, white box) (sample 4h-07-20-070).

The meta-argillite is a sulphide-rich argillaceous lithology (Plate 3.2). It is visually distinct, due to its high sulphide content, and ranges from strongly magnetic to weakly magnetic. Magnetism, in this lithology, is dependent upon the presence of both magnetic- and non-magnetic pyrrhotite, as well as minor disseminated fine-grained magnetite.

The unit is well laminated when not deformed (Plate 3.2c and d). However, it is usually deformed. Typical deformation features observed in this lithology are shear fabric (Plate 3.2b), folding (Plate 3.2c and d), and 'brecciation' (Plate 3.2 e and f). Due to a thin and discontinuous nature, the meta-argillite has not been observed in the trenches or underground.

The meta-argillite has a variable appearance. It is most often light tan-brown when dominated by grunerite, but ranges to green-grey when dominated by hornblende-rich material. This lithology is typically massive, but ranges to layered, in appearance. When layered it consists of alternating layers, on the order of 0.3-1.0 cm thick, of ~80% dark-tan argillaceous material and ~20% light-grey meta-chert (Plate 3.4c and d). A unique feature seen in this lithology is the presence of black wisps of carbon-rich material (Plate 3.4a).

Three types of compositional layers are observable in hand sample. Layers range from 0.01cm to 2.00 cm thick in samples that are less deformed. Grain size is consistently fine-grained throughout the compositional layers except in proximity to quartz-veining in which case most grains have coarsened. The compositional layers can be divided into; 1) biotite-hornblende-garnet-pyrrhotite  $\pm$  chlorite, 2) quartz-grunerite-carbonate-pyrrhotite, 3) primary pyrrhotite, and 4) quartz-pyrrhotite.

*Biotite-grunerite-hornblende-garnet-pyrrhotite  $\pm$  chlorite layers*

The mineral assemblage: biotite-grunerite-hornblende-garnet-pyrrhotite  $\pm$  chlorite, composes the homogeneous argillaceous groundmass. As such, when layering is present, these layers make up the bulk of the lithology (Plate 3.4b). Chlorite is relatively common and can make up a large part of this type of layer (Plate 3.4d). This mineral assemblage reflects the original chemistry of the sedimentary protolith to this lithology.



#### *Quartz-grunerite-carbonate-pyrrhotite layers*

These layers likely represent metamorphosed chert layers. They are less common than the meta-argillite layers. Grunerite and carbonate are mainly found along the contact between quartz-dominant layers and the above described meta-argillite layers. Due to its fine-grained nature in this lithology, in hand-sample, carbonate is mainly detected through the use of hydrochloric acid.

#### *Primary pyrrhotite*

The meta-argillite contains a semi-massive to massive pyrrhotite component (pyrrhotite  $\pm$  minor chalcopyrite). Pyrrhotite content ranges from ~15% to ~70% of the lithology. Primary pyrrhotite is found as disrupted, roughly conformable, millimetre-scale laminations as well as disseminated material.

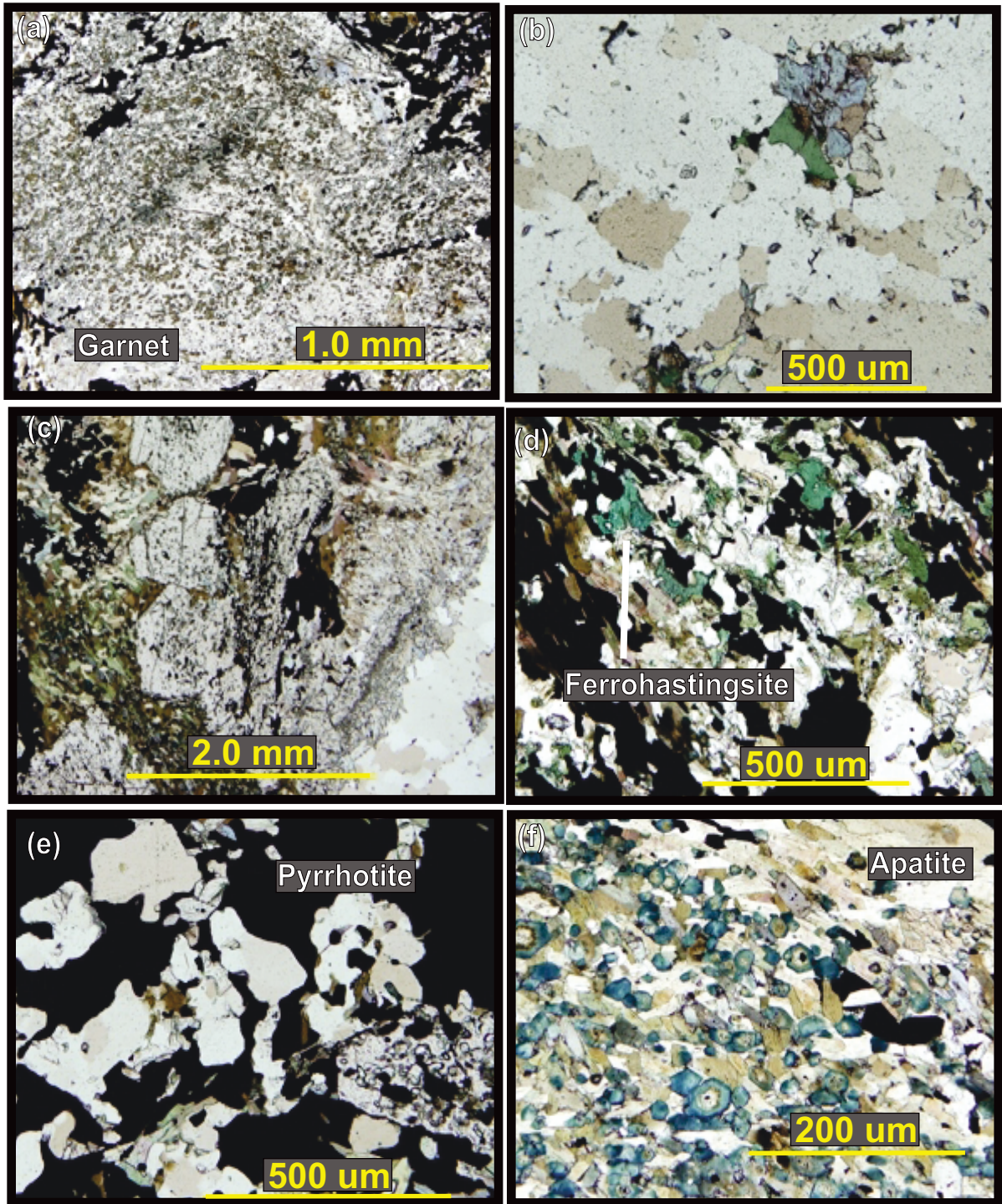
#### *Quartz-pyrrhotite layers*

Like other units in the NIF assemblage the meta-argillite is often crosscut by quartz-veins. Unlike other units in the NIF assemblage the meta-argillite is often brecciated. Remobilized pyrrhotite, as well as minor biotite, is often associated with these quartz-veins and brecciation. Within the brecciated meta-argillite pyrrhotite is associated with the margins and fractures in meta-chert 'clasts.' The majority of the pyrrhotite in the meta-argillite appears to be locally remobilized. It should be noted that minor chalcopyrite and arsenopyrite are disseminated within pyrrhotite agglomerates.

### 3.3.2 Petrographic Character

Petrographic observations are based on six thin-sections of meta-argillite. Thin-sections were only made from samples sent for geochemical analysis. Representative samples, exhibiting a range of commonly observed features such as layering, folding, and shear fabrics, were specifically selected. Refer to Appendix B for the individual thin-section descriptions.

On a microscopic level samples of the meta-argillite are a reflection of the macroscopic appearance of the lithology. Grain-size is variable and ranges from very fine- (0.01mm)



**Plate 3.5. Photomicrographs of meta-argillite, sample 4h-07-20-070, from the Musselwhite mine showing the variations in mineralogy layers.** a) Coarse-grained garnet with abundant inclusions of bladed biotite and minor inclusions of magnetite (ppl), b) Deformed quartz vein showing coarse-grained quartz grains surrounding residual ferrohastingsite crystals (ppl), c) Biotite-garnet-quartz-pyrrhotite-rich groundmass surrounding subhedral almandine garnet porphyroblasts (ppl), d) Blue-green ferrohastingsite (ppl), e) Quartz- and pyrrhotite-rich layer (ppl), f) Hexagonal, pleochroic- blue tourmaline (ppl).

up to fine grained (0.4mm). This lithology is compositionally layered with three types of layers prevailing: 1) biotite-garnet-pyrrhotite-ferrohastingsite, grunerite,  $\pm$  chlorite and tourmaline layers (Plate 3.5c), 2) quartz, pyrrhotite, and chlorite layers (meta-chert) (Plate 3.5d), and 3) Pyrrhotite, quartz, and chlorite layers (Plate 3.5e). In addition, this lithology is cross-cut by coarser-grained quartz- (Plate 3.5b), carbonate-, and pyrrhotite-veins. The layers are described sequentially below:

*Biotite-garnet-pyrrhotite-ferrohastingsite-grunerite  $\pm$  chlorite, layers*

These layers are composed of a finer-grained groundmass of biotite, ferrohastingsite, grunerite, pyrrhotite,  $\pm$  chlorite, surrounding abundant coarser-grained almandine garnet porphyroblasts.

Biotite grains are fine grained and pleochroic dark to light brown. Moderately abundant zircons, with associated dark radiation haloes, occur in the biotite grains. Another common mineral in this layer is pleochroic light-green to dark blue-green ferrohastingsite. Ferrohastingsite and grunerite are closely associated in this lithology, but on average, grunerite is finer grained than ferrohastingsite. However, coarse secondary grunerite in the form of fan and bowtie aggregates have been reported by previous workers (Klipfel, 2002b).

Pyrrhotite, on average, is coarser grained than the other groundmass minerals. It also appears to be predated by biotite, grunerite, quartz, carbonate, and cordierite as these minerals are normally found as inclusions within pyrrhotite aggregates.

Coarser-grained, anhedral to subhedral, almandine garnets, range between 0.1-0.5 cm in diameter. These garnet porphyroblasts are surrounded by a fine-grained groundmass. The garnets also contain abundant inclusions of fine-grained quartz and blades of biotite.

Sample 4h-07-20-070 contains an abundant fine-grained zoned hexagonal mineral. This mineral is most likely a type of tourmaline. It is even finer grained than the other groundmass minerals. The core is inclusion-rich appearing pleochroic brown to green-brown, whereas the rim is inclusion free and pleochroic light-blue to dark-blue (Plate 3.2f). In 4h-07-20-070, this hexagonal mineral makes up 10-15% biotite-garnet-

pyrrhotite-ferrohastingsite-grunerite  $\pm$  chlorite layers, but it is particularly closely associated with biotite.

#### *Pyrrhotite, quartz, and chlorite layers*

Pyrrhotite accounts for between 10-70% of the meta-argillite. The majority of the pyrrhotite is associated with contacts between quartz-dominant layers and the ferrohastingsite, grunerite, pyrrhotite,  $\pm$  chlorite groundmass. Pyrrhotite is primarily found as semi-massive replacements and interstitial material. Minor amounts of chalcopyrite and pyrite are found as inclusions within the pyrrhotite. The close association of pyrrhotite and quartz-veins suggests they are syngenetic.

#### *Quartz-pyrrhotite layers*

The quartz-pyrrhotite layers consist of medium-grained quartz with undulating extinction. The quartz-pyrrhotite layers in the meta-argillite represent deformed quartz- and pyrrhotite veins. These layers consist of between 5% to 30% quartz and 70% to 95% pyrrhotite. These veins were likely emplaced relatively early as many are deformed, dismembered, and realigned into the metamorphic fabric. Coarsening of minerals at the margin of quartz-veins is a common feature in thin-section.

### 3.3.3 Mineral Composition

As mentioned in Section 3.3.2, the meta-argillite is mineralogically more complex than the structurally underlying Southern Iron Formation oxide-dominant BIF. It is primarily composed of biotite, grunerite, hornblende, quartz, magnetite, pyrrhotite, garnet, titanomagnetite, and carbonate (Plate 3.6a-f). Less common constituent minerals are apatite, zircon, rare-earth minerals, and tourmaline. Minerals analyzed with the scanning electron microscope include hornblende, garnet, carbonate, titanomagnetite, biotite, grunerite, apatite, and tourmaline (Plate 3.6a-f). However, quartz, magnetite, and pyrrhotite were not analysed because their chemistry is uniform and consequently the amount of information gained from them is negligible. Plate 3.6 shows SEM backscatter electron images of the meta-argillite. Numbered points on Plate 3.6 correspond to mineral analysis results summarized in Table 3.3.

Hornblende grains occur in aggregates with pyrrhotite, quartz, and biotite. In the meta-argillite, hornblende consists of roughly 7.0 wt.% MgO, 7.8-12 wt.% Al<sub>2</sub>O<sub>3</sub>, 42-51 wt.% SiO<sub>2</sub>, 9-12 wt.% CaO, and 23-25 wt.% FeO.

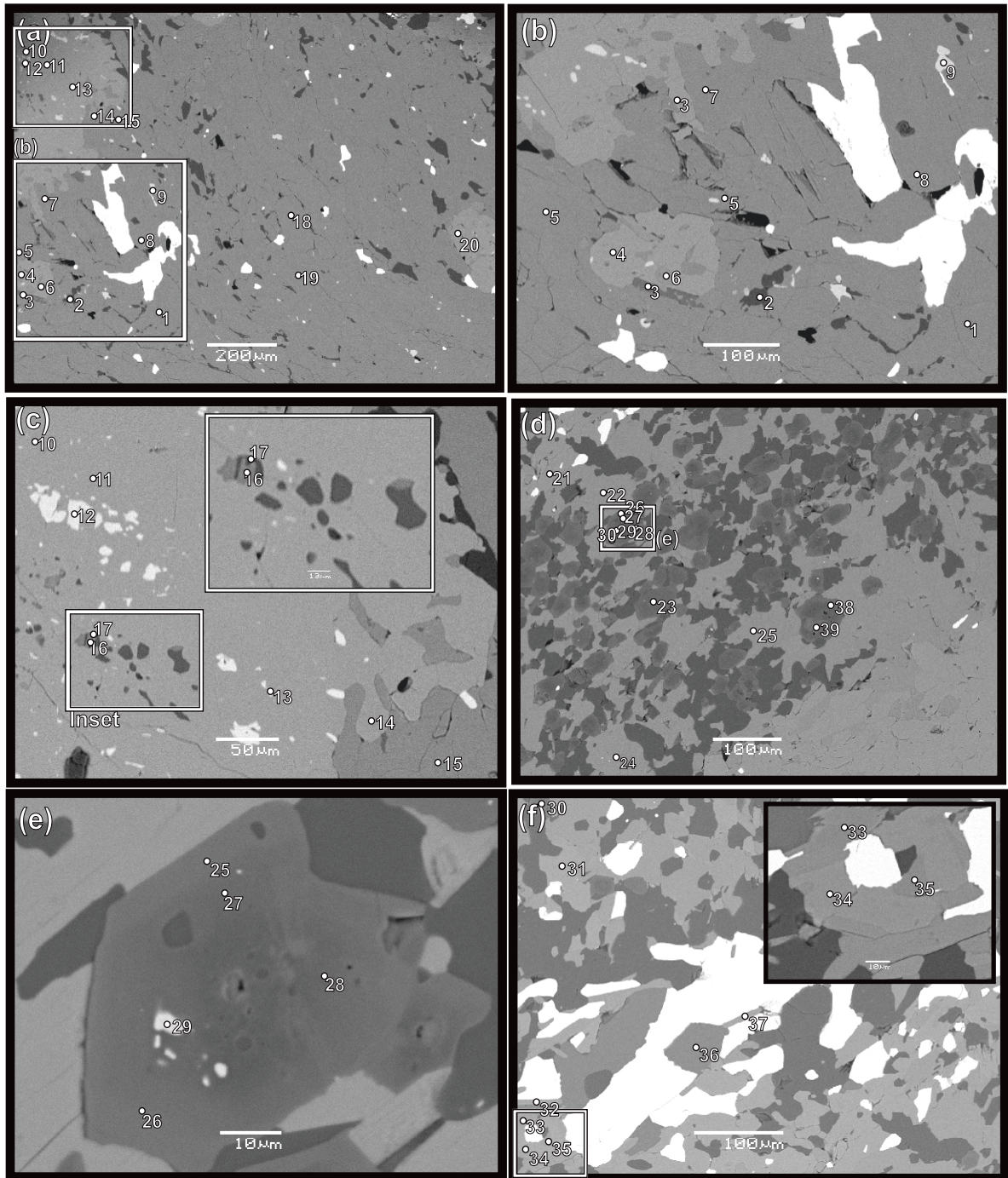
Garnet grains occur as subhedral porphyroblasts and are composed of approximately 21 wt.% Al<sub>2</sub>O<sub>3</sub>, 36-38 wt.% SiO<sub>2</sub>, 5.0-11 wt.% CaO, 4-5 wt.% MnO, and 27-32 wt.% FeO.

Biotite is a moderately abundant mineral in the meta-argillite and is commonly found as euhedral inclusions within pyrrhotite grains and aggregates (Plate 3.6f). There appears to be two types of biotite present in this lithology. The dominant variety is composed of on average ~16-17 wt.% Al<sub>2</sub>O<sub>3</sub>, ~34 wt.% SiO<sub>2</sub>, ~9.5 wt.% K<sub>2</sub>O, ~1-2 wt.% TiO<sub>2</sub> and ~28 wt.% FeO. The less common variety (Plate 3.6c, pt17, and Table 3.3, pt 17) is found as an inclusion within a garnet porphyroblast and is inter grown with chlorite (both grains are well defined). It has the following chemical composition: ~17 wt.% Al<sub>2</sub>O<sub>3</sub>, ~62 wt.% SiO<sub>2</sub>, ~16 wt.% K<sub>2</sub>O, N.D. TiO<sub>2</sub>, and ~2 wt.% FeO.

Tourmaline is only present in one thin-section and in this instance it is associated with biotite grains. However, its presence is significant since tourmaline is not a common mineral at Musselwhite Mine. In this lithology tourmaline is present as pseudo hexagonal, fine-grained, zoned, and pleochroic grains in transmitted light (Plate 3.6f). On examination with the SEM these grains contain abundant fine-grained inclusions of titanomagnetite and quartz (Plate 3.6e). In terms of chemistry this mineral is composed of ~35-37 wt.% SiO<sub>2</sub>, ~30-33 wt.% Al<sub>2</sub>O<sub>3</sub>, 9 wt.% FeO, ~6-7 wt.% MgO, 2-3 wt.% Na<sub>2</sub>O, and roughly 0.2-1.0 wt.% TiO<sub>2</sub>.

Titanomagnetite is the second most abundant opaque mineral after pyrrhotite and magnetite. Titanomagnetite, in this lithology, is found mainly as inclusions within garnet porphyroblasts and to a lesser extent as inclusions within hornblende, biotite, and tourmaline aggregates. It is composed of approximately 50 wt.% TiO<sub>2</sub>, 46 wt.% FeO and 1-2 wt.% MnO.

Iron-rich carbonate is a minor, disperse, component of the meta-argillite. This mineral is composed of ~0.5-2.0 wt.% MgO, ~1.6-3.0 wt.% FeO, and 0.5 wt.% MnO.



**Plate 3.6. Backscatter electron images (BSE) of meta-argillite collected from Musselwhite mine. Note that the numbered points correspond to the point analysis in Table 3.3.** a) Typical groundmass of hornblende, quartz, magnetite, and anhedral masses of sulphide surrounding garnet porphyroblasts (sample 4h-07-20-053), b) Enlarged area from micrograph 3.6a showing garnet porphyroblasts and anhedral sulphide masses (sample 4h-07-20-053), c) Another enlarged portion of 3.6a showing numerous inclusions within garnet porphyroblast (sample 4h-07-20-053), d) Groundmass of quartz, biotite, tourmaline, and minor titanomagnetite (sample 4h-07-20-070), e) Enlarged image from 3.6d showing zonation and numerous inclusions within tourmaline (sample 4h-07-20-070), f) Euhedral biotite crystal enclosed within pyrrhotite mass (sample 4h-07-20-070).



### 3.3.3 Geochemical Composition

The geochemistry of this lithology, summarized in Table 3.4, is variable. Differences in chemistry are primarily attributed to different combinations of the two end-member components which comprise this lithology: 1) exhalite-dominated and 2) siliciclastic-dominated. The geochemistry of this lithology can, therefore, be discussed in terms of samples dominated by either component. However, it should be noted that, in terms of geochemistry, the samples exhibit a spectrum from exhalite-dominant to siliciclastic-dominant compositional end-members.

Exhalite-dominant layers exhibit the following ranges, of major elements, in their geochemical composition: 0.05-4.0 wt.%  $\text{Fe}_2\text{O}_3$ , 13-43 wt.% FeO, 26-77 wt.%  $\text{SiO}_2$ , 2-4 wt.% MgO, 2-12 wt.% CaO, 0.02-0.15 wt.%  $\text{TiO}_2$ , 1-4 wt.%  $\text{Al}_2\text{O}_3$ , 0.4-1.0 wt.% MnO, 0.07-0.26 wt.%  $\text{Na}_2\text{O}$ , 0.04-0.76 wt.%  $\text{K}_2\text{O}$ , and 0.01-0.30 wt.%  $\text{P}_2\text{O}_5$ . In addition, relevant trace elements exhibit the following ranges: 0-32 ppm Zr, 0.04-0.63 ppm U, 0.1-1.9 ppm Th, 31-254 ppm Cu, 70-688 Zn, 14-1117 ppm Cr, 1-12 ppm Pb. Relative to the siliciclastic-dominant samples, concentrations of trace elements such as  $\text{P}_2\text{O}_5$ , Zn, Cu, and Cr are highest in the exhalite-dominant samples.

Of the ten meta-argillite samples sent for analysis, sample 4h-07-20-042 represents the exhalite-dominant end-member. Categorizing this sample as the exhalite-dominant end member is based on the fact that it has the highest  $\text{Fe}_2\text{O}_3$ , FeO, Zn content of all the samples. These are elements associated with high-temperature exhalative activity (Peter, 2003). The exact concentration of these elements are as follows: 1.5 wt.%  $\text{Fe}_2\text{O}_3$ , 43 wt.% FeO, 0.33 wt.%  $\text{P}_2\text{O}_5$ , 1117 ppm Cr, 0.68 ppm Ho, 0.32 ppm Lu, and 688 ppm Zn. Sample 4h-07-20-042 also contains low concentrations siliciclastic elements: 4 wt.%  $\text{Al}_2\text{O}_3$ , 0.15 wt.%  $\text{TiO}_2$ , and 22 ppm Zr.

In addition to 4h-07-20-042, samples 4h-07-20-043, 4h-07-20-056, 4h-07-20-057, and 4h-07-20-071 are categorized as exhalite-dominant samples. Again, this is based on the samples high  $\text{Fe}_2\text{O}_3$ , FeO,  $\text{P}_2\text{O}_5$ , and low  $\text{Al}_2\text{O}_3$ ,  $\text{TiO}_2$ , and Zr content.



Siliciclastic-dominant samples exhibit the following ranges, in major-element composition: 0.0-12 wt.% Fe<sub>2</sub>O<sub>3</sub>, 0.2-35 wt.% FeO, 43-60 wt.% SiO<sub>2</sub>, 2-9 wt.% MgO, 1-12 wt.% CaO, 0.2-0.9 wt.% TiO<sub>2</sub>, 4-15 wt.% Al<sub>2</sub>O<sub>3</sub>, 0.13-1.0 MnO, 0.08-2.0 wt.% Na<sub>2</sub>O, 0.02-2.0 wt.% K<sub>2</sub>O, and 0.02-0.17 wt.% P<sub>2</sub>O<sub>5</sub>. In addition, relevant trace-elements exhibit the following ranges: 43-52 ppm Zr, 0.77-1.54 ppm U, 2.4-4.6 ppm Th, 99-195 ppm Cu, 97-299 Zn, 63-454 ppm Cr, and 11-33 ppm Pb. Relative to the exhalite-dominant samples, concentrations of trace elements such as Zr, U, and Th are highest in the siliciclastic-dominant samples.

Of the ten meta-argillite samples analysed, sample 4h-07-20-070 represents the siliciclastic-dominant end-member. Categorizing this sample as the siliciclastic-dominant end-member is based on the fact that it has high concentrations of Al<sub>2</sub>O<sub>3</sub>, CaO, MgO, Zr, and TiO<sub>2</sub> it also contains comparatively low amounts of Fe<sub>2</sub>O<sub>3</sub> and MnO. In sedimentary rocks, Al<sub>2</sub>O<sub>3</sub>, Zr, and TiO<sub>2</sub> are associated with zircon and clay-mineral-rich siliciclastic detritus (Peter, 2003). The exact concentrations of these elements are as follows: 14.95 wt.% Al<sub>2</sub>O<sub>3</sub>, 0.88 wt.% TiO<sub>2</sub>, 1.62 wt.% Na<sub>2</sub>O, 9.06 wt.% MgO, and 12.46 wt.% CaO. In addition, relevant trace elements exhibit the following concentrations: 3254 ppm Gd, 12.2 ppm La, 2.8 ppm Nb, 12.1 ppm Nd, 3.6 ppm Th, 1.2 ppm U, 52 ppm Zr. High percentages of these elements are associated with siliciclastic-detrital clay minerals (Peter, 2003). Sample 4h-07-20-070 contains the lowest values of the following elements at 10.64 wt.% Fe<sub>2</sub>O<sub>3</sub> and 0.02 wt.% K<sub>2</sub>O. Samples similar to 4h-07-20-070 are sample 4h-07-20-051.

In addition to 4h-07-20-070, samples 4h-07-20-046, 4h-07-20-051, 4h-07-20-053a, 4h-07-20-053b, and 4h-07-20-070 are siliciclastic-dominant samples. Sample 4h-07-20-051 is particularly similar to 4h-07-20-070. Again this is based on their high concentrations of Al<sub>2</sub>O<sub>3</sub>, CaO, MgO, Zr, and TiO<sub>2</sub>. It also contains comparatively low amounts of Fe<sub>2</sub>O<sub>3</sub> and MnO. Fe<sub>2</sub>O<sub>3</sub> and FeO in samples usually differ by no more than 3-6 wt.%.

**Table 3.4. Whole-rock geochemical data for the meta-argillite.**

Sample ID	Exhalite-Dominant				Siliciclastic-Dominant					
	07-20-042	07-20-043	07-20-056	07-20-057	07-20-071	07-20-053a	07-20-053b	07-20-046	07-20-051	07-20-070
units	wt%	wt%	wt%	wt%	wt%	wt%	wt%	wt%	wt%	wt%
<b>MAJOR Elements</b>										
SiO <sub>2</sub>	31.56	76.79	54.57	54.14	25.92	45.13	59.82	43.31	53.47	47.52
Al <sub>2</sub> O <sub>3</sub>	4.32	1.49	1.32	3.38	2.13	5.34	4.44	4.89	7.7	14.95
TiO <sub>2</sub>	0.15	0.02	0.07	0.12	0.02	0.2	0.18	0.19	0.29	0.88
Fe <sub>2</sub> O <sub>3</sub>	1.51	1.11	0.05	3.60	0.80	0.00	0.00	0.00	11.67	10.42
FeO	42.58	13.00	24.85	21.52	36.42	33.31	22.67	34.69	11.12	0.20
MnO	1.15	0.41	0.72	0.74	0.41	0.58	0.69	1.08	0.13	0.17
MgO	3.94	1.68	3.7	2.68	3.44	2.3	2.76	2.84	2.70	9.06
CaO	4.22	1.96	8.09	6.34	11.56	3.1	3.11	3.81	1.34	12.46
Na <sub>2</sub> O	0.17	0.08	0.16	0.07	0.26	0.16	0.13	0.15	0.08	1.62
K <sub>2</sub> O	0.40	0.04	0.22	0.76	0.28	1.59	1.43	0.38	0.72	0.02
P <sub>2</sub> O <sub>5</sub>	0.33	0.01	0.14	0.08	0.24	0.17	0.09	0.10	0.03	0.02
LOI	3.75	1.73	1.57	2.66	2.82	5.4	2.28	3.9	9.20	2.60
TOTAL	98.82	99.77	98.23	98.49	88.36	100.71	100.02	99.16	99.69	99.94
units	ppm	ppm	ppm	ppm	ppm	ppm	ppm	ppm	ppm	ppm
<b>REE, LILE, HFSE</b>										
Ce	11.71	3.50	17.9	11.57	8.77	24.76	24.30	13.13	6.90	25.85
Cs	0.88	0.135	0.467	0.163	0.806	0.849	0.883	0.418	2.531	1.411
Dy	3.012	0.495	2.121	1.799	2.491	2.489	2.95	2.294	1.101	3.5
Er	2.106	0.333	1.391	1.196	1.597	1.615	2.013	1.512	0.803	2.281
Eu	1.183	0.332	1.031	0.612	1.023	1.191	1.375	0.875	0.214	1.41
Gd	2.435	0.48	2.012	1.665	2.198	2.508	2.805	1.996	0.969	3.254
Hf	0.50	0.10	0.80	0.50	N.D.	1.1	1.1	1.2	1.4	1.3
Ho	0.678	0.109	0.46	0.398	0.544	0.535	0.645	0.494	0.244	0.74
La	5.28	1.78	9.51	5.97	4.31	12.79	12.41	6.21	3.21	12.22
Lu	0.318	0.058	0.224	0.181	0.213	0.292	0.339	0.247	0.169	0.377
Nb	1.40	N.D.	1.70	1.50	N.D.	2.7	2.2	2.1	2.7	2.8
Nd	6.55	1.67	7.91	5.80	5.2	10.93	11.06	6.47	3.32	12.13
Pr	1.501	0.41	2.018	1.399	1.126	2.812	2.794	1.578	0.828	3.077
Rb	15.36	1.33	23.8	4.99	6.33	89.81	91.63	14.62	21.62	62.29
Sm	1.73	0.40	1.71	1.34	1.48	2.41	2.46	1.56	0.84	2.86
Sr	19.7	14.4	39.4	75	76.3	23.6	21.5	18.8	15.6	40.9
Ta	N.D.	N.D.	N.D.	N.D.	N.D.	0.23	0.19	0.19	0.22	0.25
Tb	0.431	0.077	0.317	0.267	0.371	0.391	0.452	0.348	0.164	0.533
Th	0.8	0.3	1.9	0.93	0.06	3.74	3.20	2.40	4.60	3.64
Tm	0.318	0.052	0.212	0.175	0.226	0.246	0.299	0.23	0.133	0.343
U	0.515	0.12	0.629	0.311	0.04	1.163	1.052	0.768	1.535	1.185
Y	18.58	3.24	13.78	11.67	15.85	14.46	18.33	13.1	5.74	19.21
Yb	2.12	0.37	1.41	1.17	1.44	1.74	2.09	1.56	0.97	2.39
Zr	22	5.0	31.7	19.1	N.D.	43.1	43.8	47.8	52.4	51.7
units	ppm	ppm	ppm	ppm	ppm	ppm	ppm	ppm	ppm	ppm
<b>TRACE</b>										
Ag	N.D.	N.D.	N.D.	N.D.	5	N.D.	N.D.	N.D.	N.D.	N.D.
As	39	2	37	3	66	351	68	21	64	46
Ba	49	62	72	77	134	145	104	89	164	219
Co	16	21	25	N.D.	13	28	16	29	17	30
Cr	1117	14	103	42	51	454	80	225	100	63
Cs	N.D.	N.D.	N.D.	N.D.	N.D.	N.D.	N.D.	N.D.	N.D.	7
Cu	140	89	160	31	254	195	99	135	119	135
Ga	10	4	3	3	9	8	7	9	14	9
K	3837	362	7370	2029	2769	15544	13330	3397	6574	40766
Mn	3402	2977	7370	3397	3634	4364	13330	3397	1003	2916
Mo	4	N.D.	N.D.	N.D.	N.D.	4	N.D.	2	3	2
Na	735	550	424	970	1222	987	840	723	344	1310
Nb	2	N.D.	3	N.D.	N.D.	4	3	2	4	3
Ni	89	48	84	28	66	127	61	103	53	96
P	1633	60	414	705	972	776	448	450	155	632
Pb	12	5	12	N.D.	10	33	18	11	20	18
Rb	18	N.D.	26	6	7	100	99	17	24	61
Sb	N.D.	N.D.	N.D.	N.D.	N.D.	6	N.D.	N.D.	5	N.D.
Sc	15	N.D.	8	7	20	12	7	10	15	10
Se	2	2	3	N.D.	27	11	2	N.D.	4	4
Sn	8	N.D.	N.D.	N.D.	6	8	N.D.	8	N.D.	N.D.
Sr	22	14	43	79	82	26	22	20	17	40
Th	4	4	6	4	N.D.	8	6	6	9	8
Ti	974	86	780	392	140	1302	1041	1090	1948	1245
V	94	21	36	21	130	73	50	51	108	64
W	18	48	26	25	24	17	33	34	24	22
Y	22	3	15	12	20	15	19	15	7	19
Zn	688	143	138	70	72	237	278	138	97	299
Zr	26	4	33	11	N.D.	46	47	55	61	53

Note that REE, LILE, and HFSE values are the result of ICP-MS analysis whereas other trace element values and major elements are the result of XRF analysis. In the case of duplicate element values, i.e. Y and Zr, ICP-MS values are used. N.D.= not detected i.e. below detection limit (detection limits are presented in Table 1.2).

## 3.4 Quartz-Grunerite Iron Formation

### 3.4.1 Macroscopic Character

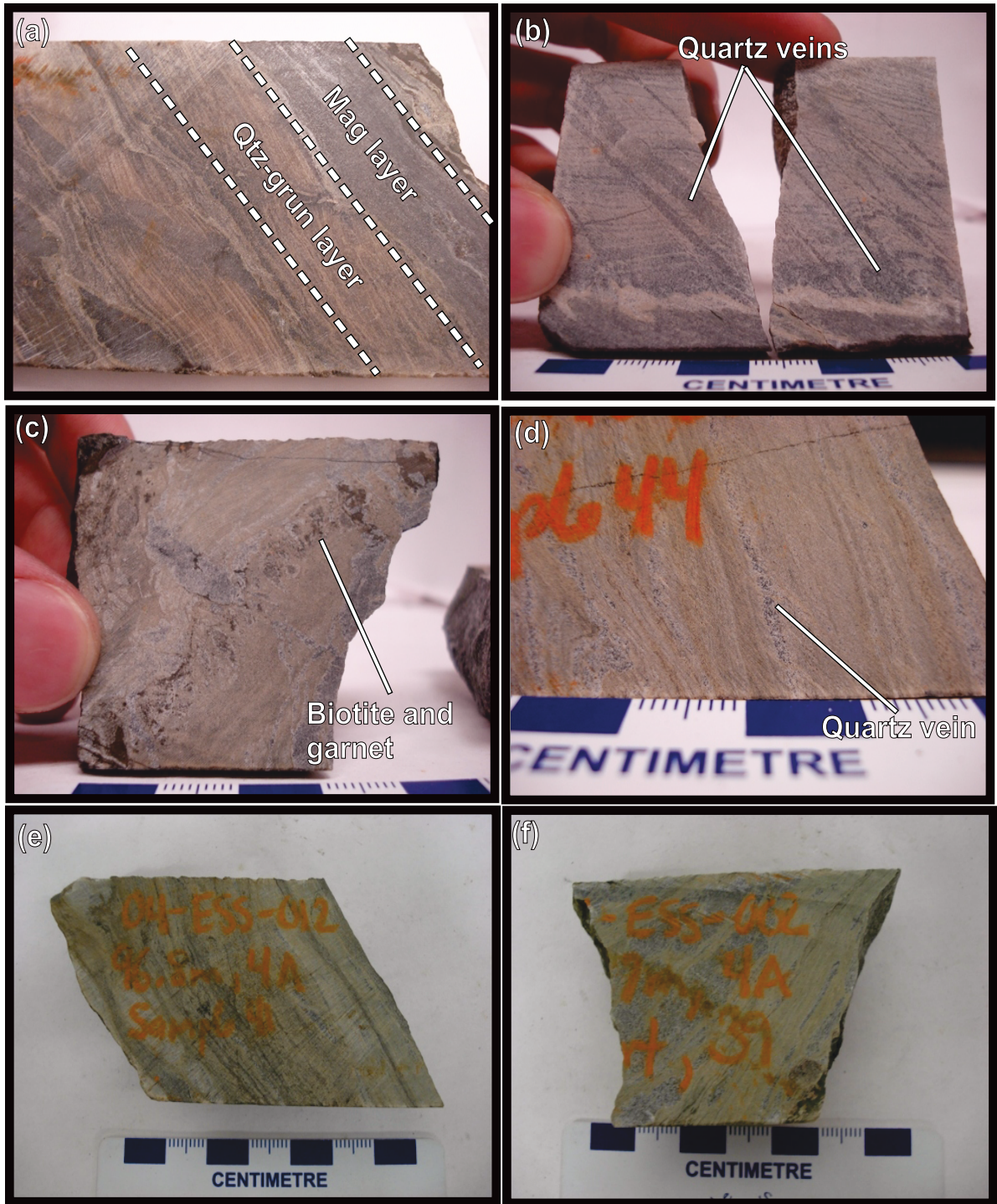
Five samples of quartz-grunerite BIF, all from drill core, were collected for the current study. All five samples were collected from the bottom of the NIF assemblage. For detailed hand sample descriptions please refer to Appendix A.

The quartz-grunerite BIF, as its name implies, is a grunerite-rich lithology (Plate 3.7). It is visually distinct, due to its high grunerite content, and ranges from weakly magnetic to moderately magnetic. Magnetism, in this lithology, is dependent upon the presence of disseminated fine-grained magnetite.

In its 'original', less deformed state, this lithology consists of intercalated thinly-laminated quartz and grunerite layers (Plate 3.7a and b). However, it is common to find this lithology in its more deformed state. Typical deformation features observed in this lithology are shear fabric (Plate 3.7c-f) and folding (Plate 3.2c). Due to its thin and discontinuous nature, the quartz-grunerite BIF has not been observed in the trenches or underground.

The quartz-grunerite BIF has a variable appearance. Samples containing abundant grunerite are light tan when dry (Plate 3.7a-f) and orange when wet. Samples containing abundant quartz are grey when dry and semi-translucent when wet. Thinly layered versions of this lithology are observed (Plate 3.7a and b). The thin laminations are a primary feature, which may have been present in all samples, but are easily destroyed by deformation (Plate 3.7c-f). More typically this lithology is found as a homogeneous assemblage of grunerite and quartz  $\pm$  biotite, garnet, and quartz veins. In its laminated form the quartz-grunerite BIF consists of alternating lamina, on the order of 0.01-0.2 cm thick, of ~40% fine-grained yellow grunerite and ~60% fine-grained, slightly thicker laminations, of grey quartz (Plate 3.7a and b).

Sample 4a-07-20-054 (Plate 3.7a) consists of ~1-1.5 cm layers of typical thinly-laminated quartz-grunerite BIF intercalated with ~1-2 cm layers of magnetite. The magnetite layers



**Plate 3.7. Photographs of quartz-grunerite banded iron formation collected from Musselwhite mine.** a) 1-1.5 cm wide layers of typical thinly laminated quartz and grunerite alternating with 1.2cm wide layers of grunerite-magnetite (sample 4a-07-20-054), b) Slightly translucent grey quartz veins cross-cutting roughly perpendicular to thinly laminated quartz-grunerite iron formation (sample 4a-07-20-012), c) Approximately 1cm wide biotite and garnet layer (sample 4a-07-20-028), d) 2mm wide deformed quartz vein in quartz-grunerite iron formation (sample 4a-07-20-044), e) Deformed quartz-grunerite iron formation (sample 4a-07-20-041), f) Deformed quartz-grunerite iron formation (sample 4a-07-20-039).

are a typical feature of the overlying oxide-dominant BIF, which is described later in this chapter. These alternating layers may represent a transition to the thickly layered oxide-dominant layered iron formation.

The grunerite and quartz laminations are cross-cut by quartz and calcite veins (Plate 3.7b), as well as biotite- and garnet-rich layers (Plate 3.7c). These deformed samples appear to have syntectonically emplaced quartz veins that are to some extent aligned with the shear fabric (Plate 3.7f).

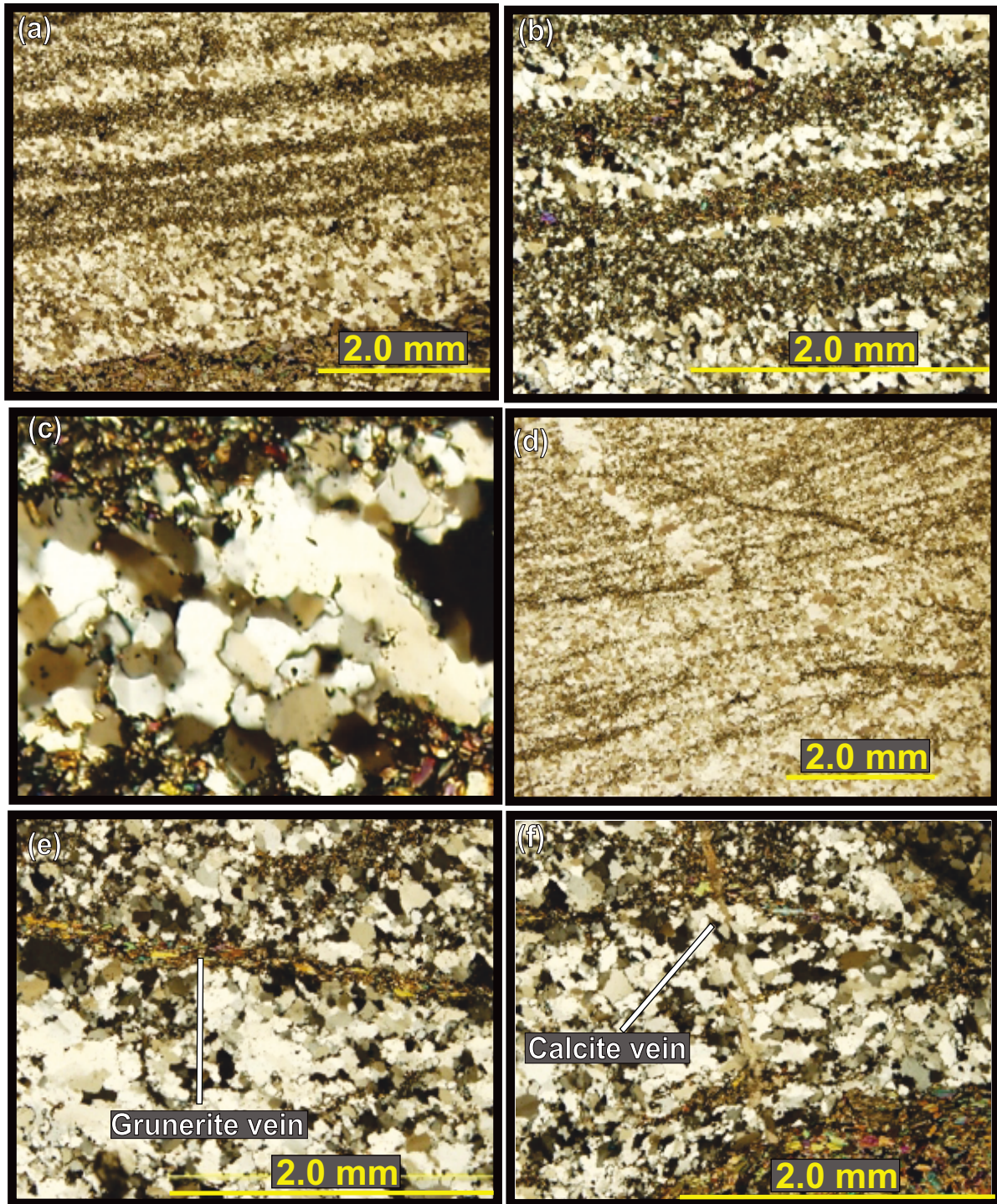
### 3.4.2 Petrographic Character

Petrographic observations are based on three thin-sections of the quartz-grunerite BIF. Thin-sections were only made from samples sent for geochemical analysis. Representative samples, exhibiting a range of commonly observed features such as layering, folding, and shear fabrics, were specifically selected. Refer to Appendix B for the individual thin-section descriptions.

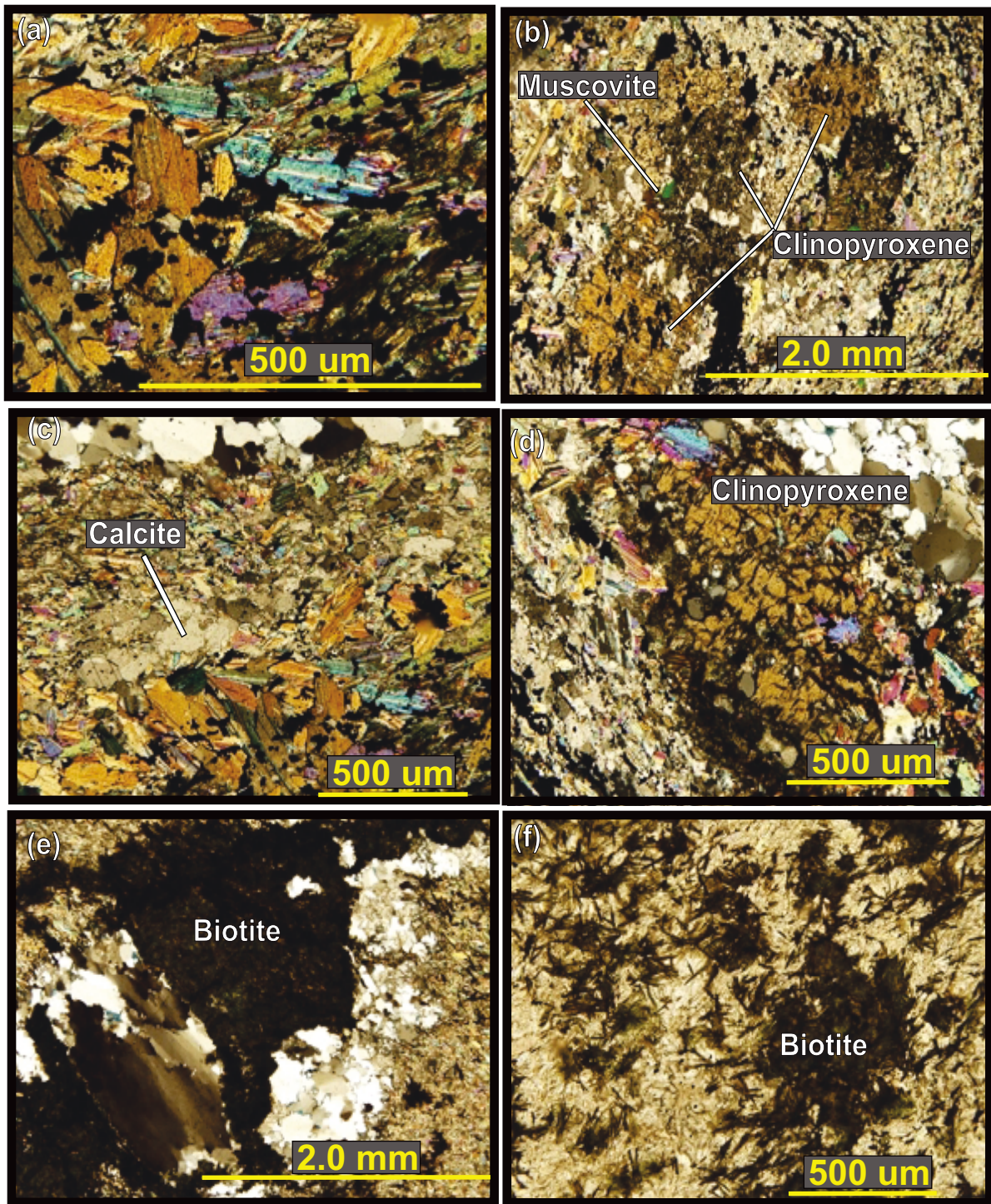
On a microscopic level samples of the quartz-grunerite BIF are a reflection of the macroscopic appearance of the lithology. Samples consist of 60% quartz- and 40% grunerite-dominated layers. Typically these two types of compositional layers prevail: 1) quartz-dominated (meta-chert); (Plate 3.8a), 2) grunerite-pyroxene-carbonate-dominated (Plate 3.8b). Less commonly a third, magnetite-dominated (Plates 3.7a, 3.9a-f), layer is observed.

#### *Quartz Dominant Layers*

In the more pristine state of this lithology, quartz layers range from ~0.1 mm to ~2 mm thick and consist of 0.01 mm to 0.2 mm diameter anhedral to subhedral quartz grains (Plate 3.8b and c). These layers are composed of fine-grained quartz with minor disseminated magnetite, grunerite, and carbonate grains (Plate 3.8c). On average the quartz layers contain >95% quartz grains with <5% magnetite, grunerite, and carbonate grains. Quartz grains exhibit undulatory extinction, have slightly wavy margins (planar grain boundaries), and moderately developed triple point (120°) junctions. The layers can be zoned, consisting of finer-grained quartz in the middle and coarser-grained



**Plate 3.8. Photomicrographs of quartz-grunerite banded iron formation collected from Musselwhite mine. All photomicrographs are of pristine thinly-laminated quartz-grunerite BIF from thin-section (sample 4a-07-20-054). a) Fine-grained laminations of quartz and grunerite (xpl), b) Magnified view of fine-grained laminations of quartz and grunerite, showing typical quartz crystals (xpl), c) Magnified view of quartz lamination with very fine-grained magnetite and grunerite crystals visible (xpl), d) Quartz vein crosscutting quartz lamination (ppl), e) Grunerite vein cross-cutting quartz vein (xpl), f) Carbonate vein cross-cutting grunerite vein (xpl).**



**Plate 3.9. Photomicrographs of quartz-grunerite banded iron formation collected from Musselwhite mine. All photomicrographs are of a magnetite-dominant band from thin-section (sample 4a-07-20-054). a) Coarser, fine-grained grunerite from magnetite-dominant band (xpl), b) Clinopyroxene, muscovite, calcite, grunerite, found as a group (xpl), c) Calcite found in reaction zone at contact between grunerite and quartz laminations (xpl), d) Clinopyroxene porphyroblast (xpl), e) Biotite mass in quartz vein (xpl), f) Radiating biotite aggregates in grunerite groundmass (xpl).**

grains at the margins.

The quartz-dominated layers contain a disseminated very fine-grained magnetite, grunerite, and carbonate component (<5%) (Plate 3.8c). The magnetite and grunerite grains are on the order of 10% the size, and found along the boundaries, of the quartz grains. Grunerite grains are euhedral, needle- to diamond-shaped, whereas magnetite grains are equidimensional, anhedral to subhedral, and 0.01  $\mu\text{m}$  in diameter.

#### *Grunerite-Dominant layers*

These layers (Plate 3.8a and b) are principally composed of grunerite with lesser amounts (<1%) of magnetite, quartz, pyroxene, and carbonate. The layers are generally 0.01 mm to 0.1 mm thick, which is slightly less than the width of the above described quartz-dominant layers.

Very fine-grained,  $\sim 20$   $\mu\text{m}$  diameter, grunerite grains occur as subhedral to euhedral blades. The grunerite grains in this lithology are unusually fine-grained compared to those observed in the other lithologies of the NIF assemblage. These grains exhibit typical twinning,  $54/126^\circ$  amphibole cleavage, and high-birefringence characteristic of grunerite.

As mentioned in the previous section, the highly deformed variety of the quartz-grunerite iron formation is more often seen in drill core than the relatively pristine, thinly laminated variety. In thin-section the more deformed quartz-grunerite BIF consists of homogeneous masses of fine-grained grunerite grains  $\pm$  calcite, biotite and garnet (Plate 3.9f) cross-cut by minor quartz and calcite veins. Grunerite laths, sometimes in 'fan'-shaped aggregates, are frequently found at the edges of these masses. Within the masses grunerite grains are commonly anhedral to subhedral, range from 20  $\mu\text{m}$  to 100  $\mu\text{m}$  in diameter, and form a chaotic and disrupted metamorphic fabric. Local disseminated fine-grained carbonate is a moderately abundant component of the grunerite groundmass. Carbonate is present as infilling between grunerite grains. Biotite grains are found within the grunerite-rich groundmass of the more deformed version of the quartz-grunerite BIF.



These grains occur as aggregates of, 200  $\mu\text{m}$  to 400  $\mu\text{m}$  diameter, radiating grains. The grains are dark-green under both plane and crossed polarized light.

### *Magnetite layers*

Typically, in the quartz-grunerite BIF, magnetite layers are found as thin, millimetre-scale, monomineralic laminations within quartz- and grunerite-dominant layers. However, 4a-07-20-054 (Plate 3.7a) is an interesting and unique sample as it consists of 1.0 to 1.5 cm layers of quartz-grunerite BIF intercalated with 1.0 to 2.0 cm layers of magnetite.

When viewed in thin-section, the magnetite-dominant layers in sample 4a-07-20-054 (Plate 3.7a), are revealed to be mostly grunerite with a significant xenomorphic magnetite component (Plate 3.9a). Originally these layers were likely pure magnetite, but have been altered to grunerite over time. On average the magnetite layers are between 1.0 to 2.0 cm thick and contain 50% to 60% grunerite grains, 20% to 30% magnetite grains and ~10% clinopyroxene porphyroblasts  $\pm$  minor quartz and pleochroic green muscovite (Plate 3.9b).

Grunerite grains are typically anhedral to subhedral in these layers and are coarser-grained, ranging between 20  $\mu\text{m}$  to 150  $\mu\text{m}$ , relative to grunerite grains in the thin laminations discussed above. Near the margins bordering quartz veins, grunerite grains become even coarser grained, ranging from 100  $\mu\text{m}$  to 250  $\mu\text{m}$ .

Clinopyroxene porphyroblasts are found in association with grunerite and carbonate (Plate 3.9d). The porphyroblasts, range from 0.9 to 1.5 mm in diameter, poikiloblastically enclose fine-grained magnetite grains, and make up <5% of the magnetite-rich layers.

Grains are typically found near the contact between quartz-dominated layers and magnetite/grunerite-dominant layers (Plate 3.9c and d).

Carbonate grains are a minor component, making up 1-5% of the magnetite-rich layer proper (Plate 3.9c). Like clinopyroxene, carbonate is found near the contact between quartz-dominated layers and magnetite/grunerite-dominant layers (Plate 3.8c and d)

#### *Quartz, Grunerite, and Carbonate Veins*

Deformed quartz veins (Plate 3.8d), grunerite veins (Plate 3.8e), and carbonate veins (Plate 3.8f) perpendicularly cross-cut the quartz- and grunerite-dominated layers. These quartz veins are distinguished from quartz layers by their coarser grain size. Quartz grains in the veins average between 2-4 mm in width, are anhedral with irregular margins and exhibit well-developed undulatory extinction. Equigranular triple point junctions are rarely developed. Smaller fine-grained quartz grains, with associated calcite, are found between the larger grains. Quartz veins appear to only cross-cut the quartz-dominant layers. The apparent absence of quartz veins in the grunerite-dominant layers may be a result of shear deformation being focused along these layers.

Fine-grained, locally cryptocrystalline, biotite or chlorite is found in association with quartz veins (Plate 3.9e) and to a lesser extent within the grunerite groundmass (Plate 3.9f). Grains are dark-green under both plane and crossed polars. These grains occur in aggregates of radiating lath-like grains, 0.5 mm to 3.5 mm in diameter.

Grunerite veins, possibly tension gashes filled with grunerite, cross-cut this lithology at a different angle than the quartz veins (Plate 3.8e). Much like the previously mentioned veins, these veins are distinguished from grunerite-dominant layers by their coarser grain size (20  $\mu\text{m}$ -200  $\mu\text{m}$ ). Carbonate veins, between 50  $\mu\text{m}$  and 100  $\mu\text{m}$  wide, cross-cut the quartz and grunerite veins (Plate 3.8f). These carbonate veins also cross-cut the quartz-dominant and grunerite-dominant layers.

### 3.4.3 Geochemical Composition

The geochemistry of this lithology, summarized in Table 3.6, is variable. Differences in chemistry are primarily attributed to different combinations of the two end-member components that comprise this lithology. These end-member lithologies are; 1) grunerite-dominated (n=3), 2) quartz-dominated layers (n=2), and 3) magnetite-dominated layers (n=1). The geochemistry of this lithology can therefore be discussed in terms of varying grunerite-dominated and quartz-dominated layer content.

Grunerite-dominant layers exhibit the following ranges, of major elements, in their geochemical composition: 1-3 wt.% Fe<sub>2</sub>O<sub>3</sub>, 22-26 wt.% FeO, 53-61 wt.% SiO<sub>2</sub>, 3-4 wt.% MgO, 4-8 wt.% CaO, 0.01-0.05 wt.% TiO<sub>2</sub>, 0.14-0.99 wt.% Al<sub>2</sub>O<sub>3</sub>, 1-2 MnO wt.%, 0.03-0.04 wt.% Na<sub>2</sub>O, 0.05-0.15 wt.% K<sub>2</sub>O, and 0.08-0.14 wt.% P<sub>2</sub>O<sub>5</sub>. In general concentrations of elements in the grunerite-dominant layers are higher than in quartz-dominant layers, but lower than the magnetite-dominant layers.

Of the six quartz-grunerite BIF samples sent for analysis, sample 4a-07-20-039 represents the grunerite-dominant layer end-member. Categorizing this sample as the grunerite-dominant layer end member is primarily based on this sample's grunerite-rich nature. The exact concentrations of these elements are as follows: ~1.2 wt.% Fe<sub>2</sub>O<sub>3</sub>, ~26 wt.% FeO, ~54 wt.% SiO<sub>2</sub>, ~4 wt.% MgO, ~7 wt.% CaO, ~0.03 wt.% TiO<sub>2</sub>, ~1 wt.% Al<sub>2</sub>O<sub>3</sub>, ~1 MnO wt. %, ~0.04 wt.% Na<sub>2</sub>O, ~0.15 wt.% K<sub>2</sub>O, and ~0.14 wt.% P<sub>2</sub>O<sub>5</sub>. Geochemically similar samples, to 4a-07-20-039, are 4a-07-20-028 and 4a-07-20-044. Together these samples delineate a spectrum of chemical characteristics observed in the sheared, grunerite-rich, variety of the quartz-grunerite BIF.

Quartz-dominant layers exhibit the following ranges, of major elements, in their geochemical composition: N.D-0.15 wt.% Fe<sub>2</sub>O<sub>3</sub>, 7-9 wt.% FeO, 84-88 wt.% SiO<sub>2</sub>, 1-2 wt.% MgO, 1-3 wt.% CaO, N.D-0.03 wt.% TiO<sub>2</sub>, 0.03-0.13 wt.% Al<sub>2</sub>O<sub>3</sub>, 0.23-0.60 MnO wt. %, N.D-0.01 wt.% Na<sub>2</sub>O, N.D-0.01 wt.% K<sub>2</sub>O, and ~0.01 wt.% P<sub>2</sub>O<sub>5</sub>. In general concentrations of elements, except SiO<sub>2</sub> in the quartz-dominant layers, are lower than in grunerite-dominant layers and magnetite-dominant layers.

Of the six quartz-grunerite BIF samples analysed, sample 4a-07-20-012 represents the quartz-dominant layer end-member. Categorizing this sample as the quartz-dominant layer end member is based on the fact that it has the highest SiO<sub>2</sub> and lowest values of other major elements, trace elements, as well as REE, LILE, and HILE. The exact concentrations of these elements are as follows: ~0.2 wt.% Fe<sub>2</sub>O<sub>3</sub>, ~7.4 wt.% FeO, ~88 wt.% SiO<sub>2</sub>, ~1 wt.% MgO, ~1 wt.% CaO, ~N.D wt.% TiO<sub>2</sub>, ~0.03 wt.% Al<sub>2</sub>O<sub>3</sub>, ~0.23 MnO wt.%, ~N.D wt.% Na<sub>2</sub>O, ~N.D wt.% K<sub>2</sub>O, and ~0.01 wt.% P<sub>2</sub>O<sub>5</sub>. Sample 4a-07-20-012 contains the lowest values of the following trace elements Cu, K, Mn, Ni, Sr, Y, and Zn.

Geochemically, sample 4a-07-20-054c contains ~84 wt.% SiO<sub>2</sub> and is comparable to 4a-07-20-012. Interestingly sample 4a-07-20-012, along with sample 4a-07-20-054c, contain the highest value of W at 43 ppm. Physically, both of these samples are relatively pristine quartz-grunerite BIF, suggesting that W is associated with chert. It should be noted that 4a-07-20-054c is a pristine quartz-grunerite BIF layer closely associated with a magnetite-dominant layer (4a-07-20-054m)

Sample 4a-07-20-054m is a magnetite-rich layer that was intercalated with pristine quartz-grunerite BIF (Plate 3.7a, 4a-07-20-054c). This sample is the only magnetite layer from this lithology making it unique. As such it is discussed on its own. It probably represents a transition from quartz-grunerite BIF to oxide-dominant BIF. The oxide-dominant BIF is described in the next section. This hypothesis is elaborated on in Chapter Five.

The magnetite-dominant layer exhibits the following concentrations of major elements: ~23 wt.% Fe<sub>2</sub>O<sub>3</sub>, ~25 wt.% FeO, ~18 wt.% SiO<sub>2</sub>, ~8 wt.% MgO, ~10 wt.% CaO, ~0.06 wt.% TiO<sub>2</sub>, ~1 wt.% Al<sub>2</sub>O<sub>3</sub>, ~2 MnO wt. %, ~0.05 wt.% Na<sub>2</sub>O, ~0.03 wt.% K<sub>2</sub>O, and ~0.08 wt.% P<sub>2</sub>O<sub>5</sub>. In general concentrations of elements in the magnetite dominant layers are higher than in the grunerite-dominant layers and the quartz-dominant layers.

**Table 3.5. Whole-rock geochemical data for the quartz-grunerite BIF.**

Sample ID	Quartz-Dominant		Grunerite-Dominant				Magnetite-	
	4a-07-20-012	4a-07-20-054c	4a-07-20-028	4a-07-20-039	4a-07-20-041	4a-07-20-044	4a-07-20-54m	
units	wt%	wt%	wt%	wt%	wt%	wt%	wt%	
MAJOR Elements	SiO <sub>2</sub>	87.75	83.89	55.11	53.45	60.83	60.58	17.71
	Al <sub>2</sub> O <sub>3</sub>	0.03	0.13	0.14	0.99	0.43	0.78	1.13
	TiO <sub>2</sub>	N.D.	0.03	0.01	0.03	0.03	0.05	0.06
	Fe <sub>2</sub> O <sub>3</sub>	0.15	N.D.	1.52	1.18	2.73	0.83	22.86
	FeO	7.38	9.10	24.82	26.37	22.3	24.73	24.65
	MnO	0.23	0.60	1.04	1.26	1.49	0.91	2.21
	MgO	1.07	1.63	3.75	4.19	3.98	3.39	7.43
	CaO	1.25	2.65	8.38	6.69	4.08	4.29	9.74
	Na <sub>2</sub> O	N.D.	0.01	0.04	0.04	0.03	0.03	0.05
	K <sub>2</sub> O	N.D.	0.01	0.05	0.15	0.05	0.05	0.29
	P <sub>2</sub> O <sub>5</sub>	0.01	0.01	0.08	0.14	0.13	0.14	0.08
	LOI	0.72	1.74	2.28	2.26	1.30	1.29	10.12
	TOTAL	99.41	100.38	99.98	99.69	99.86	99.81	99.09
	units	ppm	ppm	ppm	ppm	ppm	ppm	ppm
REE, LILE, HFSE	Ce	0.56	2.35	2.24	7.06	4.52	7.90	12.09
	Cs	0.021	0.118	1.372	0.23	1.868	0.132	0.418
	Dy	0.156	0.452	0.593	1.51	1.284	1.549	2.137
	Er	0.132	0.348	0.528	1.083	0.931	1.14	1.596
	Eu	0.067	0.215	0.15	0.609	0.55	0.641	0.926
	Gd	0.117	0.377	0.475	1.221	1.064	1.384	1.838
	Hf	N.D.	0.20	N.D.	0.30	0.20	0.30	0.30
	Ho	0.039	0.11	0.151	0.346	0.294	0.372	0.519
	La	0.33	1.42	1.13	3.56	2.1	3.87	6.68
	Lu	0.022	0.056	0.089	0.165	0.151	0.18	0.269
	Nb	N.D.	N.D.	N.D.	0.6	0.4	0.5	0.5
	Nd	0.29	1.16	1.37	3.65	2.57	4.18	5.96
	Pr	0.067	0.278	0.307	0.884	0.574	0.978	1.429
	Rb	0.11	0.60	3.14	6.39	3.29	2.15	8.48
	Sm	0.07	0.26	0.33	0.88	0.70	1.00	1.33
	Sr	8.90	22.1	14.2	28.1	16.1	18.6	72.4
	Tb	0.019	0.062	0.082	0.214	0.179	0.225	0.302
	Th	N.D.	0.06	N.D.	0.44	0.25	0.54	0.67
	Tm	0.02	0.053	0.086	0.157	0.139	0.169	0.24
	U	0.011	0.045	0.045	0.172	0.102	0.148	0.313
Y	1.47	3.82	4.89	10.36	8.54	10.86	16.35	
Yb	0.14	0.36	0.59	1.06	0.94	1.11	1.63	
Zr	N.D.	6.30	N.D.	12.2	9.20	10.8	14.0	
units	ppm	ppm	ppm	ppm	ppm	ppm	ppm	
TRACE	As	N.D.	36	24	85	96	17	65
	Ba	N.D.	108	31	68	69	N.D.	52
	Cr	N.D.	12	N.D.	8	N.D.	11	17
	Cu	1	10	35	25	15	15	46
	K	23	128	486	1453	418	438	3170
	Mn	1811	4759	8275	10547	5000	7267	19385
	Na	N.D.	110	216	120	67	144	209
	Nb	N.D.	N.D.	N.D.	N.D.	N.D.	N.D.	2
	Ni	5	10	16	27	18	17	43
	P	64	49	393	820	673	719	462
	Pb	N.D.	N.D.	N.D.	N.D.	N.D.	N.D.	8
	Rb	N.D.	N.D.	3	7	4	2	9
	Sc	N.D.	N.D.	7	N.D.	N.D.	N.D.	11
	Sn	N.D.	N.D.	N.D.	6	N.D.	N.D.	6
	Sr	9	21	14	34	16	19	78
	Th	N.D.	4	4	6	5	7	N.D.
	Ti	N.D.	N.D.	13	191	70	170	377
	V	N.D.	N.D.	5	13	9	13	25
	W	43	43	24	22	26	29	26
	Y	1	4	6	12	10	12	20
Zn	13	22	54	75	38	55	87	
Zr	N.D.	4	N.D.	6	5	8	14	

Note that REE, LILE, and HFSE values are the result of ICP-MS analysis whereas other trace element values and major elements are the result of XRF analysis. In the case of duplicate element values, i.e. Y and Zr, ICP-MS values are used. N.D.= not detected i.e. below detection limit (detection limits are presented in Table 1.2).

## 3.5 Oxide-Dominant Layered Iron Formation

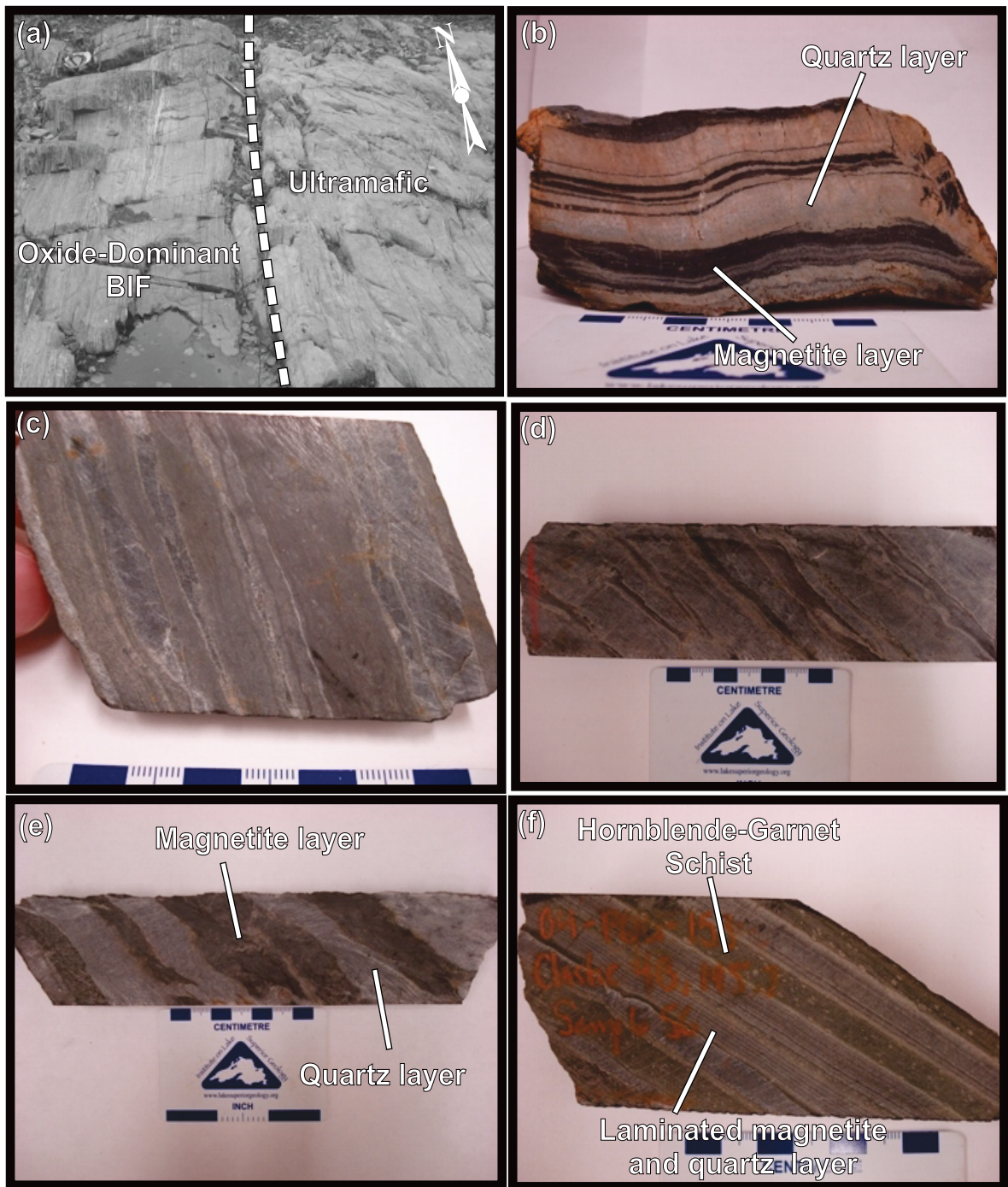
### 3.5.1 Macroscopic Character

The NIF assemblage oxide-dominant BIF is the most widely observable metasedimentary lithology at Musselwhite. It is extensive in outcrop (Plate 3.10a), underground drifts, and in drill core (Plate 3.10b-f). The NIF assemblage oxide-dominant layered iron formation is a quartz-magnetite BIF. As such it is a strongly magnetic lithology. Visually, the oxide-dominant BIF is distinct due to its layered black, white, and beige appearance (Plate 3.10b). Its appearance is primarily a reflection of its relatively simple mineralogy (Plate 3.10c). It consists of alternating layers, typically between 0.5-3.0 cm thick, of dark-grey magnetite-dominated, light-grey quartz-dominated, and tan grunerite-dominated layers (Plate 3.10d). Contacts between the different layers are sharp. Common deformation features in this lithology are open to tight folding (Plate 3.11b) and slightly sheared fabric (Plate 3.10d).

There are several variations of the oxide-dominant BIF. This lithology can be subdivided into three distinct subtypes; 1) a thinly-laminated oxide-dominant BIF, found in the lower part of the NIF assemblage just above the previously described quartz-grunerite BIF, that comprises <50% of the unit, 2) a thickly layered oxide-dominant BIF that comprises >50-85% of this unit (Plate 3.10a-e), and 3) a transitional lithology composed of intercalated layered hornblende-garnet schist and magnetite and quartz laminations (Plate 3.10f), (mine-terminology: clastic 4b), which is found in the stratigraphically upper portion of this unit and represents the transition between the oxide-dominant and silicate-dominant BIF.

Thirteen samples were collected from trenches four and five, sample locations are shown in Figure 1.8, and sample descriptions are given in Appendix D. In addition, ten samples were collected from drill core. Sample locations and descriptions are given in Appendix D.

On average the NIF assemblage oxide-dominant BIF is composed of ~ 40% magnetite layers, 40% quartz, <15% grunerite, and <5% sulphides (pyrrhotite ± arsenopyrite, and



**Plate 3.10. Photographs of NIF assemblage oxide-dominant banded iron formation.** a) Photograph of outcrop (trench #5, see Fig. 1.8 for exact location) showing contact between oxide-dominant BIF on the left and ultramafic rock on the right, b) Photograph of hand sample (4b-PM05-031) collected from surface at Musselwhite mine showing black, white, and beige striped appearance of the oxide-dominant BIF, c) Photograph of core sample (4b-07-20-004) showing translucent grey appearance of meta-chert layers, d) Photograph of core sample (4b-07-20-005) showing beige coloured grunerite-rich layers between quartz and magnetite layers, e) Photograph of core showing typical thickly banded oxide facies BIF, f) Photograph of transitional lithology, found between the oxide- and silicate-dominant BIFs, showing hornblende-garnet schist bands intercalated with thinly-laminated magnetite and quartz.

chalcopyrite). Quartz and magnetite layers tend to have comparable thickness in the same samples.

The NIF assemblage oxide-dominant BIF consists of a simple mineral assemblage of magnetite, quartz, grunerite, carbonate, and sulphides  $\pm$  apatite. Compositional layering is well developed in the NIF assemblage oxide-dominant BIF with sharp contacts between the various layers. Macroscopically the oxide-dominant BIF can be derived into; 1) magnetite dominated layers, 2) quartz-dominated layers (meta-chert), and 3) iron-silicate reaction layers between quartz and magnetite layers.

#### *Magnetite Layers*

In the NIF assemblage oxide-dominant BIF, the magnetite-dominant layers are well defined up to a relatively high degree of strain. Magnetite-dominant layers are dark grey to black and strongly magnetic. Magnetite layers range from homogeneous pure magnetite to containing thin quartz laminations on the order of 0.1-0.2 cm thick.

Disseminated pyrrhotite, arsenopyrite, and chalcopyrite are confined to the magnetite-layers whereas secondary pyrrhotite and arsenopyrite occur in fractures crosscutting magnetite and quartz layers. Chalcopyrite is found as minor inclusions within pyrrhotite. Arsenopyrite, although rare compared to pyrrhotite, is observed in the NIF assemblage oxide-dominant BIF more than other lithologies.

#### *Quartz Layers*

Quartz-dominant layers in the NIF oxide-dominant BIF are light-grey to translucent, slightly magnetic, have a sugary texture, and are commonly boudinaged. Magnetism is caused by fine-grained disseminated magnetite. These layers represent meta-chert layers. The quartz-dominant layers are more resilient than the magnetite-dominant layers as such they exhibit both brittle and ductile deformation features. Depending on the degree of deformation, quartz-layers range from moderately to strongly defined in the NIF assemblage oxide-dominant BIF.



Quartz veins preferentially form in the meta-chert layers. A high degree of quartz veining is indicated by a more translucent appearance (Plate 3.10d) and less magnetic nature. Secondary sulphides, hornblende, and visible gold are associated with quartz-veins crosscutting the oxide-dominant BIF.

#### *Grunerite Layers*

Grunerite-layers range between ~0.2 to ~0.7 cm thick and are found as reaction layers between the magnetite- and quartz-layers (Plate 3.10d and e). Grunerite layers are typically fine to medium grained, tan-yellow in appearance, and are approximately half the thickness of average quartz and magnetite layers. Medium-grained, disseminated, carbonate occurs as an accessory mineral in these layers. In hand sample the presence of carbonate is primarily identified using hydrochloric acid.

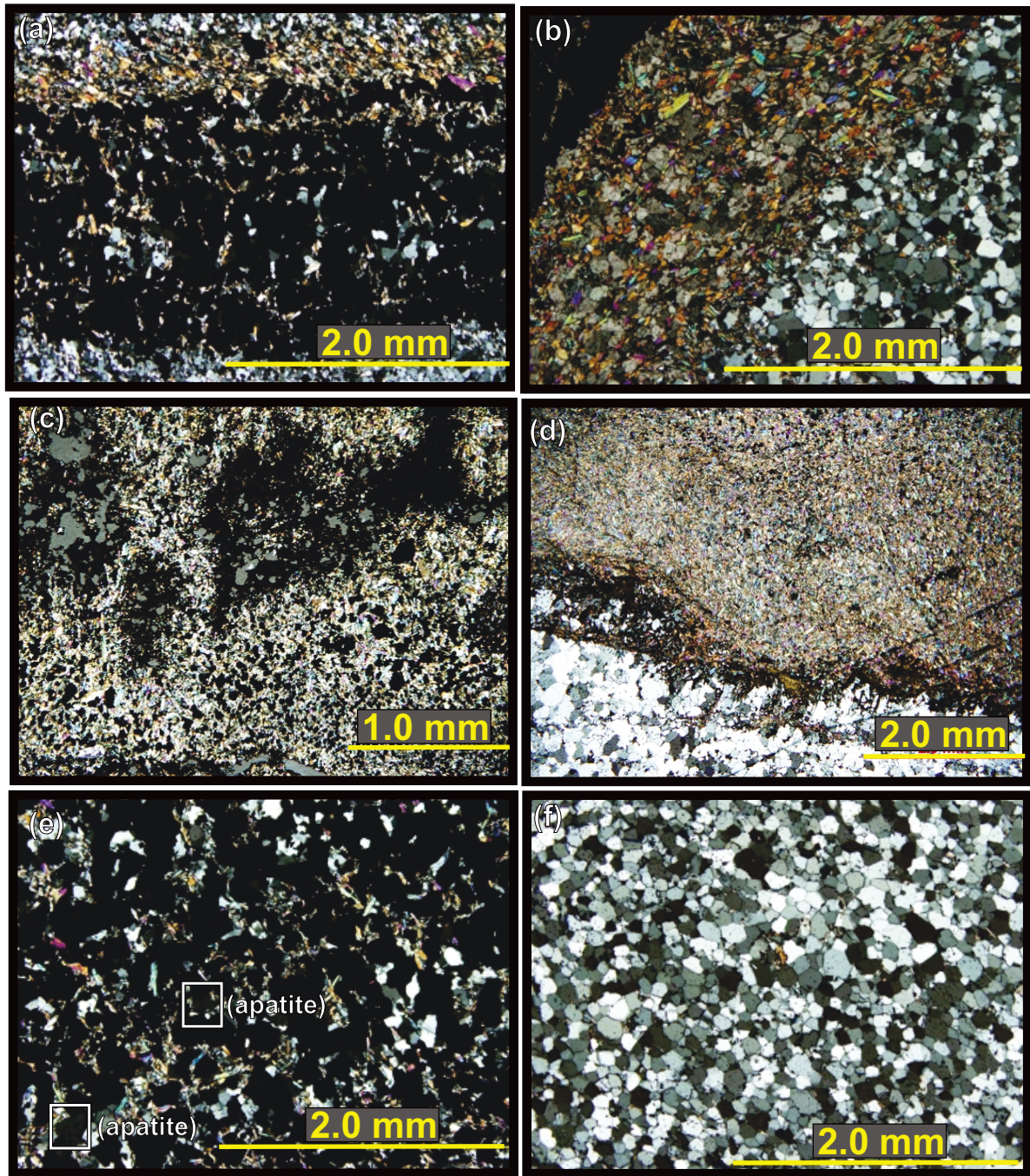
### 3.5.2 Petrographic Character

Petrographic observations are based on twenty-one thin-sections of the NIF assemblage oxide-dominant BIF. Thin-sections were made from samples sent for geochemical analysis as well from hand samples. Representative samples, exhibiting a range of commonly observed features such as layering, folding, and shear fabrics, were specifically selected. Refer to Appendix B for the individual thin-section descriptions.

The mineralogy of the oxide-dominant layered iron formation is relatively simple compared to the other lithologies in the NIF assemblage. On a microscopic level samples of the NIF oxide-dominant BIF are a reflection of the macroscopic appearance of the lithology. They consist of 60% magnetite and 40% quartz and grunerite. This lithology is compositionally layered with three types of layers prevailing; 1) magnetite-dominated (Plate 3.11a), 2) quartz-dominated (meta-chert) (Plate 3.11b), and 3) grunerite-pyroxene-carbonate-dominated (Plate 3.11b).

#### *Magnetite layers*

Magnetite-dominant layers (Plate 3.11a) are on average between 0.5-1.0 cm thick and contain from 80% to near 100% anhedral to subhedral very fine-grained magnetite



**Plate 3.11. Photomicrographs of NIF assemblage oxide-dominant BIF.** a) Photomicrograph (ppl) of 2mm thick magnetite-dominated layer with associated minor grunerite layer (sample 4b-PM05-028), b) Photomicrograph (ppl) of grunerite-dominant layer between quartz- and magnetite- dominated layers (sample 4b-PM05-038), c) Photomicrograph (xpl) of grunerite-rich magnetite- dominant layer, note xenomorphic magnetite grains (sample 4b-PM05-005), d) Photomicrograph (xpl) of grunerite-rich layer, note the lack of magnetite (sample 4b-PM05-019), e) Photomicrograph (xpl) of magnetite-dominant from oxide-dominant BIF showing subhedral magnetite grains with interstitial anhedra quartz, subhedral grunerite, and anhedra apatite crystals (sample 4b-PM05-028), f) Photomicrograph (xpl) of chert layer from oxide facies BIF showing well developed triple point junctions between quartz grains, as well as minor disseminated magnetite and grunerite grains (sample 4b-PM05-043).

grains, 3% to 20% quartz grains and <5% grunerite, apatite, and carbonate grains. The magnetite and quartz grains are approximately 5  $\mu\text{m}$  to 20  $\mu\text{m}$  in diameter, which is roughly twice as large as the quartz grains in the quartz-dominant layers (Plate 3.11a and b).

Petrographically, there is a difference between the oxide-dominant BIF from the trenches and that seen in the drill core. Magnetite layers in typical core samples consist mostly of magnetite with lesser amounts of quartz (Plate 3.11a and b). These layers have sharp contacts with the grunerite dominant layers (Plate 3.11b). However, magnetite layers in typical trench samples contain up to 50% grunerite, with equal amounts of fine-grained relict magnetite and little to no quartz (Plate 3.11c and d). These layers are commonly zoned and consist of fine-grained relict xenomorphic magnetite at their core with the rest of the layer being made up of coarser-grained grunerite grains.

It should be noted that quartz grains are preserved in magnetite layers from drill core, but rarely in trench samples. Additionally, in oxide-dominant BIF samples from core, magnetite grains often contain fine-grained apatite, calcite, and sulphide inclusions. Relatively large apatite grains (Plate 3.11e) occur outside of the magnetite grains with associated quartz and grunerite.

#### *Quartz layers*

Quartz layers, on average, are between 0.5-3.0 cm thick, and consist of >95% fine-grained quartz with <5% disseminated magnetite, grunerite, and carbonate grains (Plate 3.11b). Quartz grains range between 3  $\mu\text{m}$  to 5  $\mu\text{m}$  in diameter, display moderately developed triple point junctions, and are characterized by straight grain boundaries. However, in deformed samples, the margins of the quartz grains become sutured as grain-size reduction comes into play. Occasionally, quartz grains are finer grained in the centre of the layer and coarser grained nearer the margins of the layer.

Very fine-grained magnetite, grunerite, and carbonate grains are disseminated throughout the quartz layers. Grains of these minerals are much finer-grained than the quartz grains and are found along grain boundaries rather than as inclusions. Magnetite grains, in the quartz-dominant layers, are roughly 10% the size of the surrounding quartz grains.

Grunerite grains are needle-like to euhedral diamond-shaped whereas carbonate grains are subhedral.

Thin quartz veins perpendicularly crosscut the quartz layers. These veins are distinguished from quartz-dominant layers by their coarser grain size and linear nature. Pyrrhotite is mainly associated with these crosscutting quartz veins. Minor chalcopyrite and pyrite are associated with the pyrrhotite as annealed grains.

#### *Grunerite-pyroxene-carbonate layers*

Again, as discussed in the section on magnetite dominant layers, there is an incongruity between grunerite-dominant layers seen in core samples (Plate 3.11a and b) versus what is seen in trench samples (Plate 3.11c and d). Regardless, these layers are principally composed of iron-rich silicate minerals, primarily grunerite with lesser amounts of pyroxene, and carbonate.

As the name implies, the grunerite-dominant layers consist predominantly of grunerite with minor iron-rich carbonate  $\pm$  pyroxene. Fine- to medium-grained grunerite grains occur as both laths and euhedral typical amphibole 'diamond' shapes. These grains have 54/126° cleavage, well developed twinning, and high birefringence characteristic of grunerite. Grunerite laths, sometimes in 'fan'-shaped aggregates, are frequently found at the edges of the grunerite-pyroxene-carbonate layers radiating into the quartz layers. In petrographic examination one can see the reduction in magnetite grain size in association with grunerite growth (Plate 3.11c).

In oxide-dominant BIF samples, collected from core, layers are generally 0.1-0.4 cm thick, which is less than half the width of the surrounding quartz and magnetite layers. The grunerite-pyroxene-carbonate layers typically occur between quartz and magnetite layers. Grains in the grunerite-dominant layers are slightly coarser grained than grains in the quartz and magnetite layers.

Accessory minerals, in oxide-dominant BIF collected from core, include fine- to medium-grained, anhedral to subhedral, orthopyroxene. These grains are first- to second-order yellow-orange in colour, exhibit well developed cleavage, and have parallel extinction. Carbonate grains are confined to the centre of the layers and exhibit

characteristic well developed calcite twinning with high-birefringence. Carbonate and pyroxene are minor components, composing up to 10%, of the grunerite-pyroxene-carbonate layers.

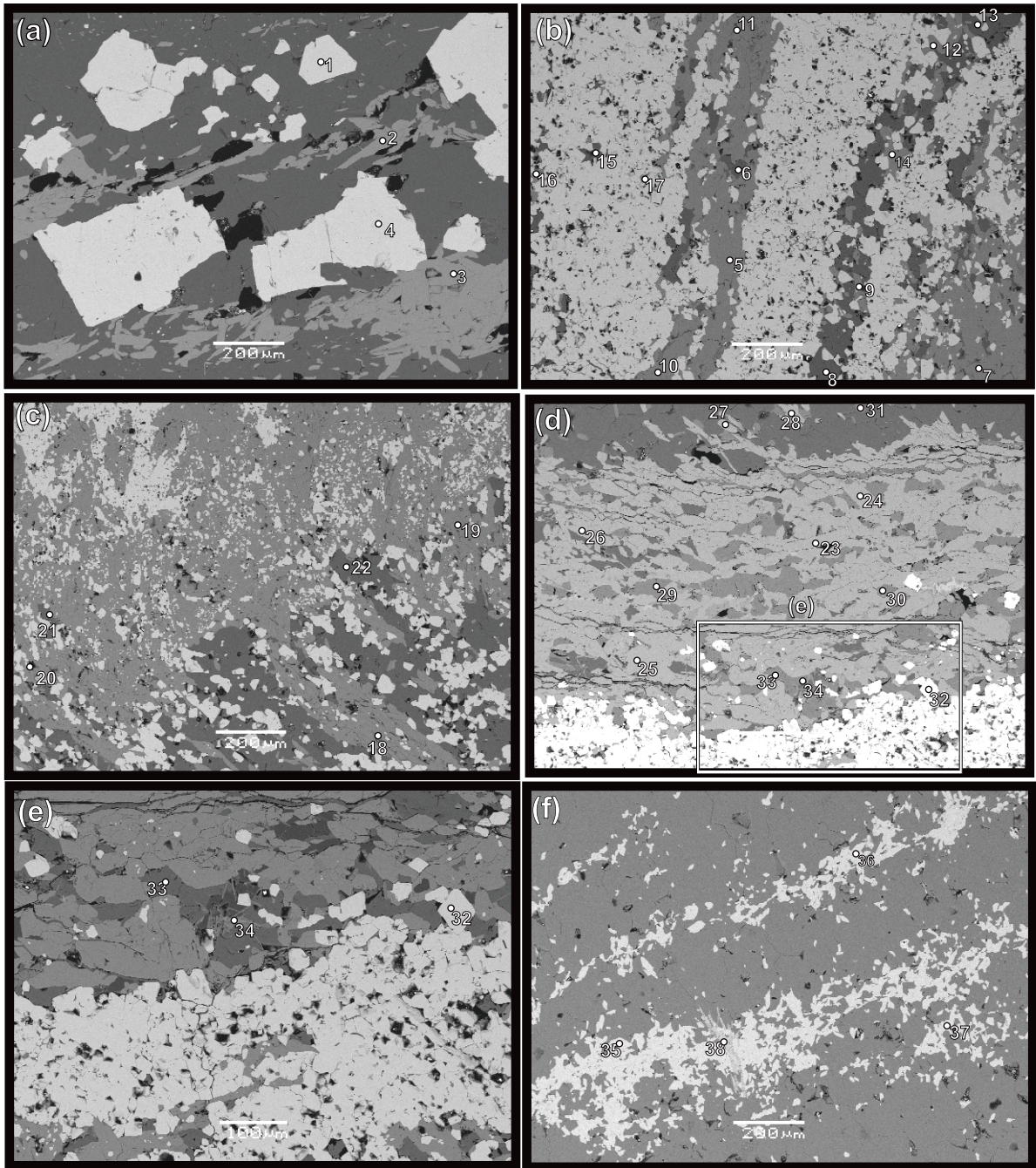
Typical trench samples do not have well defined grunerite-dominant layers as the magnetite-dominant layers have been altered to grunerite. These layers consist of between 40% to 100% grunerite, surrounding relict magnetite grains, with little to no quartz content. Grunerite grains are fine- to medium-grained and form a homogeneous mass. Carbonate is a minor component in these layers, but pyroxene appears to be absent.

### 3.5.3 Mineral Compositions

As mentioned in Section 3.5.2, the NIF assemblage oxide-dominant BIF is composed primarily of quartz and magnetite with lesser amounts of grunerite, carbonate, pyroxene and pyrrhotite. Grunerite and carbonate were analysed with the SEM for mineral chemistry. However, a limited amount of quartz and magnetite were analysed because their chemistry is uniform and consequently the amount of information gained from them is negligible. Plate 3.12a-f shows SEM backscatter electron images of the NIF assemblage oxide-dominant BIF. Numbered points on Plate 3.12 correspond to mineral analysis results summarized in Table 3.6. Most analyses focused on the composition of the grunerite grains.

Grunerite is the third most abundant mineral, after quartz and magnetite, in the NIF assemblage oxide-dominant BIF. Grunerite grains in the NIF assemblage oxide-dominant BIF typically consist of 6.0-8.0 wt.% MgO, 50-51 wt.% SiO<sub>2</sub>, and 38-39 wt.% FeO. Grunerite chemistry appears to be consistent in the NIF assemblage oxide-dominant BIF regardless of whether it occurs in a quartz- or magnetite-dominant layer.

Carbonate is found predominantly in the grunerite-rich layers found between the quartz- and magnetite-dominant layers (Plate 3.12d). Carbonate mineral chemistry was not known prior to examination of the NIF assemblage oxide-dominant BIF with the SEM. The most abundant carbonate mineral in this lithology is iron-rich calcite. Iron-rich calcite, in this lithology, contains on average ~48-51 wt.% CaO and ~2-4 wt.% FeO.



**Plate 3.12. SEM-BSE images of the NIF assemblage oxide-dominated banded iron formation collected from Musselwhite mine. Note that the numbered points correspond to the point analysis in Table 3.6. a) BSE image of minor magnetite-dominated layer composed of euhedral magnetite crystals (sample 4b-PM05-046), b) BSE image of more typical magnetite-dominant layer with minor layers of Fe-carbonate and grunerite (sample 4b-PM05-019), c) BSE image of grunerite grains growing at the expense of magnetite grains (sample 4b-PM05-019), d) BSE image of typical grunerite-carbonate layer found between quartz and magnetite dominated layers (sample 4b-PM05-048), e) BSE image of magnetite-dominant layer next to iron silicate minerals (sample 4b-PM05-019), f) BSE image of thin magnetite dominated layers found between quartz-dominated layers, note biotite bowtie in the middle of the lowest layer (sample 4b-PM05-019).**



### 3.5.4 Geochemical Composition

The chemistry of this lithology, summarized in Tables 3.7 and 3.8, is variable. Differences in composition are primarily attributed to different combinations of the three end-member components which comprise this lithology. These end-member components are; 1) magnetite-dominated layers (n=10), 2) quartz-dominated layers (n=13), and 3) siliciclastic-dominated layers (n=6). The geochemistry can therefore be discussed in terms of magnetite-dominated, quartz-dominated, and siliciclastic-dominant layers. It should be noted that compositional layers in the NIF oxide-dominant BIF represent a spectrum from magnetite-dominant to quartz-dominant end-members. Siliciclastic-dominant layers are comparatively rare.

#### *Magnetite-Dominant Layers*

Magnetite-dominant layers exhibit the following ranges of major elements in their geochemical composition: 7.0-65 wt.% Fe<sub>2</sub>O<sub>3</sub>, 12-32 wt.% FeO, 10-41 wt.% SiO<sub>2</sub>, 1-6 wt.% MgO, 0.1-6.0 wt.% CaO, <0.01-0.03 wt.% TiO<sub>2</sub>, 0.04-0.06 wt.% Al<sub>2</sub>O<sub>3</sub>, 0.1-1.0 MnO, 0.02-1.0 wt.% Na<sub>2</sub>O, <0.01-3.0 wt.% K<sub>2</sub>O, and 0.02-0.3 wt.% P<sub>2</sub>O<sub>5</sub>. Relative to the quartz-dominant layers, concentrations of trace elements such as TiO<sub>2</sub>, Zr, P, Zn, and Cu are highest in the magnetite layers. Variations in Fe<sub>2</sub>O<sub>3</sub>, FeO, SiO<sub>2</sub>, and MnO are primarily reflected mineralogically by the ratio of magnetite to quartz to grunerite.

Of the fifteen magnetite-dominant layer samples sent for analysis, sample 4b-PM05-039 represents the magnetite-dominant layer end-member. Categorizing this sample as the magnetite-dominant layer end-member is based on the fact that it has the highest Fe<sub>2</sub>O<sub>3</sub>, and lowest SiO<sub>2</sub>, content of all the samples. The exact concentration of relevant elements are as follows: 59 wt.% Fe<sub>2</sub>O<sub>3</sub>, 27 wt.% FeO, 0.03 wt.% P<sub>2</sub>O<sub>5</sub>, 44 ppm Cr, 22 ppm Cu, 13 ppm Ni, 12 ppm Sn, and 25 ppm Zn. Sample 4b-07-20-039 contains the lowest value of the following elements at 10 wt.% SiO<sub>2</sub> and 0.13 wt.% CaO.

#### *Quartz-Dominant Layers*

The NIF assemblage oxide-dominant BIF quartz-dominant layers exhibit the following ranges, of major elements, in their geochemical composition: <0.01-8.0 wt.% Fe<sub>2</sub>O<sub>3</sub>, 1-31 wt.% FeO, 56-97 wt.% SiO<sub>2</sub>, 0.2-7.0 wt.% MgO, 0.03-4.0 wt.% CaO, <0.01-0.05 wt.% TiO<sub>2</sub>,







0.02-2.0 wt.% Al<sub>2</sub>O<sub>3</sub>, 0.02-1.0 MnO, <0.01-0.2.0 wt.% Na<sub>2</sub>O, 0.01-1.0 wt.% K<sub>2</sub>O, and 0.01-0.20 wt.% P<sub>2</sub>O<sub>5</sub>. The trace elements Nb, Sb, Se, Sn, Ta, and U are undetectable in all the quartz-dominant layer samples.

All quartz-dominant layers in the NIF assemblage oxide-dominant BIF contain measurable amounts of Fe<sub>2</sub>O<sub>3</sub> and FeO. Fe<sub>2</sub>O<sub>3</sub> and FeO are incorporated into magnetite and iron-silicate minerals. The presence of disseminated fine-grained magnetite and iron-silicate minerals is evident in thin-section suggesting these layers are meta-chert layers as opposed to quartz-veins.

Of the thirteen quartz-dominant layer samples sent for analysis, sample 4b-PM05-018 represents the quartz-dominant layer end-member. Categorizing this sample as the quartz-dominant layer end member is based on the fact that it has the highest SiO<sub>2</sub> and lowest Fe<sub>2</sub>O<sub>3</sub> content. Sample 4b-PM05-018 contains the lowest values of the following elements at 0.03 wt.% CaO, 1.5 wt.% Fe<sub>2</sub>O<sub>3</sub>, 0.71wt.% FeO, 0.16 wt.% MgO, 0.02 wt.% MnO, and <0.01 wt.% TiO<sub>2</sub>. The low concentrations of these elements, in conjunction with minimal quartz-veins observable in thin-section, suggest that sample 4B-PM05-018 is the purest and most representative sample of the quartz-dominated layers.

Sample 4B-PM05-040c contains the lowest percentage of SiO<sub>2</sub> at 55.76 wt.% compared to the other meta-chert samples. This sample also contains the highest percentages of the following elements at 30.56 wt.% Fe<sub>2</sub>O<sub>3</sub>, 30.56 wt.% FeO, 6.94 wt.% MgO, 1.07 wt.% MnO, and 0.22 wt.% P<sub>2</sub>O<sub>5</sub>. Additionally this sample contains high concentrations of the majority of the REE, LILE, and HFSE relative to other quartz-dominant samples. Sample 4b-PM05-040c therefore represents a transition between quartz- and magnetite-dominant layers.

Sample 4b-07-20-005c contains the highest concentrations of the vast majority of the REE, LILE, and HFSE (excluding Ce, Cs, La, Rb, and Sr). This sample also contains high concentrations of other trace elements. Sample 4b-PM05-038 contains the lowest concentrations of the vast majority of the REE, LILE, HFSE and other trace elements (excluding Ce, Cs, Ho, and La).

Aside from Fe<sub>2</sub>O<sub>3</sub> and SiO<sub>2</sub> concentrations, the geochemical makeup of the magnetite- and quartz-dominant layers does not differ dramatically. Concentrations of FeO, MnO, MgO, CaO, Na<sub>2</sub>O, and P<sub>2</sub>O<sub>5</sub> are comparable between magnetite- and quartz-dominant layers. However, Al<sub>2</sub>O<sub>3</sub> and TiO<sub>2</sub> values are multiple times higher in the magnetite-dominated layers compared to the quartz-dominant layers. Additionally the ratio between Fe<sub>2</sub>O<sub>3</sub> and FeO is higher in the quartz-dominant layers and lower in the magnetite dominant layers. This suggests Fe is primarily found in iron-silicate minerals in the quartz-dominant layers and magnetite in the magnetite-dominant layers. This geochemical trend correlates to observed petrographic features.

#### *Siliciclastic-Dominant Layers*

Siliciclastic layers exhibit the following ranges, of major elements, in their geochemical composition: 7-37 wt.% Fe<sub>2</sub>O<sub>3</sub>, 22-29 wt.% FeO, 17-81 wt.% SiO<sub>2</sub>, 2-6 wt.% MgO, 1-6 wt.% CaO, 0.03-0.5 wt.% TiO<sub>2</sub>, 0.05-9.0 wt.% Al<sub>2</sub>O<sub>3</sub>, 0.04-1.0 wt.% MnO, 0.03-1.0 wt.% Na<sub>2</sub>O, 0.15-3.0 wt.% K<sub>2</sub>O, and 0.07-0.30 wt.% P<sub>2</sub>O<sub>5</sub>.

Of the six siliciclastic layer samples sent for analysis, sample 4b-07-20-056 represents the siliciclastic-dominant layer end-member. Categorizing this sample as the siliciclastic-dominant layer end-member is based on the fact that it has the highest Al<sub>2</sub>O<sub>3</sub>, TiO<sub>2</sub>, K<sub>2</sub>O, Na<sub>2</sub>O, Zr, Rb, and Sr content. These elements are associated with siliciclastic detrital clay minerals (Boström, 1973). Sample 4b-07-20-056 exhibits the following concentrations of relevant major elements at: 46.2 wt.% SiO<sub>2</sub>, 8.74 wt.% Al<sub>2</sub>O<sub>3</sub>, 0.5 wt.% TiO<sub>2</sub>, 7 wt.% Fe<sub>2</sub>O<sub>3</sub>, 24.29 wt.% FeO, 3 wt.% MgO, 3.17 wt.% CaO, 1.37 wt.% Na<sub>2</sub>O, 2.62 wt.% K<sub>2</sub>O, 0.67 wt.% MnO, and 0.10 wt.% P<sub>2</sub>O<sub>5</sub>. Sample 4b-07-20-056 exhibits the following concentrations of relevant trace elements at: 150 Rb ppm, 89 Sr ppm, and 54 ppm Zr. The higher concentration of these elements is reflected mineralogically by the presence of abundant tschermakite-hornblende and almandine-rich garnet in sample 4b-PM05-056. This sample is transitional between the oxide- and silicate-dominant BIF.

In addition to 4b-07-20-056, samples 4b-07-20-004m, 4b-07-20-040m, 4b-07-20-067m, 4b-PM06-028m, and 4b-07-20-055m contain a siliciclastic component. This is based on the samples high Al<sub>2</sub>O<sub>3</sub> content relative to other NIF oxide-dominant BIF samples.

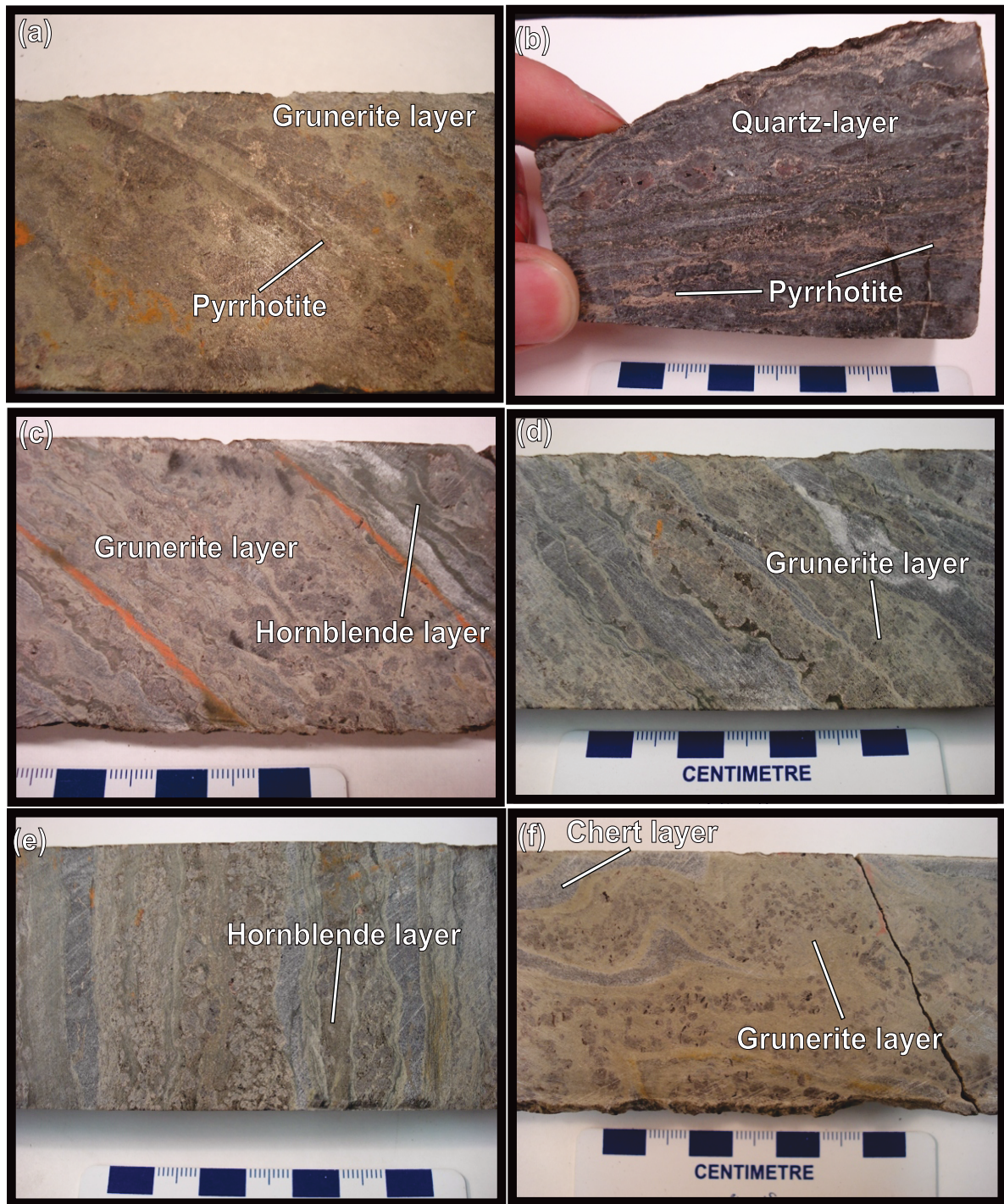
## 3.6 Silicate-Dominant Layered Iron Formation

### 3.6.1 Macroscopic Character

The NIF assemblage silicate-dominant BIF (Plate 3.13) is the second-most frequently observed metasedimentary lithology after the oxide-dominant BIF. Historically this lithology is the principal ore at Musselwhite Mine, and as such, it is widespread in drill core and underground drifts. However, it is rarely seen in outcrop, with one notable exception being near the PQ shallows open pit (Figure 1.4). Refer to Chapter One for the general stratigraphic location of this lithology and Chapter Two for a detailed description of its stratigraphy.

The NIF assemblage silicate-dominant BIF ranges from broadly folded to sheared. In terms of mineralogy it is more complex than the underlying oxide-dominant BIF and is composed of, on average, ~30% to ~40% quartz and ~60% to ~70% Fe-silicate minerals. This lithology consists of a relatively complex mineral assemblage made up of varying combinations of the following minerals: quartz, grunerite, hornblende, garnet, pyrrhotite, magnetite, carbonate  $\pm$  chlorite, arsenopyrite, and chalcopyrite. Magnetite is rarely visible, but its presence is denoted by magnetism in hand samples. Pyrrhotite, in this lithology is rarely magnetic, and can occur in percentages up to 10-20% over small intervals (<1m). The presence of these minerals is supported by X-ray diffraction work carried out by Otto (2002), which indicated the silicate-dominant BIF contains abundant quartz, garnet, cummingtonite-grunerite, and hornblende along with minor magnetite, pyrrhotite, biotite, calcite, and chlorite.

Several variations of the silicate-dominant BIF exist. These variations are primarily a product of the degree of deformation (i.e., shearing). Quartz-veining, carbonate-veining, and sulphidation are associated with shearing at Musselwhite. The exploration geologists at Musselwhite Mine subdivide the silicate-dominant BIF into three distinct subtypes (John Biczok, personal communication, 2007). These subtypes are as follows; 1) 'Well developed' consisting of sheared and sulphidized silicate-dominant BIF, with abundant quartz veins, coarse-grained garnet porphyroblasts, and pyrrhotite, usually found where the silicate-dominant BIF intersects a shear-zone (Plate 3.13a and b), 2) 'Moderately developed'



**Plate 3.13. Photographs of silicate dominant banded iron formation in core samples collected from Musselwhite Mine.** a) Photograph of garnet-grunerite-dominated layers with high pyrrhotite content, sample taken from C-block ore zone (sample 4ea-07-20-004), b) Photograph of sheared, silicate-dominated BIF with abundant quartz veins, pyrrhotite, and visible gold (sample 4ea-0620-UG004), c) Photograph of garnet-grunerite dominated layers with garnet-hornblende-dominated layers visible in upper right hand corner (sample 4ea-PM06-002), d) Photograph of garnet-grunerite-dominated layers (sample 4ea-PM06-043), e) Photograph of garnet-hornblende dominated layers (sample 4ea-0830-002), f) Photograph of broadly folded garnet-grunerite dominated layers (sample 4ea-PM06-007).

consisting of slightly sheared, less sulfidized, silicate-dominant BIF with finer grained garnet porphyroblasts, and less abundant pyrrhotite (Plate 3.13c and d); and 3) “Poorly developed” consisting of relatively undeformed broadly folded, unsulfidized, silicate-dominant BIF, containing finer-grained garnet porphyroblasts and minimal pyrrhotite (Plate 3.13e, and f). At this point it should be noted that fourteen drill-core samples and one large underground sample of silicate-dominant BIF were collected in total. Five samples of each subtype were collected. Relevant sample information, such as drill hole number and meterage, as well as the sample descriptions are provided in Appendix D.

Visually, the silicate-dominant BIF is distinct due to its compositionally layered nature. Alternating layers, typically on the order of 0.5-3.0 cm thick, can be broadly grouped into Fe-silicate-dominant and quartz-dominant layers. More specifically the layers in the silicate-dominant BIF can be divided into; 1) garnet-grunerite-dominant layers, 2) garnet-hornblende-dominant layers, and 3) quartz-dominant layers (meta-chert). Contacts between the different compositional layers range from sharp to deformed in nature.

The silicate-dominant BIF ranges from tan-yellow (Plate 3.13a, c, and f) to dark-green (Plate 3.13b, d and e) in appearance depending on which compositional layers predominate. The appearance of this lithology is also affected by common deformation features such as open to tight folding (Plate 3.13f) and slightly- to strongly-sheared fabric (Plate 3.13b).

#### *Garnet-Grunerite-Dominant Layers*

The garnet-grunerite layers consist of a fine- to medium-grained grunerite groundmass surrounding coarser-grained (~0.2-1.5cm diameter) almandine garnet porphyroblasts. These layers have a tan-yellow appearance (Plate 3.13a, c, and f) and typically range from 0.5 cm to 3.0 cm in thickness. The layers are usually thicker than the surrounding quartz-dominant layers. Disseminated magnetite and carbonate occur as accessory minerals in these layers. In hand sample the presence of carbonate is primarily identified using hydrochloric acid. These layers range from homogeneous pure garnet and grunerite

mixtures which may contain thin laminations of quartz-, magnetite-, biotite, or hornblende-rich laminations on the order of 0.1-0.5 cm thick.

#### *Garnet-Hornblende-Dominant Layers*

In the NIF assemblage silicate-dominant BIF, the garnet-hornblende-dominant layers are well defined and usually associated with relatively high degrees of shearing as well as quartz and carbonate veining (Plate 3.13d and e). The garnet-hornblende layers are dark-green and weakly magnetic. These layers range from homogeneous pure garnet and hornblende mixtures to containing thin laminations of quartz-, magnetite-, or grunerite-rich laminations on the order of 0.1-0.5 cm thick.

The garnet-hornblende dominant layers of the silicate-dominant BIF can resemble the hornblende-garnet schist layers of the transitional oxide-dominant BIF (Plate 3.10f) described in the previous section. As well, these layers can resemble the overlying hornblende-garnet schist described in the following section.

#### *Quartz Layers*

Quartz-dominant layers in the NIF silicate-dominant BIF are light-grey to translucent, slightly magnetic, have a sugary texture, and are commonly boudinaged. Magnetism is caused by fine-grained disseminated magnetite. The presence of magnetite indicates these layers represent meta-chert layers. The quartz-dominant layers are more competent than the Fe-silicate-dominant layers as such they exhibit both brittle and ductile deformation features. Depending on the degree of deformation, quartz-layers range from moderately to strongly defined in the NIF assemblage silicate-dominant BIF.

#### *Quartz and Carbonate Veins*

Like other lithologies in the NIF assemblage this one is cross cut by quartz and carbonate veins that range from <1cm to ~5cm wide, although much larger veins also occur (<1m). Quartz veins preferentially form in the meta-chert layers especially where the silicate-dominant BIF is sheared. A high degree of quartz veining is indicated by a more translucent appearance (Plate 3.13b) and less magnetic nature of the rock. Chlorite patches are found at the margins, and within, quartz veins associated with shear zones.



Secondary sulphides, hornblende, and gold are associated with quartz-veins crosscutting the silicate-dominant BIF. Disseminated pyrrhotite is found in the Fe-silicate layers, as well as in small veins crosscutting quartz-dominant layers. Chalcopyrite and arsenopyrite are found as minor inclusions within pyrrhotite. Sulphides are the predominant indicator of gold mineralization at Musselwhite with ~10-12% pyrrhotite over 1m roughly indicating 5g/t gold in the rock (John Biczok, personal communication, 2007).

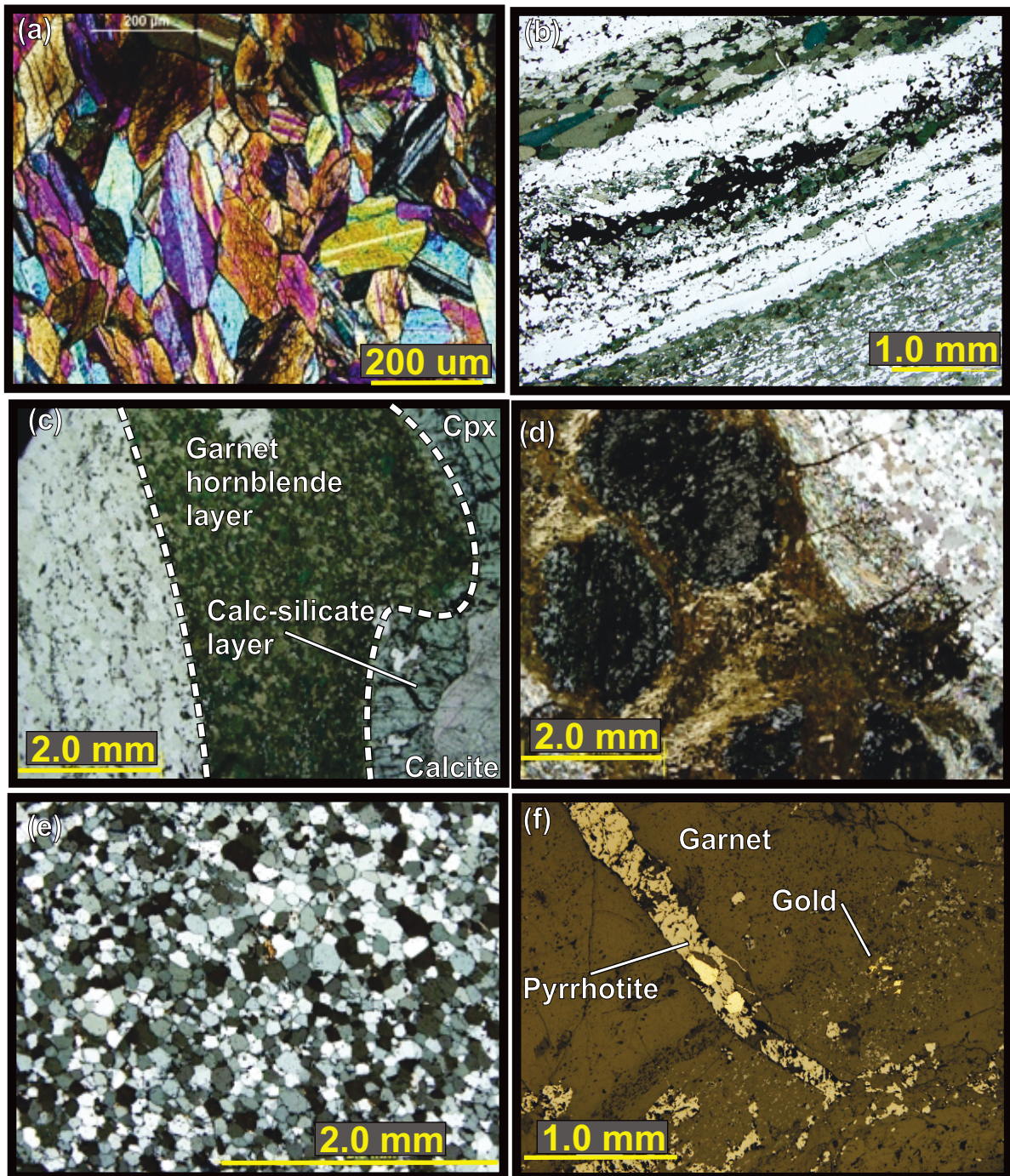
### 3.6.2 Petrographic Character

Petrographic observations are based on eighteen thin-sections of silicate-dominant BIF. Thin-sections were made from samples sent for geochemical analysis as well as from hand samples. Representative samples, exhibiting a range of commonly observed features such as layering, folding, and shear fabrics, were specifically selected. Refer to Appendix B for the individual thin-section descriptions.

On a microscopic level samples of the silicate-dominant BIF are a reflection of the macroscopic appearance of the lithology. Grain-size is variable and ranges from very fine (0.01 mm) up to fine grained (0.5 mm). As mentioned in the macroscopic description section, this lithology is compositionally layered. Additional compositional layers are observable in thin-section. Five types of layers prevail; 1) garnet-grunerite,  $\pm$  pyrrhotite, chlorite (Plate 3.14a), 2) ferrohastingsite-garnet  $\pm$  grunerite, quartz, and pyrrhotite (Plate 3.14b and c), 3) pyroxene-carbonate (calc-silicate) (Plate 3.14c), 4) biotite-garnet  $\pm$  pyrrhotite, ferrohastingsite, grunerite, and chlorite (Plate 3.14d), and 5) quartz-dominant layers (meta-chert) (Plate 3.14e). In addition, this lithology is cross-cut by coarser-grained quartz-carbonate-, and pyrrhotite-veins. The layers are described sequentially below:

#### *Garnet-Grunerite-Dominant Layers*

These layers consist of a finer-grained groundmass of grunerite and magnetite surrounding coarser-grained, subhedral to euhedral garnet porphyroblasts. Garnet grains are 0.2-3.0 mm in diameter. Garnet grains are colourless to light brown in plane polarized light (ppl), isotropic in crossed polarized light (xpl). These grains contain euhedral inclusions



**Plate 3.14. Photomicrographs of silicate-dominated banded iron formation from Musselwhite mine showing the various mineral assemblage layers.** a) Photomicrograph of euhedral coarse-grained grunerite crystals displaying typical first to second order birefringence and twinning (xpl), (b) Photomicrograph of hornblende-dominant layers separated by quartz-dominant layers (ppl), (c) Photomicrograph showing quartz-dominant, hornblende-dominant, and calc-silicate-dominant layers (ppl), (d) Photograph of garnet-biotite-dominant layer showing subhedral isotropic garnet porphyroblasts, inclusions preserve original or earlier layering (xpl), (e) Photomicrograph of quartz-dominant layer, note polygonal grains and minor grunerite grains (xpl), (f) Photomicrograph showing fracture in garnet filled with pyrrhotite and gold (reflected light).

of grunerite. Chlorite is found as inclusions and infilling fractures in garnet grains. Additionally, grain boundaries of the garnet grains can be irregular and inter grown with grunerite grains.

Grunerite grains range in size from ~50  $\mu\text{m}$  to ~850  $\mu\text{m}$  in diameter, are subhedral to euhedral, non-pleochroic in plane polarized light (ppl), with high interference colours in crossed polarized light (xpl). The grains exhibit multiple twinning characteristic of grunerite (Plate 3.14).

Pyrrhotite, when present in these layers, is coarser grained than the grunerite-magnetite groundmass. It also appears to be predated by grunerite and magnetite as these minerals are normally found as inclusions within pyrrhotite aggregates.

#### *Garnet-Hornblende-Dominant Layers*

These layers consist of a finer-grained groundmass of hornblende and magnetite surrounding coarser-grained, subhedral to euhedral almandine-rich garnet porphyroblasts. Minor accessory minerals seen include grunerite and titanomagnetite  $\pm$  pyrrhotite (Plate 3.14c). Garnet grains are 0.1-1.5 mm in diameter. Garnet grains are colourless to light brown in plane polarized light (ppl) and isotropic in crossed polarized light (xpl). These grains contain inclusions of hornblende, magnetite, and euhedral grunerite and often exhibit rotated, snowball-type, inclusion trails.

Hornblende (ferrohastingsite) grains range in size from ~50  $\mu\text{m}$  to ~1 mm in diameter, are anhedral to subhedral, and pleochroic light-green to blue. Hornblende and grunerite are closely associated, but on average grunerite is coarser-grained than hornblende. Interestingly, hornblende and grunerite are in equilibrium, although there appears to be replacement of grunerite by hornblende. Previous workers have noted hornblende/ferrohastingsite overprinting earlier grunerite (Otto, 2002).

### *Garnet-Biotite-Dominant Layers*

These layers are composed of a finer-grained groundmass of biotite and quartz  $\pm$  ferrohastingsite, grunerite, pyrrhotite, and chlorite surrounding abundant coarser-grained almandine-rich garnet porphyroblasts (Plate 3.14d). Biotite grains are fine-grained and pleochroic light to dark brown. Moderately abundant zircons, with associated dark radiation haloes, are found in the biotite grains.

Garnet porphyroblasts are coarse-grained, ranging between 0.2-3.0 mm in diameter, inclusion-rich, and have irregular grain margins that exhibit euhedral garnet overgrowths. Inclusions consist of fine-grained grunerite and titanomagnetite grains. Again, the garnets often exhibit rotated, snowball-type, inclusion trails.

### *Calc-Silicate-Dominant Layers*

These layers are thinner and less common than the garnet-grunerite and garnet-hornblende-dominant layers. The calc-silicate dominant layers are layers consisting primarily of clinopyroxene and iron-rich calcite,  $\pm$  grunerite and hornblende (Plate 3.14c). The clinopyroxene ranges from  $\sim$ 180  $\mu$ m to 2000  $\mu$ m in diameter. Pyroxene grains are anhedral, colourless to light brown and non-pleochroic in plane polarized light, high-birefringence in crossed polarized light. Calcite grains are typically coarser grained and exhibit twinning.

### *Quartz-Dominant layers*

The quartz-dominant layers (metamorphosed chert layers) primarily consist of recrystallized quartz-grains exhibiting polygonal shapes (i.e., 120° triple point junctions) and strong undulose extinction (Plate 3.14e). Grains range in diameter from 100  $\mu$ m to 200  $\mu$ m. It is common to see minor fine-grained grunerite and magnetite inter grown with the coarser-grained quartz grains. This is analogous to the quartz-dominant layers in the oxide-dominant BIF.

Coarser-grained quartz layers are quartz veins as opposed to meta-chert layers. These veins were likely emplaced relatively early as many are deformed, dismembered, and

realigned into the metamorphic fabric. Coarsening of minerals at the margin of quartz-veins is a common feature in thin-section.

### *Pyrrhotite*

Pyrrhotite accounts for between <1% up to 10% of the silicate-dominant BIF. The majority of the pyrrhotite is associated with contacts between quartz veins and the Fe-silicate dominant layers. Minor amounts of chalcopyrite and pyrite are found as inclusions within the pyrrhotite. Otto (2002) came to the conclusion that there are two polytypes of pyrrhotite present in well mineralized samples of silicate-dominant BIF. This conclusion was based on X-ray diffraction work. The two types are observable in hand sample, with one type being magnetic and the other non-magnetic.

### 3.6.3 Mineral Compositions

As mentioned in Section 3.6.2, the NIF assemblage silicate-dominant BIF is composed primarily of silicate minerals and quartz with lesser amounts of magnetite, pyrrhotite, biotite, titanomagnetite, apatite, carbonate, scheelite, and various REE minerals present. Grunerite, hornblende, garnet, titanomagnetite, apatite, scheelite, and carbonate were analysed with the SEM for mineral composition. However, quartz, magnetite, and pyrrhotite were not analysed because their chemistry is uniform and consequently the amount of information gained from them is negligible. Plate 3.15 shows SEM-BSE images of the SIF assemblage oxide-dominant BIF. Numbered points on Plate 3.15 correspond to mineral analysis results summarized in Table 3.9.

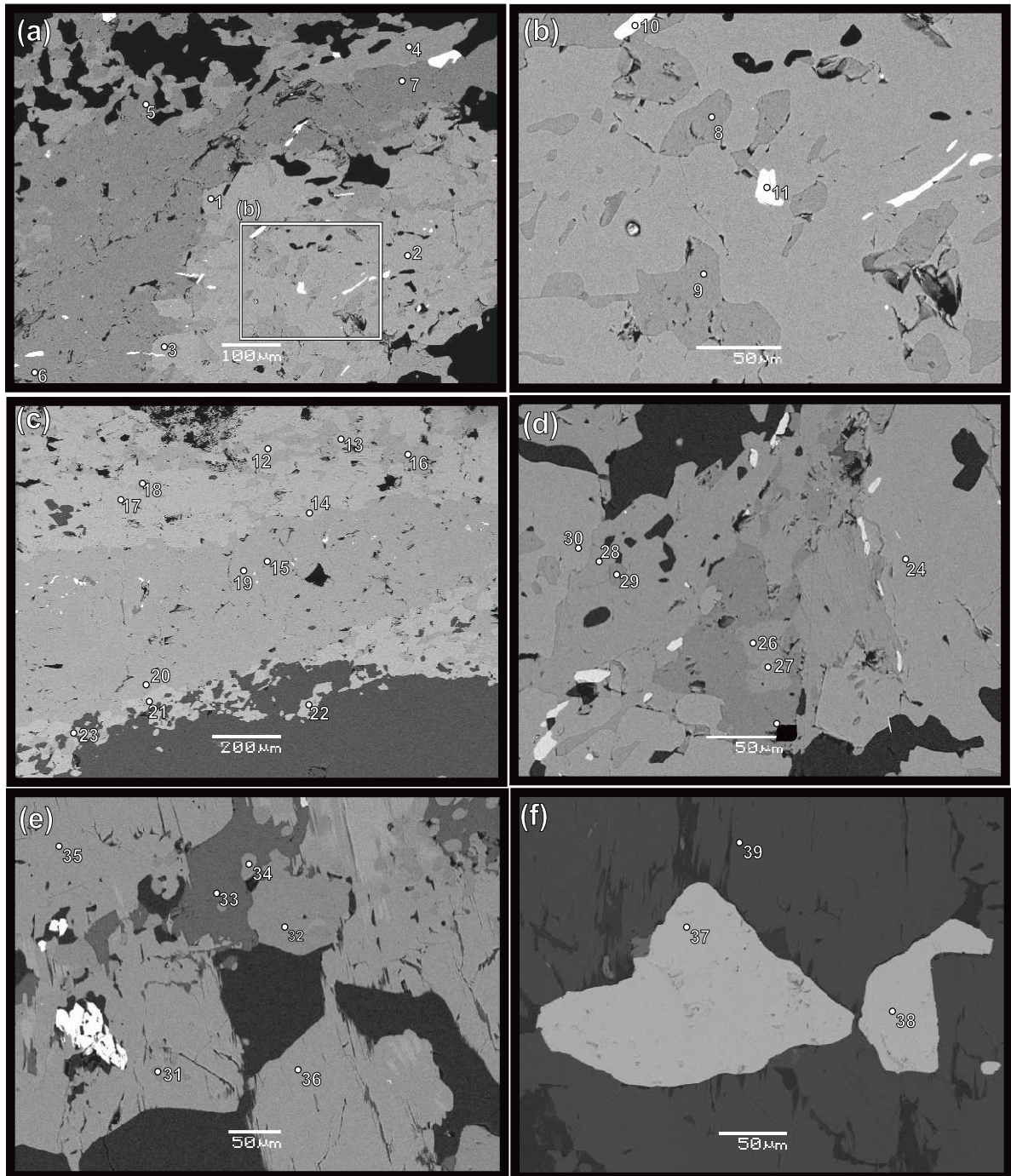
The silicate-dominant BIF is mineralogically more diverse than the oxide dominant BIF. Of the iron-silicate minerals grunerite is more abundant than hornblende. In this lithology grunerite grains are typically composed of: 48-51 wt.% SiO<sub>2</sub>, 36-39 wt.% FeO, and 7-9 wt.% MgO. Minor Na<sub>2</sub>O and Al<sub>2</sub>O<sub>3</sub> are also present. The hornblende grains consists of 36-41 wt.% SiO<sub>2</sub>, 26-27 wt.% FeO, ~20 wt.% Al<sub>2</sub>O<sub>3</sub>, 2-3 wt.% Na<sub>2</sub>O, and ~1-3 wt.% MgO.

Garnet is the fourth most abundant silicate mineral after quartz, grunerite, and hornblende in the silicate-dominant BIF. It has been conventionally thought of as the 'trap' for gold (Otto, 2002). Grunerite, hornblende, magnetite, titanomagnetite and quartz are all found as inclusions within the garnet porphyroblasts. Titanomagnetite is the most common opaque inclusion in the garnet grains. Garnets appear to have inclusion-rich interiors with relatively inclusion free rims. In terms of composition garnet consists of 37 wt.% SiO<sub>2</sub>, 35 wt.% FeO, 21 wt.% Al<sub>2</sub>O<sub>3</sub>, 6 wt.% CaO, and ~1 wt.% MgO.

On examination with the SEM a number of previously un-noticed minerals were found including apatite (Plate 3.15d) and scheelite. Apatite is relatively abundant in one sample (4ea-PM05-061), less abundant in the rest of the samples, and is composed of roughly 43 wt.% P<sub>2</sub>O<sub>5</sub> and 56 wt.% CaO with up to 1 wt.% FeO. Scheelite was identified in the silicate-dominant layered iron formation (Plate 3.15f) for the first time. However, the analysis of scheelite is less reliable as tungsten was not calibrated for. This mineral appears to be composed of roughly 56 wt.% WO<sub>3</sub> and 20 wt.% CaO.

Carbonate is found predominantly in the grunerite-hornblende-garnet layers with lesser amounts found disseminated in the quartz layers. Carbonate mineral chemistry was not known prior to examination of the NIF assemblage silicate-dominant BIF with the SEM. The most abundant carbonate mineral in this lithology is iron-rich calcite (Fe-calcite). Iron-rich calcite, in this lithology, contains on average ~54 wt.% CaO and ~1 wt.% FeO with a total of ~53-54 wt.% (low total due to inability of EDS to detect CO<sub>2</sub>).

The sulphides tend to occur clumped together as well as disseminated throughout the groundmass. Pyrrhotite is the most abundant sulphide. Magnetite is also a common opaque mineral.



**Plate 3.15. SEM-BSE images of the silicate-dominant banded iron formation collected from Musselwhite Mine.** a) Garnet porphyroblast surrounded by grunerite, hornblende, and quartz (sample 4ea-PM05-061). Note that inset-rectangle is enlarged in Fig. 3.15b, b) Enlarged view of rectangle from Fig. 3.15a showing amphibole and titanomagnetite grains within garnet porphyroblast (sample 4ea-PM05-061), c) Banded nature of various amphibole- and biotite-dominant layers, dark mineral in lower portion of image is quartz (sample 4ea-PM05-061), d) Aggregate of various minerals including garnet, grunerite, hornblende, and calcite (sample 4ea-PM05-061), e) Abundant subhedral apatite grains found as inclusions in grunerite and hornblende (sample 4ea-PM05-061), f) Several anhedral grains of scheelite surrounded by hornblende (sample 4ea-PM05-061).





### 3.6.4 Geochemical Composition

The chemistry of the silicate-dominant BIF, summarized in Table 3.10 as well as Appendix D, is more consistent than expected given that it is typically the most mineralized lithology in the NIF assemblage and, therefore, more likely to have experienced geochemical changes. Like previously described lithologies, differences in chemistry are primarily attributed to different combinations of several end-member components. In the silicate-dominant BIF, these end-member components are; 1) aluminosilicate/Fe-silicate-dominated layers (i.e., siliciclastic) (n=5), 2) magnetite-dominated layers (i.e., exhalite; n=2). The remaining nine samples form a continuum from siliciclastic- to exhalite-dominant. However, these samples exhibit similar chemistry and a new control must be invoked to differentiate them; 3) based on gold values samples are divided into weakly mineralized (<1 g/t) (n=5), moderately mineralized (1-5 g/t) (n=5), and well mineralized (> 5g/t) (n=6). The author of the current study collected a sample set, which reflects the different lithogeochemical spectrum and end members.

The chemistry can therefore be discussed in terms of magnetite-dominated, aluminosilicate/Fe-silicate dominant and gold mineralization. It should be noted that compositional layers in the NIF silicate-dominant BIF represent a spectrum from siliciclastic-dominant to magnetite-dominant end-members, whereas gold mineralization can have sharp boundaries.

#### *Magnetite-Dominant Layers*

Magnetite-dominant layers exhibit the following ranges of major elements in their geochemical composition: 46-50 wt.%  $\text{Fe}_2\text{O}_3^{\text{T}}$ , 37-44 wt.%  $\text{SiO}_2$ , 3-4 wt.%  $\text{MgO}$ , 1-2 wt.%  $\text{CaO}$ , ~0.03 wt.%  $\text{TiO}_2$ , 6-7 wt.%  $\text{Al}_2\text{O}_3$ , ~1 wt.%  $\text{MnO}$ , 0.1-0.5 wt.%  $\text{Na}_2\text{O}$ , 0.04-0.5 wt.%  $\text{K}_2\text{O}$ , and 0.1-0.2 wt.%  $\text{P}_2\text{O}_5$ . Concentrations of relevant trace elements are as follows: 35-44 ppm Zr, 31-125 ppm Cu, 220-920 ppm Au, 22-25 ppm W, and 31-125 ppm Cu. Relative to the siliciclastic-dominant layers, concentrations of major elements such as  $\text{Al}_2\text{O}_3$ ,  $\text{TiO}_2$ , and Zr are lower in the magnetite layers. Variations in  $\text{Fe}_2\text{O}_3$ ,  $\text{FeO}$ ,  $\text{SiO}_2$ , and  $\text{MnO}$  are primarily reflected mineralogically by the presence of magnetite, quartz, and grunerite.



Of the fifteen silicate-dominant BIF samples sent for analysis, samples 4ea-PM06-002 and 4ea-PM06-007 represent the magnetite-dominant layer end-member. Categorizing these samples as the magnetite-dominant layer end member is based on the fact that they have anomalously high Fe<sub>2</sub>O<sub>3</sub> values and the lowest FeO values of all the samples. High concentrations of Fe<sub>2</sub>O<sub>3</sub> indicate that these samples contain magnetite and lesser amounts of other minerals.

Both 4ea-PM06-002 and 4ea-PM06-007 contain the average silicate-dominant BIF Al<sub>2</sub>O<sub>3</sub> values at 7.4 wt.% and 5.6 wt.%, respectively. This is interesting when compared to average oxide-dominant BIF magnetite samples, which have an average Al<sub>2</sub>O<sub>3</sub> value of roughly 0.7 wt.%.

#### *Siliciclastic-Dominant Layers*

Siliciclastic layers exhibit the following ranges, of major elements, in their geochemical composition: 4.4-16 wt.% Fe<sub>2</sub>O<sub>3</sub>, 21-31 wt.% FeO, 37-46 wt.% SiO<sub>2</sub>, 3-12 wt.% MgO, 1.5-4.3 wt.% CaO, 0.5-1.6 wt.% TiO<sub>2</sub>, 9.4-14 wt.% Al<sub>2</sub>O<sub>3</sub>, 0.3-0.7 wt.% MnO, 0.1-3.3 wt.% Na<sub>2</sub>O, 0.05-0.5 wt.% K<sub>2</sub>O, and 0.1-0.2 wt.% P<sub>2</sub>O<sub>5</sub>.

Of the six siliciclastic layer samples sent for analysis, sample 4ea-07-20-069 represents the siliciclastic-dominant layer end-member. In hand sample, it is a garnet-hornblende dominant layer. Categorizing this sample as the siliciclastic-dominant layer end-member is based on the fact that it has the highest concentrations of Al<sub>2</sub>O<sub>3</sub>, TiO<sub>2</sub>, Na<sub>2</sub>O, and Zr. These elements are associated with siliciclastic detrital clay minerals (Boström, 1973). Sample 4ea-07-20-069 exhibits the following concentrations of relevant major elements: 43.1 wt.% SiO<sub>2</sub>, 14 wt.% Al<sub>2</sub>O<sub>3</sub>, 1.6 wt.% TiO<sub>2</sub>, 7 wt.% Fe<sub>2</sub>O<sub>3</sub>, 21 wt.% FeO, 4.1 wt.% MgO, 4.3 wt.% CaO, 3.3 wt.% Na<sub>2</sub>O, 0.12 wt.% K<sub>2</sub>O, 0.3 wt.% MnO, and 0.2 wt.% P<sub>2</sub>O<sub>5</sub>. Sample 4ea-07-20-069 exhibits the following concentrations of relevant trace elements: 106 ppm Zr, as well as the highest concentrations of REE, LILE, and HFSE of all silicate-dominant BIF samples. The higher concentration of these elements is reflected mineralogically by the presence of abundant hornblende, biotite, zircon, titanomagnetite, and almandine-rich garnet.

In addition to 4ea-07-20-069, samples 4ea-07-20-065, 4ea-07-20-067, 4ea-08-30-001, and 4ea-08-30-004, contain a significant siliciclastic component. This is based on these samples high  $\text{Al}_2\text{O}_3$  content relative to other NIF assemblage silicate-dominant BIF samples.

#### *Quartz-Dominant Layers*

Of the fifteen silicate-dominant BIF samples sent for analysis, sample 4ea-06-20-UG04 represents the quartz-dominant layer end-member. However, the high  $\text{SiO}_2$  value in sample 4ea-06-20-UG04 is the result of later quartz-veining.

Sample 4ea-06-20-UG04 is significant as it is a large sample, which contains visible gold as well as abundant quartz veins, and was collected from the main ore zone. This sample is important because it illustrates the connection between abundant quartz veins and the resulting dilution of the silicate-dominant BIF chemistry. In general sample 4ea-06-20-UG04 contains average concentrations of most major elements. However, this sample has the second highest  $\text{SiO}_2$  concentration at ~61 wt.% and the highest loss on ignition of all samples at 2.85 wt.%. These values indicate a high percentage quartz and hydrous minerals, and/or  $\text{CO}_2$  (carbonate), and/or S respectively. This sample also contains the lowest concentrations of  $\text{Al}_2\text{O}_3$  (4.73 wt.%) and  $\text{TiO}_2$  (0.19 wt.%) of all samples. Concentration of REE, LILE, and HFSE, as well as many trace elements, are very low in this sample compared to other silicate-dominant BIF samples.

Aside from  $\text{Fe}_2\text{O}_3$  and  $\text{SiO}_2$  concentrations, the geochemical makeup of the magnetite- and quartz-dominant layers does not differ dramatically. Concentrations of FeO, MnO, MgO, CaO,  $\text{Na}_2\text{O}$ , and  $\text{P}_2\text{O}_5$  are comparable between magnetite- and quartz-dominant layers. However,  $\text{Al}_2\text{O}_3$  and  $\text{TiO}_2$  values are multiple times higher in the magnetite-dominated layers compared to the quartz-dominant layers. Additionally the ratio between  $\text{Fe}_2\text{O}_3$  and FeO is higher in the quartz-dominant layers and lower in the magnetite-dominant layers. This suggests Fe is primarily found in iron-silicate minerals in the quartz-dominant layers and magnetite in the magnetite-dominant layers. This geochemical trend correlates to observed petrographic features.

### *Well Mineralized*

Well mineralized samples exhibit the following ranges, of major elements, in their geochemical composition: <0.01-16 wt.% Fe<sub>2</sub>O<sub>3</sub>, 24-35 wt.% FeO, 37-61 wt.% SiO<sub>2</sub>, 0.2-4.0 wt.% MgO, 2-4 wt.% CaO, 0.2-0.7 wt.% TiO<sub>2</sub>, 5-11 wt.% Al<sub>2</sub>O<sub>3</sub>, 0.5-0.6 wt.% MnO, <0.1-0.4 wt.% Na<sub>2</sub>O, 0.04-1.0 wt.% K<sub>2</sub>O, and 0.1-0.2 wt.% P<sub>2</sub>O<sub>5</sub>. Well mineralized samples exhibit the following range in concentration of relevant trace elements: 22-95 ppm Zr, 41-445 ppm Cu, <5-6 ppm Ag, 8350-13100 ppb Au, and 30-56 ppm W.

### *Moderately Mineralized*

Moderately mineralized samples exhibit the following ranges, of major elements, in their geochemical composition: 3-50 wt.% Fe<sub>2</sub>O<sub>3</sub>, 28-31 wt.% FeO, 37-47 wt.% SiO<sub>2</sub>, 3-4 wt.% MgO, 2-4 wt.% CaO, 0.3-0.6 wt.% TiO<sub>2</sub>, 7-11 wt.% Al<sub>2</sub>O<sub>3</sub>, 0.5-1.0 wt.% MnO, 0.1-0.3 wt.% Na<sub>2</sub>O, 0.01-0.6 wt.% K<sub>2</sub>O, and <0.1-0.2 wt.% P<sub>2</sub>O<sub>5</sub>. Moderately mineralized samples exhibit the following range in concentration of relevant trace elements: 44-71 ppm Zr, 53-125 ppm Cu, <5 ppm Ag, 920-2150 ppm Au, and 22-34 ppm W.

### *Poorly Mineralized*

Poorly mineralized samples exhibit the following ranges, of major elements, in their geochemical composition: 2-46 wt.% Fe<sub>2</sub>O<sub>3</sub>, 28-35 wt.% FeO, 43-47 wt.% SiO<sub>2</sub>, 3-4 wt.% MgO, 1-8 wt.% CaO, 0.3-2 wt.% TiO<sub>2</sub>, 6-14 wt.% Al<sub>2</sub>O<sub>3</sub>, 0.3-1 wt.% MnO, 0.1-3 wt.% Na<sub>2</sub>O, 0.03-1.0 wt.% K<sub>2</sub>O, and 0.1-0.2 wt.% P<sub>2</sub>O<sub>5</sub>. Poorly mineralized samples exhibit the following range in concentration of relevant trace elements: 35-107 ppm Zr, 31-219 ppm Cu, <5 ppm Ag, N.D-220 ppm Au, and 22-44 ppm W.

## 3.7 Hornblende-Garnet Schist

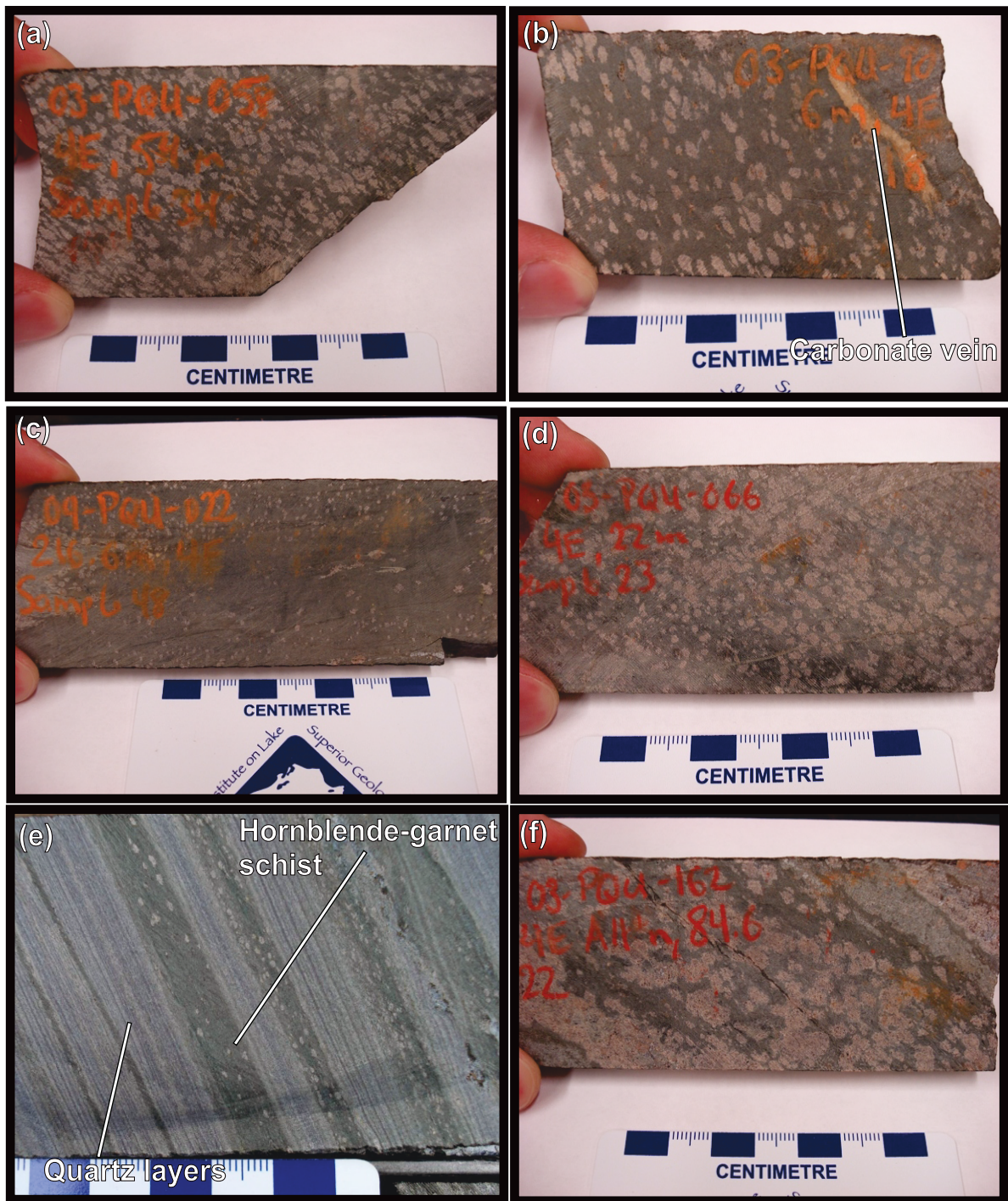
### 3.7.1 Macroscopic Character

The NIF assemblage hornblende-garnet schist (Plate 3.16a-f) is a thin lithology found intercalated with, and stratigraphically above, the NIF assemblage silicate-dominant BIF. It is locally present as centimetre- to decimetre-scale layers in the silicate-dominant BIF. These layers are one of the silicate-dominant BIF end-members described in Section 3.6.1. The predominant occurrence of this lithology is in the siliciclastic-dominant sedimentary package stratigraphically above the silicate-dominant BIF. In this stratigraphic location it ranges from centimetre- to decimetre-scale thick layers of pure hornblende-garnet schist intercalated amongst other lithologies. This lithology is locally present in drill core, but is rarely observed in underground drifts and outcrop due to its thin nature. Refer to Chapter One for the general stratigraphic location of this lithology and Chapter Two for a detailed description of its stratigraphy.

This lithology is variable, typically it is dark-green in appearance with elongated 1 mm to 2 cm pink almandine-rich garnet porphyroblasts. It is occasionally cut by late stage carbonate, and to a lesser extent, quartz veins (Plate 3.16b). The hornblende-garnet schist usually has a dark-green appearance.

In terms of mineralogy the hornblende-garnet schist is less complex than the underlying silicate-dominant BIF and is composed of, on average, ~10% to ~20% elongate garnet porphyroblasts and ~80% to ~90% fine-grained hornblende-rich groundmass. This fine-grained groundmass consists of a relatively simple mineral assemblage made up of varying combinations of hornblende, quartz, garnet, magnetite,  $\pm$  pyrrhotite, grunerite, carbonate, and chalcopyrite. Magnetite is rarely visible, but its presence is denoted by magnetism in hand samples.

Several variations of the hornblende-garnet schist exist. These variations are primarily a reflection of the mineralogic make-up of the lithology. The hornblende-garnet schist can be subdivided into two distinct subtypes. These subtypes are as follows; 1) relatively undeformed massive hornblende-garnet schist consisting of medium elongated subhedral



**Plate 3.16. Photographs of hornblende-garnet schist collected from Musselwhite Mine.** a) Photograph of typical dark-green appearance of the hornblende-garnet schist, notice pink garnet porphyroblasts elongated parallel to the metamorphic fabric (sample 4e-07-20-034), b) Photograph of typical hornblende-garnet schist which also contains a 0.7cm wide calcite vein (sample 4e-07-20-018), c) Photograph of an a-typical hornblende-garnet schist, composed of >60% garnet (sample 4e-07-20-048), d) Photograph of another a-typical version of hornblende-garnet schist, made up of ~90% hornblende (sample 4e-07-20-023), e) Photograph of transitional oxide- to silicate-dominant IF notice hornblende-garnet schist intercalated with quartz-layers, f) Photograph of hornblende-garnet schist, made up of ~50/50% hornblende and garnet (sample 4e-07-20-022).

almandine porphyroblasts surrounded by a homogeneous fine-grained hornblende-rich groundmass (Plate 3.16a-d), and 2) silicate-dominant BIF containing 0.3-1.5 cm thick intercalated layers of hornblende-garnet schist and meta-chert layers (Plate 3.16e).

It should be noted that eight samples of hornblende-garnet schist were collected in total. All samples were of the massive variety of the hornblende-garnet schist stratigraphically about the silicate iron formation. Relevant sample information, such as drill hole number and meterage, as well as the sample descriptions are provided in Appendix D.

Visually, the hornblende-garnet schist is distinct due to its dark-green appearance and porphyroblastic nature. In the silicate-dominant BIF it consists of alternating layers, typically on the order of 0.5-3.0 cm thick of hornblende-garnet schist and meta-chert. Contacts between the different compositional layers range from sharp to deformed in nature.

Aside from what is typically seen, the ratio of garnet porphyroblasts to hornblende-rich groundmass can be variable in this lithology. This ratio influences the rock's general appearance, which can be dark-green when composed of >95% hornblende with little to no garnet content (Plate 3.16c), to having a brownish-pink appearance when garnet content is in excess of roughly 60% (Plate 3.16d). Garnet size is relatively consistent in individual samples, being dominated by one size faction, and varies between samples from fine grained (<1 mm) to coarse grained (1-1.5 cm).

The hornblende-garnet schist, or at least its mineralogic composition, is a component in the transitional lithology occurring between the oxide- and silicate- dominant layered iron formations. In this lithology, quartz and magnetite layers are intercalated with well defined hornblende-garnet layers (Plate 3.16e).

In the NIF assemblage silicate-dominant BIF, the garnet-hornblende-dominant layers are usually associated with shear-zones and quartz-(carbonate) veining (Plate 3.13d and e). These layers range from homogeneous pure garnet and hornblende to containing thin quartz-, magnetite-, or grunerite-rich laminations on the order of 0.1-0.5 cm thick.



The garnet-hornblende dominant layers of the silicate-dominant BIF and the transitional oxide-dominant BIF (Plate 3.10f) resemble the massive hornblende-garnet schist.

### 3.7.2 Petrographic Character

Petrographic observations are based on five thin-sections of hornblende-garnet schist. Thin-sections were made from samples sent for geochemical analysis as well from hand samples. Representative samples, exhibiting a range of commonly observed features were specifically selected. Refer to Appendix B for the individual thin-section descriptions.

On a microscopic level samples of the hornblende-garnet schist are somewhat a reflection of the macroscopic appearance of the lithology. However, there is more mineral diversity in thin-section than the relatively homogeneous hand samples would suggest. As mentioned in the macroscopic description section, this lithology consists of a fine-grained groundmass surrounding coarser-grained garnet porphyroblasts. In thin-section the groundmass is dominated by fine-grained hornblende, but also contains minor disseminated quartz, magnetite, pyrrhotite, and grunerite (Plate 3.17a). Proportions of minerals differ from sample to sample. Grain-size is variable and ranges from very fine (0.01mm) up to fine grained (0.5mm).

#### *Hornblende-Rich Groundmass*

The groundmass is composed of roughly 90% hornblende with the following additional disseminated minerals: roughly 5% magnetite, 3-4% quartz, 1-2% grunerite, <1% pyrrhotite with chalcopyrite inclusions  $\pm$  minor carbonate and biotite. Pleochroism in hornblende ranges from light yellow-green to aquamarine (Plate 3.17b) and light yellow-green to dark-green (Plate 3.17c) depending on the sample. Based on the different pleochroic schemes, the composition of the hornblende is presumed to be variable in this lithology.

Thin-sections 4e-70-20-019 and 4e-07-20-34a exhibit typical mineralogic variations seen in the hornblende-garnet schist groundmass. Hornblende grains in sample 4e-70-20-019 are subhedral and range between 30  $\mu$ m-60  $\mu$ m in diameter. They are pleochroic yellow-green to dark-green (Plate 3.17c) and first-order yellow to purple birefringence. Quartz

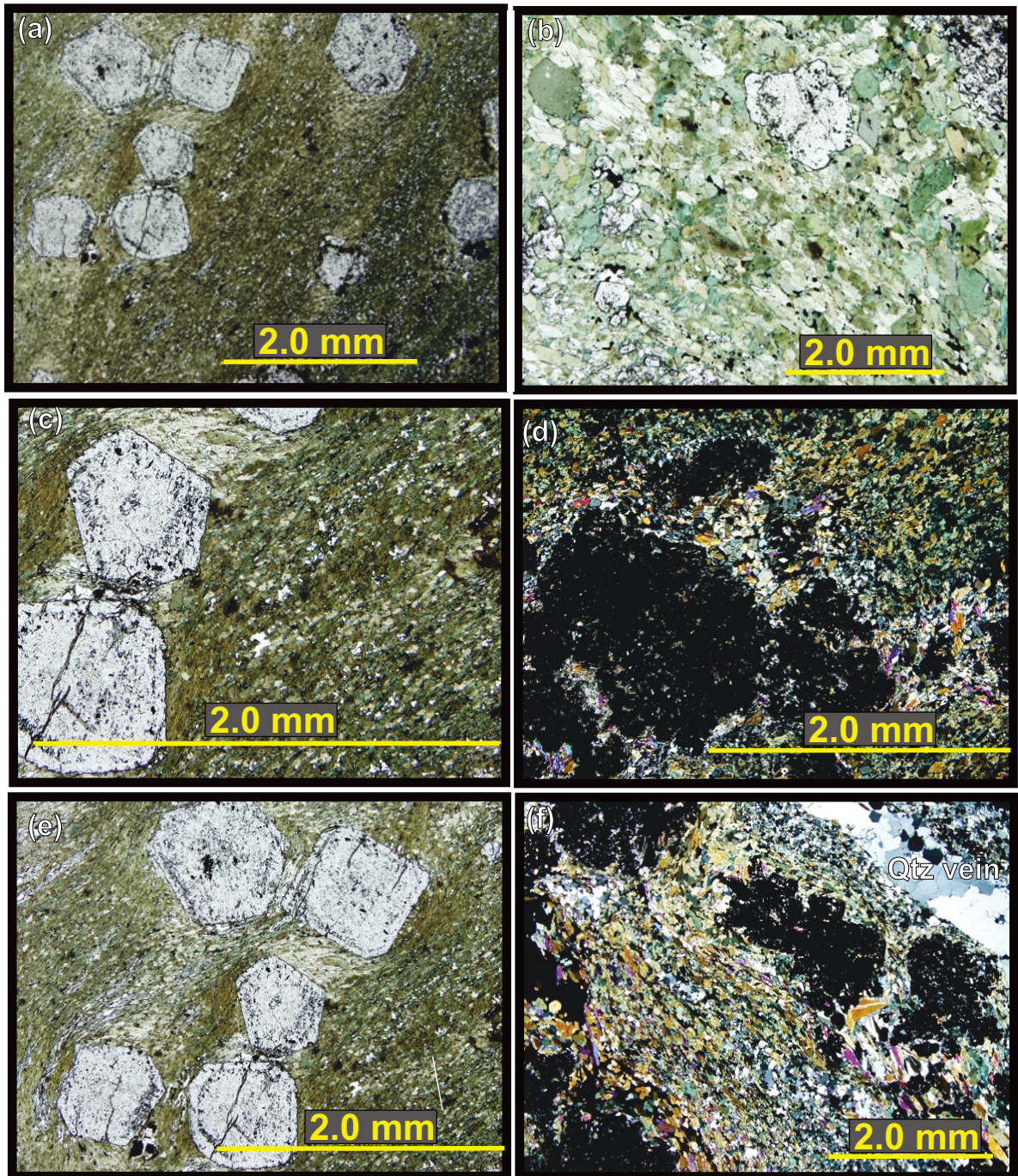
grains are a less abundant component of the groundmass. However, when present they are anhedral and exhibit a wide range of grain-sizes from 20  $\mu\text{m}$ -100  $\mu\text{m}$  in diameter (Plate 3.17c). Hornblende grains in sample 4e-07-20-34a range between 50  $\mu\text{m}$  -200  $\mu\text{m}$  in width, are pleochroic yellow-green to aquamarine (Plate 3.17b) and first order yellow to orange birefringence. Grunerite grains are present in sample 4e-07-20-34a. They are slightly coarser-grained than hornblende, ranging between 50  $\mu\text{m}$  -250  $\mu\text{m}$ , and on average are closer to the higher end of that scale. When present, grunerite grains are primarily found in close association with garnet porphyroblasts (Plate 3.17d).

### *Garnet Porphyroblasts*

Normally the hornblende-garnet schist contains roughly 30% slightly zoned euhedral almandine-rich garnet porphyroblasts. It is important to note that the garnet in this lithology does not preserve an earlier fabric, original layering, or exhibit snowball rotation features. The porphyroblasts sit in a fine-grained hornblende-rich groundmass (Plate 3.17a, c, and e).

Garnet porphyroblasts are medium to coarse grained, ranging from 0.1 to 0.7 mm in diameter, and elongated parallel to the metamorphic fabric. Grains span the spectrum from anhedral with xenomorphic rims (Plate 3.17d and f) to well formed euhedral grains (Plate 3.17a, b, and e). Quartz grains, along with minor grunerite, are the primary inclusions within the garnets. Euhedral grains tend to have fewer inclusions, mostly quartz, whereas anhedral grains tend to have abundant inclusions, again mostly of quartz, but with additional grunerite, magnetite, and surprisingly little hornblende given the groundmass.

Thin-sections 4e-70-20-019 and 4e-07-20-34a display typical variations seen in the garnet porphyroblasts. For example garnet porphyroblasts in sample 4E-07-20-019 are euhedral and display two stages of grain growth recorded as a ring of inclusions found near the edge of the porphyroblasts (Plate 3.17a, b, and e). The second stage of grain growth was possibly shorter lived, due to its thin nature. On the other hand sample 4E-07-20-034a, a slightly sheared hornblende-garnet schist sample, contains garnet porphyroblasts that are anhedral with xenomorphic rims and contain numerous inclusions



**Plate 3.17. Photomicrographs of hornblende-garnet schist collected from Musselwhite Mine.** a) Typical euhedral almandine garnet porphyroblasts surrounded by a groundmass of fine-grained hornblende-quartz-magnetite (xpl) (sample 4e-07-20-019), b) Pleochroic aquamarine hornblende crystals with associated quartz and garnet (ppl) (sample 4e-07-20-019), c) Pleochroic dark-green hornblende crystals with associated quartz and garnet (xpl) (sample 4e-07-20-019), d) Anhedral, slightly xenomorphic garnet porphyroblasts, surrounded by a ring of grunerite and quartz, found in the hornblende groundmass (xpl) (sample 4e-07-20-022), e) Typical euhedral almandine-rich garnet porphyroblasts surrounded by a fine-grained hornblende-quartz-magnetite groundmass (xpl) (sample 4e-07-20-019), f) Various layers seen in one sample of hornblende-garnet schist: hornblende-quartz, biotite-grunerite-garnet, and hornblende-garnet layers (xpl) (sample 4e-07-20-034b).

of quartz, grunerite, and carbonate as well as minor inclusions of hornblende (Plate 3.17d). Due to the xenomorphic habit of the garnet grains, and the accumulation of quartz and grunerite around of the grains edge, grunerite appears to be growing at the expense garnet (Plate 3.17d).

#### *Layered Hornblende-Garnet Schist*

Aside from the above described massive type of hornblende-garnet schist, there is a layered variety; sample 4e-07-20-034b is slightly layered in hand sample (Plate 3.16d). However, compositional layering is obvious in thin-section with this sample bearing a passing resemblance to the silicate-dominant BIF. Layers can be broken down into several subtypes. Four types of layers prevail; 1) hornblende-garnet layers (Plate 3.18a), 2) quartz-hornblende (Plate 3.18b), 3) biotite-grunerite-garnet (Plate 3.18c), and 4) quartz and magnetite layers (Plate 3.18d). In addition, this lithology is cross-cut by coarser-grained quartz and carbonate veins. The layers are described sequentially below.

#### *Hornblende-Garnet Layers*

These layers are between 0.2 mm to 0.5 mm in thickness. They are dominated by relatively coarser-grained (70  $\mu\text{m}$  -250  $\mu\text{m}$ , averages 100  $\mu\text{m}$ ) pleochroic yellow-green to aquamarine hornblende grains (80%) (Plate 3.18a). Hornblende grains range from anhedral to euhedral, and are on average subhedral. Garnet porphyroblasts (20%) range from 0.3 mm to 3 mm in diameter, are anhedral to subhedral, and contain abundant inclusions of quartz, hornblende, and magnetite. These layers contain minor magnetite and zircon (<1%).

#### *Quartz-Hornblende Layers*

These layers are between 1 mm and 4 mm thick, are dominated by fine-grained (50  $\mu\text{m}$  - 150  $\mu\text{m}$ ), anhedral inequigranular quartz grains (~65%), with a significant (~35%) hornblende component (Plate 3.18b). The quartz grains are disseminated in nature and separated by slightly coarser grained (60  $\mu\text{m}$  to 220  $\mu\text{m}$ ) anhedral grains of pleochroic light-green to aquamarine hornblende grains.

### *Biotite-Grunerite-Garnet Layers*

The biotite-grunerite-garnet layers range between 1 mm and 5 mm in thickness (Plate 3.18c). These layers are composed roughly of 50% biotite (100  $\mu\text{m}$ -500  $\mu\text{m}$ ), 35% garnet (0.5 mm-2 mm), 10% grunerite (90  $\mu\text{m}$ -300  $\mu\text{m}$ ), 4% hornblende (50  $\mu\text{m}$ -100  $\mu\text{m}$ ), 1% magnetite (50  $\mu\text{m}$ ), and minor chlorite (50  $\mu\text{m}$ -100  $\mu\text{m}$ ). Grains in this layer are several orders of magnitude coarser than the aforementioned layer. The garnet porphyroblasts are subhedral to euhedral and contain minor inclusions of biotite, quartz, grunerite, and opaque minerals.

### *Quartz and Magnetite Layers*

The presence of quartz- and magnetite-rich layers in sample 4e-07-20-019 (Plate 3.18e) suggests that hydrothermal activity was somewhat active during deposition of this sample.

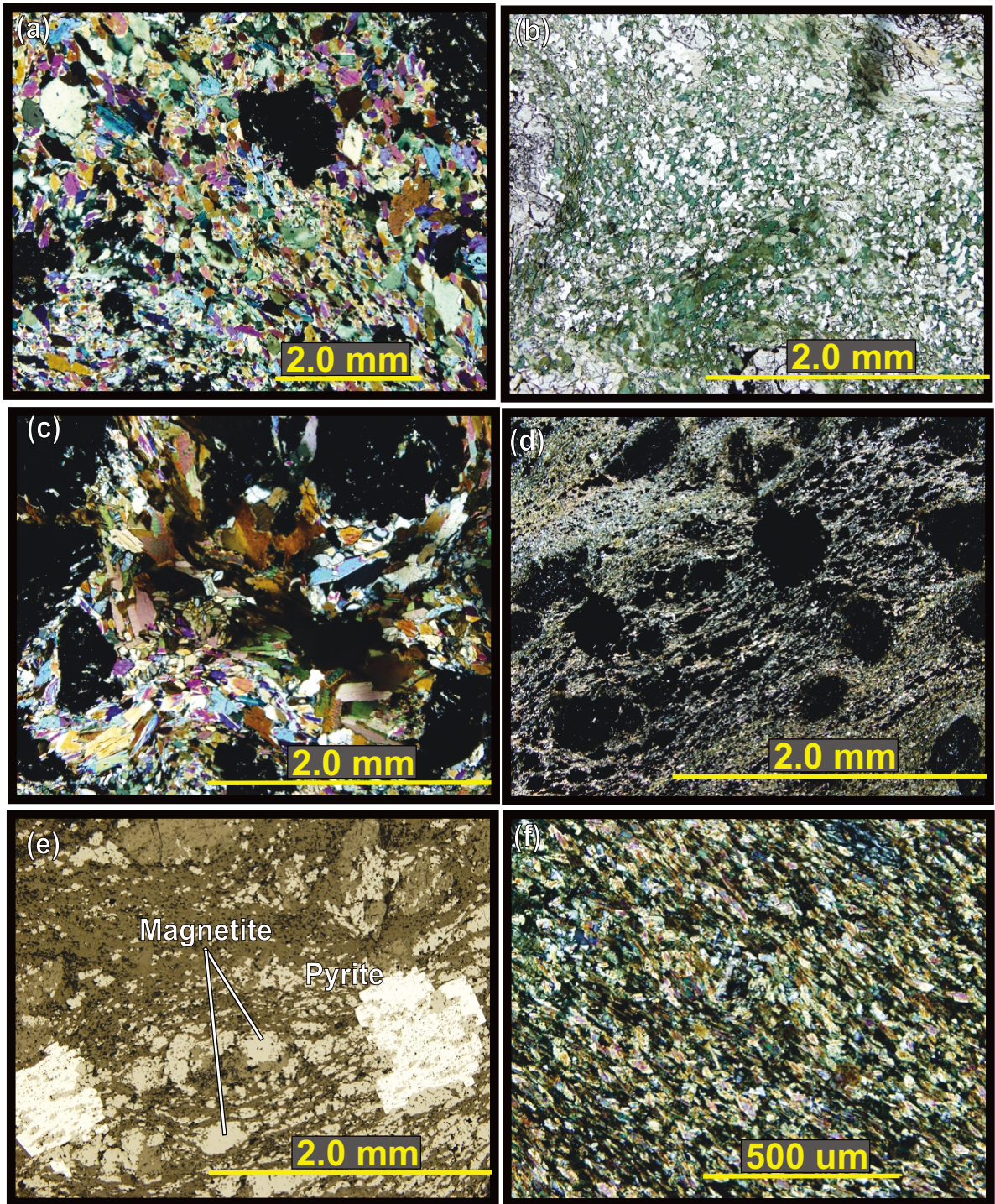
### 3.7.3 Mineral Composition

As mentioned in Section 3.7.2, the garnet-hornblende schist is composed primarily hornblende and garnet with lesser amounts quartz, grunerite, biotite, chlorite, sulphide (pyrite, pyrrhotite, chalcopyrite), titanomagnetite and Fe-rich calcite. Plate 3.19 shows SEM-BSE images of the hornblende-garnet schist. Numbered points on Plate 3.19 correspond to mineral analysis results summarized in Table 3.11.

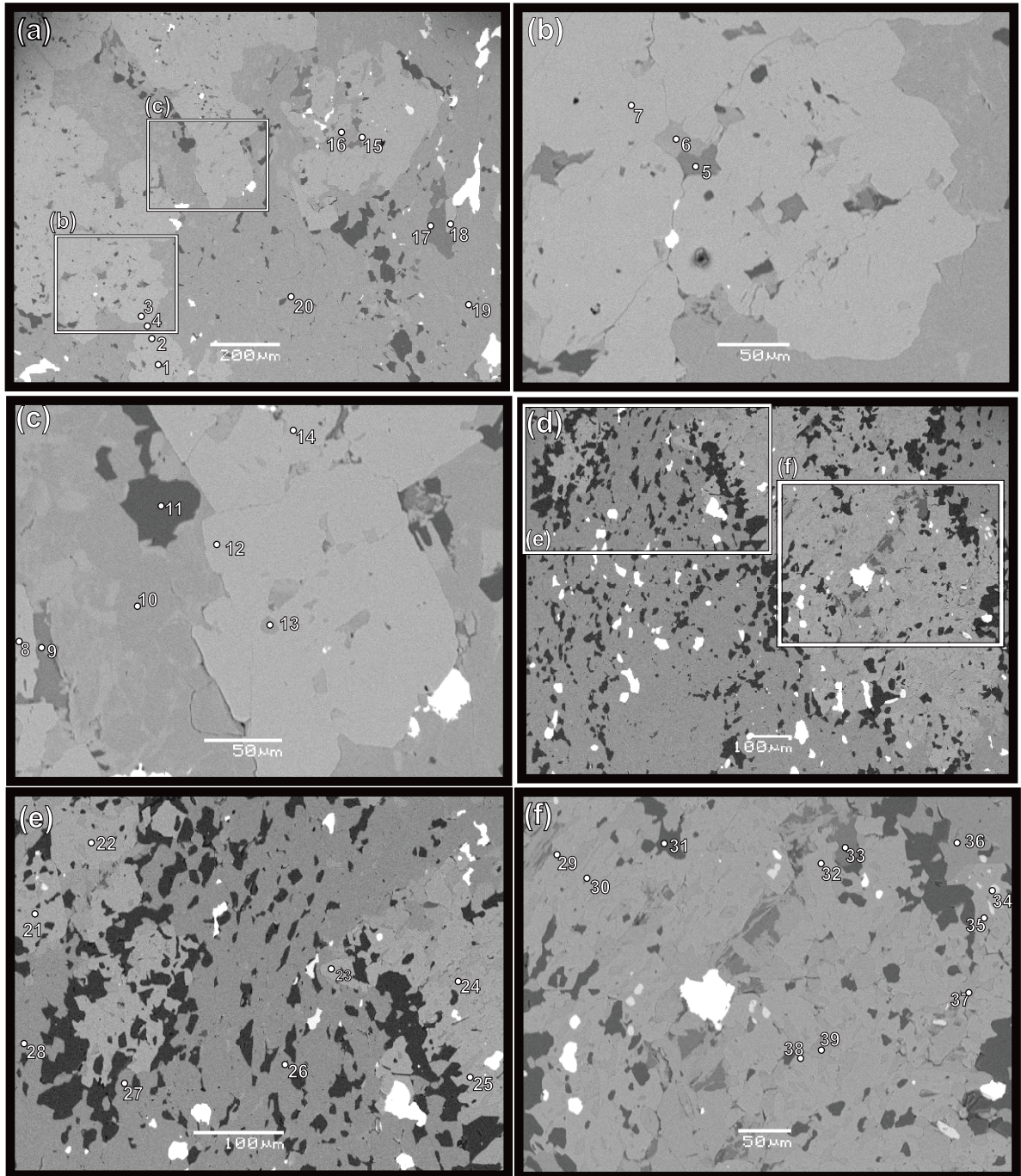
Hornblende is the primary component of the hornblende-garnet schist. In this lithology hornblende consists of 44-45 wt.%  $\text{SiO}_2$ , 9-11wt.%  $\text{Al}_2\text{O}_3$ , 5-7 wt.%  $\text{MgO}$ , 11-12 wt.%  $\text{CaO}$ , and ~23 wt.%  $\text{FeO}$ . Grunerite is the second most abundant amphibole in this lithology and contains approximately ~53 wt.%  $\text{SiO}_2$ , ~35 wt.%  $\text{FeO}$ , and ~9.3 wt.%  $\text{MgO}$ .

Under examination with the SEM, garnet is anhedral to subhedral grains that do not exhibit zonation. Grunerite and quartz are the most common inclusions within the garnet. Garnet is composed of approximately ~1 wt.%  $\text{MgO}$ , ~21 wt.%  $\text{Al}_2\text{O}_3$ , ~37-38 wt.%  $\text{SiO}_2$ , 3-5 wt.%  $\text{MnO}$ , 27-30 wt.%  $\text{FeO}$ , and variable  $\text{CaO}$  ranging from 6 to 9 wt.%.

Pyrite and various sulphides are the dominant opaque minerals. The carbonate present is Fe-calcite was analyzed and contains roughly ~51-52 wt.%  $\text{CaO}$  and ~2 wt.%  $\text{FeO}$ .



**Plate 3.18. Photomicrographs of hornblende-garnet schist collected from Musselwhite Mine.** a) Hornblende-garnet layers (xpl) (sample 4e-07-20-019), b) Fine-grained hornblende-quartz-magnetite matrix (xpl) (sample 4e-07-20-022), c) Biotite-garnet-grunerite layer (xpl) (sample 4e-07-20-034b), d) Hornblende-garnet layer (xpl) (sample 4e-07-20-034b), e) Quartz-magnetite-pyrite layer found within hornblende dominated matrix (xpl) (sample 4e-07-20-019), f) Euhedral pyrite cubes encompassing anhedral magnetite grains (reflected light) (sample 4e-07-20-019), g) Fine-grained hornblende-quartz layer (ppl) (sample 4e-07-20-019).



**Plate 3.19. SEM-BSE images of the hornblende-garnet schist collected from Musselwhite Mine.** (a) Anhedral garnet porphyroblast surrounded by a finer grained matrix of amphibole, inset rectangles are Plates 3.20b and c respectively, b) Enlarged area from Fig. 3.20a showing subhedral relatively inclusion free garnet porphyroblast, c) Enlarged area from Fig. 3.20a showing anhedral garnet porphyroblast surrounded by amphibole, quartz, and carbonate grains, d) Typical amphibole and quartz groundmass surrounding anhedral garnet porphyroblast, notice concentration of quartz around garnets, e) Enlarged area from Fig. 3.20d showing same characteristics, f) Enlarged area from Fig. 3.20d showing anhedral garnet with inclusions.





### 3.7.4 Geochemical Composition

The chemistry of the hornblende-garnet schist, summarized in Tables 3.12, as well as Appendix D, is relatively consistent. Like previously described lithologies, differences in chemistry are primarily attributed to different combinations of several end-member components. In the hornblende-garnet schist these end-member components are; 1) Fe-silicate-dominated layers (i.e., siliciclastic) (n=8), and 2) magnetite-dominated layers (i.e. exhalite) (n=1). However, the majority of samples exhibit similar composition and are considered to be siliciclastic dominant; therefore, the chemistry of this lithology is discussed in terms of siliciclastic dominant sedimentary material.

Hornblende-garnet schist samples exhibit the following ranges in composition: 2.1-19 wt.% Fe<sub>2</sub>O<sub>3</sub>, 15-23 wt.% FeO, 41-51 wt.% SiO<sub>2</sub>, 2.5-5 wt.% MgO, 1-8 wt.% CaO, 0.4-1.0 wt.% TiO<sub>2</sub>, 8.2-16.0 wt.% Al<sub>2</sub>O<sub>3</sub>, 0.2-1.3 wt.% MnO, <0.01-3.0 wt.% Na<sub>2</sub>O, 0.1-5.8 wt.% K<sub>2</sub>O, 0.03-0.20 wt.% P<sub>2</sub>O<sub>5</sub>, and 46-94 ppm Zr.

Of the eight hornblende-garnet schist samples analyzed, sample 4e-07-20-048 represents the siliciclastic-dominant layer end-member. In hand sample, it is a mostly hornblende with <5% garnet porphyroblasts. Categorizing this sample as the siliciclastic-dominant layer end member is based on the fact that it has the highest Al<sub>2</sub>O<sub>3</sub>, K<sub>2</sub>O, Na<sub>2</sub>O, and Zr content. These elements are associated with siliciclastic detrital clay minerals (Boström, 1973). This sample also has the lowest MnO content. Sample 4e-07-20-048 exhibits the following concentrations of relevant major elements: 49.6 wt.% SiO<sub>2</sub>, 15 wt.% Al<sub>2</sub>O<sub>3</sub>, 0.57 wt.% TiO<sub>2</sub>, 2.2 wt.% Fe<sub>2</sub>O<sub>3</sub>, 19.1 wt.% FeO, 2.5 wt.% MgO, 1.4 wt.% CaO, 1.5 wt.% Na<sub>2</sub>O, 5.1 wt.% K<sub>2</sub>O, 0.2 wt.% MnO, and 0.03 wt.% P<sub>2</sub>O<sub>5</sub>. Sample 4e-07-20-048 exhibits the following concentrations of relevant trace elements: 94.4 ppm Zr. The higher concentration of these elements is reflected mineralogically by the presence of abundant hornblende, biotite, zircon, and titanomagnetite in sample 4e-07-20-048.

In addition to 4e-07-20-048, samples 4e-07-20-018, 4e-07-20-022, 4e-07-20-023, 4e-07-20-034a, 4e-07-20-034b, and 4e-07-20-047 contain a significant siliciclastic component. This is based on the samples high Al<sub>2</sub>O<sub>3</sub>, TiO<sub>2</sub>, and Zr content.

**Table 3.12. Whole-rock lithochemistry of the hornblende-garnet schist from the Northern Iron Formation at Musselwhite Mine.**

		Hornblende-garnet schist							
Sample ID		4e-0720-018	4e-0720-019	4e-0720-022	4e-0720-023	4e-0720-034a	4e-0720-034b	4e-0720-047	4e-0720-048
units		wt%	wt%	wt%	wt%	wt%	wt%	wt%	wt%
MAJOR Elements	SiO <sub>2</sub>	47.01	40.64	50.02	50.99	46.77	48.56	45.31	49.64
	Al <sub>2</sub> O <sub>3</sub>	12.15	8.22	13.19	13.5	10.86	11.74	16.04	14.78
	TiO <sub>2</sub>	0.54	0.38	0.54	0.63	0.44	0.56	1.02	0.57
	Fe <sub>2</sub> O <sub>3</sub>	3.50	18.64	8.32	5.25	4.86	7.47	2.05	2.23
	FeO	19.65	22.47	15.51	15.59	21.66	17.81	14.77	19.07
	MnO	0.6	0.61	0.78	0.65	0.76	1.26	0.25	0.17
	MgO	4.08	2.5	3.18	3.48	4.05	3.78	4.99	2.54
	CaO	7.87	0.86	6.34	6.31	7.57	5.89	7.57	1.38
	Na <sub>2</sub> O	0.37	N.D.	0.18	0.33	0.4	0.17	2.82	1.47
	K <sub>2</sub> O	1.23	1.74	0.39	0.74	0.13	0.79	1.76	5.08
	P <sub>2</sub> O <sub>5</sub>	0.08	0.17	0.07	0.09	0.1	0.14	0.09	0.03
	LOI	N.D.	1.16	N.D.	0.37	N.D.	N.D.	1.61	0.66
	TOTAL	99.23	99.92	99.89	99.67	99.88	99.91	99.93	99.76
units		ppm	ppm	ppm	ppm	ppm	ppm	ppm	ppm
REE, LILE, HFSE	Ce	18.04	17.42	12.3	15.04	19.79	16.12	10.42	15.04
	Cs	0.859	6.944	0.454	0.666	0.045	0.758	20.89	4.932
	Dy	2.976	2.593	3.242	3.051	2.78	3.404	3.823	1.499
	Er	1.921	1.735	2.204	1.998	1.857	2.245	2.482	1.139
	Eu	0.81	0.683	0.744	0.818	0.869	1.019	0.839	0.484
	Gd	2.674	2.502	2.676	2.758	2.593	3.144	3.151	1.375
	Hf	1.6	1.2	1.5	2.0	1.6	1.4	1.9	2.5
	Ho	0.632	0.574	0.719	0.652	0.606	0.74	0.828	0.349
	La	9.14	10.65	5.54	6.89	10.15	7.96	4.38	8.55
	Lu	0.296	0.222	0.362	0.308	0.284	0.321	0.366	0.192
	Nb	2.8	2.1	2.4	3.4	2.7	2.5	3.0	3.9
	Nd	8.93	8.3	7.27	8.35	9.51	8.89	7.12	6.05
	Pr	2.161	2.016	1.633	1.948	2.35	2.058	1.523	1.64
	Rb	24.38	94.91	7.32	20.48	0.48	26.54	72.33	146.65
	Sm	2.15	1.86	2.04	2.17	2.16	2.31	2.26	1.3
	Sr	15.8	14.0	38.6	27.1	19.4	14.5	133.4	40.5
	Ta	0.21	N.D.	N.D.	0.26	0.22	0.18	0.2	0.3
	Tb	0.446	0.392	0.471	0.453	0.419	0.511	0.551	0.224
	Th	1.88	1.56	1.05	2.05	2.11	1.34	0.74	3.12
	Tm	0.284	0.237	0.336	0.289	0.273	0.318	0.362	0.176
	U	0.615	0.462	0.322	0.658	0.662	0.423	0.21	0.928
Y	17.13	20.92	18.3	17.8	16.7	21.13	20.92	9.57	
Yb	1.91	1.46	2.3	1.96	1.84	2.09	2.43	1.23	
Zr	60.8	46.2	61.5	72.9	59.9	51.7	68.4	94.4	
units		ppm	ppm	ppm	ppm	ppm	ppm	ppm	ppm
TRACE	Ag	N.D.	N.D.	N.D.	N.D.	N.D.	N.D.	N.D.	5
	Au	20	210	10	1720	410	1000	10	20
	As	3	6	18	33	1	55	6	12
	Ba	39	209	60	81	N.D.	82	286	617
	Co	41	14	34	41	32	29	60	27
	Cr	163	107	203	214	154	198	360	151
	Cs	N.D.	N.D.	N.D.	N.D.	N.D.	N.D.	N.D.	N.D.
	Cu	208	69	103	171	255	240	170	34
	Ga	11	10	12	13	11	10	19	15
	K	11383	17734	3774	7042	1110	7664	16109	44585
	Mn	4390	4521	5475	4363	5217	8671	518	1222
	Na	2100	162	1132	2045	2212	1096	1848	9512
	Nb	4	3	3	3	3	3	5	4
	Ni	120	79	116	107	102	114	155	83
	P	469	932	445	475	589	830	334	146
	Pb	5	N.D.	7	6	N.D.	N.D.	N.D.	6
	Rb	23	97	7	20	N.D.	26	86	187
	Sc	27	17	32	29	24	28	50	19
	Se	N.D.	N.D.	N.D.	N.D.	2	2	N.D.	N.D.
	Sn	N.D.	7	N.D.	N.D.	N.D.	N.D.	N.D.	N.D.
	Sr	14	14	36	25	16	13	19	39
	Th	5	7	N.D.	6	5	4	6	7
	Ti	3361	2631	3463	3963	2736	3550	7427	3763
	V	170	119	200	205	138	202	377	168
	W	N.D.	14	17	20	18	19	18	N.D.
	Y	17	20	19	17	17	21	16	9
	Zn	319	76	157	274	331	143	208	135
	Zr	69	54	67	79	65	58	111	106

Note that REE, LILE, and HFSE values are the result of ICP-MS analysis whereas other trace element values and major elements are the result of XRF analysis. In the case of duplicate element values, i.e. Y and Zr, ICP-MS values are used. N.D.= not detected, i.e., below detection limit (detection limits are presented in Table 1.2).

## 3.8 Biotite-Garnet Schist

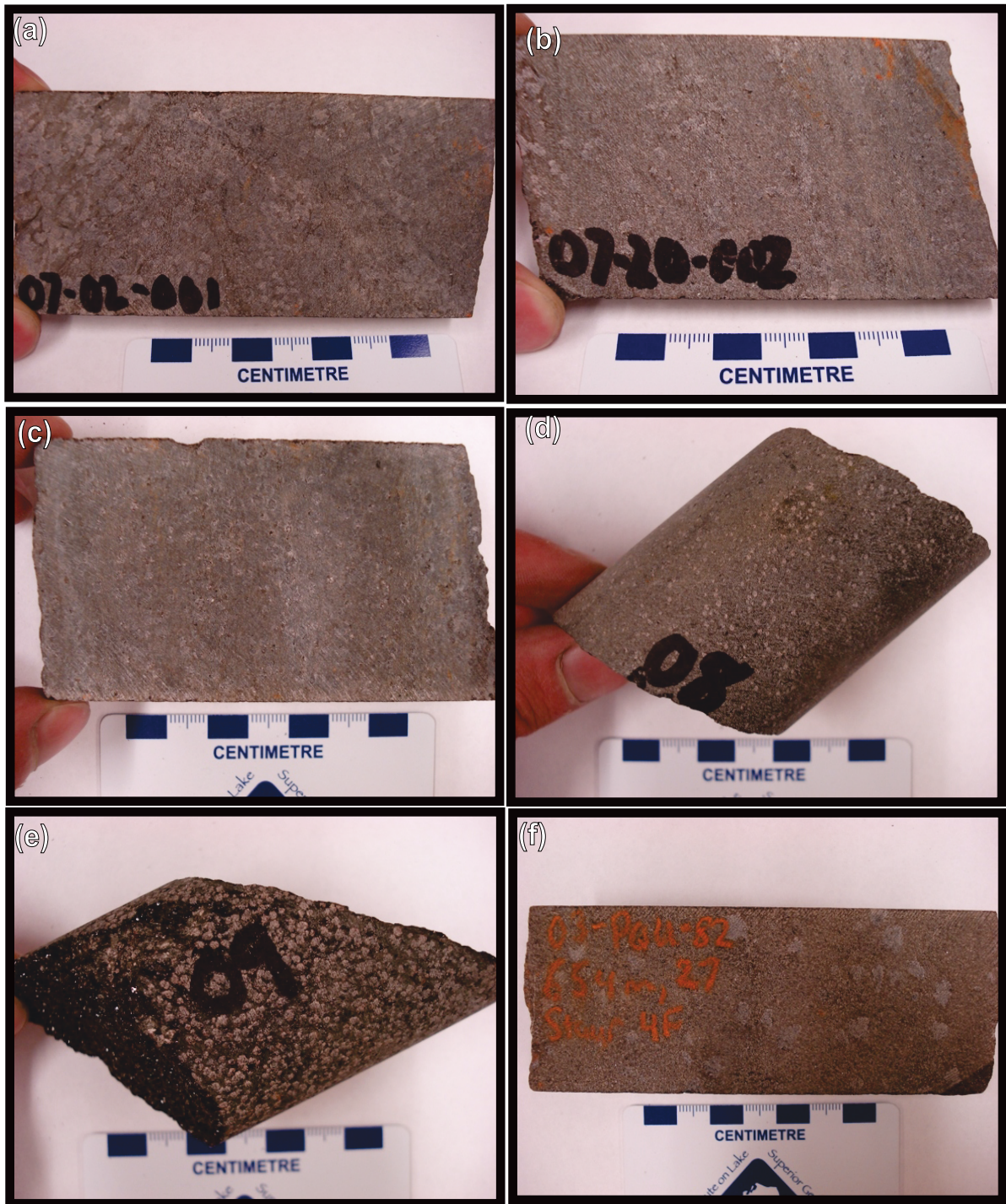
### 3.8.1 Macroscopic Character

The NIF assemblage biotite-garnet schist (4f, mine terminology) (Plate 3.20) is the third-most abundant metasedimentary lithology, after the oxide- and silicate-dominant BIFs, at Musselwhite Mine. It is usually present as a metre-scale unit located stratigraphically above the NIF assemblage silicate-dominant BIF. A staurolite-rich variety is found in the intraformational units overlying the NIF Assemblage. The biotite-garnet schist is commonly present in drill core and underground drifts. However, it is rarely seen in outcrop, with the exception of scattered glacial erratic boulders. Refer to Chapter One for the general stratigraphic location of this lithology and Chapter Two for a detailed description of its stratigraphy.

The biotite-garnet schist is typically dark-brown in appearance with subhedral to euhedral, ~1 mm to 2 cm diameter, pink almandine garnet porphyroblasts surrounded by a finer-grained biotite-rich groundmass. Meta-chert and meta-tuff layers are present in this lithology and commonly compose up to 5% of the rock. These layers are on a millimetre- to centimetre-thick scale and often broadly folded and locally boudinaged. The biotite-garnet schist varies from magnetic to non-magnetite depending on the amount of magnetite present. Occasionally the biotite-garnet lithology is cross-cut by late-stage quartz veins and rarer carbonate veins. It should be noted that the biotite-garnet schist locally grades into garnet-bearing quartzite. The garnet-bearing quartzite is described in detail further on in Chapter Three (Section 3.9).

In terms of mineralogy the biotite-garnet schist is quite simple. It is composed of, on average, ~5% to ~30% garnet porphyroblasts and ~70% to ~95% fine grained biotite-rich groundmass. This fine-grained groundmass consists of a mineral assemblage made up of varying combinations of biotite, quartz, feldspar, magnetite, zircon  $\pm$  staurolite, pyrrhotite, grunerite, zoisite, and carbonate. Magnetite is rarely visible but its presence is denoted by magnetism in hand samples.

Two primary variations of the biotite-garnet schist exist. These variations are principally a reflection of the mineralogy of the lithology. The biotite-garnet schist can be subdivided



**Plate 3.20. Photographs of biotite-garnet schist in core samples collected from Musselwhite Mine.** a) Typical looking biotite-garnet schist (sample 4f-07-20-001), b) Typical, slightly more meta-chert-rich, biotite-garnet schist (sample 4f-07-20-002), c) Another example of typical, slightly more meta-chert-rich, biotite-garnet schist (sample 4f-07-20-011), d) Biotite-garnet schist, with very low percentage of garnets, as well as their uniformly small size (sample 4f-07-20-008), e) Biotite-garnet schist, note the very high percentage of garnets as well as their uniform size (sample 4f-07-20-009), f) Staurolite-bearing biotite-garnet schist, with grey-orange colour of the sample (sample 4f-07-20-027a).

into: 1) massive biotite-garnet schist consisting of garnet porphyroblasts surrounded by a homogeneous fine-grained biotite-rich groundmass (Plate 3.20a-e), and 2) massive biotite-garnet schist consisting of garnet and staurolite porphyroblasts surrounded by a homogeneous fine-grained biotite-rich groundmass (Plate 3.20f). A third meta-chert-rich variation of this lithology also occurs (Plate 3.20b and c).

It should be noted that of the eight biotite-garnet schist drill-core samples collected, only two were of the staurolite-rich variety (sample 4f-07-20-002 and 4f-07-20-027a). The remaining seven samples were of the massive variety containing garnet porphyroblasts but devoid of staurolite porphyroblasts. Relevant sample information, such as drill hole number and meterage, as well as the sample descriptions are provided in Appendix D.

Visually, the biotite-garnet schist is distinct due to its massive grey-brown appearance and porphyroblastic nature. Garnets are anhedral to subhedral and range in size from fine grained (0.2 -0.3 cm) to coarse grained (0.5 -1.0 cm). Garnet porphyroblasts tend to be equigranular in each hand sample taken, but in the unit as a whole garnet size varies from fine to coarse grained. Staurolite porphyroblasts, when present, are finer grained than the garnet porphyroblasts. Staurolite grains appear as distinct disseminated yellow to orange-yellow anhedral grains (Plate 3.20f).

Aside from what is typically seen in this lithology, the ratio of garnet porphyroblasts to biotite-dominated groundmass can be variable. This ratio influences the rock's general appearance, which can be dark grey-brown when composed of >95% biotite-rich groundmass with little to no garnet content (Plate 3.20d) to having a brownish-pink appearance when garnet content is in excess of roughly 30% (Plate 3.20e). This lithology can even appear orange-grey when staurolite content is high (Plate 3.20f). Garnet size is relatively consistent in individual samples, being dominated by one size fraction, and varies between samples from fine grained (<1 mm) to coarse grained (1-1.5 cm).

### 3.8.2 Petrographic Character

Petrographic observations are based on seven thin-sections of biotite-garnet schist. Thin-sections were made from samples sent for geochemical analysis as well from hand samples. Representative samples, exhibiting a range of commonly observed features such as layering, folding, and metamorphic fabrics, were specifically selected. Refer to Appendix B for the individual thin-section descriptions.

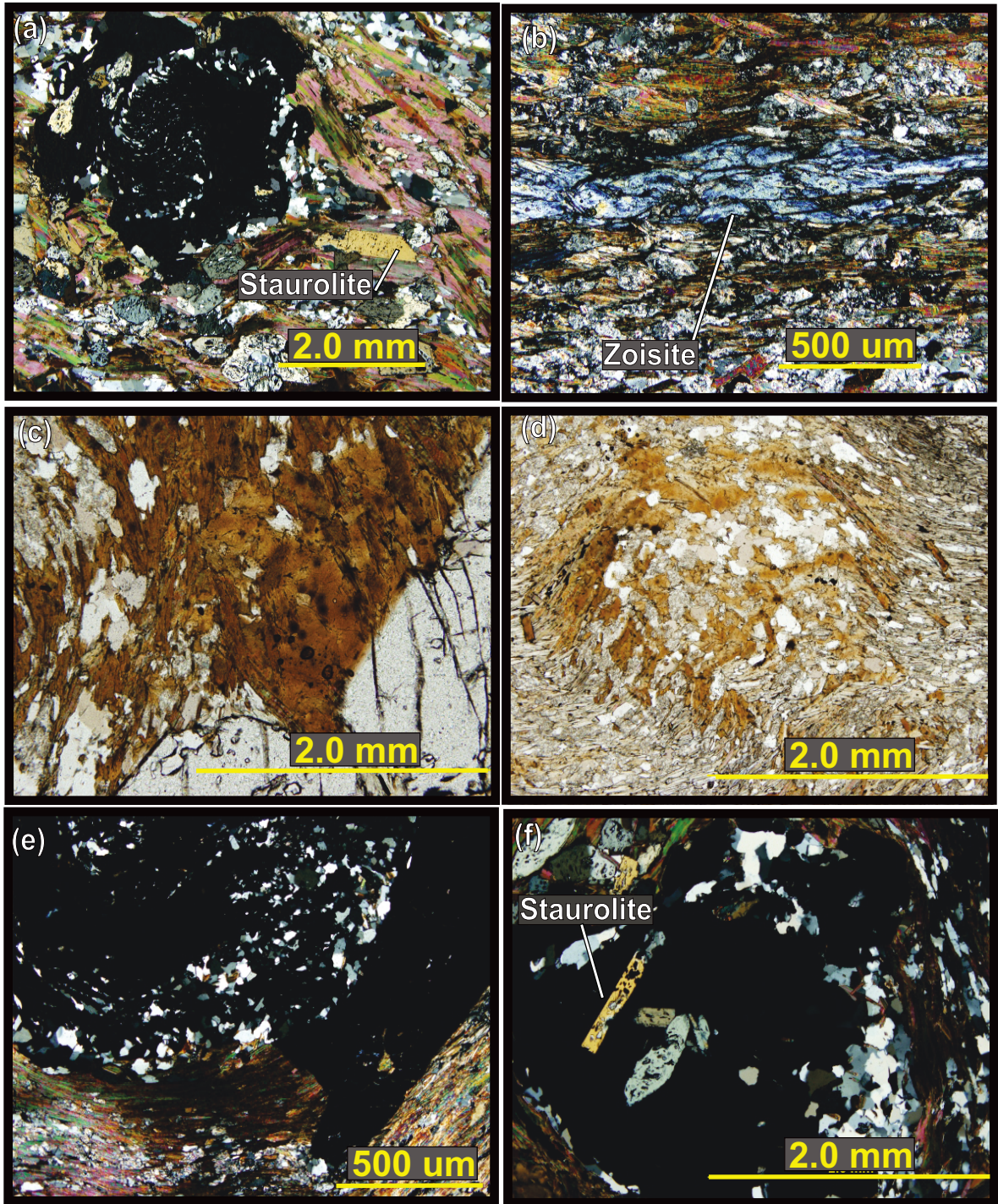
On a microscopic level samples of the biotite-garnet schist are a reflection of the macroscopic appearance of the lithology. As mentioned in section 3.8.1, this lithology typically consists of a fine-grained, biotite-rich groundmass surrounding coarser-grained garnet porphyroblasts (Plate 3.21a). In thin-section the groundmass consists of biotite, quartz, plagioclase, with additional but minor potassium feldspar, magnetite, and zircon  $\pm$  zoisite and chalcopyrite (Plate 3.21b). The grain-size of groundmass minerals is variable ranging from very fine up to fine grained, whereas the garnet porphyroblasts range from fine to coarse grained and staurolite porphyroblasts range from fine to medium grained (Plate 3.21a).

#### *Biotite-Rich Groundmass*

The biotite-rich groundmass, as its name implies, contains from 50-80% biotite (Plate 3.21c and d). In addition to biotite the groundmass is composed of biotite, quartz, plagioclase, with additional but minor potassium feldspar, magnetite, and zircon  $\pm$  zoisite and chalcopyrite.

Biotite grains are typically subhedral to euhedral lath-shaped grains ranging between 0.3 to 0.4 mm. They are pleochroic light- to dark-honey brown in plane polarized light (Plate 3.21c and d) and exhibit first-order birefringence colours in crossed polarized light (xpl). Distinct radiation haloes surround very fine-grained zircon-inclusions within these biotite grains. The biotite grains delineate a locally crenulated cleavage which surrounds the garnet porphyroblasts.

Quartz grains are the second most abundant mineral composing the groundmass. These grains are equidimensional in shape and are finer grained than biotite. Quartz grains



**Plate 3.21. Photomicrographs, showing variation, of the biotite-garnet schist collected from the Northern Iron Formation Assemblage at Musselwhite Mine.** a) Subhedral, rotated, garnet porphyroblast surrounded by finer-grained groundmass of biotite-quartz-staurolite (sample from Hollings, PMU95-13), b) Zoisite in siliciclastic groundmass (sample 4f-PM05-060), c) Biotite and garnet, biotite has zircon with pleochroic halos (sample 4f-PM05-060), d) Photomicrograph of biotite and quartz aggregate in matrix, e) Coarse-grained garnet porphyroblast with xenomorphic core and inclusion-free outer rim (sample 4f-PM05-060), f) Staurolite inclusions within garnet porphyroblast (sample 4f-PM05-060)

range from 0.05 to 0.2 mm in diameter (Plate 3.21a). Plagioclase grains are roughly the same size as the quartz grains, but exhibit distinct albite twinning.

Pyrrhotite is a minor component of the biotite-rich groundmass. It mainly occurs as disseminated anhedral grains, which contain minor chalcopyrite inclusions, and range between 0.1 to 0.4 mm in diameter. Pyrrhotite also occurs in concordant fractures within garnets and quartz grains.

Together, the biotite, quartz, and plagioclase grains form a fine-grained foliated to crenulated groundmass, which encompasses abundant coarser-grained almandine garnet porphyroblasts (Plate 3.21a-d). The minor crenulation and kink layers represent a later structural event.

#### *Garnet Porphyroblasts*

In the biotite-garnet schist, almandine garnet porphyroblasts range from fine to coarse grained, roughly 0.3-1.0 cm in diameter, and exhibit anhedral to euhedral grain forms. In plane polarized light the garnet grains are colourless to light brown and isotropic in crossed polarized light. These grains contain anhedral inclusions of quartz, and euhedral inclusions of titanomagnetite and, if present, euhedral staurolite inclusions. Additionally, garnet porphyroblasts in this lithology are very euhedral and occasionally exhibit rotated inclusion trails (Plate 3.21a).

In general the garnets tend to have inclusion-rich cores with rims free of inclusions (Plate 3.21e). When present, inclusion trails are typically linear, reflecting the original bedding or foliation. These garnets have been rotated and the internal foliation is perpendicular, therefore non-concordant, to the foliation of the surrounding fine-grained groundmass. Rotated, snow ball-type garnets are less common, but when present are exceptional examples (Plate 3.21a).

Dimorphism is observed among the garnet porphyroblasts. Coarser-grained garnets, greater than 0.5 cm in diameter, are typically anhedral to skeletal/xenomorphous in shape.



The more xenomorphic examples exhibit reabsorption textures, manifested as garnet-biotite-quartz aggregates, which occur along their margins. Finer-grained garnets tend to be euhedral and have inclusion-rich cores. Mineral inclusions within the garnets are titanomagnetite, quartz, apatite, magnetite, pyrrhotite (with minor chalcopyrite),  $\pm$  zoisite, staurolite, and biotite.

#### *Staurolite Porphyroblasts*

Two samples, 4f-07-20-002 and 4f-07-20-027a, from the current study contain between ~5% to 20% staurolite, respectively. When present in this lithology, staurolite is typically subhedral and porphyroblastic with grains ranging from 0.3 to 0.6 cm in length. Some grains are rotated. Staurolite grains are typically pleochroic yellow to light-blue, and poikiloblastically enclose fine-grained, anhedral quartz inclusions. As mentioned above staurolite grains are also found as inclusions within garnet porphyroblasts (Plate 3.21f).

#### *Quartz Layers*

There are a small number of recrystallized, 0.2 to 0.3 mm thick, quartz veins, which display 'z' or 's' shapes. These are interpreted to be relict early quartz-veins (F1), which have been strongly deformed (rootless folds) since emplacement.

### 3.8.3 Mineral Compositions

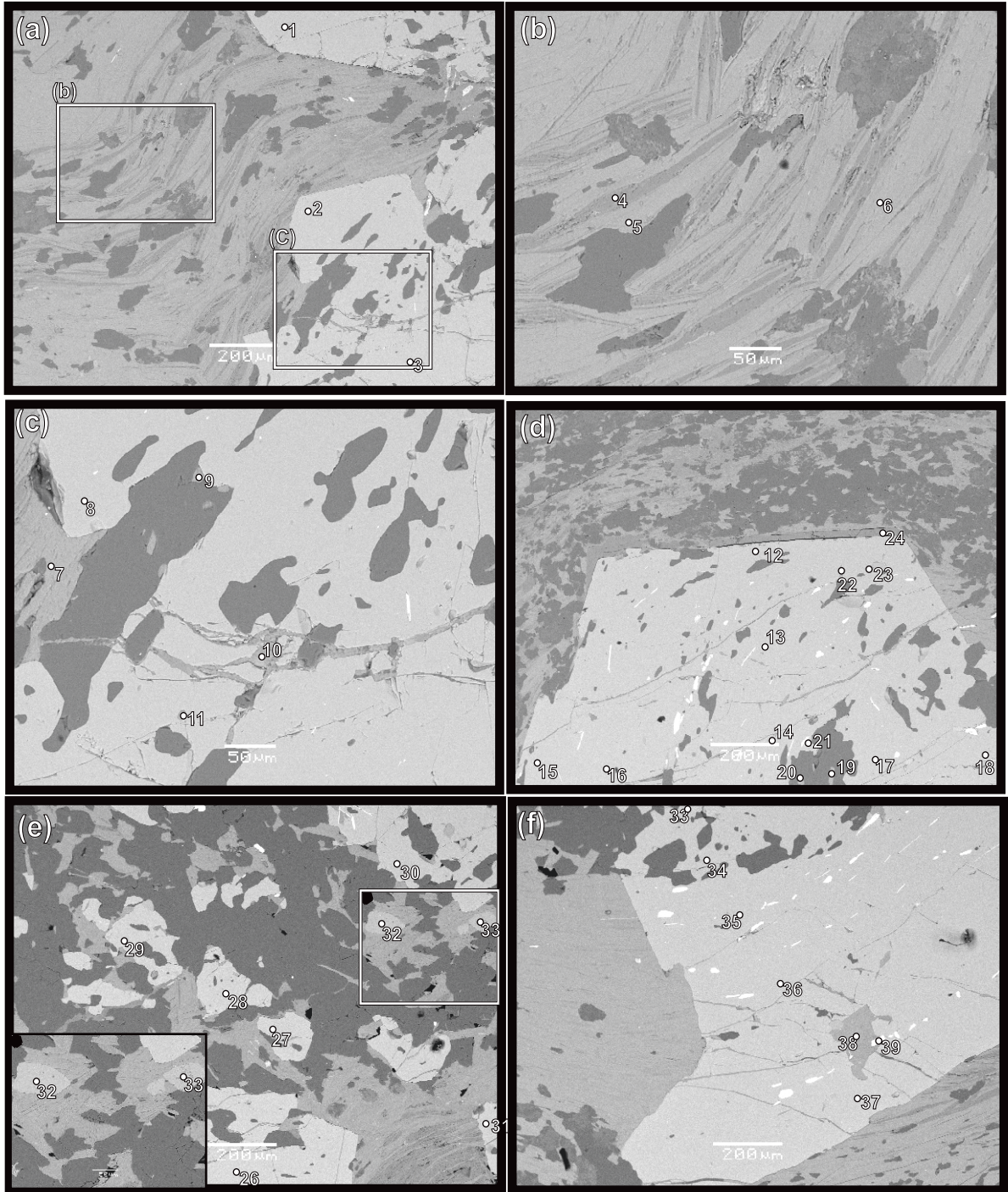
The mineralogy and mineral composition of the biotite-garnet schist is relatively complex when compared to the other lithologies in the stratigraphy (Plate 3.22). Examination of polished SEM disks was carried out to quantitatively analyze the minerals in the biotite-garnet schist. Most analyses focused on the composition of the biotite and garnet grains. The chemistry of the sulphides and titanomagnetite is more straightforward and, therefore, less time was allotted to them. Plate 3.22 shows SEM backscatter electron images of the biotite-garnet schist. Numbered points on Plate 3.22 correspond to mineral analysis results summarized in Table 3.13.

Biotite is the most abundant mineral in this lithology. It is composed of 34-36 wt.% SiO<sub>2</sub>, 17-22 wt.% FeO, 17-19 wt.% Al<sub>2</sub>O<sub>3</sub>, 9-11 wt.% MgO, 6-10 wt.% K<sub>2</sub>O, and 1-7 wt.%

TiO<sub>2</sub>, and CaO values vary dramatically from <0.5 wt.% to 5 wt.%. There is an unusual inter-growth texture associated with the biotite grains. Some biotite grains exhibit an intergrowth with a potassium-poor mineral (possibly margarite, CaAl<sub>2</sub>(Al<sub>2</sub>Si<sub>2</sub>)O<sub>10</sub>(OH)<sub>2</sub>; Deer *et al.*, 1996). This mineral has grown along the cleavage plains of the biotite grains. It is composed of ~24 wt.% Al<sub>2</sub>O<sub>3</sub>, ~43 wt.% SiO<sub>2</sub>, and 27 wt.% CaO and has a total that ranges between 95 to 96 wt.%. So it is similar to biotite, in that it contains some of the same elements as components, but its chemical makeup is slightly different in that it contains no potassium.

Garnet is the second most abundant mineral in this lithology after biotite. The mineral composition of the garnet is as follows: 2.5-3.5 wt.% MgO, 20-22 wt.% Al<sub>2</sub>O<sub>3</sub>, 36-39 wt.% SiO<sub>2</sub>, 2-3 wt.% CaO, and 36-39 wt.% FeO. Garnet porphyroblasts are commonly rotated and contain moderately abundant inclusions especially within their cores. Rims contain less inclusion and exhibit euhedral grain faces. The euhedral inclusion free rims of the garnet porphyroblasts appear to be more calcium-rich than the xenomorphic interiors. There is some evidence for a late stage tectonic event (Plate 3.22d), where there is obvious movement of a euhedral garnet porphyroblast which created a void that was then filled with calcite.

Commonly the garnet contains titanomagnetite, quartz, and grunerite inclusions. Titanomagnetite is also a common mineral and appears to contain higher TiO<sub>2</sub> values relative to previously mentioned titanomagnetite chemistry in other lithologies.



**Plate 3.22. SEM-BSE images of biotite-garnet schist collected from Musselwhite Mine.** a) Euhedral garnet porphyroblasts surrounded by finer-grained groundmass of crenulated biotite grains, biotite grains exhibit interesting intergrowth, rectangles represent Plate 3.22b and c, respectively, b) Enlarged area from Plate 3.22a showing well developed intergrowth of biotite, c) Enlarged area from Plate 3.22a showing inclusions within garnet porphyroblast as well as mineral growth along cracks, d) Euhedral garnet porphyroblast showing late-stage movement as indicated by presence of calcite filled gap on top edge of crystal, e) typical matrix from biotite-garnet schist, f) Euhedral rim and xenomorphic interior of garnet porphyroblast, notice apparent alignment of titanomagnetite in rim.



### 3.7.4 Geochemistry

The geochemistry of the biotite-garnet schist, summarized in Tables 3.14 as well as Appendix D, is relatively consistent. Like previously described lithologies, differences in chemistry are primarily attributed to different combinations of several end-member components. In the biotite-garnet schist, these end-member components are; 1) biotite-garnet  $\pm$  staurolite dominated groundmass (n=6), 2) biotite-garnet-magnetite-quartz  $\pm$  staurolite dominated groundmass (n=1). However, the majority of samples exhibit relatively similar and consistent chemistry. The presence of staurolite appears to be a reflection of metamorphic grade rather than geochemistry. The geochemistry of this lithology is discussed in terms of magnetite-absent versus magnetite-present dominant material.

Samples of the magnetite-absent, biotite-garnet schist exhibit the following ranges, of relevant elements, in their geochemical composition: <0.01.-20 wt.% Fe<sub>2</sub>O<sub>3</sub>, 8-24 wt.% FeO, 45-53 wt.% SiO<sub>2</sub>, 2.0-4 wt.% MgO, 0.3-5.0 wt.% CaO, ~1 wt.% TiO<sub>2</sub>, 16-22 wt.% Al<sub>2</sub>O<sub>3</sub>, 0.08-0.66 wt.% MnO, 0.04.-0.66 wt.% Na<sub>2</sub>O, 3.2-4.5 wt.% K<sub>2</sub>O, 0.06-0.10 wt.% P<sub>2</sub>O<sub>5</sub>, 80-133 ppm Zr, 2-118 ppm Sr, and 10-150 ppm Rb.

Of the seven biotite-garnet schist samples analyzed, samples 4f-07-20-011 and 4f-07-20-027a are geochemically similar, and represents the most siliciclastic-dominant end-member. In hand sample, 4f-07-20-027a contains abundant staurolite porphyroblasts in addition to the normal biotite-garnet mineral assemblage. However sample 4f-07-20-027a does not contain staurolite.

Categorizing these samples as the siliciclastic-dominant end member is based on the fact that they have the highest Al<sub>2</sub>O<sub>3</sub>, TiO<sub>2</sub>, and Zr content out of all the samples. These elements are associated with siliciclastic detrital clay minerals (Boström, 1973). Samples 4f-07-20-011 and 4f-07-20-027a exhibit the following ranges in concentration of relevant elements at: ~53 wt.% SiO<sub>2</sub>, ~22 wt.% Al<sub>2</sub>O<sub>3</sub>, ~1.1 wt.% TiO<sub>2</sub>, 3.2-7.8 wt.% Fe<sub>2</sub>O<sub>3</sub>, 7.5-11 wt.% FeO, 2.1-3.7 wt.% MgO, 0.3-1.5 wt.% CaO, 0.2-0.4 wt.% Na<sub>2</sub>O, 3.6-4.3 wt.% K<sub>2</sub>O, 0.1-0.5 wt.% MnO, and ~0.01 wt.% P<sub>2</sub>O<sub>5</sub>. These samples exhibit ~97-99 ppm Zr. The higher concentration of these elements is reflected mineralogically by the presence of abundant biotite, zircon, and titanomagnetite in the above described samples.

**Table 3.14. Whole-rock lithogeochemistry of the biotite-garnet schist from the Northern Iron Formation at Musselwhite Mine.**

	Biotite-garnet schist					Staurolite-	
Sample ID	4f-0720-01	4f-0720-011	4f-0720-008	4f-0720-009	4f-PM05-50	4f-0720-002	4f-0720-027a
	wt%	wt%	wt%	wt%	wt%	wt%	wt%
MAJOR Elements	SiO <sub>2</sub>	52.04	53.09	46.77	45.2	38.74	51.56
	Al <sub>2</sub> O <sub>3</sub>	18.10	21.44	19.74	16.29	6.19	20.05
	TiO <sub>2</sub>	0.96	1.12	1.04	0.96	0.29	0.96
	Fe <sub>2</sub> O <sub>3</sub>	N.D.	3.18	1.83	12.52	20.12	5.44
	FeO	20.67	11.03	15.06	15.34	24.36	9.92
	MnO	0.43	0.45	0.36	0.66	0.50	0.27
	MgO	2.72	2.08	2.25	2.51	3.04	2.52
	CaO	3.80	1.50	5.13	1.85	1.59	2.71
	Na <sub>2</sub> O	0.28	0.35	0.28	0.04	0.19	0.52
	K <sub>2</sub> O	3.19	4.27	4.46	3.64	2.64	4.22
	P <sub>2</sub> O <sub>5</sub>	0.11	0.07	0.06	0.06	0.18	0.06
	LOI	0.05	1.09	0.56	N.D.	N.D.	0.61
	TOTAL	100.86	100.9	99.22	99.92	99.61	99.94
	ppm	ppm	ppm	ppm	ppm	ppm	ppm
REE, LILE, HFSE	Ce	20.0	14.9	8.9	8.2	16.4	14.2
	Cs	13.065	2.625	3.589	2.957	5.619	3.734
	Dy	5.512	3.082	2.929	2.919	2.051	2.637
	Er	3.445	2.133	1.982	2.152	1.374	1.79
	Eu	1.197	0.736	0.734	0.627	0.749	0.699
	Gd	4.833	2.468	2.277	2.172	2.03	2.183
	Hf	3.6	2.7	2.2	2.2	1	2.5
	Ho	1.174	0.673	0.655	0.665	0.469	0.584
	La	8.98	6.7	3.38	3.71	10.97	6.45
	Lu	0.463	0.334	0.319	0.363	0.189	0.285
	Nb	4.6	4.5	4.0	4.2	1.7	4.4
	Nd	13.09	8.3	5.49	4.96	7.3	7.6
	Pr	2.771	1.896	1.219	1.089	1.81	1.772
	Rb	150	42.4	116.39	67.85	90.69	38.41
	Sm	3.68	2.15	1.69	1.53	1.52	1.9
	Sr	57.1	16.0	117.9	1.9	30.9	39.5
	Ta	0.38	0.28	0.26	0.29	N.D.	0.32
	Tb	0.819	0.441	0.418	0.4	0.305	0.376
	Th	1.42	1.71	1.47	1.21	1.3	1.94
	Tm	0.481	0.323	0.306	0.328	0.189	0.27
	U	0.452	0.601	0.477	0.559	0.401	0.683
Y	30.9	17.9	16.9	17.0	19.2	14.3	
Yb	3.15	2.19	2.07	2.31	1.19	1.84	
Zr	133.0	97.0	82.0	80.0	39.0	92.0	
	ppm	ppm	ppm	ppm	ppm	ppm	ppm
TRACE	Ag	N.D.	N.D.	N.D.	5	N.D.	N.D.
	As	25	50	45	23	3	8
	Ba	285	290	471	369	347	307
	Co	43	60	53	49	N.D.	49
	Cr	317	417	410	398	62	347
	Cs	N.D.	N.D.	7	N.D.	N.D.	N.D.
	Cu	142	211	35	54	54	83
	Ga	21	23	22	17	6	18
	K	28753	38734	38158	41029	13500	42131
	Mn	3143	3211	2593	4069	3733	1615
	Na	2191	2946	1954	406	1578	3721
	Nb	5	5	5	5	3	5
	Ni	173	158	153	202	50	139
	P	578	343	289	344	973	278
	Pb	N.D.	N.D.	10	N.D.	6	7
	Rb	81	97	187	154	101	102
	Sc	34	46	52	34	12	37
	Sr	47	27	148	3	35	47
	Th	6	6	6	4	8	4
	Ti	6016	7076	6635	7184	2047	6705
	V	302	371	380	393	77	332
	W	28	20	17	21	20	18
	Y	20	19	16	15	20	13
	Zn	205	152	141	218	53	134
	Zr	101	104	78	87	42	102

Note that REE, LILE, and HFSE values are the result of ICP-MS analysis whereas other trace element values and major elements are the result of XRF analysis. In the case of duplicate element values, i.e., Y and Zr, ICP-MS values are used. N.D.= not detected i.e. below detection limit (detection limits are presented in Table 1.2).

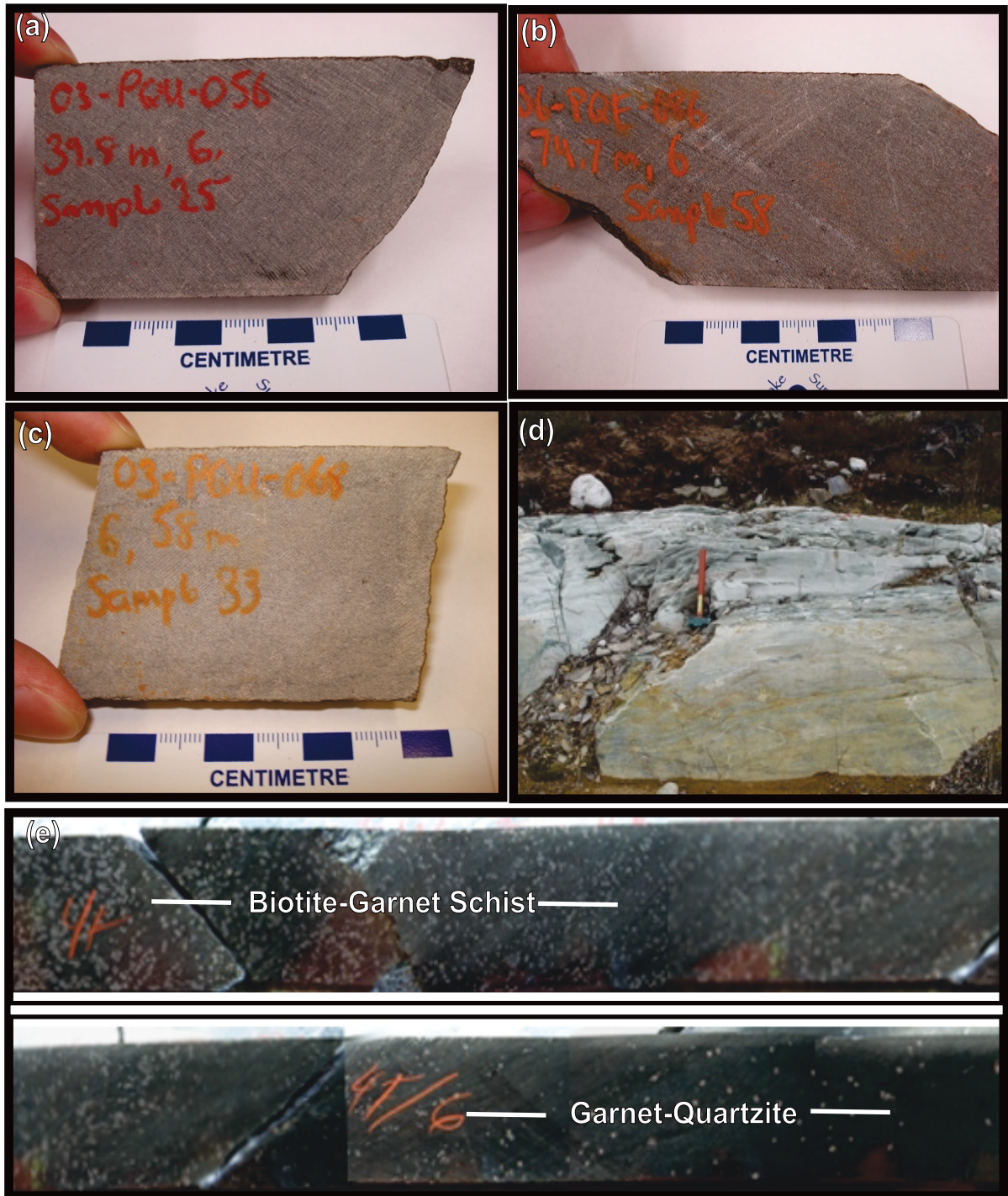
## 3.9 Garnet-Bearing Quartzite

### 3.9.1 Macroscopic Character

The garnet-bearing quartzite (Plate 3.23a-e) is a minor lithology in the Northern Iron Formation Assemblage. It is usually present as decimetre- to metre-scale intercalations in the stratigraphically upper portions of the biotite-garnet schist. Typically, it is found along the contact between the NIF assemblage and the overlying meta-volcanic rocks. Therefore, it is an important stratigraphic marker. Additionally the garnet-bearing quartzite is found in contact with the hornblende-garnet schist. The garnet-bearing quartzite is usually present in drill core; however, it is rarely seen in underground drifts or outcrop. Refer to Chapter One for the general stratigraphic location of this lithology and Chapter Two for a detailed description of its stratigraphy.

In total, five samples of garnet-bearing quartzite were collected for the current study. Relevant sample information, such as drill-hole number and meterage, as well as the sample descriptions are provided in Appendix D.

The garnet-bearing quartzite is normally moderately foliated and light to dark grey in appearance. It contains, minor scattered subhedral ~1 to 0.5 cm diameter, pink almandine garnet porphyroblasts (Plate 3.23a and b). Garnet porphyroblasts are surrounded by a finer-grained quartz-biotite-rich groundmass. The groundmass ranges from dominated by felsic minerals to dominated by mafic minerals, which in turn affects the colour of the rock (Plate 3.23b and c, respectively). It is a result of the alignment of the sheet silicate minerals in the fine-grained groundmass (biotite ± muscovite, and chlorite). The garnet-bearing quartzite is less-distinct compared to other lithologies in the NIF due to its massive grey appearance and resemblance to metavolcanic rock. This lithology consists of pyroclastic material with the bulk of the groundmass composed of fine grained quartz, biotite, muscovite, plagioclase, potassium feldspar, and garnet. Garnet content is



**Plate 3.23. Photographs of garnet-bearing quartzite collected from Northern Iron Formation Assemblage at Musselwhite Mine.** a) Typical dark grey quartz-biotite-rich groundmass surrounding minor medium-grained subhedral garnet porphyroblasts (sample 6-07-20-025), b) Typical dark-grey quartz-biotite-rich groundmass surrounding minor medium-grained subhedral garnet porphyroblasts, notice resemblance to metavolcanic material (sample 6-07-20-058), c) Light tan-grey garnet-quartzite containing more felsic mineral assemblage (sample 6-07-20-033), d) Possible quartzite in out cropping (location trench five, for exact location refer to Fig. 1.8), e) Photograph of gradational contact between garnet-bearing quartzite and biotite-garnet schist, in drillcore 04-ESN-010, core is roughly 4 cm wide (note left is the way up).



minor and ranges from ~1% to <5% of the rock. Garnet porphyroblasts tend to be equigranular in hand sample, but in the unit as a whole garnet size varies from fine to medium grained.

The garnet-bearing quartzite is usually non-magnetic. It should be noted that this lithology typically locally grades, over 5-10 cm, into biotite-garnet schist (Plate 2.23e). However thin, 0.3 to ~1 cm thick, boudinaged quartz-veins are a common feature and compose up to 1% of the rock. These 0.3 to 1 cm wide veins are dismembered and often have a lens-like shape, they are aligned into the foliation. There is minor primary disseminated sulphide and magnetite in this unit. Less commonly this unit contains large muscovite porphyroblasts.

There is only one variety of garnet-bearing quartzite in terms of macroscopic appearance (Plate 3.23a-e). The macroscopic appearance is principally a reflection of the mineralogy. In terms of mineralogy the garnet-bearing quartzite is quite simple. It is composed of, on average, <5% garnet porphyroblasts and >95% fine-grained quartz-biotite-rich groundmass. This fine-grained groundmass consists of a mineral assemblage made up of varying combinations of quartz, biotite, feldspar, magnetite, zircon  $\pm$  pyrrhotite and carbonate.

This lithology represents metamorphosed sandstone, as opposed to a metamorphosed intermediate tuff, as ascertained by the presence of what was originally graded-bedding. It is important to note that graded bedding can also occur in air fall ash deposits. However, this lithology does not represent an ash fall deposit as graded ash deposits are size-sorted but do not show the aluminum enrichment in the fine-grained tops that can be attributed to clay (formed by weathering) in sedimentary deposits. In some places the garnet content can be seen to increase up through a layer gradually and then be abruptly overlain by a garnet-poor layer that goes through the same transition (graded-bedding) with the garnets denoting clay-rich material produced by weathering. Thus, it is sedimentary.

### 3.9.2 Petrographic Character

Petrographic observations are based on three thin-sections of garnet-bearing quartzite. Thin-sections were only made from samples sent for geochemical analysis. Representative samples, exhibiting a range of commonly observed features such as metamorphic fabric, foliation, and boudinaged quartz veins were selected. Refer to Appendix B for the individual thin-section descriptions.

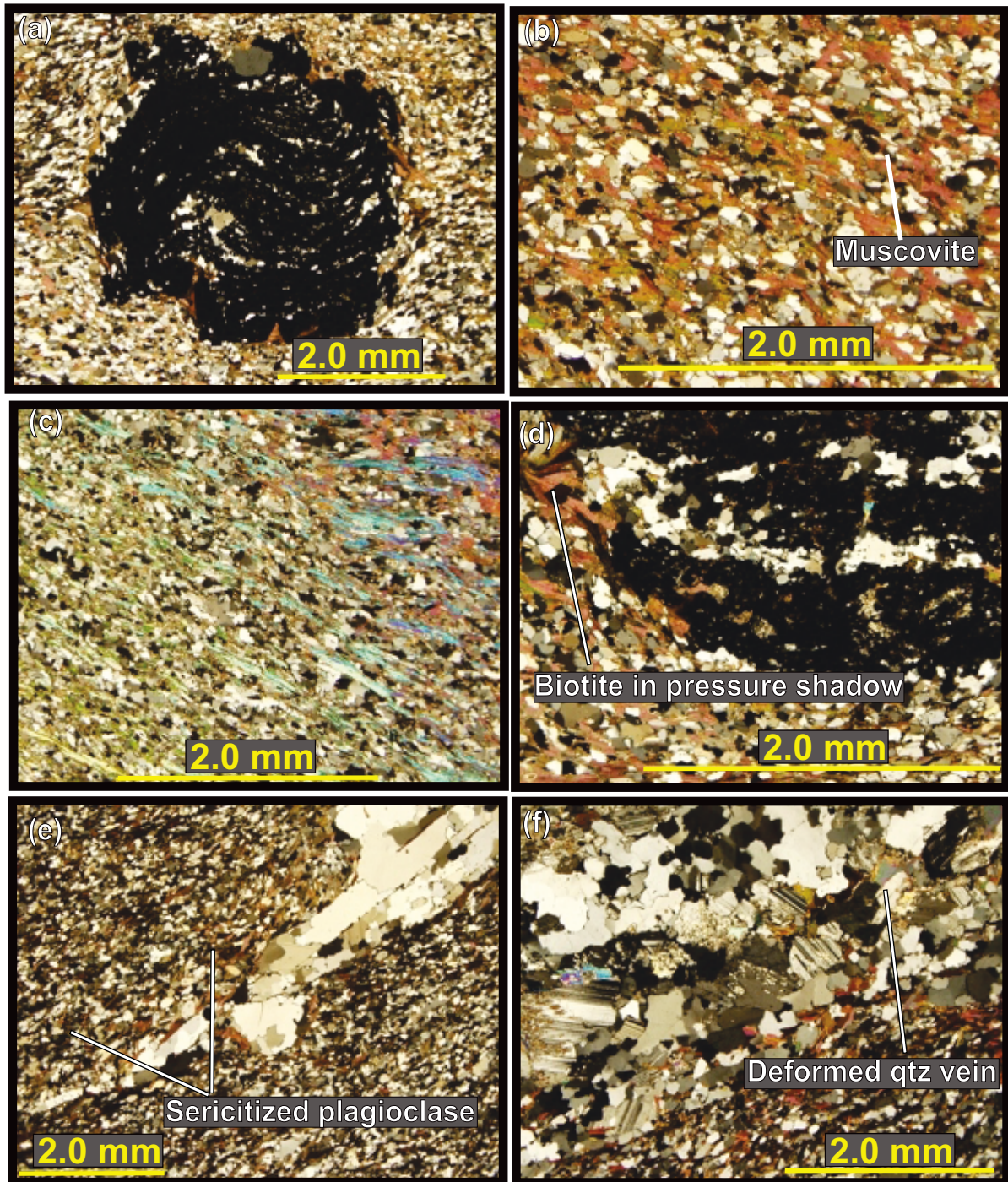
On a microscopic level samples of the biotite-garnet schist are a reflection of the macroscopic appearance of the lithology. As mentioned in section 3.9.1, this lithology typically consists of a fine-grained quartz- and biotite-rich groundmass surrounding coarser-grained garnet porphyroblasts (Plate 3.24a). In thin-section the groundmass consists of quartz, biotite, muscovite, and plagioclase, with additional but minor potassium feldspar, zircon  $\pm$  magnetite and pyrrhotite (Plate 3.24b). The grain-size of groundmass minerals is variable ranging from very fine up to fine grained, whereas the garnet porphyroblasts range from fine- to medium-grained (Plate 3.24a).

#### *Quartz-Biotite-Rich Groundmass*

The garnet-bearing quartzite, as its name implies, is a metamorphosed siliciclastic rock, typically consisting of a fine-grained anhedral to subhedral equigranular groundmass containing quartz, biotite, muscovite and plagioclase grains (Plate 3.24b and c). Grain size ranges from  $\sim$ 0.01 to  $\sim$ 0.03 mm.

In terms of mineralogy this lithology is dominated by biotite which comprises anywhere from 20% to 50% of the groundmass. Quartz is the second most abundant mineral composing anywhere from 15% to 30% of groundmass. The remaining portion of the groundmass is composed of fine-grained plagioclase, potassium-feldspar and disseminated finer-grained magnetite, titanomagnetite and zircon,  $\pm$  pyrrhotite and muscovite. Muscovite, when present, makes up  $<$ 5% of the rock and is usually confined to muscovite-biotite rich layers (Plate 3.24c).

Biotite grains are typically found as aligned subhedral to euhedral lath-shaped grains ranging between 0.1 to 0.3 mm. These grains are slightly coarser grained than the



**Plate 3.24. Photomicrographs of typical garnet-quartzite collected from Musselwhite Mine.** a) Coarse-grained rotated garnet surrounded by typical quartz-biotite-rich groundmass containing minor plagioclase (xpl) (sample 6-07-20-058), b) Fine-grained groundmass made of quartz, biotite, with minor plagioclase, and magnetite (xpl) (sample 6-07-20-058), c) Muscovite-rich matrix (xpl) (sample 6-07-20-058), d) Xenomorphic garnet containing abundant inclusions. Note biotite and quartz grains in pressure shadow (sample 6-07-20-058), e) Deformed, medium-grained quartz vein (sample 6-07-20-058), f) Medium- to coarse-grained quartz, plagioclase, calcite, and hornblende, vein crosscutting rock matrix (sample 6-07-20-058).

quartz and plagioclase grains (Plate 3.24b). They are pleochroic light to dark brown, and occasionally brown-green, in plane polarized light, and exhibit first-order birefringence colours in crossed polarized light. Minor very fine-grained zircons, surrounded by pleochroic haloes, are found within the biotite grains. Biotite grains delineate a locally crenulated cleavage which surrounds the garnet porphyroblasts.

The biotite grains are aligned in a metamorphic fabric with all grain grains going extinct at roughly the same angle. There appears to be a second biotite growth event associated with cracks and pressure shadows within and around garnet porphyroblasts (Plate 3.24d).

Quartz grains, in the quartz-biotite-rich groundmass, are fine- to medium-grained grains with irregular margins. These grains are equidimensional in shape and are finer grained than biotite. Quartz grains range from 0.05 to 0.2 mm in diameter (Plate 3.24b). Quartz-grain aggregates exhibit poorly developed triple point junctions indicating deformation during the crystallization process. Plagioclase and quartz grains are found together in the groundmass. Plagioclase grains are approximately the same size as the quartz grains, but exhibit distinct albite twinning.

Muscovite grains are pleochroic white to light cream in plane polarized light, second order blues and pinks in crossed polars, and are comparable in size to the biotite grains (Plate 3.24c). If present, muscovite occurs in close association with biotite grains and follows the same metamorphic fabric. Thin muscovite-rich layers are found within this lithology suggesting muscovite is not homogeneously distributed throughout the groundmass.

Plagioclase grains make up a minor component of the groundmass and are found in association with quartz and biotite as fine-grained subhedral grains. These grains exhibit typical albite twinning.

Together, the biotite, quartz, and plagioclase grains form a fine-grained foliated to crenulated groundmass, which encompasses abundant coarser-grained anhedral to euhedral almandine garnet porphyroblasts (Plate 3.24a and d). The minor crenulation and kink layers represent a later structural event.

### *Garnet Porphyroblasts*

Garnet grains are typically coarse-grained, but range from 0.06 to 5.00 mm in diameter. In plane polarized light the garnet grains are colourless to light brown, and isotropic in crossed polarized light. Grains are subhedral to euhedral and contain inclusions of anhedral quartz and biotite and euhedral inclusions of titanomagnetite. If present, inclusion trails are typically linear, reflecting the original bedding or foliation. The majority of the garnets have been rotated and the internal foliation is perpendicular, therefore non-concordant, to the foliation of the surrounding fine-grained groundmass. Some garnets also show moderately developed snowball rotation features (Plate 3.24a).

Dimorphism is observed among the garnet porphyroblasts. Occasional, atypical, xenomorphic garnets containing abundant inclusions of quartz and biotite are observed in the garnet-bearing quartzite (Plate 3.24d). These garnets appear to be in disequilibrium with the surrounding mineral assemblage. Interestingly, quartz and biotite grains are coarser grained around these xenomorphic garnet grains.

### *Quartz Layers*

Medium- to coarse-grained quartz agglomerates are found in the unit (Plate 3.24e). Grain margins are slightly wavy with poorly developed equianble triple point junctions. These most likely represent dismembered quartz veins. They appear to be recrystallized, 0.2 to 0.3 mm thick, quartz veins which have also been boudinaged (Plate 3.24e). Minerals associated with the quartz veins are also medium to coarse grained. These minerals include calcite, blue-green amphibole, and plagioclase,  $\pm$  xenomorphic garnet are associated with the veins (Plate 3.24f) and probably represent metasomatic alteration associated with the vein contact. The plagioclase grains exhibit noticeable grain-size increase from very fine grained in the quartz-biotite groundmass, up to 2 mm diameter grains in association with the quartz veins. These grains are moderately to strongly sericitized (Plate 3.24f).

### 3.8.3 Geochemical Composition

The geochemistry of the garnet-bearing quartzite, summarized in Tables 3.15 as well as Appendix D, is relatively consistent across samples. In total five samples were sent for

geochemical analysis. Overall, the garnet-bearing quartzite samples exhibit comparatively similar, purely siliciclastic, geochemical signatures. These geochemical signatures are elaborated on below.

Samples of the garnet-bearing quartzite exhibit the following ranges, of relevant elements, in their geochemical composition: 0.2-2.2 wt.% Fe<sub>2</sub>O<sub>3</sub>, 3.0-8.0 wt.% FeO, 61-66 wt.% SiO<sub>2</sub>, 1.6-6.3 wt.% MgO, 2.1-5.2 wt.% CaO, 0.4-0.5 wt.% TiO<sub>2</sub>, 17-20 wt.% Al<sub>2</sub>O<sub>3</sub>, 0.1-0.2 wt.% MnO, 0.2-2.0 wt.% Na<sub>2</sub>O, 3.1-5.8 wt.% K<sub>2</sub>O, ~0.1 wt.% P<sub>2</sub>O<sub>5</sub>, 137-191 ppm Zr, 1.5-2.0 ppm U, and 46-115 ppm Rb.

Of the five garnet-bearing quartzite samples analyzed, sample 6-07-20-033 is the most siliciclastic-dominant end-member, although its chemistry is only slightly above the average for the sample set. Categorizing this sample as the siliciclastic-dominant end member is based on the fact that it has the highest Al<sub>2</sub>O<sub>3</sub> and Zr content out of all the samples. These elements are associated with siliciclastic detrital clay minerals (Boström, 1973). Sample 6-07-20-033 exhibits the following concentration of relevant elements: ~63 wt.% SiO<sub>2</sub>, ~22 wt.% Al<sub>2</sub>O<sub>3</sub>, ~2.0 wt.% TiO<sub>2</sub>, ~2 wt.% Fe<sub>2</sub>O<sub>3</sub>, ~3 wt.% FeO, ~2 wt.% MgO, ~2 wt.% CaO, 0.4 wt.% Na<sub>2</sub>O, ~5 wt.% K<sub>2</sub>O, 0.2 wt.% MnO, and ~0.01 wt.% P<sub>2</sub>O<sub>5</sub>. This sample exhibits the following concentrations of relevant trace elements: ~191 ppm Zr. The higher concentration of these elements is reflected mineralogically by the presence of abundant quartz, biotite, zircon, and titanomagnetite in sample the above described sample.

The garnet-bearing quartzite is a geochemically distinct unit within the stratigraphic succession of the Northern Iron formation. It represents the purest siliciclastic sediment based on examination of the thin-sections as well as its whole-rock geochemistry. An interesting feature of this unit is the relatively homogeneous geochemical nature of the rock (suggesting a well sorted protolith). The samples have very similar chemistry. The garnet-bearing quartzite appears to represent metamorphosed sandstone with a silt component. This interpretation is based on its mineralogy and geochemistry. Upon examining the basic geochemistry of the samples this lithology falls into the pure siliciclastic end member sediment. These trends are discussed further in Chapter Four.

**Table 3.15. Whole-rock lithochemistry of the garnet-quartzite from the Northern Iron Formation at Musselwhite Mine.**

		Garnet-Quartzite				
Sample ID		07-20-024	07-20-025	07-20-033	07-20-038	07-20-058
MAJOR Elements	units	wt%	wt%	wt%	wt%	wt%
	SiO <sub>2</sub>	65.65	64.84	62.78	65.3	61.04
	Al <sub>2</sub> O <sub>3</sub>	18.15	17.52	20.44	17.22	17.66
	TiO <sub>2</sub>	0.38	0.38	0.40	0.36	0.46
	Fe <sub>2</sub> O <sub>3</sub>	1.46	0.15	2.20	0.18	0.71
	FeO	3.34	4.16	2.66	4.24	7.67
	MnO	0.22	0.11	0.18	0.07	0.2
	MgO	1.78	1.8	1.64	1.70	2.26
	CaO	3.79	3.48	2.06	2.36	5.18
	Na <sub>2</sub> O	0.18	1.94	0.37	1.82	0.23
	K <sub>2</sub> O	3.74	4.36	5.17	5.78	3.06
	P <sub>2</sub> O <sub>5</sub>	0.08	0.08	0.08	0.07	0.12
	LOI	1.21	0.69	1.68	0.40	0.53
TOTAL	100.36	99.96	99.96	99.97	99.97	
REE, LILE, HFSE	units	ppm	ppm	ppm	ppm	ppm
	Ce	32.93	34.55	40.68	34.41	29.46
	Cs	1.78	2.61	2.51	3.04	2.24
	Dy	1.94	1.81	1.88	1.47	1.96
	Er	1.03	0.98	1.03	0.80	1.12
	Eu	0.93	0.78	0.95	0.70	0.88
	Gd	2.18	2.15	2.20	1.82	2.24
	Hf	3.80	3.70	4.80	4.00	3.40
	Ho	0.37	0.35	0.37	0.28	0.40
	La	17.71	19.02	22.55	19.35	14.47
	Lu	0.14	0.13	0.14	0.12	0.16
	Nb	6.00	5.90	7.60	6.50	5.60
	Zd	12.24	12.84	14.22	12.20	12.12
	Pr	3.45	3.60	4.15	3.51	3.26
	Rb	50.80	80.46	102.60	115.47	46.20
	Sm	2.30	2.36	2.54	2.11	2.35
	Sr	60.10	73.40	40.60	52.60	83.00
	Ta	0.58	0.57	0.74	0.63	0.51
	Tb	0.32	0.31	0.32	0.25	0.32
	Th	5.18	5.59	7.28	6.32	4.18
	Tm	0.14	0.14	0.15	0.12	0.16
	U	1.68	1.67	2.33	1.89	1.47
Y	9.78	9.25	9.68	7.32	10.18	
Yb	0.95	0.90	0.98	0.78	1.04	
Zr	152.80	142.50	190.50	160.90	136.70	
TRACE	units	ppm	ppm	ppm	ppm	ppm
	As	2	2	4	2	6
	Ba	383	306	465	290	264
	Bi	N.D.	N.D.	N.D.	N.D.	N.D.
	Co	14	13	12	13	19
	Cr	63	61	48	39	94
	Cs	N.D.	N.D.	8	N.D.	N.D.
	Cu	18	24	1	7	3
	Ga	17	16	19	15	17
	K	37212	39790	51690	51074	30983
	Mn	1472	866	1237	575	1381
	Mo	N.D.	N.D.	N.D.	N.D.	N.D.
	Na	1534	14801	2938	11982	1676
	Nb	6	6	7	6	6
	Ni	29	30	28	25	53
	P	418	366	422	345	558
	Pb	11	15	9	13	8
	Rb	107	97	134	113	106
	Sc	14	13	11	10	17
	Sr	68	71	44	50	84
	Ta	N.D.	N.D.	N.D.	N.D.	N.D.
	Th	6	8	8	8	8
	Ti	2813	2741	2882	2580	3267
	V	79	74	62	54	104
W	17	16	13	16	15	
Y	8	8	7	7	8	
Zn	53	64	60	60	77	
Zr	160	152	201	168	143	

Note that REE, LILE, and HFSE values are the result of ICP-MS analysis whereas other trace element values and major elements are the result of XRF analysis. In the case of duplicate element values, i.e. Y and Zr, ICP-MS values are used.

## 3.10 Minor Lithologies

### 3.10.1 Introduction

This section introduces the reader to a number of minor, but important, lithologies at Musselwhite that do not occur in specific stratigraphic positions. Three lithologies are covered in Section 3.10 and they are discussed in the following order: 1) metasomatic biotite-garnet schist, 2) metasomatised oxide-dominant BIF, and 3) chlorite schist. Both the metasomatised oxide-dominant BIF and the chlorite schist are only found in the trenches (Figure 1.8). Conversely the metasomatic biotite-garnet schist does not occur in the trenches and is the only lithology found proximal to the main ore zones.

### 3.10.2 Macroscopic Character

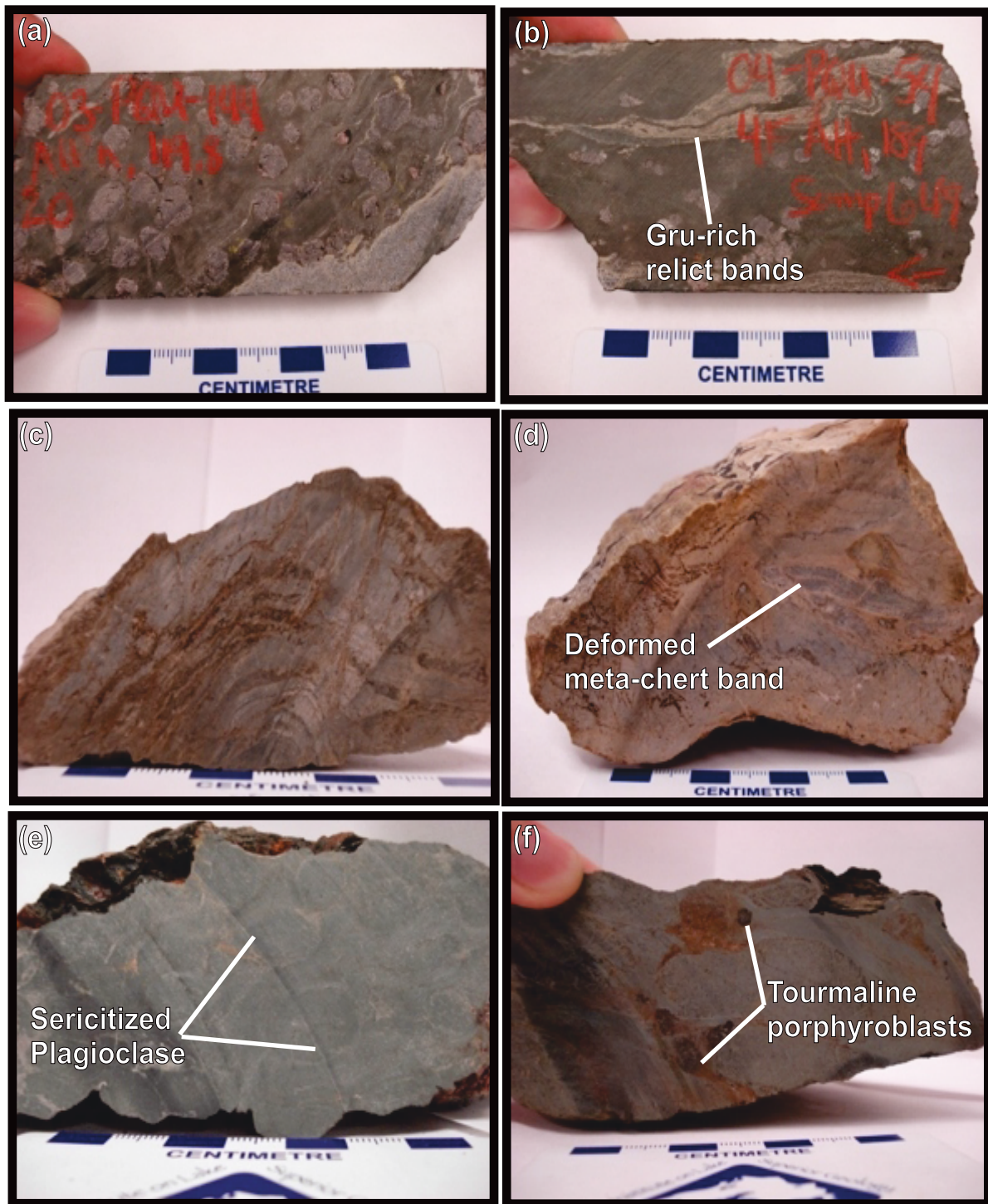
#### *Metasomatic Biotite-Garnet Schist*

The metasomatic biotite garnet-schist, as the name implies, is mineralogically similar to the regular biotite-garnet schist (described in Section 3.8.1). It is usually present as millimetre- to centimetre-scale and more rarely decimetre-scale layers in the lithologies of the Northern Iron Formation Assemblage; although, it tends to be concentrated around the most tectonically disrupted areas as well as at the contacts between quartz and magnetite layers in the oxide-dominant BIF. This lithology is commonly present in drill core and underground drifts, but is rarely seen in outcrop.

Six metasomatic biotite-garnet schist samples were collected for the current study. Relevant sample information, such as drill hole number and meterage, as well as the sample descriptions are provided in Appendix A.

Visually the metasomatic biotite-garnet schist consists of a fine- to medium-grained, dark green-brown, biotite-rich groundmass (Plate 3.25a). The groundmass has a satiny, somewhat shiny, appearance due to the crenulated nature of the biotite grains. The groundmass surrounds euhedral medium- to very coarse-grained porphyroblastic almandine garnets. The garnet grains range from <0.5 cm to ~2 cm in diameter.





**Plate 3.25. Photographs of typical miscellaneous lithologies collected from Musselwhite Mine.** a) sample of biotite-garnet schist showing fine- to medium-grained biotite-rich groundmass, displaying satiny appearance, surrounding coarser-grained garnet porphyroblasts, b) Sample of biotite-garnet schist showing relict grunerite-rich layer surrounded by biotite groundmass, c) Sample of metasomatized oxide-dominant BIF showing grunerite-rich nature and pseudomorphed quartz and magnetite layers, d) sample of oxide-dominant BIF showing deformed meta-chert layer surrounded by massive grunerite-rich groundmass, e) Chlorite-schist sample showing chlorite-rich nature and pseudomorphed augens, f) Chlorite-schist sample containing anhedral to euhedral tourmaline porphyroblasts.

The metasomatic biotite-garnet schist is mineralogically simple. It is composed of, on average, ~5% to <20% garnet porphyroblasts and >80% to ~95% biotite-rich groundmass. The groundmass contains minimal (<5%) additional minerals. Common accessory minerals are limited to quartz, grunerite, and zircon. It should be noted that when present quartz and grunerite are concentrated in millimetre-scale, broadly folded and locally boudinaged, relict layers (Plate 3.25b).

This lithology is visually distinct, compared to the regular biotite-garnet schist, primarily due to the darker and more coarse-grained nature of the groundmass. Additionally, the presence of sparser but significantly coarser-grained garnet porphyroblasts imparts a distinct appearance to the metasomatic biotite-garnet schist. Garnet porphyroblasts tend to be equigranular in each hand sample taken, but in the unit as a whole garnet size varies from medium to very coarse grained.

#### *Metasomatised Oxide-Dominant BIF*

The metasomatised oxide-dominant BIF, as stated above, only occurs in the trenches at Musselwhite (Figures 1.4 and 1.8). The geologic map, presented in Figure 1.8, reveals that this lithology is moderately abundant in the trenches and is closely associated with the oxide-dominant BIF. It is typically present in diffuse contact with the surrounding oxide-dominant BIF; although, it is in higher concentrations around the most tectonically disrupted area of trench five. This lithology is identified as metasomatized oxide-dominant BIF because of its mottled appearance and the fact that it grades laterally, over 10-15 cm, into surrounding 'pristine' oxide BIF over. In terms of mineralogy, this lithology is somewhat similar to the oxide-dominant BIF in that it contains grunerite, magnetite, and quartz. As such, hand samples range from magnetic to non-magnetic depending on the magnetite concentration. The reader should note that this lithology is not present in drill core or underground drifts.

Ten metasomatic oxide-dominant BIF samples were collected from the trenches for the present study. Locations are shown in Figure 1.8. and relevant sample information such as sample descriptions are provided in Appendix A.

Visually the metasomatised oxide-dominant BIF consists of a fine-grained, tan-yellow, grunerite-rich groundmass (Plate. 3.25c). Grunerite grains range from anhedral to subhedral and can be up to 1 mm in diameter. The groundmass has a granulated appearance. Its appearance is primarily a reflection of its relatively simple mineralogy.

The metasomatised oxide-dominant BIF is mineralogically simple. It is composed of, on average, ~50% to ~99% grunerite and <50% to ~1% relict magnetite and/or quartz material. Common accessory minerals are limited to minor biotite. It should be noted that when present quartz and magnetite layers have a relict, almost skeletal, appearance and are boudinaged and broadly folded (Plate. 3.25d).

This lithology is visually distinct compared to the regular oxide-dominant BIF (described in Section 3.5) mainly due to its massive nature and tan-yellow appearance. The reader should note that this lithology, for the most part, resembles the grunerite-reaction layers commonly observed in samples of the oxide-dominant BIF (except on a larger scale).

#### *Chlorite Schist*

The chlorite schist, as stated above, only occurs in the trenches at Musselwhite (Plates 1.4 and 1.8). The geologic map (Figure 1.8) reveals that this lithology is minor in its extent. It is present as dyke-like features, with distinct margins, crosscutting the oxide-dominant BIF. In terms of mineralogy this lithology is composed primarily of chlorite with lesser amounts of biotite, carbonate, and tourmaline. The reader should note that this lithology is not present in drill core or underground drifts.

At this point it should be noted that three chlorite schist samples were collected from the trenches (tb-PM05-100, tb-PM05-007, and tb-PM05-024). Relevant sample information such as sample descriptions are provided in Appendix A.

Visually the chlorite schist is striking, due to its green appearance, especially when compared to the black and white appearance of the surrounding oxide-dominant BIF. It consists of a fine-grained, dark green, chlorite-rich groundmass. The groundmass has a

satiny appearance due to the crenulated nature of the chlorite grains. Additionally, an interesting texture is observed in the groundmass. This texture has the appearance of pseudomorphed, very coarse-grained (~2-4cm diameter), augen structures or porphyroblasts (Plate. 3.25e). The groundmass surrounds euhedral medium- to coarse-grained porphyroblastic tourmaline grains (Plate. 3.25f). Tourmaline grains range from <0.2 cm to ~0.5 cm in diameter.

As stated above the mineralogy of the chlorite schist is rather simple. It is composed of, on average, ~99% chlorite-rich groundmass, and ~<1% tourmaline porphyroblasts. Common accessory minerals are limited to biotite and carbonate. Biotite and carbonate in this lithology can compose up to <5% of individual samples.

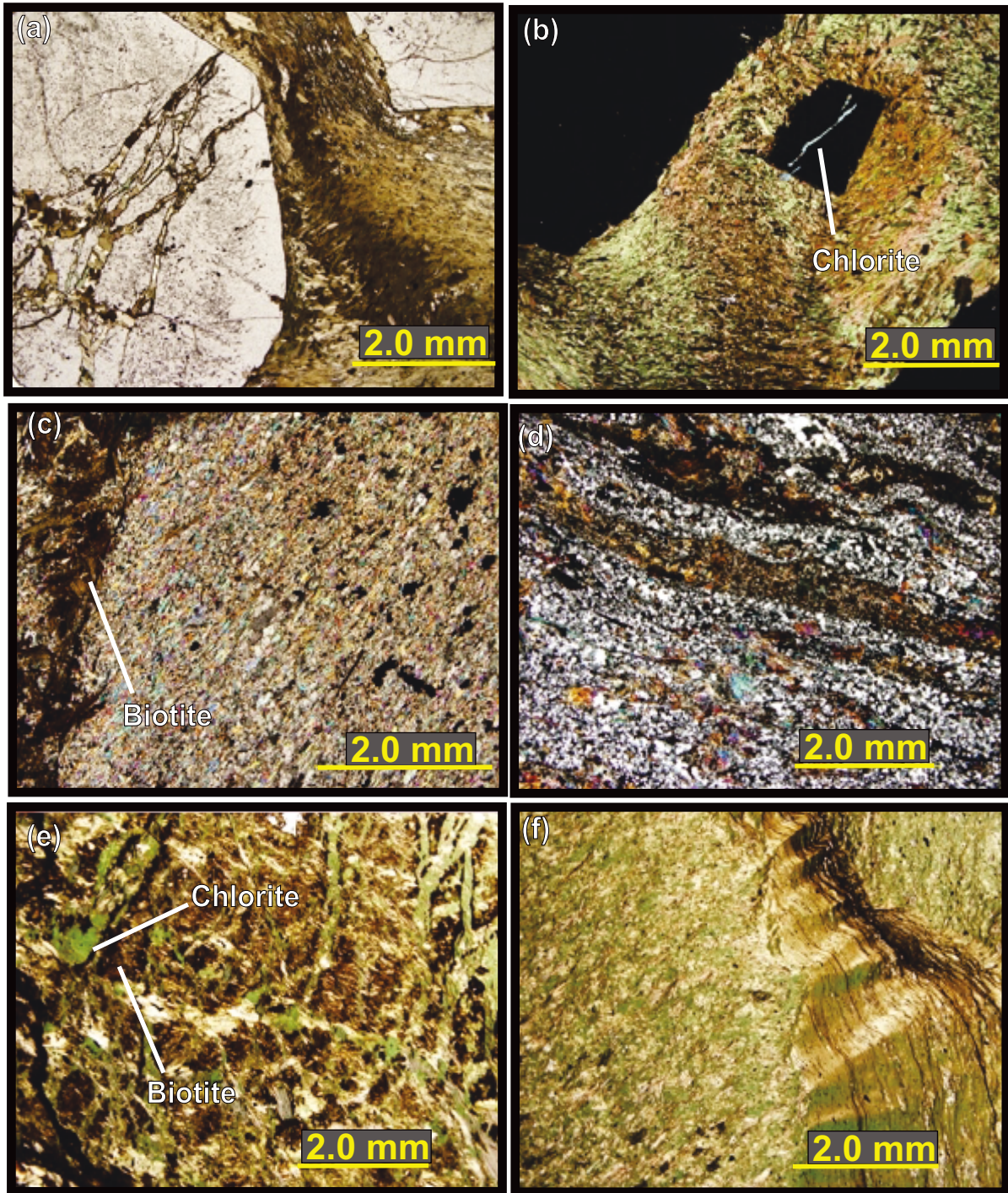
### 3.10.2 Petrographic Character

#### *Metasomatic Biotite-Garnet Schist*

Petrographic observations are based on three thin-sections of metasomatic biotite-garnet schist. Thin-sections were only made from samples sent for geochemical analysis. Representative samples, exhibiting a range of commonly observed features such as relict layering, folding, and metamorphic fabrics, were specifically selected. Refer to Appendix B for the individual thin-section descriptions.

On a microscopic level samples of the biotite-garnet schist are a reflection of the macroscopic appearance of the lithology. As mentioned in section 3.10.1, this lithology typically consists of a fine- to medium-grained biotite-rich groundmass surrounding coarse-grained euhedral garnet porphyroblasts (Plate. 3.26a).

In thin-section the groundmass consists predominantly of biotite. Minor accessory minerals (<5%), in the groundmass, consist of carbonate, quartz, magnetite, grunerite, hornblende, chlorite, and zircon. The grain-size of groundmass minerals is variable ranging from very fine- up to medium-grained, whereas the garnet porphyroblasts range from medium to very coarse grained (Plate. 3.26a and b).



**Plate 3.26. Photomicrographs of minor lithologies collected from Musselwhite Mine.** a) Fine-grained groundmass of crenulated biotite surrounding garnet porphyroblast (ppl), note biotite growth along fractures in garnet (ppl) (sample: bt.gran-0720-020), b) Garnet porphyroblast with chlorite growth along central fracture (xpl) (sample: bt.gran-0720-049), c) Fine-grained grunerite-rich groundmass, containing some biotite aggregates, of the metasomatised oxide-dominant BIF (xpl) (sample: alt-PM05-032), d) Siliciclastic metasediment sample showing quartz bands and Fe-silicate layers (xpl) (sample: alt-PM05-049), e) Fine-grained biotite- and chlorite-rich groundmass of the chlorite schist, note the presence of cross-cutting chlorite-rich veins (ppl) (sample: tb-PM05-007), f) Fine- to medium-grained crenulated chlorite-rich groundmass of the chlorite schist (ppl)(sample: tb-PM05-024).

The biotite-rich groundmass, as its name implies, contains abundant biotite (Plate 3.26a and b). Biotite grains are typically subhedral to euhedral lath-shaped grains ranging between  $<100\ \mu\text{m}$  and  $\sim 400\ \mu\text{m}$ . The biotite grains delineate a well developed crenulation cleavage present throughout the groundmass (Plate 3.26a and b). They are pleochroic light- to dark-green in plane polarized light and exhibit first-order birefringence colours in crossed-polarized light. The biotite grains in the regular biotite-garnet schist exhibit light brown to dark brown pleochroism.

In addition to biotite the groundmass is composed of minor carbonate, quartz, magnetite, grunerite, hornblende, chlorite, and zircon. However, these minerals together do not compose more than 5% of the sample. Quartz grains are usually associated with grunerite grains in relict layers but can also occur as disseminated grains in the groundmass. These grains are equidimensional in shape and are finer grained than the biotite grains. Quartz grains range from  $>20\ \mu\text{m}$  to  $\sim 50\ \mu\text{m}$  in diameter.

There are a small number of recrystallized, 0.2 mm to 0.3 mm thick, quartz-grunerite-amphibole layers, which have been folded into crenulated patterns. These are interpreted to be relict meta-chert layers, which have been strongly deformed since emplacement.

Chlorite is a minor component of the biotite-rich groundmass and is also found as inclusions within fractured garnets (Plate 3.26b). It mainly occurs as individual subhedral grains, which are comparable in size to the biotite grains. Interestingly, these grains look primary and therefore probably do not represent alteration of the biotite. Additionally, the presence of chlorite grains in the fractures of garnets suggests a somewhat later stage of formation. Together, the biotite and minor accessory minerals form a foliated to crenulated groundmass, which encompasses abundant coarser-grained almandine garnet porphyroblasts (Plate 3.26a and b).

The almandine garnet porphyroblasts in the metasomatic biotite-garnet schist range from medium- to very coarse-grained, being roughly 0.5 -1.5 cm in diameter, and exhibit primarily euhedral grain forms. In plane polarized light the garnet grains are colourless to light brown and isotropic in crossed-polarized light. These grains contain anhedral

inclusions of biotite and chlorite as well as euhedral inclusions of titanomagnetite and magnetite. Additionally, garnet porphyroblasts in this lithology are very euhedral and in certain cases exhibit three generations of growth consisting of an inclusion-free core and rim with a central inclusion-rich layer. Rotated, snowball-type, garnets are not present in the three thin-sections examined.

#### *Metasomatised Oxide-Dominant BIF*

Petrographic observations are based on nine-sections of metasomatised oxide-dominant BIF. Thin-sections were made from samples sent for geochemical analysis. Representative samples, exhibiting a range of commonly observed features such as relict layering and massive texture were specifically selected. Refer to Appendix B for the individual thin-section descriptions.

On a microscopic level samples of the metasomatised oxide-dominant BIF are a reflection of the macroscopic appearance of the lithology. As mentioned in section 3.10.1, this lithology typically consists of a fine-grained grunerite-rich groundmass surrounding fine- to medium-grained relict magnetite grains (Plate 3.26c).

In thin-section the groundmass consists predominantly of grunerite. Grunerite typically composes greater than 85% of this lithology with the remainder of the rock made up of a combination of magnetite, carbonate, biotite,  $\pm$  quartz. The latter minerals are considered minor accessory minerals in this lithology. The grain-size of groundmass minerals is variable ranging from very fine up to medium grained.

Grunerite grains (Plate 3.26c) are typically subhedral to euhedral roughly diamond-shaped grains ranging between  $<40 \mu\text{m}$  and  $\sim 60 \mu\text{m}$ . They exhibit high birefringence colours in crossed polarized light and the characteristic twinning pattern of grunerite.

In addition to grunerite the groundmass is composed of minor carbonate, quartz, magnetite, and biotite. However, these minerals together do not compose greater than 15% of individual samples. Quartz grains are usually associated with carbonate grains in distorted veins. Additionally, both carbonate and quartz grains can occur as disseminated

grains in the groundmass. If present quartz grains occur in later veins, which cross-cut this lithology. These grains are equidimensional in shape and are finer grained than the grunerite grains. These grains are usually <40 µm in diameter.

The reader should note the unusual absence of primary quartz in the metasomatised oxide-dominant BIF. It is assumed that quartz must have been a component of the original lithology. It is hypothesised, at this point, that all the quartz reacted to form the grunerite grains presently seen.

Biotite is a minor, but important, component in this lithology. These grains exhibit light brown to dark brown pleochroism. Biotite grains are on average between 500 µm to 900 µm long with grains primarily found as euhedral blades forming radiating agglomerates (Plate 3.26c). Most importantly, the biotite grains appear to be concentrated around fractures which crosscut this lithology.

Two samples (alt-PM05-048 and alt-PM05-049) were originally identified and collected as metasomatised oxide-dominant BIF. These samples are probably siliciclastic metasediment based on their mineralogy. In thin section these samples consist of quartz, hornblende, grunerite, and clinopyroxene (Plate 3.26d). Quartz is the main component of this lithology. Quartz grains range between 50 µm to 150 µm in diameter and compose layers between 1 mm and 1.5 mm in thickness.

Hornblende, grunerite, and pyroxene grains are confined to thinner, wispy-layers, ranging between 0.5 mm to 1.0 mm in thickness are intercalated amounts the quartz-rich layers (Plate 3.26d). Within the Fe-silicate layers amphibole grains range between 300 µm to 700 µm and pyroxene grains range between 200 µm to 500 µm.

#### *Chlorite Schist*

Petrographic observations are based on two-sections of chlorite schist. Thin-sections were made from samples sent for geochemical analysis. Representative samples, exhibiting a range of commonly observed features such as pseudomorphed augen



structures and tourmaline porphyroblasts were specifically selected. Refer to Appendix B for the individual thin-section descriptions.

On a microscopic level samples of the biotite-garnet schist are a reflection of the macroscopic appearance of the lithology. As mentioned in section 3.10.1, this lithology typically consists of a very fine- to medium-grained, chlorite-rich groundmass surrounding medium- to coarse-grained, tourmaline porphyroblasts. Note tourmaline is only found in samples from trench 5.

Chlorite typically composes greater than 97% of this lithology with the remainder of the rock made up of a combination of biotite, carbonate,  $\pm$  garnet and tourmaline. However, biotite can compose a significant part of this lithology (Plate 3.26e). Biotite grains actually appear to predate chlorite. The later minerals are considered minor accessory minerals in this lithology. The grain-size of groundmass minerals is variable ranging from very fine up to medium grained. Texturally, the chlorite schist exhibits a number of different features. The most notable is a pervasive crenulation cleavage (Plate 3.26f).

#### 3.10.4 Geochemical Composition

##### *Metasomatic Biotite-Garnet Schist*

The geochemistry of the metasomatic biotite-garnet schist, summarized in Tables 3.16 as well as Appendix D, is relatively consistent across the sample set. In total six samples were sent for geochemical analysis. Overall, the metasomatic biotite-garnet schist samples exhibit similar mixtures of exhalative- and siliciclastic-derived elements and derivative geochemical signatures. These geochemical signatures are elaborated on below.

Samples of the metasomatic biotite-garnet schist exhibit the following ranges, of relevant elements, in their geochemical composition: 3.0-42 wt.% Fe<sub>2</sub>O<sub>3</sub>, 0.2-27 wt.% FeO, 27-39 wt.% SiO<sub>2</sub>, 4-6 wt.% MgO, 1.5-6 wt.% CaO, 0.5-1.7 wt.% TiO<sub>2</sub>, 11-22 wt.% Al<sub>2</sub>O<sub>3</sub>, 0.2-0.8 wt.% MnO, 0.1-0.8 wt.% Na<sub>2</sub>O, 4-5 wt.% K<sub>2</sub>O, 0.02-0.2 wt.% P<sub>2</sub>O<sub>5</sub>, 52-130 ppm Zr, 0.3-1.5 ppm U, 20-150 ppm Rb, 2.6-20 ppm Cs, 0.3-4.1 ppm Th, and 0-2 ppm Se.



As stated above, samples of the metasomatic biotite-garnet schist exhibit similar values across a range of elements. Interestingly, the most noticeable geochemical difference is between iron values. Out of the six metasomatic biotite-garnet schist samples sent for analysis, three samples (bt.garn-07-20-017, bt.garn-07-20-020, and bt.garn-07-20-049) have low FeO values and high Fe<sub>2</sub>O<sub>3</sub> values and the other three samples (bt.garn-07-20-001, bt.garn-07-20-007, and bt.garn-07-20-054) have high FeO values and low Fe<sub>2</sub>O<sub>3</sub> values.

Samples bt.garn-07-20-017, bt.garn-07-20-020, and bt.garn-07-20-049 exhibit the following ranges in concentration of relevant elements at: 27-42 wt.% Fe<sub>2</sub>O<sub>3</sub>, 0.2-0.3 wt.% FeO, 32-38 wt.% SiO<sub>2</sub>, 4-5 wt.% MgO, 1.5-2.3 wt.% CaO, 0.5-1.0 wt.% TiO<sub>2</sub>, 14-22 wt.% Al<sub>2</sub>O<sub>3</sub>, ~0.2 wt.% MnO, 0.13-0.6 wt.% Na<sub>2</sub>O, 4-5 wt.% K<sub>2</sub>O, 0.02-0.09 wt.% P<sub>2</sub>O<sub>5</sub>, 52-130 ppm Zr, 0.3-1.5 ppm U, 24-150 ppm Rb, 2.6-15.3 ppm Cs, 0.3-4.1 ppm Th, and <1-2 ppm Se. The higher concentration of Fe<sub>2</sub>O<sub>3</sub> is reflected mineralogically by the presence of relatively abundant magnetite in the above described samples.

Samples bt.garn-07-20-001, bt.garn-07-20-007, and bt.garn-07-20-054 exhibit the following ranges in concentration of relevant elements at: 3.0-8.0 wt.% Fe<sub>2</sub>O<sub>3</sub>, 21-23 wt.% FeO, 27-39 wt.% SiO<sub>2</sub>, 4-6 wt.% MgO, 3-6 wt.% CaO, 0.6-2.0 wt.% TiO<sub>2</sub>, 11-16 wt.% Al<sub>2</sub>O<sub>3</sub>, 0.2-0.3 wt.% MnO, 0.3-0.8 wt.% Na<sub>2</sub>O, ~4.0 wt.% K<sub>2</sub>O, 0.1-0.2 wt.% P<sub>2</sub>O<sub>5</sub>, 56-114 ppm Zr, 0.32-0.59 ppm U, 20-150 ppm Rb, 2.6-19.8 ppm Cs, 1-21 ppm Th, and <1 ppm Se.

An interesting feature of this unit is the unexpected relatively homogeneous geochemical nature of the rock. Samples exhibit very similar geochemical values. The metasomatic biotite-garnet schist contains roughly 10-15 wt.% less SiO<sub>2</sub> than the regular biotite-garnet schist (see Section 3.9.4). Other than the difference in SiO<sub>2</sub> content the two lithologies are geochemically similar.

#### *Metasomatised Oxide-Dominant BIF*

The geochemistry of the metasomatised oxide-dominant BIF, summarized in Tables 3.16 as well as Appendix D, is relatively consistent across the sample set. In total nine samples

were analyzed geochemically. Two out of the nine samples are distinct and represent metamorphosed siliciclastic sediment; these are broken out and discussed on their own. However, the remaining seven samples exhibit comparatively similar geochemical signatures. These geochemical signatures are elaborated on below.

Samples of the metasomatic oxide-dominant BIF exhibit the following ranges, of relevant elements, in their geochemical composition: 7.5.-21 wt.% Fe<sub>2</sub>O<sub>3</sub>, 28-34 wt.% FeO, 39-48 wt.% SiO<sub>2</sub>, 4-6 wt.% MgO, 0.2-3 wt.% CaO, 0.01-0.4 wt.% TiO<sub>2</sub>, 0.1-0.3 wt.% Al<sub>2</sub>O<sub>3</sub>, ~1.0 wt.% MnO, 0-0.25wt.% Na<sub>2</sub>O, 0-0.6 wt.% K<sub>2</sub>O, 0.07-1.0 wt.% P<sub>2</sub>O<sub>5</sub>, 10-14 ppm Zr, 0.04-0.13 ppm U, 0-4 ppm Rb, 0.2-2.8 ppm Cs, 0-0.2 ppm Th, and <1 ppm Se.

It should be noted that the siliciclastic metasediment samples are different from the metasomatised oxide-dominant BIF samples. Please refer to Appendix A for detailed descriptions of the individual samples.

The two samples of the siliciclastic metasediment exhibit the following ranges, of relevant elements, in their geochemical composition: ~4.0 wt.% Fe<sub>2</sub>O<sub>3</sub>, ~4 wt.% FeO, 63-64 wt.% SiO<sub>2</sub>, 4-6 wt.% MgO, 7-8 wt.% CaO, 0.6-0.9 wt.% TiO<sub>2</sub>, 8-11 wt.% Al<sub>2</sub>O<sub>3</sub>, 0.12-0.15 wt.% MnO, 1-1.5 wt.% Na<sub>2</sub>O, 0.3-0.4 wt.% K<sub>2</sub>O, 0.03-0.06 wt.% P<sub>2</sub>O<sub>5</sub>, 87-130 ppm Zr, 1.33-2.53 ppm U, 10-12 ppm Rb, ~3.0 ppm Cs, 4-10.92 ppm Th, and 2-3 ppm Se.

#### *Chlorite Schist*

The geochemistry of the chlorite schist, summarized in Tables 3.17 as well as Appendix D, is relatively consistent across the sample set. However, this lithology is of limited extent and as such only three samples were analyzed geochemically. Overall, these chlorite schist samples exhibit similar geochemical signatures. The geochemical signatures are elaborated on below.

Samples of the chlorite schist exhibit the following ranges, of relevant elements, in their geochemical composition: 3.0.-11 wt.% Fe<sub>2</sub>O<sub>3</sub>, 27-33 wt.% FeO, 28-30 wt.% SiO<sub>2</sub>, 5-8wt.% MgO, 0.1-0.2 wt.% CaO, 0.7-0.8 wt.% TiO<sub>2</sub>, 16-17 wt.% Al<sub>2</sub>O<sub>3</sub>, ~0.1 wt.% MnO, 0.04-0.1 wt.% Na<sub>2</sub>O, 0.1-0.8 wt.% K<sub>2</sub>O, 0.03-0.05 wt.% P<sub>2</sub>O<sub>5</sub>, 35-55 ppm Zr, 0.07-0.09 ppm U, 3-172 ppm Rb, N.D-25 ppm Cs, N.D-4.0 ppm Th, and N.D ppm Se.

## Chapter 4

### Whole-Rock Lithochemochemistry

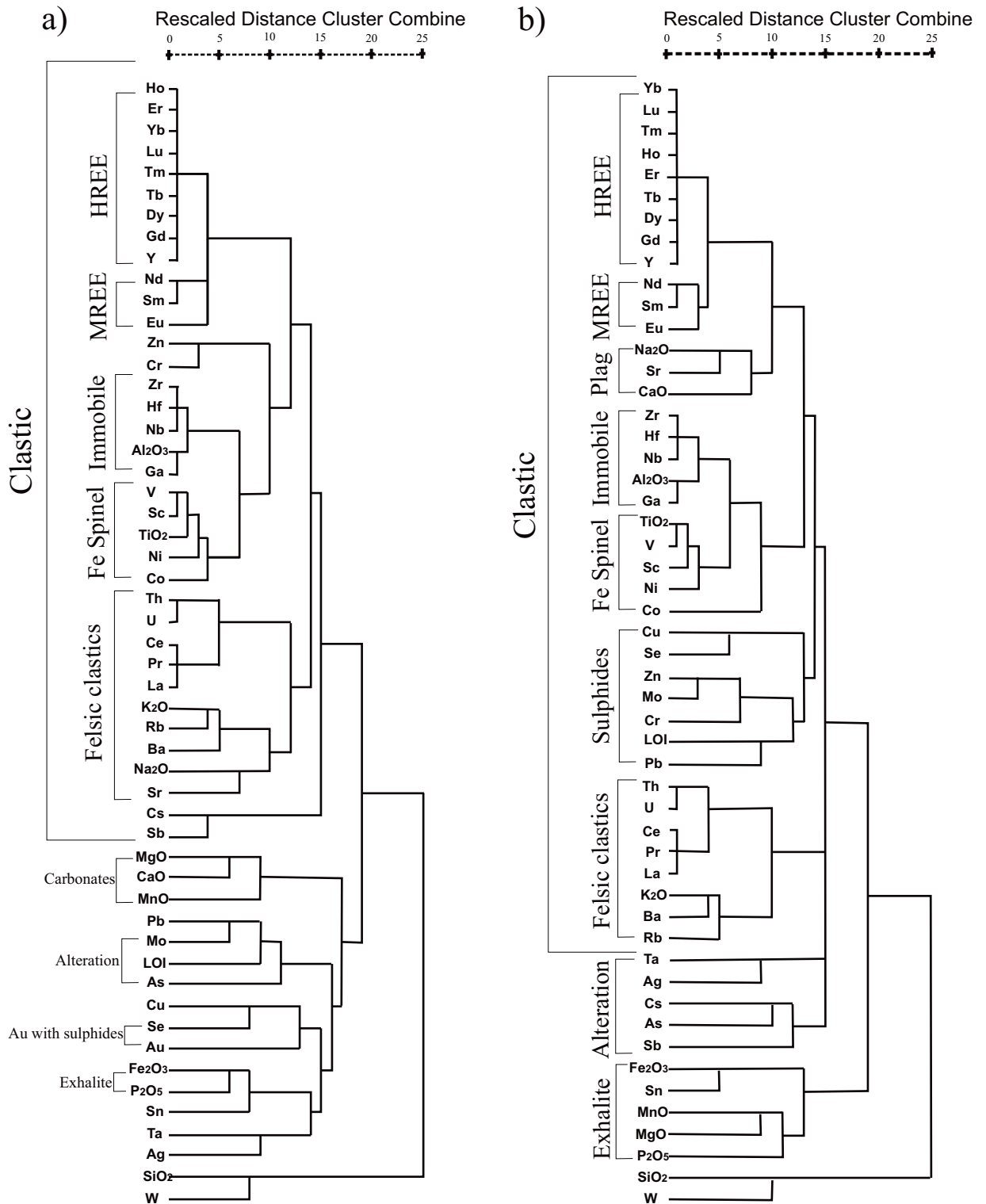
#### 4.1 Introduction

Chapter Four focuses on the geochemistry of the various lithologies sampled from the Musselwhite gold deposit. In total one hundred and twenty-three samples were sent for whole-rock geochemical analysis. The reader will find detailed description of methods, detection limits, and analytical procedures in section 1.12 (p. 39) of Chapter One. Please refer to Appendix A for detailed sample descriptions and Appendix D for lithochemochemistry data.

Due to the number of samples, plots in Chapter Four are divided into two groups; chemical and clastic dominated. Groups were established after a broad examination of the geochemistry of lithologies from the standpoint of their protolith.

The objectives of this chapter revolve around relating the macroscopic appearance and characteristics of the lithologies to their geochemistry in order to gain a more complete understanding of the drill core, stratigraphy, and mineralization patterns. Importantly this chapter establishes the protolith of the metasedimentary rocks, their tectonic setting, and post-depositional chemical alteration.

Examination of the geochemical trends began on a fundamental level by using the statistical procedure of cluster analysis. Cluster analysis is a technique designed to determine similarities between items, in this case elements, using algorithms which consider all the variables measured (Till, 1974). The elements are arranged into uniform groups based on their collective mathematical similarities (Neuendorf *et al.*, 2005). Cluster analysis works through comparing points (items) in space. The position of these points is based on the value of the variables measured. Initially, the items closest in space (i.e., the most similar) are paired together. Clustering proceeds in this fashion until all items are grouped. This hierarchical grouping results in a dendrogram (Fig. 4.1). The



**Figure 4.1. Cluster analysis dendrograms for samples from the current study. Note elements which behaved in a similar manner plot closest to each other on the dendrogram. a) Cluster analysis dendrogram for seventy-two samples (including Au values) from the NIF assemblage at Musselwhite gold deposit, b) Cluster analysis dendrogram for 106 samples from the NIF assemblage at Musselwhite gold deposit (excluding Au values).**

closer the items link on the dendrogram the more similar they are. For instance, in Figure 4.1a and b, the HREE group together on a first order basis suggesting these elements behaved in a similar manner the samples analysed. This result is not surprising since these elements are considered strongly immobile.

The geochemical dataset from the present study was given to Dr. Wendy Huang, head of the statistical consulting service (part of the Mathematical Sciences Department at Lakehead University), who completed cluster analysis on the dataset using an SPSS computer program. Further interpretation and investigation of the data was completed by the author. The reader should note that this preliminary statistical analysis is only one component in clarifying the exact nature and relationship elements have to each other. However, the cluster analysis dendrograms do provide basic information on element mobility as well as the behaviour of critical elements. When conducting geochemical research, it is important to first establish element behaviour, especially mobility and immobility of Al, Ti, and Zr. This is critical, as mobility can be an indication as to the degree the rocks have been 'altered'. Additionally, proving element immobility gives credit to and validates the geochemical trends seen in other diagrams dealing with more mobile elements such as Fe and Mn.

#### 4.2 Element Mobility and Relationships

Numerous cluster-analysis dendrograms (Hartigan, 1975), using different combinations of samples were generated. In total one hundred and eight geochemical analyses were provided to Dr. Huang. Only the metasedimentary samples were compared because mineralization is primarily confined to these lithologies. Metavolcanic samples (n=15) were not included in the cluster analyses sample set because the study is focused on the metasedimentary lithologies. Additionally, the metavolcanic samples were not compared because they contain low concentrations of elements associated with exhalative activity (i.e. Fe, Mn, Mg etc.) relative to the metasedimentary samples. Therefore, their inclusion in the dataset would generate meaningless results.

Analysis was completed by both clustering the variables (elements) and clustering the cases (samples). The dendrogram comparing samples is discussed further on in this

chapter (Section 4.8). Sample combinations are summarized in the following table (refer to p. xvii in the introduction for explanation of abbreviations):

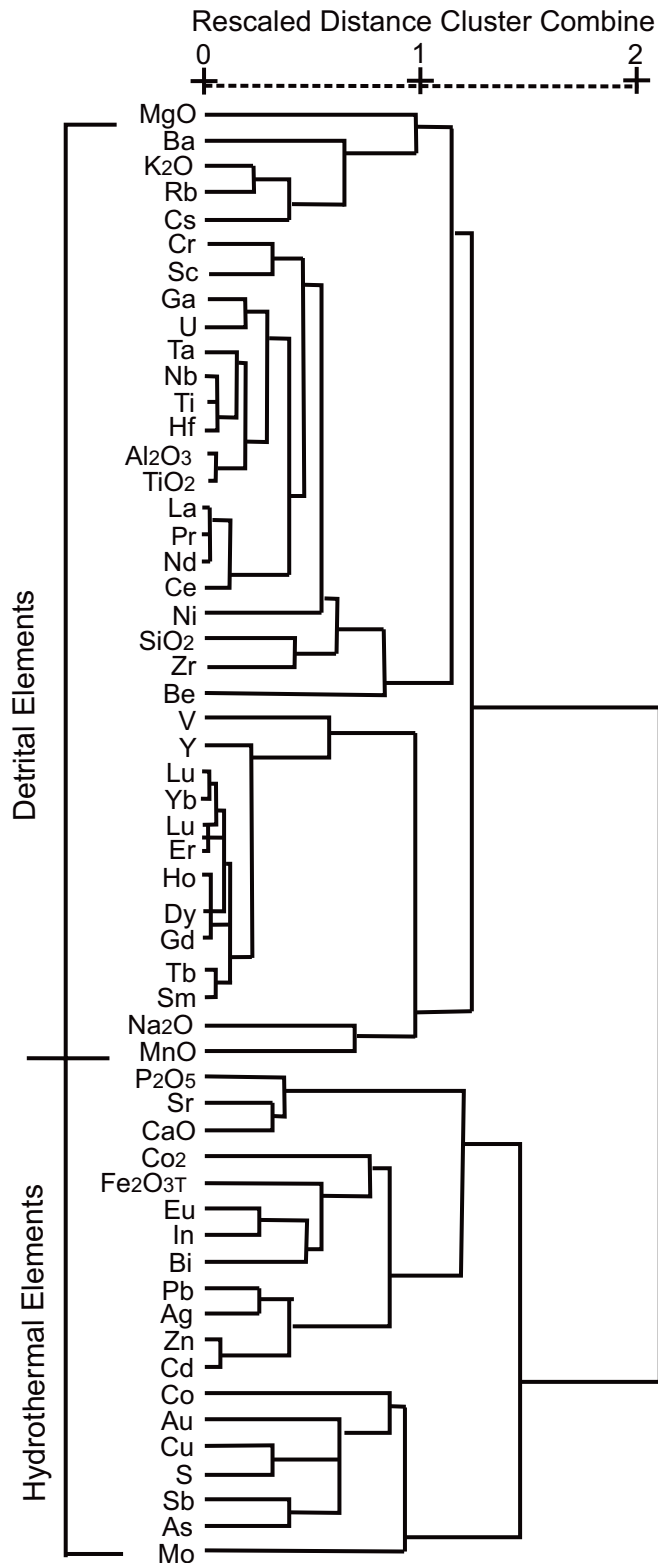
Group	Sample combination (out of n=108)
1	n=72, entire dataset is smaller as it is limited to drill core samples with Au values (4h, 4a, 4b, metasomatic bt.garn-, 4ea-, 4e-, 4f-)
2	n=49, siliciclastic dominated samples (no Au data input) (biotite-garnet-, 4ea-, 4f-, 4e-, alt-, tb-, altb-)
3	n=57, exhalite-dominated samples (no Au data input) (4h, 4a, 4b, SIF)
4	n=106, entire dataset including exhalite- and siliciclastic-dominated lithologies, all samples (no Au data input)

**Table 4.1. Table listing the sample groupings used to produce the dendrograms in Fig. 4.1a and b. Note abbreviations are explained on p. xvii of the thesis introduction.**

Figure 4.1a is a cluster analysis dendrogram generated from group one, which contains seventy-two samples with Au values, from the metasedimentary rocks at Musselwhite Mine. Figure 4.1b is a cluster analysis dendrogram generated from group four, and does not include gold values (all samples in dataset, with gold values omitted because gold was not measured in all samples). The elements can be broadly divided into two clusters, those which came from a clastic detrital source and those which came from an exhalite hydrothermal source. These elemental groupings, along with others, are broken out in Figures 4.1a and 4.1b. There are also numerous smaller sub-clusters which are controlled primarily by specific minerals. These clusters are based on Peter's (2003) dendrogram interpretations (Fig. 4.2).

The mid- to heavy-REE's (MREE-HREE) are known immobile elements. These elements cluster together in Figure 4.2a-b and therefore behaved in their predicted immobile manner. The HREE (Ho, Er, Yb, Lu, Tm, Tb, Dy, Gd, and Y) show the same relationship in both Figures 4.1a and b. These elements are related because they behave in a chemically similar way. However, Eu clusters with Nd and Sm in Figures 4.1a and b, not with the other mid- to heavy-REE, due to its ability to exist in the +2 state.





**Figure 4.2 Peter's (2003) Cluster Analysis dendrogram for iron formation samples collected from the Bathurst Mining Camp in the Heath Steele belt. Note elements which behaved in a similar manner plot closest to each other on the dendrogram.**

Interestingly, in Figure 4.1a, the light-REEs (LREE) La, Ce and Pr do not cluster with the HREE and MREEs, but with Th, U, K<sub>2</sub>O, Rb, Ba, Na<sub>2</sub>O, and Sr. A slightly different grouping occurs in Figure 4.1b where Na<sub>2</sub>O, Sr, and CaO group together, not with Th, U, K<sub>2</sub>O, Rb, and Ba. The Na<sub>2</sub>O, Sr, CaO group is controlled by plagioclase and the other elements denote the influence of a felsic source. It is likely that significant quantities of feldspars were weathered and transported as clay minerals (this is discussed in more detail in Chapter Five). The fact that, in Figure 4.1a, the immobile LREEs and Th cluster with K<sub>2</sub>O, Rb, Ba, Na<sub>2</sub>O, and Sr indicates the latter elements probably commonly behaved in a relatively immobile manner as well. The immobile nature of Th and U is confirmed by the positive linear relationship the two elements exhibit (see Figures 4.7g and h). However, it is important to note that metavolcanic rocks from the major shear zones exhibit potassium addition (John Biczok, personal communication, 2007).

The elements Zr, Hf, Nb, Al<sub>2</sub>O<sub>3</sub>, and Ga group together, in both Figures 4.1a and b, because of their shared strong immobile nature. Ga groups next to Al<sub>2</sub>O<sub>3</sub> because it commonly substitutes for Al due to similar atomic properties (Deer *et al.*, 1992).

Titanium dioxide, V, Sc, Ni, and Co cluster together in Figure 4.1a suggesting these elements behaved in a similar manner. Cobalt does not group with the aforementioned elements in Figure 4.1b. The fact that these elements cluster with TiO<sub>2</sub> suggests they were relatively immobile. It is likely that this cluster is controlled by titanomagnetite. Titanomagnetite is part of a solid solution series, between magnetite and ulvöspinel (Fe<sub>2</sub>TiO<sub>4</sub>). The solid solution series occurs because the magnetite crystal structure can accommodate a substantial amount of Ti. In addition it is common to have partial substitution of Fe<sup>3+</sup> by V and Cr and Fe<sup>2+</sup> by Zn, Co, and Ni (Deer *et al.*, 1992). SEM examination of thin-sections revealed abundant titanomagnetite in the clastic-dominated lithologies. In Figure 4.1a these elements do not group with Fe<sub>2</sub>O<sub>3</sub> suggesting the titanomagnetite represents original clastic material as opposed to exhalite material.

In Figure 4.1a Fe<sub>2</sub>O<sub>3</sub> and P<sub>2</sub>O<sub>5</sub> cluster together and represent the core of the exhalite cluster. Figure 4.1b exhibits a more developed exhalite cluster containing: Fe<sub>2</sub>O<sub>3</sub>, Sn,

MnO, MgO, and P<sub>2</sub>O<sub>5</sub>. Iron and phosphorous were originally deposited as gels, which were later transformed into magnetite and apatite through diagenesis and metamorphism (Toth, 1980). Iron and phosphorous are precipitated together in non-buoyant hydrothermal plumes due to completing of P (oxyanion, from seawater) with Fe-oxide (oxyhydroxide, from hydrothermal fluid; Peter, 2003). Interestingly, in Figure 4.1a, CaO clusters with MgO and MnO suggesting these elements were primarily controlled by a carbonate phase (i.e., dolomite and Ferroan calcite).

The opposite geochemical behaviour defines SiO<sub>2</sub>, which shows the least correlation of all elements in both Figures 4.1a and b, suggesting SiO<sub>2</sub> behaved in a mobile manner. The disconnect between SiO<sub>2</sub> and the other elements is an example of a constant sum problem, that is to say a whole sample must sum to 100 wt. % so more SiO<sub>2</sub> in a sample will result in most other elements having lower values. Interestingly W is the one element that clusters with SiO<sub>2</sub> suggesting W is coming into various lithologies with quartz veining. However not all samples contain quartz veins leaving questions as to the exact relationship. This quandary is addressed further on in the chapter.

Molybdenum and As cluster together in Figure 4.1a and probably suggests small amounts of these elements were added during a phase of alteration. It is common to have elevated contents of As in BIF-hosted gold deposits (Lhotka and Nesbitt, 1989). This ‘alteration’ pattern is elaborated on later in this chapter as well as in Chapter Five. Selenium and Cu are the only elements that cluster directly with Au. Selenium substitutes for S in sulfide minerals (Deer *et al.*, 1992). Therefore, Au can be considered to cluster with S (S was not analyzed) and is associated with sulfide minerals (such as pyrrhotite and chalcopyrite).

Dendrogram 4.1b was generated using the entire dataset, which includes a significant number of samples collected away from the ore zones. Therefore, the strong similarities between the cluster analyses of both groups (Fig. 4.1a and b) suggest that there has not been a large amount of element mobility associated with the gold-bearing samples. The most significant difference between Figures 4.1a and 4.1b is the Cu, Se, Zn, Mo, Cr, LOI,

and Pb cluster, which is observed Figure 4.1b, but not Figure 4.1a. This cluster is likely controlled to some degree by sulfide minerals.

#### 4.3 Chemical Versus Clastic Detrital Protoliths: Geochemical Trends

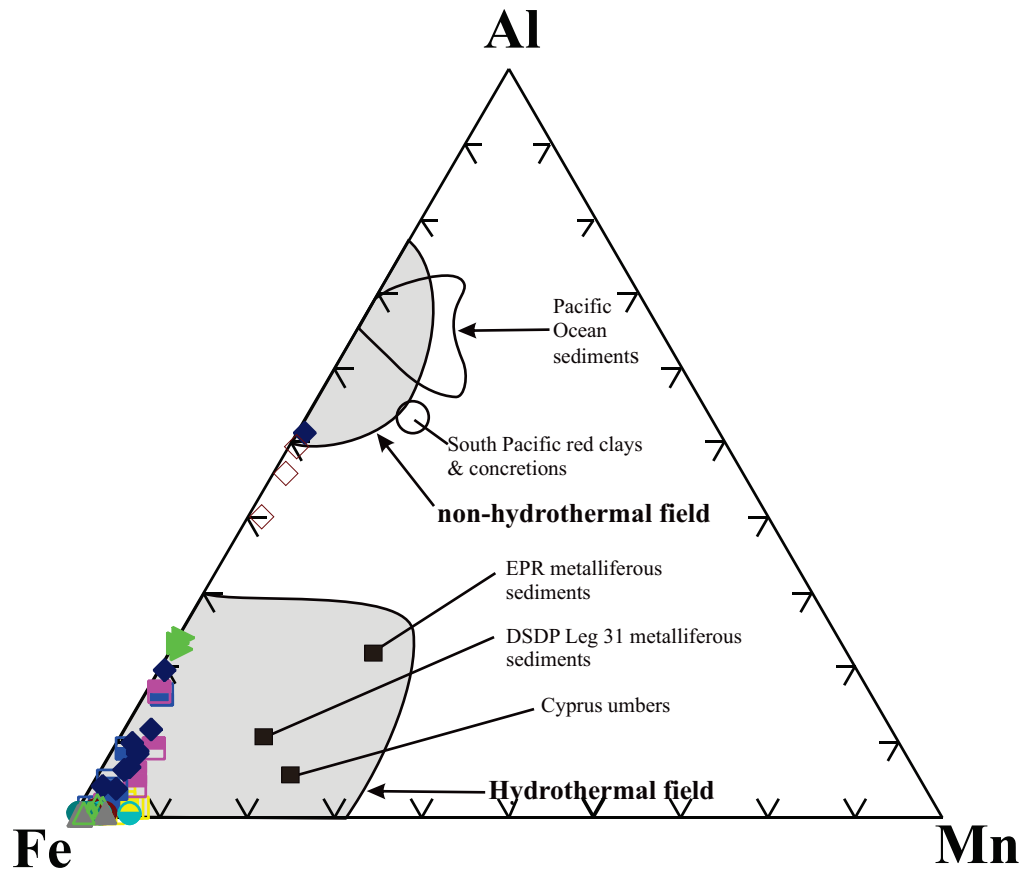
One trend that has already been recognized (Otto, 2002), but not examined in detail, is the increasing siliciclastic component upwards in the stratigraphic succession of the Northern Iron Formation Assemblage. In terms of geochemistry, siliciclastic material has elevated amounts of Al, Zr, and Ti compared to chemical sediments. These elements are contained in detrital feldspars, clay minerals, as well as zircon, titanomagnetite, and titanite. Together these minerals compose silt material, which settles directly out of the water column onto the ocean floor. The general geochemical trend seen in the NIF assemblage indicates the meta-argillite, quartz-grunerite BIF, and oxide-dominant BIF precipitated from submarine hydrothermal fluids and can be broadly classified as exhalites (Fig. 4.3a). The remaining lithologies, the silicate-dominant BIF, hornblende-garnet schist, and biotite-garnet schist are a varying combination of chemical and terrigenous sediment (Fig. 4.3b). Only one lithology, the garnet-bearing quartzite, formed from pure terrigenous/siliciclastic sediment settling out of the water column (Fig. 4.3b).

Relatively simple geochemical diagrams are used to distinguish between exhalite- and siliciclastic-dominated sedimentary rocks. Figures 4.3a and 4.3b are Al-Fe-Mn ternary plots from modified from Boström (1973). The diagrams depict hydrothermal and non-hydrothermal fields. Average samples of various types of modern day seafloor sediments are included for comparison and to add perspective (Toth, 1980; Bonatti *et al.*, 1979; Boström, 1973; Dymon *et al.*, 1973; Robertson and Hudson, 1973).

The basis of the Al-Fe-Mn ternary plot, and many of the plots that follow, is that in both siliciclastic and chemical sediments deposited in the deep ocean, aluminum is primarily a component of detrital clays, the end product of erosion, whereas iron and manganese are mainly contained in exhalite material deposited from hydrothermal black smoker fluids or as hydrogenous crusts and concretions. Boström (1973) empirically arrived at the spatially separated ‘hydrothermal’ and ‘non-hydrothermal’ fields seen on the ternary

## Legend

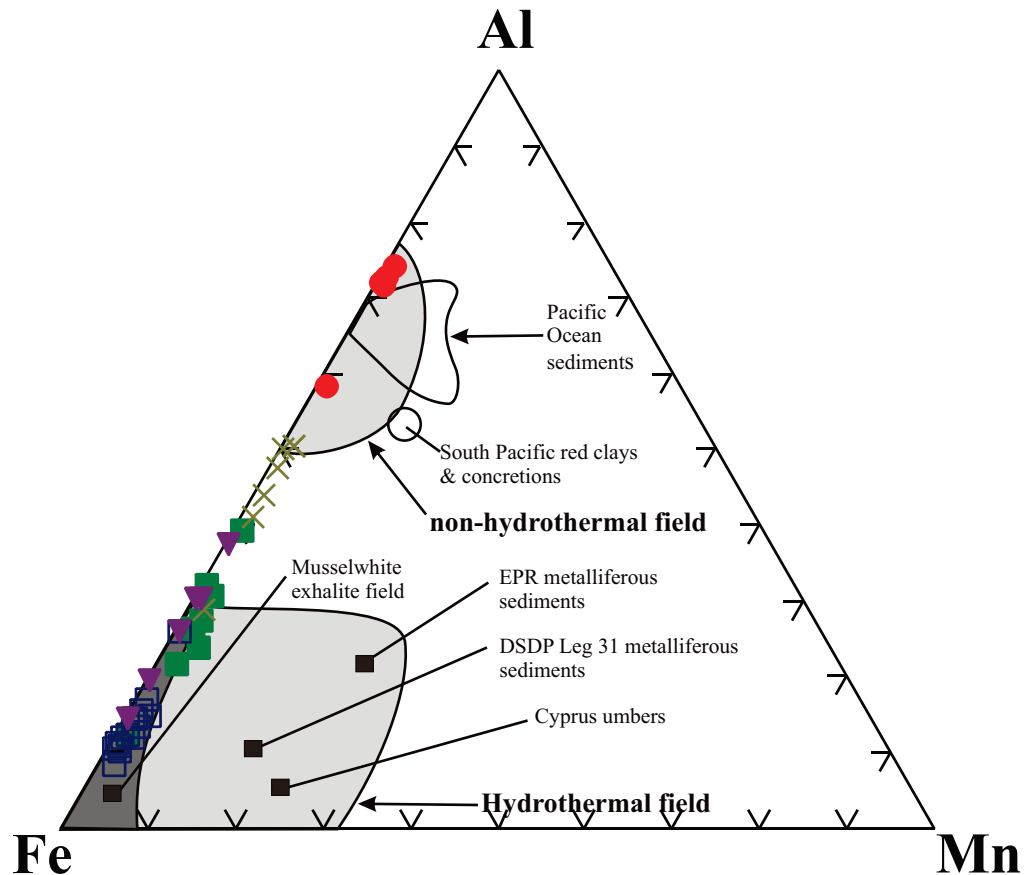
- |  |   |
|--|---|
| <ul style="list-style-type: none"> <li>● Quartz Bands, SIF Oxide-Dominant BIF</li> <li>● Magnetite Bands, SIF Oxide-Dominant</li> <li>◆ Meta-Argillite</li> <li>■ Quartz-Grunerite Banded Iron Formation</li> <li>■ Magnetite bands, NIF assemblage Oxide-</li> <li>■ Quartz bands, NIF assemblage Oxide-</li> <li>▲ Magnetite Bands, NIF Oxide-Dominant BIF</li> <li>△ Quartz Bands, NIF Oxide-Dominant BIF</li> <li>□ Silicate-Dominant Banded Iron</li> </ul> | <ul style="list-style-type: none"> <li>■ Hornblende-Garnet Schist</li> <li>× Bitotie-Garnet Schist</li> <li>▼ Metasomatic Biotite-Garnet Schist</li> <li>● Garnet-Quartzite</li> <li>○ Metasomatised NIF Oxide-Dominant BIF</li> <li>◇ Metasediment Rock (Trench #4)</li> <li>▶ Chlorite Schist (Trench)</li> <li>● Metabasalt</li> </ul> |
|--|---|



**Figure 4.3a. Ternary diagram showing hydrothermal and non-hydrothermal sediment fields based on the relative concentration of aluminum, iron, and manganese for exhalite-dominant samples collected from the Musselwhite gold deposit.** Note: Hydrothermal and non-hydrothermal sediment fields were developed by Boström (1973), oceanic sediments (Dymon et al., 1973; Toth, 1980), umbers from Cyprus massive sulfide deposits (Robertson and Hudson, 1973), East Pacific Rise metalliferous sediments (Boström, 1973) and Deep Sea Drilling Project Leg 31 (Figure modified from Bonatti *et al.*, 1979).

## Legend

- |  |   |
|--|---|
| <ul style="list-style-type: none"> <li>● Quartz Bands, SIF Oxide-Dominant BIF</li> <li>● Magnetite Bands, SIF Oxide-Dominant</li> <li>◆ Meta-Argillite</li> <li>■ Quartz-Grunerite Banded Iron Formation</li> <li>■ Magnetite bands, NIF assemblage Oxide-</li> <li>■ Quartz bands, NIF assemblage Oxide-</li> <li>▲ Magnetite Bands, NIF Oxide-Dominant BIF</li> <li>△ Quartz Bands, NIF Oxide-Dominant BIF</li> <li>□ Silicate-Dominant Banded Iron</li> </ul> | <ul style="list-style-type: none"> <li>■ Hornblende-Garnet Schist</li> <li>× Bitotie-Garnet Schist</li> <li>▼ Metasomatic Biotite-Garnet Schist</li> <li>● Garnet-Quartzite</li> <li>○ Metasomatised NIF Oxide-Dominant BIF</li> <li>◇ Metasediment Rock (Trench #4)</li> <li>▶ Chlorite Schist (Trench)</li> <li>● Metabasalt</li> </ul> |
|--|---|



**Figure 4.3b. Ternary diagram showing hydrothermal and non-hydrothermal sediment fields based on the relative concentration of aluminum, iron, and manganese for siliciclastic-dominant samples collected from the Musselwhite gold deposit.** Note hydrothermal and non-hydrothermal sediment fields were developed by Boström (1973), oceanic sediments (Dymon et al., 1973; Toth, 1980), umbers from Cyprus massive sulfide deposits (Robertson and Hudson, 1973), East Pacific Rise metalliferous sediments (Boström, 1973) and Deep Sea Drilling Project Leg 31 (Figure modified from Bonatti *et al.*, 1979).

diagrams in Figure 4.3. These separated fields create a problem in Fig. 4.3b, because some of the lithologies plot between the hydrothermal and non-hydrothermal fields. Peter (2003) notes that it would be logical for these fields to overlap slightly or grade into each other as these lithologies are controlled by two factors: detrital and hydrothermal inputs.

As mentioned above the lithologies of the Northern Iron Formation Assemblage have been broadly subdivided into two groups due to the number of samples. Subdivision is based on trends in Figures 4.1a, 4.1b, 4.3a, and 4.3b. Figure 4.3a contains samples of lithologies that are characteristically exhalative in nature including the meta-argillite, quartz-grunerite BIF, and oxide-dominant BIF. Figure 4.3b contains samples of lithologies that are slightly more siliciclastic in nature including the silicate-dominant BIF, hornblende-garnet schist, biotite-garnet schist, and garnet-bearing quartzite. Most of the siliciclastic-dominant lithologies plot in the hydrothermal field but are separated from the lithologies in Figure 4.3a, because they contain somewhat higher levels of Al.

The samples in Figure 4.3a and 4.3b depict the general trend of increasing siliciclastic component stratigraphically upward in the Northern Iron Formation Assemblage. The stratigraphically lower lithologies in the NIF assemblage are exhalite-dominant, whereas the stratigraphically higher lithologies are siliciclastic-dominant. Overall the lithologies form a continuum from exhalite-dominated to terrigenous-dominated.

The majority of the NIF assemblage lithologies plot in the hydrothermal field (Fig. 4.3a). This trend is significant from the standpoint of duration of exhalative activity relative to the duration of siliciclastic sedimentation. This topic will be discussed, in detail, in Chapter Five.

Several key trends are observed amongst the samples in Figure 4.3a. One of the most interesting trends is seen in the metasediment samples collected from trench four (alt-PM05-042, alt-PM05-043, and alt-PM05-044). These samples likely represent the only true siliciclastic sediment samples collected from the trenches.

Additional trends seen in Figure 4.3a include a weak correlation between high Fe values and slightly higher Mn values in the exhalite-dominant lithologies particularly in samples of Southern Iron Formation oxide-dominant BIF. Quartz- and magnetite-dominant bands from the SIF are the purest exhalite material as they contain very low aluminium and very high iron and silica values. It should be noted that the quartz-grunerite BIF exhibits comparatively low aluminium values to the SIF oxide-dominant BIF samples.

Magnetite- and quartz-dominated band samples, from the NIF assemblage oxide-dominant BIF, exhibit a moderate amount of scatter. The geochemical variability is probably due to the relatively thick nature of the unit as a whole. Siliciclastic content increases stratigraphically upward in the oxide-dominant BIF unit making it likely that samples collected from near the top contain some aluminous material.

Meta-argillite samples, from the NIF assemblage, exhibit the most scatter out of the exhalite-dominant lithologies, primarily because this lithology is composed of both exhalite and siliciclastic components. There is one anomalous meta-argillite sample which plots within the non-hydrothermal field (sample: 4H-07-20-070).

Figure 4.3b contains samples of the more aluminous lithologies (i.e., units with higher siliciclastic content). It should be noted that these lithologies still contain a significant exhalite constituent with most samples plotting within the hydrothermal field. However, it is obvious from looking at the diagrams in Figure 4.3 that these lithologies contain higher aluminium than the lithologies in Figure 4.3a. As mentioned above the lithologies of the NIF assemblage form a continuum from exhalite- to siliciclastic dominant and this trend is clearly visible in Figure 4.3.

The best example of geochemical overlap exists between the oxide- and silicate-dominant banded iron formations. This overlap is the result of the silicate-dominant BIF being more iron-rich compared to the other siliciclastic-dominant lithologies. Overlap between these two lithologies is not unexpected since they are in gradational contact. It is interesting to reflect on how this slight geochemical difference dramatically affects the



mineralogy of the two BIFs (refer to sections 3.5 and 3.6 of Chapter Three for petrologic descriptions of the two BIFs). This topic will be discussed, in more detail, in Chapter Five.

The silicate-dominant BIF samples plot consistently close to each other, relative to samples of other lithologies, in Figure 4.3b. The unexpectedly similar and consistent geochemical trends of the silicate-dominant BIF are seen in Figure 4.3b and continue on into other diagrams further on in the chapter. However, there are two anomalous samples which overlap with the hornblende-garnet schist (samples: 4ea-PM05-057 and 4ea-07-20-069). The silicate-dominant BIF and the hornblende-garnet schist overlap due to their similar iron and aluminium contents.

Samples of the hornblende-garnet schist, on average, contain lower iron and higher aluminium values compared to the silicate-dominant BIF. Samples of this lithology primarily plot in the upper portion of the hydrothermal field. Two samples (4e-07-20-023 and 4e-07-20-048) plot just outside the hydrothermal field but are a continuation of the trend formed by the other hornblende-garnet schist samples. It should be noted that there is one anomalous sample (4e-07-20-047) which plots with the biotite-garnet schist samples between the hydrothermal and non-hydrothermal fields.

Biotite garnet-schist samples primarily plot between the hydrothermal and non-hydrothermal fields tending to be closer to the non-hydrothermal end of the scale. One biotite-garnet schist sample (4f-07-20-011) even plots slightly within the non-hydrothermal field. This indicates there are roughly equal amounts of aluminium relative to iron in this lithology. Due to both high aluminium and iron content this lithology likely represents metamorphosed ferruginous shale (elaborated on in Chapter Five).

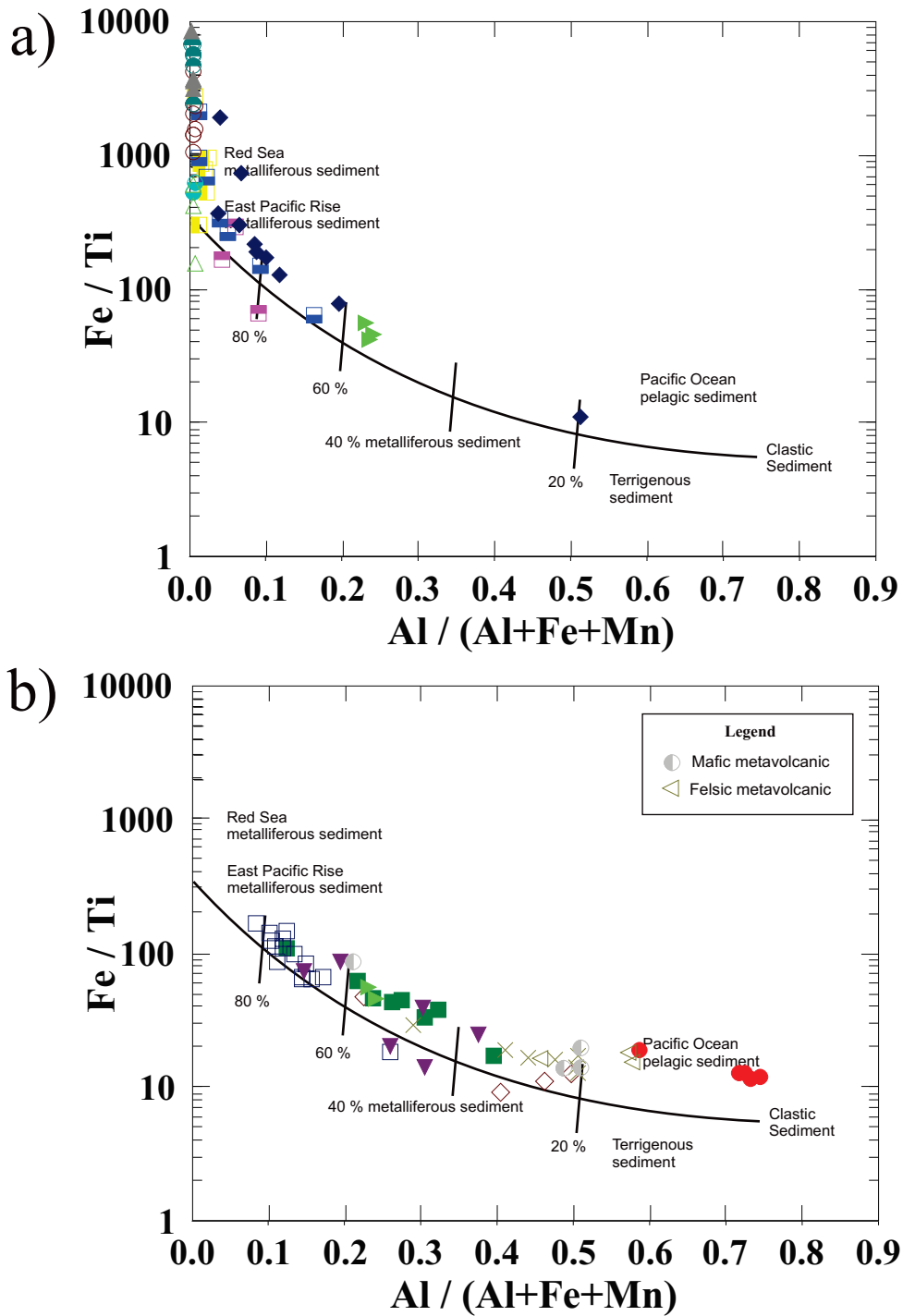
The majority of biotite-garnet schist samples plot close to one and other. However, there is one anomalous sample which plots away from the others in the hydrothermal field overlapping with the hornblende-garnet schist (sample: 4f-07-20-009). This geochemical

trend reaffirms the relationship observed in drill-core where hornblende-garnet schist is found as intercalated bands within the biotite-garnet schist.

The only lithology that plots exclusively in the non-hydrothermal field is the garnet-bearing quartzite. Samples of this lithology plot just above modern day Pacific Ocean sediment in Figure 4.3b. The garnet-bearing quartzite is usually found at the top of and overlying the NIF assemblage. For all intents and purposes, as the garnet-bearing quartzite follows similar geochemical trends to the other lithologies, it is considered part of the NIF assemblage. The garnet-bearing quartzite represents the culmination of increasing siliciclastic component stratigraphically upward in the NIF assemblage. In addition to this lithology having the highest aluminium content, there are various other geochemical factors that make it distinct. These factors will be presented further on in this chapter.

Figures 4.4a and 4.4b consist of a relevant and practical binary discrimination diagram. In this diagram  $Fe/Ti$  is plotted against  $Al/(Al+Fe+Mn)$ . The diagram is more complex than the previously discussed diagrams because it is based on ratios of elements. This diagram was designed by Boström (1973) and is used to interpret the amount of exhalative versus the amount of siliciclastic component in lithologies. Average samples of Red Sea metalliferous sediments (Backer, 1976), East Pacific Rise metalliferous sediment (Cronan, 1976), terrigenous sediment (Boström, 1973), and average pelagic Pacific Ocean sediment (Cronan, 1976) are plotted on the diagram for comparison and to add perspective.

The roughly horizontal curved mixing-line represents a spectrum of pure exhalative sediment on the left end to pure siliciclastic sediment on the right end. The sub-vertical lines perpendicular to the curved mixing-line delineate the amount (percentage) of metalliferous material contained at those particular points. Note a basic assumption is made, in this diagram, that titanium and aluminium are both completely siliciclastic in origin.



**Figure 4.4. Discrimination diagram for estimating the amount of exhalative versus siliciclastic sedimentary material in samples. Diagram modified after Boström (1973). Note that the symbols are the same as in Fig. 4.3. a) diagram depicting the exhalite-dominant samples (lithologies) from the current study, b) diagram depicting the siliciclastic-dominated samples (lithologies). Note that 4 mafic and 3 felsic metavolcanic samples, from the current study, are plotted for comparison. Also note that, in Fig. 4.4b, samples plot above the mixing line which is the result of lower Ti in Archean clays. Average samples of Red Sea metalliferous sediments (Backer, 1976), East Pacific Rise metalliferous sediment (Cronan, 1976), terrigenous sediment (Boström, 1973), and average pelagic Pacific Ocean sediment (Cronan, 1976) are plotted on the diagram for reference.**

Figure 4.4a contains the exhalative-dominated lithologies (n=68), whereas Figure 4.4b contains siliciclastic-dominated lithologies (n=41). Figure 4.4b also contains mafic (n=4) and felsic (n=3) metavolcanic samples, collected during the current study, and plotted for comparison.

There are several trends observable in Figures 4.4a and 4.4b: 1) aluminium and titanium along with iron and manganese have maintained proper ratios because the samples plot on the mixing line, 2) samples form a continuous trend from pure exhalative hydrothermal sediment to pure pelagic siliciclastic sediment, 3) samples plot above the mixing line which is the result of lower titanium in the Archean clays that formed the original (Musselwhite) sediment relative to Boström's (1973) samples, 4) the remaining sedimentary lithologies fall surprisingly concisely between mixing lines, and 5) samples of felsic metavolcanic rock plot close to the garnet-bearing quartzite and samples of the mafic metavolcanic rock plot close to the biotite-garnet schist (similar trend is observed in the REE spider diagrams which are discussed further on in this chapter).

It is evident in Figure 4.4a that most of the exhalite-dominant lithologies contain between 80% to 100% hydrothermally-derived exhalite material including the following samples: the SIF oxide-dominant BIF, meta-argillite, quartz-grunerite BIF, and the NIF assemblage oxide-dominant BIF.

The SIF oxide-dominant BIF magnetite and quartz band samples, with all samples plotting in the 100% exhalite field, exhibit the most exhalite-dominant nature of all the lithologies shown in Figure 4.4a. This is the same trend observed in Figure 4.3a.

Interestingly, NIF assemblage oxide-dominant BIF magnetite and quartz band samples exhibit more scatter compared to SIF samples, ranging between 80% to 100% exhalite material. The remaining portion of these samples is composed of up to 20% non-hydrothermal material (i.e., aluminum-rich siliciclastic sediment). Again, this is the same trend seen in Figure 4.3a. The quartz-grunerite BIF, much like the SIF and NIF oxide-dominant BIF samples plots within the purely chemical field.

Unlike the BIF samples, samples of the meta-argillite plot further to the right suggesting they have higher siliciclastic content than the previously discussed lithologies. In general the meta-argillite is enigmatic as it contains both siliciclastic and exhalite material. This is the same trend observed in Figure 4.3a. However, there is one anomalous sample of meta-argillite that contains a relatively low value of 20% metalliferous material (4h-07-20-070).

Figure 4.4b contains samples of the more aluminous lithologies (i.e., units with higher siliciclastic content). It should be noted that these lithologies still contain a significant exhalite constituent. Figure 4.4b shows that the siliciclastic-dominant lithologies contain between 20% to 60% exhalite material. Note that the stratigraphy of these lithologies, from lowest to highest, is in the following order: silicate-dominant BIF, hornblende-garnet schist, biotite-garnet schist, and garnet-bearing quartzite. Figure 4.4b depicts the increasing siliciclastic component stratigraphically upward in the NIF assemblage quite well. The lithologies form a concise trend with the siliciclastic-dominant BIF containing between 20% to 40% siliciclastic material, the hornblende-garnet schist containing 40% to 60% siliciclastic material, the biotite-garnet schist containing between 20% to 40% siliciclastic material, and the garnet-bearing quartzite containing > 80% siliciclastic material.

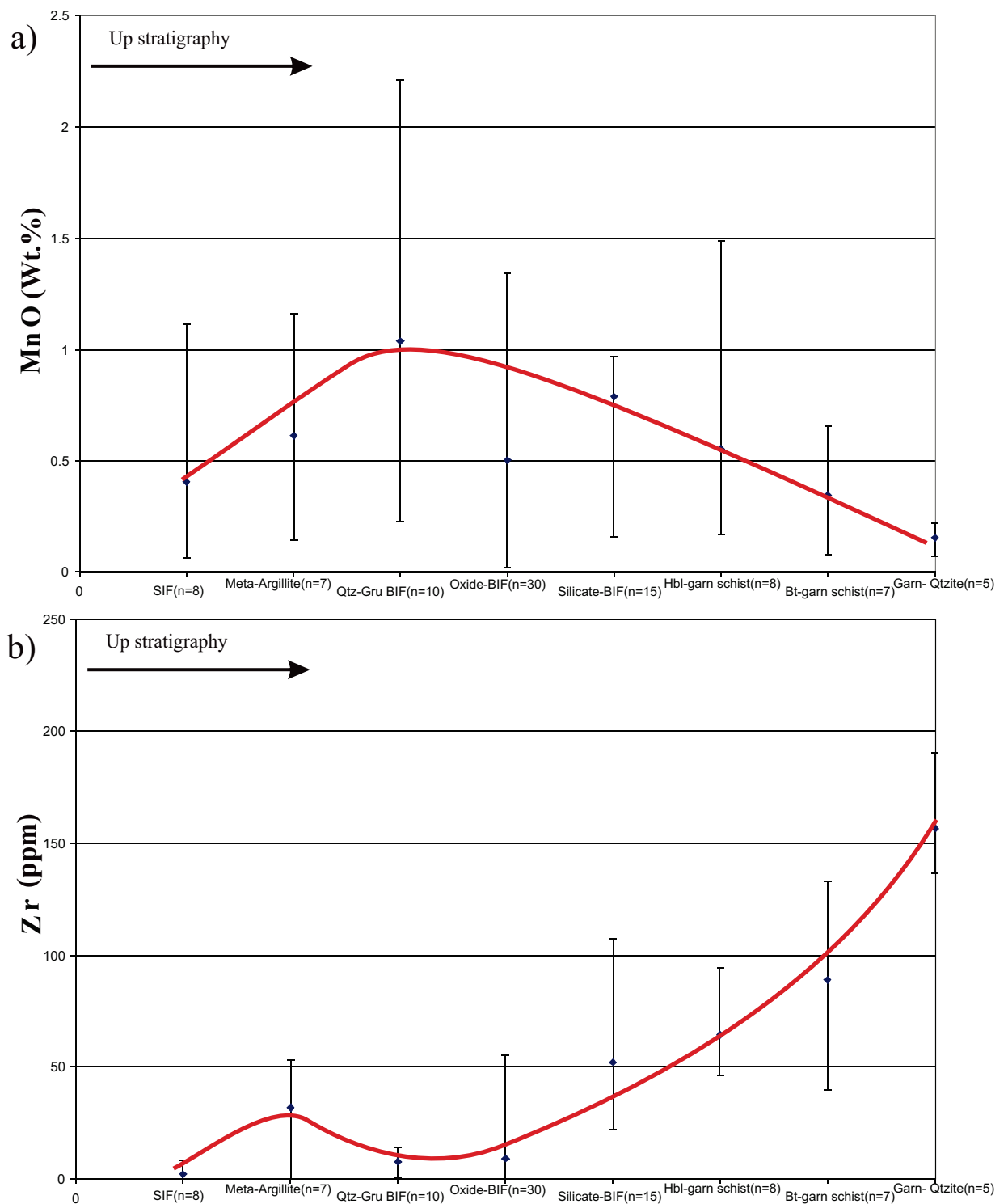
The silicate-dominant BIF contains considerable aluminium, titanium, and iron content relative to the oxide-dominant BIF. As mentioned above the silicate-dominant BIF contains between 20% to 40% siliciclastic material. Again, like in Figure 4.3a and b, the silicate-dominant BIF exhibits more concise geochemistry compared to the oxide-dominant BIF. These two lithologies also slightly overlap geochemically. It should be noted that samples of silicate-dominated BIF were separated into aluminosilicate-dominant bands and quartz-dominant bands with only aluminosilicate-dominant bands sent for analysis. This may be the reason for their similar geochemistry compared to the oxide-dominant BIF (as both quartz and magnetite samples were sent from this lithology). However, there is one anomalous sample of silicate-dominant BIF, which does not plot with the other samples. Instead it contains roughly 50% siliciclastic sediment and overlaps with the hornblende-garnet schist samples.

The hornblende-garnet schist, biotite-garnet schist, and garnet-bearing quartzite contain even higher aluminium, titanium, and iron values compared to the silicate-dominant BIF. These lithologies are at the top of the stratigraphic succession and plot in systematic manner between the mixing lines. As mentioned above the hornblende-garnet schist contains between 40% and 60% siliciclastic material, the biotite-garnet schist contains between 20% to 40% siliciclastic material, and the garnet-bearing quartzite contains >80% siliciclastic material. The biotite-garnet schist and hornblende-garnet schist overlap slightly in terms of geochemistry. However, the garnet-bearing quartzite does not overlap geochemically with any of the other lithologies, instead samples from this lithology plots squarely in the purely clastic, terrigenous sediment field (similar to Pacific Ocean pelagic sediment) with samples containing minimal metalliferous sediment. It should be noted that individual lamina can be analyzed in the future by laser-ablation ICP-MS. This may be a useful way of obtaining the geochemistry of individual layers in the more thinly laminated lithologies.

Samples in Figure 4.4a and 4.4b exhibit similar trends to those observed in the preceding diagrams. There is overlap and clustering of samples, especially among the exhalite-dominated lithologies like the quartz-grunerite BIF, oxide dominant BIF, and Southern iron formation samples. Again, samples and by extension lithologies form a continuum from pure exhalite to pure siliciclastic sediment.

Figure 4.5a is a histogram which depicts the average MnO value (wt. %) for individual lithologies, whereas Figure 4.5b is a histogram which depicts the average Zr value (ppm) for individual lithologies. The lithologies, in both diagrams are organized from stratigraphically lowest on the left to stratigraphically highest on the right.

The reader should note that in the Archean ocean, which was O<sub>2</sub> poor, precipitation was not only governed by hydrothermal input but also availability of O<sub>2</sub> to form oxides. Fe<sup>2+</sup> will come out of solution at lower  $fO_2$  than manganese and thus, it will more effectively scavenge the scarce O<sub>2</sub> compared manganese (Gross, 1996). This will effect the concentration of Mn in the precipitate. Figure 4.6b shows MnO is increasing relative to



**Figure 4.5** a) Binary diagram with lithologies on the x-axis versus MnO (wt.%) on the y-axis. Note average MnO value for each lithology is plotted (symbol represents average value, and bars represent the highest and lowest values measured). Lithologies are organized up stratigraphy from left to right. b) Binary diagram with lithologies on the x-axis versus Zr (ppm) on the y-axis. Note average Zr value for each lithology is plotted (symbol represents average value, and bars represent the highest and lowest values measured). Lithologies are organized up stratigraphy from left to right.

$\text{Fe}_2\text{O}_3^{\text{T}}$  upwards through the lower three units then it rapidly decreases in importance relative to  $\text{Fe}_2\text{O}_3^{\text{T}}$  in the oxide-dominant BIF.

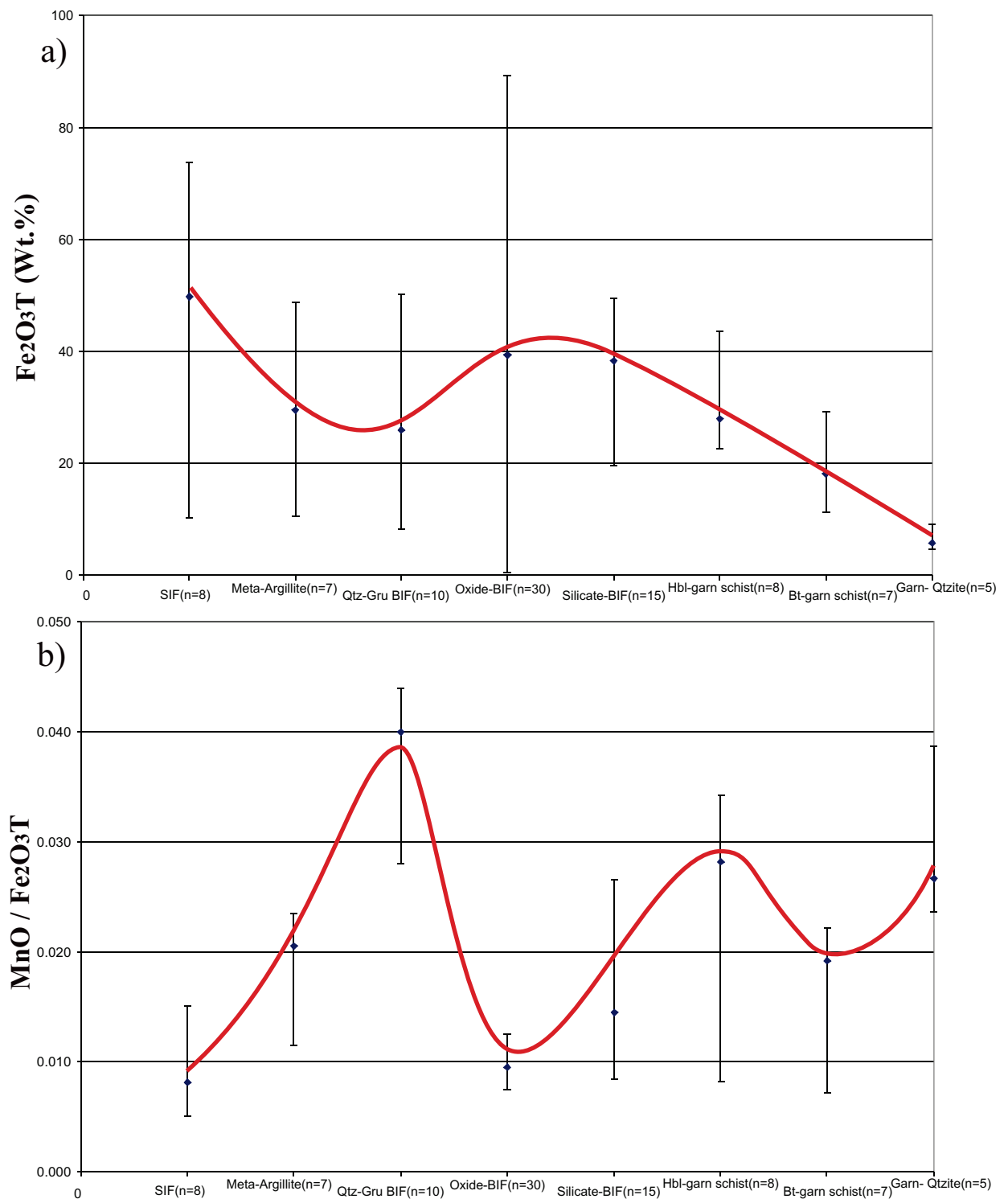
MnO content is one of the best indications of the degree of hydrothermal activity and  $f\text{O}_2$  at the time of deposition. In Figure 4.5a there is an increase in the MnO content stratigraphically upward from the SIF oxide-dominant BIF through to the quartz-grunerite BIF. Therefore, it appears, maximum favourable conditions for the precipitation of manganese peaked during the deposition of the quartz-grunerite BIF, after which, the intensity of hydrothermal activity and/or suitable  $f\text{O}_2$  appears to have steadily declined.

The NIF assemblage oxide-dominant BIF, rather counter-intuitively, has a lower average MnO value compared to the other exhalite-dominant lithologies in Figure 4.5a. Since the NIF assemblage oxide-dominant BIF is typically the thickest unit associated with exhalative activity in the NIF assemblage, and a classic Algoma-type BIF, the MnO values are expected to be higher indicating peak hydrothermal activity. This is especially true since MnO values are higher in the units both above and below the oxide-dominant BIF does not follow the established trend. However, the average iron content in the oxide-dominant BIF is the highest out of all the lithologies (Fig. 4.6a) suggesting conditions were prime for iron precipitation during its deposition. In this situation iron is preferentially scavenged by anions over manganese (Gross, 1996).

The MnO values decrease in a stepwise manner from the silicate-dominant BIF, stratigraphically upward, through to the garnet quartzite. This trend could be an indication of decreasing hydrothermal activity. Likewise this trend could be the result of increasing siliciclastic material, which would dilute both manganese and iron, in the rocks as is indicated in Figure 4.5b.

As mentioned above, Figure 4.5b depicts the average Zr content (ppm) for each lithology. There is a clear trend of increasing zirconium content stratigraphically upward from the Southern Iron Formation upward through the entire Northern Iron Formation Assemblage. The zirconium concentration increases in an almost exponential nature. All lithologies, except the meta-argillite, have higher zirconium content than the lithology directly below them.





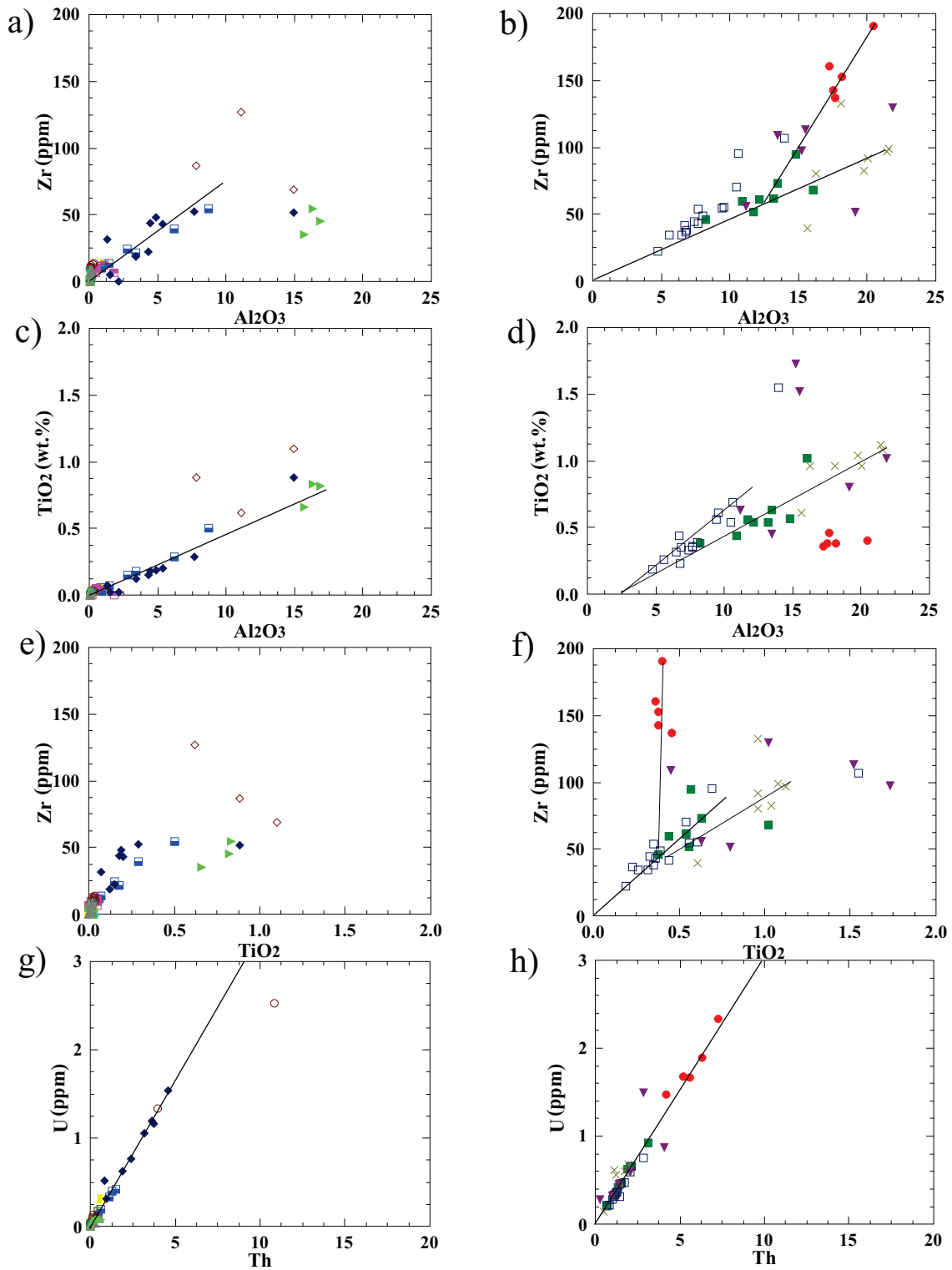
**Figure 4.6** a) Binary diagram with lithologies on the x-axis versus Fe<sub>2</sub>O<sub>3</sub><sup>T</sup> (wt.%) on the y-axis. Note average Fe<sub>2</sub>O<sub>3</sub><sup>T</sup> value for each lithology is plotted (symbol represents average value, and bars represent the highest and lowest values measured). Lithologies are organized up stratigraphy from left to right. b) Binary diagram with lithologies on the x-axis versus MnO/Fe<sub>2</sub>O<sub>3</sub><sup>T</sup> on the y-axis. Note average MnO/Fe<sub>2</sub>O<sub>3</sub><sup>T</sup> value for each lithology is plotted (symbol represents average value, and bars represent the highest and lowest values measured). Lithologies are organized up stratigraphy from left to right.

The meta-argillite is anomalous because it contains a moderate amount of zirconium, which is multiple times greater than the zirconium contents of the surrounding lithologies. The meta-argillite's anomalous nature is visually evident in Figure 4.5b. The moderate concentration of zirconium indicates this lithology contains a siliciclastic component unlike the surrounding lithologies.

Figure 4.6a depicts the average  $\text{Fe}_2\text{O}_3^{\text{T}}$  value (wt. %) for individual lithologies, whereas Figure 4.6b is a histogram that depicts the average ratio between  $\text{MnO}/\text{Fe}_2\text{O}_3^{\text{T}}$  for individual lithologies. The lithologies, in both diagrams are organized from stratigraphically lowest on the left to stratigraphically highest on the right.

Trends in these diagrams are not as well developed as in Figures 4.5a and 4.5b. However, the broad trend observable in Figure 4.6a is of decreasing  $\text{Fe}_2\text{O}_3^{\text{T}}$  in the lower three lithologies, high  $\text{Fe}_2\text{O}_3^{\text{T}}$  in the oxide- and silicate-dominant BIFs, and both high and low  $\text{Fe}_2\text{O}_3^{\text{T}}$  in the upper three lithologies. The broad trend observable in Figure 4.6b is of increasing MnO relative to  $\text{Fe}_2\text{O}_3^{\text{T}}$  concentration in the lower three lithologies, low  $\text{MnO}/\text{Fe}_2\text{O}_3^{\text{T}}$  concentration in the oxide- and silicate-dominant BIFs, and higher  $\text{MnO}/\text{Fe}_2\text{O}_3^{\text{T}}$  in the upper three lithologies.

Figure 4.7 is composed of multiple diagrams all of which are designed to infer the basic sedimentary composition of the various lithologies. Figure 4.7a and b are binary diagrams of Zr vs.  $\text{Al}_2\text{O}_3$ . Figure 4.7c and d are binary diagrams of  $\text{TiO}_2$  vs.  $\text{Al}_2\text{O}_3$ . Figure 4.7e and f are binary diagrams of Zr vs.  $\text{TiO}_2$ . These diagrams serve a twofold purpose: 1) to establish the immobile nature of these elements (Fralick, 2003) and 2) to further examine the clastic detrital content of the lithologies. The logic of these plots is that if both elements were chemically immobile and contained in mineral phases that behaved in hydrodynamically similar ways during transport a linear trend should exist between combinations of  $\text{Al}_2\text{O}_3$ , Zr, and  $\text{TiO}_2$  (Fralick, 2003). Increases in either element will result in equal increase in the opposing element.



**Figure 4.7** Note that the symbols are the same as in Fig. 4.3. a) Al<sub>2</sub>O<sub>3</sub> vs. Zr plot, exhalite-dominated lithologies, b) Al<sub>2</sub>O<sub>3</sub> vs. Zr plot, siliciclastic-dominated lithologies, c) Al<sub>2</sub>O<sub>3</sub> vs. TiO<sub>2</sub> plot, exhalite-dominated lithologies, d) Al<sub>2</sub>O<sub>3</sub> vs. TiO<sub>2</sub> plot, siliciclastic-dominated lithologies, e) Zr vs. TiO<sub>2</sub> plot, exhalite-dominated lithologies, f) Zr vs. TiO<sub>2</sub> plot, siliciclastic-dominated lithologies, g) U vs. Th plot, exhalite-dominated lithologies, h) U vs. Th plot, siliciclastic-dominated lithologies. Note that trend-lines are drawn based on visually observed linear trends.

Aluminum is primarily contained in sheet silicate minerals, which are the end product of weathered rock. Zirconium is primarily found in zircons, which by and large are eroded from a felsic source. Titanium is found in titanomagnetite and titanite. All of the aforementioned minerals are resilient enough to survive the erosion process so they are concentrated in detrital siliciclastic sedimentary material.

The plots in Figure 4.7 build on similar trends observed in Figures 4.3 and 4.4. The lithologies are again broken up into the same groups as in the previous figures. Figure 4.7a, c, e, and g contain the exhalite-dominated lithologies (n=68), whereas Figures 4.7b, d, f, and h contains siliciclastic-dominated lithologies (n=41). Note that positive trends are observable in all diagrams.

In general the exhalite-dominant lithologies contain low concentrations of the elements normally associated with siliciclastic sediment such as  $Al_2O_3$ ,  $TiO_2$ , and Zr. Samples from these lithologies therefore tend to cluster close to the origin. However, it should be noted, that there is overlap between exhalite- and siliciclastic-dominant lithologies in terms of concentration of these elements; specifically between the meta-argillite, the NIF assemblage oxide-dominant BIF, and the silicate-dominant BIF.

Figure 4.7a, c, e, and g contains the SIF and NIF oxide-dominant BIF, quartz-grunerite BIF, metargillite, meta-sediment (trench), and chlorite schist samples. These samples form a coherent positive linear trend in Figures 4.7a, c, and f. The slopes of the linear trend-lines are comparable to those formed by the siliciclastic-dominant samples, which are described below.

Most of the exhalite-dominant samples plot close to the origin on these diagrams, including samples of the SIF oxide-dominant BIF, quartz-grunerite BIF, and NIF assemblage quartz- and magnetite-dominant bands. However, four NIF assemblage oxide-dominant BIF magnetite samples, and all the meta-argillite samples, plot away from the origin and form a linear trend-line.

Five magnetite samples, from the NIF assemblage oxide-dominant BIF, form a clear positive linear trend between aluminium to zirconium in Figure 4.7a. This supports the concept of a minor siliciclastic component in this lithology. Similarly, in this figure, there

is a slightly scattered relationship between aluminium and zirconium in the meta-argillite samples. It should be noted that in Figure 4.7a samples of the trench, meta-sediment and chlorite schist have high values of zirconium and aluminum, but do not form coherent trends. A more coherent linear trend is formed by the magnetite and meta-argillite samples when  $\text{Al}_2\text{O}_3$  is plotted against  $\text{TiO}_2$  (Fig. 4.7b), as well as when Th is plotted against U (Fig. 4.7g).

In general samples of the meta-argillite have anomalous concentrations of  $\text{Al}_2\text{O}_3$ ,  $\text{TiO}_2$ , Zr, Th, and U relative to the other exhalite-dominated lithologies. The higher concentration of these elements suggests the meta-argillite contains a significant siliciclastic component. The fact that this lithology has a siliciclastic component makes it unique as it is found at the base of the NIF assemblage. However, when compared to the majority of the siliciclastic-dominated samples, it has slightly lower  $\text{Al}_2\text{O}_3$  and  $\text{TiO}_2$  relative to the siliciclastic-dominant lithologies.

Samples from the silicate-dominant lithologies exhibit slightly more variation in the concentration of the respective elements compared to samples from the exhalite-dominated lithologies. There are two distinct trends observable in Figures 4.7b, d, and f; 1) the aluminosilicate bands from the silicate-dominant BIF exhibit the most consistent trend of all the lithologies and 2) the garnet-bearing quartzite does not plot along the same trend as the other siliciclastic-dominated lithologies. Regardless of this, samples of the garnet-bearing quartzite do cluster together and form coherent linear trends. This lithology likely has a different source than the other three siliciclastic-dominated lithologies.

As stated in the previous paragraph, the immobile elements maintain concise positive linear ratios across all silicate-dominant BIF samples. This is counterintuitive to the expected scattered trend, as the silicate-dominant BIF is host to gold at Musselwhite and presumably would be the most altered rock. The concise trend indicates any metasomatic alteration associated with the mineralizing event did probably did not differently mobilize  $\text{Al}_2\text{O}_3$ ,  $\text{TiO}_2$ , Zr, Th, or U.

The stratigraphically overlying hornblende-garnet schist geochemically overlaps with, and delineates the same linear trend as, the silicate-dominant BIF. However, the trends are not as concise as those in the silicate-dominant BIF as hornblende-garnet schist samples exhibit more scatter than the previously discussed lithology. It is also not surprising that these lithologies share similar trends since the hornblende-garnet schist is intercalated within the silicate-dominant BIF. Relative to the silicate-dominant BIF, the hornblende-garnet schist contains higher  $\text{Al}_2\text{O}_3$  and comparable  $\text{TiO}_2$ , and Zr values.

There is one somewhat anomalous sample of hornblende-garnet schist (sample: 4e-07-20-019), which tends to overlap with silicate-dominated BIF sample (sample: 4ea-08-20-002, ore-zone) in Figures 4.7b, d, and f. This sample exhibits the same geochemical overlap in Figure 4.3b. Similar trends are manifested in other elements and are discussed further on in this chapter. It should also be noted that there is some geochemical overlap between the hornblende-garnet schist and the biotite-garnet schist. This relationship is not completely unexpected since the hornblende-garnet schist is found as intercalated bands within the biotite-garnet schist.

Samples of the biotite-garnet schist plot in a disperse pattern, relative to the other siliciclastic-dominant lithologies, which delineates a weaker linear trend compared to underlying silicate-dominant BIF and the hornblende-garnet schist. However, this weak linear trend is inline with the stronger linear trend formed by samples from the other lithologies. Overall the biotite-garnet schist has higher  $\text{TiO}_2$  and  $\text{Al}_2\text{O}_3$  values, and comparable Zr values to the previously discussed lithologies.

There are two anomalous samples of biotite-garnet schist, 4f-07-20-001 and 4f-PM05-052, which do not group with the other samples in Figures 4.7b, d, f. These anomalous samples also plot off the trend-line established by the other samples, which may be a result of metasomatic alteration.

Additionally there is one anomalous sample of biotite-garnet schist that plots, on Figure 4.7b, with samples of the garnet-bearing quartzite (sample: 4f-07-20-001 plots next to garnet-bearing quartzite sample 6-07-20-058). The garnet-bearing quartzite is found as minor laminations and beds within the biotite-garnet schist. These two lithologies are

commonly in gradational contact. So it is no surprise that there is some geochemical overlap between these two lithologies.

Samples of the garnet-bearing quartzite are significantly geochemically different from other lithologies in the NIF assemblage. They tend to plot as a concise group away from samples of other lithologies. This group does not fall on the positive linear trend delineated by the other lithologies.

Al<sub>2</sub>O<sub>3</sub> values in the garnet-bearing quartzite are comparable to the biotite-garnet schist: both lithologies have the highest Al<sub>2</sub>O<sub>3</sub> values out of all the lithologies analyzed. Samples of the garnet-bearing quartzite also have the highest zirconium values out of all the lithologies. The garnet-bearing quartzite samples, rather enigmatically, have comparatively low TiO<sub>2</sub> values relative to the high Al<sub>2</sub>O<sub>3</sub> and Zr values.

Based on its geologic nature, universally similar sample chemistry, and relationship with the other siliciclastic-dominant metasediments, the garnet-bearing quartzite is probably a metamorphosed volcanoclastic felsic ash layer. This topic will be discussed in further detail in Chapter Five.

Nesbitt and Young (1982) introduced the concept of ‘Chemical Index of Alteration’ (CIA), which is used as a tool for quantifying the degree of weathering sediment has undergone relative to the parent/source rock. CIA is equal to:

$$\text{CIA} = [\text{Al}_2\text{O}_3 / (\text{Al}_2\text{O}_3 + \text{CaO}^* + \text{Na}_2\text{O} + \text{K}_2\text{O})] \times 100$$

CaO\* = CaO in silicate minerals

The formula for deducing CIA is based around the breakdown (weathering) of feldspars, which compose the majority (62%) of the earth’s crust and therefore make up the bulk of material weathered (Nesbitt and Young, 1982). Feldspars primarily weather to illite clay (Deer *et al.*, 1992). The breakdown of the feldspar crystal structure releases K, Na, and Ca to solution (Nesbitt *et al.*, 1980). By comparing these elements to aluminium, an element that does not enter solution easily, the strength of weathering can be inferred. It should also be noted that mafic minerals such as olivine, pyroxene, biotite, amphibole, and opaques weather to smectite-vermiculite type clay minerals.

The large ternary diagrams, in Figure 4.8a and 4.8b, depict the molecular proportions of  $\text{Al}_2\text{O}_3$ – $(\text{Na}_2\text{O}+\text{CaO})$ – $\text{K}_2\text{O}$  and are designed to portray CIA trends (modified after Gu *et al.*, 2002). In addition to visually portraying the degree of CIA, the diagram shows the possible original composition of the siliciclastic sedimentary protolith to the samples: note the smectite and illite fields.

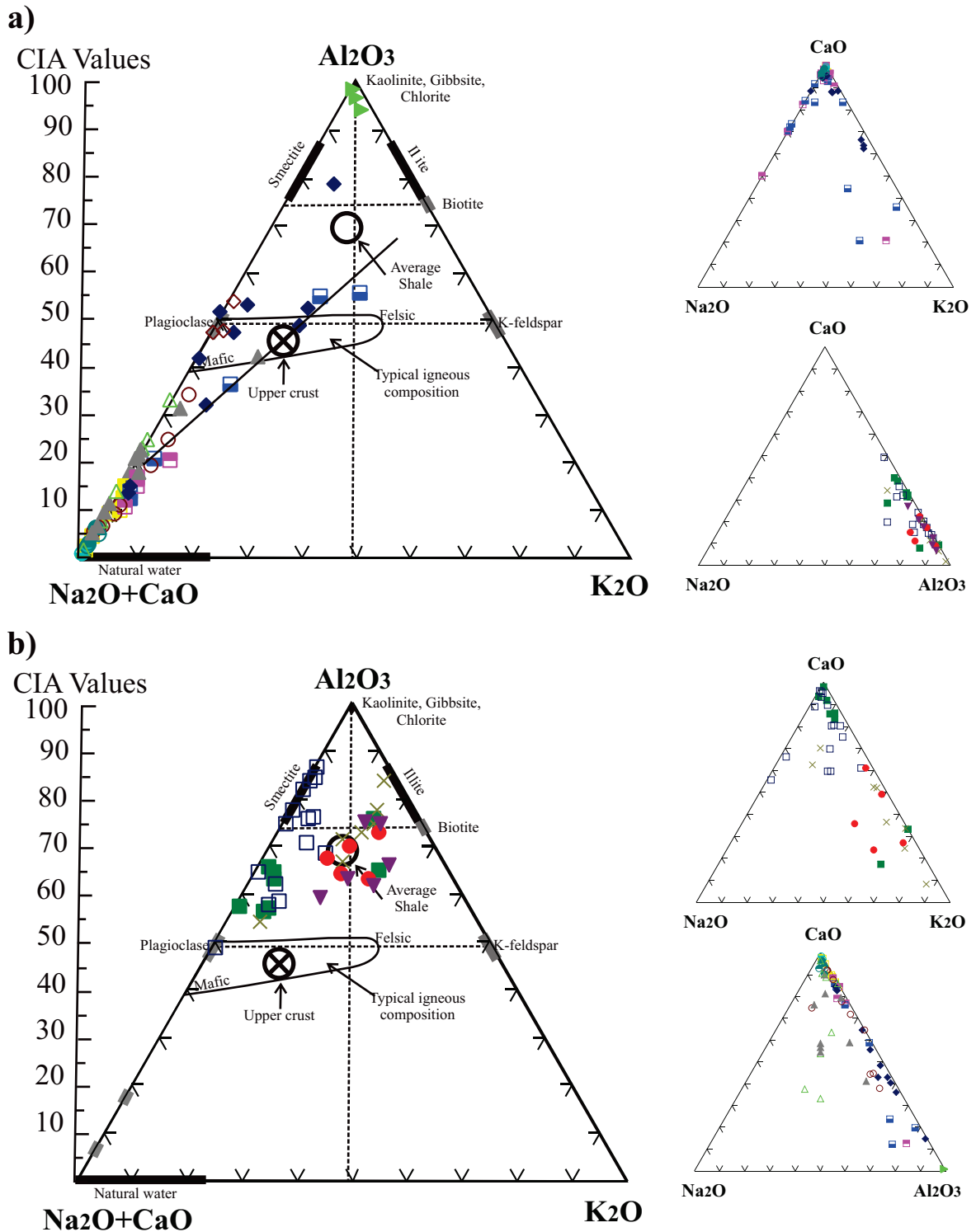
The four smaller ternary diagrams are included in Figure 4.8 to demonstrate the relative concentrations of the elements to one another. These diagrams indicate that the majority of the exhalite- and siliciclastic-dominated lithologies do not contain significant  $\text{Na}_2\text{O}$  compared to their  $\text{CaO}$  and  $\text{K}_2\text{O}$  content. This relationship is not unusual as potassium is commonly retained during sub-aerial chemical weathering whereas sodium is leached (Nesbitt *et al.*, 1980). The high  $\text{K}_2\text{O}/\text{Na}_2\text{O}$  ratios of samples from all lithologies may also be the result of preferential decomposition of plagioclase over potassium-feldspar during weathering of source rocks (Gu *et al.*, 2002).

Figure 4.8a contains the exhalite dominant lithologies. These lithologies contain high  $\text{CaO}$  values relative to  $\text{Al}_2\text{O}_3$ ,  $\text{K}_2\text{O}$ , and  $\text{Na}_2\text{O}$  values, even higher than what is seen in the siliciclastic-dominated lithologies. The  $\text{CaO}$  in these samples is likely contained in carbonate minerals, which are observed in thin-section samples of these lithologies. It should be noted that particular attention was paid to selecting samples that did not contain secondary (vein) carbonate material.

An interesting feature observed in Figure 4.8a is the well developed trend-line delineated by several NIF assemblage oxide-dominant BIF (magnetite) and meta-argillite samples. This trend is interesting because it is in line with the biotite field suggesting the trend is a result of the biotite content in these samples. Another interesting trend in Figure 4.8a is a cluster of meta-argillite samples around the plagioclase field indicating that these samples originally contained un-weathered plagioclase as opposed to clay minerals.

The chlorite schist (described in section 3.10) lithology exhibits an anomalous trend relative to other exhalite-dominant lithologies. These samples do plot in the “Kaolinite, Gibbsite, and Chlorite”





**Figure 4.8.** Larger ternary discrimination diagram, used to determine original loose sediment material, is based on the relative molecular proportions of  $Al_2O_3$ - $Na_2O$ - $CaO$ - $K_2O$ . Note that the symbols are the same as in Fig. 4.3. Fields are from Gu et al. (2002). Hornblende and clinopyroxene are idealized compositions from Taylor and McLennan (1985). Smaller inset  $CaO$ - $Na_2O$ - $K_2O$  and  $CaO$ - $Na_2O$ - $Al_2O_3$  ternary diagrams show the relative concentrations of these elements, a) Samples from exhalite-rich lithologies, b) Samples from siliciclastic-rich lithologies.

field. Samples contain very high  $\text{Al}_2\text{O}_3$  values, which are much greater than even the siliciclastic-dominated lithologies. This lithology is likely a product of metasomatic alteration. The topic of alteration is discussed further on in this chapter as well as expanded upon in Chapter Five.

Figure 4.8b contains samples of the siliciclastic-dominated lithologies. Samples from these lithologies plot in the upper half of the diagram as opposed to exhalite-dominated lithologies whose samples plot mostly in the lower half of the diagram (Fig. 4.8a). Samples of the various lithologies form a loose trend from the plagioclase field to the illite and smectite fields. This indicates the original siliciclastic sedimentary material was composed of a combination of plagioclase, illite, and smectite clays. The ratio of original components depends on how close individual samples plot to the end-member fields.

In Figure 4.8b samples of the silicate-dominant BIF form a concise trend with the majority of samples plotting in the smectite field. This trend is unique to the silicate-dominant BIF; however, the other lithologies may have contained a relatively minor smectite component. Note that smectite is the end product of weathered volcanic glass and can also be formed from the breakdown of Ca- and/or Na-rich silicate minerals (Neuendorf *et al.*, 2005). It should be noted that because the silicate-dominant BIF was composed of smectite clay it has the highest CIA of all the lithologies sampled (other than the chlorite schist).

There is overlap between samples of silicate-dominant BIF and hornblende-garnet schist. The hornblende-garnet schist, as well as several silicate-dominant BIF, samples form a relatively concise group which plots roughly halfway between the plagioclase / mafic volcanic field and the smectite field. This is an indication that the original sedimentary material was a combination of poorly weathered mafic volcanic material, plagioclase, and smectite clay.

The biotite-garnet schist samples plot close to the average shale field (CIA of 70-75, Taylor and McLennan 1985). This indicates these samples resulted from moderate

weathering (CIA between 54-79; Gu *et al.*, 2002) probably of a combination of mafic and felsic material. It should be noted that clay minerals produced from moderate weathering still retain alkali and alkaline earth elements as opposed to removal of these elements in more deeply weathered clays (Taylor and McLennan, 1985).

#### 4.4 Environment of Deposition

A good deal of academic work has previously been conducted on the area regarding tectonic setting. Hollings and Kerrich (1998) completed a study on the metavolcanic rocks closest to the Musselwhite gold deposit, specifically: the Opapimiskan metavolcanic assemblage (OMV) and the South Rim metavolcanic assemblage (SRMV) (Fig. 1.3). They conclude that the mafic and ultramafic rocks of the OMV were produced by a mantle plume erupting through the proto-continental Superior Province. During ascent the komatiitic plume melt assimilated continental crust (TTG type material). However, they draw a slightly different conclusion about the origins of the directly overlying SRMV. The rocks of the SRMV are also plume related but they do not have a crustally-contaminated signature, instead they possess similar trace-element patterns to modern ocean plateaus. Additionally, Hollings and Kerrich (1998) suggest that the two metavolcanic assemblages were deposited as an oceanic plateau due to the intercalated nature of the volcanic rocks with banded iron formation, as well as the general lack of arc-related volcanism.

The genetic relationship between the two assemblages is a product of plume dynamics with the komatiite- and tholeiite-rich OMV representing melting associated with the ascent of the plume head. Hollings and Kerrich (1998) postulate that the same volcanic plumbing system was supplying both the OMV and SRMV; however, in order to deposit the OMV the ascending plume had to melt and assimilate continental crust. By the time the SRMV was deposited a well developed and open plumbing system was in place so ascending magma passed through at an accelerated rate and therefore did not assimilate crustal material.

Hollings and Kerrich (1998) suggest that the North Caribou Lake Belt (NCLB) is more comparable to the Yilgarn Block than to the greenstone belts in the southern Superior Province. This is due to the fact that mafic and ultramafic rocks of the Yilgarn block display crustally contaminated signatures and are known to have erupted through continental crust (Barley, 1986; Sun *et al.*, 1989), whereas the southern Superior greenstone belts formed in intra-oceanic tectonic settings (c.f., Jochum *et al.*, 1991; Desrochers *et al.*, 1993; Xie *et al.*, 1995).

One of the main objectives of the present study, as stated in Section 1.2 (p. 6), was to determine the environment of deposition of the lithologies at Musselwhite Mine. The simplest route to establishing the tectonic setting is to dissect the geochemistry of the volcanic lithologies from Musselwhite. Unfortunately only a small number of igneous samples were collected during the present study. However, the exploration department at Musselwhite generously provided geochemical data for 197 mafic volcanic samples and 51 intermediate volcanic samples (John Biczok, personal communication, 2007).

An equally valid, but slightly more complex, route to establishing the tectonic setting is to examine the geochemistry of the metasedimentary lithologies. This is the most viable option since the focus of the present study is on the meta-sedimentary lithologies from Musselwhite. The geochemistry of the meta-sediments in terms of tectonic setting will be expanded upon in Chapter Five.

Section 4.4 begins with an examination of geochemistry of the volcanic samples provided by the Musselwhite exploration department. The reader should note that these samples were not analyzed for a full spread of elements.

In Figures 4.9, 4.10 and 4.11 the volcanic samples are plotted on plots a, c, e, and g, whereas the siliciclastic-dominant samples are plotted on plots b, d, f, and h for comparative purposes. The author fully realizes these diagrams are designed for volcanic rocks and would like to stress that sedimentary samples are plotted for comparison to possible parental material. Note that the mafic volcanic samples are represented as green

diamonds and the intermediate volcanic samples are represented as grey diamonds. The symbols for the siliciclastic-dominant sedimentary samples are the same as in previous diagrams (legend is displayed in Figure 4.3).

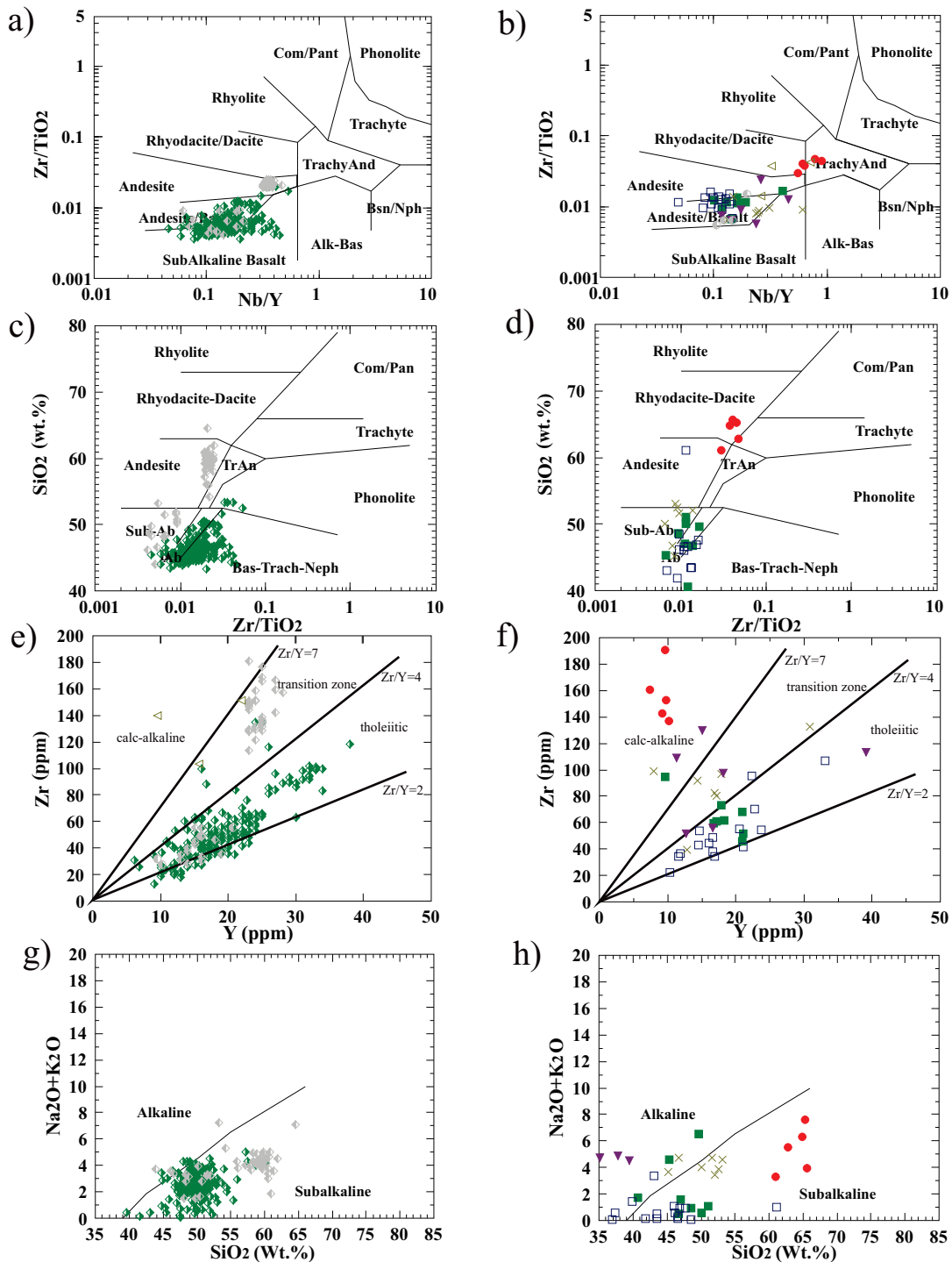
Figures 4.9a and 4.9b consist of the same Nb/Y versus  $\text{TiO}_2$  igneous discrimination diagram used to differentiate between intermediate to felsic volcanic rocks. Figure 4.9a indicates the majority of mafic volcanic samples plot in the andesite/basalt field with a smaller number plotting in the sub-alkaline basalt field. The mafic samples probably exhibit scatter for several reasons, namely, the samples were collected from different stratigraphic levels out of a thick volcanic sequence.

On the other hand, the intermediate samples plot in a concise group within the andesite field, close to the rhyodacite/dacite field as opposed to basalt field. These samples do not exhibit scatter possibly because the intermediate volcanic flows are confined to a limited interval in the upper levels of the stratigraphic succession.

The siliciclastic metasedimentary samples, in Figure 4.9b, geochemically overlap with the volcanic samples in Figure 4.9a suggesting there is an evolutionary link between the two. However, the garnet-bearing quartzite is the only lithology which plots in the trachyandesite field. None of the volcanic samples plot within this field.

Samples of the garnet-bearing quartzite plot in the trachyandesite field due to their relatively high Nb content. It should be noted that the high Nb values coincides with high  $\text{K}_2\text{O}$  in this lithology. This suggests the garnet-bearing quartzite was possibly derived from an alkalic lithology as opposed to potassium-enriched altered material.

Figures 4.9c and 4.9d consist of the same Zr/ $\text{TiO}_2$  versus  $\text{SiO}_2$  igneous discrimination diagram used to differentiate between intermediate to felsic volcanic rocks. For the most part, samples and lithologies exhibit the same patterns seen in Figures 4.9a and 4.9b.



**Figure 4.9** Binary discrimination diagrams containing the mafic and intermediate volcanic samples. Note that green-diamonds are mafic samples and grey-diamonds are intermediate samples (Figs 4.9b, d, f, and h: symbols are the same as in Fig. 4.3). Siliciclastic-dominant samples from the current study are plotted on separate diagrams for comparative purposes. a) Nb/Y vs. Zr/TiO<sub>2</sub> for volcanic samples (Winchester and Floyd), b) Nb/Y vs. Zr/TiO<sub>2</sub> for metasediment samples (Winchester and Floyd), c) Zr/TiO<sub>2</sub> vs. SiO<sub>2</sub> for volcanic samples (Winchester and Floyd), d) Zr/TiO<sub>2</sub> vs. SiO<sub>2</sub> for metasediment samples (Winchester and Floyd), e) Y vs. Zr for volcanic samples (McLean), f) Y vs. Zr for metasediment samples, modified after Shervais (1982), g) SiO<sub>2</sub> vs. Na<sub>2</sub>O+K<sub>2</sub>O for volcanic samples (Irvine and Baragar, 1971), h) SiO<sub>2</sub> vs. Na<sub>2</sub>O+K<sub>2</sub>O for siliciclastic samples (Irvine and Baragar, 1971).

Figure 4.9c indicates the majority of mafic volcanic samples plot in the basalt field and the intermediate samples again plot in a concise group within the andesite field. However, in this diagram they plot close to the trachyandesite field as opposed to rhyodacite-dacite field. The intermediate samples exhibit slightly more scatter in this diagram compared to what is seen in Figure 4.9a. These samples possibly exhibit scatter because of quartz veining.

For the most part the siliciclastic samples in Figure 4.9d, excluding the garnet-bearing quartzite, overlap with the range of the volcanic samples in Figure 4.9c. This is the same trend as observed in Figure 4.9b. Unlike in Figure 4.9b, where the garnet-bearing quartzite plots in the trachyandesite field, the garnet-bearing quartzite plots in the rhyodacite-dacite field in Figure 4.9d. The garnet-quartzite may plot in this field due to higher zircon content. Hydraulic sorting of zircon, during the transportation of volcanoclastic sediment, concentrates zircon crystals in the final sediment. Therefore, it is possible the garnet-quartzite actually represents ash deposits from distal felsic eruptions. Note that Figure 4.9a and 4.9b are based on immobile elements they provides a more accurate assessment of the lithologies than Figure 4.9c and 4.9d.

Figures 4.9e and 4.9f are the same diagram, consisting of the immobile elements Y versus Zr, designed to reveal the chemical affinity of intermediate to felsic volcanic rocks. Figure 4.9e indicates that the majority of the mafic volcanic samples have tholeiitic affinity and the intermediate metavolcanic samples are transitional to calc-alkaline chemical affinity.

The siliciclastic samples, plotted on Figure 4.9f, geochemically overlap with the volcanic samples plotted on Figure 4.9e. More specifically, the silicate-dominant BIF and hornblende-garnet schist primarily plot in the tholeiitic field. The biotite-garnet schist samples primarily plot in the transitional field and the garnet-bearing quartzite samples plot in the calc-alkaline field. This is not surprising since it is theorized, by the author, the siliciclastic material composing the silicate-dominant BIF and the hornblende-garnet schist came from eroded mafic igneous rock. Likewise the siliciclastic material composing the biotite-garnet schist is theorized to have come from eroded intermediate igneous rock.

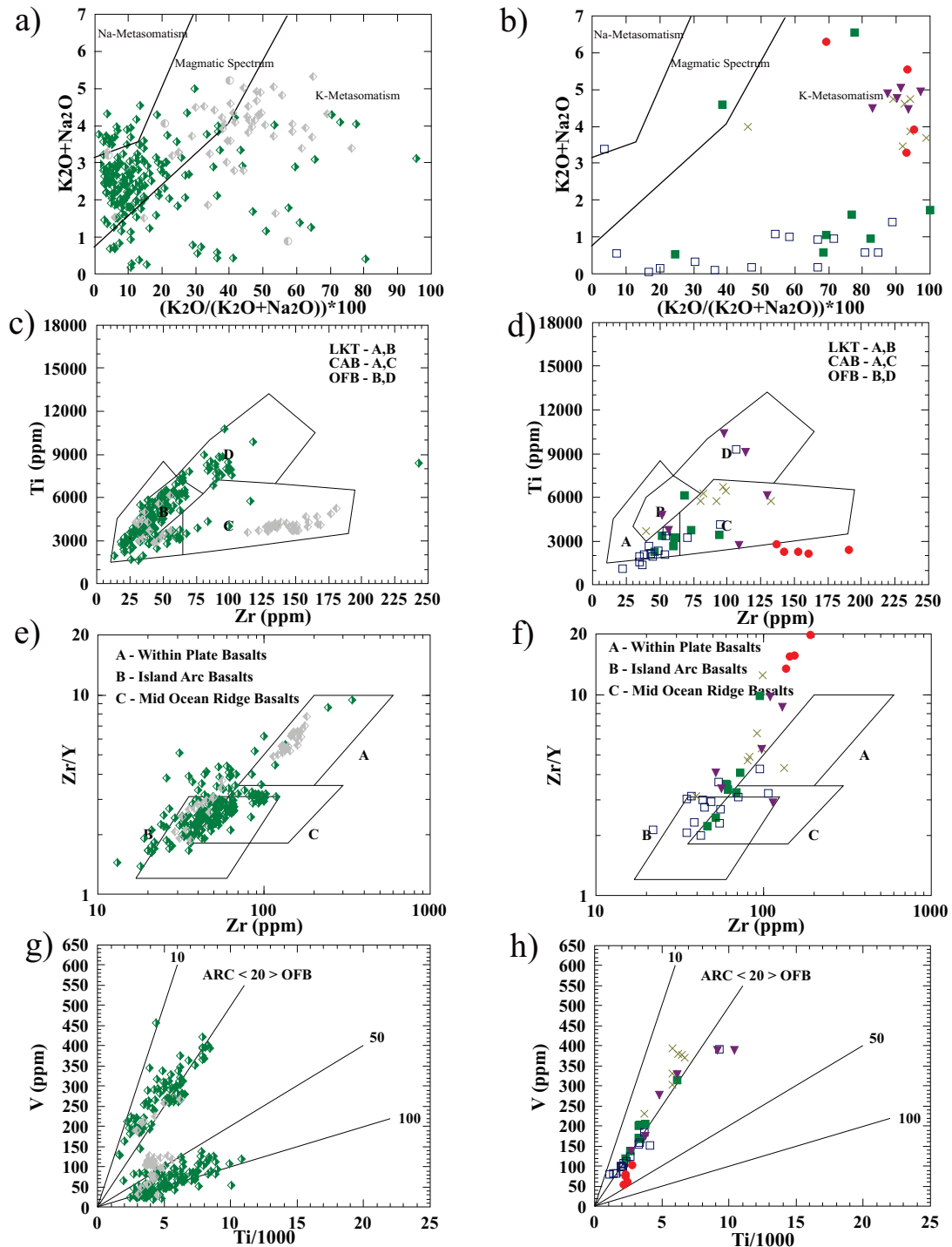
Figures 4.9g and 4.9h are the same diagram, consisting of the mobile elements  $\text{SiO}_2$  versus  $\text{Na}_2\text{O}+\text{K}_2\text{O}$ , designed to elucidate the chemical affinity of volcanic rocks. The diagram is divided into two fields (alkaline and subalkaline) separated by a single inclined line. Both the mafic and intermediate metavolcanic samples in Figure 4.9g plot in the subalkaline field. Not surprisingly the mafic samples plot in a similar pattern to what is observed in Figures 4.9a-d. However, samples of the siliciclastic lithologies (Fig. 4.9h) exhibit a general depletion of the respective elements compared to the volcanic lithologies. The garnet-bearing quartzite is a notable exception as it contains high  $\text{SiO}_2$  and  $\text{Na}_2\text{O}+\text{K}_2\text{O}$  relative to the other samples.

Figures 4.10a and 4.10b consist of the same  $(\text{K}_2\text{O}/(\text{K}_2\text{O}+\text{Na}_2\text{O}))\cdot 100$  versus  $\text{K}_2\text{O}+\text{Na}_2\text{O}$  diagram. This diagram is designed to reveal whether mafic volcanic samples experienced sodium and/or potassium metasomatism (note that these diagrams are designed for mafic volcanic rocks; intermediate volcanic and sedimentary samples have been plotted for comparative purposes). The diagram is based on the premise that during prograde metamorphism, potassium is leached from potassium-feldspar and sodium is precipitated as albite, whereas during retrograde metamorphism sodium is replaced by potassium (Ellis, 1979). Note that intermediate volcanic rocks naturally contain more  $\text{K}_2\text{O}$  than mafic rocks. Therefore the intermediate volcanic samples are plotted on Figure 4.10a simply for comparison to the siliciclastic samples.

The majority of the mafic samples in Figure 4.10a plot within the normal magmatic spectrum indicating these samples did not experience potassium or sodium metasomatism. However, a considerable number of samples appear to be sodium or potassium metasomatised. Potassium metasomatism dominates over sodium metasomatism.

The siliciclastic samples form two, disperse, groups in Figure 4.10b. The first group consists of the silicate-dominant BIF and the hornblende-garnet schist. Both lithologies exhibit a reduction in  $\text{K}_2\text{O}$  and  $\text{Na}_2\text{O}$  relative to the mafic and intermediate volcanic material. It should be noted that the silicate-dominant BIF and hornblende-garnet schist are mixed with chemical sediment which dilutes the sodium and potassium content. This makes it difficult to compare the absolute amounts of these elements with the igneous





**Figure 4.10. Binary discrimination diagrams containing the mafic and intermediate volcanic samples. Note that green-diamonds are mafic samples and grey-diamonds are intermediate samples (Figs 4.10b, d, f, and h: symbols are the same as in Fig. 4.3). Intermediate volcanic and siliciclastic-dominant samples are plotted for comparative purposes. a)  $(K_2O/(K_2O+Na_2O)) * 100$  vs.  $K_2O+Na_2O$  for volcanic samples (Huges, 1971), b)  $(K_2O/(K_2O+Na_2O)) * 100$  vs.  $K_2O+Na_2O$  for siliciclastic samples (Huges, 1971), c) Zr vs. Ti for volcanic samples (Pearce and Cann, 1973), d), Zr vs. Ti for siliciclastic samples (Pearce and Cann, 1973), e) Zr vs. Zr/Y for volcanic samples, f) Zr vs. Zr/Y for siliciclastic samples, g) Ti/1000 vs. V for Musselwhite igneous samples (Shervais, 1982), h) Ti/1000 vs. V for metasediment samples (Shervais, 1982).**

rocks. The second group consists of the biotite-garnet schist and the garnet-bearing quartzite. These lithologies do not exhibit a change in the amount of  $K_2O$ , but they do display a loss in  $Na_2O$  relative to the intermediate volcanic material.

Figures 4.10c and 4.10d consist of a zirconium versus titanium binary plot. This is a tectonic setting discrimination diagram where polygons A and B represent low potassium tholeiites (LKT), polygons A and C represent continental arc basalt (CAB), and polygons B and D represent ocean floor basalt (OFB).

Most mafic volcanic samples plot in the low potassium tholeiite (LKT) and ocean floor basalt (OFB) polygons in Figure 4.10c. The mafic volcanic samples form two linear trends in Figure 4.10c. The majority of mafic samples form a loose linear trend from LKT to OFB. A second less pronounced trend, formed from a subset of mafic samples, is the linear evolution from LKT to CAB. Additionally there is a small, but distinct, group of mafic samples in 'polygon D' (OFB). Note that the intermediate samples are simply included on this diagram for comparison purposes. However these samples also form a linear trend and plot in the continental arc basalt (CAB) polygon.

Samples of the siliciclastic-dominated lithologies, in Figure 4.10d, form a less concise trend relative to the volcanic lithologies. However, they do geochemically overlap with the smaller group of mafic volcanic samples which form a linear trend from LKT to CAB in Figure 4.10d. Again the garnet-bearing quartzite exhibits the least similarity to the volcanic samples as it does not even plot within a polygon. The garnet-bearing quartzite samples have comparable Zr content, but lower Ti than the intermediate volcanic samples.

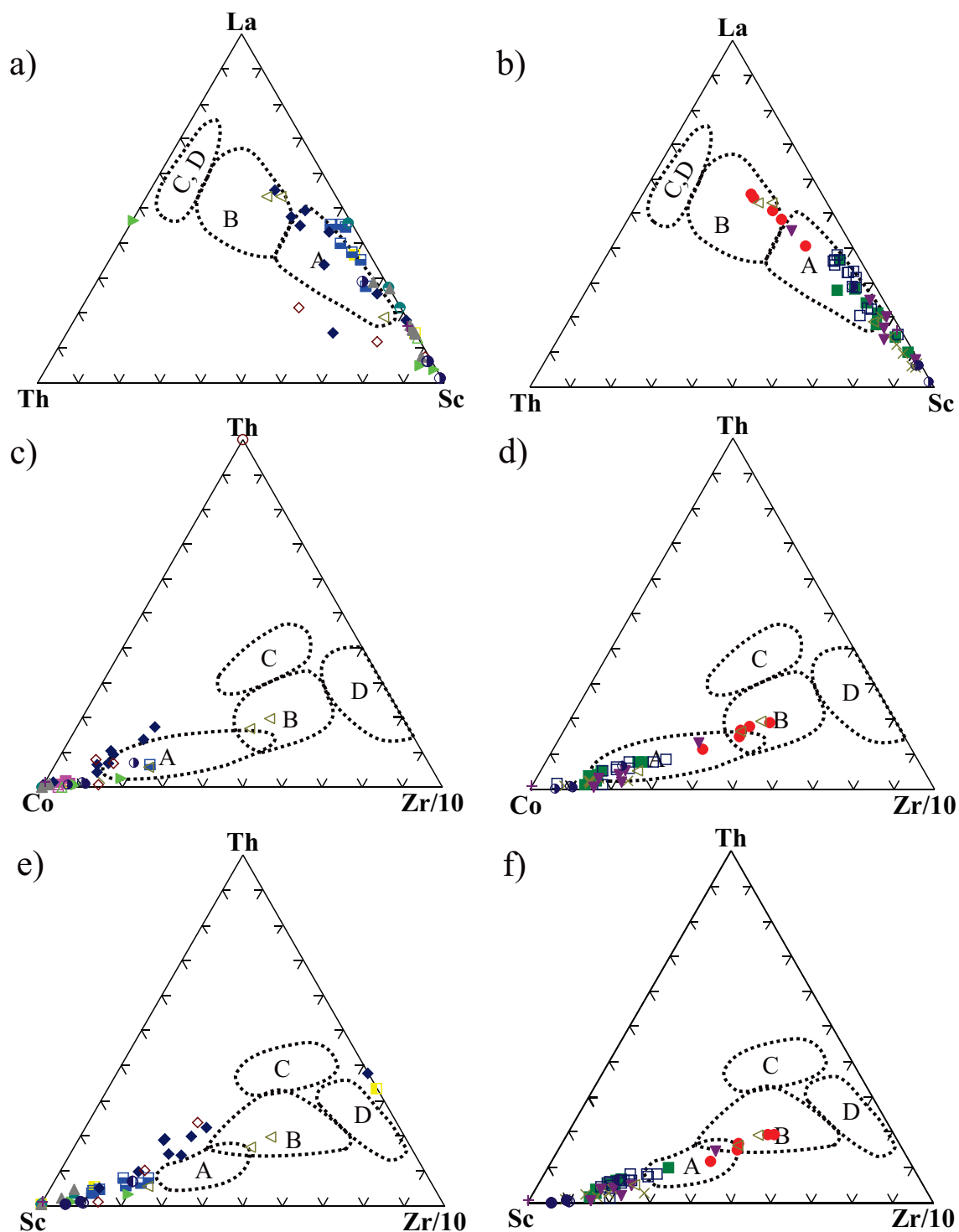
Figures 4.10e and 4.10f consist of a Zr versus Zr/Y binary plot. This is a tectonic setting discrimination diagram where polygon A represents within plate basalt, polygon B represents island arc basalt, and polygon C represents mid-ocean ridge basalts.

Figure 4.10e shows that the mafic samples are roughly divided fifty-fifty between ocean floor basalts and island arc basalts. It should be noted that there is considerable overlap between the two polygons though. Again as seen in the previous diagrams, the siliciclastic-dominated samples in Figure 4.10f overlap with the mafic volcanic samples and the garnet-bearing quartzite exhibits little similarity to the intermediate volcanic samples. Note that the intermediate samples are included on this diagram simply for comparison and plot in the within plate basalts field.

Figures 4.10g and 4.10h are binary tectonic discrimination diagrams consisting of Ti/1000 versus V. Samples with a Ti/1000 to V ratio greater than twenty fall into the arc field (ARC) and those with Ti/1000 to V ratio less than twenty fall into the ocean floor basalt field (OFB). Several significant trends are observed in Figures 4.10g and 4.10h. Firstly, there are two distinct groups of volcanic samples in Figure 4.11g. One group falls in the OFB field and the other in the ARC field. Figure 4.10h contains the siliciclastic-dominant samples plotted for comparison. These samples plot in a linear trend and overlap with the arc basalts but not with the ocean floor basalts.

Discerning the environment of deposition and provenance of the metasediments, containing a weathered siliciclastic component, is possible using trace elements with low mobility and low residence times in seawater such as Ti, Zr, Ce, Nd, La, Th, Nb, Sc, and Hf. These elements are retained and incorporated quantitatively into clastic detritus (Taylor and McLennan 1985; McLennan *et al.* 1990; McLennan and Taylor 1991; Bhatia and Crook 1986). Among the most sensitive tectonic setting discriminators are values for Nd, Nb, Zr/Nb, and Sc/Ni (and possibly Ce, and Zr/Th). Metasedimentary samples from the current study are similar to active margin graywackes; values of K/Th, Zr/Hf, La/Th, Sc, V, Th/Sc, and Ti/Zr are more like those of island arc graywackes; whereas Th, Zr, Hf, Th/U, La/Sc, Eu/Eu\*, La/Yb, (La/Yb)<sub>n</sub>, and (Gd/Yb)<sub>n</sub> are comparable with sediments from both tectonic settings. These ratios are discussed in more detail below.

Figure 4.11 consists of three ternary tectonic discrimination diagrams: La–Th–Sc, Th–Co–Zr/10, and Th–Sc–Zr/10, which have been modified after Bhatia and Crook (1986). Figures 4.11a, c, and e contain exhalite-dominated samples and Figures 4.11b, d, and f



**Figure 4.11. Ternary discrimination diagrams examining the original tectonic setting of sediment deposition. Fields are from Bhatia and Crook (1986). Note: A= oceanic island arc; B= continental island arc; C= active continental margin; D= passive margin. Note that the symbols are the same as in Fig. 4.3. a) La-Th-Sc diagram of exhalite-dominant lithologies, b) La-Th-Sc diagram of siliciclastically-dominant lithologies, c) Th-Co-Zr/10 diagram of exhalite-dominant lithologies, d) Th-Co-Zr/10 diagram of siliciclastically-dominant lithologies, e) Th-Sc-Zr/10 diagram of exhalite-dominant lithologies, f) Th-Sc-Zr/10 diagram of siliciclastically-dominant lithologies.**

contain siliciclastic samples. Volcanic samples are not plotted because some of the respective elements were not analyzed. It is stressed that the fields on these diagrams were originally delineated based on sandstones and not igneous rocks. Note that samples plotting along the edges of the ternary diagram have exceedingly low amounts of the element on the corner directly opposite them.

It is important to note that there is a minor issue with these diagrams. Bhatia and Crook (1986) used sandstones from oceanic island arcs dominated by mafic volcanic rock to construct the fields on the diagrams, but did not take into account within-plate volcanic islands such as Hawaii or hotspots on ridges like Iceland. These discrimination plots just differentiating between volcanic sources and do not prove the tectonic setting. This problem is addressed by using spider diagrams (Fig. 4.15) modified after Fralick (2003). Regardless Figure 4.11 still provides useful information, which is further expanded upon in Figure 4.15.

The samples form surprisingly linear trends on the various ternary diagrams in Figure 4.11. Not only is this an indication the samples are relatively unaltered in terms of these elements but the various lithologies exhibit similar trends on all three diagrams. These diagrams indicate that sediment at the base of the NIF assemblage was deposited in an ocean floor setting. Stratigraphically higher siliciclastic samples indicate development of a larger oceanic island towards the stratigraphic top of the NIF assemblage. The linear trends seen in Figure 4.11 probably represent an original igneous trend that is preserved in the sediments. The preservation of these trends may be an indication that these elements have not been mobilized. Prolonged weathering and/or sorting would have distorted these trends.

The garnet-bearing quartzite has higher ratio of Zr/Co, Zr/Sc, and La/Sc relative to other siliciclastic lithologies. The protolith to this lithology is most likely sandstone. The higher ratios may be a result of sorting but are more likely due to the garnet-bearing quartzite being formed from sediment that weathered from more felsic igneous rock. Felsic rocks are normally enriched in Zr and La and depleted in Sc and Ti relative to mafic volcanic

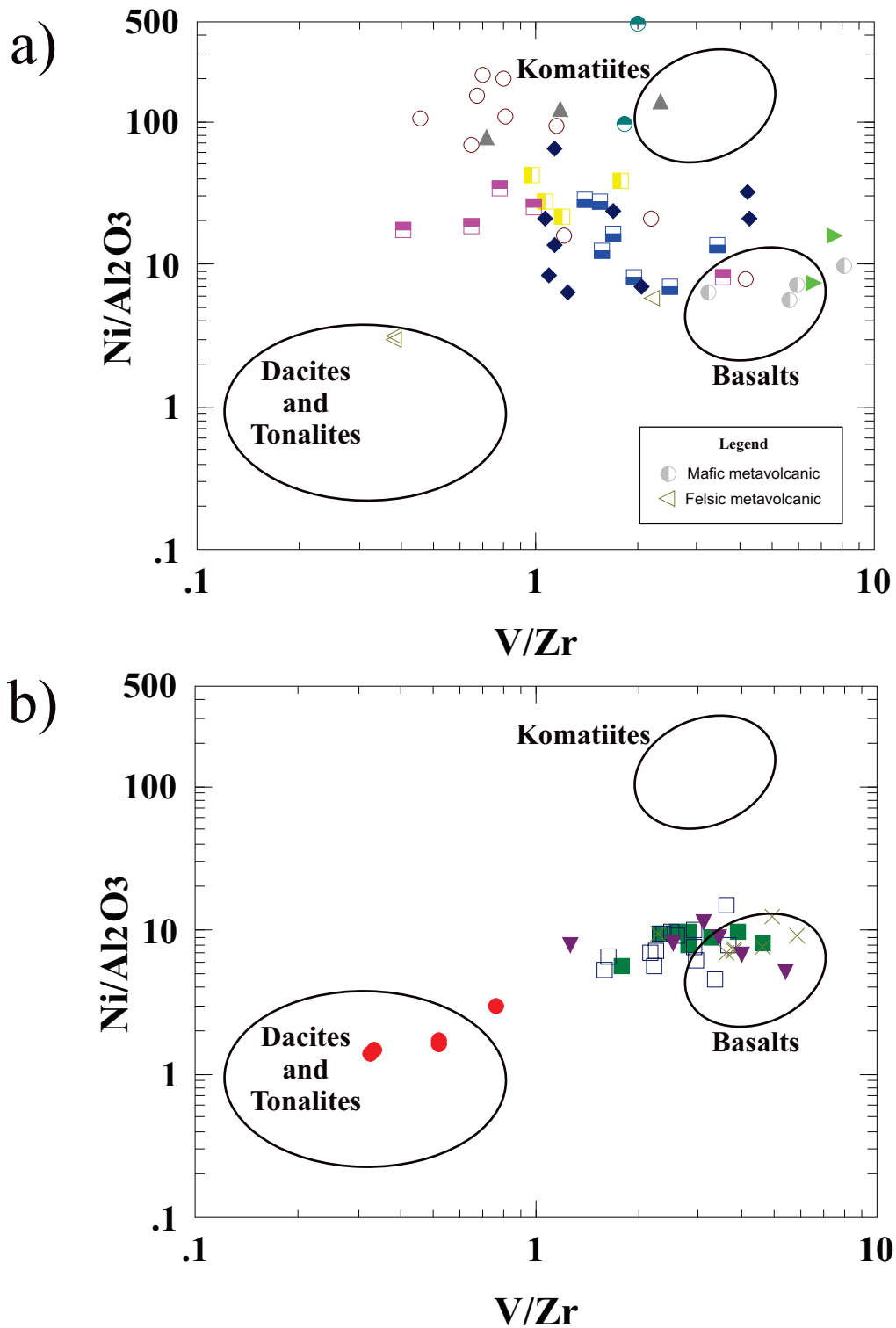
rocks (Gu *et al.*, 2002). In addition the garnet-bearing quartzite is found in close proximity to intermediate metavolcanic rock.

Several trends are repeated throughout the ternary diagrams of Figure 4.11 including: 1) the garnet-bearing quartzite is always transitional from oceanic island arc to continental island arc (not necessarily derived from an continental island arc, but weathered from mafic to felsic parent material), 2) the meta-argillite plots consistently in the oceanic island arc setting, 3) the lithologies plot in a positive linear trend line that more or less parallels up stratigraphy, however, many samples plot outside of the established fields indicating relatively low Th and Zr, and 4) in Figure 4.11d and 4.11f the silicate-dominant BIF and several hornblende-garnet schist samples plot in the oceanic island arc field.

It should be noted that the ternary diagrams in Figure 4.11 were not designed with ultramafic source rocks in mind. Hence Figure 4.12 is introduced in order to compare samples of the siliciclastic lithologies to average ultramafic, mafic, and felsic rocks. Figures 4.12a and 4.12b are logarithmic binary tectonic discrimination diagrams consisting of V/Zr versus Ni/Al<sub>2</sub>O<sub>3</sub>. The ratio of both V/Zr and Ni/Al<sub>2</sub>O<sub>3</sub> increase from felsic to ultramafic volcanic lithologies and this is the basis for the fields depicted on the diagram. Figure 4.12a contains the exhalite-dominant lithologies and 4.12b the siliciclastic-dominant lithologies. Figure 4.12a also contains the volcanic samples collected for the present study (note inset legend). However, the large volcanic sample set is not plotted because vanadium was not analyzed.

Samples of the exhalite-dominant lithologies are scattered and do not form a coherent trend in Figure 4.12a. The exhalite samples do plot closer to the komatiite field than the siliciclastic-dominant samples. Samples of the mafic and intermediate volcanics plot in or near the appropriate fields.

Samples of the siliciclastic-dominant lithologies form a more concise group with a weak linear trend in Figure 4.12b. Samples of the silicate-dominant BIF, hornblende-garnet



**Figure 4.12. Binary plot of V/Zr versus Ni/Al<sub>2</sub>O<sub>3</sub>.** Note that the symbols are the same as in Fig. 4.3. Average komatiite, basalt, dacite, and tonalite fields are plotted on this diagram for comparative purposes. V/Zr and Ni/Al<sub>2</sub>O<sub>3</sub> ratios normally decrease during the evolution of igneous systems. Note that the symbols are the same as in Fig. 4.3. a) exhalite-dominant lithologies b) Siliciclastic-dominant lithologies.

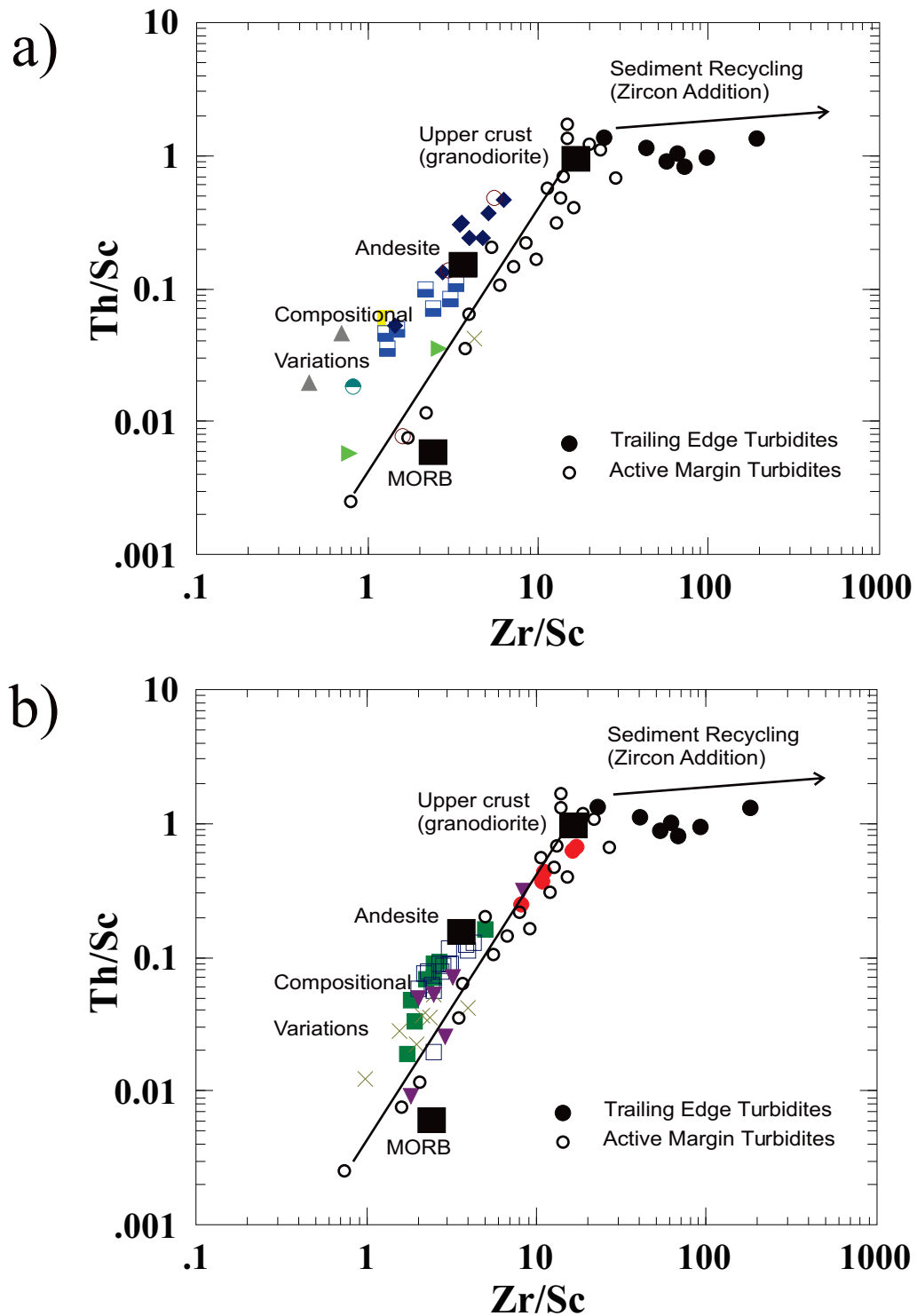
schist, and biotite-garnet schist plot close to the basalt field, whereas samples of the garnet-bearing quartzite plot close to the dacite and tonalite field.

The stratigraphically lower lithologies in the NIF assemblage contain minor clastic material possibly weathered from ultramafic and mafic source rock (see Figure 4.12a). Lithologies closer to the top of the NIF assemblage are produced mostly from the weathering of mafic with some intermediate or felsic lithologies (Figure 4.12b). There is only one lithology produced mostly from the weathering of felsic volcanic rocks and that is the garnet-bearing quartzite. These conclusions are also supported by the geology seen at the mine with decreasing ultramafic and mafic volcanic rocks up section.

Figures 4.13a and 4.13b consist of the same binary plot of Th/Sc versus Zr/Sc modified after McLennan *et al.* (1990) and McLennan and Murray (1999). Average modern mid-ocean ridge basalt, andesite, and granodiorite, as well as modern active margin and trailing edge turbidites are plotted on this diagram for comparative purposes. Th/Sc and Zr/Sc ratios normally increase during the evolution of igneous systems. Increasing Th/Sc and Zr/Sc ratios are preserved in active margin sediments that have simple provenance and have not undergone extensive sediment recycling (note that active margin can theoretically include an actively growing volcanic island). However, Th/Sc and Zr/Sc ratios are less likely to be preserved in trailing margin sediments (i.e., passive margin) due increased sediment recycling. Sediment recycling hydraulically concentrates zircon due to this minerals heavy nature. Concentration of zircon results in decoupling of the Th/Sc and Zr/Sc ratios where Zr/Sc will increase nearly independently of Th/Sc (McLennan and Murray, 1999).

Figure 4.13a contains the exhalite-dominant lithologies. These lithologies plot slightly above the mixing line. Magnetite samples from the NIF assemblage oxide-dominant BIF, and meta-argillite samples, plot close to average andesite. Figure 4.13b contains the siliciclastic-dominant samples. These samples plot closer to the mixing line, relative to the exhalite-dominant lithologies, and cluster between MORB and andesite. The garnet-





**Figure 4.13. Binary plot of Th/Sc versus Zr/Sc modified after McLennan et al. (1990) and McLennan and Murray (1999). Note that the symbols are the same as in Fig. 4.3. Average modern mid-ocean ridge basalt, andesite, granodiorite, and modern active margin and trailing edge turbidites are plotted for comparative purposes. Note that Th/Sc and Zr/Sc ratios normally increase during the evolution of igneous systems. a) exhalite-dominant lithologies, b) Siliciclastic-dominant lithologies.**

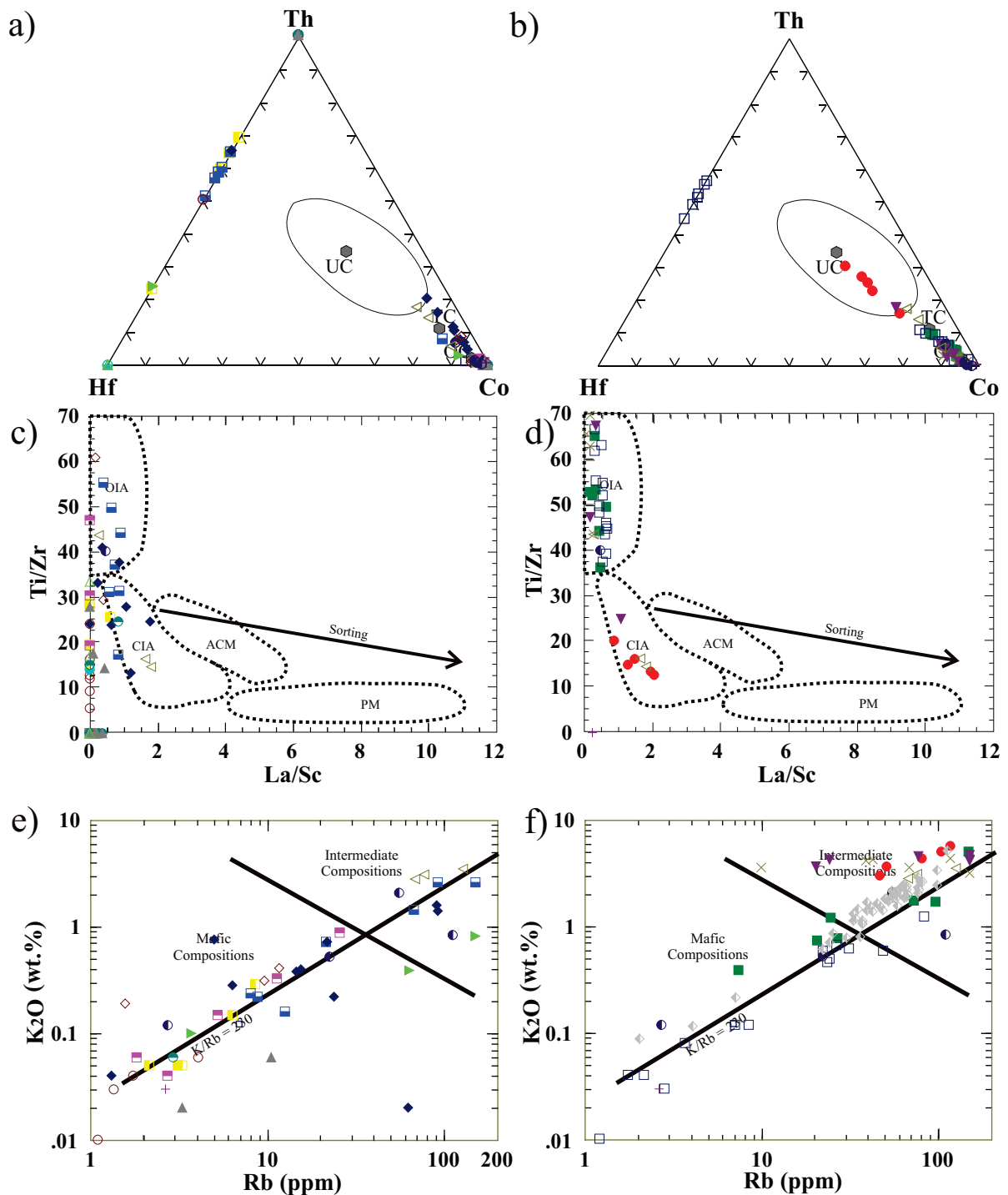
quartzite plots close to upper crust (granodiorite) composition. Importantly, Figures 4.13a and 4.13b indicate all sediment was deposited on an active margin (i.e., actively growing volcanic island) and not a trailing edge.

Figure 4.14 contains an assortment of diagrams designed to extrapolate the environment of deposition from sedimentary geochemical characteristics. Figure 4.14a and 4.14b consists of a Th-Hf-Co ternary diagram with three average points for reference: UC= upper crust, TC= bulk continental crust, OC= average oceanic crust (Taylor and McLennan, 1985). Both exhalite-dominated and clastic-dominated lithologies form a linear trend from average oceanic to upper continental crust. An interesting feature in Figure 4.14b is the distinct UC nature of the garnet-bearing quartzite whereas all other lithologies lump together. This indicates the garnet-bearing quartzite, has similarities to a dacite and/or granodiorite.

Figure 4.14c and 4.14d are La/Sc vs. Ti/Zr plots. The Ti/Zr vs. La/Sc plot is designed to interpret original tectonic setting of the sediment. Note that fields are from Bhatia and Crook (1986) where PM= passive margin, OIA= oceanic island arc, CIA= continental island arc, ACM= active continental margin, and PM= passive continental margin. Most of the lithologies plot within the active continental margin field, close to the field for continental island arc. The exhalite-dominant samples in Figure 4.14c are scattered. However, a much better developed trend is formed by the siliciclastic-dominant samples in Figure 4.14d. The silicate-dominant BIF, hornblende-garnet schist, and biotite-garnet schist plot in the OIA field. Samples of the garnet-bearing quartzite again display a distinctly different trend from the other lithologies plotting solidly in the CIA field and overlap with samples of felsic volcanic rock.

Figure 4.14e and 4.14f are  $K_2O$  vs. Rb plots modified after Floyd and Leveridge (1987) and McCann (1991). These plots are designed to distinguish between mafic and felsic source rocks. In Figure 4.14 the  $K_2O$  vs. Rb diagram is used to see if the sedimentary lithologies were weathered from mafic, felsic, or a mix of parent sources.

Ultimately both  $K_2O$  and Rb are reflected in the overall biotite content of the sample.  $K_2O$  and Rb should maintain a similar ratio to the sediment it formed from. Intermediate



**Figure 4.14** Note that the symbols are the same as in Fig. 4.3. Thorium-Hafnium-Cobalt ternary diagram, used to determine original tectonic setting of sediment deposition. Fields are from Taylor and McLennan (1985). OC= average oceanic crust; TC= bulk continental crust; UC= Upper continental crust. a) Samples from exhalite-dominant lithologies, b) Samples from siliciclastic-dominant lithologies. Ti/Zr vs. La/Sc plot designed to interpret original tectonic setting of deposition of sediment. Fields are from Bhatia and Crook (1986): PM= passive margin, OIA= oceanic island arc, CIA= continental island arc, and ACM= active continental margin. c) Samples from exhalite-dominant lithologies d) Samples from siliciclastic-dominant lithologies. K<sub>2</sub>O vs. Rb diagram designed to show if sedimentary material came from mafic, felsic, or a mix of parent sources. Fields after Floyd and Leveridge (1987). e) Samples from exhalite dominant lithologies, f) Samples from siliciclastic-dominant lithologies.

to felsic igneous rocks have higher concentrations of K<sub>2</sub>O and Rb relative to mafic igneous rocks. This relationship is in the biotite-garnet schist and garnet-bearing quartzite, two biotite-rich lithologies, which plot very far into the intermediate field.

Most samples of the silicate-dominant BIF appear to be weathered from mafic igneous source rocks. Samples of the hornblende-garnet schist are evenly divided between mafic and intermediate/felsic source rock. Samples of the biotite-garnet schist and garnet-bearing quartzite are composed mostly of weathered intermediate/felsic igneous material.

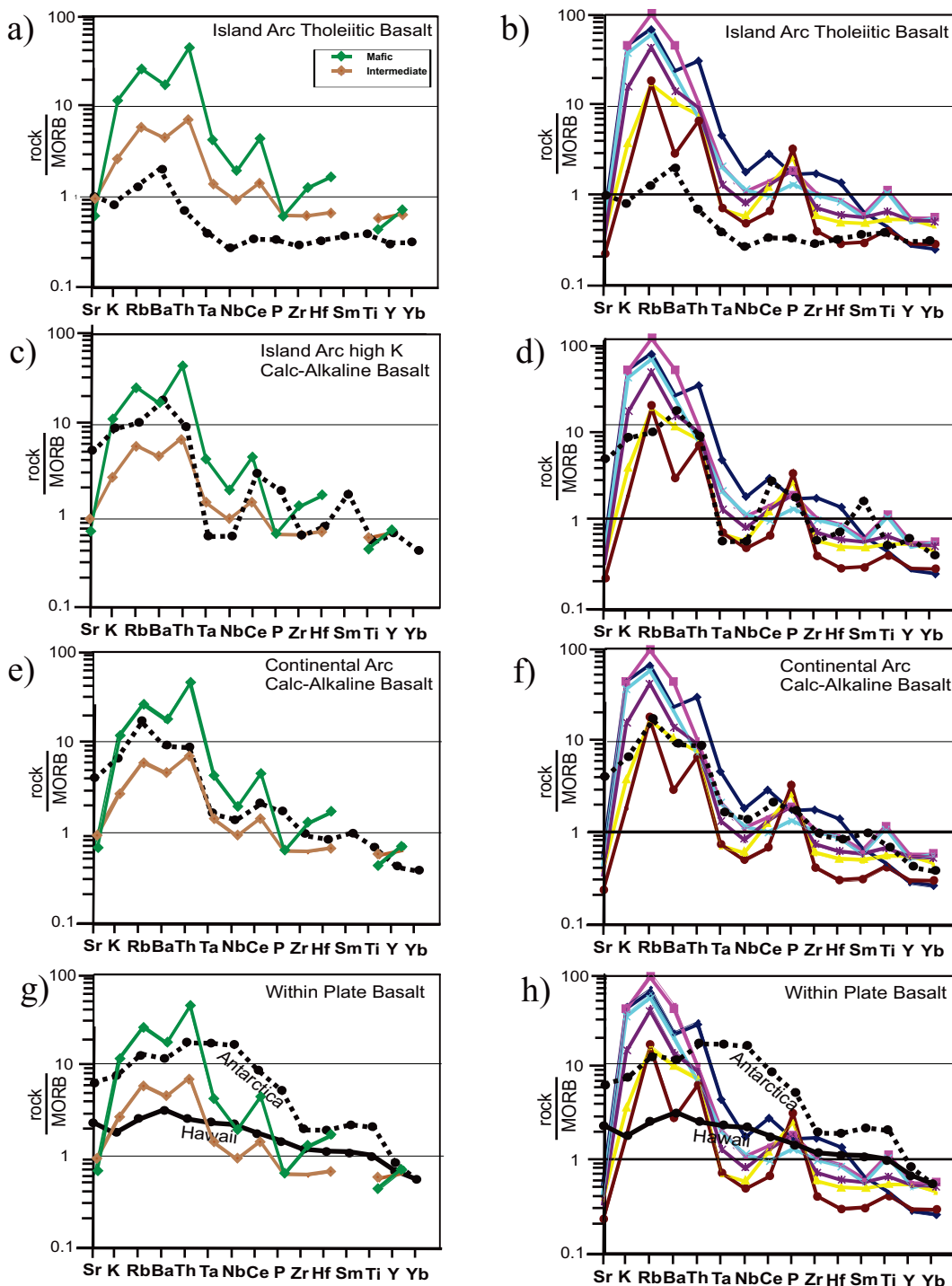
It should be noted that due to the mobile nature of K and Rb inferences from Figure 4.14e and 4.14f are made with a good deal of caution. However, the samples form similar trends to those observed in the preceding diagrams and plot along the K/Rb=230 trend line indicating K and Rb were not substantially remobilized.

Figure 4.15 is composed of four MORB normalized incompatible-element spider diagrams modified from Pearce (1983). Fralick (2003) showed the applicability of these spider diagrams to sediment geochemistry. Note the MORB-normalizing values (Pearce *et al.*, 1981) are as follow:

	Sr	K <sub>2</sub> O	Rb	Ba	Th	Ta	Nb	Ce	P	Zr	Hf	Sm	TiO <sub>2</sub>	Y	Yb
	ppm	ppm	ppm	ppm	ppm	ppm	ppm	ppm	ppm	ppm	ppm	ppm	ppm	ppm	ppm
N-MORB	120	1500	2	20	0.2	0.18	3.5	10	1200	90	2.4	3.3	15000	30	3.4

**Table 4.2. N-MORB normalizing values for Figure 4.10**

The bold-dashed lines on the diagrams in Figure 4.15 represent average curves for basalts from particular tectonic settings. These curves are the product of different magmatic melts. The island-arc tholeiitic basalt pattern is characterised by high REE values between Sr to Th with horizontal values between Ta to Yb. The island-arc calc-alkaline basalt pattern is more erratic containing high levels of Th, Ba, Rb, K, and Sr in addition to less significant amounts of Sm, P, and Zr. The continental-arc calc-alkaline basalt pattern has higher levels of Ta, Zr, Nb, and Hf (Pearce, 1983).



**Figure 4.15. Incompatible-element spider diagrams modified from Pearce (1983).** Bold-dashed lines represent average basalt from particular settings. MORB-normalizing values are found in Table 4.2. Coloured lines represent average values for individual Musselwhite lithologies. Symbols in Fig. 4.15b, d, f, and h are the same as in Fig. 4.3 (legend for Figs. 4.15a, c, e, and g is inset in Fig. 4.15a). Number of samples averaged as follows: Mafic (n=197), intermediate (n=51), trench meta-sediment (n=9), silicate-dominant BIF (n=15), biotite-garnet schist (n=7), hornblende-garnet-schist (n=8), garnet-quartzite (n=5). a) Musselwhite mafic and intermediate volcanic values plotted against Island Arc Tholeiitic Basalt, b) Musselwhite metasediment values plotted against Island Arc Tholeiitic Basalt, c) Musselwhite mafic and intermediate volcanic values plotted against Island Arc High K Calc-Alkaline Basalt, d) Musselwhite metasediment values plotted against Island Arc High K Calc-Alkaline Basalt, e) Musselwhite mafic and intermediate volcanic values plotted against Continental Arc Calc-Alkaline Basalt, f) Musselwhite metasediment values plotted against Continental Arc Calc-Alkaline Basalt, g) Musselwhite mafic and intermediate volcanic values plotted against Within Plate Basalt, h) Musselwhite metasediment values plotted against Within Plate Basalt.

The reader should note that the average mafic and average intermediate curves are plotted on a, c, e, and g. These curves are based on the igneous geochemistry provided by the Musselwhite exploration department. The mafic curve represents 197 mafic volcanic samples and the intermediate curve represents 51 intermediate volcanic samples. The average sedimentary curves are plotted on b, d, f, and h. These curves are based on the samples collected for the present study.

In general the metasediment, mafic, and intermediate metavolcanic samples exhibit the same style of curve and therefore have similar concentrations of the elements in question. Similarities include high concentrations of K, Rb, Ba, and Th. Differences between the curves include higher overall average element concentrations in the sediments relative to the volcanic samples. The volcanic lithologies also exhibit a pronounced positive Ce anomaly, whereas the metasediments do not. Overall both the metavolcanic and metasedimentary lithologies exhibit curves similar to island-arc calc-alkaline basalt and continental-arc calc-alkaline basalt curves (Figures 4.15c-f).

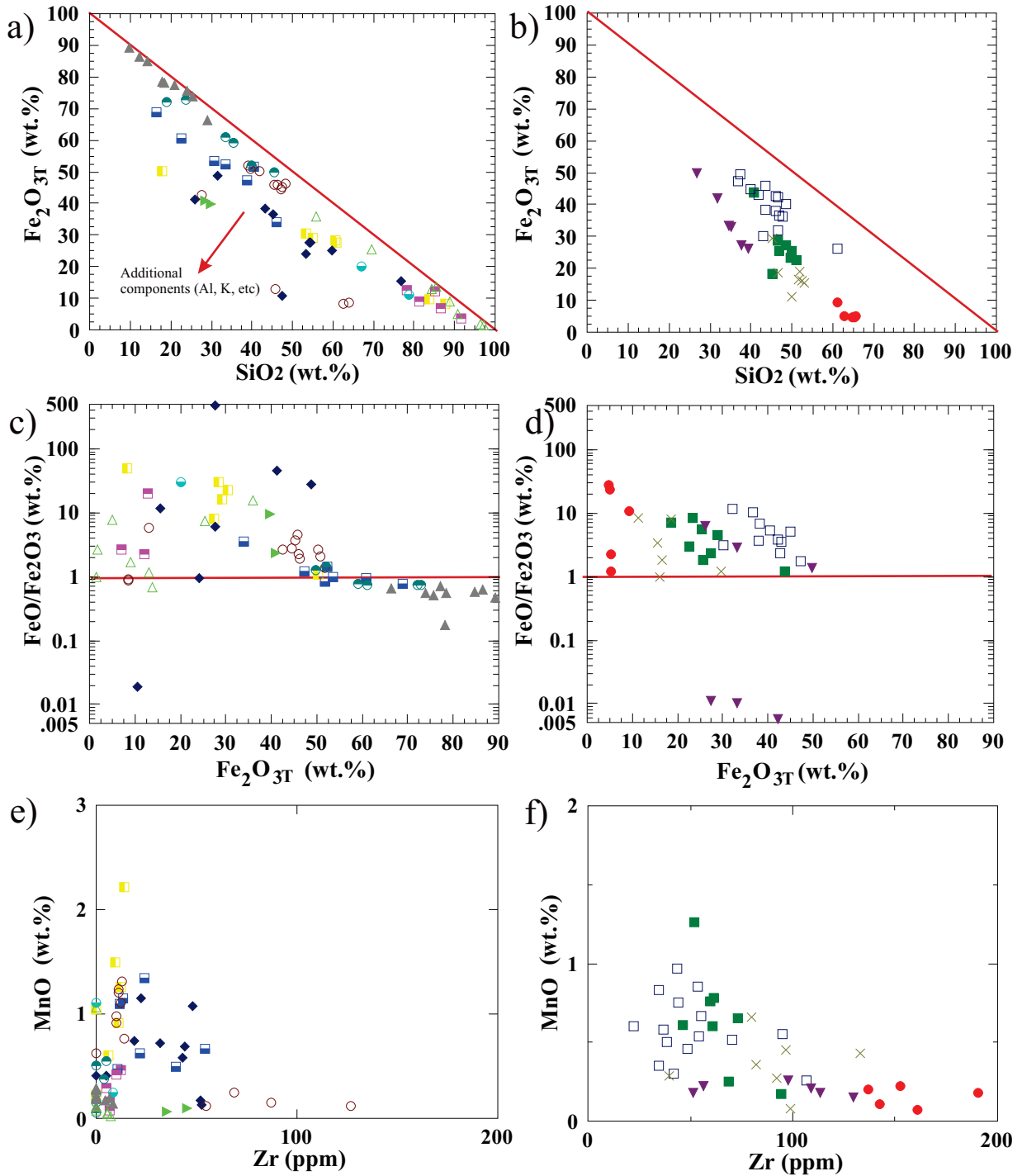
The most likely source for the sediments is the volcanic lithologies in the immediate vicinity of the NIF assemblage. Together the diagrams in Figures 4.11, 4.12, 4.13, and 4.14 indicate that preliminary sedimentation of the NIF assemblage (and therefore hydrothermal black smoker activity) took place in a primitive oceanic island setting, which progressed gradually into a mature oceanic island setting. An evolving oceanic island takes into account the plume model proposed by Hollings and Kerrich (1998). It is possible that the oceanic island(s) were part of a large igneous province. The geochemical trend evident in the Musselwhite metasediments would develop in a large igneous province if flows are thick enough. Melting at the base of ultramafic and mafic flows may produce a felsic melt. The felsic melt could have erupted and eroded to produce the more felsic siliciclastic lithologies.

#### 4.5 Major Elements: General Characteristics

A great amount of discussion has already been devoted to the partitioning of elements in terms of exhalite and siliciclastic dominant lithologies. Section 4.5 is devoted to a general description of the major elements and how they relate to the trace and REE elements in the different lithologies. This is done through the diagrams in Figures 4.16 and 4.17. The reader should note that in Figures 4.16 and 4.17 the exhalite samples are plotted on a, c, and e whereas the siliciclastic samples are plotted on b, d, and f.

Figures 4.16a and 4.16b are binary diagrams of  $\text{Fe}_2\text{O}_3^{\text{T}}$  vs.  $\text{SiO}_2$ . The exhalite-dominant lithologies are composed primarily of quartz, iron-silicates, magnetite, and/or sulfide, the mineralogy is primarily a reflection of the chemistry. Together samples from these lithologies form an interesting trend-line in Figure 4.16a. This line is drawn in red and represents a mixing line theoretically ranging from a sample composed of 100%  $\text{Fe}_2\text{O}_3^{\text{T}}$  (i.e., pure magnetite) in the upper left corner to a sample composed of 100%  $\text{SiO}_2$  (i.e., pure quartz) in the lower right corner. Samples that plot on this line are composed of varying percentages of magnetite and quartz. Samples that plot off the mixing line contain additional material besides  $\text{Fe}_2\text{O}_3^{\text{T}}$  and  $\text{SiO}_2$ .

Only samples of NIF assemblage and SIF oxide-dominant BIF plot directly on this line, which indicates they are the simplest lithologies in terms of chemistry and mineralogy. Both the NIF assemblage and SIF oxide-dominant banded iron formations are homogenous and composed of <95% alternating magnetite and quartz bands. The major-element geochemistry of the oxide-dominant BIF is relatively straight forward since this lithology is primarily composed of alternating monomineralic magnetite and quartz bands. As stated in Chapter One the bands were separated for geochemical analysis. Samples of magnetite cluster at the upper left end of the line and samples of meta-chert cluster in the lower left end of the line. There are several anomalous samples of both meta-chert and magnetite that plot away from their respective groupings. In this case magnetite bands contain some quartz and the quartz bands contain some magnetite. This is not unusual to see in thin-section.



**Figure 4.16. Various binary diagrams.** a) Binary diagram of  $\text{Fe}_2\text{O}_3$  vs.  $\text{SiO}_2$  for samples from the exhalite-dominant lithologies, b) Binary diagram of  $\text{Fe}_2\text{O}_3$  vs.  $\text{SiO}_2$  for samples from the siliciclastic-dominant lithologies, c)  $\text{FeO}/\text{Fe}_2\text{O}_3$  vs.  $\text{Fe}_2\text{O}_3$  total for samples from the exhalite-dominant lithologies, d)  $\text{FeO}/\text{Fe}_2\text{O}_3$  vs.  $\text{Fe}_2\text{O}_3$  total for samples from the siliciclastic-dominant lithologies, e) Zr vs. MnO for samples from the exhalite-dominant lithologies, f) Zr vs. MnO from the siliciclastic-dominant lithologies.



A number of samples, specifically the meta-argillite and quartz-grunerite BIF lithologies along with some magnetite and quartz bands from the oxide-dominant BIF and SIF, do not plot on the mixing line. This indicates that these samples are not pure magnetite and quartz and there are other elements (and therefore minerals) in these samples that are 'pulling' them off the trend line. In thin-section and hand sample, the meta-argillite is composed of quartz, pyrrhotite, biotite, and various amphiboles so it makes sense for this lithology to not plot on the mixing line. The same can be said for the quartz-grunerite BIF as it contains a high degree of Mn-rich grunerite. The reason some of the SIF and NIF assemblage oxide-dominant BIF samples do not plot along the mixing line lies in the fact that many SIF samples contain carbonate and NIF oxide-dominant BIF samples can contain some biotite. The reader should note that a biotite trend has already been established in some oxide-predominant BIF samples in the previous diagrams.

Figure 4.16b is a binary plot of  $\text{Fe}_2\text{O}_3^{\text{T}}$  vs.  $\text{SiO}_2$  containing samples of the siliciclastic lithologies. No samples plot on the previously discussed mixing line, because these lithologies contain both siliciclastic and exhalite material. However, several trends are observable in Figure 4.16b the most obvious of which is the tendency of samples to cluster together by lithology. Samples from these lithologies exhibit less scatter than the exhalite-dominant samples in Figure 4.16a, and an overall negative linear trend between  $\text{Fe}_2\text{O}_3^{\text{T}}$  and  $\text{SiO}_2$ . All samples in Figure 4.16b plot relatively close together, but not along the mixing line because of their more complex geochemical makeup, indicating similar concentrations of  $\text{Fe}_2\text{O}_3^{\text{T}}$  and  $\text{SiO}_2$ . The more complex geochemical nature of these lithologies is reflected in their mineralogy.

Figure 4.16b indicates the silicate-dominant BIF is composed of 70-90% exhalite material and 10-30% siliciclastic material as opposed to the garnet-hornblende schist and biotite-garnet schist, which are composed of between 50-70% exhalite material and 30-50% siliciclastic material. Samples of the silicate-predominant BIF, hornblende-garnet schist, and biotite-garnet schist exhibit slight overlap and form a continuum indicating decreasing exhalite material stratigraphically upwards in the NIF. The garnet-bearing quartzite plots on its own in a distinct group and contains minimal iron and, therefore, by

extension exhalite material. Interestingly, the metasomatic biotite-garnet schist samples exhibit a concise negative linear relationship between  $\text{Fe}_2\text{O}_3^{\text{T}}$  and  $\text{SiO}_2$ .

Figure 4.16c and 4.16d are the same  $\text{Fe}_2\text{O}_3^{\text{T}}$  vs.  $\text{FeO}/\text{Fe}_2\text{O}_3$  diagram designed to interpret the redox state of the various lithologies. Note that Figure 4.16c contains exhalite-dominant lithologies and Figure 4.16d contains the siliciclastic-dominant lithologies. The plots consist of the ratio of FeO (iron in silicate minerals) to  $\text{Fe}_2\text{O}_3$  (iron in oxide minerals). The logic behind the line drawn through 'one' on the y-axis is 'y ( $\text{FeO}/\text{Fe}_2\text{O}_3$ ) = 1' where  $\text{FeO} + \text{Fe}_2\text{O}_3 = \text{Fe}_3\text{O}_4$  (magnetite). Therefore if a sample plots above the line more of its iron is in silicate minerals. If a sample plots below this line more of its iron is in the oxidized state. The further away from the line a sample plots the more pronounced this difference in mineralogy. The further a sample plots to the right on the x-axis than the greater the total amount of iron in the sample (regardless of form).

There are three dominant trends observable in Figure 4.16c 1) most of the iron in the quartz-grunerite BIF, the meta-argillite, and quartz-dominant bands from the SIF and NIF oxide-dominant BIFs resides in silicate minerals, 2) most of the iron in the magnetite-dominant samples from the NIF assemblage and SIF oxide-dominant BIF resides in magnetite, and 3) in general the higher the  $\text{Fe}_2\text{O}_3^{\text{T}}$  the higher the amount of iron in the oxidized form ( $\text{Fe}_2\text{O}_3$ ). Note that the meta-argillite exhibits enigmatic trends which may be due to the abundance of sulfide in this lithology.

Supplementary features observed in Figure 4.16c include the following: SIF assemblage BIF magnetite-dominant samples, collected from the trenches, contain the highest  $\text{Fe}_2\text{O}_3^{\text{T}}$  and the greatest amount of iron in the oxide form compared to the other lithologies. On average the SIF assemblage BIF quartz-dominant bands from the trenches contain the lowest  $\text{Fe}_2\text{O}_3^{\text{T}}$  and the most iron in the form of FeO compared to the other lithologies. Additionally, samples of metasomatic oxide-dominant BIF, collected from the trenches, exhibit an interesting trend. These samples plot close to magnetite dominant bands but contain more FeO. This may be an indication that these samples were altered by reducing fluids.

Samples of the siliciclastic-dominant lithologies are plotted on Figure 4.16d. The siliciclastic-dominant lithologies exhibit less range in  $\text{Fe}_2\text{O}_3^{\text{T}}$  values compared to the exhalite-dominant lithologies. However  $\text{Fe}_2\text{O}_3^{\text{T}}$  values are comparable to samples of the meta-argillite, quartz-grunerite BIF, and oxide-dominant BIF quartz-dominant samples. Overall the siliciclastic-dominant lithologies have comparable  $\text{FeO}/\text{Fe}_2\text{O}_3$  values indicating they have a consistent ratio of silicate minerals to oxide minerals.

A weak general trend observed in Figure 4.16d is the negative linear correlation between  $\text{Fe}_2\text{O}_3^{\text{T}}$  and  $\text{FeO}/\text{Fe}_2\text{O}_3$  in individual lithologies. The main difference between these lithologies is the concentration of  $\text{Fe}_2\text{O}_3^{\text{T}}$ . The silicate-dominant BIF contains the greatest concentration followed by the hornblende-garnet schist, biotite-garnet schist, and garnet-bearing quartzite. This is further indication of decreasing exhalite activity stratigraphically upward in the NIF. It is important to note the overlap between the silicate-dominant BIF and the oxide-dominant BIF. Geochemical overlap between these two lithologies has been noted in numerous preceding diagrams.

Figure 4.16e and 4.16f are the same binary diagram of MnO vs. Zr designed to provide insight into exhalite (MnO) versus siliciclastic (Zr) content within the lithologies. Note Figure 4.16e contains the exhalite-dominant samples whereas Figure 4.16f contains the siliciclastic-dominant samples. In both diagrams samples exhibit a weak negative correlation between MnO and increasing Zr values. These two figures reinforce the already established trend of increasing siliciclastic content and decreasing hydrothermal content stratigraphically upward in the NIF assemblage. This trend is evident in Figure 4.16f with the stratigraphically lower silicate-dominant BIF having the highest MnO and lowest Zr compared to the stratigraphically highest garnet-bearing quartzite, which has the lowest MnO and highest Zr values.

An interesting feature of Figure 4.16f is the stratigraphically higher lithologies plot in more concise groups with samples of the garnet-bearing quartzite exhibiting the least scatter out of all the siliciclastic lithologies. This is a possible indication that deposition

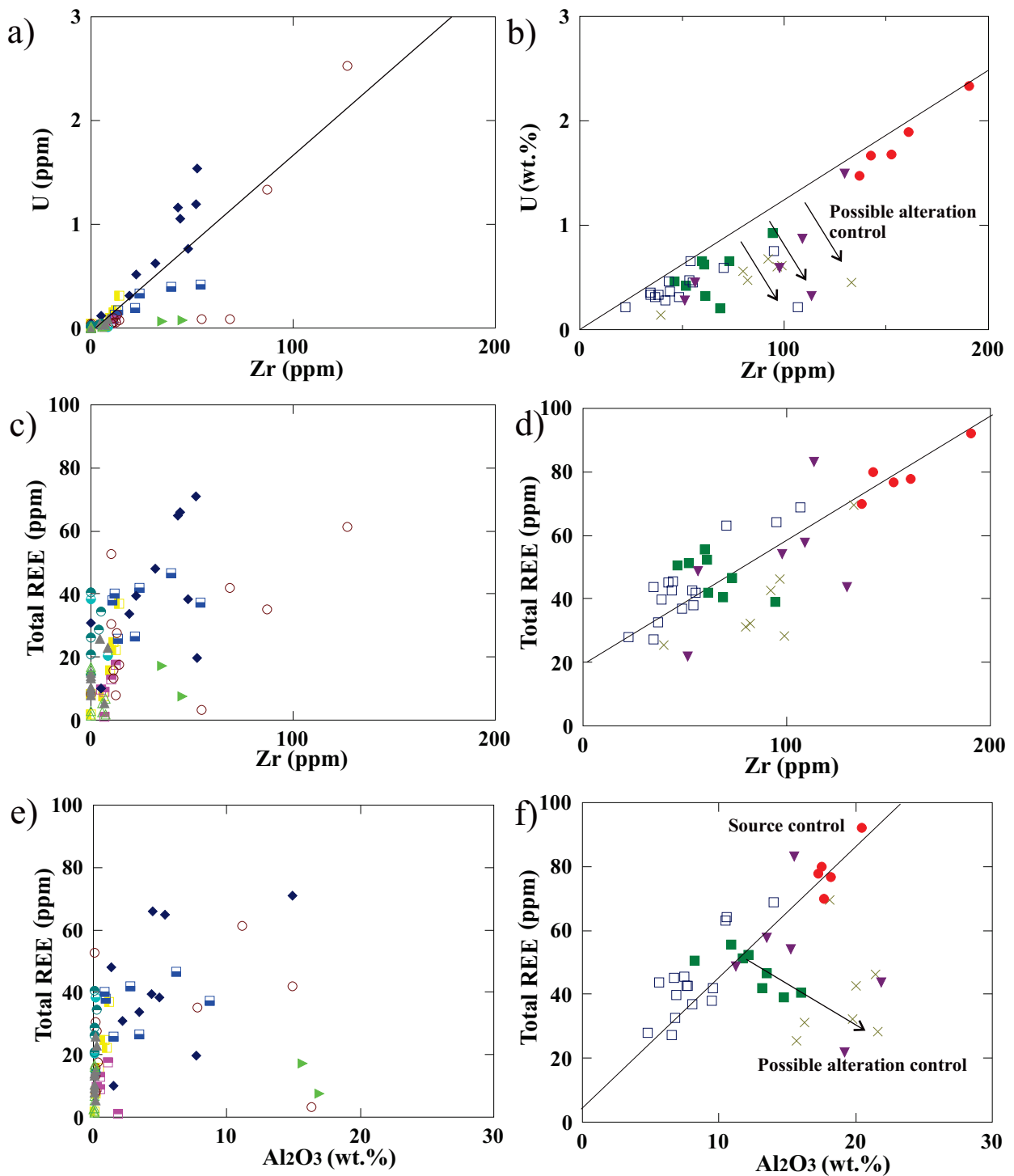
of detrital clastic material was slow initially. This is also an indication that hydrothermal black smoker activity decreases up stratigraphy in the NIF assemblage.

Figure 4.17a and 4.17b are binary plots of U vs. Zr for exhalite and siliciclastic dominated lithologies, respectively. Samples from both exhalite and siliciclastic lithologies exhibit moderate positive linear correlation between U and Zr. Note that the slope of the various trend lines varies slightly between the two sample sets. A particularly steep trend-line is formed by samples of the meta-argillite. This trend-line is steep relative to that formed from samples of the other exhalite-dominant lithologies. The high concentration, and strong positive linear correlation, of U and Zr in the meta-argillite is rather anomalous for the exhalite-dominated lithologies.

In Figure 4.7b samples of the silicate-dominant BIF and the garnet-bearing quartzite share the same trend line possibly indicating a common mineral is controlling both U and Zr (probably zircon). The majority of the hornblende-garnet schist, biotite-garnet schist, and metasomatic biotite-garnet schist samples plot off the line. This may be a result of alteration.

Figures 4.17c-f provide an appropriate lead in to the following section, Section 4.6, in which the REE chemistry discussed in more detail. Figures 4.17c and 4.17d are binary plots of “total rare earth elements (REE)” vs. Zr for exhalite- and siliciclastic-dominated lithologies, respectively. This diagram is designed to look at the relationship between concentrations of REE and Zr (siliciclastic content). The reader should note Total REE ( $\Sigma$ REE) equals La+Ce+Pr+Nd+Sm+Eu+Gd+Tb+Dy+Ho+Er+Tm+Yb+Lu.

The samples in Figure 4.17c are scattered and do not form a coherent trend. However, samples in Figure 4.17d form a very weak positive correlation between “total REE” and Zr. The siliciclastic samples also contain higher concentrations of total REE relative to the exhalite samples. This is the result of higher concentration of REE in the original clay



**Figure 4.17. Various binary diagrams. Note trend-lines are drawn on by eye.** a) Binary diagram of Zr vs. U for samples from the exhalite-dominant lithologies, b) Zr vs. U for samples from the siliciclastic-dominant lithologies, c) Total REE vs. Zr for samples from the exhalite-dominant lithologies, d) Total REE vs. Zr for samples from the siliciclastic-dominant lithologies, e) Total REE vs. Al<sub>2</sub>O<sub>3</sub> for samples from the exhalite-dominant lithologies, f) Total REE vs. Al<sub>2</sub>O<sub>3</sub> for samples from the siliciclastic-dominant lithologies.

mineral component of the siliciclastic lithologies relative to the exhalite material deposited from black smokers.

Figures 4.17e and 4.17f are binary plots of “total rare earth elements (REE)” vs.  $\text{Al}_2\text{O}_3$  for exhalite- and siliciclastic-dominated lithologies, respectively. This diagram is designed to look at the relationship between concentrations of REE and  $\text{Al}_2\text{O}_3$  (siliciclastic content). In general these plots exhibit similar trends to those seen in Figures 4.17c and 4.17d. The exhalite samples in Figures 4.17e are scattered and do not form a trend. On the other hand the siliciclastic samples in 4.17f form a moderately developed positive linear trend. Most of the samples that delineate the trend line are silicate-dominant BIF and garnet-bearing quartzite. Additionally two samples of both hornblende-garnet schist and metasomatic biotite-garnet schist fall on the trend-line.

Note that samples of the biotite-garnet schist and hornblende-garnet schist form their own trend-line. This trend-line is a negative, weakly linear, trend plotting away from the main trend-line. This trend indicates the higher the  $\text{Al}_2\text{O}_3$  value of a sample the lower the total REE will be in these lithologies. This trend might be the result of composition differences between these lithologies and the other lithologies. However, samples of biotite-garnet alteration exhibit a similar trend which supports possible alteration causality.

As seen in Figure 4.17d the average total REE concentrations are higher in samples of the siliciclastic-dominant lithologies. This is the result of higher concentration of REE in the original clay mineral component of the siliciclastic lithologies relative to the exhalite material deposited from black smokers.

#### 4.6 Rare Earth Elements

The rare-earth elements (REE) are useful in studying both ancient and modern iron formations, because their geochemical behaviour is well understood. These elements are relatively immobile and act in a consistent geochemical manner. Therefore the original controls and process operating during the deposition of iron formation can be inferred from the concentration and behaviour of the various REE. It is important to note that REE

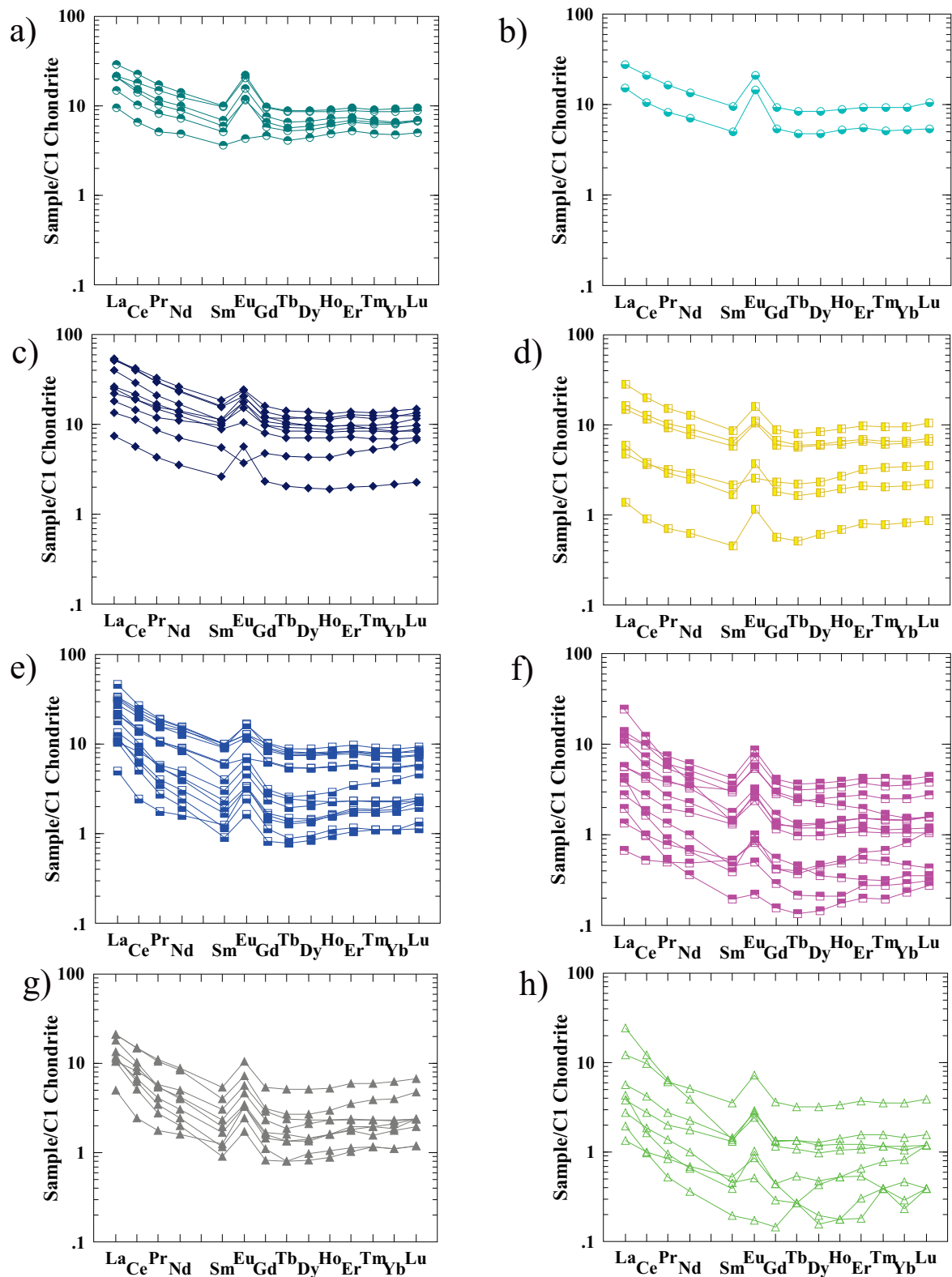
are contained in numerous sources including siliciclastic detrital, hydrothermal exhalite precipitates, and hydrogenous precipitates. Figures 4.18 and 4.19 display the C1 normalized REE curves for the various lithologies collected from the Musselwhite gold deposit. C1 chondrite normalizing values from Taylor and McLennan (1985) are found in the following table:

La	Ce	Pr	Nd	Sm	Eu	Gd	Tb	Dy	Ho	Er	Tm	Yb	Lu
ppm	ppm	ppm	ppm	ppm	ppm	ppm	ppm	ppm	ppm	ppm	ppm	ppm	ppm
0.367	0.957	0.137	0.711	0.231	0.087	0.306	0.058	0.381	0.085	0.249	0.036	0.248	0.038

**Table 4.3. C1 chondrite normalizing values from Taylor and McLennan (1985)**

Figure 4.18 contains the exhalite-dominant lithologies, whereas Figure 4.19 contains the siliciclastic lithologies. For the most part the REE spider diagrams are organized and discussed from stratigraphically lowest (SIF oxide-dominant BIF) to highest (garnet-bearing quartzite) lithologies. However there are a few exceptions to this, namely, Figures 4.18g and 4.18h contain the magnetite and quartz-bands from SIF oxide-dominant BIF collected from the trenches. Also Figure 4.19a contains the grunerite-rich metasomatic oxide-BIF samples from the trenches. The trenches are several hundred metres away from the main ore-zone and placing them into the SIF assemblage stratigraphy is problematic. The reader should note that several plots in Figure 4.19 contain multiple lithologies for comparative purposes (refer to figure caption for more information).

The concentration of the various REE in seafloor sediments, especially hydrothermally precipitated varieties like iron formation and banded iron formation, is an important indication of the processes and conditions behind their formation. Typically, pure high temperature hydrothermally precipitated chemical sediment (exhalite) exhibits one or all of the following trends on chondrite-normalized REE spider diagrams: 1) higher Europium (Eu) concentration relative to Sm and Gd and termed a “positive Eu anomaly” (Graf, 1977) 2) in addition there may be a lower Ce concentration relative to La and Pr which is termed a “negative Ce anomaly” (Graf, 1977) (both anomalies are quantified in



**Figure 4.18. C1 normalized REE spider diagrams;** a) Magnetite samples from the SIF (drill core), b) Quartz samples from the SIF (drill core), c) Meta-argillite samples (drill core), d) Quartz-grunerite BIF samples (drill core), e) Magnetite samples from the oxide-dominant BIF (drill core), f) Quartz samples from the oxide-dominant BIF (drill core), g) SIF oxide-dominant BIF magnetite samples (trench), h) SIF oxide-dominant BIF quartz samples (trench).



Figures 4.20 and 4.21), and 3) weak to strong enrichment in both light REE (LREE) and heavy REE (HREE) imparting a ‘horseshoe’ shape to the REE curve.

Note that the positive Eu anomaly occurs because of the increased solubility of Eu above 300°C (Peter, 2003). Eu is leached from plagioclase crystals in the seafloor volcanic rock and concentrated in the circulating hydrothermal fluids. The hydrothermal fluids are eventually expelled from the seafloor and upon mixing with seawater form exhalite precipitates rich in metals and having high Eu values relative to the other REE.

Two obvious trends are evident when navigating the stratigraphy of the NIF assemblage; 1) the decreasingly pronounced europium anomalies with increasing stratigraphy and 2) the general flattening of the REE curves with increasing stratigraphy.

Several general trends are repeated in the exhalite-group of lithologies. These trends are observable in the diagrams of Figure 4.18. The majority of samples from these lithologies exhibit moderate LREE enrichment and zero to weak HREE enrichment. Additionally they exhibit moderate to strong positive Eu anomalies and zero to weak negative Ce anomalies. These patterns are the same as REE patterns for other ancient iron formations such as the Windy Craggy VHMS deposit, which is Upper Triassic in age (Peter and Scott, 1999). It is important to note that these same patterns are observed in modern exhalite-dominated seafloor metalliferous sediment from the Atlantis II Deep in the Red Sea, oxide minerals on the surface of the seafloor at the TAG mound site, and pure high-temperature hydrothermal black smoker fluids venting on the present day ocean floor. This lends credibility to the fact that the IF and BIF at Musselwhite were deposited in conjunction with hydrothermal exhalite activity. This topic is discussed in more detail in Chapter Five.

SIF magnetite-dominant samples (Fig. 4.18c), on average, have higher concentrations of REE than quartz-dominant samples. However, both sample sets exhibit the same REE curve, which is slightly LREE enriched with flat HREE and a pronounced Eu anomaly. On average the SIF samples have the most pronounced positive Eu anomalies out of all

the lithologies sampled. There is one anomalous sample of magnetite, which does not follow the established trend as it has a subdued Eu anomaly (SIF-07-20-072m).

Figure 4.18c contains the meta-argillite samples. Samples from this lithology plot in a concise manner, have a flat REE trend, and contain comparable concentrations of REE to SIF magnetite-dominant samples. However, the meta-argillite samples are slightly more LREE enriched and have significantly less pronounced positive Eu anomalies compared to SIF samples.

There are two anomalous meta-argillite samples, 4h-07-20-043 and 4h-07-20-051, both of which contain lower concentrations of REE relative to the lithology average. Sample 4h-07-20-043 simply has a lower concentration of REE, but adheres to the same trend as the other samples. However, sample 4h-07-20-051 has a negative Eu anomaly suggesting this sample's protolith was mud-like and not strongly influenced by hydrothermal activity.

Figure 4.18d contains samples of the quartz-grunerite BIF. This lithology exhibits a wider range of REE values compared to the previously discussed lithologies. All samples have a similar LREE-enriched and weakly HREE-enriched REE pattern. This lithology displays a more pronounced positive Eu anomaly compared to the meta-argillite, but less pronounced than the SIF oxide-BIF. Therefore the quartz-grunerite BIF has the second most prominent average Europium anomaly. These features, combined, impart a more developed 'horseshoe'-shaped curve relative to that of the SIF and meta-argillite. The reader should note sample 4a-07-20-054m is a magnetite band interlaminated with quartz-grunerite BIF. This sample shares the same REE curve as the rest of the samples. Additionally there is one anomalous sample of quartz-grunerite BIF. This sample, 4a-07-20-028, has a subdued positive Eu anomaly relative to the other samples.

Figure 4.18e and 4.18f contain the NIF oxide-dominant BIF magnetite and quartz samples, respectively. Both the magnetite and quartz samples exhibit a large range in REE concentration and exhibit similar REE curves to the quartz-grunerite BIF in Figure

4.18d. However, the magnetite samples have higher average REE values, and exhibit a more coherent trend, compared to the quartz samples. There is considerable overlap in the concentration of the REE between quartz and magnetite samples. This is likely a reflection of the gradational relationship between quartz- and magnetite-dominant bands. Samples also have positive Eu anomalies similar to what is seen in the quartz-grunerite BIF and greater than the meta-argillite, but less than the SIF samples.

The REE curves of the magnetite and quartz samples exhibit LREE enrichment, slight HREE enrichment, and display moderately developed positive Eu anomalies. This pattern of enrichment imparts a moderate 'horseshoe' shape to the REE curves. Naturally, there is variation among the REE curves on these plots. The most common variations involve the concentration of the LREE and HREE. However, the quartz-dominant samples display more variation than the magnetite-dominant samples with HREE ranging from flat to strongly enriched. This is an interesting difference as it may indicate mobility of REE associated with the quartz-dominant bands. This is not beyond reason as grunerite is a common mineral occurring along the contact between quartz and magnetite bands. Grunerite is the result of fluid-rich chemical reactions between the quartz and magnetite. Also, it should be noted that these slight variations might be the result of temperature variations within the hydrothermal system depositing the original exhalite material.

Figure 4.18g and h contain the NIF assemblage oxide-dominant BIF samples collected from the trenches. Figures 4.18g and 4.18h contain magnetite and quartz samples, respectively. The magnetite samples plot tightly together, are LREE enriched and slightly HREE enriched, with positive Eu anomalies.

The quartz samples display very inconsistent trends. There are two anomalous samples with subdued Eu anomalies and these same samples exhibit erratic HREE values. The remaining samples display positive Eu anomalies. Samples exhibit a large variation in the degree of HREE enrichment and/or depletion. Four samples have flat HREE and four samples exhibit irregular HREE patterns, which probably indicate these elements were mobilized in the latter samples. These irregular HREE patterns, as well as the subdued

positive Eu anomalies, can be attributed to the high grunerite content in the quartz-bands from the trenches. The grunerite content in this lithology is higher than in the oxide-dominant BIF from core.

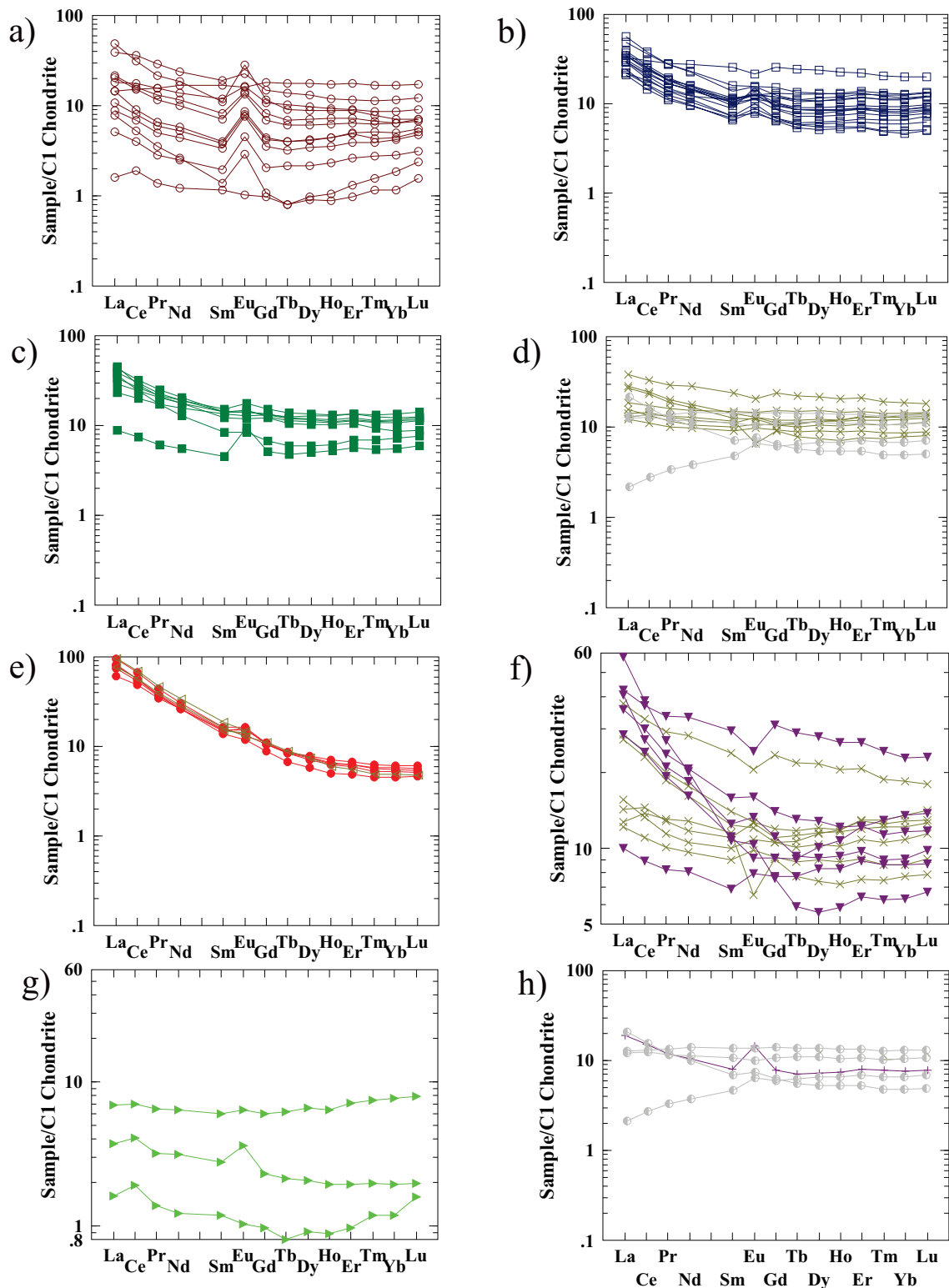
Figure 4.19a contains samples of the metasomatic oxide-dominant BIF collected from the trenches. It should be noted that that this lithology is enigmatic. It could possibly have resulted from soft sediment deformation of the oxide-dominant BIF. It may also represent hydrothermally altered oxide-dominant BIF.

This lithology has comparable REE values to the oxide-dominant BIF magnetite and quartz samples. Samples from this lithology are LREE enriched, have positive Eu anomalies, and generally flat HREE, although several samples do exhibit weak to moderate HREE enrichment. The fact that the majority of the samples have horseshoe-shaped REE curves that exhibit positive Eu anomalies suggests this lithology is not too strongly altered, if it is in fact a product of metasomatism.

Sample alt4B-PM05-045 is anomalous because it has a slight positive Ce anomaly and a subdued Eu anomaly. Additionally sample alt4B-PM05-019 is anomalous because it has a very slight negative Eu anomaly.

Figures 4.19b-h contains the siliciclastic dominant lithologies. It is important to note that some of these diagrams have multiple lithologies plotted on them for comparative purposes. In general the lithologies with a siliciclastic component have higher REE concentration and tighter, more coherent, REE curves compared to the exhalite-dominant lithologies. This is because the detrital siliciclastic sediment settling out of the water column was clay-rich (hemipelagic to pelagic). These clay minerals contain relatively high REE compared to chemically deposited exhalite precipitates.

Figure 4.19b contains samples of the silicate-dominant BIF. Samples of this lithology exhibit a tight and coherent REE curve, much more consistent than the previously



**Figure 4.19 C1 normalized REE spider diagrams;** a) Metasomatic SIF assemblage oxide-dominant BIF samples (trench), b) Silicate-dominant BIF samples (drill core), c) Hornblende-garnet schist samples (drill core), d) Biotite-garnet schist and mafic metavolcanic samples (drill core), e) Garnet-quartzite and felsic metavolcanic samples (drill core), f) Metasomatic biotite-garnet schist and regular biotite-garnet schist samples plotted together (drill core), g) Chlorite-dyke samples (trench), h) Ultramafic and mafic volcanic samples (drill core).

discussed lithologies. This lithology exhibits one of the most consistent REE curves out of all the lithologies sampled. Samples are LREE enriched, with weak positive Eu anomalies, and flat HREE curves. There is one anomalous sample, 4ea-07-20-069, which differs significantly from the established trend in that it has a slight negative Eu anomaly and a overall flat REE curve exhibiting no enrichment in either LREE or HREE. Interestingly this sample also has the highest REE values out of all the samples. Note that this sample's REE curve is similar to samples of the biotite-garnet schist.

Figure 4.19c contains samples of the hornblende-garnet schist. Samples of this lithology plot in a concise manner, although there is one anomalous sample (4e-07-20-047). The majority of the samples are LREE enriched, have zero to slightly positive Eu anomalies, and flat HREE. Note that the hornblende-garnet schist and silicate-dominant BIF exhibit similar REE curves, and REE concentrations, which continues the already well established correlation between these lithologies.

Sample 4e-07-20-047 is anomalous because it exhibits a typical exhalite REE curve, i.e., both LREE and HREE enriched (horseshoe shaped) also having a well pronounced positive Eu anomaly. These are not the dominant characteristics of the other hornblende-garnet schist samples.

Figure 4.19d contains samples of the biotite-garnet schist and mafic volcanic lithologies. The mafic volcanic samples have been included for comparison. Both lithologies exhibit similar REE curves. It should be noted that these curves are significantly different than the previously discussed REE curves. For the most part the REE curves of these two lithologies overlap suggesting the biotite-garnet schist may have been derived from weathered mafic igneous rock. In general, samples of both these lithologies exhibit flat REE curves with slight LREE enrichment and therefore resemble a MORB pattern.

There are two anomalous biotite-garnet schist samples (4f-07-20-001 and 4f-07-20-027a). These samples are anomalous because they have negative Eu anomalies. Negative Eu anomalies suggest that the protolith material to the biotite-garnet schist was a mud

uninfluenced by hydrothermal activity. This is an enigmatic trend since this lithology also contains high iron content. The reader should note there is one anomalous mafic metavolcanic sample, 2-PM05-017, which exhibits strong LREE depletion.

Figure 4.19e contains samples of the garnet-bearing quartzite and felsic volcanic lithologies. The felsic volcanic samples have been included for comparison. The garnet-bearing quartzite samples plot in an extremely concise manner with no anomalous samples. Both lithologies exhibit similar REE curves, which display the greatest degree of LREE enrichment, and therefore the steepest curve, out of all the lithologies. The samples form a REE curve that is unique amongst the lithologies in the NIF. Additionally, some samples display a very minor positive Eu anomaly. The presence of the slight europium anomaly is probably a reflection of the plagioclase content. The reader should note that the HREE appear to be slightly depleted relative to the previously discussed lithologies.

Figure 4.19f contains samples of the metasomatic biotite-garnet schist. Note that the previously discussed biotite-garnet schist samples have been plotted on for comparison. The scale of this diagram has been reduced from the previous REE diagrams in order to highlight the differences between these two mineralogically similar lithologies. Although there are similarities between the curves, there are also significant differences; namely stronger LREE enrichment, and less concise curves, in the metasomatic biotite-garnet schist samples.

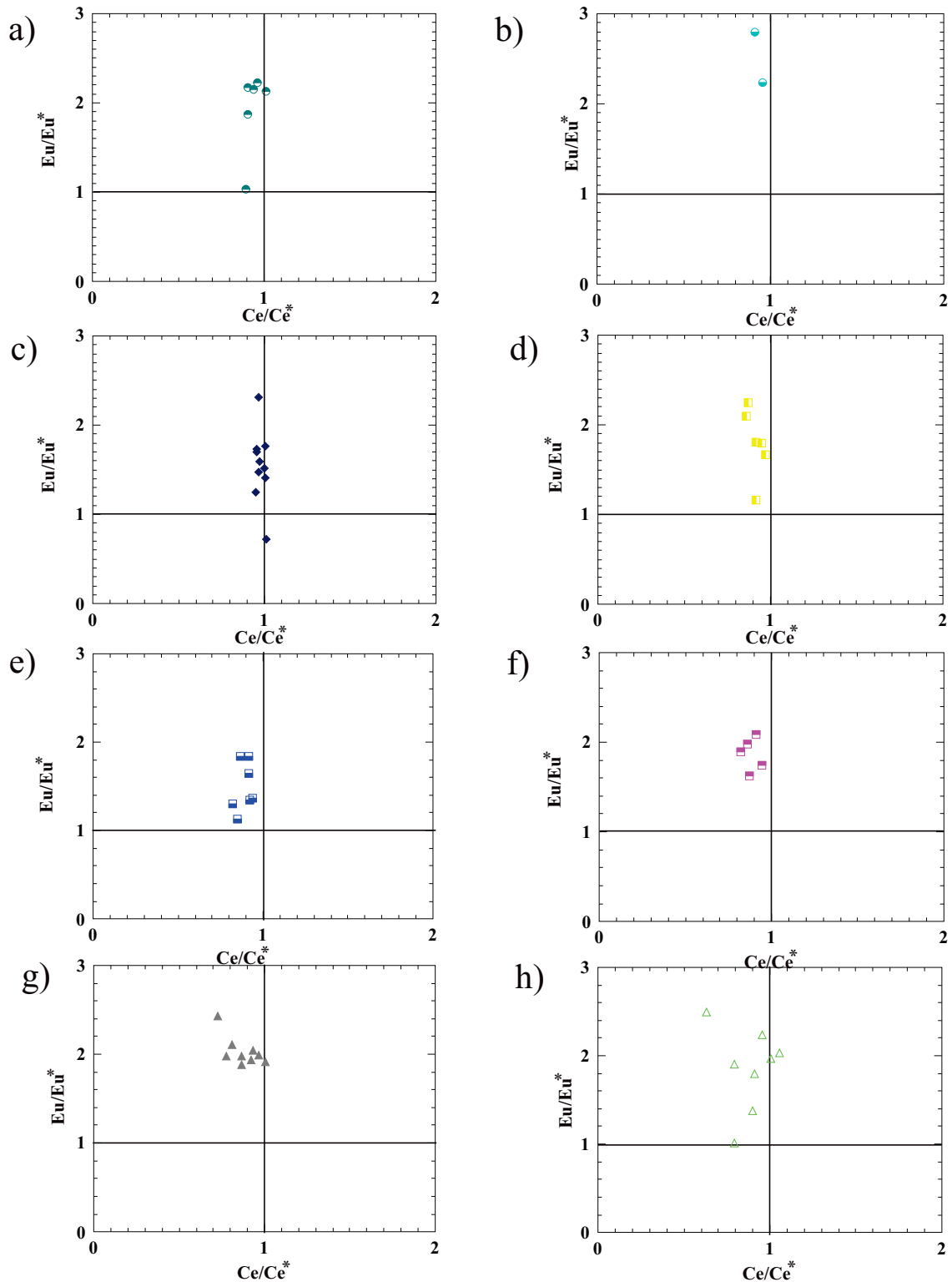
Sample bt.garn-07-20-007 has a REE curve identical to the REE curve of a biotite-garnet schist sample 4f-07-20-001. The remaining metasomatic biotite-garnet schist samples exhibit more variation in their REE values, such as extremely strong LREE enrichment, relative to the regular biotite-garnet schist and less consistent REE curves. Although both lithologies have the same mineralogical makeup there are obvious physical differences, such as coarser grain-size and more euhedral crystals in the metasomatic biotite-garnet schist, which imply these two lithologies are not one in the same.

Figure 4.19g contains chlorite-schist samples from the trenches. Again, note the reduced scale in order to highlight subtle differences in the REE curves. Overall this lithology has low REE concentrations and flat REE curves. The most interesting feature of two of these samples, tb-PM05-007 and tb-PM05-024, is their positive Ce anomaly. Sample tb-PM05-024 also exhibits a positive Eu anomaly. The chlorite-schist samples exhibit low concentrations of REE relative to the other lithologies and positive Ce anomalies. These features suggest this lithology is a chloritic ultramafic dyke (diatreme) which may have undergone metasomatic alteration.

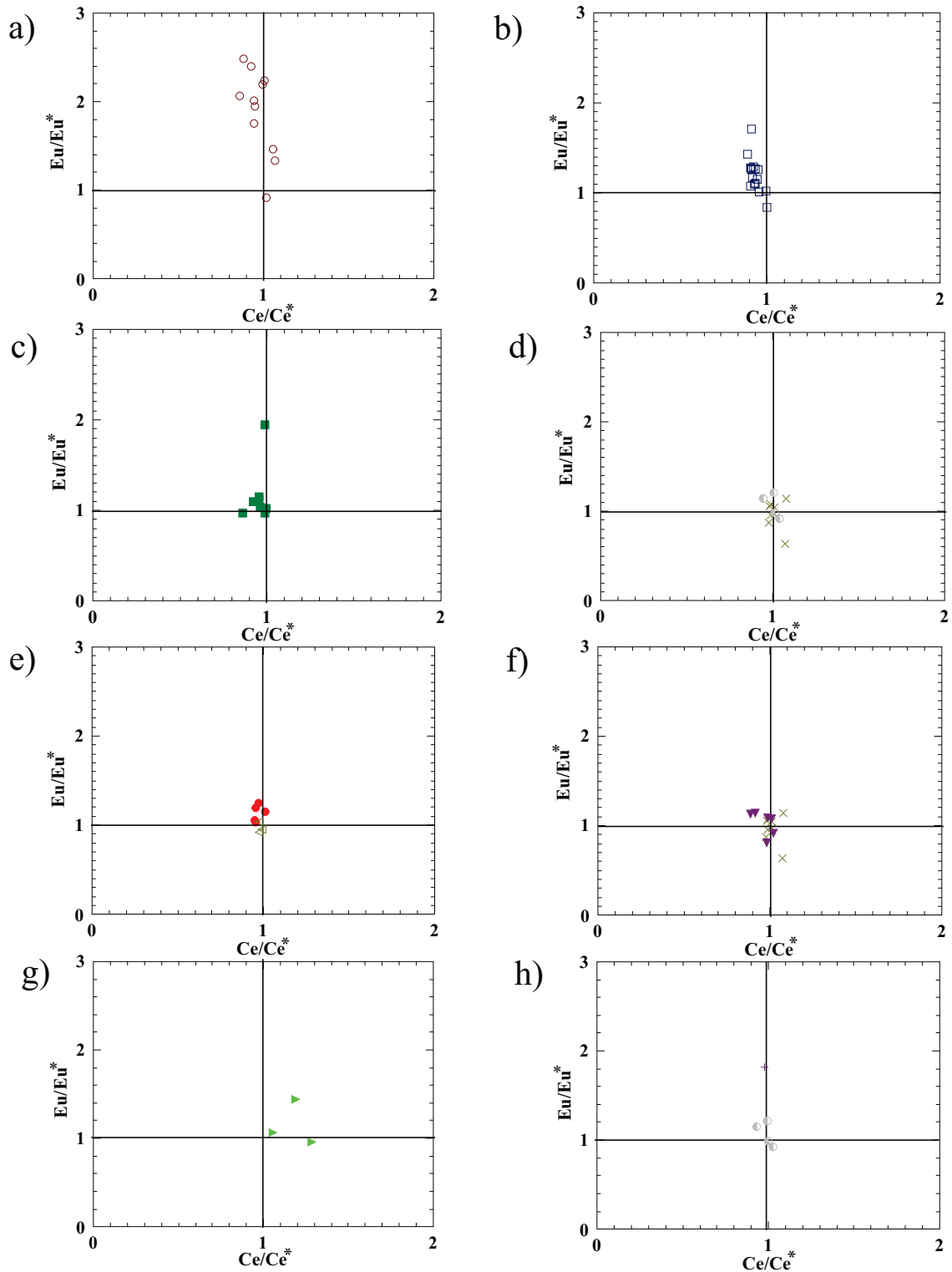
Figure 4.19h contains what was thought to be an ultramafic volcanic sample. This sample is LREE enriched, has flat HREE, and a positive Eu anomaly. This trend is indicative of an exhalite lithology and not an ultramafic igneous lithology. Due to the similarity between this curve and the exhalite curves, it is likely this sample is in fact an exhalite lithology. This lithology remains enigmatic as talc is visible in thin-section. It is possible that this sample represents weathered ultramafic sediment deposited in conjunction with hydrothermal activity.

Figures 4.20 and 4.21 contain plots of  $\text{Eu}/\text{Eu}^*$  vs.  $\text{Ce}/\text{Ce}^*$  where  $\text{Eu} = \text{Eu}/0.058$  and  $\text{Eu}^* = [0.5(\text{Sm}/0.153)] + [0.5(\text{Gd}/0.2055)]$  and  $\text{Ce} = \text{Ce}/0.612$  and  $\text{Ce}^* = [0.5(\text{Pr}/0.095)] + [0.5(\text{La}/0.2370)]$ . Note that all REE values are normalized (C1 chondrite). This plot is designed to visually represent the degree of Eu anomaly versus the degree of Ce anomaly in samples. There are two lines on the plot, one horizontal and one vertical, which intersect '1' on both the x- and y-axis. Together these lines segregate the diagram into four fields. Samples to the right of the vertical line have positive Ce anomalies. Samples plotting above the horizontal line have positive europium anomalies. The further a samples plots from the line the stronger their respective anomaly. The dominant trend in these diagrams is decreasing positive Eu anomalies stratigraphically upwards and neutral to weakly negative Ce anomalies regardless of lithology.





**Figure 4.20. Binary diagrams of Eu anomaly (y-axis) vs. Ce anomaly (x-axis). Note samples plotting over 1 on the y-axis have positive Eu anomalies, samples plotting over 1 on the x-axis have positive Ce anomalies, samples plotting below 1 on either axis represent negative anomalies.** a) Magnetite samples from the SIF, b) Quartz samples from the SIF, c) Meta-argillite samples, d) Quartz-grunerite BIF samples, e) Magnetite samples from the NIF oxide-dominant BIF (core), f) Quartz samples from the NIF oxide-dominant BIF (core), g) Magnetite samples from the SIF oxide-dominant BIF (trench), h) Quartz samples from the SIF oxide-dominant BIF (trench).



**Figure 4.21. Binary diagrams of Eu anomaly (y-axis) vs. Ce anomaly (x-axis). Note samples plotting over 1 on the y-axis have positive Eu anomalies, samples plotting over 1 on the x-axis have positive Ce anomalies, samples plotting below 1 on either axis represent negative anomalies.** a) Samples of metasomatic SIF oxide-dominant BIF (trench), b) Silicate-dominant BIF samples, c) Hornblende-garnet schist samples, d) Biotite-garnet schist and mafic volcanic samples, e) Garnet-quartzite and felsic volcanic samples, f) Metasomatic biotite-garnet schist and biotite-garnet schist samples, g) Chlorite-schist samples (trench), h) Ultramafic and mafic volcanic samples.

Figure 4.20 contains the exhalite-dominant lithologies whereas Figure 4.21 contains the siliciclastic lithologies. For the most part the REE spider diagrams are organized and discussed from stratigraphically lowest (SIF oxide-dominant BIF) to highest (garnet-bearing quartzite) lithologies. However, there are a few exceptions to this, namely, Figures 4.20g and 4.21h contain the magnetite and quartz-bands from SIF oxide-dominant BIF collected from the trenches. Also Figure 4.21a contains the grunerite-rich metasomatic oxide-BIF samples from the trenches. The trenches are several hundred metres away from the main ore-zone and placing them into the SIF assemblage stratigraphy is difficult. The reader should note that several plots in Figure 4.21 contain multiple lithologies for comparative purposes (refer to figure caption for more information).

In general the degree of the Eu anomaly is an indication of the intensity of the hydrothermal activity at the time of deposition. A negative Eu anomaly indicates no hydrothermal influence on the deposition of sediment and is a common feature in seafloor mud (Peter, 2003). A strong positive Eu anomaly indicates high temperature exhalative activity. However, it should be noted that during the Archean hydrothermal activity was so abundant that it imparts a background signature to most chemical sediments deposited at this time. This revelation does not undermine the Algoma-type nature of the oxide-dominant BIF at Musselwhite. This topic is discussed, in greater detail, in Chapter Five.

Figures 4.20a and 4.20b contain the SIF magnetite and quartz samples, respectively. Figure 4.20a shows that the majority of the magnetite samples, except for one anomalous sample (SIF-07-20-072m), exhibit strong positive Eu anomalies. Similarly, Figure 4.20b shows that the quartz samples also have strong positive Eu anomalies. Both magnetite and quartz samples have weak negative Ce anomalies. Overall samples of the SIF oxide-dominant BIF consistently have the strongest positive Eu anomalies of all lithologies sampled.

Figure 4.20c contains samples of the meta-argillite. Samples of this lithology exhibit consistent slightly negative to neutral Ce anomalies. However Eu anomalies are less consistent and range from moderate to strongly positive. There is one anomalous sample which has a negative Eu anomaly (4h-07-20-051).

Figure 4.20d contains the quartz-grunerite BIF samples. Samples from this lithology exhibit a range of Eu anomalies from moderate to strongly positive. Samples of Quartz-grunerite BIF have slightly more pronounced negative Ce anomalies, exhibiting a less consistent trend, relative to samples of the meta-argillite but similar to magnetite samples from the SIF.

Figures 4.20e and 4.20f contain the oxide-dominant BIF magnetite and quartz samples, respectively. These samples are from the NIF assemblage BIF. Interestingly there does not appear to be much difference between the two sample sets. Both the magnetite and quartz samples exhibit; 1) Eu anomalies that range from weak to strongly positive and 2) Ce anomalies that range from roughly neutral to weakly negative. Both magnetite and quartz samples from the oxide-dominant BIF exhibit more scatter than the previously discussed lithologies.

Figures 4.20g and 4.20h contain the oxide-dominant BIF magnetite and quartz samples, respectively. These samples are collected from the trench oxide-dominant BIF. The magnetite samples exhibit consistently strong positive Eu anomalies relative to magnetite samples collected from drill core.

Interestingly the quartz samples display the most variation in Eu and Ce anomalies out of all the lithologies collected. Samples range from having strong to zero positive Eu anomalies and slightly positive Ce to moderately negative Ce anomalies. This scatter may be an indication of preferential metasomatic alteration of the quartz bands in the oxide-dominant BIF collected from the trenches. This hypothesis is supported by the presence of abundant secondary grunerite in thin sections and hand samples. This raises additional questions about the relationship between the oxide-dominant BIF in the trenches relative

to that in the core (i.e., mine stratigraphy). This topic is discussed, in greater detail, in Chapter Five.

Figure 4.21a contains samples of the metasomatic oxide-dominant BIF collected from the trenches. Eu anomalies range from weakly to strongly positive and Ce anomalies range from moderately negative to weakly positive. This lithology has comparable Eu and Ce anomalies to the oxide-dominant BIF magnetite and quartz samples.

Figures 4.21b-h contain the siliciclastic dominant lithologies. It is important to note that some of these diagrams have multiple lithologies plotted on them for comparative purposes. In general, samples of lithologies with a siliciclastic component plot close to the intersection of the horizontal and vertical lines relative to the previously discussed lithologies. This indicates these lithologies have subdued Eu and Ce anomalies. The subdued nature of the anomalies is the result of the high siliciclastic content of the lithologies. The siliciclastic component has REE concentrations multiple times higher than any exhalite component these samples may contain thus masking the exhalite signature.

Figure 4.21b contains samples of the silicate-dominant BIF. Samples range from having moderately developed positive Eu anomalies with slight negative Ce anomalies to slightly negative Eu anomalies with neutral Ce anomalies. Together these samples form a concise slightly negative linear correlation between increasingly positive Ce anomalies and decreasing intensity of Eu anomalies.

Figure 4.21c contains the hornblende-garnet schist samples. The majority of the samples have a slightly positive Eu anomaly and a slightly negative Ce anomaly. For the most part samples cluster around the “1, 1” origin and have a weak negative correlation between increasing Ce and decreasing Eu anomalies. This is similar to the trend formed by silicate-dominant BIF samples. There is one obvious anomalous sample, 4e-07-20-047, with a strong positive Eu anomaly.

Figure 4.21d contains the biotite-garnet schist and mafic volcanic samples. Note that the mafic volcanic samples have been included for comparison. These samples plot in a concise group. The majority of samples exhibit neutral Ce anomalies and Eu anomalies, which range from slightly negative to slightly positive. Samples from both lithologies cluster around the “1, 1” origin indicating subdued Eu or Ce anomalies. There is one anomalous sample which has a moderate negative Eu anomaly (4f-07-20-027a). It is important to note that this sample also contains a high concentration of andalusite.

Figure 4.21e contains the garnet-bearing quartzite and felsic volcanic samples. Note that the felsic volcanic samples have been included for comparative purposes. The garnet-bearing quartzite samples plot in a tight group close to the ‘1, 1’ origin indicating subdued Eu and Ce anomalies. Interestingly and unexpectedly, samples of the garnet-bearing quartzite exhibit weak positive Eu anomalies suggesting the presence of abundant plagioclase as opposed to an exhalite component. The reader should note that the felsic volcanic samples do not display Eu anomalies.

Figure 4.21f contains samples of both metasomatic biotite-garnet schist and regular biotite-garnet schist. The biotite-garnet schist has already been discussed above and is simply included for comparison due to the similar mineralogy between the two lithologies. Interestingly, the metasomatic biotite-garnet schist samples overlap with the regular biotite-garnet schist samples. This simply indicates that these lithologies have near negligible Eu and Ce anomalies.

Figure 4.21g contains the chlorite-schist samples. Samples exhibit neutral to moderately positive Eu anomalies. This lithology is very interesting because it is the only lithology with samples that exhibit positive Ce anomalies. It should be noted that positive Ce anomalies can be an indication of metasomatic alteration.

Figure 4.21h contains the ultramafic volcanic sample. The mafic volcanic samples have been included for comparative purposes. This sample exhibits a strong positive Eu anomaly and no Ce anomaly. The mafic volcanic samples do not exhibit Eu or Ce anomalies. The positive Eu anomaly, exhibited by the ultramafic sample, is more in line

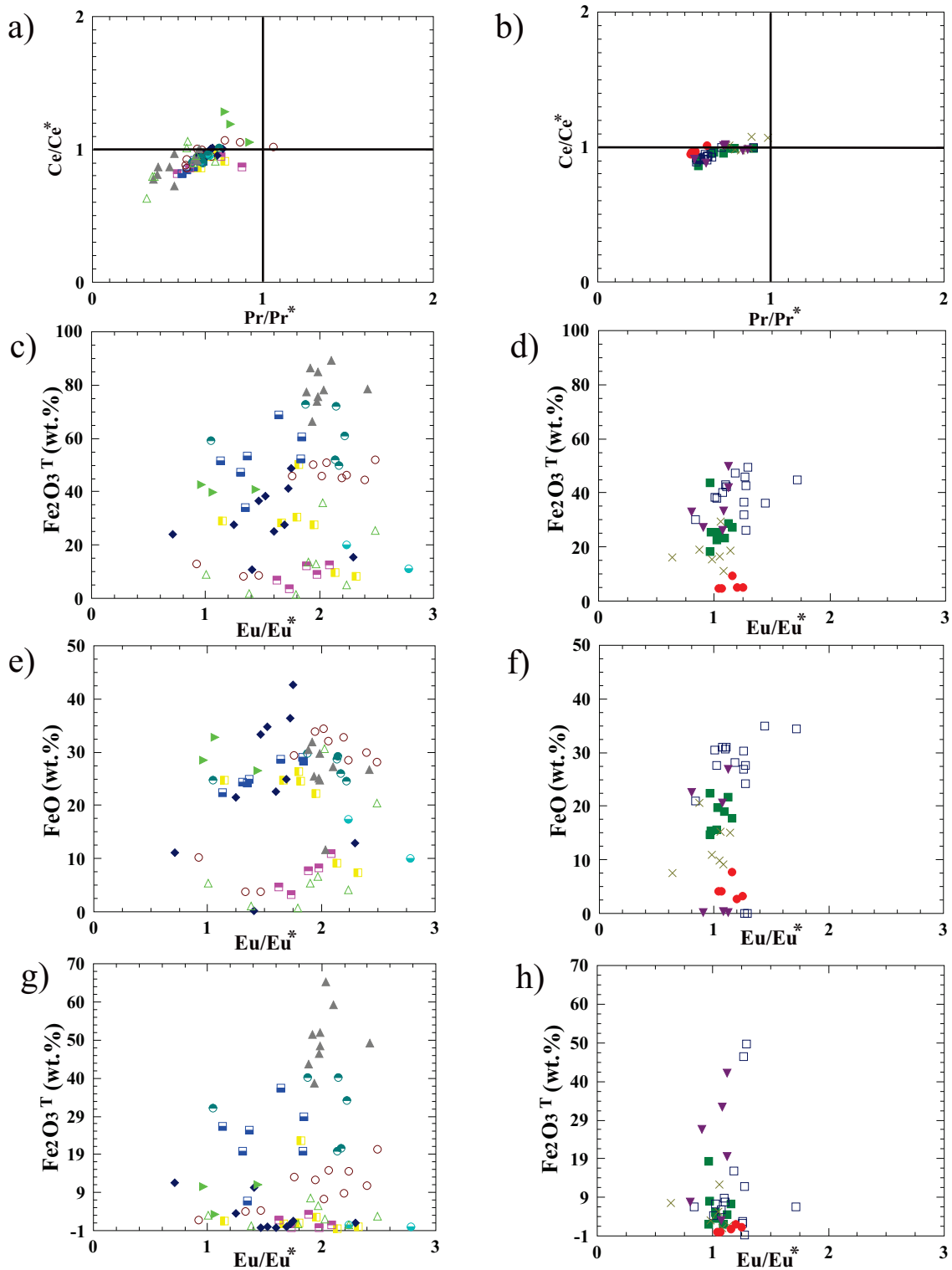
with the exhalite-dominated lithologies. The geochemistry of this sample is enigmatic and will be explained in further detail in Chapter Five.

Figures 4.22a and 4.22b contain plots of  $Ce/Ce^*$  vs.  $Pr/Pr^*$  for the exhalite and siliciclastic dominant lithologies respectfully. The reader should note that  $Ce = Ce/0.612$  and  $Ce^* = [0.5(Pr/0.095)] + [0.5(La/0.2370)]$  whereas  $Pr = Pr/0.095$  and  $Pr^* = [0.5(Ce/0.095)] + [0.5(Nd/0.467)]$ . All REE values are normalized (C1 chondrite). This plot is designed to visually represent the degree of cerium anomaly versus the degree of praseodymium anomaly in samples. There are two lines on the plot, one horizontal and one vertical, which intersect '1' on both the x- and y-axis. Together these lines segregate the diagram into four fields. Samples to the right of the vertical line have positive Pr anomalies. Samples plotting above the horizontal line have positive Ce anomalies. The further a samples plots from the line the stronger their respective anomaly.

The dominant trend in these diagrams, regardless of lithology, is weak to moderately negative Pr anomalies and neutral to weakly negative Ce anomalies. Note that the exhalite samples, in Figure 4.22a, exhibit a positive linear correlation between increasingly positive Pr anomalies and increasingly positive Ce anomalies. In Figure 4.22b the clastic-dominated lithologies exhibit a subdued positive linear correlation between  $Ce/Ce^*$  and  $Pr/Pr^*$ .

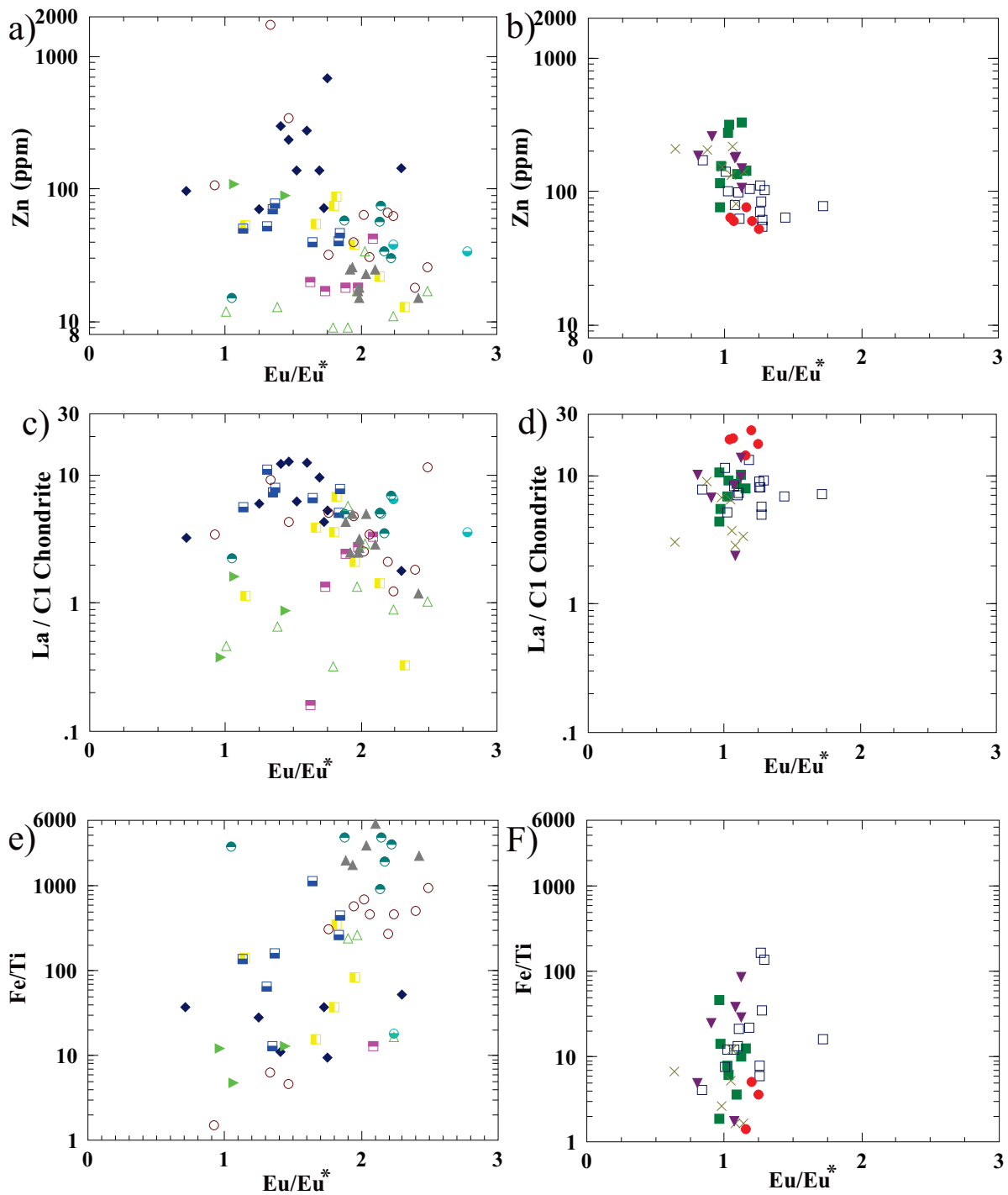
The remaining plots in Figures 4.22 and 4.23 are binary diagrams with various elements plotted on the y-axis versus  $Eu/Eu^*$  on the x-axis. The plots are designed to see if there is a correlation between these elements and the degree of a sample's Eu anomaly. Since a pronounced Eu anomaly indicates high-temperature hydrothermal black smoker activity correlation suggests that the element on the y-axis is related to this activity.

Establishing the relationship between Eu anomalies and various elements is important in understanding where these elements came from. Many other iron formations exhibit clear geochemical links between their Eu anomalies and element concentrations. This is an indication of coprecipitation, as hydrothermal oxides and sulfides, through interaction of hydrothermal fluid and seawater (Peter, 2003).



**Figure 4.22. Various binary diagrams relating the Eu, Ce, and Pr anomalies to various elements.** a) Ce/Ce\* vs. Pr/Pr\* for exhalite-dominant lithologies, b) Ce/Ce\* vs. Pr/Pr\* for siliciclastic-dominant lithologies, c) Fe<sub>2</sub>O<sub>3</sub>T vs. Eu/Eu\* for exhalite-dominant lithologies, d) Fe<sub>2</sub>O<sub>3</sub>T vs. Eu/Eu\* for siliciclastic-dominant lithologies, e) FeO vs. Eu/Eu\* for exhalite-dominant lithologies, f) FeO vs. Eu/Eu\* for siliciclastic-dominant lithologies, g) Fe<sub>2</sub>O<sub>3</sub>T vs. Eu/Eu\* for exhalite-dominant lithologies, h) Fe<sub>2</sub>O<sub>3</sub>T vs. Eu/Eu\* for siliciclastic-dominant lithologies.





**Figure 4.23. Various binary diagrams relating Eu anomalies to various elements.** a) Zn vs.  $Eu/Eu^*$  for the exhalite-dominant lithologies, b) Zn vs.  $Eu/Eu^*$  for the siliciclastic-dominant lithologies, c) C1 normalized La vs.  $Eu/Eu^*$  for the exhalite-dominant lithologies, d) C1 normalized La vs.  $Eu/Eu^*$  for the siliciclastic-dominant lithologies, e) Fe/Ti vs.  $Eu/Eu^*$  for the exhalite-dominant lithologies, f) Fe/Ti vs.  $Eu/Eu^*$  for the siliciclastic-dominant lithologies.

The general trends, observed in Figures 4.22 and 4.23, are that the exhalite-dominant samples exhibit more variable iron concentration and Eu anomalies compared to the siliciclastic-dominant lithologies. The siliciclastic-dominant lithologies exhibit more concise Eu anomalies, compared to the exhalite-dominant lithologies, and tend to cluster together by lithology. However, overall there does not appear to be a correlation between  $\text{Fe}_2\text{O}_3^{\text{T}}$ , FeO,  $\text{Fe}_2\text{O}_3$ , and Zn with Eu/Eu\*. These are the elements normally associated with hydrothermal black smoker exhalative precipitates.

It should be noted that there is a weak negative correlation between  $\text{La}_n/\text{C1}$  Chondrite and Eu/Eu\* in the exhalite-dominant lithologies (Fig. 4.23c). Figures 4.23e and 4.23f depict the ratio of Fe/Ti plotted against the Eu anomaly of each sample. There is a moderate positive linear relationship between Fe/Ti versus Eu/Eu\*. This indicates decreasing Ti values and increasing Fe values relative to Eu/Eu\*.

However, Figures 4.22 and 4.23, show that there is minimal correlation between the various elements and the degree of the Eu anomalies in the samples from Musselwhite. This raises an interesting quandary over the SIF and NIF assemblages at Musselwhite. These are Algoma-type iron-formations and it is well known that iron in Algoma-type iron-formations originated from hydrothermal sources (e.g., Jacobsen and Pimentel-Klose, 1988). So why is there no positive correlation at least between  $\text{Fe}_2\text{O}_3^{\text{T}}$  and Eu/Eu\* in the Musselwhite dataset? This topic is discussed, in more detail, in Chapter Five.

#### 4.7 Metasomatic Alteration

Section 4.7 serves to address the subject of ‘hydrothermal alteration’, henceforth referred to as metasomatic alteration, within the rocks of the Musselwhite gold deposit. Metasomatic alteration is used because this terminology is more appropriate considering the metamorphic nature of the Musselwhite gold deposit. Metasomatic alteration refers to the chemical development of a rock, which is part of an open metamorphic system, as it reacts with fluids derived from an external source. This process may occur through a number of ways depending on the physical conditions under which the rock exists. At low pressure fluid flow dominates whereas at high-pressure metasomatism occurs through grain-boundary diffusion (Neuendorf *et al.*, 2005).

Enrichment of alkali elements is typically associated with gold mineralization (Kerrick, 1983). An important observation noted by the mine geologists, and confirmed by the author, is the presence of apparently secondary metasomatic biotite-garnet schist. Consequently, much of the Section 4.7 is focused around alkali element mobility and utilizing this characteristic as a possible vector to gold mineralization.

The alkali elements, in orogenic gold deposits, are derived from the breakdown of feldspars (Kerrick, 1983). The breakdown of feldspars releases K, Cs, Rb, and other LILE into the weathering/diagenetic/metamorphic system. The liberated alkali elements are preferentially incorporated into crystallizing secondary micas. Sericite is the stable mica at greenschist facies, whereas biotite is stable at higher metamorphic facies (Mikucki and Ridley, 1993). The rocks at Musselwhite are between mid-greenschist to amphibolite facies and contain zero to abundant biotite. Therefore alkali distribution patterns may provide useful information on ‘fluid pathways’ (Heath and Campbell, 2004).

Some of the lithologies at Musselwhite, specifically the biotite-garnet schist and garnet-bearing quartzite, contain abundant metamorphic biotite. As such, it is important to note that Cs and Rb may be better indicators of fluid flow than potassium; because, Cs and Rb can replace potassium in micas resulting in significant LILE exchange between fluid and rock (Melzer, 1999).

Heath and Campbell (2004) devised an ‘alkali alteration index’ based on the above described properties of alkali elements in gold deposits. They note that in their sample set, consisting of Paringa basalts from the Golden Mile, potassium exhibited the least variability and Cs the most variability. In their study the best alteration index is the ratio  $((Cs+Rb)/Th)_N$  where  $_N$  is normalization using primitive mantle values of Sun and McDonough (1989).

The alkali alteration index can be used as a vector to gold mineralization because, theoretically, the closer a sample is to mineralization the higher its ratio of  $((Cs+Rb)/Th)_N$ . A  $((Cs+Rb)/Th)_N$  value of 5, based on empirical evidence, was used to distinguish between depleted ( $<5$ ) and enriched ( $>5$ ) samples. Samples with values  $\gg 5$

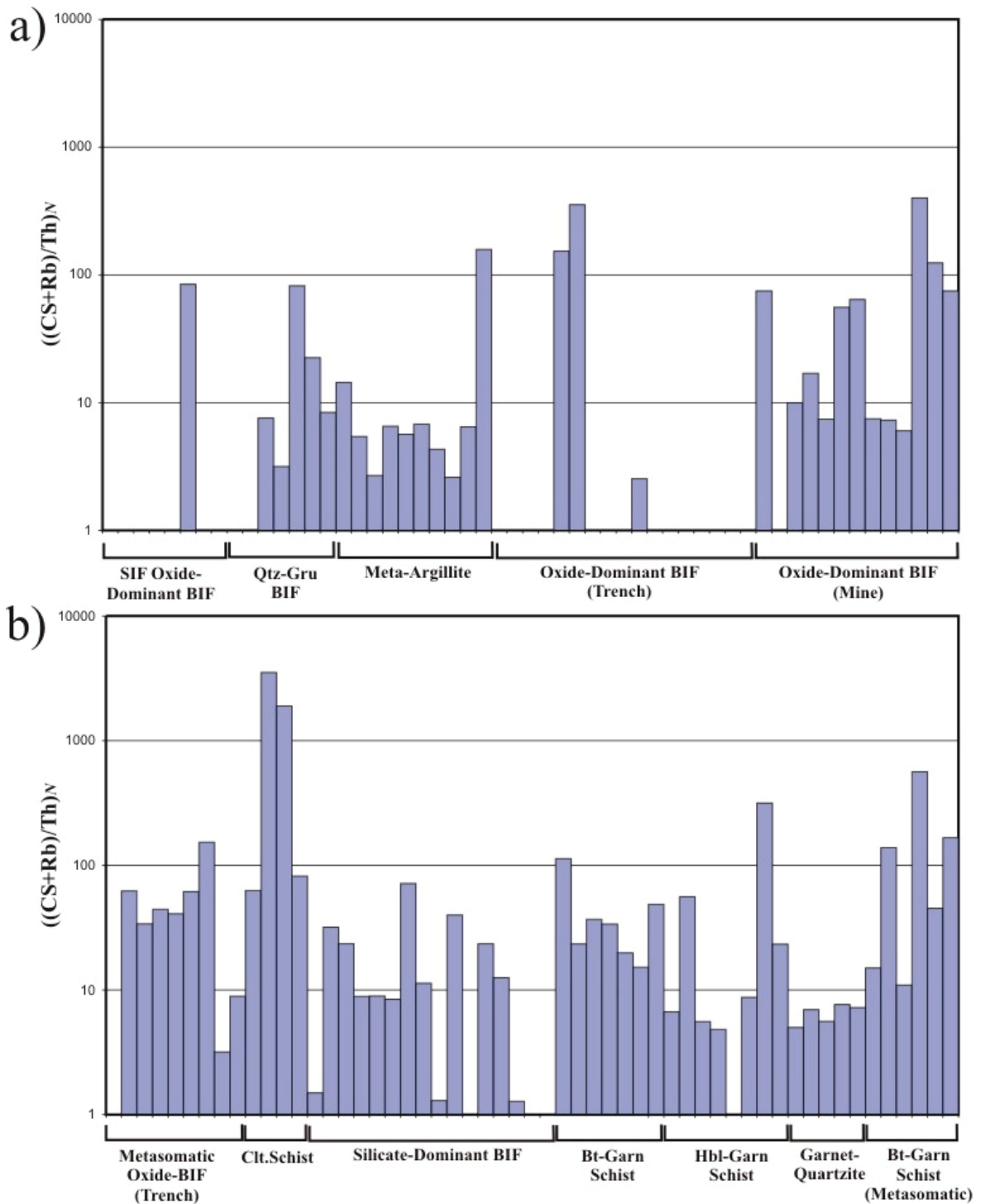
represent rocks which have interacted extensively with fluids, presumably mineralizing, rich in LILE.

Figures 4.24a and 4.24b are histograms that depict the  $((Cs+Rb)/Th)_N$  value for individual samples. Note the y-axis is logarithmic. Figure 4.24a contains the exhalite-dominant lithologies and Figure 4.24b contains the siliciclastic-dominant lithologies. Samples from the lithologies at Musselwhite exhibit a diverse array of  $((Cs+Rb)/Th)_N$  values ranging from 0 to  $\gg 5$  suggesting zero to very strong alkali enrichment.

Figure 4.24a contains samples from the exhalite dominant lithologies. In general the SIF oxide-dominant BIF and the trench oxide-dominant BIF samples do not exhibit alkali alteration. A potential explanation for the lack of alkali alteration is the distal nature of these lithologies to the mineralized zones. This is reinforced by the pattern of alkali alteration exhibited by the NIF assemblage oxide-dominant BIF samples from core. These samples are closer to mineralization and exhibit pronounced alkali index of alteration values. However, it should be noted that the chlorite-schist and the metasomatised oxide-dominant BIF from the trenches do exhibit strong alkali index of alteration values (in fact a chlorite schist sample in Figure 4.24b, has the highest alkali anomaly out of all the samples collected).

Figure 4.24b contains the siliciclastic-dominant, as well as metasomatically-altered, lithologies (the reader should note that the metasomatically altered lithologies were preliminarily deemed such, by the author, based on their stratigraphic relations, mineralogy, and petrographic characteristics). The biotite-garnet schist, hornblende-garnet schist, and garnet-bearing quartzite each have a mean  $((Cs+Rb)/Th)_N$  value of  $>5$ . The garnet-bearing quartzite anomalies are very consistent relative to the other lithologies. In general, the siliciclastic lithologies exhibit pronounced alkali index of alteration values. The reader should note that the biotite-garnet schist, since it is already biotite-rich, could possibly take up Cs and Rb more easily.

The metasomatic biotite-garnet schist, and metasomatised oxide-dominant BIF samples (trench) exhibit the most consistent  $\gg 5$  alkali index of alteration values suggesting these



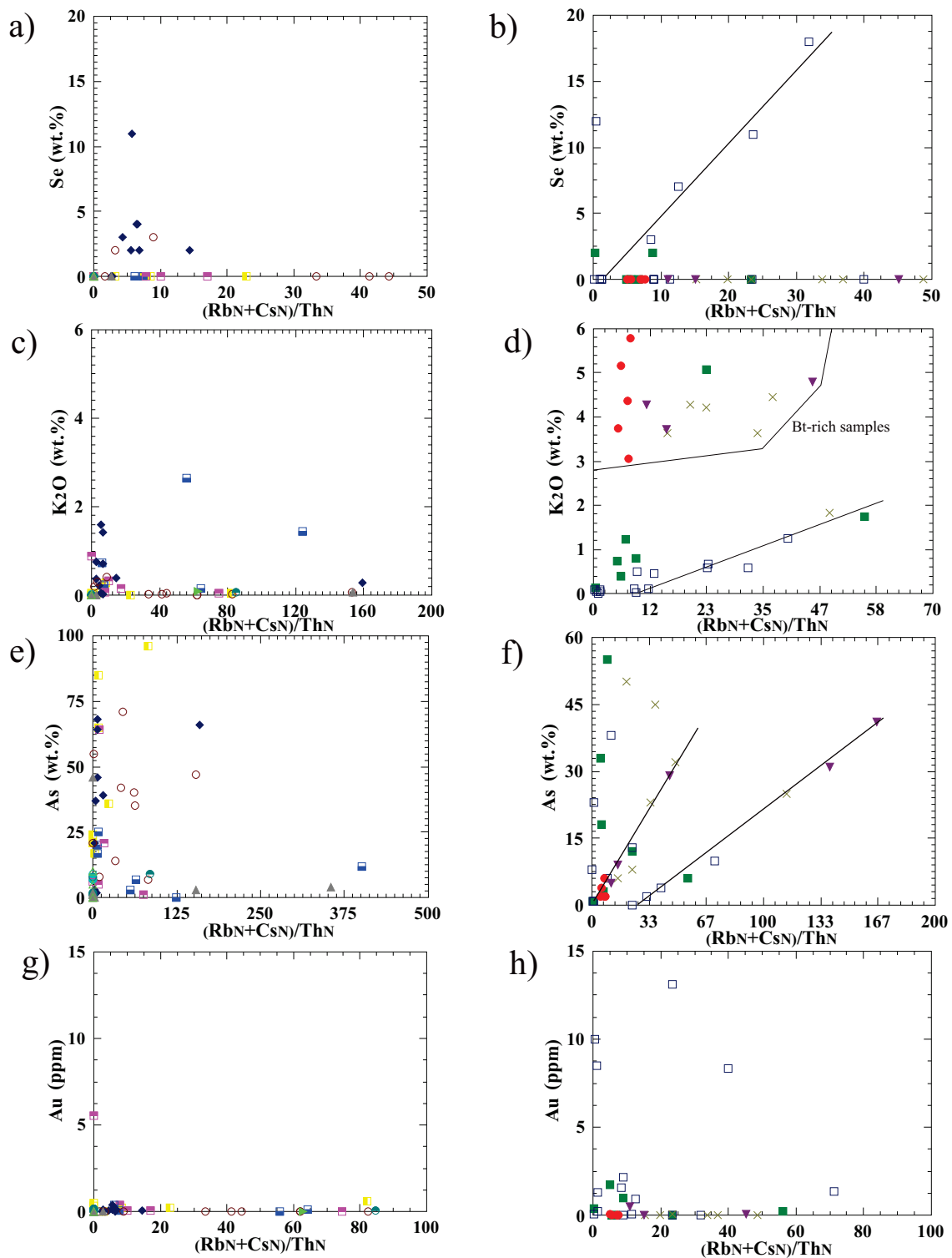
**Figure 4.24. Histograms displaying the  $((Cs+Rb)/Th)N$  values for individual samples.** a) Exhalite-dominant lithologies, b) Siliciclastic-dominant lithologies. Individual bars represent single samples. Samples are grouped together by lithology as indicated by the horizontal brackets. Note the following: SIF= SIF assemblage oxide-dominant BIF, Qtz-Gru BIF= quartz-grunerite BIF, Clt.Schist= chlorite schist, Bt-Garn Schist= biotite-garnet schist, Hbl-Garn Schist= hornblende-garnet schist, and Bt-garn Schist (Metasomatic)= metasomatic biotite-garnet schist.

lithologies are associated with fluid pathways. Interestingly, samples of the silicate-dominant BIF exhibit minimal alkali index of alteration values. This suggests  $((Cs+Rb)/Th)_N$  is not an appropriate geochemical indicator of gold mineralization within the silicate-dominant BIF. However it may be a useful tool for regional gold exploration.

Figure 4.25 expands on the histograms depicted in Figure 4.24. It contains various Harker diagrams of  $((Cs+Rb)/Th)_N$  as the x-variant plotted against a variety of elements, associated with gold mineralization, on the y-axis. Figures 4.25a, c, e, and g contain the exhalite-dominant lithologies. The reader should note the exhalite-dominant lithologies do not form discernable trends in these plots. They are therefore not discussed, but included for comparison. Figures 4.25b, d, f, and h contain the silicate-dominant lithologies.

Figure 4.25b depicts  $((Cs+Rb)/Th)_N$  vs. Se for the siliciclastic-dominant lithologies. A strong positive linear correlation is formed by four silicate-dominant BIF samples and one hornblende-garnet schist sample. This indicates Se, in these samples, is likely being brought in with the alkali enriched fluids. It is important to note that Se substitutes for sulphur in sulfide minerals: an indication that sulphur is also being transported in alkali enriched fluids. This trend is significant because Au is strongly associated with pyrrhotite in the silicate-dominant BIF. A positive correlation between Se/S and  $((Cs+Rb)/Th)_N$  lends credence to the alkali index of alteration being a reliable vector to gold mineralization.

Figure 4.25d depicts  $((Cs+Rb)/Th)_N$  versus  $K_2O$  for the siliciclastic-dominant lithologies. The samples form two groups 1) a high  $K_2O$  group consisting of biotite-garnet schist, metasomatic biotite-garnet schist, garnet-bearing quartzite, and 2) a low  $K_2O$  group consisting of silicate-dominant BIF and hornblende-garnet schist. A positive linear correlation between  $((Cs+Rb)/Th)_N$  and  $K_2O$  is observed in the latter group. The positive linear correlation indicates there was some  $K_2O$  addition associated with the alkali-rich mineralizing fluids in the silicate-dominant BIF and hornblende-garnet schist. However, the main group of  $K_2O$  enriched samples do not correlate with the  $((Cs+Rb)/Th)_N$  enrichment event. These samples contain abundant primary biotite.



**Figure 4.25** Harker binary plots displaying  $((Cs+Rb)/Th)N$  as the x-variante versus various elements associated with gold mineralization (as the y-variante). a)  $((Cs+Rb)/Th)N$  vs. Se for exhalite-dominant lithologies, b)  $((Cs+Rb)/Th)N$  vs. Se for siliciclastic-dominant lithologies, c)  $((Cs+Rb)/Th)N$  vs  $K_2O$  for exhalite-dominant lithologies, d)  $((Cs+Rb)/Th)N$  vs  $K_2O$  for siliciclastic-dominant lithologies, e)  $((Cs+Rb)/Th)N$  vs. As for exhalite-dominant lithologies, f)  $((Cs+Rb)/Th)N$  vs. As for siliciclastic-dominant lithologies, g)  $((Cs+Rb)/Th)N$  vs. Au for exhalite-dominant lithologies h)  $((Cs+Rb)/Th)N$  vs. Au for siliciclastic-dominant lithologies

Figure 4.25f depicts  $((Cs+Rb)/Th)_N$  versus As for the siliciclastic-dominant lithologies. It should be noted that arsenopyrite is commonly associated with Au mineralization in orogenic gold deposits and that is why this diagram is relevant. Two separate positive linear trends are present in Figure 4.25f. Both these trends contain samples from the same lithologies. However, both trends appear to be associated with alkali enrichment as they contain samples of metasomatic biotite-garnet schist.

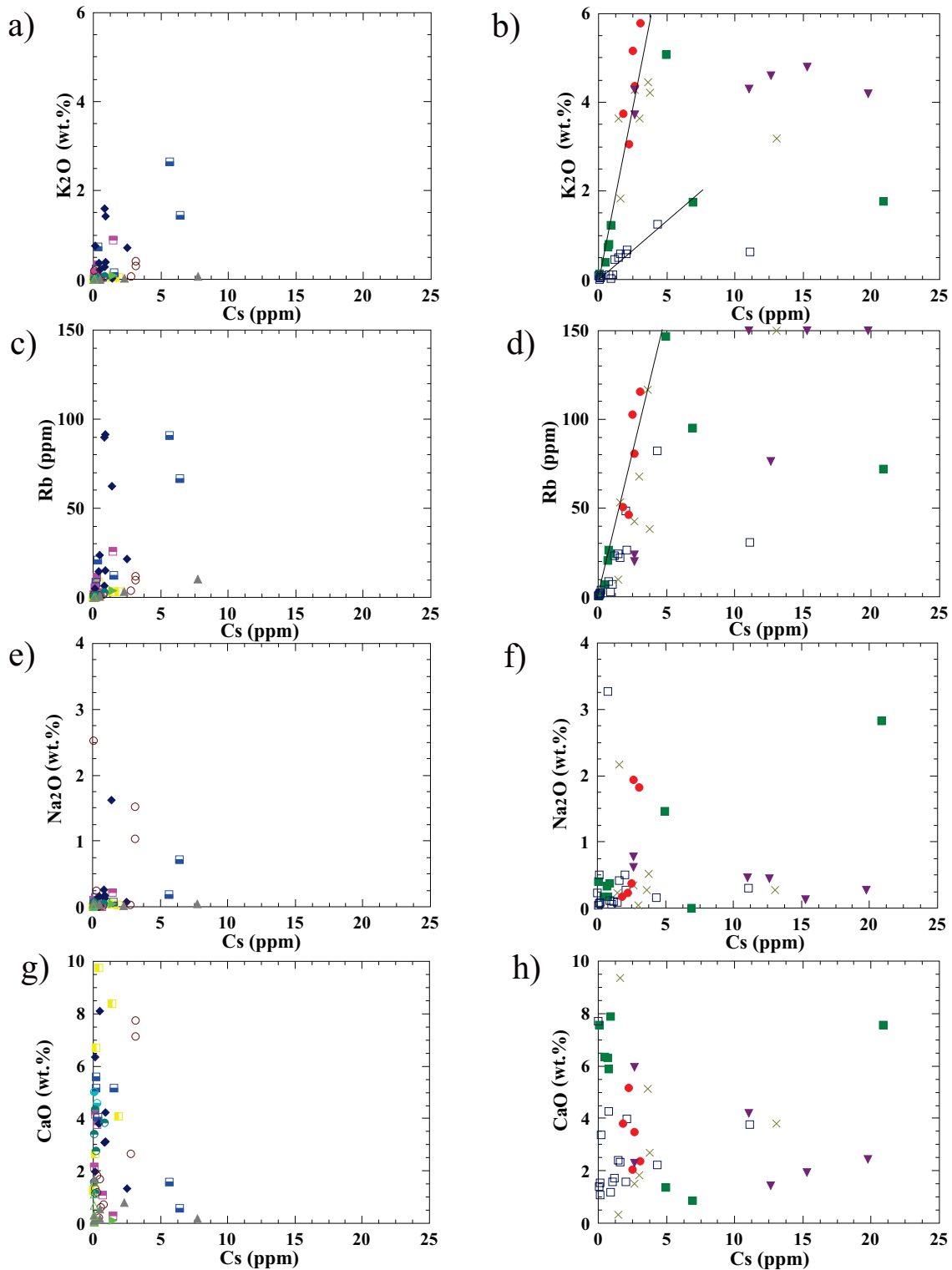
Figure 4.25h depicts  $((Cs+Rb)/Th)_N$  versus Au. Two of the four highest gold values also have high  $((Cs+Rb)/Th)_N$ . Overall, there does not appear to be a correlation between the alkali index of alteration and gold mineralization (possibly the result of low resolution gold measurements).

Figure 4.26 expands on the histograms depicted in Figure 4.24 and Figure 4.25. This figure consists of binary-diagrams with Cs as the x-variant plotted against a variety of elements, associated with metasomatic alteration, on the y-axis. Figures 4.26a, c, e, and g contain the exhalite-dominant lithologies. The reader should note the exhalite-dominant lithologies do not form discernable trends in these plots. They are therefore not discussed, but included for comparative purposes. Figures 4.25b, d, f, and h contain the silicate-dominant lithologies.

Figure 4.26b depicts Cs vs.  $K_2O$  for the siliciclastic-dominant lithologies. The samples form two positive linear trends in Figure 4.26b. A steep positive linear trend primarily delineated by samples of the hornblende-garnet schist, biotite-garnet schist, and garnet-bearing quartzite. This is likely the result of the high concentration of original biotite in these lithologies. A second, shallower positive linear trend is delineated by samples of the silicate-dominant BIF. This shallower trend is likely the result of mobilization of alkali elements associated with the mineralization of the silicate-dominant BIF.

Figure 4.26d depicts Cs vs. Rb for the siliciclastic-dominant lithologies. Samples from all the siliciclastic-dominant lithologies form a weak positive linear correlation between Cs and Rb on this diagram. The remaining Figures, 4.26f and 4.26h, contain Cs vs.  $Na_2O$  and CaO, respectively. Samples from all lithologies exhibit a scattered nature and do not form coherent trends.





**Figure 4.26. Binary plots of Cs versus various elements associated with metasomatic alteration. Note that linear trend-lines are based on visual observations.** a) Cs vs. K<sub>2</sub>O for exhalite-dominant lithologies, b) Cs vs. Rb for siliciclastic-dominant lithologies, c) Cs vs. Rb for exhalite-dominant lithologies, d) Cs vs. Rb for siliciclastic-dominant lithologies, e) Na<sub>2</sub>O vs. Cs for exhalite-dominant lithologies, f) Na<sub>2</sub>O vs. Cs for siliciclastic-dominant lithologies, g) Cs vs. CaO for exhalite-dominant lithologies, h) Cs vs. CaO for siliciclastic-dominant lithologies.

#### 4.8 Alteration Dendrograms

Figure 4.27 is a cluster analysis dendrogram comparing all samples for which there are gold values (n=72). This dendrogram was produced by the same means as the dendrograms presented earlier in Chapter Four. Please refer to section 4.2 for a detailed description of the methodology behind their generation. It should be noted that samples are compared through factor analysis to see how closely they are related. This is opposed to the earlier dendrograms where elements are compared. Samples are compared to see if they plot together by lithology and/or mineralogy. In theory this is how they should group together.

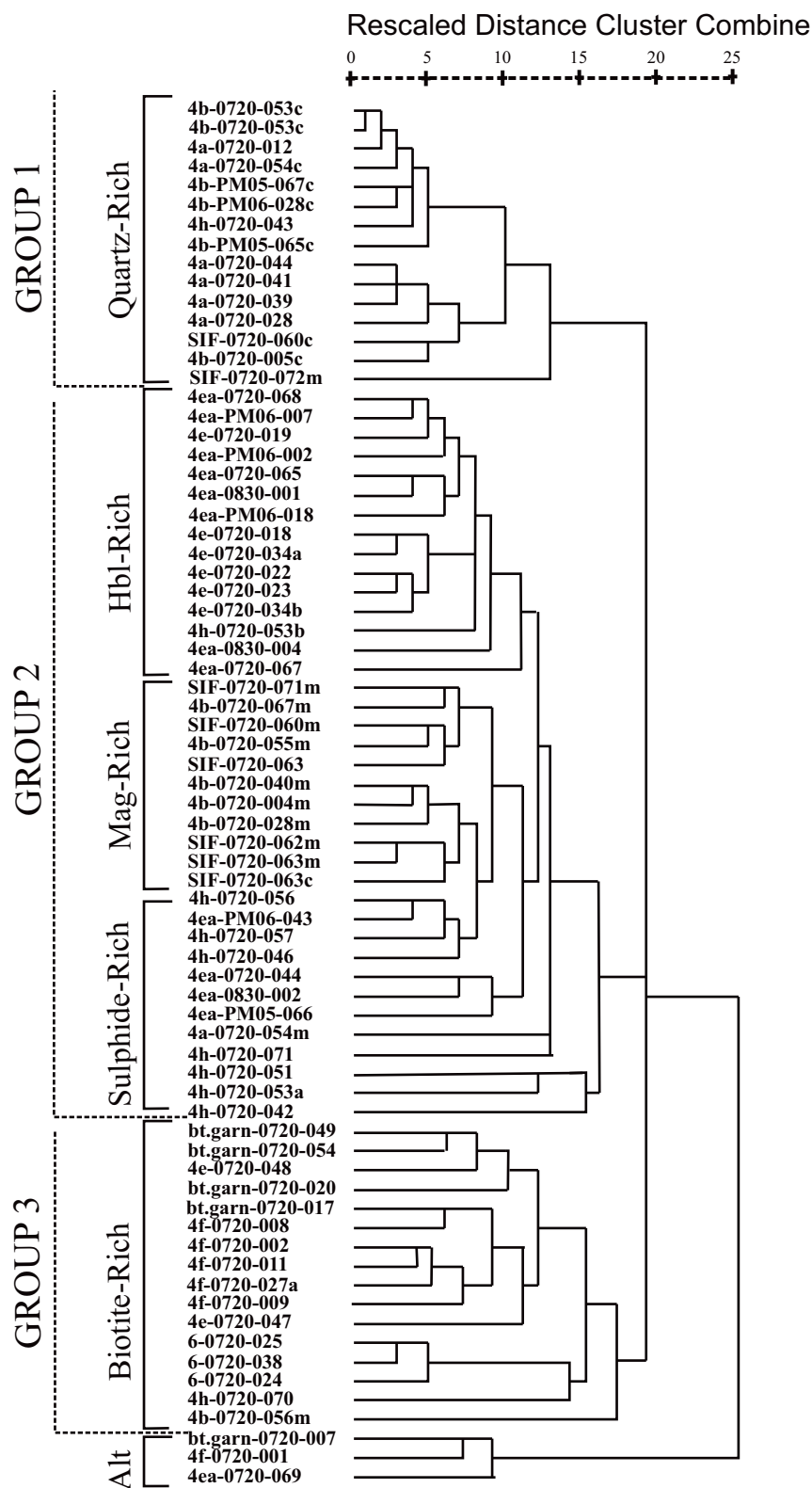
The majority of samples, in this dendrogram, group together based on a common lithology and/or mineralogy. It should be noted that there does not appear to be a subgroup of samples with high Au values or an alteration sub-group. The sample groups are primarily based on the original sample chemistry, which is reflected by the sample's mineralogy. Samples can be broadly divided into three main groups. These groups are termed group one: consisting of quartz-rich samples, group two: consisting of transitional exhalite- to silicate-dominant samples, and three: consisting solely of siliciclastic-dominant samples.

Group One is formed by SIF and NIF assemblage quartz-dominant samples, as well as quartz-grunerite BIF samples. These samples group together because they are composed primarily of quartz.

Group Two is the largest group of samples. This group is formed from the following lithologies: meta-argillite, SIF and NIF assemblage magnetite, hornblende-garnet schist, and silicate-dominant BIF samples. These samples group together for various reasons.

It is evident, from the dendrogram, that a number of smaller subgroups form Group Two. These subgroups appear to be controlled by the mineralogy of the samples. The subgroups are as follow: hornblende- and garnet-rich, magnetite-rich, and sulphide-rich sample groupings. Note that these groups are delineated by brackets in Figure 4.27.

The hornblende- and garnet-rich subgroup is formed from samples of the hornblende-



**Figure 4.27.** Cluster analysis dendrograms for seventy-two samples (these are the samples for which Au values were available) from the NIF assemblage at Musselwhite gold deposit. Samples can be broadly divided into three groups. Note samples which behaved in a similar manner plot closest to each other on the dendrogram.

garnet schist and silicate-dominant BIF. Both of these lithologies can contain abundant hornblende and garnet, which are a reflection of their high  $\text{Al}_2\text{O}_3$  and  $\text{FeO}$  concentrations.

The magnetite-rich subgroup is formed from the NIF assemblage and SIF magnetite-dominant samples. These are the magnetite samples separated from the oxide-dominant banded iron formation lithologies. Both of these lithologies contain abundant magnetite which is a reflection of their high  $\text{Fe}_2\text{O}_3^{\text{T}}$  concentrations.

The sulphide-rich subgroup is formed from samples of the meta-argillite and silicate-dominant BIF. Both of these lithologies can contain abundant pyrrhotite, which is a reflection of their high  $\text{Fe}_2\text{O}_3^{\text{T}}$  and sulphur concentrations.

Group Three is roughly the same size as Group One in terms of the number of samples it contains. This group is formed from the following lithologies: biotite-garnet schist, metasomatic biotite-garnet schist, and garnet-bearing quartzite samples. These lithologies group together due to their high potassium and alkali-element concentrations. The high concentration of these elements is reflected by abundant biotite in these lithologies. The reader should note that the metasomatic biotite-garnet schist is part of Group Three as opposed to plotting in a separate alteration group.

The final group is formed by three samples, which are significantly different from the other samples in this factor analysis collection. It is hypothesised that their chemistry has been significantly affected by alteration. The samples forming this group are one of each of the following: biotite-garnet schist, a silicate-dominant BIF, and metasomatic biotite-garnet schist. The geochemical dissimilarity these samples exhibit, to the rest of the samples, is highlighted by the fact they are the last set of samples linking into the dendrogram. One likely reason these samples group together is their potassium content since all three lithologies can contain abundant biotite. However, the reason these samples do not cluster with the above mentioned samples is enigmatic.

Figure 4.28 is another cluster analysis dendrogram. As mentioned above this dendrogram was produced by the same means as the dendrograms presented earlier in Chapter Four. However, this dendrogram differs from the one in Figure 4.27 in that it is comparing the entire database of samples ( $n=106$ ). The reader should note that gold values were omitted

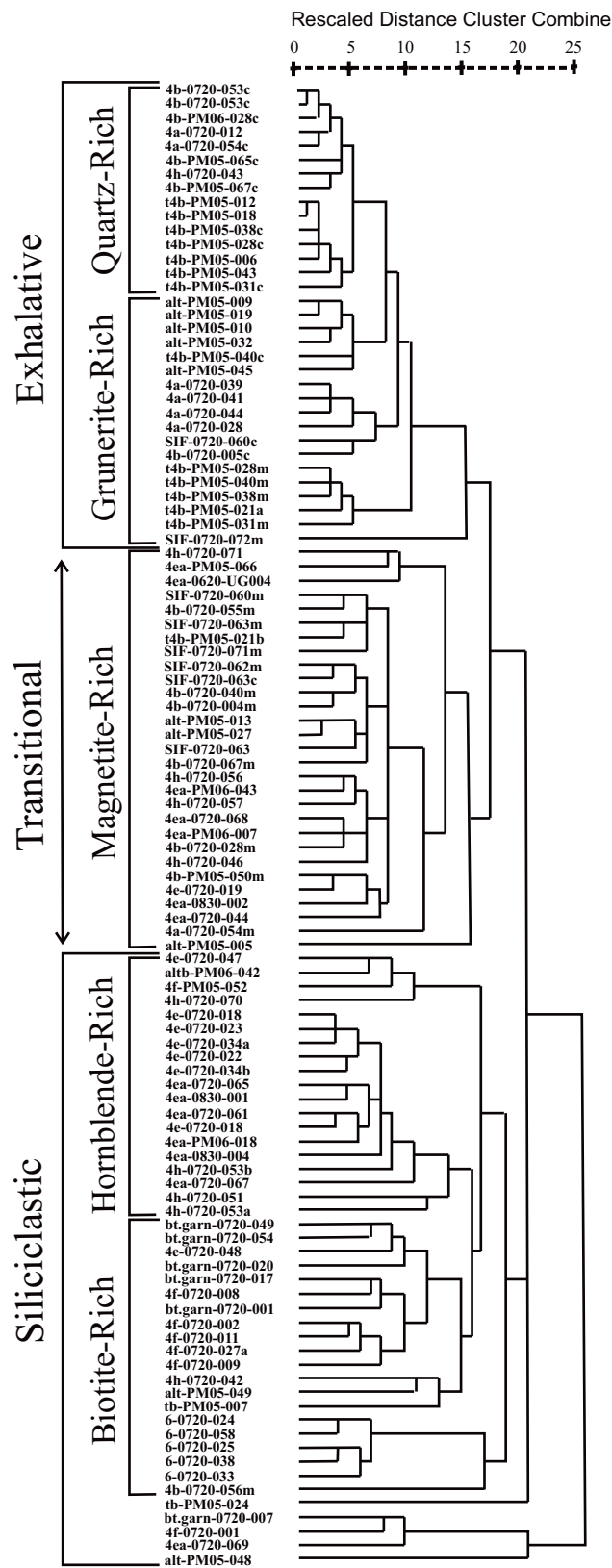
from the factor analysis due to statistical implications. This is because in order to draw mathematical comparisons properly the SPSS program requires a value for all fields. In the instance a value was not measured a number must be used as a placeholder (typically zero). Roughly half the samples were not analyzed for gold so a placeholder would have to be used if we wished to compare these samples to the samples, which do have gold values. The number used as a placeholder would be treated as a real value by the SPSS program and would therefore generate inaccurate results.

The primary reason for the dendrogram in Figure 4.28 is to see how all the samples relate to one and other. It is important to see how the samples from the previous dendrogram (Fig. 4.27) relate to the larger sample group. Overall, the samples from the previous dendrogram form similar groups and trends in the dendrogram seen in Figure 4.28.

The majority of samples, in this dendrogram, group together based on a common lithology and/or mineralogy. It should be noted that there does not appear to be an alteration sub-group. The sample groups are primarily based on the original sample chemistry, which is reflected by the sample's mineralogy. Samples can be broadly divided into three main groups. These groups are as follow; 1) exhalite-dominant, 2) siliciclastic-dominant, and 3) transitional between exhalite- and siliciclastic-dominant.

These broad groupings are sub-divided based on mineralogy. The exhalite-dominant group is composed of quartz-, magnetite-, and grunerite-rich samples. The siliciclastic-dominant group is composed of hornblende-, biotite, and garnet-rich samples. The transitional group is slightly enigmatic as it contains a number of different lithologies. However, the justification for calling this group transitional, is that it contains both exhalite- and siliciclastic-dominant samples compose this group.

All sample groups can be explained based on their shared lithology and/or mineralogy. The similar sample groupings between dendrograms in Figure 4.27 and 4.28 suggest that gold mineralization is not associated with a large-scale geochemical alteration halo. Instead a more likely scenario is that gold mineralization is associated with narrow alteration zones that are primarily structurally controlled (i.e., shear zones). These hypotheses are expanded upon in Chapter Five.



**Figure 4.28. Cluster analysis dendrograms for 106 samples (omitting Au values) from the NIF assemblage at Musselwhite gold deposit. Samples can be broadly divided into three groups: exhalative, transitional, and siliciclastic. These broad groups can be further subdivided by the dominant minerals in the samples. Note samples which behaved in a similar manner plot closest to each other on the dendrogram. Refer to page XVII of thesis intro for abbreviation definitions.**

## Chapter 5

### Discussion

#### 5.1 Introduction

Chapter Five serves to build a logical discussion on the evolution of the Musselwhite gold deposit, from deposition to present state, by tying together the data presented in the preceding chapters; specifically the whole rock and mineral geochemistry of the various lithologies. It is important to note that, as with other Archean-aged orogenic gold deposits, the complexity of the deposit is compounded by the deformed nature of the host rocks, therefore, making interpretation difficult. This problem is overcome due to numerous drill holes resulting in a well established stratigraphic succession.

The first part of the discussion revolves around utilizing the litho-geochemistry and stratigraphic relationships of the lithologies to elucidate the conditions of metalliferous sediment genesis and the tectonic setting. Once established the discussion is expanded by building on these fundamental properties, using the litho-geochemistry and mineral chemistry, to look at gold mineralization patterns as they relate to lithology. Finally the discussion turns toward placing Musselwhite in a global context by comparing it to other world class BIF-hosted orogenic gold deposits. Answering these questions and drawing comparisons to similar deposits will aid in the future exploration and detection of concealed BIF-hosted orogenic gold deposits.

#### 5.2 Type of Iron Formation: Implications for Conditions of Deposition

The deposition of iron formation, whether or not the iron formation is banded, and the mineralogy of the precipitates, is dependant on physiochemical parameters such as fluid temperature, pH, Eh, pE,  $fO_2$ ,  $fS_2$  and  $fCO_2$ . Other important influences on the presence, composition, and mineralogy of iron formation include the amount of siliciclastic-detrital input and the location of the basin relative to the source of input, the duration and strength of exhalative activity, fluid/rock ratio in an exhalative feeder zone, and bottom currents (Peter, 2003).

The original definition of iron formation (IF), first used by James (1954), is laminated to thinly-bedded chemical sediment containing at least 15 wt.% Fe. However, contemporary researchers classify rocks containing >10 wt.% Fe as IF (Peter, 2003). Ridler (1971) coined the term 'exhalite' for iron-rich chemical sedimentary rocks, which may or may not be intercalated with volcanic, volcanoclastic, and/or siliciclastic rocks (Note: In this paper 'exhalite' refers to IF precipitated in association with black smoker activity). The aforementioned siliciclastic and volcanoclastic components are eroded volcanic/volcanoclastic material, shale, siltstone, and sandstone. Geochemical studies indicate that in addition to chemically precipitated material the IFs can contain various amounts of siliciclastic detrital material.

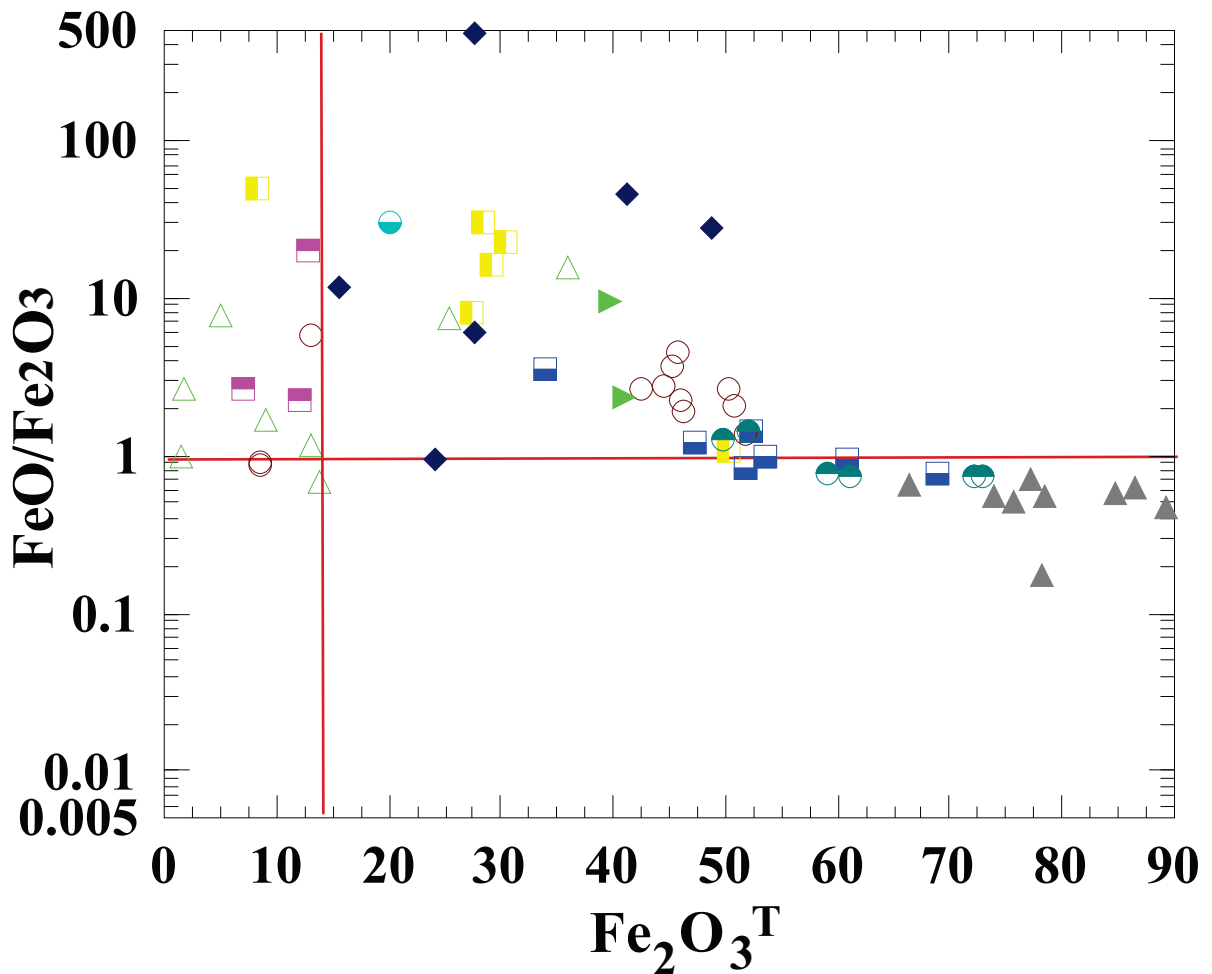
The majority of sedimentary lithologies at Musselwhite can be classified as iron formation based on the above described criteria. Figure 5.1a and 5.1b consist of the same binary diagram of  $\text{Fe}_2\text{O}_3^T$  vs.  $\text{FeO}/\text{Fe}_2\text{O}_3^T$ . The plots in Figure 5.1 demonstrate that the bulk of the samples from the current study contain >10% Fe (>14 wt.%  $\text{Fe}_2\text{O}_3^T$ ) and are therefore iron formation. Even the lithologies containing siliciclastic material such as the silicate-dominant BIF, hornblende-garnet schist, and biotite-garnet schist are technically IF. However, they have been termed siliciclastic-dominant IF, because of their aluminium, titanium, and zirconium content. These lithologies are mineralogically different from the pure iron-rich IF lithologies and they are discussed in more detail below.

There are three major categories of iron formation lithologic assemblages: Superior-, Algoma-, and Rapitan-type (Fig. 5.2). Superior-type iron formations are the largest by volume and are primarily the type of IF mined for iron ore. These IFs are chiefly associated with siliciclastic sedimentary rocks, and their metamorphic equivalents, mainly sandstone, arkose, conglomerate, and dolomite. Since Superior-type IFs are associated with siliciclastic sedimentary rocks they are hypothesized to have been deposited on continental shelf settings through mixing of up-welling anoxic iron-rich water from marine basins with oxygen-rich water on a stable shelf platform (Cloud, 1973). Rapitan-type iron formations are associated with glaciation events and, therefore, are relatively rare in the geologic record.



### Legend

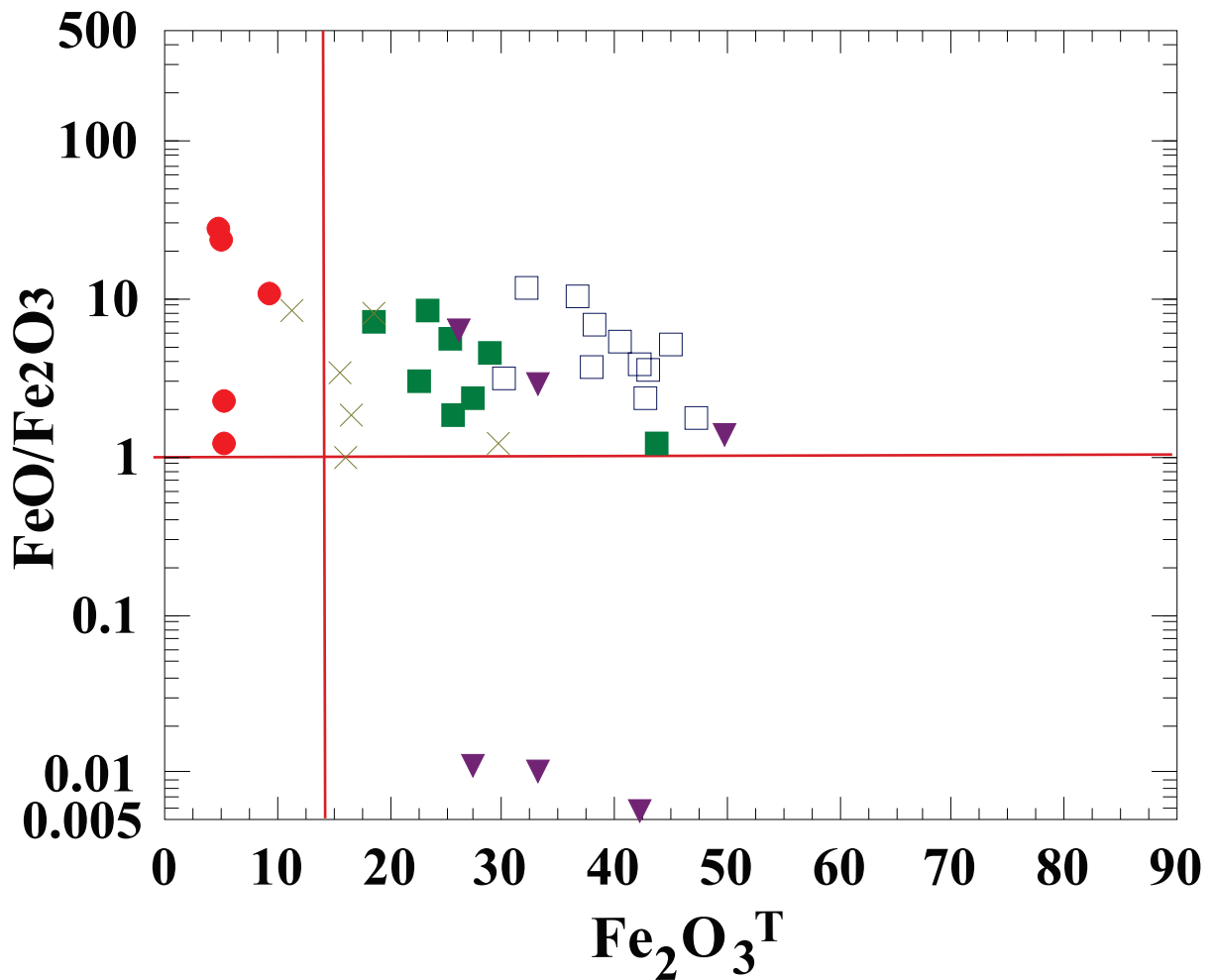
- |  |   |
|--|---|
| <ul style="list-style-type: none"> <li>● Quartz Bands, SIF Oxide-Dominant BIF</li> <li>● Magnetite Bands, SIF Oxide-Dominant</li> <li>◆ Meta-Argillite</li> <li>■ Quartz-Grunerite Banded Iron Formation</li> <li>■ Magnetite bands, NIF assemblage Oxide-</li> <li>■ Quartz bands, NIF assemblage Oxide-</li> <li>▲ Magnetite Bands, NIF Oxide-Dominant BIF</li> <li>△ Quartz Bands, NIF Oxide-Dominant BIF</li> <li>□ Silicate-Dominant Banded Iron</li> </ul> | <ul style="list-style-type: none"> <li>■ Hornblende-Garnet Schist</li> <li>× Bitotie-Garnet Schist</li> <li>▼ Metasomatic Biotite-Garnet Schist</li> <li>● Garnet-Quartzite</li> <li>○ Metasomatised NIF Oxide-Dominant BIF</li> <li>◇ Metasediment Rock (Trench #4)</li> <li>▶ Chlorite Schist (Trench)</li> <li>● Metabasalt</li> </ul> |
|--|---|



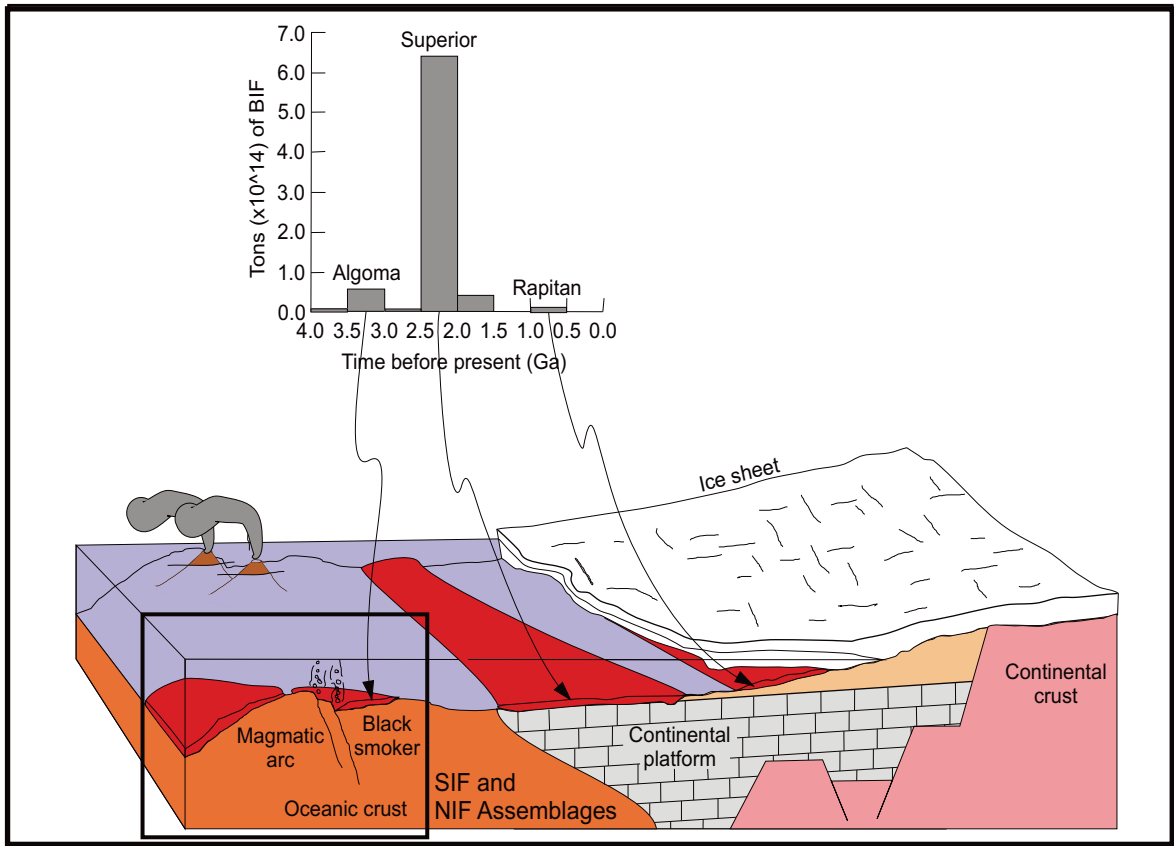
**Figure 5.1a)** FeO/Fe<sub>2</sub>O<sub>3</sub> vs. Fe<sub>2</sub>O<sub>3</sub> (total) for samples from the exhalite-dominant lithologies. It should be noted that samples plotting to the left of the vertical line contain less than 14 wt.% Fe<sub>2</sub>O<sub>3</sub> (total). In Figure 5.1a these samples are meta-chert rich and still considered exhalite material.

### Legend

- |  |   |
|--|---|
| <ul style="list-style-type: none"> <li>● Quartz Bands, SIF Oxide-Dominant BIF</li> <li>● Magnetite Bands, SIF Oxide-Dominant</li> <li>◆ Meta-Argillite</li> <li>■ Quartz-Grunerite Banded Iron Formation</li> <li>■ Magnetite bands, NIF assemblage Oxide-</li> <li>■ Quartz bands, NIF assemblage Oxide-</li> <li>▲ Magnetite Bands, NIF Oxide-Dominant BIF</li> <li>△ Quartz Bands, NIF Oxide-Dominant BIF</li> <li>□ Silicate-Dominant Banded Iron</li> </ul> | <ul style="list-style-type: none"> <li>■ Hornblende-Garnet Schist</li> <li>× Bitotie-Garnet Schist</li> <li>▼ Metasomatic Biotite-Garnet Schist</li> <li>● Garnet-Quartzite</li> <li>○ Metasomatised NIF Oxide-Dominant BIF</li> <li>◇ Metasediment Rock (Trench #4)</li> <li>▶ Chlorite Schist (Trench)</li> <li>● Metabasalt</li> </ul> |
|--|---|



**Figure 5.1b)** FeO/Fe<sub>2</sub>O<sub>3</sub> vs. Fe<sub>2</sub>O<sub>3</sub> (total) for samples from the siliciclastic-dominant lithologies. It should be noted that samples plotting to the left of the vertical line contain less than 14 wt.% Fe<sub>2</sub>O<sub>3</sub> (total). In Figure 5.1b these samples are siliciclastic rich and do not contain enough iron to be considered iron formation.



**Figure 5.2.** Diagram showing the hypothesized locations and environments of deposition for various iron formations (modified after Clemmey, 1985; Maynard, 1991). The grey bars on the histogram represent the amount of a particular type of IF world-wide (Holland, 1984). The schematic diagram displays the three main types of iron formation: Algoma-, Superior-, and Rapitan-type iron formations. Algoma-type iron formation is depicted next to a hydrothermal seafloor vent, Superior-type iron formation is depicted on a stable continental platform and Rapitan type iron formation is depicted in association with a glacier. This diagram is idealized, there is no scale, and it is only meant to depict the environment of deposition for the respective formations and does not represent a real situation. Note: inset box is highlights the environment of deposition for the SIF and NIF assemblages.

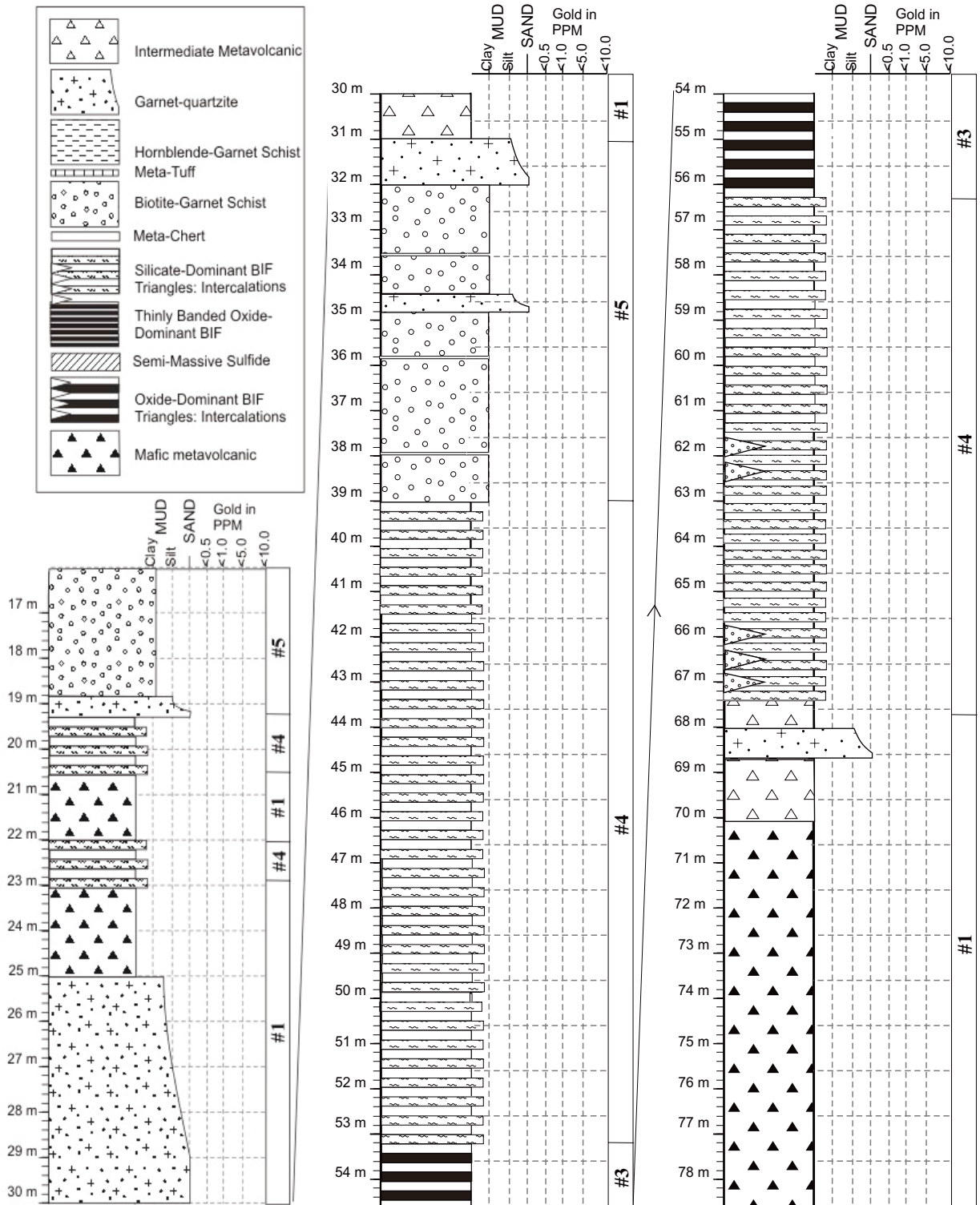
Algoma-type IFs (Gross, 1980) are primarily associated with volcanic, volcanoclastic, greywacke, and turbiditic rocks. Deposition of Algoma-type IF occurs at the same time as deposition of volcanic rocks. Due to the close proximity between Algoma-type IFs and volcanic rocks associated with spreading ridges, back-arcs and rifts they are thought to have been deposited in association with hydrothermal seafloor activity and may be evidence for paleo-hydrothermal black smoker systems (Gross, 1996). Algoma-type IF chemical sediment precipitated due to mixing of hydrothermal fluids with ocean water. These IFs are not as voluminous as Superior-type IFs.

Both the Southern and Northern Iron Formations are Algoma-type, based on the above described criteria. This conclusion is formulated around lithologic associations as well as the geochemistry of the lithologies composing the SIF and NIF. Given that the SIF and NIF are Algoma-type IFs, the remainder of Section 5.2 is devoted to the dynamics of Algoma-type IF deposition.

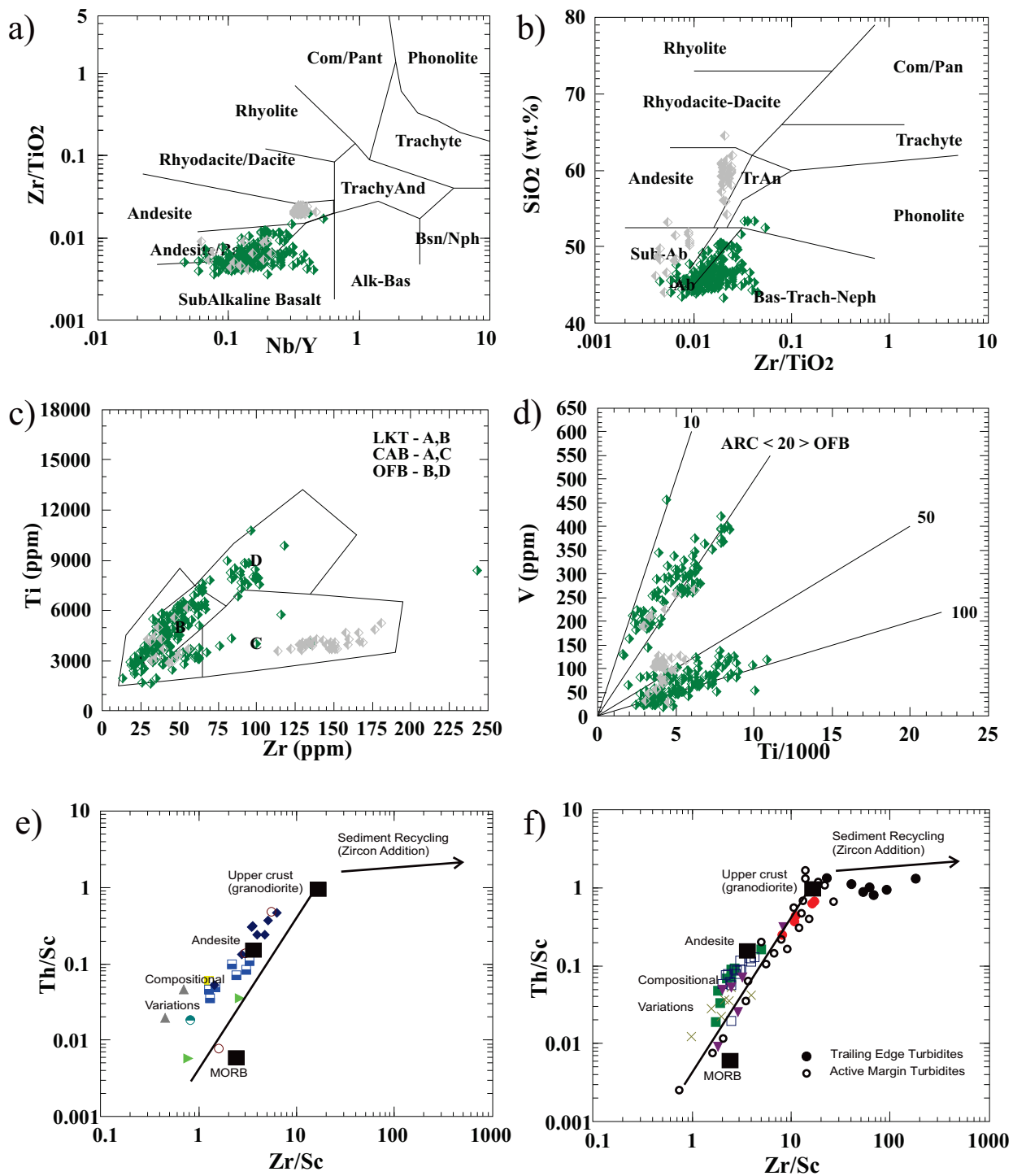
The Southern and Northern Iron Formation assemblages are contained in a larger package of volcanic rocks as described in Chapter One Section 1.9. Volcanic flows also occur as intercalated units within the SIF and NIF assemblages. Additionally, siliciclastic and volcanoclastic units are intercalated with IF in the stratigraphically upper part of the NIF.

These characteristic Algoma-type lithologic associations are unequivocally exhibited by the iron formation at Musselwhite. Figure 5.3 is a stratigraphic column depicting part of the NIF assemblage. The detailed characteristics and lithologic associations of the stratigraphic column are explained in detail in Chapter Two. What is important to note is the intercalated nature of the iron formation, volcanic flows, and siliciclastic sediment. This is the lithologic grouping, as outlined above, which characterizes Algoma-type IFs.

Figure 5.4 contains multiple geochemistry plots which are included at this point to show that the volcanic flows consist of basaltic to andesitic rocks (Fig. 5.4a-b). The volcanic lithologies form two groups one which appears to be associated with ocean floor



**Figure 5.3 Detailed stratigraphic log of drill hole 05-PQE-012.** Note the lithologic associations to the right of each stratigraphic column, these lithologic associations are described in Chapter Two.



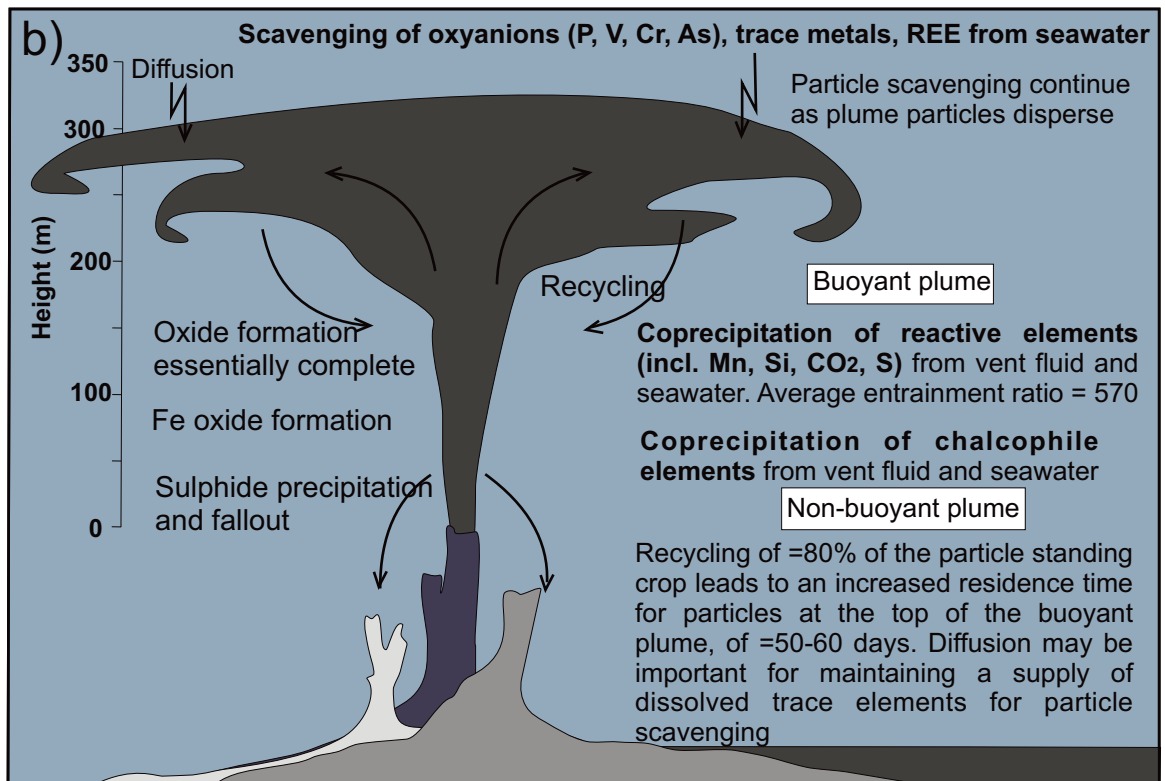
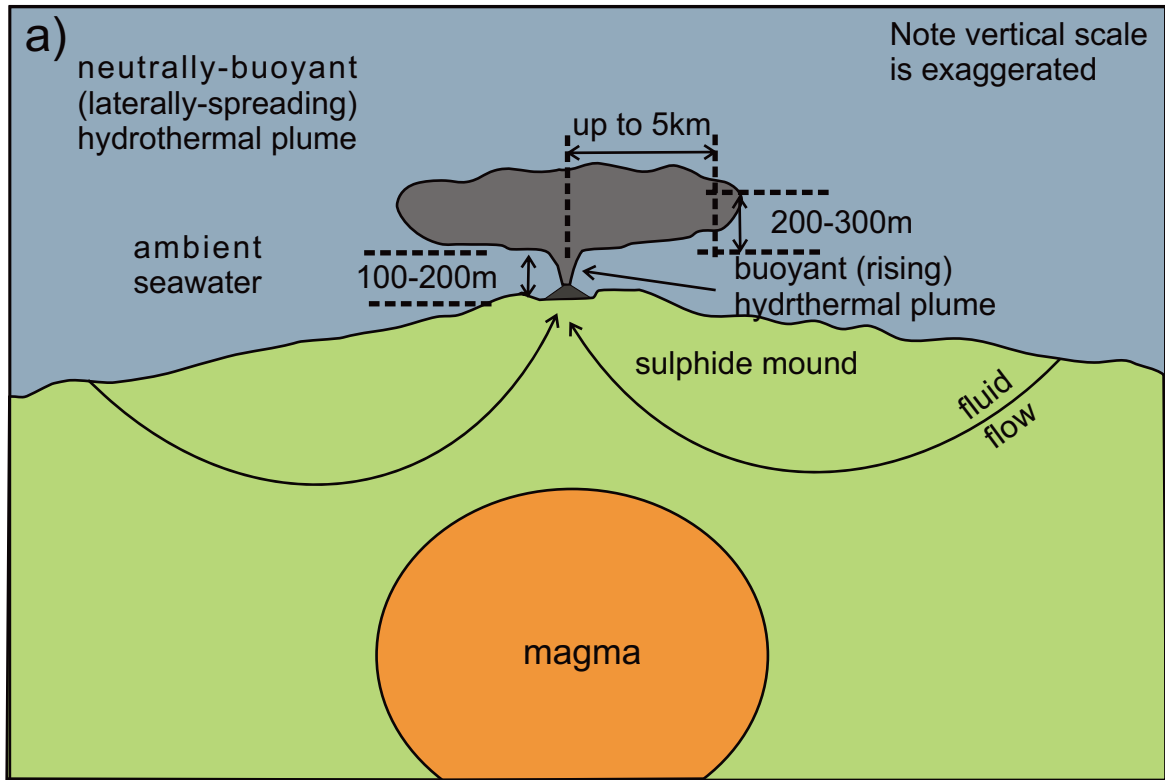
**Figure 5.4. a-d) Binary discrimination diagrams containing the mafic and intermediate volcanic samples. Note that green-diamonds are mafic samples and grey-diamonds are intermediate samples. Figures e and f contain the sedimentary samples (symbols are the same as in Fig. 5.1). a) Nb/Y vs. Zr/TiO<sub>2</sub>\*0.001 for volcanic samples (Winchester and Floyd), b) Zr/TiO<sub>2</sub>\*0.001 vs. SiO<sub>2</sub> for volcanic samples (Winchester and Floyd), c-d) Ti/1000 vs. V for volcanic samples (Pearce and Cann, 1973 and Shervais, 1982 respectively), e-f) Binary plot of Th/Sc versus Zr/Sc for exhalite- and siliciclastic- dominant lithologies, respectively. Both sample groups contain at least some sediment associated with active margin turbidites (Note diagrams modified after McLennan et al., 1990; McLennan and Murray, 1999).**

volcanism and the other with arc volcanism (Fig. 5.5c-d). It is also evident, in Figures 5.5e and 5.5f, that the principal siliciclastic component of the sedimentary lithologies has an active margin turbidite geochemical signature. The presence of turbiditic rock, volcanic rocks, and iron formation indicates the SIF and NIF are Algoma rather than Superior-type iron formation. As described above Superior-type iron formation is found principally in association with siliciclastic sedimentary rocks on passive continental margins.

Algoma-type iron formation is thought to form in association with primordial black smoker systems (Peter, 2003). Hydrothermal black smoker systems are associated with volcanically and tectonically active areas. Figure 5.5 contains several comprehensive schematic diagrams depicting black smoker hydrothermal systems. Hydrothermal plumes, generated by black smoker activity, range up to hundreds of metres in height and kilometres in diameter (Fig. 5.5a). These hydrothermal plumes are composed of hot metal-rich fluids.

Figure 5.5b depicts typical hydrothermal plume fluids containing Fe, Mn, Si, CO<sub>2</sub>, and S. These fluids react with seawater to form precipitates, which settled out of the water column. The reactions scavenge P, V, Cr, and REE from seawater (Fig. 5.5b). Iron and phosphorous are precipitated together in non-buoyant hydrothermal plumes due to the complexing of phosphorous (oxyanion, from seawater) with Fe-oxide (oxy-hydroxide, from hydrothermal fluid; Peter, 2003). The precipitates form a gelatinous layer on the ocean floor, which is later transformed into magnetite- and apatite-rich metasediment through diagenesis and metamorphism (Gross, 1996). In terms of geochemistry, this exhalite material is rich in Fe<sub>2</sub>O<sub>3</sub><sup>T</sup> and, P<sub>2</sub>O<sub>5</sub>, CaO, Sr, Ag, As, Au, Bi, Cu, Cd, Eu, Eu/Eu\*, Mo, Pb, Sb, Zn, and Se.

It is important to note that exhalite material associated with Algoma-type IF possesses a fairly distinctive REE curve. Figure 5.6 contains numerous REE spider diagrams representing both ancient and modern metalliferous sediment. Figure 5.6a depicts the chemistry of modern black smoker and white smoker hydrothermal fluids as well as the precipitated sediment associated with them (TAG mound mid-Atlantic ridge). These REE curves exhibit pronounced positive europium anomalies.



**Figure 5.5. Schematic diagrams related to the formation of Algoma-type iron formation.**  
 a) Generalized diagram showing the relative scale of a hydrothermal black smoker plume b) Generalized diagram of modern TAG hydrothermal system found at the mid-Atlantic ridge, diagram modified from Rudnicki (1995).

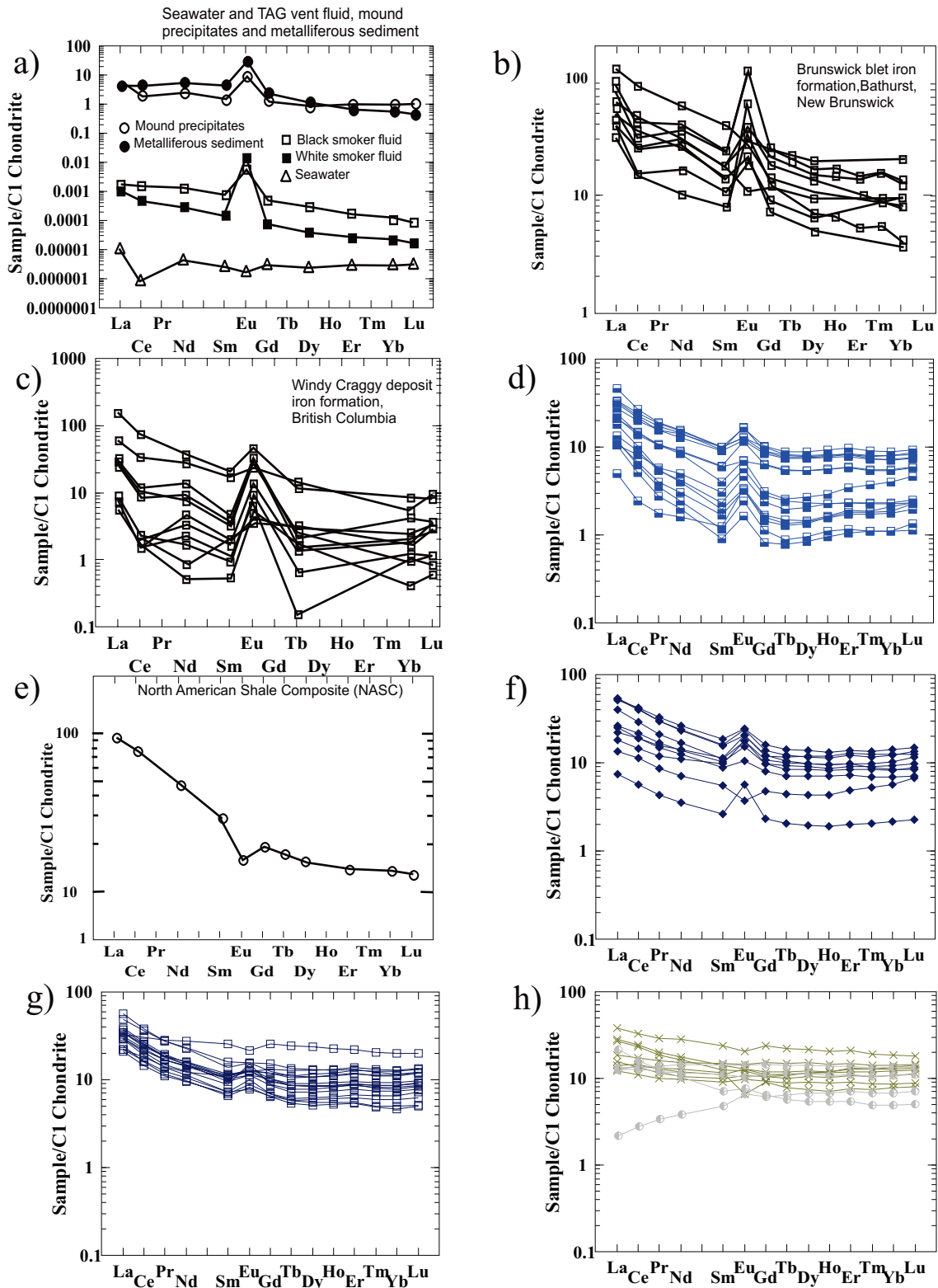


Figure 5.6b depicts the chemistry of ancient iron formation from the Bathurst mining belt, a well known Algoma-type IF. These REE curves exhibit even more pronounced positive europium anomalies, as well as enrichment of the LREE. Note that IF samples from the Windy Craggy deposit exhibit a comparatively similar REE curve (Fig. 5.6c). This is considered by researchers (P. Fralick, personal communication, 2007) to be the classic shape of ancient hydrothermally associated REE curves. It is important to note that during Archean times hydrothermal black smoker activity was so pervasive that it imparts a positive europium anomaly to most seafloor chemical sediment deposited at this time. As such, this REE curve pattern, on its own, should not be taken as evidence that an iron formation formed entirely in association with black smoker activity. However, when combined with other evidence it provides useful insight into the genesis of iron formation.

The majority of the exhalite-dominant lithologies from Musselwhite exhibit positive europium anomalies and LREE enrichment. The magnetite samples, collected from the oxide-dominant BIF of the NIF assemblage, are depicted in Figure 5.6e as they exhibit the best REE curves.

Figure 5.6e depicts the North American Shale Composite REE curve (Taylor and McLennan, 1985). This curve has a distinct negative europium anomaly, which is characteristic of seafloor mud. Figures 5.6g and 5.6h contain samples of the silicate-dominant BIF and the biotite-garnet schist. It should be noted by the reader that several samples in Figures 5.6g and 5.6h exhibit slight negative europium anomalies. This suggests these particular samples originally contained a mud component. Additionally the silicate-dominant BIF exhibits higher overall REE concentration and reduced positive europium anomalies. This is a result of the lithologies clay-rich protolith (mud). Clay minerals contain high concentrations of REE relative to exhalite material and therefore suppress the exhalite REE trend.

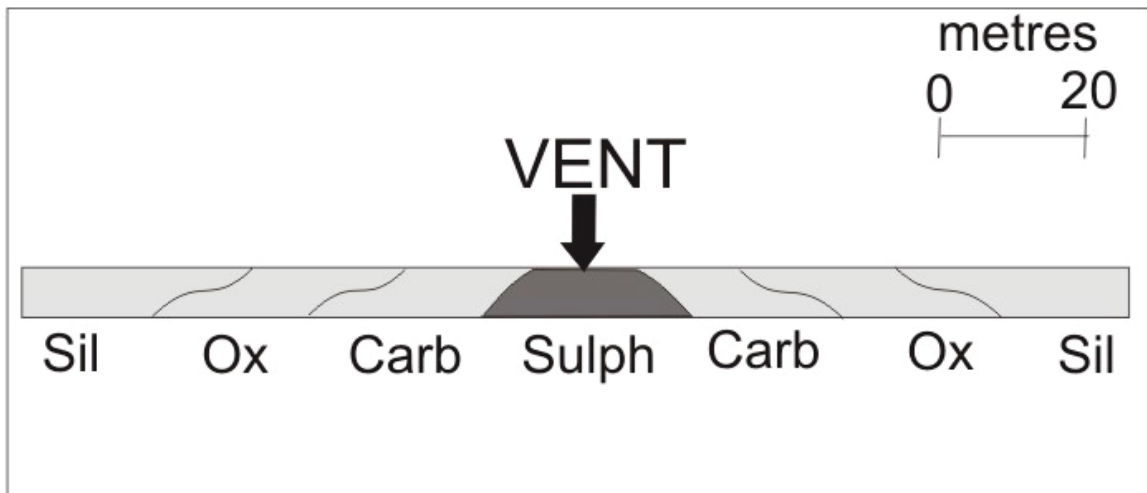
Figures 5.6h contains samples of the biotite-garnet schist, which exhibit flat REE curves and reduced europium anomalies. Again, these curves are the result of higher siliciclastic content in these lithologies. The flat REE curve resembles MORB. The siliciclastic content of the lithologies is discussed below.



**Figure 5.6. C1 normalized REE spider diagrams;** (a) REE curves for modern seawater, mound and metalliferous sediment, as well as black and white smoker hydrothermal fluids (Mills and Elderfield, 1995), (b) REE curves for Brunswick belt iron formation (Peter and Goodfellow, 1996), (c) REE curves for Windy Craggy deposit iron formation (Peter and Scott, 1999), (d) REE curves for NIF assemblage oxide-dominant BIF (magnetite) samples, (e) North American shale composite (NASC) REE curve, (f) Meta-argillite REE curves (Taylor and McLennan, 1985), (g) Silicate-dominant REE curves, (h) Biotite-garnet schist REE curves.

Iron formations, in general, are broadly subdivided into sulphide-, oxide-, carbonate-, and silicate-dominant varieties based on the amount of Fe-Si-Ca-S-Al they contain. The type of IF deposited is subject to the prevailing environmental and chemical conditions as well as local sediment sources.

Three types of iron formation exist, in gradational contact, at Musselwhite. The three types are; 1) sulphide-dominant, 2) oxide-dominant, and 3) silicate-dominant. Figure 5.7 is a schematic diagram illustrating the possible original arrangement of these different iron formations at Musselwhite. This diagram shows the sulphide-dominant IF is deposited proximal to the vent under reducing conditions. Oxide-dominant IF is deposited, under oxidizing conditions, distal to the vent. Silicate-dominant IF is most distal to the vent because this location allows for deposition of both siliciclastic detrital sediment and exhalite precipitates. The reader should note that Figure 5.8 is a generalized and schematic diagram. In reality the IF at Musselwhite formed under changing spatial-temporal conditions, which are discussed in detail in Section 5.3.

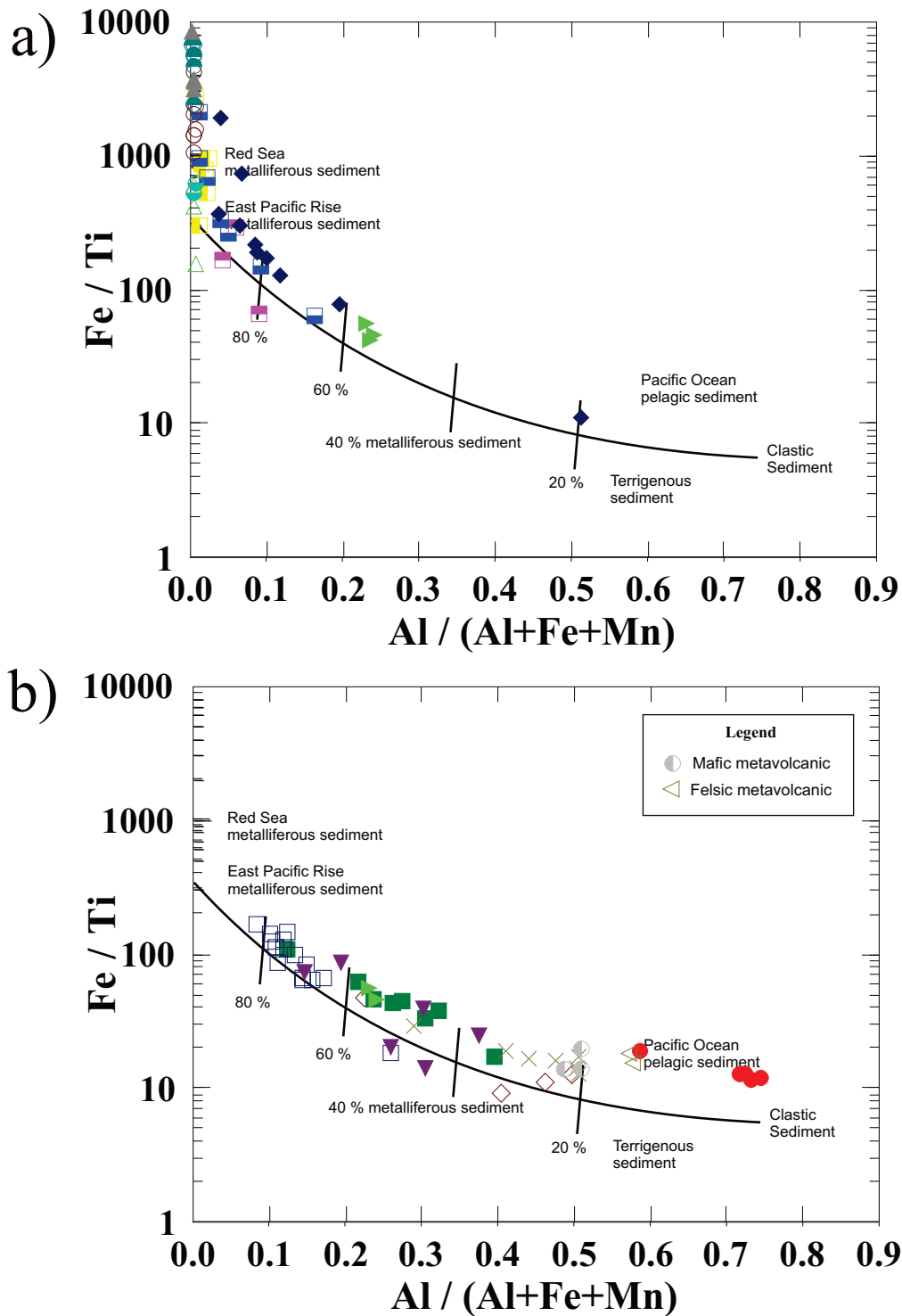


**Figure 5.7.** Schematic cross-section of a possible original layout of the zoned, sulphide-oxide-silicate-dominant iron formation in the NIF assemblage at the Musselwhite gold deposit. Note that conditions are reducing nearest the vent ranging to oxidizing distal to the vent, modified from Peter (2003).

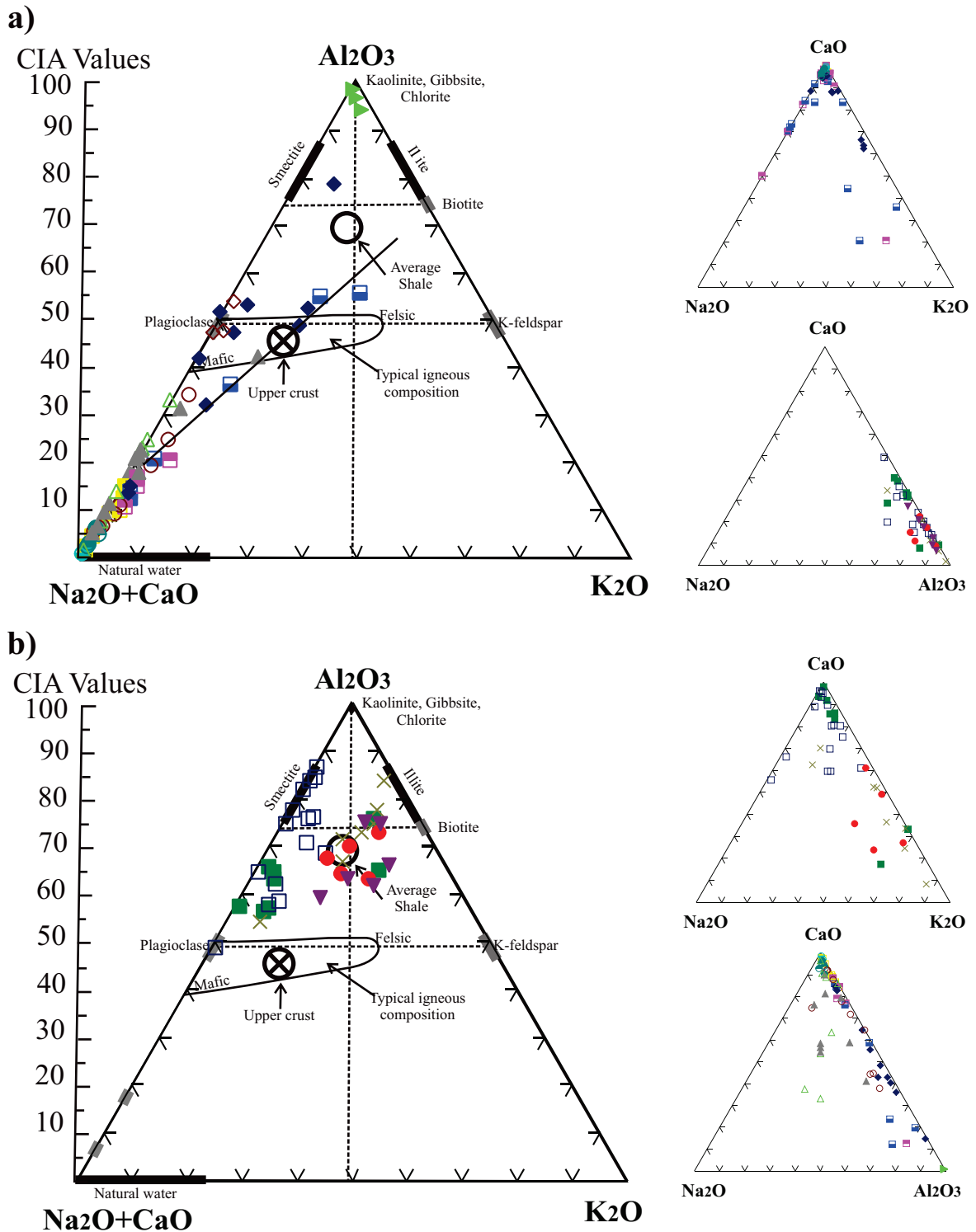
The meta-argillite forms a basal sulphide-dominant IF to the SIF and NIF assemblages. This lithology is classified as sulphide-dominant IF based on its high pyrrhotite content. The oxide- and silicate-dominant IFs are classified based on both mineralogy and geochemical properties.

Figures 5.8a and 5.8b were introduced in Chapter Four to show the amount of chemical vs. siliciclastic material samples contain. Figure 5.8a illustrates that the quartz-grunerite BIF, and NIF/SIF quartz-magnetite BIFs are principally composed of iron-rich material. Together the chemistry and mineralogy designates these lithologies as oxide-dominant IFs. It should be noted that the metasomatised quartz-magnetite BIF, collected from the trenches, falls into the iron-rich exhalite-dominant range. Figure 5.8b illustrates that the silicate-dominant BIF, hornblende-garnet schist, and biotite-garnet schist are composed of both iron- and siliciclastic-rich material. Together the chemistry and mineralogy designates these lithologies as silicate-dominant IFs. It should also be noted that the metasomatic biotite-garnet schist falls into the silicate-dominant IF range. Overall Figure 5.8 shows that the Northern Iron Formation assemblage at Musselwhite is not pure oxide-dominant BIF. The NIF assemblage contains an increasing amount of siliciclastic material stratigraphically upward. This siliciclastic material originally consisted of clay minerals, which settled out of the water column during periods of quiescence. These clay minerals are the end weathering product of feldspars and ferromagnesian minerals from igneous rocks.

The large ternary diagrams, in Figure 5.9a and 5.9b were introduced in Chapter Four. These diagrams depict the molecular proportions of  $\text{Al}_2\text{O}_3$ – $(\text{Na}_2\text{O}+\text{CaO})$ – $\text{K}_2\text{O}$  and are designed to portray chemical index of alteration (CIA) trends (modified after Gu *et al.*, 2002). In addition to visually portraying the degree of CIA the diagram shows the possible original composition of the siliciclastic sedimentary protolith to the samples. The reader should note that protoliths of the stratigraphically lower exhalite-dominant lithologies contained minimal clay minerals. However, the protoliths of the upper lithologies contained a mix of smectite, illite, chlorite, and plagioclase in addition to iron-rich exhalite material.



**Figure 5.8. Discrimination diagram for estimating the amount of exhalative versus siliciclastic sedimentary material in samples. Diagram modified after Boström (1973). Note that the symbols are the same as in Fig. 5.1. a) diagram depicting the exhalite-dominant samples (lithologies) from the current study, b) diagram depicting the siliciclastic-dominated samples (lithologies). Also note that, in Fig. 4.4b, samples plot above the mixing line which is the result of lower Ti in Archean clays. Average samples of Red Sea metalliferous sediments (Backer, 1976), East Pacific Rise metalliferous sediment (Cronan, 1976), terrigenous sediment (Boström, 1973), and average pelagic Pacific Ocean sediment (Cronan, 1976) are plotted on the diagram for reference.**



**Figure 5.9.** Larger ternary discrimination diagram, used to determine original loose sediment material, is based on the relative molecular proportions of  $Al_2O_3$ - $Na_2O+CaO$ - $K_2O$ . Note that the symbols are the same as in Fig. 5.1. Fields are from Gu et al. (2002). Hornblende and clinopyroxene are idealized compositions from Taylor and McLennan (1985). Smaller inset  $CaO$ - $Na_2O$ - $K_2O$  and  $CaO$ - $Na_2O$ - $Al_2O_3$  ternary diagrams show the relative concentrations of these elements; a) Samples from exhalite-rich lithologies, b) Samples from siliciclastic-rich lithologies

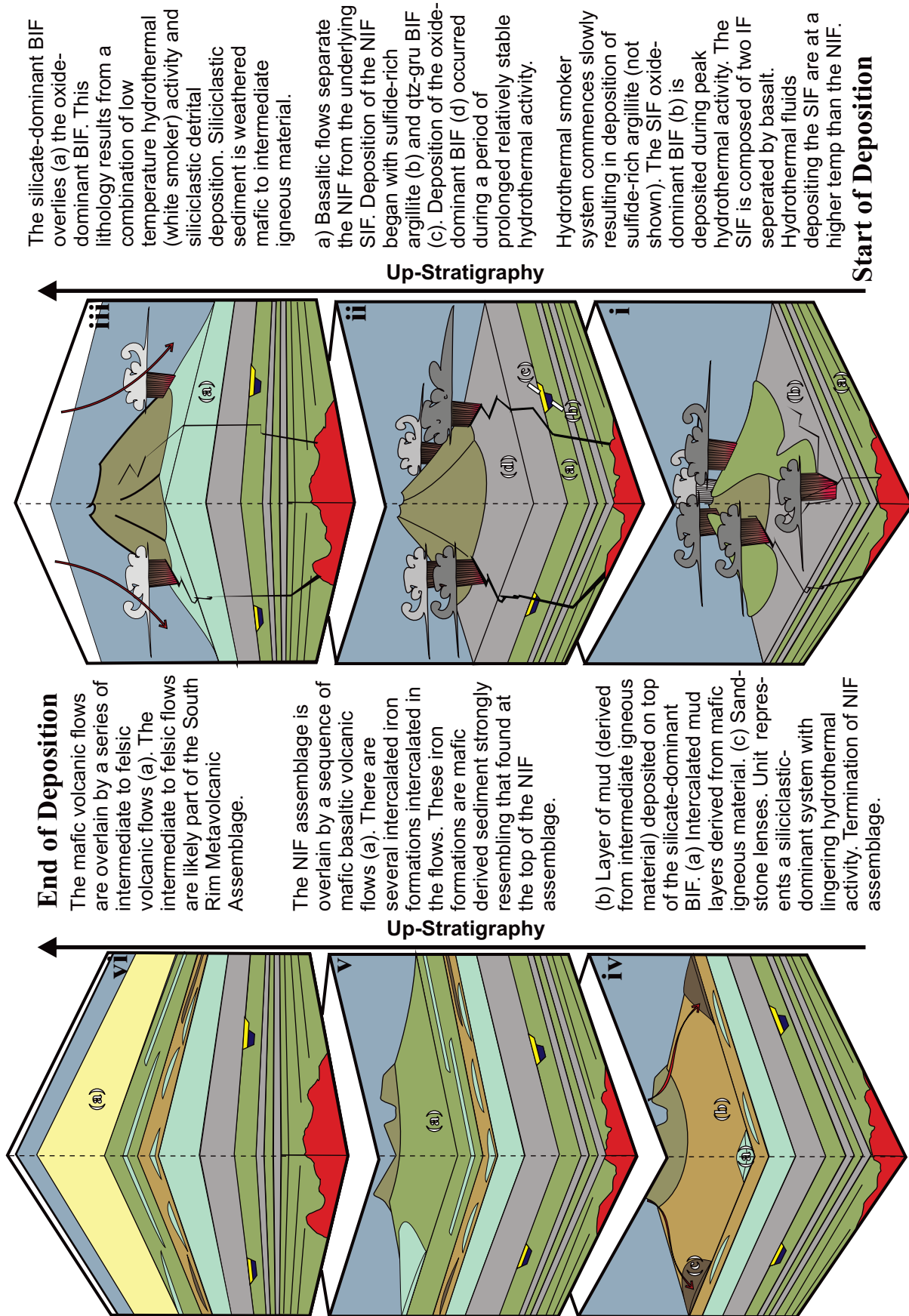
### 5.3 Mine Lithology Protoliths and Stratigraphic Succession

Classifying the protoliths of the lithologies, in the Musselwhite stratigraphy, is important for several reasons; namely, for determining changing facies conditions as well as interpreting the original environment of deposition. In Chapter Four it was shown that alteration is confined to narrow zones associated with shear-zones and, for the most part, the chemistry of the lithologies has not changed significantly since deposition of the sediment on the seafloor. As such identifying protoliths to the lithologies at Musselwhite was principally based on whole rock geochemistry and to a lesser extent the macroscopic lithologic characteristics of the rocks. Such macroscopic characteristics were identified through detailed core logging and include relict meta-chert bands, graded bedding preserved as varying garnet content in the rocks, and shifting magnetite contents. For the most part the mineralogy is not used as it is only a reflection of metamorphism and is not a primary feature. The protoliths to the lithologies at Musselwhite are fairly straight forward.

The ensuing discussion is organized from stratigraphically lowest to highest lithologies; it begins at the bottom of the stratigraphy and builds stratigraphically upward. Figure 5.10 is a visual representation of the evolution of the Musselwhite stratigraphy showing the SIF assemblage, NIF assemblage, as well as the encompassing and intervening volcanic units. This schematic diagram is not to scale and is used solely as a visual aid when describing the depositional sequence of the lithologies at Musselwhite.

Ultramafic and mafic volcanic rocks are the lowest normally encountered lithologies in drill core at Musselwhite (Fig. 5.10i-a). These rocks represent ultramafic and mafic subaqueous volcanic flows, which predate both the SIF and NIF (J. Biczok, personal communication, 2007). These lower volcanic rocks represent ocean floor basalts (Fig. 5.4c-d).

The Southern Iron Formation assemblage was deposited on top of these flows. This assemblage is an Algoma-type IF composed of a basal sulphide-rich argillite overlain by quartz-magnetite BIF (Fig. 5.10i-b). The meta-argillite marks both a period of quiescence, after the volcanic eruptions that deposited the basalts and komatiites, and initiation of hydrothermal black smoker activity. Quiescence, in this case, is



**Figure 5.10.** Schematic representation of the evolution of the Musselwhite stratigraphy showing the SIF and NIF assemblages as well as the encompassing and intervening volcanic units. This diagram is not to scale and is used as a visual aid.



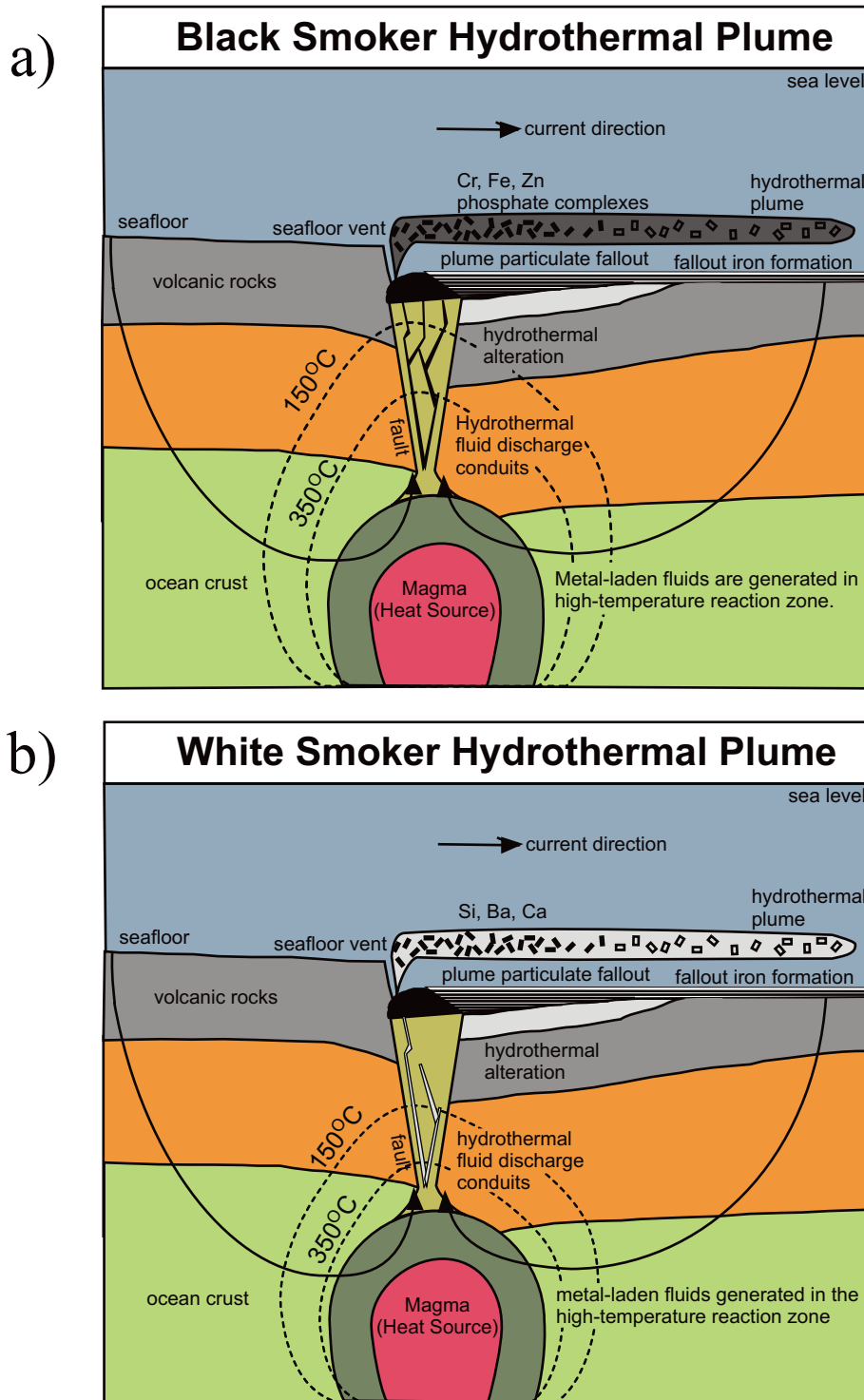
indicated by relatively high Zr, Ti, and Al concentrations which were originally contained in detrital clay and associated minerals. Hydrothermal activity is indicated by pronounced positive Eu anomalies, as well as high metal and sulphide concentrations.

The quartz-magnetite, oxide-dominant BIF is the most significant component of the SIF assemblage. This lithology was originally deposited on the seafloor as alternating bands of iron- and silica-rich gelatinous precipitates during peak hydrothermal black smoker activity. The iron- and silica-rich gelatinous material was later converted to magnetite and chert through diagenesis. The alternating banded nature of the iron formation is a result of changing heat-flow in the hydrothermal regime.

Figure 5.11a and 5.11b are schematic diagrams depicting the deposition of Algoma-type oxide-dominant banded iron formation in general. The diagrams have been modified from Spry *et al.* (2000). Figure 5.11a represents a high heat flow regime, resulting from well developed and open fracture plumbing network, producing black smokers. The higher temperature of black smoker hydrothermal fluid allows it to transport metals (mainly iron). These fluids deposit iron-rich precipitates upon interacting with seawater. The precipitates go on to become the magnetite bands after diagenesis.

Over time the fracture networks supplying the hydrothermal system became clogged with precipitated material, which reduces the flow of fluid through the system. Declining fluid circulation also curbs the heat flow in the system. The reduced heat flow results in lower temperature fluids, which are under-saturated in metals but contain appreciable silica, barite, and sulphate. These fluids give rise to hydrothermal white smoker systems. Figure 5.11b represents a hydrothermal white smoker system. The fluids, upon interacting with seawater, deposit silica-rich precipitates which go on to form the quartz (chert) bands.

Periodic disruptions, such as an earthquake, re-open the fracture networks in the rock allowing for increased fluid-flow/heat flow and the cycle repeats. The thinly-banded nature of the SIF is an indication that the hydrothermal system cycled rapidly between white and black smoker regimes.



**Figure 5.11. Schematic diagrams related to the formation of banded oxide-dominant Algoma-type iron formation at Musselwhite. Figures depict buoyant hydrothermal plumes and are modified from Spry *et al.*, (2000). a) Black smoker hydrothermal plume resulting from increased fluid flow and associated temperature increase: deposits magnetite protolith, b) White smoker hydrothermal plume resulting from decreased fluid flow and associated temperature decrease: deposits quartz-protolith.**

The pronounced positive Eu anomalies in the quartz (meta-chert) and magnetite samples from the SIF oxide-dominant BIF (Fig. 4.18a and b) indicate that the hydrothermal fluids depositing this lithology were relatively hot. The connection between positive Eu anomalies and hydrothermal smoker systems was described above. These Eu anomalies are more pronounced than those seen in other IF samples from Musselwhite. This is an indication that the hydrothermal system depositing the SIF assemblage was operating at a higher temperature than the hydrothermal system depositing the exhalite-dominant lithologies of the NIF assemblage. In addition the more thinly banded nature of the SIF oxide-dominant BIF relative to the NIF oxide-dominant BIF indicates a comparatively faster hydrothermal cycling.

The SIF is overlain, and separated from the NIF assemblage, by a sequence of mafic volcanic rock (Fig. 5.10ii-a). This mafic sequence represents sub-aqueous basaltic volcanic flows. These flows indicate eruptive volcanism took place. The number of flows and the amount of time it took to deposit them is unknown. The eruptive volcanism buried the hydrothermal smoker systems resulting in cessation of deposition of the SIF assemblage.

The Northern Iron Formation assemblage was deposited on top of these flows. The hydrothermal system which participated in the deposition of the NIF assemblage likely represented the resurgence of the original hydrothermal system, which deposited the SIF assemblage. However, there are key differences between the SIF and NIF assemblages, which will be discussed further on in the chapter.

The NIF assemblage, much like the SIF assemblage, has at its base a thin discontinuous sulphide-rich argillite unit (Fig. 5.10ii-b). Again, the argillite marks both a period of quiescence, after volcanism, and initiation of hydrothermal smoker activity. Quiescence is indicated by relatively high Zr, Ti, and Al concentrations originally contained in detrital clay and associated minerals. Hydrothermal activity is indicated by pronounced positive Eu anomalies, as well as high metal and sulphide concentrations. The high sulphide content could also be an indication of anoxic conditions during deposition. Unlike the argillite in the SIF assemblage, which if present is in contact with the oxide-

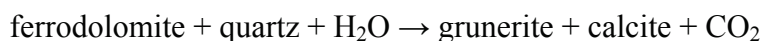
dominant BIF, the argillite in the NIF assemblage is separated from the oxide-dominant BIF by a thinly banded quartz-grunerite BIF (Fig. 5.10ii-c).

The thinly laminated quartz-grunerite BIF is a discontinuous, absent to locally quite thick (~15-20 m), unit in the NIF assemblage. However, although both the quartz-grunerite BIF and argillite are discontinuous lithologies; when present they occur together suggesting there is a genetic link between the two.

The defining characteristics of the quartz-grunerite BIF are its thinly-banded nature, high calcium, magnesium and silica contents, as well as lack of magnetite. Explaining the presence of grunerite- and quartz-laminations instead of magnetite- and quartz-laminations is problematic. It is probable that the grunerite laminations resulted from the diagenesis and metamorphoses of an original Fe/Mg-rich hydroxide gel.

Another possible explanation is that the thin grunerite laminations were originally thin magnetite laminations. The abundance of quartz is the result of the low temperature, initial stages, of hydrothermal smoker activity. It is logical to assume that, at its onset, fluid temperatures were lower and therefore primarily deposited silica-rich precipitates. As the hydrothermal system became fully operational temperatures increased and follow the above described cyclical pattern. Grunerite laminations could have originally been magnetite bands deposited during sporadic temperature spikes in the hydrothermal system. These laminations are thin enough to be completely altered to grunerite through metamorphic reactions with surrounding quartz-crystals.

Metamorphic reactions do not explain the slightly higher magnesium concentration in the quartz-grunerite BIF relative to the oxide-dominant BIF. The magnesium content of the quartz-grunerite BIF is possibly a reflection of the seawater conditions at the time (pH, Eh,  $fO_2$ , etc.) of its deposition. Under certain chemical conditions magnesium is precipitated more easily out of water than iron. Another possibility, which can explain both the magnesium content and the much higher calcium content of the quartz-grunerite BIF, is that this lithology represents a thinly laminated carbonate-dominant/facies BIF. This argument is based on the following chemical reaction:



Therefore it is possible that the thin grunerite laminations originally consisted of iron-rich dolomite, which reacted with quartz under metamorphic conditions to form grunerite. This hypothesis is supported by the lithologies relatively high magnesium and calcium contents. Additionally, Figure 5.7 indicates carbonate-facies BIF forms between the sulphide- and oxide-dominant BIFs. At Musselwhite, the quartz-grunerite BIF is situated between the sulphide-rich meta-argillite (below) and the oxide-dominant BIF (above) further supporting its nature as a carbonate-BIF.

The meta-argillite and quartz-grunerite BIF represent sulphide- and carbonate-dominant varieties of IF, respectively. Note that the plausible location these types of IF are deposited, relative to the hydrothermal vent and other types of IF, is depicted in Figure 5.7. It is probable that these lithologies were deposited in ocean floor depressions. Sheltered depressions would explain why these lithologies are discontinuous, occur together, and are of limited thickness. The depressions would protect loose sediment thus preventing the siliciclastic component of the meta-argillite from being carried away by bottom currents. The reader should note that the siliciclastic component indicates that this lithology was deposited slowly. The depressions would allow sulphides to precipitate due to more anoxic conditions. The depressions would have been filled with brine pools created as dense metal laden hydrothermal fluids collected in them. These brine pools precipitated the exhalite material that formed the lithologies.

Overlaying the quartz-grunerite BIF is a thick sequence of oxide-dominant BIF (Fig. 5.10ii-d). This quartz-magnetite BIF is a classic Algoma-type IF and represents the peak output of hydrothermal smoker activity in the NIF assemblage. It was deposited in the same manner as the oxide-dominant BIF component of the SIF assemblage (alternating bands of Fe- and Si-rich gelatinous precipitates). Again, the alternating banded nature of the iron formation is a result of changing heat-flow in the hydrothermal regime (Fig. 5.11a-b). For a detailed description of this system refer to the earlier paragraph on the deposition of the oxide-dominant BIF in the SIF assemblage.

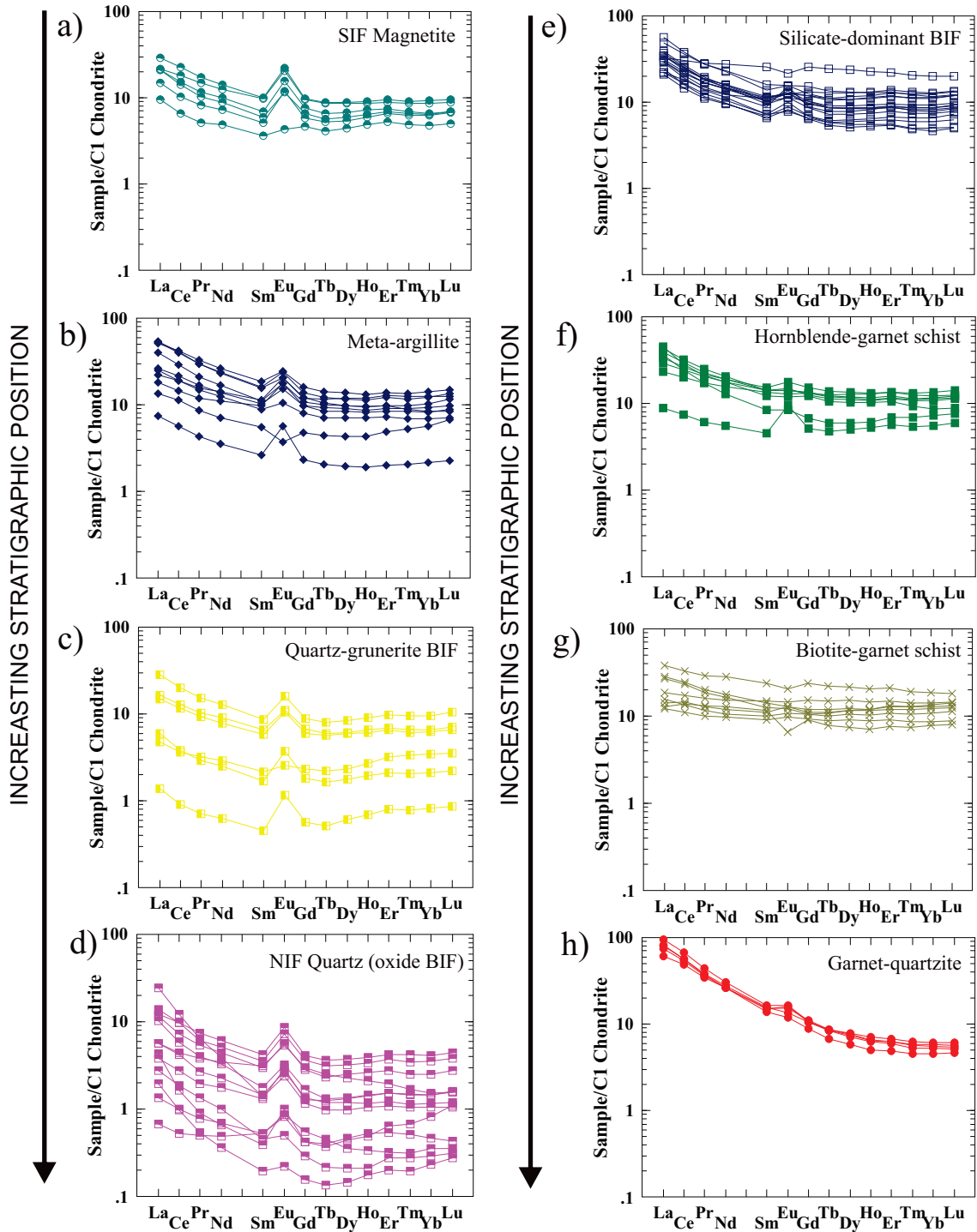
There are notable differences between the SIF and NIF oxide-dominant BIFs. In the NIF oxide-dominant BIF bands are on average ~1 cm thick, whereas in the SIF oxide-

dominant BIF bands are on the order of ~0.2-0.5 cm thick. The different magnitude bands indicates that the hydrothermal system depositing the NIF oxide-dominant BIF was cycling more slowly with prolonged periods of black smoker and white smoker activity relative to the SIF. Another possibility is that a greater number of hydrothermal vents were operating during deposition of the NIF relative to the SIF.

Interestingly positive Eu anomalies are slightly less pronounced in the NIF oxide-dominant BIF relative to the SIF oxide-dominant BIF (Figs. 5.12a and d). This indicates that, although the hydrothermal system depositing the NIF was more voluminous, it was operating at a lower temperature relative to the hydrothermal system depositing the SIF assemblage.

A discontinuous, but important, transitional lithology is found at the top of the NIF oxide-dominant BIF. This lithology consists of alternating hornblende-garnet schist and meta-chert bands (mine terminology: clastic 4b). Originally these bands were composed of siliciclastic detrital material and silica-gel. This lithology is significant because it represents and physically preserves the facies change from oxide- to silicate-dominant BIF. This facies change is the result of a combination of decreased heat flow driving the hydrothermal system and an influx of siliciclastic detritus. The influx of siliciclastic detritus may have been the result of changes in ocean floor topography and bottom currents whereas changes in the hydrothermal system were driven by shifts in tectonic and volcanic activity.

The transitional lithology marks a permanent reduction of heat flow in the hydrothermal smoker system. This conclusion is based on chert being the dominant exhalite material in the overlying lithologies. Magnetite bands are less common in these lithologies. The hydrothermal REE curves also become less and less pronounced with increasing stratigraphic position (Fig. 5.12a-f). This implies the stratigraphically overlying lithologies to the transitional lithology, of the NIF assemblage, were primarily deposited in association with white smoker activity.



**Figure 5.12. C1 normalized REE spider diagrams.** The reader should note that some lithologies have been omitted to conserve space. Additionally this diagram is organized in a different manner to other geochemical figures (vertical instead of horizontal alphabetical order). Symbols are the same as in Fig. 5.1. a) Magnetite samples from the SIF (drill core), b) Meta-argillite samples (drill core), c) Quartz-grunerite IF samples (drill core), d) Quartz samples from the oxide-dominant BIF (drill core), e) Silicate-dominant BIF samples (drill core), f) Hornblende-garnet schist samples (drill core), g) Biotite-garnet schist samples (drill core), h) Garnet-quartzite samples (drill core).

It is important to note that the transitional lithology signals the shift from exhalite-dominant sedimentation to a combination of siliciclastic- and exhalite-dominant sedimentation. The latter lithologies are the result of both white smoker activity and increased siliciclastic sedimentation.

The transitional BIF is in gradational contact with the overlying silicate-dominant BIF. The silicate-dominant BIF (Fig. 5.10iii-a) consists of alternating bands with individual bands composed of either quartz or varying combinations of hornblende-grunerite-almandine-biotite. Like the previously discussed lithologies, the quartz bands represent metamorphosed chert layers deposited as silica-rich gel. The hornblende-grunerite-almandine bands were originally clay-rich layers  $\pm$  iron hydroxides. Together these bands indicate that both hydrothermal exhalative and siliciclastic deposition were taking place at the same time.

The presence of chert in this lithology, and its banded nature, indicate that cyclic hydrothermal activity contributed to its formation. However, quartz is more common than magnetite suggesting white smokers predominated during the deposition of the silicate-dominant BIF. Again, the lack of black smoker input indicates a low heat flow regime. This is in line with the reduced heat flow indicated by the aforementioned underlying transitional lithology. Therefore, the silicate-dominant BIF represents continuation of the diminishing hydrothermal system. Periodically the white smoker hydrothermal system would shut down allowing siliciclastic detrital material to accumulate.

The Fe-silicate mineral bands in the silicate-dominant BIF consist of variable combinations of hornblende-grunerite-almandine-biotite. The bands range from being composed exclusively of grunerite and almandine garnet to exclusively hornblende and garnet.

The chemistry is relatively consistent between samples of the Fe-silicate bands regardless of the combination of minerals. The Fe-silicate bands from the silicate-dominant BIF exhibit geochemical similarities to mafic and intermediate volcanic samples from the

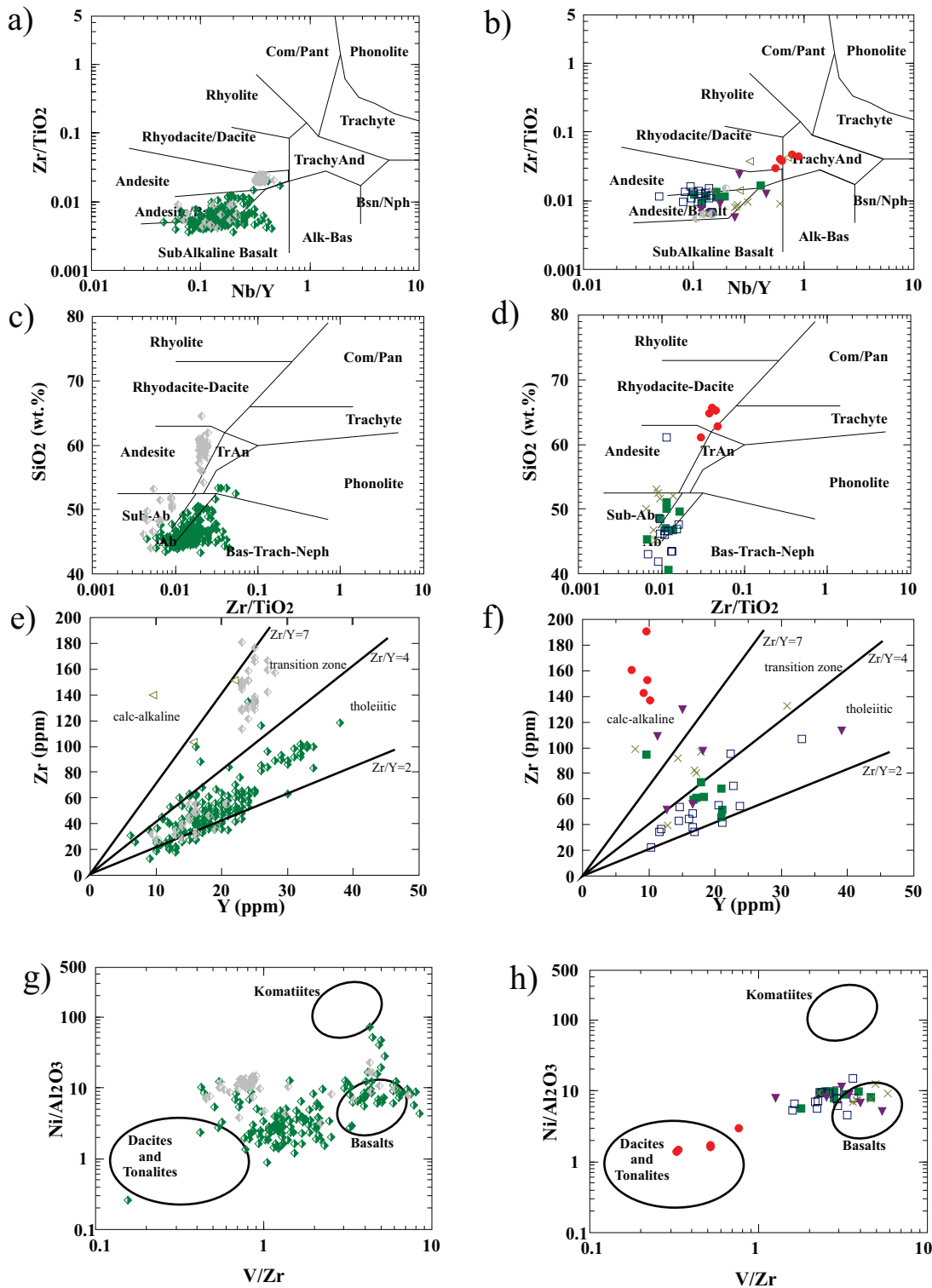


Musselwhite mine stratigraphy. This suggests the siliciclastic component of the silicate-dominant BIF represents weathered mafic to intermediate igneous rock.

Figure 5.13 contains mafic and intermediate volcanic rocks (from Musselwhite, introduced in Chapter Four) in one series of plots and siliciclastic samples on different plots for comparison. Figure 5.13a-b and 5.13c-d show that silicate-dominant BIF samples geochemically overlap with volcanic samples. Both sample sets plot between basalt and andesite fields. Figure 5.13e-f show that both mafic and silicate-dominant BIF samples share tholeiitic geochemical affinity. Figure 5.13g-h is slightly enigmatic as the silicate-dominant BIF samples plot closer to the basalt field than the basalt samples themselves.

In Figure 5.9 samples of the silicate-dominant BIF consistently plot in the smectite field. This diagram has previously been explained in Chapter Four as well as earlier in this chapter. It is important to note that smectite is the end product of weathered volcanic glass and can also be formed from the breakdown of Ca and/or Na-rich silicate minerals (Neuendorf *et al.*, 2005). Smectite contains no potassium. It is logical to assume that if this siliciclastic material was eroding from intermediate to felsic source rocks at least some illite would have been formed due to the fact that these rock types contain potassium.

The grunerite content, in the silicate-dominant BIF, is a reflection of the original mineralogy as well. Figure 5.1a-b shows that the NIF oxide- and silicate-dominant BIF geochemically overlap in terms of total iron values suggesting the silicate-dominant BIF in some instances contains abundant magnetite. The grunerite observed in the silicate-dominant BIF is the result of magnetite and quartz reacting together under metamorphic conditions. This reaction requires fluid to reach completion. Therefore abundant grunerite is an indication of high fluid content in this lithology during metamorphism.



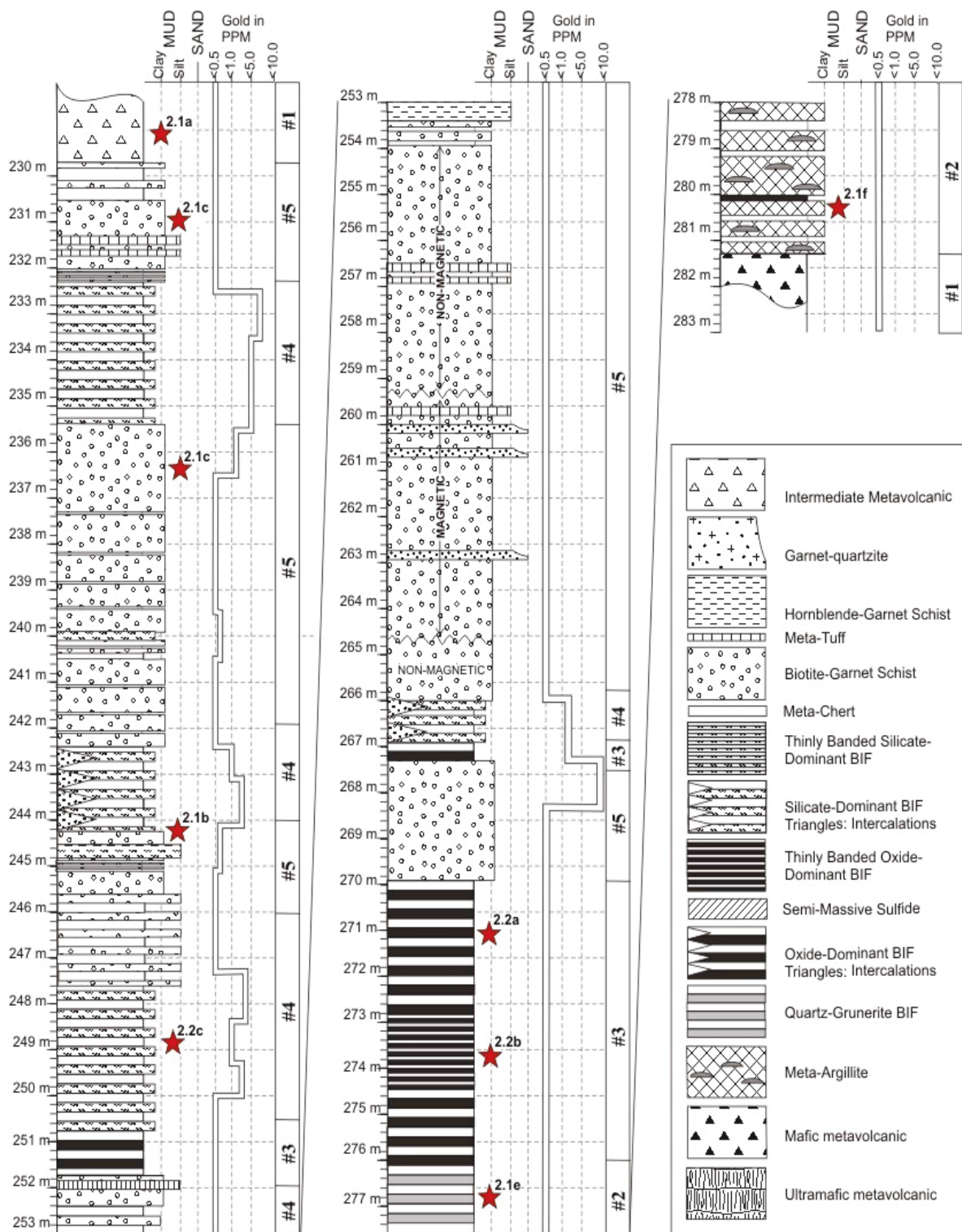
**Figure 5.13. Binary discrimination diagrams containing the mafic/intermediate volcanic samples. Note that green-diamonds are mafic samples and grey-diamonds are intermediate samples. Siliciclastic-dominant samples from the current study are plotted on separate diagrams for comparative purposes, symbols are the same as in Fig. 5.1. a) Nb/Y vs. Zr/TiO<sub>2</sub> for volcanic samples (Winchester and Floyd), b) Nb/Y vs. Zr/TiO<sub>2</sub> for metasediment samples (Winchester and Floyd), c) Zr/TiO<sub>2</sub> vs. SiO<sub>2</sub> for volcanic samples (Winchester and Floyd), d) Zr/TiO<sub>2</sub> vs. SiO<sub>2</sub> for metasediment samples (Winchester and Floyd), e) Y vs. Zr for volcanic samples (McLean), f) Y vs. Zr for metasediment samples, g) V/Zr vs. Ni/Al<sub>2</sub>O<sub>3</sub> for volcanic samples h) V/Zr vs. Ni/Al<sub>2</sub>O<sub>3</sub> for metasediment samples.**

At this point it is important to note that the lithologies stratigraphically above the silicate-dominant BIF have historically been arranged in the following manner: biotite-garnet schist, garnet-bearing quartzite, and hornblende-garnet schist. However, based on the observed geochemical trends in Chapter Four, it is suggested that the stratigraphy be arranged in the following order: hornblende-garnet schist (Fig. 5.10iv-a), biotite-garnet schist (Fig. 5.10iv-b), and garnet-bearing quartzite (Fig. 5.10iv-c). These lithologies will be discussed in this stratigraphic order. It should be noted that the biotite-garnet schist is more voluminous compared to the hornblende-garnet schist and garnet-bearing quartzite, which are intercalated within the biotite-garnet schist (Fig. 5.14, see 230-247m).

The hornblende-garnet schist is a largely continuous unit within the NIF assemblage. It is most commonly found intercalated with other siliciclastic-dominant lithologies stratigraphically above the silicate-dominant BIF. Note that the hornblende-garnet schist is also found as bands within the silicate-dominant BIF, as well as in the transitional BIF between the oxide- and silicate-dominant BIFs.

The principal hornblende-garnet schist horizon ranges up to one or two metres thick and represents metamorphosed mudstone. This lithology is also an IF due to its high iron content. The hornblende-garnet schist is composed primarily of clay minerals derived from mafic to intermediate igneous material. This conclusion is based on the persistent overlap between the hornblende-garnet schist samples and the igneous samples seen in Figure 5.13a-g. Thicker beds, containing few chert layers, were likely deposited slowly. The lack of chert layers indicates that hydrothermal activity in the immediate area was minimal. However, the hornblende-garnet schist has high iron content and is in fact an iron formation (Fig. 5.1b). This indicates the waters in which this lithology was deposited were saturated and precipitating iron compounds. The iron was possibly put into the water by hydrothermal smoker systems further a field.

As well as stratigraphic overlap the hornblende-garnet schist and silicate-dominant BIF exhibit similar geochemistry and geochemical trends. Similar geochemical trends are observed in Figures 5.1b, 5.8b, 5.12e-f, and 5.13f. This further supports a sedimentary-genetic link between these two lithologies. Out of the three stratigraphically



**Figure 5.14. Detailed stratigraphic log of drill hole 04-ESN-010 showing the relative abundance of biotite-garnet schist compared to hornblende-garnet schist and garnet quartzite in the interval 230-247m. White lines represent Au values. Note the lithologic associations to the right of each stratigraphic column, these lithologic associations are described in Chapter Two.**

overlying siliciclastic lithologies (i.e. hornblende-garnet schist, biotite-garnet-schist, and garnet-bearing quartzite) the hornblende-garnet schist is the lithology most consistently associated with the silicate-dominant BIF in both geochemical and stratigraphic terms. Due to similar geochemical trends, this is likely the same siliciclastic detrital material in the silicate-dominant BIF. It should be noted that the hornblende-garnet schist also exhibits geochemical similarities to the biotite-garnet schist.

The biotite-garnet schist comprises the thickest sedimentary unit stratigraphically above the silicate-dominant BIF (Fig. 5.10iv-b). This lithology has high aluminium, potassium, and iron concentration indicating it was originally ferruginous shale. The potassium-rich nature of this lithology is an indication it was weathered from intermediate to felsic igneous source rocks. The high iron content of the biotite-garnet schist is enigmatic as intense black smoker hydrothermal activity appears to have diminished by the time this lithology was deposited. However, the high iron-content may be the result of lingering, less intense, hydrothermal black smoker activity.

Again, much like the hornblende-garnet schist, the biotite-garnet schist was deposited as siliciclastic detritus settling out of the water column in iron-rich waters. However, unlike the hornblende-garnet schist this siliciclastic detritus was eroded primarily from intermediate to felsic igneous sources based on the high potassium content of the rock. The potassium content does not appear to be the result of secondary enrichment. This is because samples of the biotite-garnet schist maintain positive linear relationships between immobile elements like aluminium, titanium, and zirconium. In fact biotite-garnet schist samples plot on the linear trend-lines delineated by the silicate-dominant BIF and hornblende-garnet schist (Fig. 5.15a-d).

Figure 5.14 shows that meta-chert bands are a less common feature in the biotite-garnet schist (see 236-240m) compared to the underlying lithologies (see 243-253m). The reduced presence of meta-chert layers in the biotite-garnet schist indicates hydrothermal smoker activity was minimal by the time this lithology was deposited.

The garnet-bearing quartzite, although intercalated with the biotite-garnet schist, is typically the uppermost lithology in the NIF assemble (Fig. 5.10iv-d). This lithology is

the only truly volcanoclastic lithology in this assemblage (Fig. 5.8b). It represents the end of sedimentation of the NIF assemblage proper as only a few, separate, metasedimentary horizons are present in the overlying mafic to intermediate volcanic rocks (Fig. 5.10 v-a). Based on the garnet-bearing quartzite's chemistry and mineralogy, the protolith to this lithology is felsic volcanoclastic sediment.

The garnet quartzite exhibits very pronounced LREE enrichment (Fig. 5.12h) indicating that the sediment was derived from a felsic igneous source. There is a significant difference between the REE curves of the garnet-bearing quartzite and the biotite-garnet schist. The biotite-garnet schist exhibits a flat, MORB-like, trend (Fig. 5.12g) compared to the garnet-bearing quartzites steeply inclined REE curve. The garnet-bearing quartzite probably represents volcanic ash deposits from distal felsic volcanic eruptions.

The garnet-bearing quartzite does not plot on the trend-line delineated by the other lithologies in the NIF assemblage (Fig. 5.15a-c). However, it does share some geochemical similarities to the biotite-garnet schist. Both lithologies also contain a biotite-quartz-garnet mineral assemblage. It is possible these two lithologies were derived from similar source material. The differences between the two lithologies could result from mechanical sorting during sediment transport. Mechanical sorting would produce geochemical partitioning of various elements (geochemical partitioning depends on grain size).

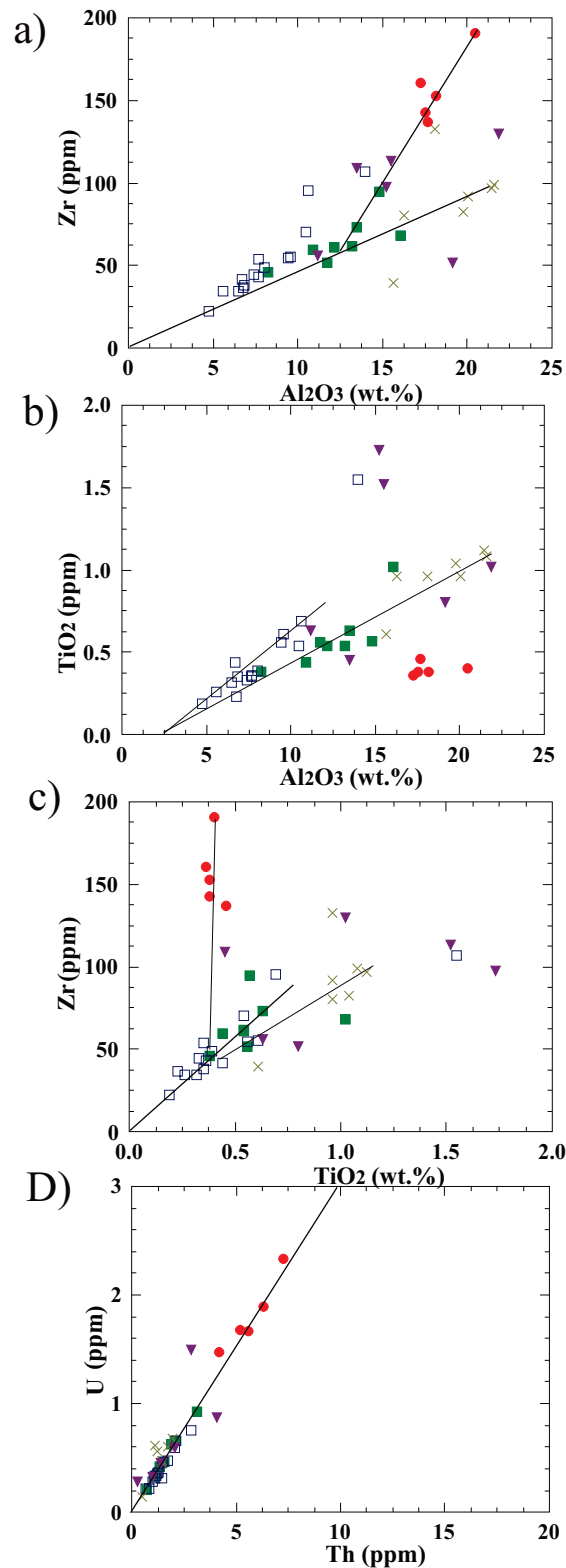
The garnet-bearing quartzite marks the end of the NIF sedimentary assemblage proper (several thinner metasedimentary horizons exist above the NIF assemblage). The volcanic rocks overlying the NIF assemblage range from mafic to felsic (Fig. 5.10vi-a). It is a likely possibility that the felsic volcanic rocks are part of the South Rim Metavolcanic assemblage of the NCLB (refer to Section 1.6.4). The SIF and NIF sedimentary assemblages have historically been grouped with the Opapimiskan Lake Metavolcanic assemblage (refer to Section 1.6.7).

In summary the SIF argillite and oxide-dominant BIF as well as the NIF argillite, quartz-grunerite BIF, and oxide-dominant BIF are primarily composed of exhalite material and represent lithologies deposited in association with peak hydrothermal smoker activity.

The transitional BIF and silicate-dominant BIF record the initial demise of the hydrothermal system and the start of a siliciclastic regime of sedimentation. The diminishing hydrothermal system is further reinforced by the lack of quartz and magnetite bands in the stratigraphically highest units (hornblende-garnet schist, biotite-garnet schist, and garnet-bearing quartzite, there are minor disperse quartz bands in these units). The hornblende-garnet schist, biotite-garnet schist, and garnet-bearing quartzite primarily consist of siliciclastic material and therefore represent the peak of siliciclastic sedimentation.

The Northern Iron Formation is characterized by a decreasing degree / strength / duration of subaqueous hydrothermal activity, as well as a general increase in siliciclastic sedimentation rates stratigraphically. The source of the siliciclastic material becomes more felsic stratigraphically upward (see Figure 5.12e-h and Figure 5.13b, d, f, and h). Source rocks for the silicate-dominant BIF and hornblende-garnet schist range from mafic to intermediate in composition, whereas source rocks for the biotite-garnet schist and garnet-bearing quartzite range from intermediate to felsic in composition. This interpretation of source material is also based on the high potassium content of the biotite-garnet schist and garnet-bearing quartzite. The logical source of potassium-rich sediment is intermediate to felsic igneous source rocks.

In terms of tectonic setting both the volcanics and siliciclastic sediments exhibit the same style of incompatible element REE curves (Fig 4.15). These REE curves have a general arc signature. Taking into account the plume model proposed by Hollings and Kerrich (1998), it is possible these rocks represent plume-arc contaminated MORB. It has already been established that volcanic lithologies range from being associated with ocean floor basalts to ocean island volcanism. The author of the current study proposes that the SIF and NIF assemblages, as well as the volcanic lithologies, were deposited in oceanic island component of a large-igneous province, which was formed in association with plume-driven magmatism. This can explain all the features seen in the lithologies at Musselwhite. Such features include the presence of hydrothermal smoker systems, associated with volcanically active oceanic-island settings, as well as rapid



**Figure 5.15.** a) Al<sub>2</sub>O<sub>3</sub> vs. Zr plot, siliciclastic dominated lithologies, b) Al<sub>2</sub>O<sub>3</sub> vs. TiO<sub>2</sub> plot, siliciclastic dominated lithologies, c) Zr vs. TiO<sub>2</sub> plot, siliciclastic dominated lithologies, d) U vs. Th plot, siliciclastic dominated lithologies. Note that trend-lines are drawn based on visually observed linear trends. Symbols are the same as in Fig. 5.1.



sedimentation, which can be explained by the formation of volcanic islands associated with the accumulation of volcanic flows.

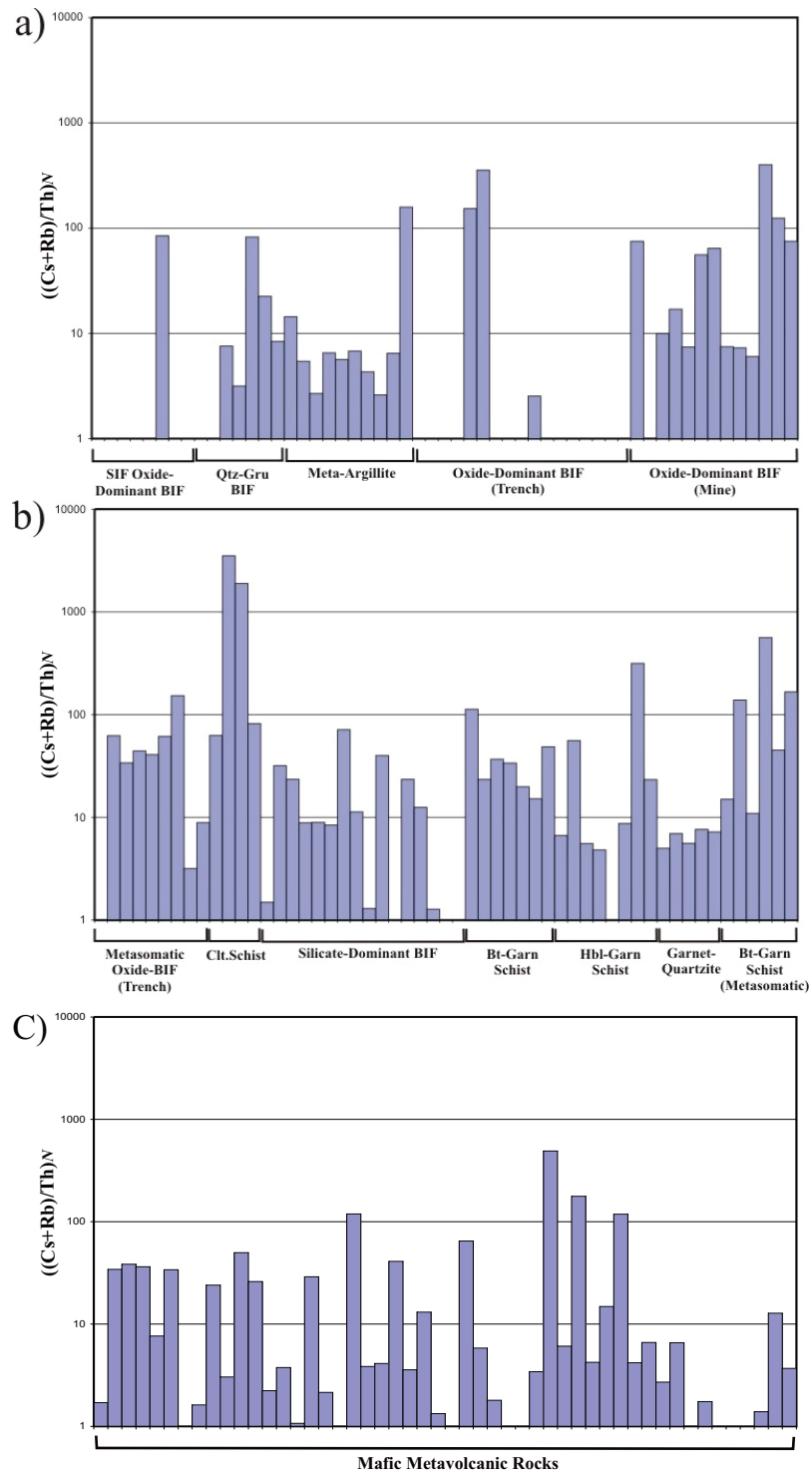
The author hypothesizes that the siliciclastic sediment was derived from the weathering of the northern part of the NCLB (Fig. 1.3). This is because intermediate and felsic igneous rocks are abundant in the north relative to the southern part of the belt.

#### 5.4 Metasomatic Alteration as a Vector to Mineralization

It is possible to use geochemical methods to explore for gold deposits. Gold mineralization in orogenic terranes is commonly accompanied by amplified Se, W, As, Bi, Te, and Sb abundances (Barnes, 1997). Further geochemical changes associated with gold mineralization include enrichment of major elements (Na, K, Mg; Heath and Campbell, 2004) and trace elements (Ag, Sc, Ba, Rb, Te, As, and Bi; Barnes, 1997). Enrichment of these elements can be used as a vector to mineralization. In addition to mineral and whole-rock chemistry, it is possible to use more traditional methods of exploration, including lithologic and structural associations in the exploration for concealed gold deposits. It should be noted that the following associations are for Musselwhite and interpreting mineralization patterns in other banded iron formations should be done on an individual basis depending on the characteristics of those deposits.

Enrichment of alkali-elements is typically associated with gold mineralization (Kerrich, 1983). Consequently, much of the ensuing discussion is constructed around alkali element mobility and utilizing this characteristic as a possible vector to gold mineralization. In addition to utilizing the mobility of alkali-elements as indicators of gold mineralization, factor analysis dendrograms, examining the relationship of elements to one and other and samples to one and other, were used to determine probable alteration patterns.

Possible metasomatic hydrothermal trends and signatures, within the rocks of the Musselwhite gold deposit, were introduced in Section 4.7. Figures 5.16a, b, and c are histograms, which depict the  $((Cs+Rb)/Th)_N$  value for individual samples from the current study. Note the y-axis is logarithmic. Figure 5.16a contains the exhalite-dominant lithologies, Figure 5.16b contains the siliciclastic dominant lithologies, and Figure 5.16c



**Figure 5.16. Histograms displaying the  $((Cs+Rb)/Th)_N$  values for individual samples. Samples are grouped by lithology as indicated by the horizontal lines. a) Exhalite dominant lithologies where SIF= SIF assemblage oxide-dominant BIF, 4h= meta-argillite, 4a= quartz-grunerite BIF, Trench 4B= NIF assemblage oxide-dominant BIF collected from trenches, Mine 4B= NIF assemblage oxide-dominant BIF collected from drill core (i.e. Close to mineralization), b) Siliciclastic dominant lithologies where: Alt= altered NIF assemblage oxide-dominant BIF from trenches, TB= chlorite dyke from trenches, 4EA= silicate-dominant BIF, 4F= biotite-garnet schist, 4E= hornblende-garnet schist, 6= garnet-quartzite, B-alt= metasomatic biotite-garnet schist, c) Metavolcanic samples.**

contains the mafic volcanic lithology. Samples from the lithologies at Musselwhite exhibit a diverse array of  $((Cs+Rb)/Th)_N$  values from 0 to  $\gg 5$  suggesting a range of depletion to very strong alkali enrichment.

The majority of samples, regardless of lithology, exhibit alkali alteration values of  $>5$  suggesting they have undergone alkali-element metasomatism (enrichment). However, there does not appear to be a definitive pattern of alkali-element enrichment and/or depletion amongst the sample set at least in terms of individual lithologies.

Common, albeit weak, trends observed include: 1) pervasive alkali element enrichment in the samples closest to the ore-zones, whereas alkali element enrichment/depletion appears to be more selective in the trench lithologies, 2) possible alkali-element depletion in the oxide-dominant BIF (collected from the trenches) as well as SIF assemblage oxide-dominant BIF, and 3) in general the mafic volcanic samples exhibit lower average alkali metasomatism values of  $\sim 5$  to  $<5$  with multiple anomalous samples exhibiting strong alkali-element enrichment.

The biotite-garnet schist and garnet-bearing quartzite are biotite-rich lithologies found close to the ore-zones. Note, in the previous section it was established that these are primary lithologies and are not formed in association with mineralization. Since both lithologies are biotite-rich and biotite contains abundant alkali-elements, it may be expected that these lithologies should have higher alkali-element metasomatism values. However, this is not the case; in fact, these lithologies have lower ratios than the metasomatised oxide-dominant BIF from the trenches and even some oxide-dominant BIF samples. These latter lithologies do not contain much biotite at all. This geochemical trend indicates that not all alkali-element metasomatic enrichment (Cs, Rb, Th) results in higher biotite content.

Interestingly and rather counter intuitively, samples of the silicate-dominant BIF, which is the main ore-hosting lithology, exhibit moderate-average alkali index of alteration values. However, it should be noted that when  $((Cs+Rb)/Th)_N$  is plotted against elements associated with gold mineralization (specifically Se), for samples of the silicate-dominant

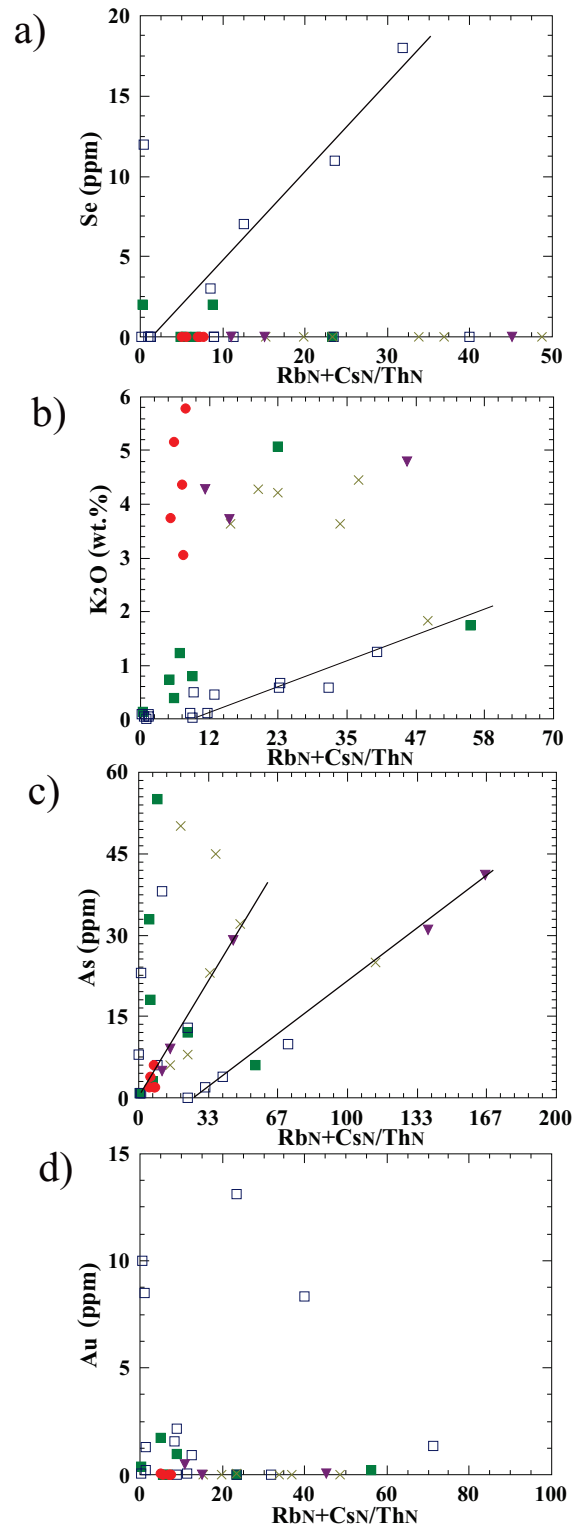
BIF, a positive linear trend is formed. This positive correlation between  $((Cs+Rb)/Th)_N$  and Se suggests Se was brought into the rocks with the alkali-rich metasomatic fluid.

Both the SIF assemblage and SIF assemblage (trench) oxide-dominant banded iron formations are relatively distal to the main ore-zones at Musselwhite. There is a stark contrast in alkali alteration values between the SIF oxide-dominant BIF ( $<5$ ), SIF assemblage oxide-dominant BIF collected from the trenches ( $<5$ ) and that collected from closer to the ore-zones ( $>5$ ) (labelled 'mine' in Fig. 5.16a). This pattern suggests that alkali element depletion may have occurred locally distal to the ore-zones whereas alkali element enrichment occurs proximal to the ore-zones.

The samples collected from closest to the main ore-zones exhibit consistently high ( $>5$ ) alkali-element metasomatism values. A different pattern of alkali-element metasomatism is observed in samples collected distal to the main ore-zones (trenches). The reader should note that Figure 1.4 is a map of the mine property showing the relative location of the main ore-zones and trenches whereas Figure 1.8 is an enlarged view of the trenches themselves. As stated above, alkali element enrichment and depletion can be loosely correlated to lithology in the trenches. This is in contrast to the universal pattern of alkali-enrichment enrichment near the ore-zones.

In the trenches, samples of the oxide-dominant BIF exhibit alkali-element depletion whereas samples of the metasomatic-oxide-dominant BIF and chlorite schist exhibit alkali-element enrichment. It should be noted that alkali-element enrichment is astonishingly high in the chlorite schist leaving no doubt that it is a product of focused metasomatic alteration. The chlorite schist occurs as a dyke which cross-cuts the oxide-dominant BIF. Both the chlorite schist and metasomatised oxide-dominant BIF are distinct units enclosed within a thick sequence of oxide-dominant BIF (Fig. 1.8).

The metasomatised oxide-dominant BIF and chlorite schist samples (trench) exhibit the most consistent  $>>5$  alkali index of alteration values suggesting these lithologies are associated with metasomatic-fluid pathways.



**Figure 5.17. Binary plots displaying  $((Cs+Rb)/Th)N$  as the x-variate versus various elements associated with gold mineralization (as the y-variate). Symbols are the same as in Fig. 5.1. a)  $((Cs+Rb)/Th)N$  vs. Se for siliciclastic dominant lithologies, b)  $((Cs+Rb)/Th)N$  vs  $K_2O$  for siliciclastic dominant lithologies, c)  $((Cs+Rb)/Th)N$  vs. As for siliciclastic-dominant lithologies, d)  $((Cs+Rb)/Th)N$  vs. Au for siliciclastic-dominant lithologies.**

Figure 5.17 expands on the histograms depicted in Figure 5.16. It contains various binary diagrams of  $((Cs+Rb)/Th)_N$  as the x-variant plotted against a variety of elements, associated with gold-mineralization, on the y-axis. Figures 5.17a, b, c, and d contain the silicate-dominant lithologies. The reader should note the exhalite-dominant lithologies do not form discernable trends in these plots. Therefore they are not discussed in this chapter. If the reader is interested these diagrams are presented as Figure 4.25a, c, e, and f in Chapter Four.

Figure 5.17a depicts  $((Cs+Rb)/Th)_N$  vs. selenium for the siliciclastic-dominant lithologies. A strong positive linear correlation is formed by four silicate-dominant BIF samples and one hornblende-garnet schist sample (samples: 4ea-PM05-066, 4ea-PM06-002, 4ea-06-20-UG004, 4ea-07-20-067, and 4e-07-20-034b). This indicates selenium in these samples is associated with alkali-element metasomatism (enrichment). It is important to note that selenium substitutes for sulphur in sulphide minerals (Deer *et al*, 1992). By extension, this substitution relationship almost certainly indicates sulphur was also transported/ remobilized by alkali enriched metasomatic fluids. This positive linear trend is significant because gold is strongly associated with pyrrhotite in the Musselwhite gold deposit. A positive correlation between Se/S and  $((Cs+Rb)/Th)_N$  lends credence to the alkali index of alteration being a reliable vector to gold mineralization associated with sulphidation in the silicate-dominant BIF.

Figure 5.17b depicts  $((Cs+Rb)/Th)_N$  versus  $K_2O$  for the siliciclastic-dominant lithologies. The samples form two groups; 1) a high  $K_2O$  group consisting of biotite-garnet schist, metasomatic biotite-garnet schist, garnet-bearing quartzite, and 2) a low  $K_2O$  group consisting of silicate-dominant BIF and hornblende-garnet schist. A positive linear correlation between  $((Cs+Rb)/Th)_N$  and  $K_2O$  is observed in the latter group. The positive linear correlation indicates there was some  $K_2O$  addition associated with the alkali-rich mineralizing fluids in the silicate-dominant BIF and hornblende-garnet schist. As such, the presence of biotite can be interpreted as yet another sign of possible gold mineralization in the silicate dominant BIF. Samples in the  $K_2O$ -rich sample grouping do not exhibit positive linear correlations between  $((Cs+Rb)/Th)_N$  and  $K_2O$ . The lack of linear trends may be due to the high concentration of primary biotite in these lithologies.

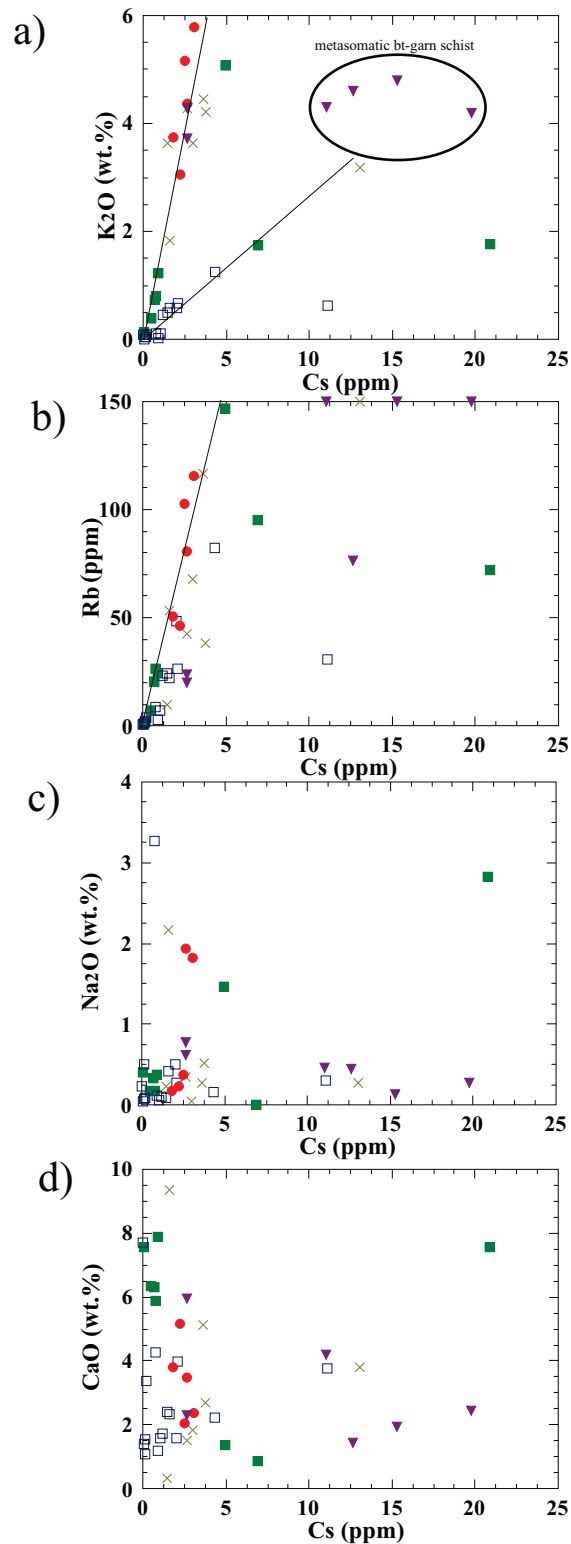
Figure 5.17c depicts  $((Cs+Rb)/Th)_N$  versus arsenic for the siliciclastic-dominant lithologies. It should be noted that arsenopyrite is commonly associated with gold mineralization in orogenic gold deposits and that is why this diagram is relevant. Two separate positive linear trends are present in Figure 5.22c. Both these trends contain samples from the same lithologies. These trends suggest that arsenopyrite is brought into the rocks with alkali-element-rich metasomatic fluids. Additionally, the positive linear correlations suggest the presence of arsenopyrite in the silicate-dominant BIF can be an indication of gold mineralization.

Figure 5.17d depicts  $((Cs+Rb)/Th)_N$  versus gold. Unfortunately there is no direct correlation between gold and  $((Cs+Rb)/Th)_N$ . However, two out of the four samples with the highest gold values also have high  $((Cs+Rb)/Th)_N$ .

Figure 5.18 expands on the histograms depicted in Figure 5.16 and the binary diagrams of Figure 5.17. This figure consists of binary-diagrams with Cs as the x-variant plotted against a variety of mobile elements on the y-axis. Figures 5.28b, d, f, and h contain the silicate-dominant lithologies. The reader should note the exhalite-dominant lithologies do not form discernable trends in these plots. Therefore they are not discussed in this chapter. If the reader is interested, these diagrams are presented as Figure 4.26a, c, e, and f in Chapter Four.

Figure 5.18a depicts Cs vs.  $K_2O$  for the siliciclastic-dominant lithologies. The samples form two positive linear trends in Figure 5.18a. A steep positive linear trend primarily delineated by samples of the hornblende-garnet schist, biotite-garnet schist, and garnet-bearing quartzite. This is likely the result of the high concentration of primary biotite in these lithologies.

A second, shallower positive linear trend is delineated by samples of the silicate-dominant BIF. This shallower trend is likely the result of mobilization of alkali-elements associated with the mineralization of the silicate-dominant BIF. Part of the reason for this inference is that the shallower linear trend evolves toward a group of metasomatic



**Figure 5.18. Binary plots of Cs versus various elements associated with metasomatic alteration. Note that linear trend-lines are based on visual observations and symbols are the same as in Fig. 5.1. a) Cs vs. Rb for siliciclastic-dominant lithologies, b) Cs vs. Rb for siliciclastic-dominant lithologies, c) Na<sub>2</sub>O vs. Cs for siliciclastic-dominant lithologies, d) Cs vs. CaO for siliciclastic-dominant lithologies.**



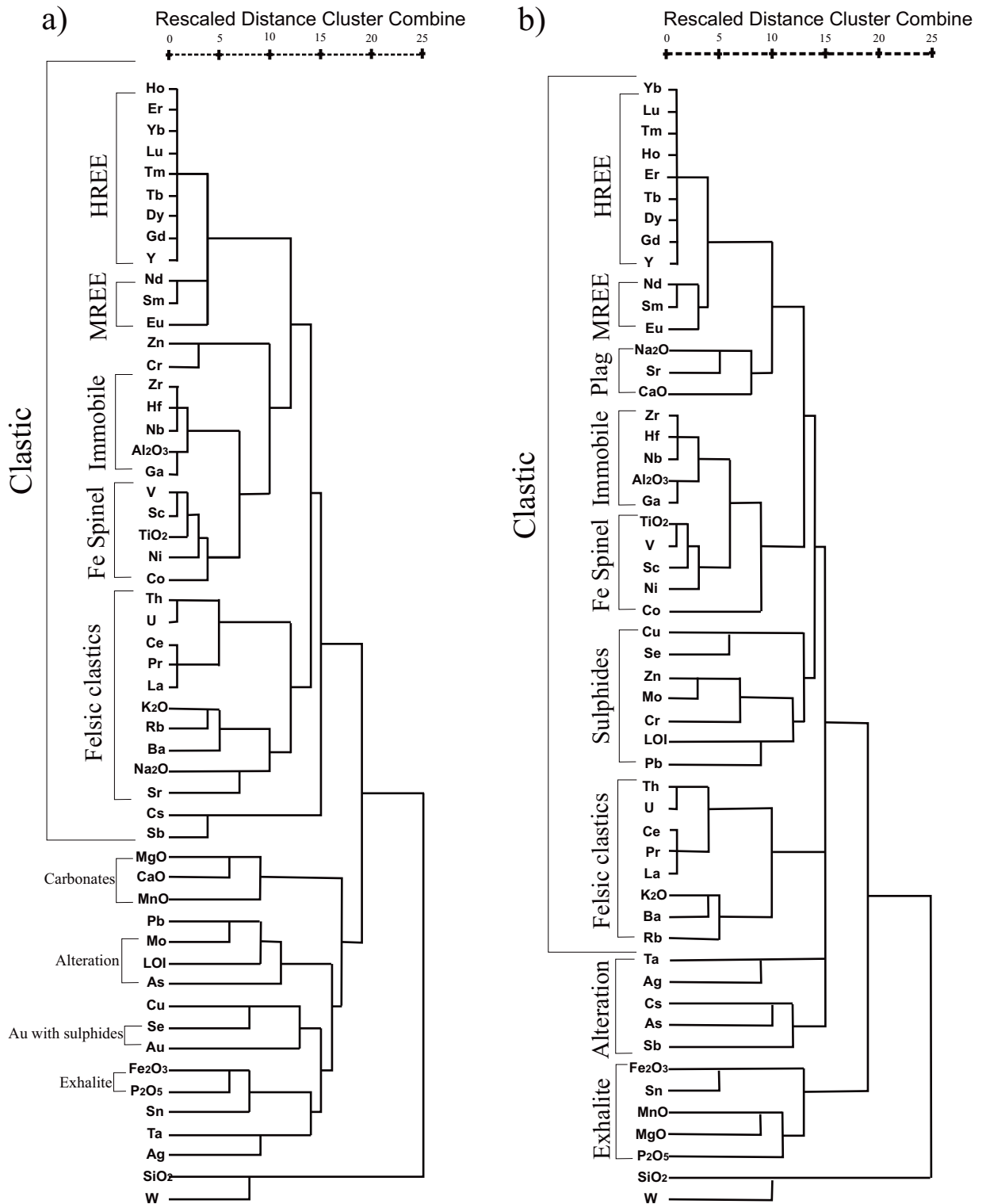
biotite-garnet schist samples. This group of samples does not plot with the regular biotite-garnet schist, which plots along the steeper, primary biotite, trend-line. This trend reinforces the notion of minor secondary biotite in the silicate-dominant BIF, which was formed from potassium and alkali-element rich metasomatic fluid.

Figure 5.18b depicts Cs vs. Rb for the siliciclastic-dominant lithologies. Samples from all the siliciclastic-dominant lithologies form a weak positive linear correlation between Cs and Rb on this diagram. The remaining Figures 5.18c and 5.18d contain Cs vs. Na<sub>2</sub>O and CaO, respectively. Samples from all lithologies exhibit a scattered nature and do not form coherent trends in these plots. This suggests that sodium and calcium are enriched and depleted seemingly at random and are less useful elements to examine when looking for gold close to the mineralized zones at Musselwhite.

Figure 5.19 consists of factor analysis dendrograms comparing element behaviour between the various samples. Elements which behaved in a similar manner plot closest to each other on the dendrograms. If a pronounced metasomatic mobilization of elements occurred within the lithologies at Musselwhite, this statistical analysis procedure should reveal it. As such the dendrograms are a logical progression from the above discussed diagrams.

Figure 5.19a is a cluster analysis dendrogram generated from seventy-two samples having gold values. Figure 5.19b is a cluster analysis dendrogram generated from the entire sample set and does not include gold values. The latter sample set contains all samples from the current study including samples collected distal to the ore-zones.

The dendrograms reveal that the majority of elements can be broadly divided into two clusters, those which came from a siliciclastic detrital source and those which came from an exhalite source. The reader should note that since elements group together in an expected manner fully explainable by mineralogical controls. In combination with the trends in Figures 5.16-5.18, the dendrograms imply that metasomatic alteration at Musselwhite was not pervasive and/or omnipresent throughout the rocks. This does not mean metasomatic alteration altogether is not present; on the contrary, it is likely confined to focused metasomatic fluid-pathways, primarily shear-zones.



**Figure 5.19. Cluster analysis dendrograms for samples from the current study. Note elements which behaved in a similar manner plot closest to each other on the dendrogram. a) Cluster analysis dendrogram for seventy-two samples (including Au values) from the NIF assemblage at Musselwhite gold deposit, b) Cluster analysis dendrogram for 106 samples from the NIF assemblage at Musselwhite gold deposit (excluding Au values).**

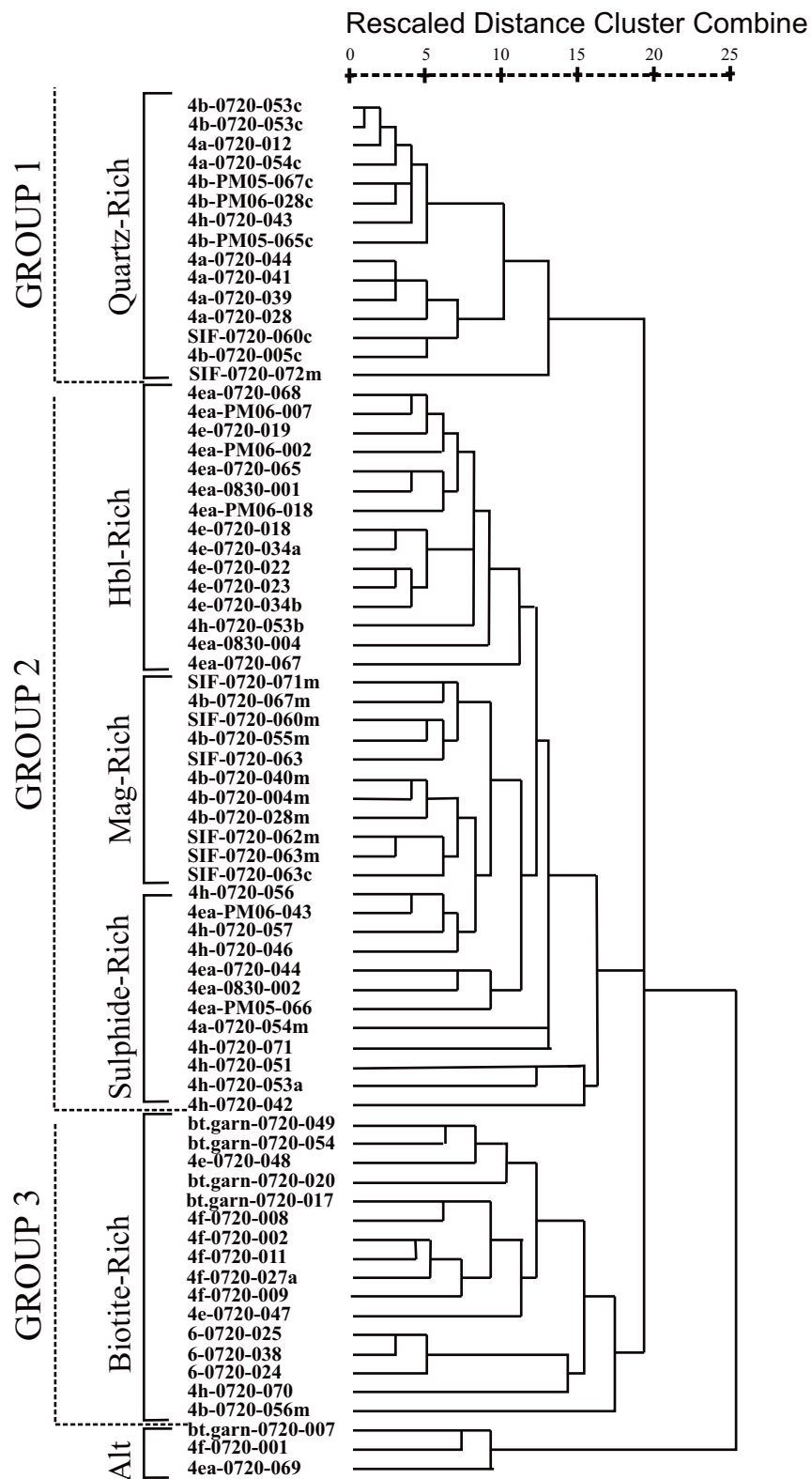
sum to 100 wt. % so more SiO<sub>2</sub> in a sample will result in most other elements having lower values. Interestingly W is the one element that clusters with SiO<sub>2</sub> suggesting W is coming into various lithologies with quartz veining. Tungsten enrichment is associated with, orogenic gold deposits.

Additional element clusters in Figure 5.24a include Mo, LOI, and As which along with Au, Se, and Cu probably represent elements added during alkali-element metasomatism. Molybdenum and copper are commonly associated elements with gold mineralization. The fact that LOI is grouping with these elements suggest that metasomatic fluids formed minerals with a hydrous component, such as biotite and amphiboles.

Selenium and Cu are the elements which cluster closest to gold. As stated above selenium substitutes for sulphur in sulphide minerals (Deer *et al.*, 1992) and copper is an element commonly associated with gold mineralization. Therefore Au can be considered to cluster with sulphur (S was not analyzed) and is associated with sulphide minerals as described above.

The most significant difference between Figures 5.19a and 5.19b is the Cu, Se, Zn, Mo, Cr, LOI, and Pb cluster which is observed Figure 5.19b but not Figure 5.19a. This cluster is likely controlled to some degree by sulphide minerals. The strong similarities between the cluster analyses of both groups (Fig. 5.19a and 5.19b) suggest that there is not a large difference in between lithologies and samples distal to the main ore-zone and those which are proximal. The similarities between the two dendrograms suggest that element behaviour at the Musselwhite deposit is universal across the area sampled (i.e., between the trenches and the main ore-zones).

Figure 5.20 is a cluster analysis dendrogram comparing all samples for which there are gold values (n=72). This is opposed to the earlier dendrograms where elements are compared (Fig. 5.19a and 5.19b). It should be noted that samples are compared through factor analysis to see how closely they are related. Please refer to Section 4.2 for a detailed description of the methodology behind the generation of dendrograms. Samples are compared to see if they plot together by lithology and/or mineralogy. In theory, as



**Figure 5.20.** Cluster analysis dendrograms for seventy-two samples (those with Au values) from the NIF assemblage at Musselwhite gold deposit. Samples can be broadly divided into three groups. Note samples which behaved in a similar manner plot closest to each other on the dendrogram.

long as the samples are not altered, this is how they should group together.

The sample groups, in this dendrogram, are primarily based on the original sample chemistry, which is reflected by the sample's mineralogy. It should be noted that there does not appear to be a subgroup of samples with high gold values or an alteration subgroup. Samples can be broadly divided into three main groups. These groups are termed group one: consisting of quartz-rich samples, group two: consisting of transitional exhalite- to silicate-dominant samples, and three: consisting solely of siliciclastic-dominant samples. It should be noted that there is a sulphide-rich subgroup in group two. Some samples in this group are likely the result of sulphidation, while other samples contain abundant original sulphide.

Group one is formed by SIF and NIF assemblage quartz-dominant samples, as well as quartz-grunerite BIF samples. These samples group together because they are composed primarily of quartz. Group Two is the largest group of samples. This group is formed from the following lithologies: meta-argillite, SIF and NIF assemblage magnetite, hornblende-garnet schist, and silicate-dominant BIF samples. Group Three is roughly the same size as Group One and is formed from the following lithologies: biotite-garnet schist, metasomatic biotite-garnet schist, and garnet-bearing quartzite samples. These lithologies group together due to their high potassium and alkali-element concentrations. The reader should note that the metasomatic biotite-garnet schist is part of Group Three as opposed to plotting in a separate alteration group.

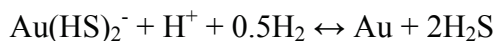
A number of smaller subgroups compile to form Group Two. These subgroups appear to be controlled by the mineralogy of the samples. The subgroups are as follow: hornblende- and garnet-rich, magnetite-rich, and sulphide-rich sample groupings. Note that these groups are delineated by brackets in Figure 5.20.

The first two groupings reflect the original chemistry of the lithologies and are not a product of metasomatic alteration. However, the present mineralogy *is* a reflection of the original chemistry of the rocks as well as the metamorphic grade.

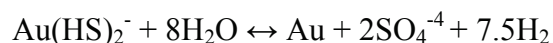
The third, sulphide-rich, subgroup is a reflection of both original chemistry as well as later sulphidation. Samples of the meta-argillite (4h-) are rich in primary sulphide. Justification for this conclusion is presented in the previous section. Interestingly, several silicate-dominant BIF samples (4ea-PM05-066, 4ea-PM06-043, 4ea-07-20-044, and 4ea-08-30-002) are included in the sulphide-rich group. These samples were probably enriched in sulphide through a sulphidation process associated with alkali-element metasomatism (see Fig. 5.17).

The sulphide-rich samples of silicate-dominant BIF were likely produced through sulphidation of the host rock. This sulphidation of these rocks appears to be at least partially related to the alkali-element metasomatism described above. The reader should note that in order for gold to be transported in fluids circulating through the Earth's crust it is necessary for gold to go into solution. The solubility of gold will increase if it forms a complex with anionic species (ligands) such as sulphide ( $\text{HS}^-$ ) or chloride ( $\text{Cl}^-$ ) (Seward and Barnes, 1997). Gold is transported as  $\text{Au}(\text{HS})_2^-$  complex when in a fluid of a near-neutral pH and reduced state (low-sulphidation systems).

Boiling and fluid mixing are the two processes that induce precipitation of gold in low-sulphidation systems. The  $\text{Au}(\text{HS})_2^-$  complexes destabilizes when boiling takes place, as boiling results in the loss of the bisulphide ion to the vapour phase:



Mixing of oxidized meteoric water which migrates from the surface with metasomatic and / or magmatic fluid will also cause gold to precipitate from the solution, as in the following reaction:



Therefore, the sulphide in the silicate-dominant BIF is possibly an indication of gold being transported as an  $\text{Au}(\text{HS})_2^-$  complex. When metasomatic fluid, rich in  $\text{Au}(\text{HS})_2^-$ ,

interacted with the silicate-dominant BIF it became destabilized through chemical reactions with the iron-rich silicate-dominant BIF. That is to say, the silicate-dominant BIF acted as a chemical trap. The products of the chemical reaction between the bisulphide-complex and the BIF include the gold and pyrrhotite.

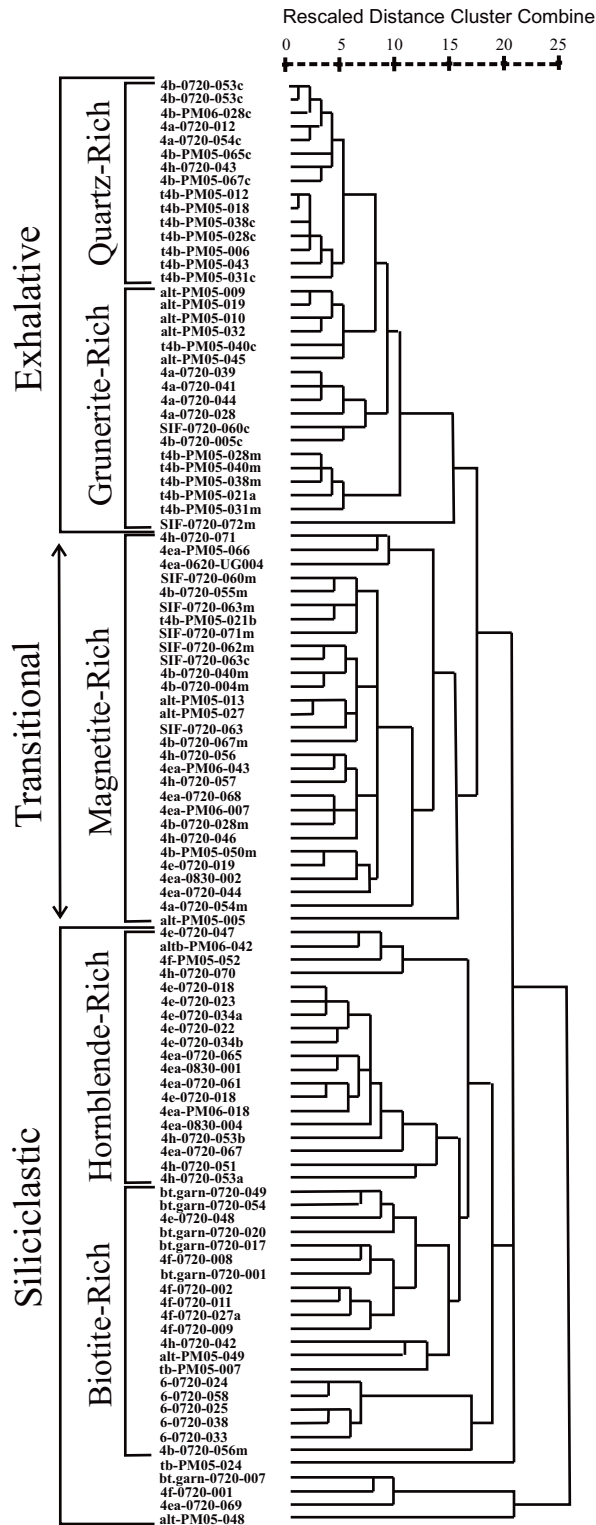
Figure 5.21 is another cluster analysis dendrogram with samples as the variant. However, this dendrogram is comparing the entire database of samples (n=106). The reader should note that gold values were omitted from this factor analysis due to statistical implications (not all samples were analyzed for gold).

The main reason for the Figure 5.21 dendrogram is to see how all the samples, in the entire sample set, relate to one and other. It is important to see how the mineralized samples relate to the sample set as a whole. Overall, mineralized samples form similar groups and trends in this dendrogram as they do in the previously discussed dendrogram. This implies that samples both mineralized and unmineralized, regardless of whether they are distal or proximal to ore-zones, have evolved in a similar manner.

The majority of samples, in this dendrogram, group together based on a common lithology. Again, it should be noted that there is no alteration subgroup. The sample groups are primarily based on the original sample chemistry, which is reflected by the sample's present mineralogy. Samples can be divided into three main groups, which are 1) exhalite-dominant, 2) siliciclastic-dominant, and 3) transitional between exhalite- and siliciclastic-dominant.

These broad groupings are sub-dividable based on mineralogy. The exhalite-dominant group is composed of quartz-, magnetite-, and grunerite-rich samples. The siliciclastic-dominant group is composed of hornblende-, biotite, and garnet-rich samples. The transitional group is slightly enigmatic as it contains a number of different lithologies. However, the justification for calling this group transitional, is that it contains both exhalite- and siliciclastic-dominant samples composing this group.

There is one notable difference between Figures 5.21 and 5.20. Samples in Figure 5.20 are from close to as well as within the ore-zones. This dendrogram contains a sub-grouping of samples which are high in sulphide. However, Figure 5.21 contains samples



**Figure 5.21. Cluster analysis dendrograms for 106 samples (omitting Au values) from the NIF assemblage at Musselwhite gold deposit. Samples can be broadly divided into three groups: exhalative, transitional, and siliciclastic. These broad groups can be further subdivided by the dominant minerals in the samples. Note samples which behaved in a similar manner plot closest to each other on the dendrogram. Refer to page xvii of thesis introduction for abbreviation definitions.**



from close to, as well as distal, to the ore-zones and does not contain a sub-group of sulphide-rich samples. Overall, the similar sample groupings between the dendrograms in Figure 5.21 and 5.20 suggest that gold mineralization does not produce a significant alteration halo. The confined nature of the gold mineralization itself is one possible reason for this statistical signature.

The previously discussed geochemical diagrams, as a group, show that there are no strong unifying geochemical trends associated with gold mineralization at Musselwhite. Geochemical changes instead appear to be limited to individual samples rather than being pervasive throughout the deposit. In fact, most samples retain their original geochemical signatures enough to group together by lithology in the dendrograms.

It is well known that many factors affect gold mineralization in orogenic gold deposits. One possibility is that main control on gold mineralization is structural. The association between structurally disrupted IF and gold mineralization is well documented at Musselwhite (Andrew Cheatle, personal communication, 2007). Additionally the main ore-zones at Musselwhite Mine are constricted, elongate bodies that plunge northwestwardly, with flattening parallel to the vertical foliation (Fig. 1.4) (Andrew Cheatle, personal communication, 2007). These elongate ore-bodies are roughly parallel to the large shear-zone recognized by Rayner and Stott (2005), which occurs along the eastern margin of the NCLB (Fig. 1.3). These characteristics indicate an association between mineralization and structural deformation at Musselwhite.

The best macroscopic indicators of gold mineralization at Musselwhite include: quartz and (minor) carbonate veins, abundant pyrrhotite, in conjunction with shear fabric and structural disruption of the silicate-dominant banded iron formation. It has already been mentioned that the silicate-dominant BIF is the main host lithology to gold mineralization at Musselwhite. The reason(s) that this lithology is preferentially mineralized over other lithologies is likely twofold due to the unique geochemistry of the silicate-dominant BIF.

The primary host to gold mineralization is the silicate-dominant BIF. This lithology is a combination of iron-rich exhalite material and Fe-silicate-rich siliciclastic material. When the metasomatic fluid, carrying gold as a bisulphide complex, interacts with the iron-rich

rock a chemical reaction occurs between the bisulphide complex and the iron resulting in gold and sulphide dropping out of solution. The chemical reaction destabilizes the bisulphide-complex allowing gold to precipitate.

It should be noted that the majority of the sedimentary lithologies at Musselwhite are iron-rich, which again raises the question as to why they are less commonly mineralized compared to the silicate-dominant BIF. Figure 5.14, a stratigraphic column of hole 04-ESN-010, displays this observation very well. Distinct peaks in gold values coincide with the presence of silicate-dominant BIF whereas gold values are universally low in the biotite-garnet schist and oxide-dominant BIF.

It is likely that combination of chemistry and banded nature of the silicate-dominant BIF allow this lithology to; 1) react with mineralizing metasomatic fluids to force gold out of solution and 2) deform in such a manner as to retain the gold. This is opposed to the oxide-dominant BIF, which has the favourable chemistry, but not the correct rheologic nature (too plastic) to trap gold (in this deposit).

The reader should note that the present mineral assemblage, of the silicate-dominant BIF, is a reflection of the chemistry and the metamorphic facies of the rock. The chemistry allows for the formation of minerals, such as garnet, which trap gold during their growth (because gold is already present in the rock when the garnet is growing) (Otto, 2002). It is evident that garnet was growing during shearing as many crystals exhibit rotated inclusion trails. Gold is also found along fractures within the garnet crystals. These characteristics further strengthen the connection between gold mineralization and shearing at Musselwhite (Hill *et al.*, 2006).

The connection between pyrrhotite enrichment and gold mineralization in the silicate-BIF has already been established through petrographic observations (Otto, 2002), as well as the use of geochemical diagrams and statistical analysis (i.e., S, Se, and Au). The sulphide is a result of sulphidation of the silicate-dominant BIF. Sulphidation is a result of metasomatic fluids reacting with the silicate-dominant BIF. These fluids were migrating along the shear zones, but did not actively penetrate into the surrounding rafts of more coherent rock. This is a common feature of BIF-hosted orogenic gold deposits.

## 5.5 Comparison to Other BIF Hosted Orogenic Gold Deposits

The connection between banded iron formations and gold mineralization in Archean metasedimentary/metavolcanic belts has long been recognized. As such banded iron formations in association with major shear zones present excellent exploration targets for concealed gold mineralization. Significant iron formation-hosted gold deposits are found in the following countries; Canada (Lupin: Lhotka and Nesbitt, 1989; Musselwhite: Hall and Rigg, 1986), as well as Zimbabwe (Vubachikwe: Saager *et al.*, 1987), South Africa (Fumani: Pretorius *et al.*, 1988), Brazil (Morro Velho: Ladeira, 1991), and Australia (Mt. Morgans: Vielreicher *et al.*, 1994).

There are three genetic types of mineralization associated with BIF: syngenetic, epigenetic, and mixture of both epi- and syngenetic (Fripp, 1976; Phillips *et al.*, 1984; Groves *et al.*, 1987; Saager *et al.*, 1987; Ladeira, 1991). In the case of syngenetic mineralization gold is contained in hydrothermal black smoker fluid and is precipitated along with chert, sulphide and carbonate minerals during the deposition of the BIF (e.g., Vubachikwe: Fripp, 1976; Morro Velho: Ladeira, 1991). Epigenetic mineralization is more common and occurs at some point after the deposition of the BIF. The Musselwhite gold deposit is epigenetic and gold mineralization is likely related to a large crustal-scale shear zone (Hill *et al.*, 2006).

Section 5.5 compares the Musselwhite deposit to three other BIF-hosted orogenic gold deposits (Lupin, Meadowbank, and Ajjanahalli). Homestake, the most well-known BIF hosted gold deposit, was not compared to Musselwhite because it is mainly a carbonate-BIF hosted gold deposit.

### 5.5.1 Lupin Gold Mine

The Lupin gold mine is Canada's premier example of a world class BIF-hosted gold deposit. It is located in the central Slave Province, Northwest Territories, Canada. Lupin is similar to Musselwhite in numerous ways, which are expanded on in this section. Like Musselwhite this deposit is Archean in age, the metamorphic grade of the rocks ranges

from greenschist to amphibolite, and the rocks have experienced multiple deformation events.

Mineralization is primarily confined to the Lupin BIF (mine terminology; Lhotka and Nesbitt, 1989). Like the banded iron formation in the NIF assemblage at Musselwhite the Lupin BIF is associated with siliciclastic lithologies. Unlike the IF at Musselwhite, which sits on top of a metavolcanic sequence, the Lupin BIF sits on top of a psammitic meta-graywacke sequence. The Lupin BIF is overlain by a sequence of phyllites. The surrounding siliciclastic metasediments are turbiditic in origin (Bostock, 1980; Lhotka and Nesbitt, 1988). Discontinuous garnet-amphibole-biotite-chlorite schist is intermittently found between the BIF and overlying phyllites (Bullis *et al.*, 1994). This stratigraphic sequence is reminiscent of the stratigraphy of the upper portion of the NIF assemblage. Here the garnet-biotite schist, which probably represents turbiditic sediment due to the presence of graded bedding (described in section 5.3), overlies the silicate-dominant BIF.

The overlying garnet-amphibole-biotite-chlorite schist at Lupin may have acted as an impermeable layer and played a significant role in the mineralization of the Lupin BIF (Geusebroek and Duke, 2005). This has interesting implications for the biotite-garnet schist overlying the silicate-BIF at Musselwhite. It is possible that this scenario took place at Musselwhite.

The mineralized silicate-dominant BIF at Lupin consists of millimetre- to centimetre-scale bands of quartz and hornblende  $\pm$  chlorite  $\pm$  pyrrhotite  $\pm$  arsenopyrite. Intercalated within this unit are 10 to 30 cm thick layers of garniferous amphibolite. These layers may be analogous to the intercalated hornblende-garnet schist layers in the Musselwhite silicate-dominant BIF.

The Musselwhite silicate-dominant BIF shares a similar mineralogy to the Lupin BIF. It consists of millimetre- to centimetre- scale bands of quartz, grunerite, almandine garnet, and hornblende  $\pm$  pyrrhotite,  $\pm$  chlorite,  $\pm$  arsenopyrite (the reader should note that

arsenopyrite is rare in the silicate-dominant BIF at Musselwhite). In places sulphides compose between 5% to 30% of the BIF at both Lupin and Musselwhite.

At Lupin sulphide-rich bands are thought to be sulphidized silicate-dominant bands (Lhotka and Nesbitt, 1989). A similar pattern of sulphidation is proposed to have occurred in the silicate-dominant BIF at Musselwhite. It should be noted that the sulphide-rich silicate-dominant BIF is a secondary feature. These bands do not represent a sulphide-dominant BIF which is a primary feature.

Away from zones of mineralization the barren BIF at Lupin is composed of quartz-grunerite  $\pm$  magnetite. This is reminiscent of the unmineralized oxide-dominant BIF in the NIF assemblage at Musselwhite.

The mineralized Lupin BIF, like the mineralized Musselwhite silicate-dominant BIF, contains abundant quartz veins which in some cases destroy primary textures. At Lupin hedenbergite and chlorite are common minerals found in association with the quartz veins. Otto (2002) noted the presence of hedenbergite in the silicate-dominant BIF at Musselwhite. Unlike at Lupin chlorite is a minimal at Musselwhite, but when present is associated with gold mineralization (Otto, 2002).

At Lupin hornblende is the main amphibole in mineralized BIF, in some cases, composing up to 35% of the rock. However many hornblende crystals have grunerite crystals at their core (Bullis *et al.*, 1994). Mineralized Lupin BIF does not contain significant amounts of grunerite. This is not the case at Musselwhite where grunerite-rich silicate-dominant BIF can be well mineralized. The amount of hornblende and grunerite in the Lupin BIF varies significantly over small distances much the same as the Musselwhite silicate-dominant BIF. In both deposits silicate minerals (i.e., hornblende and grunerite) are replaced by pyrrhotite mineralization. Kerswill (1985) observed that gold occurs both with pyrrhotite and interstitially in silicate minerals at Lupin. Ruslan Liferovich (personal communication, 2006) reached the same conclusion for the Musselwhite deposit.

Geusebroek and Duke (2005) suggest mineralization of the Lupin BIF occurred through focused metamorphic fluid flow similar to that proposed by Ford and Duke (1993). Gold is contained in metamorphic fluids derived from dehydration of rock at depth and deposition of gold occurs during metamorphic reactions taking place at the greenschist-amphibolite recrystallization front. This mineralization model should be considered for Musselwhite due to the numerous similarities between Lupin and Musselwhite. Additionally the Musselwhite deposit is associated with a crustal-scale shear-zone and is at the right metamorphic facies.

Like Musselwhite, gold mineralization at Lupin is primarily confined to the silicate-dominant BIF with mineralized intervals corresponding with a high degree of quartz-veining, as well as the presence of hedenbergite and pyrrhotite. At Musselwhite there is noticeable amplification of hornblende and pyrrhotite in the silicate-dominant BIF flanking large quartz veins (John Biczok, personal communication, 2007). Gold is associated with the replacement of part of the silicate-dominant BIF by pyrrhotite is common in the Lupin deformation zone (Bullis *et al.*, 1994). Mineralization is associated with garnet-arsenopyrite-chlorite crystallization, driven by prograde and retrograde metamorphic fronts, near late-stage quartz veins (Bullis *et al.*, 1994). Geusebroek and Duke (2005) propose an epigenetic metamorphic model for mineralization at Lupin. In the epigenetic model gold is structurally trapped in the amphibolite recrystallization front.

From an exploration standpoint there are three critical requirements for mineralization of the Lupin BIF: 1) proper metamorphic conditions (amphibolite metamorphic front), 2) shear zone (fluid conduit), 3) chemical trap (Lupin BIF) (Geusebroek and Duke, 2005). Some of these requirements are met by the Musselwhite deposit which; 1) is between upper greenschist to amphibolite facies, 2) is associated with a shear zone, and 3) has a chemical trap (Musselwhite silicate-dominant BIF). In addition the silicate-dominant BIF is intrinsically important, at both Lupin and Musselwhite, because of its inherent chemical properties, as well as rigidity contrasts generated under amphibolite metamorphism (Geusebroek and Duke, 2005).

### 5.5.2 Meadowbank Gold Deposit

The Meadowbank gold deposits are BIF-hosted orogenic gold deposits located in the Western Churchill Province, Nunavut, Canada. The host rocks to this deposit have a U-Pb age of  $2711 \pm 3$  Ma (Zaleski *et al.*, 2000) and are therefore Archean like the rocks at Musselwhite (deKemp, 1987). Like Musselwhite, but unlike Lupin, the Meadowbank BIFs are hosted in a sequence of predominantly mafic volcanic rocks with lesser amounts of ultramafic volcanic rocks. Unlike Musselwhite, there is a quartz-pebble conglomerate in the stratigraphic succession at Meadowbank, which probably represents some prograding terrigenous formation (Sherlock *et al.*, 2003).

At Musselwhite the geochemistry of the silicate-dominant BIF indicates it weathered from mafic to intermediate volcanic material. Similar to the Musselwhite silicate-dominant BIF, the Meadowbank amphibolitic BIF represents the incorporation of detritus weathered from intermediate volcanic rocks and indicates intermediate volcanism was active during deposition of the BIF (Sherlock *et al.*, 2003).

The REE geochemistry of the Meadowbank BIF, with its pronounced positive Eu anomalies, indicates the hydrothermal fluids precipitating the iron formations were  $>250^{\circ}\text{C}$  and probably acidic and reducing, while circulating in the black smoker hydrothermal plumbing system (Sherlock *et al.*, 2003). The pronounced positive Eu anomalies observed in the Musselwhite IF indicates similar conditions of deposition.

Much like Musselwhite and Lupin, mineralization at Meadowbank is primarily controlled by pyrrhotite (and pyrite) replacement of minerals in the BIF. Unlike Lupin, where the mineralogy changes close to mineralization (Geusebroek and Duke, 2005), but similar to Musselwhite, the mineralogy at Meadowbank is consistent across the extent of the BIF and is unaffected by mineralization (this is possibly due to the high iron-content of the rocks which buffer chemical reactions; Sherlock *et al.*, 2003).

The intermediate volcanic rocks at Meadowbank exhibit observable geochemical changes, likely during metasomatism, mainly decreases in CaO, MgO, and Na<sub>2</sub>O, and an increase in K<sub>2</sub>O. Similar geochemical changes have been reported at Musselwhite (Otto, 2002). At Meadowbank gold mineralization is mainly associated with replacement of

magnetite by pyrite and pyrrhotite in high-strain passageways. This is a similar style of mineralization to what is seen both at Musselwhite and Lupin.

### 5.5.3 Ajjanahalli Gold Deposit

The Ajjanahalli gold deposit is a BIF-hosted orogenic gold deposit located in the Chitradurga greenstone belt, part of the Dharwar craton, in India (Kolb *et al.*, 2004). Like Musselwhite, and the previously discussed Lupin and Meadowbank deposits, mineralization is associated with a crustal-scale shear zone transecting Archean-aged country rock (Kolb *et al.*, 2004). The main host to mineralization at Ajjanahalli is oxide- and carbonate-dominant banded iron formation (Kolb *et al.*, 2004). The nature of the host BIF and the fact that it is found in a thicker sequence of turbidites make the Ajjanahalli deposit significantly different from Musselwhite.

Kolb *et al.* (2004) suggest the lithologies at Ajjanahalli were deposited in a back-arc basinal environment. This conclusion is based on stratigraphic progressions and whole-rock lithogeochemistry completed on the volcanic lithologies in the deposit. The banded iron formation, which hosts the mineralization, sits on top of chlorite schist. Overlying the main iron formation is a sequence of phyllites and quartz-sericite schist representing shale and turbidite-dominant lithologies, respectively (Kolb *et al.*, 2004). This stratigraphic progression is somewhat analogous to the NIF assemblage at Musselwhite (see Section 5.2).

Gold mineralization, at Ajjanahalli, is connected with a ~100 m wide antiform in the banded iron formation (Kolb *et al.*, 2004). This antiform is associated with a first-order shear zone. A similar tectonic concurrence occurs at Musselwhite, where the majority of gold mineralization is enclosed within a large antiform structure (T-antiform) loosely associated with a first order shear-zone. However, at Musselwhite, the mineralized zones are primarily associated with shear zones in the antiform (minimal work has been done linking the mineralized zones at Musselwhite to the nearby regional-scale shear zone).



The Ajjanahalli deposit is rather exceptional since gold mineralization, in this deposit, is associated with a first order structure (Kolb *et al.*, 2004). In orogenic deposits gold mineralization is usually associated with second-order shear zones, so mineralization of a first order feature is unusual (Goldfarb *et al.*, 2001). It is possible that mineralized first order structures are a result of later deformation (e.g., Paddington, in the Yilgarn craton; Kolb *et al.*, 2004).

Alteration minerals after original magnetite and siderite, at Ajjanahalli, include pyrite, pyrrhotite, arsenopyrite, chlorite, and gold (Kolb *et al.*, 2004). This is a similar mineral assemblage to that seen at Musselwhite. However, additional alteration minerals include minnesotaite, sericite, stilpnomelane, and ankerite, which are not commonly seen in the IF at Musselwhite.

Localized gold mineralization at Ajjanahalli, much like Musselwhite, is the result of extensive reaction between metasomatic-fluid and the iron-formation. Evidence for this extensive interaction, at Ajjanahalli are replacement textures, as well as enrichment of certain elements like Ca, S, Au, Cu, Se, Ag, and Te (Kolb *et al.*, 2004). Interestingly large-quartz veins at Ajjanahalli are for the most part barren of gold mineralization. This is different to Musselwhite where gold mineralization is regularly associated with diffuse quartz veining.

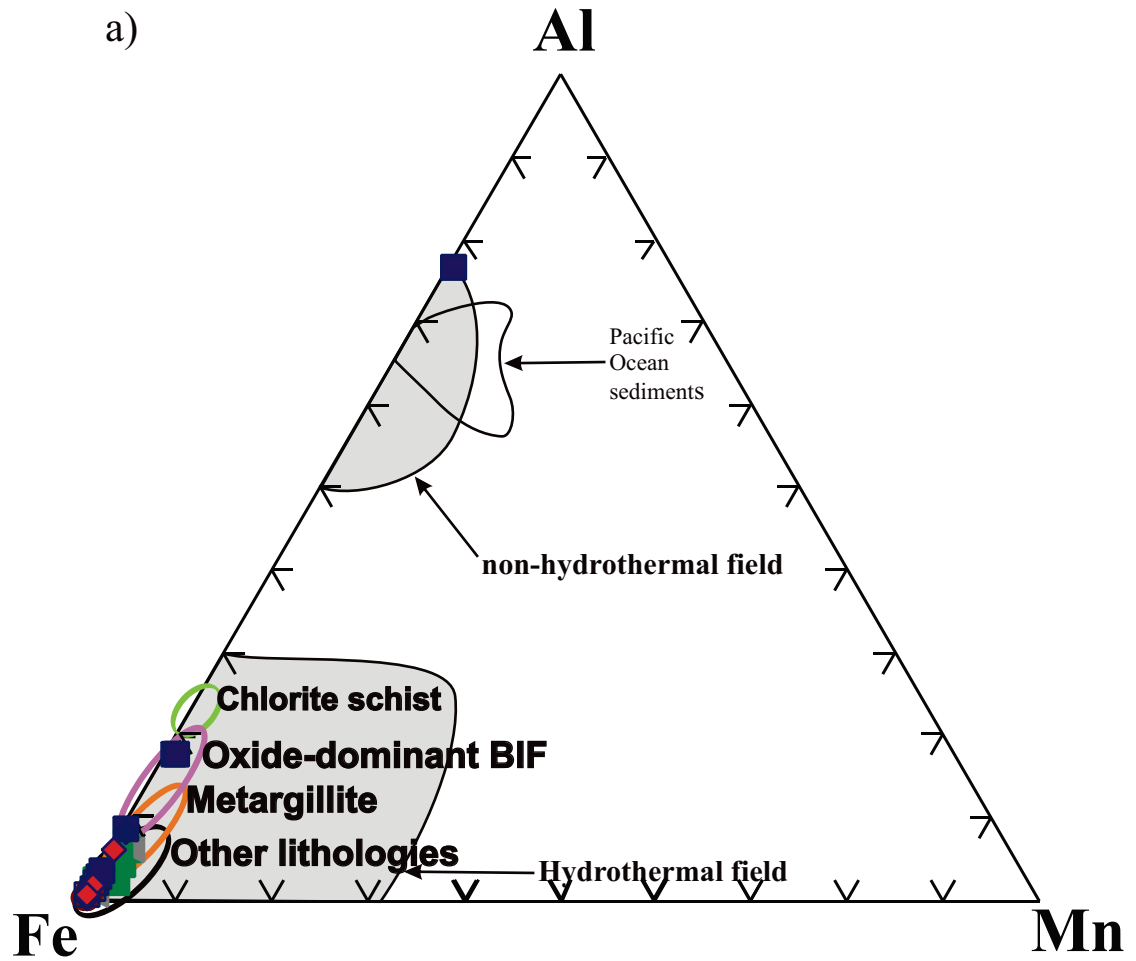
Kolb *et al.* (2004) interpret mineralization at Ajjanahalli to be lower mesozonal and taken place between 300-500°C; whereas at Musselwhite, Otto (2002) interprets mineralization to have taken place at slightly higher temperatures ranging between 540 °C to 600°C. Kolb *et al.* (2004) suggest that gold mineralization at Ajjanahalli resulted from fluid infiltration of low strain areas. Low strain areas, in this case, have formed in association with more competent units/blocks of rock. This conclusion is based on the geologic and chronologic associations between the strike-slip deformation associated with the main shear zone and local structure propagation and mineralization patterns. It is postulated that metasomatic fluids were being transported along the main shear zone. Gold mineralization at Ajjanahalli is unusual in that it is associated with low strain areas in a first order, transcrustal-scale shear zone.

5.5.4 Musselwhite Geochemistry Relative to Lupin, Meadowbank, and Ajjanahalli  
Based on the numerous similarities between the above described deposits, it was expected they would compare well geochemically. This is not necessarily the case. A general characteristic of both the Meadowbank and Ajjanahalli sample sets is that they exhibit more scatter than seen in the Musselwhite sample set. Another obvious difference is their ratio of  $\text{TiO}_2$  to Zr. Samples from Meadowbank have higher ratio of Zr to  $\text{TiO}_2$  relative to Musselwhite samples. Several silicate-dominant samples from Meadowbank compare to both the Musselwhite silicate-dominant BIF and meta-argillite samples.

Figure 5.22a-b shows that the majority of samples from both the Meadowbank and Ajjanahalli deposits cluster deep in the hydrothermal field, dominated by Fe, and therefore are more chemical than siliciclastic in nature. These samples overlap with the exhalite-dominant lithologies from Musselwhite (quartz-grunerite BIF, SIF/NIF oxide-dominant BIF). Samples from the Ajjanahalli deposit are all exhalite in nature. However, a number of the Meadowbank silicate-dominant BIF samples overlap with the Musselwhite silicate-dominant BIF field in Figure 5.22b

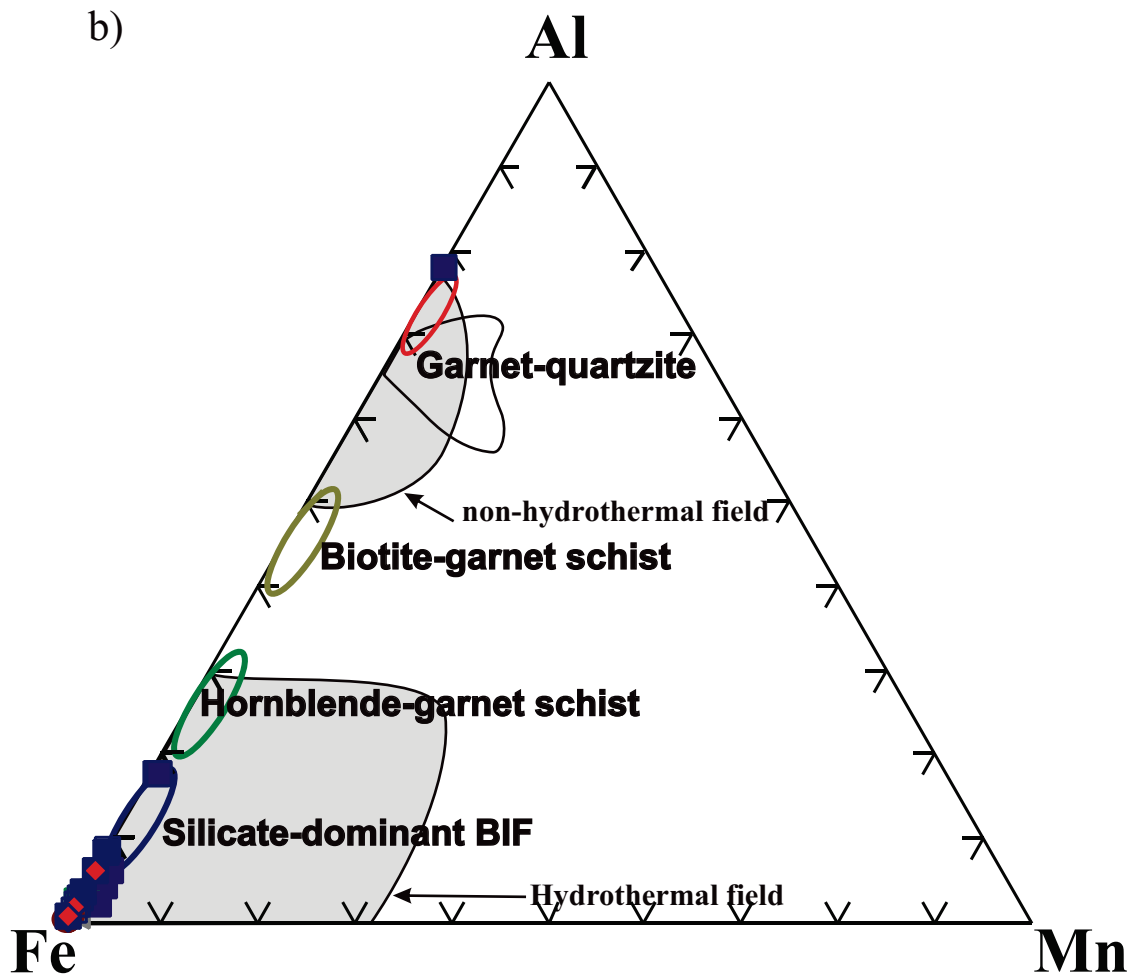
Figure 5.23a and b consist of a binary discrimination diagram where  $\text{Fe}/\text{Ti}$  is plotted against  $\text{Al}/(\text{Al}+\text{Fe}+\text{Mn})$ . This is the same diagram as depicted in Figure 4.4 (refer to Chapter 4 for detailed explanation of this diagram). Figure 5.23a shows samples from Meadowbank and Ajjanahalli plotted against the range of compositions of the exhalite dominant samples from Musselwhite. Again, like the previous diagram most of the samples compare favourably to the most exhalite-dominant lithologies at Musselwhite and not the silicate-dominant BIF. There is also one anomalous Meadowbank silicate-dominant BIF sample, which does plot in the clastic sediment field. A general trend seen in both comparison sets is their tendency to plot above the trend line even relative to Musselwhite samples (which themselves plot off the trend line). This indicates that these lithologies contain lower levels of titanium than the Musselwhite samples. Most of the Meadowbank and Ajjanahalli samples plot close to the outline for the various exhalite dominant samples (lithologies) at Musselwhite. None of the silicate-dominant BIF

- Legend**
- Range of exhalite dominant samples
  - Range of metargillite samples
  - Range of chlorite schist samples
  - Range of oxide-dominant BIF (mag)
  - Range of silicate-dominant BIF samples
  - Range of hornblende-garnet schist
  - Range of biotite-garnet schist samples
  - Range of garnet-quartzite samples
  - Silicate-dominant BIF (Meadowbank)
  - Oxide-dominant BIF (Meadowbank)
  - ◆ Sulfide-dominant BIF (Meadowbank)
  - Silicate-dominant BIF (Ajjanahalli)
  - ◀ Oxide-dominant BIF (Ajjanahalli)



**Figure 5.22a. Ternary diagrams showing hydrothermal and non-hydrothermal sediment fields based on relative concentrations of aluminum, iron, and manganese. Coloured outlines represent sample range for the lithologies from Musselwhite. Samples plotted on these diagrams are iron formation from the Meadowbank and Ajjanahalli BIF hosted gold deposits a) Meadowbank and Ajjanahalli samples plotted against exhalite-dominant Musselwhite samples. Hydrothermal and non-hydrothermal sediment fields were developed by Boström (1973), oceanic sediments (Dymon *et al.*, 1973; Toth, 1980), umbers from Cyprus massive sulphide deposits (Robertson and Hudson, 1973), East Pacific Rise metalliferous sediments (Boström, 1973) and Deep Sea Drilling Project Leg 31 (Figure modified from Bonatti *et al.*, 1979). Meadowbank and Ajjanahalli sample geochemistry from Sherlock *et al.* (2004), and Kolb *et al.* (2004), respectively.**

- Legend**
- Range of exhalite dominant samples
  - Range of metargillite samples
  - Range of chlorite schist samples
  - Range of oxide-dominant BIF (mag)
  - Range of silicate-dominant BIF samples
  - Range of hornblende-garnet schist
  - Range of biotite-garnet schist samples
  - Range of garnet-quartzite samples
  - Silicate-dominant BIF (Meadowbank)
  - Oxide-dominant BIF (Meadowbank)
  - ◆ Sulfide-dominant BIF (Meadowbank)
  - Silicate-dominant BIF (Ajjanahalli)
  - ◄ Oxide-dominant BIF (Ajjanahalli)



**Figure 5.22b.** Ternary diagrams showing hydrothermal and non-hydrothermal sediment fields based on relative concentrations of aluminum, iron, and manganese. Coloured outlines represent sample range for the lithologies from Musselwhite. Samples plotted on these diagrams are iron formation from the Meadowbank and Ajjanahalli BIF hosted gold deposits. Meadowbank and Ajjanahalli samples plotted against siliciclastic-dominant Musselwhite samples. Hydrothermal and non-hydrothermal sediment fields were developed by Boström (1973), oceanic sediments (Dymon *et al.*, 1973; Toth, 1980), umbers from Cyprus massive sulfide deposits (Robertson and Hudson, 1973), East Pacific Rise metalliferous sediments (Boström, 1973) and Deep Sea Drilling Project Leg 31 (Figure modified from Bonatti *et al.*, 1979). Meadowbank and Ajjanahalli sample geochemistry from Sherlock *et al.* (2004), and Kolb *et al.* (2004), respectively.

samples from the Ajjanahalli deposit plot close to the Musselwhite silicate-dominant BIF field. However, they do plot close to Red-Sea metalliferous sediment field. Interestingly in Figure 5.23a, the Meadowbank silicate-dominant BIF samples plot more closely to the Musselwhite meta-argillite samples than the silicate-dominant BIF samples.

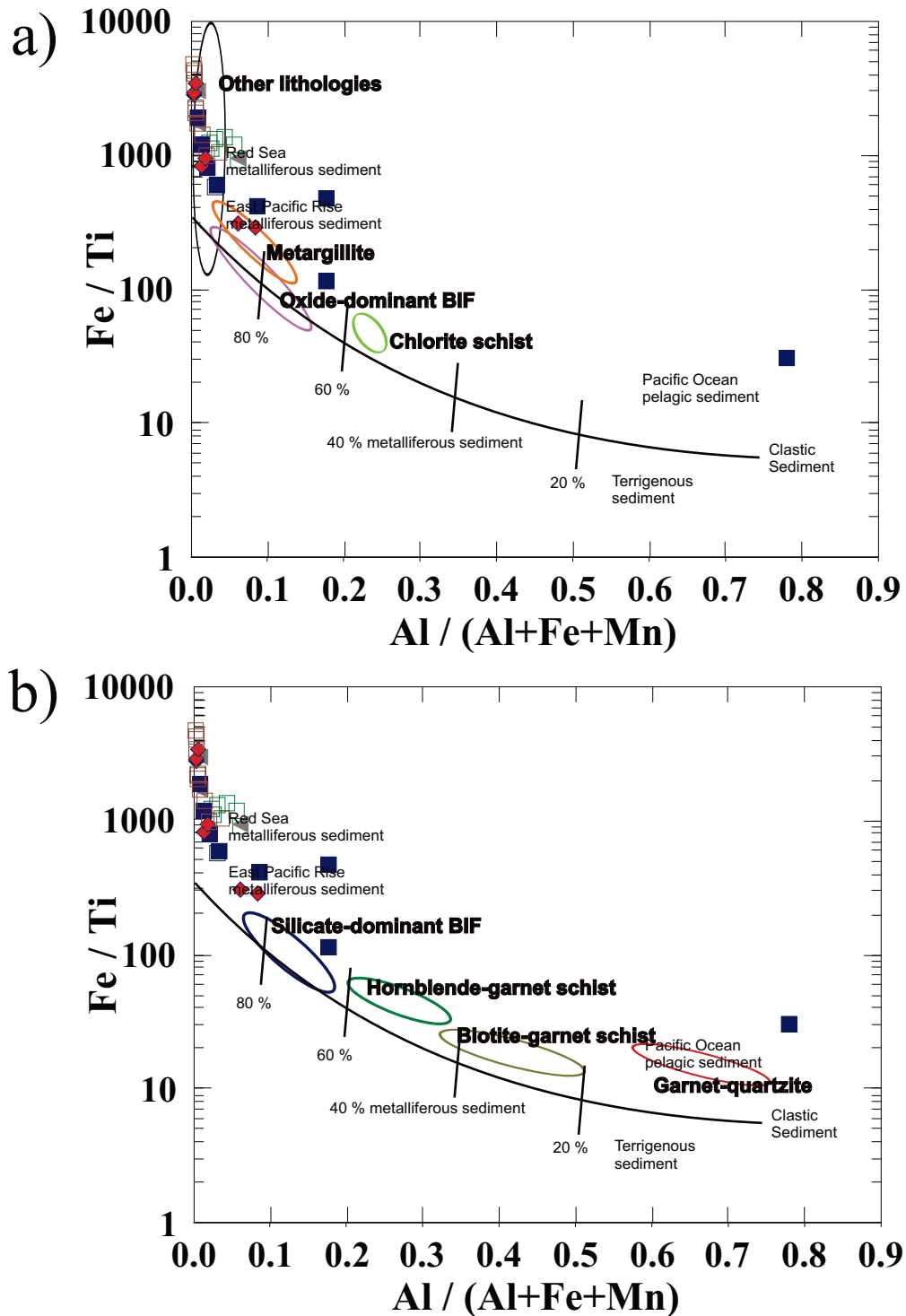
Like Musselwhite, the exhalite-dominated lithologies from Meadowbank and Ajjanahalli contain low concentrations of  $\text{Al}_2\text{O}_3$ ,  $\text{TiO}_2$ , and Zr therefore cluster close to the origin on the diagrams. Samples from Ajjanahalli only compare to the exhalite-dominant lithologies from Musselwhite. Similarly the exhalite-dominant lithologies from Meadowbank compare to those from Musselwhite. The Meadowbank silicate-dominant BIF samples more favourably compare to the Musselwhite meta-argillite than with the silicate-dominant BIF.

Additionally, iron formation samples from the Meadowbank deposit exhibit similar REE curves (Fig. 5.24a) to the exhalite-dominant lithologies at Musselwhite (Fig. 5.7). However, samples from the Ajjanahalli deposit exhibit more scatter (Fig. 5.24b).

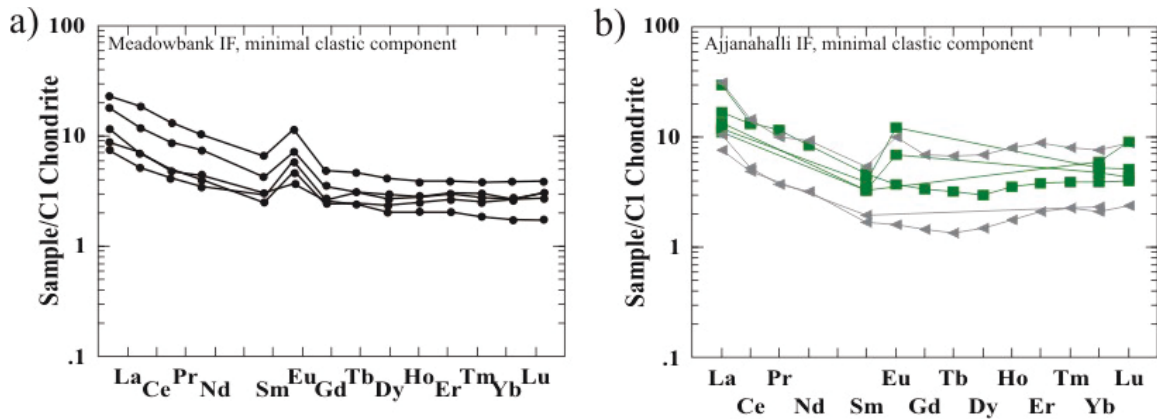
The remaining figures, presented in this section, are focused on comparing and contrasting the metasomatic alteration patterns in the various BIF-hosted orogenic deposit samples. An assortment of diagrams, designed to detect alteration, were introduced in Section 4.7 and expanded upon in Section 5.4. The underlying principles behind these diagrams were explained in the previous sections. The diagrams are based around alkali-elements as these tend to be mobilised by metasomatic fluids in orogenic systems (Heath and Campbell, 2004).

Figure 5.25 contains histograms which depict the  $((\text{Cs}+\text{Rb})/\text{Th})_N$  value for individual samples from the Musselwhite deposit. Note the y-axis is logarithmic. Figure 5.25a contains the exhalite-dominant lithologies, Figure 5.25b contains the siliciclastic dominant lithologies, and Figure 5.30c contains samples from the comparison deposits (Meadowbank and Ajjanahalli, not all samples were analysed for Cs).

Samples from Musselwhite exhibit a diverse array of  $((\text{Cs}+\text{Rb})/\text{Th})_N$  values from 0 to  $\gg 5$  suggesting a range of depletion to very strong alkali enrichment. Samples from the comparison deposits exhibit comparatively subdued  $((\text{Cs}+\text{Rb})/\text{Th})_N$  values.



**Figure 5.23.** Symbols are the same as in Fig. 5.22. a) Discrimination diagram for estimating the amount of exhalative versus siliciclastic sedimentary material in samples. Originally devised by Boström (1973), this diagram shows Meadowbank and Ajjanahalli samples plotted overtop the lithology outlines of chemically dominated samples from Musselwhite, b) this diagram shows Meadowbank and Ajjanahalli samples plotted overtop the lithology outlines of siliciclastic-dominated samples from Musselwhite. Note samples plot above the mixing line which is the result of lower Ti in these Archean clays. Average samples of Red Sea metalliferous sediments (Backer, 1976), East Pacific Rise metalliferous sediment (Cronan, 1976), terrigenous sediment (Boström, 1973), and average pelagic Pacific Ocean sediment (Cronan, 1976) are plotted on the diagram for reference. Meadowbank and Ajjanahalli sample geochemistry from Sherlock *et al.* (2004) and Kolb *et al.* (2004)

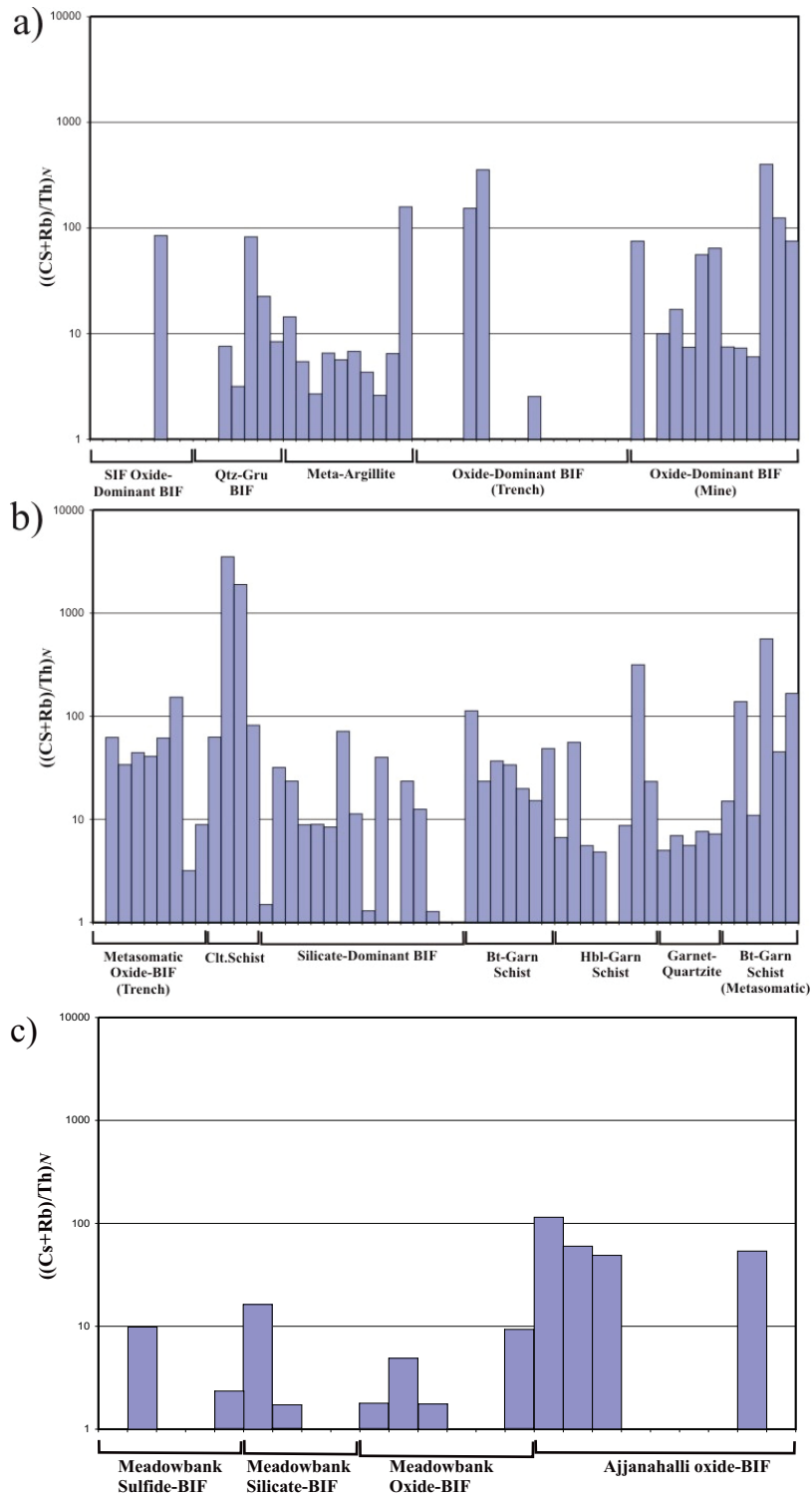


**Figure 5.24. C1 normalized REE spider diagrams** a) Meadowbank iron formation samples containing minimal siliciclastic material Sherlock *et al.* (2004), b) Ajjanahalli iron formation samples (note that some of the samples have not been analyzed for a full spectrum of elements) Kolb *et al.* (2004).

Specifically Meadowbank sample exhibit values ranging from 0 to ~5, whereas samples from the Ajjanahalli deposit exhibit higher mean values of ~70. In general there does not appear to be a definitive pattern of alkali-element enrichment and/or depletion amongst the comparison sample set at least in terms of individual lithologies.

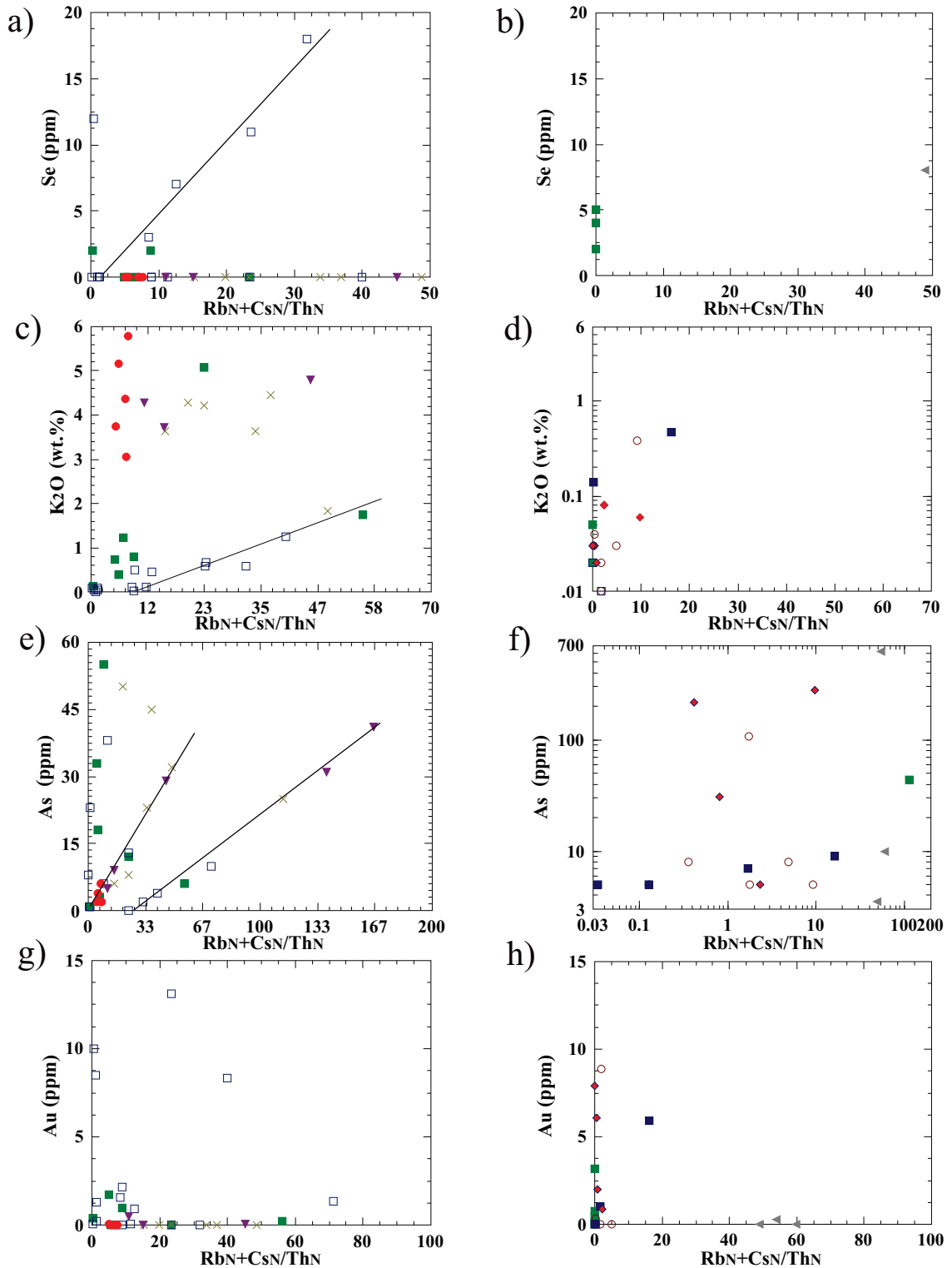
Figure 5.25 expands on the histograms depicted in Figure 5.25. It contains various binary diagrams of  $((Cs+Rb)/Th)_N$  as the x-variant plotted against a variety of elements, associated with gold mineralization, on the y-axis. Figures 5.26a, b, c, and d contain the Musselwhite silicate-dominant samples, whereas Figures 5.26b, d, f, and h contain samples from the Ajjanahalli and Meadowbank deposits. Positive linear trends are observed in the Musselwhite samples. In stark contrast samples from the comparison deposits do not exhibit any discernable trends.

Figure 5.27 expands on the histograms depicted in Figure 5.25 and the binary diagrams of Figure 5.26. This figure consists of binary diagrams with Cs as the x-variant plotted against a variety of mobile elements on the y-axis. Figures 5.26a, b, c, and d contain the Musselwhite silicate-dominant samples, whereas Figures 5.27b, d, f, and h contain samples from the Ajjanahalli and Meadowbank deposits. Again, in several diagrams (Figs. 5.27a and c) the Musselwhite samples exhibit positive linear trends. However, the comparison deposit samples do not exhibit any discernable trends in these diagrams.

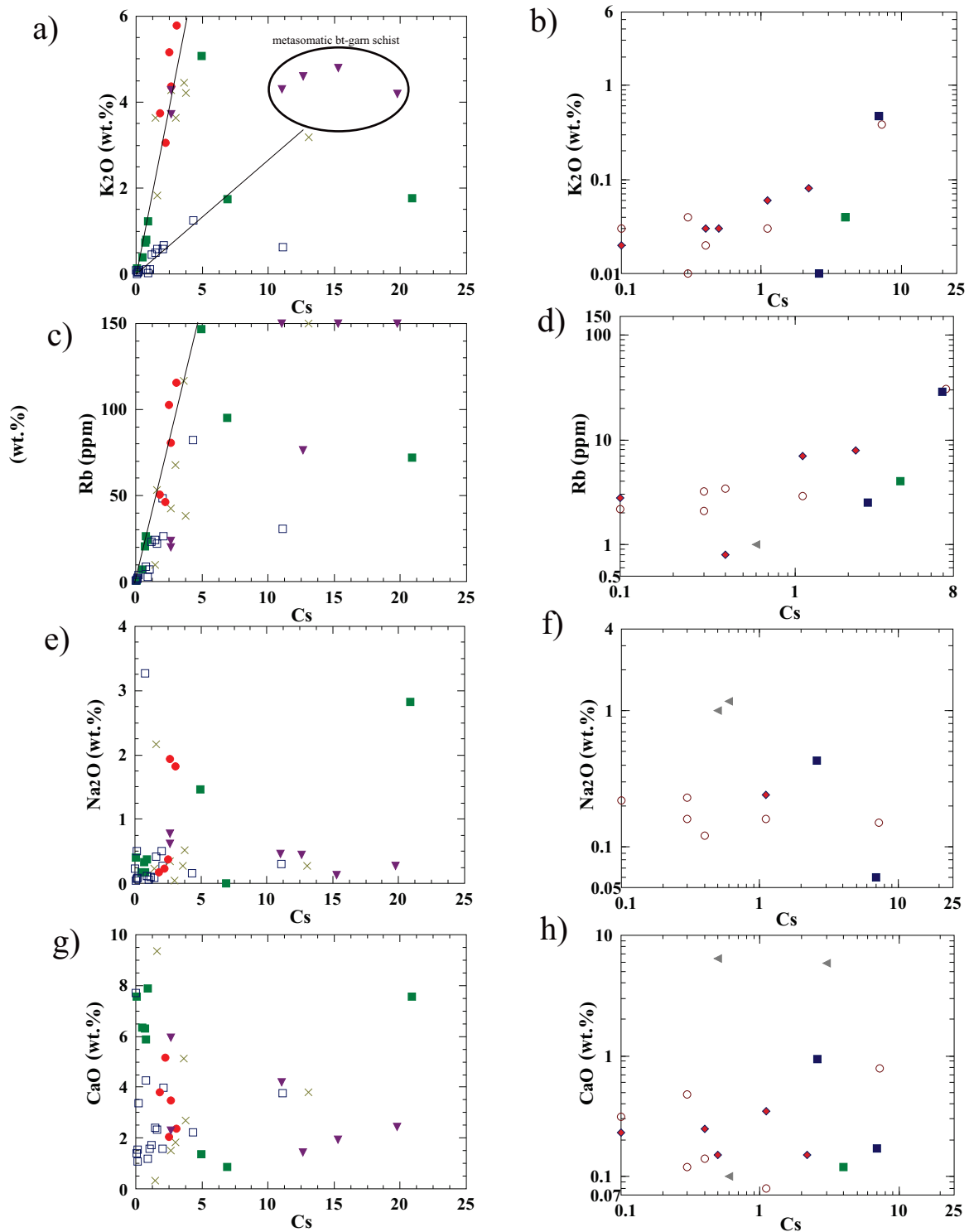


**Figure 5.25. Histograms displaying the  $((Cs+Rb)/Th)^N$  values for individual samples. Samples are grouped by lithology as indicated by the horizontal lines. a) Samples of exhalite-dominant lithologies from Musselwhite, b) Samples of siliciclastic-dominant lithologies from Musselwhite, c) Samples from the comparison deposits (Meadowbank and Ajjanahalli) where sulfide-BIF=sulfide-dominant BIF, silicate-BIF=silicate-dominant BIF, and oxide-BIF=oxide-dominant BIF.**





**Figure 5.26. Binary plots displaying  $((Cs+Rb)/Th)_N$  as the x-variate versus various elements associated with gold mineralization (as the y-variate). Symbols are the same as in Fig. 5.1. a)  $((Cs+Rb)/Th)_N$  vs. Se for siliciclastic-dominant lithologies, b)  $((Cs+Rb)/Th)_N$  vs. Se for the Ajjanahalli and Meadowbank samples, c)  $((Cs+Rb)/Th)_N$  vs. K<sub>2</sub>O for siliciclastic-dominant lithologies, d)  $((Cs+Rb)/Th)_N$  vs. K<sub>2</sub>O for the Ajjanahalli and Meadowbank samples, e)  $((Cs+Rb)/Th)_N$  vs. As for siliciclastic-dominant lithologies, f)  $((Cs+Rb)/Th)_N$  vs. As for the Ajjanahalli and Meadowbank samples, g)  $((Cs+Rb)/Th)_N$  vs. Au for siliciclastic-dominant lithologies, h)  $((Cs+Rb)/Th)_N$  vs. Au for the Ajjanahalli and Meadowbank samples.**



**Figure 5.27. Binary plots of Cs versus various elements associated with metasomatic alteration. Note that linear trend-lines are based on visual observations. Symbols are the same as in Fig. 5.1. a) Cs vs. Rb for siliciclastic-dominant lithologies, b) Cs vs. Rb for the Ajjanahalli and Meadowbank samples, c) Cs vs. Rb for siliciclastic-dominant lithologies, d) Cs vs. Rb for the Ajjanahalli and Meadowbank samples, e) Na<sub>2</sub>O vs. Cs for siliciclastic-dominant lithologies, f) Na<sub>2</sub>O vs. Cs for the Ajjanahalli and Meadowbank samples, g) Cs vs. CaO for siliciclastic-dominant lithologies, h) Cs vs. CaO for the Ajjanahalli and Meadowbank samples.**

## Chapter 6

### Conclusions

1) The Southern Iron Formation and Northern Iron Formation assemblages were included in the Opapimiskan Lake Metavolcanic Assemblage by previous workers. However, it appears that the SIF and NIF assemblages actually straddle the transition between the Opapimiskan Lake and South Rim Metavolcanic assemblages. This tentative conclusion is based on the increase in felsic volcanic lithologies with increasing stratigraphic thickness where abundant ultramafic to mafic volcanic flows dominate the lower portion of the mine stratigraphy and mafic and intermediate volcanic rocks which dominate the upper portions of the stratigraphy.

2) The SIF and NIF assemblages, at Musselwhite, are Algoma-type iron formation. Classifying these assemblages as Algoma-type is based on the association between the IF and abundant surrounding volcanic rocks. The presence of volcanic rocks in association with the iron formation suggests volcanic activity was the main factor contributing to their formation. Additionally, the presence of sulfide-, oxide-, and silicate-dominant iron formation suggests hydrothermal smoker systems were the driving force behind the IF precipitation. The sulfide-dominant IF formed proximal to hydrothermal vents, whereas oxide- and silicate-dominant lithologies were deposited distal to the vents.

The REE spider diagrams, of the exhalite-dominant lithologies, exhibit pronounced positive europium anomalies and LREE enrichment. This REE curve pattern, although ubiquitous in the Archean, is characteristic of high-temperature hydrothermal smoker systems. These curves, in conjunction with the volcanic lithologic association, reinforce the notion that the iron formation lithologies at Musselwhite were deposited in association with hydrothermal smoker systems analogous to modern black smoker systems.

3) It was already established that siliciclastic input increases stratigraphically upward in the NIF assemblage. The extensive geochemistry results and interpretation from the

current study provide further, more far-reaching, insight into the evolution of the sedimentary stratigraphy at Musselwhite.

The stratigraphically lower NIF assemblage oxide-dominant BIF, meta-argillite, quartz-grunerite-BIF, and SIF assemblage oxide-dominant BIF are for the most part exhalite-dominant lithologies with relatively minimal siliciclastic input. The stratigraphically higher silicate-dominant BIF, hornblende-garnet schist, biotite-garnet schist, and garnet-bearing quartzite contain higher siliciclastic components at the expense of their exhalative component.

The source of siliciclastic sediment also changes with stratigraphic position. Lower lithologies contain mostly sediment eroded from ultramafic to mafic igneous rocks, whereas the stratigraphically higher lithologies contain sediment eroded from mafic-intermediate to felsic igneous rocks. The changing siliciclastic detrital material reflects the evolving composition of the source volcanic rocks. The sources of the sediment therefore appear to be local rather than distal.

4) The SIF and NIF assemblages were likely deposited in an oceanic-island tectonic setting. This conclusion is based on geochemical and stratigraphic trends observed at Musselwhite. The metavolcanic lithologies form two distinct groups in terms of geochemical affinity; i) ocean floor basalts and ii) ocean-island basalts and andesites. Basalt and andesite samples both exhibit MORB REE curves. However, samples of the garnet-bearing quartzite, whose protolith is volcanic ash, exhibit steeply sloped REE curves. The remaining siliciclastic-dominant lithologies exhibit a succession, corresponding with increasing stratigraphy, from ocean floor basalt-derived sediment in the lower stratigraphy to increasingly felsic-intermediate derived sediment in the upper stratigraphy (i.e., active continental margin sediment).

5) Historically the upper stratigraphy of the Northern Iron Formation Assemblage has been organized in the following order: silicate-dominant BIF, biotite-garnet schist, garnet-bearing quartzite, and hornblende-garnet schist. However, based on the

geochemical similarities, differences, and trends observed between these lithologies, it is recommended that the stratigraphy be reorganized in the following manner: silicate-dominant BIF, hornblende-garnet schist, biotite-garnet schist, and garnet-bearing quartzite.

6) Protoliths to the present lithologies are as follows; meta-argillite was originally sulfide-rich seafloor sediment composed of both siliciclastic detrital material and exhalative precipitates. This lithology is the basal unit to the NIF assemblage. It marks initiation of the hydrothermal smoker system responsible for the deposition of the exhalite-dominant component in the NIF assemblage. The quartz-grunerite BIF, found in association with the meta-argillite, was originally deposited as hydrous-gels on the seafloor. These hydrous-gels were precipitates formed from the interaction of metal- and silica-rich hydrothermal seafloor smoker fluids and ocean water. Similar, analogous, precipitates form in modern seafloor hydrothermal smoker systems (TAG and Red sea systems). The meta-argillite and quartz-grunerite BIF are minor units compared to the overlying, volumetrically significant, NIF assemblage oxide-dominant BIF.

The oxide-dominant BIF was deposited during a steady period of prolonged hydrothermal seafloor smoker activity. Similar to the previously discussed quartz-grunerite BIF, this lithology was deposited as hydrous-gels on the seafloor. The banded nature of these lithologies results from the rhythmic variation of black to white smoker hydrothermal systems.

The silicate-dominant BIF was deposited on top of the oxide-dominant BIF and represents decreasing hydrothermal smoker activity combined with increasing siliciclastic detrital sedimentation. The Fe-silicate minerals likely represent metamorphosed clay-rich layers. The clay minerals were eroded from intermediate to mafic igneous rocks. The quartz-rich layers represent meta-chert bands.

The hornblende-garnet schist represents a metamorphosed iron-rich mudstone eroded from mafic to intermediate igneous material (i.e., weathered volcanic glass in the form of

smectite). In addition to being found as intercalated bands within the silicate-dominant BIF, the hornblende-garnet schist geochemically overlaps with the silicate-dominant BIF suggesting these two lithologies are genetically related. The siliciclastic sedimentary protolith to the hornblende-garnet schist is the same sediment that makes up the siliciclastic component of the silicate-dominant BIF.

The biotite-garnet schist represents a metamorphosed ferruginous mudstone due to its high iron and aluminum content. Unlike the hornblende-garnet schist and silicate-dominant BIF, the siliciclastic sedimentary component was derived from intermediate to felsic igneous source rocks. The biotite-garnet schist and garnet-bearing quartzite commonly occur in gradational contact. These lithologies also exhibit geochemical similarities. The garnet-bearing quartzite represents metamorphosed silt-rich sandstone (volcanic ash) eroded from the same, or similar, felsic igneous source rocks as the biotite-garnet schist.

7) The majority of samples did not experience significant metasomatic alteration. The metasomatic alteration that did take place was selective, relatively confined, and not pervasive. Typically immobile elements remained immobile as indicated by well developed linear geochemical ratios between these elements ( $\text{Al}_2\text{O}_3$ ,  $\text{TiO}_2$ , Zr, U, Th, REE etc).

More importantly normally mobile alkali elements like potassium and sodium, in some samples, appear to have remained stationary, whereas in other samples these elements were mobilized. These geochemical trends indicate that metasomatic fluids were not pervasively circulating through the rocks at Musselwhite. Rather, metasomatic alteration is likely associated with localized structures such as shear-zones.

8) The most widespread alteration seen in the oxide-dominant BIF is grunerite bands. These bands are found between the magnetite and quartz bands. Grunerite was formed as metasomatic-fluids migrated along the contact between the two monomineralic bands with quartz and magnetite reacting to form grunerite.

9) Gold mineralization at Musselwhite is largely confined to the silicate-dominant BIF. Mineralized intervals correspond with abundant diffuse quartz veins and disseminated pyrrhotite. The association between gold mineralization and pyrrhotite suggests gold was transported as  $\text{Au}(\text{HS})_2$ . Localized pyrrhotite content, in the silicate-dominant BIF, is the result of sulfidation reactions between metasomatic fluids and the wall rock.

In terms of geochemistry the  $\text{Au}(\text{HS})_2$  complex was likely being carried in the same metasomatic fluids causing the select mobilization of alkali elements at Musselwhite. This conclusion is based on positive correlations between selenium, which substitutes for sulfur in sulfide minerals, and  $((\text{Cs}+\text{Rb})/\text{Th})_N$  values in some samples of the silicate dominant BIF.

An epigenetic metamorphic model for mineralization is proposed for Musselwhite as opposed to a syngenetic model. It is hypothesized that gold mineralization is associated with garnet-pyrrhotite-chlorite crystallization, driven by prograde and retrograde metamorphic fronts, along second-order shear zones. Therefore gold mineralization is both structurally and chemically controlled. Mineralization occurs where gold-pathways (shear zones) intersect appropriate chemical traps (silicate BIF).

10) From an exploration standpoint there are three critical requirements for mineralization of the Musselwhite gold deposit: 1) proper metamorphic conditions (amphibolite recrystallization front), 2) shear zone (metasomatic fluid conduit), and 3) chemical trap (silicate-dominant BIF)

11) The silicate-dominant banded iron formation is not generated through an alteration of the oxide-dominant BIF during the mineralization process. It represents a true silicate-dominant iron formation formed from the co-deposition of exhalative precipitates and siliciclastic detritus.

12) The Musselwhite gold deposit is similar to other orogenic BIF-hosted gold deposits. More specifically, prominent similarities exist between Musselwhite, Lupin, and Meadowbank deposits. Similarities include age, metamorphic grade, mineralogy, type of iron formation, tectonic setting of formation and proximity to significant shear zones. Therefore Algoma-type iron formations, deposited near active continental margins, are prime targets when exploring for Musselwhite and Lupin style BIF-hosted gold deposits.

13) The 'metasomatic biotite-garnet schist' exhibits similar geochemistry to the regular biotite-garnet schist lithology suggesting that these bands probably resulted from the same protolith. It is likely that the 'metasomatic biotite-garnet schist' bands represent physically deformed versions of biotite-garnet schist.

However, biotite is a common alteration mineral in orogenic gold deposits that were formed between sub-greenschist and amphibolite-facies conditions. In many Archean deposits, biotite forms at or immediately following peak metamorphic conditions. There is some geochemical evidence supporting this conclusion mainly for the silicate-dominant BIF.



## References

- Andrew, A.J., Sharp, D.R., and Janes, D.A., 1981, Preliminary reconnaissance of the Weagamow-North Caribou Lake metavolcanic-metasedimentary belt, including the Opapimiskan Lake (Musselwhite) gold occurrence: Ontario Geological Survey, Miscellaneous Paper 100, p. 196-202.
- Bäcker, H., 1976, Fazies und chemische Zusammensetzung rezenter Ausfällungen aus Mineralquellen in Roten Meer: Geologisches Jahrbuch, v. 17, p. D151-D172.
- Barnes, H. [ed.], 1997, Geochemistry of hydrothermal ore deposits-3<sup>rd</sup> edition: John Wiley & Sons Inc, 963 p.
- Barley, M.E., 1986, Incompatible element enrichment in Archaean basalts, a consequence of contamination of older Sialic crust rather than mantle heterogeneity. *Geology*. 14 p, 947-950.
- Bhatia, M.R., and Crook, K.A.W., 1986, Trace element characteristics of graywackes and tectonic setting discrimination of sedimentary basins: *Contributions to Mineralogy and Petrology*, v. 92, p. 181-193.
- Blower, S. and Kiernan, J., 2003, Kinross Technical Report: Review of Musselwhite Mine Operations, Ontario, AMEC report, 20 p.
- Bonatti, E., Kolla, V., Moore, W.S., and Stern, C., 1979, Metallogenesis in marginal basins: Fe-rich basal deposits from the Philippine Sea: *Marine Geology*, v. 32, p.21-37.
- Bostock, N.H., 1980, Geology of the Itchen Lake area, District of Mackenzie: Geological Survey of Canada, Memoir 391, 101 p.
- Böstrom, K., 1973, The origin and fate of ferromanganoan active ridge sediments: *Stockholm Contributions to Geology*, v.27, p. 147-243.
- Breaks, F.W., Bartlett, J.R., and deKemp, E.A., 1985, Opapimiskan Lake project: Precambrian and economic geology of the North Caribou Lake greenstone belt, Eyapamikama Lake area, north-western Ontario, District of Kenora, Patricia Portion: Ontario Geological Survey, Miscellaneous Paper 126, p.268-276.
- Breaks, F.W., 1989, Origin and Evolution of peraluminous granite and rare-element pegmatite in the Dryden area, Superior Province of north-western Ontario; Unpublished PhD thesis, Carleton University, Ottawa, Ontario, 594 p.
- Breaks, F.W., Bartlett, J.R., deKemp, E.A., and Osmani, I.A., 1991, Geology of the Doubtful-Akow lakes area, District of Kenora: Ontario Geological Survey, Open File Report 5795, 131p.

Breaks, F.W., Osmani, I.A., and deKemp, E.A., 2001, Geology of the North Caribou Lake area, north-western Ontario: Ontario Geological Survey, Open File Report 6023, 80p.

Bullis, H.R., Hureau, R.A., and Penner, B.D., 1994, Distribution of gold and sulfides at Lupin, Northwest Territories: *Economic Geology*, v. 89, p. 1217-1227.

Card, K. D., and Ciesielski, A., 1986, Subdivisions of the Superior province of the Canadian Shield: *Geoscience Canada*, v. 13, p. 5-13

Clemmey, H., 1985, Sedimentary ore deposits. *in* P.J. Brenchley and B.P.J. Williams (eds), *Sedimentology. Recent Developments and Applied Aspects*. Geological Society London and Blackwell Scientific Publications, p. 229-247.

Cloud, P.E., 1973, Paleocological significance of banded iron-formation: *Economic Geology*, v. 68, p. 1135-1143.

Cronan, D., 1976, Basal metalliferous sediments from the eastern Pacific: *Geological Society of America, Bulletin*, v. 87, p. 928-934.

Davis, D.W. and Stott, G.M., 2001, Geochronology of several greenstone belts in the Sachigo Subprovince, north-western Ontario: Summary of Fieldwork and Other Activities 2001, Ontario Geological Survey, Open File Report 6070, p 18-1 to 18-13.

Deer, W.A., Howie, R.A., and Zussman, J., 1992, *An introduction to The Rock-Forming Minerals* 2<sup>nd</sup> edition, Addison: Wesley Longman Limited, Harlow UK, 696p.

deKemp, E.A., 1987, Stratigraphy, provenance and geochronology of Archean supracrustal rocks of western Eyapamikama Lake area, north-western Ontario: unpublished MSc thesis, Carleton University, Ottawa, Ontario, p. 98.

Derochers, J.P., Hubert, C., Ludden, J.N., Pilote, 1993, Accretion of Archean oceanic plateau fragments in the Abitibi greenstone belt, Canada: *Geology*, v. 21, p.452-454.

Dymon, J., Corliss, J.B., Heath, G.R., Field, C.W., Dasch, E.W., and Veeh, H.H., 1973, Origin of metalliferous sediments from the Pacific Ocean: *Geological Society of America, Bulletin*, v. 84, p. 3355-3372.

Emslie, R.F., 1962, Wunnummin Lake (NTS 53A), Ontario: Geological Survey of Canada, Map 1-1962.

Floyd, P.A., and Leveridge, B.E., 1987, Tectonic environment of the Devonian Gramscatho basin, south Cornwall: framework mode and geochemical evidence from turbiditic sandstones: *Journal of Geological Society, London*, v. 144, p. 531-542.

Ford, R.C., and Duke, N.A., 1993, Concentration of gold during retrograde metamorphism of Archean banded iron formations, Slave Province, Canada: *Canadian Journal of Earth Sciences*, v.30, p. 1566-1581.

Fralick, P., 2003, Geochemistry of clastic sedimentary rocks: ratio techniques, in Lentz, D.R., ed., *Geochemistry of Sediments and Sedimentary Rocks: Evolutionary Considerations to Mineral Deposit-Forming Environments*: Geological Association of Canada, *Geotext* 4, p. 85-103.

Froese, E., and Gasparinni, E., 1975, Metamorphic zones in the Snow Lake area, Manitoba: *The Canadian Mineralogist*, v.13, p. 162-167.

Fripp, R.E.P., 1976, Strata-bound gold deposits in Archean banded iron-formation, Rhodesia: *Economic Geology*, v. 71, p. 58–75.

Geusebroek, P.A., and Duke, N.A., 2005, An Update on the Geology of the Lupin Gold Mine, Nunavut, Canada: *Exploration and Mining Geology*, v. 13, p. 5-12.

Goldfarb, R.J., Groves, D.I., and Gardoll, S., 2001, Orogenic gold and geologic time: A global synthesis: *Ore Geology Reviews*, v.18, p.1-75.

Graf, J.L., Jr., 1977, Rare earth elements as hydrothermal tracers during the formation of massive sulfide deposits in volcanic rocks: *Economic Geology*, v. 72, p. 527-548.

Gross, G.A., 1980, A classification of iron formation based on depositional environments: *The Canadian Mineralogist*, v. 18, p. 215-222.

Gross, G.A., 1996, Stratiform Iron: Lake Superior-type iron-formation, Algoma-type iron formation, Ironstone, in Eckstrand, O.E., Sinclair, W.D., and Thorp, R.I., eds., *Geology of Canadian Mineral Deposit Types, The Geology of North America*, no.8: Geological Survey of Canada, p. 41-80.

Groves, D.I., and Batt, W.D., 1984, Spatial and temporal variations of Archean metallogenic associations in terms of evolution of granitoid-greenstone terrains with particular emphasis on the Western Australian Shield: in *Archean geochemistry*, Springer-Verlag, Berlin, p. 73-98.

Groves, D.I., Phillips G.N., Falconer L.J., Houstoun S.M., Ho S.E., Browning P., Dahl N., and McNaughton N.J., 1987, Evidence for an epigenetic origin for BIF-hosted gold deposits in greenstone belts of the Yilgarn block, Western Australia: in Ho, S.E., and Groves D.I. (eds.) *Recent advances in understanding Precambrian gold deposits*. Geology Department and University Extension, The University of Western Australia Publication 11, p. 167–179.

Gu, X.X., 1996, Geochemical characteristics of sediments and tectonic setting analysis of sedimentary basins: in *Developments in Geosciences and Technology*, 1995: Press of

University of Geosciences of China, Beijing, p. 205–212 (in Chinese with English abstract).

Gu, X.X., Liu, J.M., Zheng, M.H., Tang, J.X., and Qi, L., 2002, Provenance and tectonic setting of the Proterozoic turbidites in Hunan, south China: geochemical evidence: *Journal of Sedimentary Research*, v. 72, p. 393-407.

Hall, R.S. and Rigg, D.M., 1986, Geology of the West Anticline zone, Musselwhite prospect, Opapimiskan Lake, Ontario, Canada: *in Proceedings of Gold '86*, Konsult International, Toronto, Ontario, p.124-136.

Hartigan, J.A., 1975, *Clustering Algorithms*. John Wiley & Sons, Inc, New York, 185p.

Heath, C.J., and Campbell, I.H., 2004, A New Geochemical Technique for Gold Exploration: Alkali Element Mobility Associated with Gold Mineralization in the West Australian Goldfields: *Economic Geology*, v. 99, p. 313-324.

Hill, M.L. Cheatle, A., and Liferovich, R., 2006, Musselwhite Mine: An orogenic gold deposit in the Western Superior Province: *Geologic Association of Canada Abstracts*, v.31, p. 67.

Holland, H.D., 1984, *The chemical evolution of the atmosphere and the oceans*: Princeton University Press, 598p.

Hollings, P., and Kerrich, R., 1999, Trace element systematics of ultramafic and mafic volcanic rocks from the 3 Ga North Caribou greenstone belt, north-western Superior Province: *Precambrian Research*, v. 93, p. 257-279.

Hoschek, G., 1969, The stability of staurolite and chloritoid and their significance in metamorphism of pelitic rocks: *Contributions to Mineralogy and Petrology*, v. 22, p. 208-232.

Jacobsen S.B., and Pimentel-Klose, M.R., 1988, A neodymium isotopic study of the Hamersley and Michipicoten banded iron-formations: The sources of REE and iron in Archean oceans: *Earth and Planetary Science Letters*, v. 87, p. 29-44.

James, H.L., 1954, Sedimentary facies of iron-formation: *Economic geology*, v.49, p.235-293.

Jochum, K.P., Arndt, N.T., and Hofman, A.W., 1991, Nb-Th-La in Komatiites and basalts, constraints on komatiite paragenesis and mantle evolution: *Earth and Planetary Science Letters*, v.107, p. 272-289.

Kerswill, I.A., 1985, Gold Distribution in the Contwoyto Lake Area, NWT: An update to include current thoughts on gold metallogeny: Echo Bay Mines Ltd., Internal Report, 14p.

Kerrich, R., 1983, Geochemistry of gold deposits in the Abitibi greenstone belt: Canadian Institute of Mining and Metallurgy Special Paper, v. 27, 75p.

Klipfel, P., 2002a, Musselwhite Geology Model: Construction and Interpretations: Goldcorp Internal Report.

Klipfel, P., 2002b, Musselwhite U-Pb Zircon and Ar-Ar Dates, Synthesis and Interpretation: Goldcorp Internal Report.

Kolb, J., Hellmann, A., Rogers, A., Sindern, S., Vennemann, I., Bottcher, M.E., and Meyer, M.F., 2004, The role of transcrustal shear zone in orogenic gold mineralization at the Ajjanahalli Mine, Dharwar Craton, South India: *Economic Geology*, v. 99, p.743-759.

Ladeira, EA., 1991, Genesis of gold in the Quadril'tero Ferrifero: a remarkable case of permanency, recycling and inheritance, a tribute to Djalma, Guimaraes, Pierre Routhier and Hans Ramsberg. *in* Ladeira EA (ed) Gold '91. Balkama Publications, Rotterdam, p.11–30

Lhotka, P.G., and Nesbitt, B.E., 1988, Evidence for epigenetic Au mineralization in Archean silicate iron-formation, Lupin Mine, Slave Province, Canada: *Bicentennial Gold 88: Geological Society of Australia, No. 23, Poster Volume 1*, p. 89-91.

Lhotka, P.G., and Nesbitt, B.E., 1989, Geology of unmineralized and gold-bearing iron formation, Contwoyto lake- Point Lake region, Northwest Territories, Canada: *Canadian Journal of Earth Sciences*, v.26, p. 46-64.

Maynard, J.B., 1991, *Geochemistry of Sedimentary ore deposits*: Springer-Verlag, 305p.

McCann, T., 1991, Petrological and geochemical determination of provenance in the southern Welsh Basin, *in* Morton, A.C., Todd, S.P., and Haughton, P.D.W., eds., *Developments in Sedimentary Provenance Studies: Geological Society of London, Special Publication 57*, p.215–230.

McLearty, E.A., 1985, A detailed study of the mineralogy, structure, and metal distribution within the Pollux Lake banded iron formation, northwestern Ontario: unpublished BSc thesis, University of Western Ontario, London, Ontario, 78 p.

McLennan, S.M., Taylor, S.R., McCulloch, M.T., and Maynard, J.B., 1990, Geochemical and Nd–Sr isotopic composition of deep-sea turbidites: Crustal evolution and plate tectonic associations: *Geochimica et Cosmochimica Acta*, v. 54, p. 2015–2050.

McLennan, S.M., and Taylor, S.R., 1991, Sedimentary rocks and crustal evolution: Tectonic setting and secular trends: *Journal of Geology*, v. 99, p. 1–21.

McLennan, S.M., and Murray, R.W., 1999, Geochemistry of sediments, *in* Marshall, C.P., and Fairbridge, R.W., *Encyclopaedia of Geochemistry*: Kluwer Academic Publishers, p. 282-292.

Melzer, S., 1999, Experimentally determined K-Rb-Cs exchange coefficients between micas, amphiboles and aqueous chloride solutions [abs]: EOS Supplement, v. 80, no. 17, 1999, p. 361.

Mikucki, E.J., and Ridley, J.R., 1993, The hydrothermal fluid of Archean lode-gold deposits at different metamorphic grades: compositional constraints from ore and wall rock alteration assemblages: *Mineralium Deposita*, v. 28, p. 469-481.

Mills, R.A., and Elderfield, H., 1995, Rare earth element geochemistry of hydrothermal deposits from the active TAG mound 260 north, Mid-Atlantic Ridge: *Geochimica et Cosmochimica Acta*, v.59, p.3511-3524.

Nesbitt, H. Wayne, R., Markovics, G., and Price, R. C., 1980, Chemical processes affecting alkalis and alkaline earths during continental weathering: *Geochimica et Cosmochimica Acta*, v. 44, p. 1659-1666.

Nesbitt, N.W., and Young, G.M., 1982, Early Proterozoic climates and plate motions inferred from major element chemistry of lutites: *Nature*, v. 299, p. 715-717.

Neuendorf, K.K.E., Mehl, J.P. Jr., Jackson, J.A., 2005, Glossary of geology: American Geological Institute, 779p.

Otto, A., 2002, Ore forming processes in the BIF-hosted gold deposit Musselwhite Mine, Ontario, Canada. Masters thesis: Freiberg University of Mining and Technology, Institute of Mineralogy, Department of Economic Geology and Leibniz Laboratory for Applied Marine Research, 86p.

Ontario Department of Mines–Geological Survey of Canada, 1985, Airborne electromagnetic and total intensity magnetic survey; Geophysical papers 919G and 929G.

Pearce, J.A., Alabaster, T., Shelton, A.W., and Searle, M.P., 1981, The Oman ophiolites as a Cretaceous arc-basin complex: evidence and implications: *Philosophical Transactions of the Royal Society*, v. A300, p. 299-317.

Pearce, J.A., 1983, The role of sub-continental lithosphere in magma genesis at destructive plate margins, *in* Hawkesworth, C.J., and Norry, M.J., eds.: *Continental Basalts and Mantle Xenoliths*: Shiva, Nantwich, p. 230-249.

Peter, J.M., 2003, Ancient iron formations: their genesis and use in exploration for stratiform base metal sulfide deposits, with examples from the Bathurst Mining Camp: *in* Lentz, D.R., ed., *Geochemistry of Sediments and Sedimentary Rocks: Evolutionary Considerations to Mineral Deposit-Forming Environments*. Geological Association of Canada, Geotext 4, p. 145-176.

Peter, J.M., and Goodfellow, W.D., 1996, Mineralogy, bulk and rare earth element geochemistry of massive sulphide-associated hydrothermal sediments of the Brunswick

Horizon, Bathurst Mining Camp, New Brunswick: Canadian Journal of Earth Sciences, v.33, p.252-283.

Peter, J.M., and Scott, S.D., 1999, Windy Craggy, north-western British Columbia: The world's largest Besshi-type deposit, *in* Barrie, C.T. and Hannington, M.D., eds., Reviews in Economic Geology, v.8: Society of Economic Geologists, p. 261-295.

Phillips, G.N., Groves, D.I., Martyn, J.E., 1984, An epigenetic origin for Archean banded iron-formation-hosted gold deposits: Economic Geology, v. 79, p.162–171.

Pirie, J., and Mackasey, W.O., 1978, Preliminary examination of regional metamorphism in parts of Quetico metasedimentary belt, Superior Province, Ontario: in Metamorphism in the Canadian Shield, Geological Survey of Canada, Paper 78-10, p.37-48.

Piroshco, D., 1986, Structural geology and gold mineralization of the Eyapamikama Lake area of the North Caribou Lake greenstone belt, District of Kenora (Patricia Portion); Ontario Geological Survey, Miscellaneous Paper 126, p. 277-286.

Pretorius, A.I., van Reenen, D.D., and Barton, J.M., Jr., 1988, BIF-hosted gold mineralization at the *Fumani* Mine, Sutherland greenstone belt, South Africa: Transactions of the Geological Society of South Africa, v. 91, p.429-438.

Rayner, N., and Stott, G.M., 2005, Discrimination of Archean Domains in the “Sachigo Subprovince”, North-western Ontario: Ontario Geological Survey poster, Ontario Exploration and Geoscience symposium, Toronto, December 13-14 2005.

Ridler, R.H., 1971, Analysis of Archean volcanic basins in the Canadian Shield using the exhalative concept: Bulletin of the Canadian Institute of Mining and Metallurgy, v. 64, p.20.

Robertson, A.H.F, and Hudson, J.D., 1973, Cyprus umbers: chemical precipitates on a Tethyan ocean ridge: Earth and Planetary Science Letters, v. 18, p. 93-101.

Rudnicki, M.D., 1995, Particle formation, fallout and cycling within the buoyant and non-buoyant plume above the TAG vent field, *in* Parson, L.M., Walker, C.L., and Dixon, D.R., eds., Hydrothermal vents and processes: Geological Society, Special Publication, no.87, p.387-396.

Saager R., Oberthür T., and Tomschi H., 1987, Geochemistry and mineralogy of banded iron-formation-hosted gold mineralization in the Gwanda Greenstone Belt, Zimbabwe: Economic Geology, v. 82, p. 2017–2032

Satterly, J., 1994, Geology of the Windigo-North Caribou Lakes area: Ontario Ministry of Northern Development and Mines, Ontario Geologic Survey, Publication No: ARV48-09.

- Sherlock, R.L., Deyell, C., and Hyde, D., 2003, Geologic setting of gold mineralization in the Committee Bay belt, central mainland, Nunavut, Canada. In 7<sup>th</sup> International Symposium on mining in the Arctic. Edited by J.E. Udd and G. Bekkers. Canadian Institute of mining and Metallurgy and Petroleum, p. 19-34.
- Spry, P.G., Peter, J.M., and Slack, J.F., 2000, Meta-exhalites as exploration guides to ore, *in* Spry, P.G., Marshall, B., and Vokes, F.M., eds., *Metamorphosed and metamorphic ore deposits*, *Reviews in Economic Geology*, v.11, p.163-201.
- Stone, D., 2005, *Geology of the Northern Superior Area, Ontario*: Ontario Geological Survey, Open File Report 6240, 94p.
- Sun, S.S., and McDonough, W.F., 1989, Chemical and isotopic systematics of oceanic basalts: Implications for mantle composition processes: *Geological Society Special Publication* v. 42, p. 313-345.
- Taylor, S.R., and McLennan, S.M., 1985, *The continental crust: Its composition and evolution*: Blackwell, Oxford, 312p.
- Thurston, P.C., and Breaks, F.W., 1978, Metamorphic and tectonic evolution of the Uchi-English River Subprovince; *in* *Metamorphism in the Canadian Shield*, Geological Survey of Canada, Paper 78-10, p. 49-62.
- Thurston, P.C., Sage, R.P., and Siragusa, G.M., 1979, *Geology of the Winisk Lake area, District of Kenora (Patricia Portion)*: Ontario Geological Survey, Report 193, 169p.
- Thurston, P.C., Osmani, I.A., Stone, D., 1991, *North-western Superior Province Review and Terrane Analysis: Geology of Ontario*. Ontario Geological Survey, 144p.
- Thurston, P.C., Williams, H.R., Sutcliffe, R.H., and Stott, G.M. eds., 1991, *Geology of Ontario*: Ontario Geological Survey special volume, Queens Printer for Ontario, p. 83-89.
- Till, R., 1974, *Statistical Methods for the earth scientist and introduction*: Halsted press a division of John Wiley and Sons, Inc. New York, p.148.
- Toth, J.R., 1980, Deposition of submarine crusts rich in manganese and iron: *Geological Society of America Bulletin*, v. 91, p. 44-54.
- Vielreicher, R.M., Groves, D.I., Ridley, J.R., and McNaughton, N.J., 1994, A replacement origin for the BIF-hosted gold deposit at Mt. Morgans, Yilgarn Block, W.A: *Ore Geology Reviews*, v. 9, p. 325-347.
- Walshe, J.L., 1986, A Six-Component Chlorite Solid Solution Model and the Conditions of Chlorite Formation in Hydrothermal and Geothermal Systems: *Economic Geology*, v. 81, p. 681-703.
- Wells, R.C., 1995a, Petrographic and lithogeochemical report on samples from the Musselwhite project, East Bay synform including observations on the geological setting of gold mineralization: Internal report for Placer Dome Canada Limited, 40p.



Wells, R.C., 1995b, Lithogeochemical report on Bvol, ultramafic and unit8 dike samples, Musselwhite project. Internal report for Placer Dome Canada Limited, 6p.

Xie, Q., McCuaig, T.C., Kerrich, R., 1995, Secular trends in the melting depths of mantle plumes; evidence from HFSE/REE systematics of Archaean high-mg lavas and Modern oceanic basalts: *Chemical Geology*. v.126, p.29-42.

Zaleski, E., Davis, W.J., and Wilkinson, L., 2000, Basement/cover relationships, unconformities and depositional cycles of the Woodburn Lake group, western Churchill province, Nunavut. *Yellowknife Geoscience Forum*. November 2000.






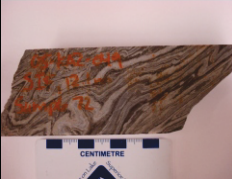
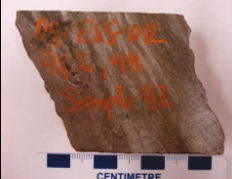
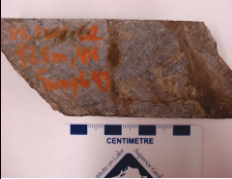

Zang, G., 1997, Structural characteristics and mechanical controls on fluid flow of gold deposit at the Musselwhite Mine, Weagamow-North Caribou Lake greenstone belt, north-western Ontario: Internal report for Placer Dome Canada, 85p.

# **Appendix A**

## **Sample Descriptions**







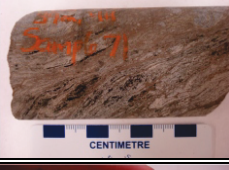

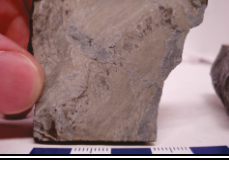
(Abbreviations used in this section are explained on pg. XIII)

## SIF ASSEMBLAGE OXIDE-DOMINANT BIF

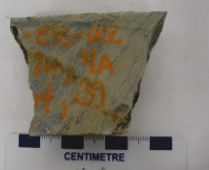








Sample	Location	Description	GEOCHEM	THIN-SECTION	SEM
	SIF-PM05-063c SIF-PM05-063m Machine Shop SIF	Only SIF assemblage oxide-dominant BIF sample collected from underground workings at Musselwhite. Taken from near machine shop on 500L. Consists of alternating, 0.2-1.0cm thick bands of fgr-mgr qtz and mag. Qtz bands are cream coloured and gru- and cal-rich. Mag bands are monomineralic consisting of ~60% mag and ~40% qtz. Separated into two samples and sent for geochemical analysis (SIF-PM05-063c: quartz band, SIF-PM05-063m: magnetite band).	X	X	
	SIF-07-20-060c SIF-07-20-060m 03-RDW-003 295.6m	Thickly banded, mod-distorted SIF assemblage oxide-dominant BIF sample (a-typical due to unusually thick bands). Consists of 50% mag-bands (0.5-2.0cm bands) 45% qtz-bands (0.5-1.5cm bands) 5% gru-bands (0.1-0.3cm bands), and minor disseminated hbl or chl. Evident folding. This sample appears carbonate rich. Collected in July 06. This sample contains a large qtz-vein (not included in geochemistry samples). Separated into 2 samples (SIF-PM05-060c: quartz-band, SIF-PM05-060m: magnetite-band)	X	X	
	SIF-07-20-062m 03-RDW-035 241.9m SIF	Thinly banded SIF assemblage oxide-dominant BIF sample. On broken surfaces mag has shiny/polished look, indicating possible highly strained nature. Consists of 55%, 0.1-0.5cm thick, white quartz-bands, and 45%, 0.1-0.6cm thick, black magnetite-bands. Contains disseminated grunerite and <1% disseminated primary sulfide. No obvious quartz veins. Only one sample sent for geochemistry (SIF-07-20-062m: magnetite-band).	X		
	SIF-07-20-063c SIF-07-20-063m 04-ESS-086 157.5m SIF	Sample of typical looking SIF assemblage oxide-dominant BIF showing 'zebra stripe' appearance. Consists of 50%, 0.1-0.3cm thick, black mag bands and 50%, 0.1-0.4cm thick, white qtz bands. Bands have 'undulating margins.' No qtz and sulfide veins. Minor calcite vein <1mm thick. Sample collected in July 2006. Separated into two samples (SIF-07-20-063c: qtz band, SIF-07-20-063m: mag.	X	X	
	SIF-07-20-070m 04-KAZ-002 141m SIF	Thinly-banded SIF assemblage oxide-dominant BIF sample. Consists of 50%, 0.1-0.3cm thick, magnetite-bands and 45%, 0.2-0.4cm thick, quartz-bands. Roughly 2% disseminated grunerite and 3% pyrrhotite. Magnetite and quartz bands are strongly sheared, resulting in distortion of the original bands. Sample collected in July '06. One sample sent for geochemistry (SIF-07-20-070m: magnetite band). Magnetite sample probably has high silica due to distorted nature of the bands.	X		
	SIF-07-20-072m 05-KAZ-049 12.1m SIF	Intensely folded SIF assemblage oxide-dominant BIF sample. Typical black and white 'zebra-striped' appearance for this lithology, however sample is crenulated and folded. The bands in this sample are thicker relative to other samples. Sample consists of 48%, 0.1-0.5cm thick, black mag-bands and 48%, 0.1-0.4cm thick, white qtz-bands. Roughly 4% gru. Sample collected in July 2006. One sample sent for geochemistry (SIF-07-20-072m: mag band).	X	X	
	4h-07-20-042 04-ESS-012 98.2m 4h	Grunerit-rich meta-argillite sample. This sample does not contain obvious carbon or graphite rich layers. Sample consists of 80% tan-yellow grunerite-rich bands (laminated), 15% light-grey distorted quartz bands, and 5% pyrrhotite which is disseminated in the grunerite-rich material. All layers appear distorted and or brecciated. Sample collected in July 2006. One sample sent for geochemistry (4h-07-20-042).	X		
	4h-07-20-043 04-ESN-012 97.8m 4h	Meta-argillite sample with high quartz-component (due to quartz-veining). Sample consists of >90% grey-semi-translucent quartz, ~7% fine-grained tan-yellow grunerite-rich selvages, and ~3% pyrrhotite. Sample is distorted and brecciated. It should be noted that this sample was collected from between sulfide rich layers. Sample collected in July 2006. One sample sent for geochemistry (4h-07-20-043). Grunerite and pyrrhotite-rich material sent for geochemistry.	X		
	4h-07-20-046 04-ESS-009 149.3m 4h	Typical looking meta-argillite sample. This sample is moderately folded and contains abundant quartz. Sample consists of roughly 50% quartz and 50% tan-yellow grunerite-rich argillaceous material. Again the siliclastic material appears to contain abundant grunerite in hand sample. Sample does not appear to contain carbon/graphite. This sample is similar to previously described meta-argillite sample. Sample collected in July '06. One sample sent for geochemistry (4h-07-20-046).	X		

## META-ARGILLITE





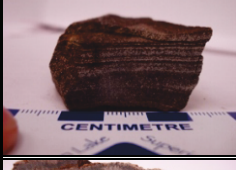
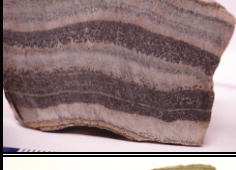



META-ARGILLITE

Sample	Location	Description	GEOCHEM	THIN-SECTION	SEM
	4h-07-20-051 04-PQD-001 28.6m 4h	Sample of typical looking meta-argillite, collected from the bottom of the NIF assemblage. Sample consists of 80% distorted, thinly-banded, dark-grey graphitic+sulfide rich siliciclastic material (contains disseminated grunerite), 7% disseminated and stinger pyrrhotite (abundant between graphite-rich and qtz-rich material). Strongly distorted laminations (graphite- versus grunerite- rich bands). Sample collected July'06. One sample sent for geochemistry (4h-07-20-051).	X		
	4h-07-20-053a 04-PQD-006 1024.2m 4h	Good example, and sample, of meta-argillite. Sample is quart-rich and contains what appear to be graphitic laminations. Sample consists of 40%, 0.2-1.0cm thick, grey graphitic-bands, 10% black biotite-bands containing garnet, 30% grey, 0.2-0.5cm thick, quartz-bands, 15%, 0.2-0.3cm thick, grunerite bands, 5% disseminated pyrrhotite in graphitic layers. Sample is distorted and brecciated. Sample collected July'06. One sample sent for geochemistry (4h-07-20-053a).	X	X	
	4h-07-20-053b 04-PQD-006 1024.2m 4h	Good example, and sample, of meta-argillite. Sample is quart-rich and contains what appear to be graphitic laminations. Sample consists of 40%, 0.2-1.0cm thick, grey graphitic-bands, 10% black biotite-bands containing garnet, 30% grey, 0.2-0.5cm thick, quartz-bands, 15%, 0.2-0.3cm thick, grunerite bands, 5% disseminated pyrrhotite in graphitic layers. Sample is distorted and brecciated. Sample collected July'06. One sample sent for geochemistry (4h-07-20-053b).	X	X	
	4h-07-30-056 04-PQU-135 34m 4h	This sample of meta-argillite was collected from within the mafic meta-volcanics just below the NIF assemblage. Upper contact was sharp while lower contact was obscured by a qtz-vein. Sample consists of: 70% grunerite-rich bands, 10% graphitic + garn bands, 15% quartz bands, and 5% disseminated and laminated pyrrhotite. Po especially abundant in graphitic layers. Sample is characterized by thin laminations. Sample collected July'06. One sample sent for geochemistry (4h-07-20-056).	X	X	
	4h-07-20-057 04-PQU-135 32.3m 4h	Unique sample, of the contact between the meta-argillite and mafic metavolcanics underlying the NIF assemblage. Thin-graphitic band occurs along contact. Meta-argillite is thinly laminated, grunerite-rich, and contains thin pyrrhotite-rich laminations: consists of 80% grunerite, 15% siliciclastic material, 5% pyrrhotite, and <5% graphite. Rather A-typical meta-argillite sample. July'06. One sample sent for geochemistry (4h-07-20-057).	X		
	4h-07-20-070 06-PQU-019 33m 4h	Good example, and sample, of typical looking meta-argillite, collected from the bottom of the NIF assemblage. Sample consist of roughly 40% siliciclastic material (graphite, hornblende, biotite), 30% quartz (disseminated in matrix + brecciated piece of meta-chert), 15% disseminated pyrrhotite (as well as agglomerates), 10% sub- to euhedral garns (0.2-0.4cm) 5% tan-gru. Contains 0.1-0.3cm thick graphitic layers. Sample collected in July '06. One sample sent for geochemistry (4h-07-20-070).	X	X	
	4h-07-20-071 05-KAZ-005 39m 4h	Excellent meta-argillite sample. Only sample of meta-argillite collected from the SIF assemblage. Sample consists of: 35% dark-yellow grunerite-rich material, 25% tan-grey grunerite/siliciclastic-rich material, 15% 0.3-1.0cm wide qtz- blobs, 10% fine-grained black carbon blebs and laminations, 15% disseminated pyrrhotite (concentrated in, and around, rounded qtz- rich bands and between carbon and qtz-rich bands). Make thin-section. July'06. One sample sent for geochemistry (4h-07-20-071).	X	X	
	4a-07-20-012 06-PQU-019 30.5m 4a	Good example, and sample, of quartz-grunerite BIF collected from bottom of NIF assemblage. Sample has relatively pristine appearance. Sample consists of alternating 0.1-0.2cm thick quartz- and grunerite-laminations. Grunerite-laminations are slightly thicker than quartz-laminations. Sample consists of: 80% fine-grained yellow grunerite-bands, 5% quartz-bands, and 15% quartz-veins (semi-translucent). (Make thin-section). Sample collected July'06. One sample sent for geochemistry (4a-07-20-012).	X		
	4a-07-20-028 03-CMP-053 27.9m 4a	Sample, of sheared and grun-rich quartz-grunerite BIF. Probably represents distorted quartz-grunerite BIF. Collected from hole 03-CMP-053 is an interesting hole b/c it contains BIF and abundant meta-argillite. This sample consists of massive grunerite crosscut by quartz-veins: 70% fgr. gru (tan-yellow, original laminations destroyed), 25% dark qtz (laminations have been stretched and distorted), 5% dismembered pyrrhotite vein on right edge of core. July'06. One sample sent for geochemistry (4a-07-20-028).	X	X	

QUARTZ-GRUNERITE BIF









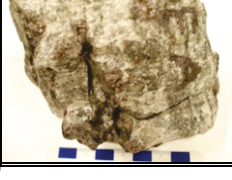
	Sample	Location	Description	GEOCHEM	THIN-SECTION	SEM
				X		
QUARTZ-GRUNERITE BIF		4a-07-20-039 04-ESS-002 148.7m 4a	Typical example of moderately deformed, thickly-laminated quartz-grunerite BIF. This samples consists of: 70%, 0.5-5.0cm thick, fine-grained yellow grunerite-rich bands with minor dark-green internal laminations (hornblende-rich?), 27%, 0.5-1.5cm thick grey quartz-bands, 3% hornblende+garn layers. This sample was collected from just below 1.3m thick gru+hbl+ mag+ qtz BIF. Make TS. Collected July'06. One sample sent for geochemistry (4a-07-20-039).	X		
		4a-07-20-041 04-ESN-012 96.8m 4a	Sheared and non-magnetic sample of quartz-grunerite BIF. Quartz- and grunerite- bands are sheared into one and other. Sample was collected from 2.5m thick quartz-grunerite BIF unit with intercalated, 0.1-0.15m thick, meta-argillite layers. Note there are minor dark-green internal laminations (hornblende-rich?). Consists of 80% grunerite, 5% 0.1-0.3cm thick grey distorted quartz-bands, 15% meta-argillite containing sulfide. Make TS. Collected July'06. One sample sent for geochemistry (4a-07-20-041).	X		
		4a-07-20-044 04-ESS-009 148.6m 4a	Well developed, grunerite-rich, thinly laminated quartz-grunerite BIF (laminations appear distorted). Sample consists of 85% fine-grained grunerite and 15% dark-grey quartz-bands (meta-chert). This sample is somewhat similar in appearance to sample 4a-07-20-041. It should be noted that quartz- and grunerite-rich laminations have been distorted by shearing. Make thin-section. Collected in July'06. One sample sent for geochemistry (4a-07-20-044).	X	X	
		4a-07-20-054c 4a-07-20-054m 04-PQU-135 28.3m 4a	The quartz-grunerite BIF bands in this sample represent the pristine appearance of the lithology. Undeformed sample. This sample is interesting b/c qtz-gru BIF bands are intercalated with mag-bands, possibly representing the transition from qtz-grun BIF to oxide-dominant BIF. Consist of: 50% qtz-gru BIF-bands and 50% mag-bands. Bands are of equal thickness (0.5-1.0cm). Sample collected in July'06. Sample 4a-07-20-054c: qtz-grun band and 4a-07-20-054m: mag band).	X	X	
NIF ASSEMBLAGE OXIDE-DOMINANT BIF		4b-PM05-006c Trench # 4 4b	Quartz-band of NIF assemblage oxide-dominant BIF. Sample was collected from the western margin of trench #4 (near mafic / ultra-mafic meta-volcanic rocks, see Fig. 1.11). This sample likely represents a meta-chert layer. Sample consists of >95% quartz, but also appears to contain disseminated fine-grained magnetite. The exterior of this sample is covered in ~1mm thick grunerite-rich rind. Collected in Oct'05. One sample (quartz-rich) sent for geochemistry (4b-PM05-006).	X		
		4b-PM05-012c Trench # 4 4b	Roughly 1.0-2.5cm thick quartz-band sample from NIF assemblage oxide-dominant BIF. Sample was collected from middle area of trench #4 (See Fig. 1.11). This sample consists of >99% qtz and ~1% fine-grained disseminated mag and grunerite. Sample has sugary texture and the interior appears to be hematite stained. There are also dark brown vugs filled with hematite (<2% of sample, see picture to left). Collected in Oct'05. One sample (quartz-rich) sent for geochemistry (4b-PM05-006).	X	X	
		4b-PM05-018c Trench # 4 4b	Roughly 5cm thick quartz-band sample from NIF assemblage oxide-dominant BIF. Sample was collected from middle area of trench #4 (See Fig. 1.11). More robust and consolidated sample compared to 4b-PM05-006c and 012c. This sample is a-typical as it resembles 'siliciclastic meta-sediment' from the trenches. Sample has high quartz content. Sample consists of ~95% qtz, and 5% hematite, mag, and grun. Collected in Oct'05. One sample (quartz-rich) sent for geochemistry (4b-PM05-018).	X	X	
		4b-PM05-021m Trench # 4 4b	Good example, and sample, of magnetite-band from NIF assemblage oxide-dominant BIF (~3cm thick). Sample collected from the western margin of trench #4 (near mafic / ultra-mafic meta-volcanic rocks, see Fig. 1.11). Sample is schistose (strong foliation), consists of >99% mag, ~1% minor disseminated fine-grained grunerite. Sample contains thin, strongly folded quartz-band which was not included in geochemistry sample. Collected in Oct'05. One sample (quartz-rich) sent for geochemistry (4b-PM05-021m).	X	X	
		4b-PM05-028c 4b-PM05-028m Trench # 5 4b	Magnetite- and quartz-bands from the NIF assemblage oxide-dominant BIF. Sample was collected from slight hill next to central water body in trench #5 (Fig. 1.11). Large sample (small part shown in pic). Sample consists of ~2cm thick magnetite and ~2cm thick quartz-bands. Magnetite band is >97% mag and ~3% qtz+grun. Qtz band is >99% qtz and ~1% fgr disseminated mag and gru. Collected in Oct'05. Separated into 2 samples (4b-PM05-028c: qtz-gru band and 4b-PM05-028c: mag band).	X	X	

NIF ASSEMBLAGE OXIDE-DOMINANT BIF

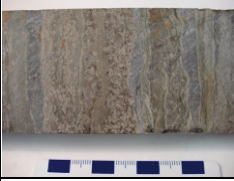



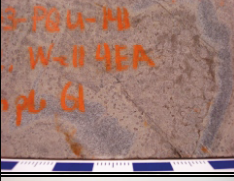
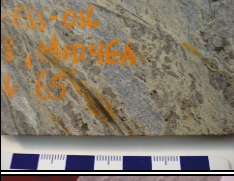
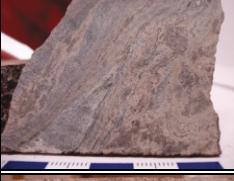
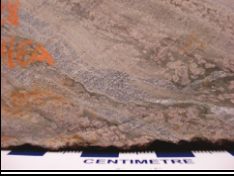
Sample	Location	Description	GEOCHEM	THIN-SECTION	SEM
	4b-PM05-031c 4b-PM05-031m Trench # 5 4b	Magnetite- and quartz-bands from NIF assemblage oxide-dominant BIF. This sample was collected from trench #5 (Fig. 1.11). Relatively large sample. Unaltered appearance compared to other trench samples. Consists of ~0.3cm-1.7cm thick mag- and ~2cm thick qtz-bands. Mag-band is >95% mag and ~5% qtz+grun. Qtz-band is >99% qtz and ~1% fgr disseminated mag and gru. Collected in Oct'05. Separated into 2 samples (4b-PM05-031c: qtz-grun-band and 4b-PM05-031m: mag-band).	X	X	
	4b-PM05-037m Trench #4 4b	Excellent example, and sample, of magnetite-band from NIF assemblage oxide-dominant BIF (large). Sample was collected by Dr. Fralick in trench #4 (Fig. 1.11). Consists of >97% fine- to medium-grained dark-grey, sparkly, magnetite. Minor, ~3%, 1-3mm thick quartz-grunerite bands contained in magnetite matrix. Magnetite matrix contains disseminated fine-grained grunerite crystals. Collected in Oct'05. One sample (magnetite-rich) sent for geochemistry (4b-PM05-037m).	X		
	4b-PM05-038c 4b-PM05-038m Trench #4 4b	Magnetite- and quartz-bands from NIF assemblage oxide-dominant BIF. This sample was collected from trench #4 (Fig. 1.11). Qtz-band (4b-PM05-038c) appears to be a true meta-chert band. It consists of ~98% fine-grained qtz and ~2% disseminated fine-grained magnetite. Mag-rich band consists of ~95% fine-grained magnetite and 5% disseminated (and in ~2mm thick band) qtz and gru. Collected in Oct'05. Separated into 2 samples (4b-PM05-038c: qtz-gru-rich band and 4b-PM05-038m: mag-rich band).	X	X	
	4b-PM05-039 Trench #4 4b	Small, ~5cm, sample of magnetite-band from NIF assemblage oxide-dominant BIF. Sample was collected by Dr. Fralick in trench #4 (Fig. 1.11). Consists of >97% fine- to medium-grained dark-grey, sparkly, magnetite. Minor, ~3%, 1-3mm thick quartz-grunerite bands contained in magnetite matrix. Magnetite matrix contains disseminated fine-grained grunerite crystals. Collected in Oct'05. One sample (magnetite-rich) sent for geochemistry (4b-PM05-039m).	X		
	4b-PM05-040c 4b-PM05-040m Trench #4 4b	Magnetite-band sample from NIF assemblage oxide-dominant BIF. Sample collected by Dr. Fralick in trench #4 (Fig. 1.11). Thinly laminated quartz and magnetite, ideal for thin-section. Consists of >95% fine- to medium grained magnetite and ~5% fine- to medium-grained quartz and grunerite. Grunerite is also disseminated in the magnetite-bands. Collected in Oct'05. Separated into 2 samples (4b-PM05-040c: quartz-grunerite band and 4b-PM05-040m: magnetite-band).	X	X	
	4b-PM05-042 Trench #5 4b	Small sample of NIF assemblage oxide-dominant BIF. This sample collected from trench #5 (Fig. 1.11). This sample is interesting because it shows an alteration type that is not seen in samples collected from drill core. Consists of: 60%, 0.5-1.0cm thick, quartz bands; and 40%, 0.4-0.7cm thick magnetite bands. Magnetite bands look 'skeletal' and contain abundant disseminated grunerite. Good sample for thin-section. Collected in Oct'05. One geochemistry sample sent (2-PM05-042).	X	X	
	4b-PM05-043c Trench # 4 4b	Excellent example, and sample, of quartz band from the NIF assemblage oxide-dominant BIF. Sample was collected by Dr. Fralick from trench #4 (Fig. 1.11). Roughly 4cm thick dark-grey quartz-rich band. Consists of ~90% fine-grained quartz, ~7% fine-grained disseminated and thinly-laminated magnetite, ~3% fine-grained disseminated grunerite. Good example of meta-chert band. Collected in Oct'05. One sample sent for geochemistry (4b-PM05-043c: qtz-grun band)	X	X	
	4b-PM05-101 Trench 4b	Good example, and sample, of magnetite-rich band from the NIF assemblage oxide-dominant BIF. Collected from the western margin of trench #4 (near mafic / ultra-mafic meta-volcanic rocks Fig. 1.11). Sample is schistose (strong foliation), consists of >99% magnetite, ~1% minor disseminated fine-grained grunerite. There is thin, strongly folded, quartz-band which was not included in geochemistry sample. Collected in Oct'05. One (magnetite-rich) geochemistry sample sent (4b-PM05-018).	X		
	4b-07-20-004m 06-PQE-071 101.6m 4b	Typical example of thickly banded NIF assemblage oxide-dominant BIF from core. Quartz-bands are semi-translucent. Overall sample consists of ~60%, 0.5-4.0cm thick, magnetite bands; 35% 0.5-1.0cm thick quartz bands; <5% 0.1-0.2cm thick grunerite bands. Sample collected in July '06. Several samples from this interval were collected. Sample A: 100.5m, Sample 4B 101.6m, Sample C 103.2m. Entire box is oxide-BIF. One sample (magnetite-rich) sent for geochem (4b-07-20-004m)	X	X	

NIF ASSEMBLAGE OXIDE-DOMINANT BIF

SILICATE BIF

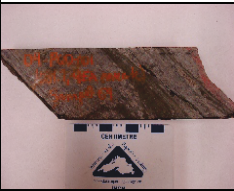






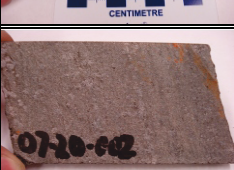

Sample	Location	Description	GEOCHEM	THIN-SECTION	SEM
	4b-PM06-005 05-PQE-013 55.5m 4b	Thickly banded NIF assemblage oxide-dominant BIF from core. Consists of 70%, 2-3cm thick, grey, semi-translucent quartz bands; 25%, 0.3-1.0cm thick, dark-grey magnetite bands; and 3%, 0.2-0.4cm thick, fine- to medium-grained yellow grunerite bands. Sample contains minor biotite-garnet schist (2%) associated with magnetite bands (not included in geochemistry sample). Normal looking sample. Sample collected in March '06. One sample (magnetite-rich) sent for geochemistry (4b-PM06-005).	X		
	4b-PM06-028m 4b-PM06-028c 05-PQE-013 147.5m 4b	Sample of thickly banded NIF assemblage oxide-dominant BIF collected from core. Consists of: ~50%, 1.0-4.0cm thick, dark-grey magnetite bands; ~50%, 1.0-3.0cm thick semi-translucent quartz-bands; and <5% 0.1-0.2cm thick tan-yellow grunerite bands. Large quartz-vein on end of sample (not included in geochemistry sample). Sample collected in March 2006. Separated into two samples (4b-PM06-028c: quartz-grunerite band and 4b-PM06-028m: magnetite band).	X		
	4b-07-20-040c 04-PQU-062 325.5m 4b	Sample of thickly banded NIF assemblage oxide-dominant BIF collected from core. This sample is moderately deformed and folded and consists of: 60%, 1.0-2.5cm thick, dark-grey magnetite bands; 35%, 0.2-2.0cm thick light-grey quartz bands; and 5% 0.2-0.3cm thick tan-yellow grunerite bands. Note there are thin lamination of quartz (~0.2cm) in magnetite bands. Sample collected July 2006. One sample (quartz-rich) sent for geochemistry (4b-07-20-040c).	X		
	4b-07-20-053c 04-PQU-130 7.1m 4b	Unusual oxide-dominant BIF sample consisting of laminated oxide-dominant BIF intercalated with thicker meta-chert bands. Consists of: 50%, ~3cm thick, sugary textured slightly magnetic quartz bands and 50% laminated (0.1-0.2cm) black magnetite, dark-tan/yellow grunerite, and meta-chert (quartz). The large amount of grunerite is typical in the thinly laminated variety of oxide-dominant BIF. Sample collected July 2006. One sample (quartz-rich) sent for geochemistry (4b-07-20-053c).	X		
	4b-07-20-055m 04-PQD-006 1270.1m 4b	Thinly laminated NIF assemblage oxide-dominant BIF. Consists of 55%, 0.05-1.0mm thick, fine-grained grey magnetite bands; 43%, 0.05-1.0mm thick light-grey fine-grained quartz bands, 2% 0.05-1.0mm thick mgr, gru bands. Darker in colour compared to thinly banded SIF oxide-dominant BIF. Disseminated po found in thicker mag bands and along contacts between mag and qtz bands (<1% total). Sample collected July 2006. One sample (magnetite-rich) sent for geochemistry (4b-07-20-055m).	X		
	4b-07-20-056 04-PQU-153 145.3m Clastic 4b	Important sample. Transitional oxide-to-silicate-dominant BIF (clastic 4b). Sample is 15cm long and consists of 45%, ~1cm thick, hornblende-garnet schist bands (95% hbl, 5% 0.1-0.2cm garn; 0.2cm thick gru bands at margins); 50%, ~1cm thick bands consisting of 0.1cm thick laminations of qtz-mag-hbl. Sample collected July 2006. One sample (hrbld-garn schist) sent for geochemistry (4b-07-20-055m). Sample was classified as 'magnetite' for index purposes.	X		
	4b-PM05-065c 05-PQE-006 141-142m 4b	Sample of NIF assemblage oxide-dominant BIF containing abundant quartz veins and secondary hornblende, grunerite, and biotite associated. This sample is roughly 15cm long. This sample is mineralized oxide-dominant BIF a (5.6g/ton gold). Sample consists of ~86% fine-grained to medium-grained semi-translucent to milky quartz, 5% pyrrhotite wisps, 10% fine-grained grunerite, and ~1% dark-green hornblende. Sample collected in Oct '05. One sample (quartz) sent for geochemistry (4b-PM05-065c).	X		
	4b-PM05-067c 4b-PM05-067m 05-PQE-016 99.3m 4b	Sample of NIF assemblage oxide-dominant BIF collected from core. This sample has a typical appearance. Sample consists of 65%, 0.3-1.0cm thick, dark-grey magnetite bands; 35%, 0.5-1.5cm thick, light-grey slightly magnetic quartz bands; <5% fine-grained disseminated grunerite in magnetite bands. Sample collected in March 2006. Separated into two samples (4b-PM06-067c: quartz-rich band and 4b-PM06-067m: magnetite-rich band).	X		
	4ea-PM05-057 500L near S2 limb 4ea	Quartz- and biotite-rich NIF assemblage silicate-dominant BIF. Sample is ~10cm in diameter and consists of: 70%, 1.0-1.5cm thick, mgr quartz bands; 25%, 0.3-1.0cm thick, mgr to cgr biotite-garnet-hornblende bands; and 5% pyrrhotite agglomerates. This sample was collected from the 500 level near the S2 limb on October 23, 2005 (Billy, senior underground geo, took Dr. Fralick and Patrick underground). Much of the qtz in this sample is likely from qtz-veins. Note the cgrd nature of the sample.	X		

NIF ASSEMBLAGE SILICATE-DOMINANT BIF

Sample	Location	Description	GEOCHEM	THIN-SECTION	SEM
	4ea-08-30-001 06-PQE-093 77.5-77.8m A+B block 4ea	Grunerite-rich silicate-dominant BIF. Consists of 70% 1.0-2.0cm thick, gru+garn bands: composed of ~60% fgr gru and ~40% 0.3-1cm diameter subhedral pink-red garn; 30%, 0.5-1.0cm thick qtz bands with distorted margins; ~1% disseminated hbl+biotite. Minor po mineralization (<1%), seems concentrated between gru and quartz bands. Sample was collected August 2006. One geochemistry sample (silicate band 4ea-08-30-001). Important sample as it was collected from one of the main ore zones.	X	X	
	4ea-08-30-002 06-PQE-098 74.2-74.4m B-block ore zone	Hornblende-rich silicate-dominant BIF from B-block ore zone. Sample consists of: 40%, 0.4-2.0cm thick, hbl+garn bands with straight margins' (possibly indicates shearing); 25%, 0.5-1.0cm thick, slightly magnetic qtz bands; 20% fgr grunerite (disseminated and at edged of hbl bands); 15% medium-to coarse-grained (an-subhedral) garn (garn found in hbl bands). Moderate amount of pyrrhotite (<5%). Collected August 2006. One geochemistry sample (silicate band: 4ea-08-30-002).	X	X	
	4ea-08-30-004 05-PQE-073 84.85-85m C-block ore zone	Grunerite-rich silicate-dominant BIF sample collected from C-block ore zone. Sample consists of: 50% fgr yellow gru matrix surrounding garnets; 40%, 0.4-1.2cm in diameter, dark red garnets (sub-euhedral); 5%, <1cm thick, qtz-bands; 5% disseminated blebs of po found mostly between garns (also found in gru matrix). Good thin-section sample. Excellent example of silicate-BIF ore in terms of large-garn and high po content. Collected August 2006. One geochem sample (silicate band: 4ea-08-30-002).	X	X	
	4ea-06-20- UG04 T- antiform limb Level 620 or 650L	Important sample. Very-large, ~20kg sample of deformed and well mineralized (v.g.) silicate-dominant BIF from main ore-zone. Consists of: 50%, 0.5-1.5cm thick, cgr translucent qtz bands (qtz-veins +meta-chert); 5% cgr 0.5-1cm diameter red, transparent sub-to euhedral garns; 25% po found along margins of qtz bands; 5% black, mgr bt (not included in geochemistry); 10% light, blue-green amphibole (+ garn) bands. Collected June 2006. One geochemistry sample (silicate band: 4ea-06-20-UG004).	X	X	
	4ea-06-044 04-ESN-010 250.7m 4ea	Silicate-dominant BIF sample collected to show diversity of this lithology. Sample comes from contact between silicate- and oxide-dominant BIF. Consists of 30%, ~0.5cm thick, fine-grained hornblende dominated bands; 45% fine-grained grunerite bands; 20% light-grey quartz bands; <5% pink-grey, an- to subhedral garnets. Bands are not distinct, probably as a result of shear deformation. Sparse po mineralization. Collected June 2006. One geochemistry sample (silicate band: 4ea-06-044).	X	X	
	4ea-07-20-061 03-PQU-141, 42m 4ea	Folded sample of grunerite-rich silicate-dominant BIF consisting of: 85%, 2-3cm thick, gru-rich bands (70% fgr-mgr, and in places fibrous, gru and 30% sub- to euhedral mgr pink-grey garn); 10%, 0.3-0.5cm thick, bt-garn bands found along contacts between gru- and qtz-dominated bands; 5%, 0.5-0.7cm thick, sugary textured light-grey folded qtz-bands. This sample contains <<5% pyrrhotite (weakly mineralized). Sample collected July 2006. One geochemistry sample (silicate band) sent (4ea-07-20-061).	X	X	
	4ea-07-20-065 04-ESS-016 225.8m 4ea	Sample of silicate-dominant BIF. Consists of: 55%, 2-3cm thick, grunerite rich bands (60% fine-grained grunerite, 30% sub- to euhedral mgr pink-grey garn, and 10% hbl); 5%, 0.3-1.0cm thick, biotite-garnet bands; 45%, 0.5-1.5cm thick, sugary textured light-grey folded quartz-bands. This sample contains <5% pyrrhotite (weakly mineralized). Sample collected July 2006. One geochemistry sample (silicate band) sent for geochemistry (4ea-07-20-065).	X	X	
	4ea-07-20-067 04-ISL-010 131.3m 4ea	Moderately sheared sample of NIF assemblage silicate-dominant BIF. This sample comes from close to undeformed transitional oxide-dominant BIF. Consists of: 85% fine-grained grunerite-garnet bands with minor hornblende (composed of 80% grunerite, 15%, 0.3-0.8cm diameter anhedral pink garnets, and 5% pyrrhotite); 15% grey quartz bands. Sample was collected in July 2006. One geochemistry sample (silicate band) sent (4ea-07-20-067).	X	X	
	4ea-07-20-068 04-PQU-028 204.3m 4ea	Moderately-sheared silicate-dominant BIF. Consists of: 65%, 1-3 cm thick, fine-grained hbl-garn bands with minor bt (composed of 40% hbl, 35%, 0.5-0.6cm diameter elongate pink anhedral garns, and 15% mgr bt); 25% grey quartz bands; 25%, 2-4cm thick, fgr gru-dominated bands (composed of 80% gru and 20% garn); <1% calcite veins (not included in geochemistry sample). Bio grades into gru-rich bands. Collected July 2006. One geochemistry sample (silicate band) sent (4ea-07-20-068).	X	X	



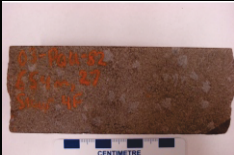
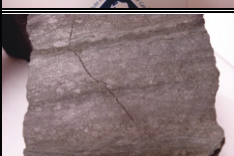
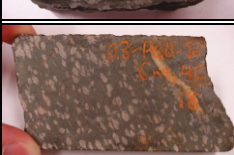

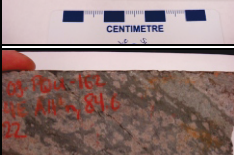
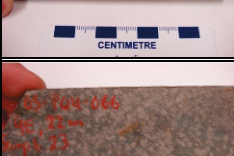



NIF ASSEMBLAGE SILICATE-DOMINANT BIF

Sample	Location	Description	GEOCHEM	THIN-SECTION	SEM
	4ea-07-20-069 04-PQD-001 1081.7m 4ea	Hbl-garn schist band from silicate-dominant BIF. Consists of 70% hbl-garn schist (composed of 75% fgr hbl, 20%, 0.2-0.6cm diameter an-to-subhedral yellow-pink garn); 20%, <1cm thick, gru-bands (consisting of 40% fgr yellow-gru and 60% 0.2-0.3cm diameter an-subhedral pink garn); 10%, ~0.1-0.2cm thick qtz-bands. Poorly mineralized in terms of po (<<5%). No (qtz and/or carb) veining. Collected July 2006. One geochemistry sample (mostly hbl with minor gru) sent (4ea-07-20-069).	X	X	
	4ea-PM05-066c 05-PQU-077 659.5m 4ea	Sheared sample of silicate-dominant BIF. This sample contains a high percentage of quartz-veins. It should be noted this sample comes from a well mineralized interval (assay value of 13.1 grames per ton). Consists of: ~75%, 0.3-1.0cm thick, semi-translucent qtz bands (likely veins as opposed to meta-chert); 10% metasomatic biotite-garnet bands (97% mgrd bio and 3% cgrd garns). Sample collected in Oct'05. One geochemistry sample (qtz-rich) sent (4ea-PM05-066c).	X	X	
	4ea-PM06-002 05-PQE-013 51.3m 4ea	Good example of silicate-dominant BIF (very-coarse-grained garn and well mineralized with po). Weakly-deformed sample. Consists of: 55%, 1-4cm thick, grunerite-rich bands (30% fgr gru matrix with 25% 0.5-1.5cm diameter dark red an-to-subhedral garn); 25%, 0.2-0.4cm thick, fgr hbl bands (contain <5% cgr dark-red garns); 20% .5-1cm thick, quartz-bands. Sample was collected in March 2006. One geochemistry sample (silicate mineral band) sent (4ea-PM06-002).	X	X	
	4ea-PM06-007 05-PQE-01363.33- 64.00m 4ea	Moderately folded grunerite-rich silicate-dominant BIF composed mainly of grunerite and garnet with minormeta-chert component. Consists of: 90%, 2-3cm thick, fgr, tan-yellow grunerite bands (80% gru, 20% 0.1-0.3cm diameter grey-red subhedral garnets); 10%, ~1cm thick, grey, slightly magnetic, quartz-bands. Weak pyrrhotite mineralization, ~1%. Sample was collected in March 2006. One geochemistry sample (silicate mineral band) sent (4ea-PM06-007).	X	X	
	4ea-PM06-018 05-PQE-013 113m 4ea	Deformed, quartz-rich silicate-dominant BIF sample. Consists of: 40%, 1-4cm thick, mgr grey translucent qtz bands (qtz-veins?); 25%, 0.5-1.0 cm thick hbl-rich bands (mainly on right side sample); 25%, 0.2-0.7cm thick, fgr tan gru bands; 10% mgr-to-cgr sub-to-euhedral red garn. Weakly mineralized in respect to pyrrhotite. Good geochemistry sample of almost pure gru and garn. Sample collected in March 2006. One geochemistry sample (silicate mineral band) sent (4ea-PM06-018).	X	X	
	4ea-PM06-043 05-PQE-012 18.38-18.67m 4ea	Sample of silicate-dominant BIF. Sample consists of: 33%, 0.5-1.5cm thick, grey qtz bands (boudined); 45% fgr grunerite-hbl-garn bands (composed of 50% gru, 30% hbl, 20% 0.3-.7cm diameter pink-red an-subhedral garn); 5% disseminated blebs of pyrrhotite. Relatively high percentage of hbl. Grunerite occurs mostly along the margins of aluminosilicate-bands. Sample collected in March 2006. One geochemistry sample (silicate mineral band) sent (4ea-PM06-043).	X	X	
	4f-07-20-001 06-PQE-001 18.1m 4f	Undistorted biotite-garnet schist sample. Consists of: 70% fgr brown biotite-rich matrix (composed of siliciclastic detrital qtz and feldspar, zircon, etc); 20% 0.3-0.5cm diameter sub-to-euhedral pink garnets (garnets, appear confined to distorted layers); 10% fgr (0.1cm) yellow-pink garnets (stauralite?). Possible minor metasomatic biotite+garnet component. Sample was collected July 2006. One geochemistry sample sent (4f-07-20-001).	X	X	
	4f-07-20-002 06-PQE-072 42.2m 4f	Typical looking biotite-garnet schist. Undistorted sample with garnet-rich bands. This sample consists of: 90% brown biotite-rich matrix (composed of siliciclastic detrital quartz, feldspar, zircon, etc); 10% 0.2-0.4cm diameter anhedral pink garnets; <5%, ~1cm thick, quartz-rich bands (represent meta-chert layers). This biotite-garnet schist sample is relatively quartz-rich. Sample was collected in July 2006. One geochemistry sample sent (4f-07-20-002).	X	X	
	4f-07-20-008 06-S2E-002 Top of hole (1m) 4f	Interesting, a-typical sample of biotite-garnet schist. Sample is a-typical due to its low percentage, and small, garnet porphyroblasts). This samples is transitional to garnet-quartzite due to low its low garn content. Consists of: 90% fine-grained bt-rich matrix (contains detrital quartz and feldspar, zircon etc); <5%, 0.1-0.2cm diameter, homogeneously distributed sub-to-euhedral pink garnet porphyroblasts. Sample was collected in July 2006. One geochemistry sample sent (4f-07-20-008).	X	X	

BIOTITE-GARNET SCHIST

## BIOTITE-GARNET SCHIST





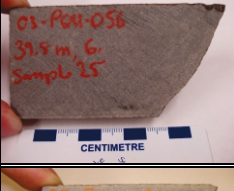
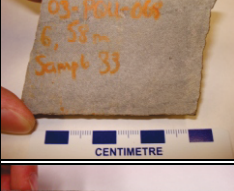

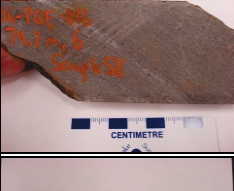

Sample	Location	Description	GEOCHEM	THIN-SECTION	SEM
	4f-07-20-009 06-S2E-002 Top of hole 4f	A-typical looking bt-garn schist sample due to high % garn and cgr bt. Appears to be metasomatically altered due to mgr-to-cgr bt and cgr euhedral garnets (recrystallized). Sample consists of: 60%, 0.2-0.3cm diameter, sub- to euhedral, pink, garnets; 40% mgr dark-black biotite (satin appearance). Possibly a good link between regular biotite-garnet schist and metasomatic biotite-garn schist. Sample was collected in July 2006. One geochemistry sample sent (4f-07-20-009).	X	X	
	4f-07-20-011 06-PQE-098 40.5m 4f	Typical looking biotite-garnet schist. Undistorted sample with homogeneous garnet distribution. Sample consists of: 80% brown biotite-rich matrix (composed of siliciclastic detrital quartz, feldspar, zircon etc); 20% 0.1-0.4cm diameter anhedral pink garnets; <1%, ~0.2cm thick, quartz-rich layers. This sample may contain some muscovite due to the lighter color of fractured surfaces relative to other samples. Sample was collected in July 2006. One geochemistry sample sent (4f-07-20-002).	X	X	
	4f-07-20-027 03-PQU-082 65.4m 4f	This sample is important, and distinct looking, due to its high percentage of staurolite. Sample consists of: 50% brown biotite-matrix (contains detrital quartz, feldspar, and zircon, etc. also minor metasomatic component); 40%, 0.1-0.2mm diameter, yellow staurolite crystals, homogeneously distributed through the bt-rich matrix; 10%, 0.4-1.0cm diameter, anhedral pink garn (relatively large for this lithology). Sample was collected in July 2006. One geochemistry sample sent (4f-07-20-009).	X	X	
	4b-PM05-050 500 level 4f/4b	Sample collected from underground workings at Musselwhite. Identified as oxide-facies BIF intercalated with biotite-garnet schist (identified as 4bf-fine-termanology by senior underground geologist). This sample consists of: ~90% siliciclastic biotite-garnet rich matrix; and ~10% oxide-dominant BIF. Matrix minerals range from fine- to medium-grained whereas the garnet porphyroblasts range from medium- to coarse-grained. Sample collected in Oct'05. One sample sent for geochemistry (4b-PM05-050).	X		
	4e-07-20-018 03-PQU-090 6m 4e	Typical looking hornblende-garnet schist. This sample was collected from interformational unit (between metavolcanic flows). Sample consists of: 85% fine-grained hornblende-rich matrix; 15%, 0.2-0.5cm diameter, elongate and anhedral pink garnets; sample also contains 0.4cm wide cgr carbonate vein. The carbonate vein was not included in the geochemistry sample. In side profile garnets appear to flattened. Sample was collected in July 2006. One geochemistry sample sent (4e-07-20-018).	X	X	
	4e-07-20-019 03-CMP-057 26.8m 4e	Rather unusual sample of hornblende-garnet schist due to the fineness and disperse nature of the garnets. Sample consists of: 70% fine-grained hornblende-rich matrix; 20%, 0.1-0.3cm diameter pink garnet porphyroblasts; 10% thin (0.1-0.4cm) quartz-laminations; ~1% pyrite, occurring mostly within qtz-laminations (more euhedral cubes occur in hbl matrix). Possible minor bio+garn metasomatism in this sample. Sample was collected in July 2006. One geochemistry sample sent (4e-07-20-019).	X	X	
	4e-07-20-022 03-PQU-162 84.6m 4e	Another usual looking sample of hornblende-garnet schist, due to abundant large agglomerates of anhedral garnets in sample. Sample consists of: 55%, 0.3-2.5cm diameter, subhedral pink-garn; 30% fgr hornblende-rich matrix occurring between garn (crenulated around garn); 15% massive garnet bands (two, 2-3cm bands at both ends of sample-not included in geochemistry sample); 2% po and 2% grunerite disseminated in the sample. Collected July 2006. One geochemistry sample sent (4e-07-20-022).	X	X	
	4e-07-20-023 03-PQU-066 22m 4e	Typical looking hornblende-garnet schist (although slightly garnet-rich). This sample is composed of: 60% fine-grained hornblende-rich matrix which surrounds 40% subhedral, 0.2-0.5cm diameter garnet porphyroblasts (not exactly elongate but appear to be either aligned to foliation or along the original bedding). Sample was collected in July 2006. One geochemistry sample sent (4e-07-20-023).	X	X	
	4e-07-20-034a 03-PQU-068 59.2m 4e	Sample of hornblende-garnet schist. Relatively a-typical looking, but right mineralogy for this lithology. Sample consists of: 40% fine-grained hornblende, occurring in 0.4-1.2cm distorted layers; 45% 0.2-0.6cm diameter subhedral pink garnets; 15% 0.1-0.3cm thick quartz laminations; Disseminated po, moderate metasomatic biotite+garnet of hornblende (possibly 15% of sample, not included in geochemistry sample). Collected July 2006. One geochemistry sample sent (4e-07-20-034a).	X	X	

## HORNBLLENDE-GARNET SCHIST

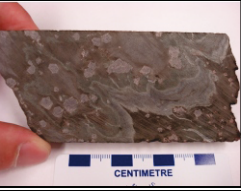


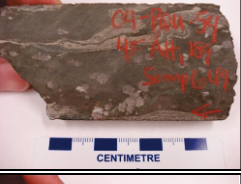



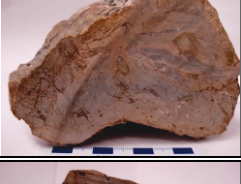

HORNBLLENDE-GARNET SCHIST

GARNET QUARTZITE

BT.GARN




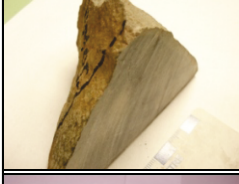





Sample	Location	Description	GEOCHEM	THIN-SECTION	SEM
 03-PQU-058 54m 4e	4e-07-20-034b 03-PQU-058 54m 4e	Typical looking hornblende-garnet schist sample. This sample consists of: 70% fine-grained hornblende; 30% elongated, 0.2-0.5cm diameter, anhedral pink garnets; 2% mostly disseminated pyrrhotite (minor vein on back side of sample (not visible in this sample picture). This sample comes from middle of sheared unit just above the silicate-dominant BIF. Sample was collected in July 2006. One geochemistry sample sent (4e-07-20-034b).	X	X	
 04-ISL-010 130.4m 4e	4e-07-20-047 04-ISL-010 130.4m 4e	Unusual garnet-poor hornblende-garnet schist sample. This sample was collected from transition between oxide- and silicate-dominant BIF. It shows the diversity observed within the hornblende-garnet schist. Sample consists of 85% fine-grained hornblende matrix; 10% finely laminated (<0.1cm) / disseminated quartz bands; 5% coarse-grained anhedral pink garnets (confined to edge of sample near band of meta-chert). Sample was collected in July 2006. One geochemistry sample sent (4e-07-20-047).	X	X	
 04-PQU-022 16.6m 4e	4e-07-20-048 04-PQU-022 16.6m 4e	A-typical hornblende-garnet schist in terms of appearance. This sample is also magnetic. It consists of: 83% fine-grained hornblende matrix containing disseminated fine-grained magnetite, quartz, and grunerite; 10% 0.1-0.2cm diameter pink garnets primarily confined to two layers on edge of sample; 5% broken up meta-chert (1cm blocks); 2% disseminated grunerite (fine-grained and yellow). Sample was collected in July 2006. One geochemistry sample sent (4e-07-20-048).	X	X	
 03-PQU-066 216.6m Unit 6	6-07-20-024 03-PQU-066 216.6m Unit 6	This sample is typical light-grey massive looking garnet-quartzite containing minor disseminated garnet porphyroblasts. Sample consists of: 98% siliciclastic matrix (very fine-grained quartz, biotite, feldspar, ± muscovite); 2%, 0.4-0.5cm diameter, anhedral pink garnets. This sample comes from the correct stratigraphic position (on top of silicate-dominant BIF). Sample was collected in July 2006. One geochemistry sample sent (6-07-20-024).	X	X	
 03-PQU-056 39.8m Unit 6	6-07-20-025 03-PQU-056 39.8m Unit 6	Another typical looking light-grey massive garnet-quartzite sample containing disseminated garnet porphyroblasts. Sample consists of ~99% siliciclastic matrix material (fine-grained quartz, biotite, feldspar, ± muscovite); <1% garnet porphyroblasts. Sample is well foliated. Medium-grained biotite porphyroblasts are obvious. Sample was collected in July 2006. One geochemistry sample sent (6-07-20-025).	X	X	
 03-PQU-068 58m Unit 6	6-07-20-033 03-PQU-068 58m Unit 6	Rather a-typical looking garnet-quartzite sample due to very light appearance. Aside from its light appearance, this sample is typical garnet-quartzite. It consists of: 97% siliciclastic matrix material (fine-grained quartz, biotite, feldspar, ± muscovite); ~3% 0.2-0.4cm diameter pink garnets. This is possibly a more siliceous sample due to lighter colour. Comes from the correct stratigraphic position (on top of silicate-dominant BIF). Collected July 2006. One geochemistry sample sent (6-07-20-033).	X	X	
 03-PQU-006 50.9m Unit 6	6-07-20-038 03-PQU-006 50.9m Unit 6	Typical looking, foliated, garnet-quartzite sample. Contains minor discontinuous quartz-veins (mine terminology: quartz-sweats) which is a defining feature of this lithology. Consists of: 99% quartz, feldspar, and biotite; ~1% discontinuous quartz-veins; and <1% garnets. Fractured surfaces are light and shiny indicating high percentage of muscovite relative to biotite. Below 51m is sheared unit 6 with minor garn-gru and hbl. Collected July 2006. One geochemistry sample sent (6-07-20-038).	X	X	
 06-PQE-086 74.7m Unit 6	6-07-20-058 06-PQE-086 74.7m Unit 6	Typical looking, well-foliated, garnet-quartzite sample. Contains minor discontinuous quartz-veins (which are a defining feature of this lithology). Sample consists of: 95% siliciclastic material (fine-grained quartz, biotite, feldspar, ± muscovite); and minor garn.; 4% dismembered quartz veins; and ~1% 0.1-0.2cm anhedral garnets. This garnet-quartzite sample comes from within a biotite-garnet schist unit. Sample was collected in July 2006. One geochemistry sample sent (6-07-20-058).	X	X	
 06-PQE-072 43.1m Bt-garn metasomatism	Bt.garn-0720-01 06-PQE-072 43.1m Bt-garn metasomatism	Metasomatic biotite-garnet schist (mine terminology:biotite-garnet alteration). Collected from sheared silicate-dominant BIF. Sample ~30cm long and consists of 49% bt-garn alteration (85% mgr satin-black bt, 14% 0.5-0.9cm diameter, sub-to-euhedral garn, 2% po) and 50% silicate-dominant BIF (45% quartz and 45% aluminosilicate minerals). Only metasomatic biotite-garnet material was sent for geochemistry. Sample collected July 2006. One geochemistry sample sent (bt.garn-07-20-001).	X	X	








METASOMATIC BIOTITE-GARNET SCHIST

Sample	Location	Description	GEOCHEM	THIN-SECTION	SEM
	Bt.garn-0720-07 06-PQU-008 151m Bt-Garn Metasomatism	Green-tinged metasomatic biotite-garnet band from strongly bt-garn altered silicate-dominant BIF (replacing aluminosilicate mineral bands). Sample is ~12cm long; consists of 90% bt-garn (90% mgr-cgr black bt with satiny appearance, 10% 0.5-1.0cm diameter, sub-to-euhedral garn, >1% po) and 10% relict silicate-dominantBIF (disseminated iron-silicate minerals). Only bt-garn material was sent for geochemsitry. Collected July 2006. One geochemistry sample sent (bt.garn-07-20-007).	X	X	
	Bt.garn-0720-17 03-PQU-044 1053.2m Bt-Garn metasomatism	Typical looking metasomatic biotite-garnet alteration band from silicate-dominant BIF (silicate-dominant BIF unit is ~1m thick and close to an ultramafic unit). Sample consists of: 80% satiny black mgr biotite-rich matrix; 10% 0.4-0.7cm diameter euhedral garn; 5% 2cm thick chunk of relict meta-chert; ~5% disseminated grunerite and hornblende in biotite-rich matrix. Only bt-garn material was sent for geochemistry. Collected July 2006. One geochemistry sample sent (bt.garn-07-20-017).	X	X	
	Bt.garn-0720-20 03-PQU-044 119.8m Bt-Garn metasomatism	Typical looking metasomatic biotite-garnet alteration band. Sample consists of: 80% satiny black medium-grained biotite matrix; 20% 0.5-1.2cm diameter euhedral garnets; ~2% disseminated pyrrhotite; 5% relict meta-chert and silicate-mineral bands. Biotite crystals are crenulated around garnet porphyroblasts. Only biotite-garnet alteration material was sent for geochemistry. Sample was collected in July 2006. One geochemistry sample sent (bt.garn-07-20-020).	X	X	
	Bt.garn-0720-49 04-PQU-054 189m Bt-Garn metasomatism	Sample of metasomatic biotite-garnet alteration containing selvages of iron-silicate mineral bands. Sample consists of: 80% medium-grained dark black satiny biotite; 15% relict grunerite-rich iron silicate-mineral bands; 5%, 0.5-0.9cm diameter euhedral pink garnets. This sample is associated with a large qtz-vein and comes from around the contact between oxide-and silicate-dominant BIF. Only bt-garn material was sent for geochemistry. Collected July 2006. One geochemistry sample sent (bt.garn-07-20-049).	X	X	
	Bt.garn-0720-54 04-PQU-130 175m Bt-Garn metasomatism	Sample of typical looking metasomatic biotite-garnet alteration. Contains minor relict grunerite-rich bands. Sample consists of: 90% mgr dark-black satiny biotite; 5% 0.5-0.9cm diameter sub-to-euhedral pink garnets; 4% wispy relict grunerite bands. This sample was collected from, in my opinion, silicate-dominant BIF (although logged by mine as oxide-dominant BIF). Only bt-garn material was sent for geochemistry. Collected July 2006. One geochemistry sample sent (bt.garn-07-20-020).	X	X	
	Alt-PM05-005 Trench #4	'Meta-sediment' sample collected from trench #4 (Fig. 1.11) by Dr. Fralick. This material was collected from a 'silty layer' in the NIF assemblage oxide-dominant BIF. Sample is ~5cm in diameter and quite grotty looking. It is possible to see distorted and folded banding in the sample in cut cross-section. Visually it is difficult to tell the mineralogy of the sample (>>grunerite). Sample was collected in Oct '05. One geochemistry sample sent (alt-PM05-005).	X	X	X
	Alt-PM05-009 Trench #4	'Meta-sediment' sample collected from trench #4 (Fig. 1.11) by Dr. Fralick. This sample has a relatively less altered and grotty looking appearance (relative to other Alt-PM05-series samples). This sample consists of homogeneous mixture of grunerite and quartz. Also contains disseminated magnetite.Check the thin-section for mineralogy. This sample was collected in Oct'05. One geochemistry sample sent (alt-PM05-009).	X	X	X
	Alt-PM05-010 Trench #4	Large (~25x15cm) 'meta-sediment' sample collected from trench #4 (Fig. 1.11) by Dr. Fralick. This sample contains obvious distorted compositional banding. In cross section deformation of original banding is obvious with dismembered meta-chert bands sitting in a homogenous grunerite-rich matrix. There are small (0.1-0.2cm diameter) shiny black porphyroblasts that may be biotite or garnet (check thin-section) Sample was collected in Oct'05. One geochemistry sample sent (alt-PM05-009).	X	X	X
	Alt-PM05-013 Trench #4	Smaller sample of greenish-grey 'meta-sediment' collected by Dr. Fralick from trench #4 (Fig. 1.11). Sample does not exhibit compositional banding, has a grotty appearance, and consists of a homogeneous looking fine-to-medium grained grunerite-rich matrix containing disseminated magnetite. Both internal and external hematite rich patches are present. Sample was collected in Oct'05. One geochemistry sample sent (alt-PM05-009).	X	X	X

TRENCH METASOMATIC BIF





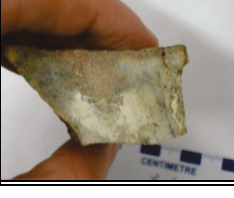
TRENCH METASOMATIC BIF

Sample	Location	Description	GEOCHEM	THIN-SECTION	SEM
	Alt-PM05-014 Trench #4	Rather large, ~10x15cm, 'meta-sediment' sample collected from trench #4 (Fig. 1.11) by Patrick. Sample has different appearance compared to the other 'meta-sediment' samples and may represent a quartz porphyry or quartzite. Dr. Fralick thinks this is a possible metamorphosed sandstone that has been silicified. Sample is fine-grained to medium-grained, is weathered to a light tan on exterior surfaces, and contains muscovite. Collected Oct'05. One geochemistry sample sent (alt-PM05-014).	X	X	
	Alt-PM05-019 Trench #4	Elongate yellowish-grey 'meta-sediment' sample collected by Patrick from trench #4 (Fig. 1.11). This sample is quite dense. Sample consists of ~95% fine-grained grunerite-rich matrix containing disseminated fine-grained magnetite crystals. Interestingly, in cross-section there is a deformed, relict, meta-chert band. Sample has grotty looking appearance. Exterior is iron/hematite-strained. Sample was collected in Oct'05. One geochemistry sample sent (alt-PM05-019).	X	X	
	Alt-PM05-023 Trench #5	Similar sample to alt-PM05-014. Collected from trench #5 (Fig. 1.11) by Patrick. Appears to be a sample of quartzite. Very hard, foliated, rock. Dr. Fralick believes that it has a sedimentary origin because you can see the original grains. Sample is fine-to medium-grained and is weathered to a light tan on exterior surfaces. Contains ~99% of sample is quartz-feldspar and ~1% muscovite + biotite. Sample was collected in Oct'05. One geochemistry sample sent (alt-PM05-023).	X	X	
	Alt-PM05-025 Trench #5	This sample is similar to sample to alt- PM05-014. It was collected from trench #5 (Fig. 1.11) by Patrick. Again, sample has different appearance compared to other 'meta-sediment' samples and may represent a quartz-porphyry or quartzite. Unidentified but felsic looking intrusive or metamorphosed sandstone. Sample is fine-to medium-grained, is weathered to a light tan on exterior surfaces, and contains muscovite. Collected Oct'05. One geochemistry sample sent (alt-PM05-025).	X	X	
	Alt-PM05-027 Trench #5	Yellowish-grey 'meta-sediment' sample collected by Pat from slight hill next to central water body in trench #5 (Fig. 1.11). Sample is~10x15cm. Selective weathering of exterior highlights compositional bands. In cross-section sample is homogeneous grun-rich matrix. Sample consists of ~85% fine-grained yellow grunerite crystals with ~15% disseminated fine-grained quartz and magnetite crystals. Sample was collected in Oct'05. One geochemistry sample sent (PM05-027).	X	X	
	Alt-PM05-032 Trench #5	Greyish-green, grotty, 'meta-sediment' sample from trench #5 (Fig. 1.11). Selective weathering of exterior highlights compositional bands (dismembered meta-chert bands). Also, fine-grained black-magnetite visible on the exterior. In cross-section the sample consists of: ~85% light-yellow-grey grunerite-rich matrix with 5% fine-grained disseminated magnetite and 10% dark-brown weathered patches. Sample was collected in Oct'05. One geochemistry sample sent (alt-PM05-032).	X	X	
	Alt-PM05-045 Trench #4	Excellent example of 'sedimentary material' from trenches. This sample resembles the other samples of this lithology except it contains obvious relict bands of magnetite and therefore represents altered rock. Dr. Fralick indicates calcite/carbonate alteration appearance. Consists of: 55% homogeneous fgr grun-rich matrix; and 45%, 0.5-1.3cm thick wispy relict magnetite bands. Sheared sample. Sample was collected in Oct'05. One geochemistry sample sent (alt-PM05-045).	X	X	
	Alt-PM05-048 Trench #4	Relatively small sample of 'carbonaceous layer' collected by Dr. Fralick from ~1m thick unit below felsic-looking unit in trench #4 (Fig. 1.11). Much darker in colour than the other 'meta-sediment' samples discussed and shown to this point. Consists of a fine-grained dark-grey (hornblende?) quartz-rich matrix, visually resembles meta-basalt on fractured surfaces. Minor brown weathering spots in cross-section. Sample was collected in Oct'05. One geochemistry sample sent (alt-PM05-048).	X	X	
	Alt-PM05-049 Trench #4	Small 'carbonaceous layer' collected by Dr. Fralick from same area as alt-PM05-048, however, represents upper silty layer and is more coarse-grained. Again, much darker than the other 'meta-sediment' samples discussed so far. Consists of a fine-grained dark-grey (hbl) quartz-rich matrix, visually resembles meta-basalt on fractured surfaces. Minor brown weathering spots in cross-section. Sample was collected in Oct'05. One geochemistry sample sent (alt-PM05-048).	X	X	

	Sample	Location	Description	GEOCHEM	THIN-SECTION	SEM
AMPHIBOLITE		2-PM05-017 Trench #4 Unit 2-mafic metavolcanic	Meta-basalt sample, collected by Patrick, from the western edge of trench #4 (Fig. 1.11). Sample comes from ~2-3m thick sheared volcanic unit in contact with NIF assemblage oxide-dominant BIF. John indicates this unit is ultramafic. Sample is strongly foliated, light greyish-green in colour, fine-to-medium grained, and contains 0.1-0.2cm diameter chlorite porphyroblasts (check thin-section) Sample was collected in Oct'05. One geochemistry sample sent (2-PM05-017).	X	X	
		2-PM05-026 Trench #5 Unit 2-mafic metavolcanic	Meta-basalt sample, collected by Patrick, from eastern edge of trench #5 (Fig. 1.11). Comes from ~1-2m thick mafic unit in contact with ~1-2m thick felsic unit. Foliated, greyish-green, fine-to medium-grained, and contains 0.1-0.2cm diameter biotite (?) porphyroblasts (check thin-section) In cross section sample looks like intermediate metavolcanic lithology seen in core. This sample is feldspar-rich compared to 2-PM05-017. Sample was collected in Oct'05. One geochemistry sample sent (2-PM05-026).	X	X	
		2-PM05-052 Hanging wall PQ 500 Level 4f	This sample was collected underground on the 500L and mistakenly identified as biotite-garnet schist. In reality it is a typical looking mafic metavolcanic sample. Consists of: ~99% fine-grained quartz-hornblende-feldspar matrix with: <1% 0.1cm long chlorite porphyroblasts. Minimal carbonate veining (not included in geochemistry sample). Sample was collected in October '05. One geochemistry sample sent (2-PM05-052).	X	X	
INTERMEDIATE META-VOLCANIC		2-PM05-055 500L Unit 2-mafic metavolcanic	Sample classified as mafic meta-volcanic. It was collected from underground, on the 500L, near S2 limb. Sample consists of: ~94% fine-grained amphibole-feldspar matrix with: ~5% 0.1-0.3cm diameter garnet porphyroblasts; <1% 0.1-0.3cm biotite porphyroblasts; and 1% 0.3cm wide carbonate vein. Due to garnet content, sample may be meta-sed (quartzite). Sample was collected in October '05. One geochemistry sample sent (2-PM05-055). Check thin-section to confirm mineralogy.	X	X	
		2-PM06-065 05-PQE-012 72.0m Unit 2-mafic metavolcanic	Typical looking, foliated, mafic-metavolcanic lithology seen in core. Sample was collected from below the NIF assemblage. Consists of: ~92% fine-grained amphibole-feldspar matrix with: ~5% 0.1-0.3cm long chlorite porphyroblasts; and <1% 0.1-0.3cm long minor biotite porphyroblasts. Porphyroblasts are aligned along the foliation plane. Roughly 2% of sample is carbonate veining (not included in geochemistry sample). Sample was collected in March '06 One geochemistry sample sent (2-PM06-065).	X	X	
		Avol-PM05-053 Unit 2t Intermediate metavolcanic	Intermediate- to felsic-metavolcanic sample (mine-terminology: AVOL) collected from 500L. Sample is ~10cmx10cm and has a banded nature imparted by shearing. This sample is medium- to coarse-grained and composed of light sericite-rich bands (19%) and dark amphibole rich bands (79%). ~2% chalcopryrite and pyrrhotite (associated with carbonate-vein) in sample. Sample was collected in October '05. One geochemistry sample sent (avol-PM06-053).	X	X	
		Avol-PM05-054 AVOL-felsic metavolcanic	Strongly sheared intermediate- to felsic-metavolcanic sample collected from 500L. Consists of: 85%, 0.5-1.0cm thick, quartz-rich sericite bands; 15%, 0.3-1.0cm thick, amphibole-sulfide bands (40% pyrrhotite and chalcopryrite, 60% amphibole). Sample is a-typical due to very pronounced banding, >>high silica content and >>sulfide content. Sample was collected in October '05. One geochemistry sample sent (avol-PM06-054).	X	X	
CHLORITE SCHIST		1-PM05-064 500L near machine shop Ultramafic	Sample of 'ultramafic' meta-volcanic from close to the southern iron formation-not sure if intrusive or extrusive. This sample is very dense, has a dark green appearance, and greasy feel to it. Collected on last stop on the tour of the mine. In cross section looks like deformed serpentinite. This sample is not sulfide rich but may be meta-argillite? Sample was collected in October 2005. One geochemistry sample sent (unit1-PM05-064). Check t.s. mineralogy.	X	X	
		Tb-PM05-007 Trench #4 Chlorite Schist	Chlorite-schist (mine terminology: Toad's back) sample collected from northern area of trench #4 (Fig. 1.11). Roughly 15cmx15cm dark-green sample. Very interesting lithology composed >99% chlorite. This lithology contains distinct pseudomorphed augen structures. Slightly fibrous on fractured surfaces and pseudomorphed augens retain their oval shape on these surfaces. Sample was collected in October '05. One geochemistry sample sent (tb-PM05-007).	X	X	

ALTERED SAMPLES

QUARTZ-VEINS, TRENCH #4, >Au

Sample	Location	Description	GEOCHEM	THIN-SECTION	SEM
	Tb-PM05-024 Trench #5 Chlorite Schist	Chlorite-schist sample collected from southern area of trench # 5 (Fig. 1.11). This chlorite schist is found as a dyke (or sill) completely cross-cutting the BIF perpendicular to the banding. The dyke is roughly 0.5m x 4m. This sample is >99% chlorite and contains distinct deformed pseudomorphed augen structures. This sample also contains, 0.1-0.5cm diameter sub-to euhedral, porphyroblasts of magnetic tourmaline (not sure because hexagonal). Collected in October '05. One geochemistry sample sent (tb-PM05-024).	X	X	
	Alt-PM05-100 Trench #5 Chlorite Schist	Chlorite-schist sample collected from southern area of trench # 5 (Fig. 1.11). This chlorite schist is found as a dyke (or sill) completely cross-cutting the BIF perpendicular to the banding. The dyke is roughly 0.5m x 4m. This sample is >99% chlorite and contains distinct deformed pseudomorphed augen structures. This sample also contains, 0.1-0.5cm diameter sub-to euhedral, porphyroblasts of magnetic tourmaline (not sure because hexagonal). Collected in October '05. One geochemistry sample sent (tb-PM05-024).	X	X	
	Vein-PM05-029 Trench #5 Qtz-vein	Coarse-grained milky to translucent, heavily hematite-stained, mineralized quartz sample from the "Horsetail shear zone" (gossin-type material) in trench #5 (Fig. 1.11). This area of trench #5 runs at approximately 45 grams per ton. A moderate-sized brittle-ductile fault, containing quartz-veins, splays out into the NIF assemblage oxide-dominant BIF in this area. Check Cs, Rb, and K ratios. Sample was collected in Oct '05. One geochemistry sample sent (Vein-PM05-029).	X	X	
	Vein-PM05-033 Trench #5 Qtz-vein	Medium- to coarse-grained milky quartz vein containing chlorite (green mineral) collected from periphery of mineralized "Horsetail shear zone" in trench #5 (Fig. 1.11). Quartz material is poorly consolidated, containing numerous mm-scale vugs/cavities, and has a sugary texture. Roughly consists of 99% quartz and 1% green-mineral. Exterior slightly hematite stained. Sample was collected in Oct '05. One geochemistry sample sent (Vein-PM05-033).	X	X	
	Vein-PM05-034 Trench #5 Qtz-vein	Fine- to coarse-grained milky to translucent mineralized quartz sample from the "Horsetail shear zone" in trench #5 (Fig. 1.11). The exterior of this sample is covered in hematite (less intense than Vein-PM05-029). Sample is roughly 10cm long by 4cm wide and contains minor grunerite content. Roughly consists of 99% quartz and 1% grunerite, hematite, and limonite. Check Cs, Rb, and K ratios. Sample was collected in Oct '05. One geochemistry sample sent (Vein-PM05-034).	X	X	

**ABBREVIATIONS**

Mine-Scale Geology		Minerals	
NIF	Northern Iron Formation	Po	Pyrrhotite
SIF	Southern Iron Formation	Qtz	Quartz
4h	Meta-Argillite (mine terminology)	Bt	Biotite
4a	(mine terminology) Quartz-Grunerite Banded Iron Formation	Garn	Garnet (Almandine)
4b	(mine terminology) Oxide-Dominant Banded Iron Formation	Gru	Grunerite
4ca	(mine terminology) Silicate-Dominant Banded Iron Formation	Hbl	Hornblende
4e	(mine terminology) Hornblende-Garnet Schist	Cord	Cordierite
4f	(mine terminology) Biotite-Garnet Schist	Staur	Staurolite
6	(mine terminology) Garnet-Quartzite	Silm	Sillimanite
2	(mine terminology) Mafic Meta-Volcanic	Cal	Calcite
2t	(mine terminology) Intermediate Meta-Volcanic	Ser	Sericite
		Ccp	Chalcopyrite
		Chl	Chlorite
		Cpx	Clinopyroxene
		Fe-Dol	Iron-rich Dolomite
		Fe-Cal	Iron-rich Calcite
		Ilm	Ilmenite
		Kfs	Potassium-Feldspar
		Mag	Magnetite
		Ms	Muscovite
		Pl	Plagioclase
	Fgr	Fine-grained	
	Mgr	Medium-grained	
	Alt	Alteration	
	Cgr	Coarse-grained	
	V.G.	Visible Gold	

# **Appendix B**

## **Thin-Section Descriptions**

(Abbreviations used in this section are explained on pg. XIII of Appendix A)



Sample ID	Section	Mineralogy													Description					
		Disk	T.S.	Qtz	Mag	Gru	Hbl	Grt	Chl	Po	Ccp	Bt	Ms	Plag		Kfs	Act	Staur	Cpx	Cal
SIF-0720-060	X			•	•															Thinly-banded meta-BIF, consisting of 60% mag-bands and 40% Qtz-bands (both mm-scale). Relatively fgr-equigranular sample. Mag-bands consist of 60% mag, 40% grunerite and nil Qtz. Qtz-bands are thinner, finer-grained, and consist of: 92% Qtz, 5% Gru, and 3% mag.
			X	•	•	•														
4h-0720-070	X	•	•	•	•	•			•											Meta-argillite sample consisting of: 25% po, 38% fgr hbl + 15% fgr Qtz + 2% Gru + 3% bt together which compose a fine-grained matrix surrounding 15% cgr subhedral-garnets. Note pleochroic blue hexagonal mineral.
4h-0720-056	X	•	•	•	•	•			•									•		Sample consists of: 30% Qtz, 20% Gru, 35% hbl, 7% po, 3% gam, 3% cpx, and <1% bt. This sample is compositionally banded. It contains Qtz-rich, grun+cpx-rich, and hbl-rich bands. This sample is also cross-cut by quartz and carbonate veins.
4h-0720-053a	X	•	•	•	•	•			•											Meta-argillite sample consisting of: 40% semi-massive pyrrhotite (contains ~1% chalcopyrite inclusions), 10% fine-grained quartz, 20% very fine-grained grunerite, 10% coarse-grained subhedral garnet porphyroblasts, 10% biotite, 5% hornblende, and 2% carbonate.
4h-0720-053b	X	•	•	•	•	•			•											Meta-argillite sample containing possible proto-mylonitic bands. Consists of: 30% quartz-rich bands intercalated with a mixture of 24% biotite, 10% medium-grained garnet porphyroblasts, 10% very fine-grained grunerite, 5% pyrrhotite, and 2% magnetite.
4a-0720-012	X	•	•	•																Sample consists of thin grunerite-rich (10%) and quartz-rich (90%) laminations. Grunerite-rich laminations are very-fine-grained compared to the quartz-laminations which themselves are fine-grained. These laminations are perpendicularly cross-cut by coarser-grained Qtz-veins.
4a-0720-025	X	•	•	•																Massive and deformed variety of the quartz-grunerite BIF consisting of: 75% Gru, 20% Qtz, 3% bt, ~1% mag, and ~1% carb. Sample is folded and deformed. Contains Qtz-veins. Gru crystals are occasionally found as radiating needles. Carb-altered sample, carb found between Qtz-crystals.
4a-0720-054	X	•	•	•	•				•											Quartz-grunerite BIF consisting of 70% Qtz-gru bands (~1cm thick) with 30% relict mag-bands (0.5-0.7cm thick). Mag-bands consists of: 15% mag, 5% carb, and 80% Gru (cpx too). Qtz-gru bands: 85% fgr equigranular Qtz with multiple ~1mm thick laminations of vfr grun.
4b-0720-004	X	•	•	•	•				•											T.s. of meta-BIF from drill core, consists of: 70% Qtz-bands and 30% relict mag-bands. Qtz-bands consist of: 98% deformed Qtz exhibiting grain-size reduction and 2% very fine-grained grun. Relict mag-bands consist of: 2% hornblende, 15% magnetite, 2% po, 1% quartz, 80% grunerite.
4b-0720-053	X	•	•	•																T.s. of thinly-laminated oxide-dominant BIF consisting of ~1mm thick monomineralic laminations of grun and mag: 52% Gru, 43% mag, and 5% Qtz. Gru-crystals are relatively cgr at 0.5mm large. Grun-laminations are on average thicker than mag-laminations. Note: the low Qtz-content.
4b-0720-055	X	•	•	•	•	•			•											T.s. of thinly-laminated transitional oxide-dominant BIF. Sample consist of 35% Qtz, 20% mag, 40% Gru, 5% hbl, and ~1% garn. Gru porphyroblasts are more common but finer-grained than garn. Qtz-crystals are very-fgr. Hbl-bands are thicker than Qtz and mag bands.
4b-0720-056	X	•	•	•	•	•			•											T.s. of thinly-laminated transitional oxide-dominant BIF, consists of thin monomineralic bands of: 33% anhedral Qtz, 33% Gru, 20% mag, 10% hbl, ~1% (1mm diameter) garn, <1% carbonate. Hbl bands are thicker than Qtz- and mag-bands. Gru, Qtz, mag, and hbl occur as inclusions in garn.

Sample ID	Section		Mineralogy													Description			
	Disk	T.S.	Qtz	Mag	Gru	Hbl	Grt	Chl	Po	Ccp	Bt	Ms	Plag	Kfs	Act		Staur	Cpx	Cal
4b-0720-065	X		•	•	•	•	•	•											T.s. of qtz-vein from oxide-dominant BIF, consists of: 92% anhedral elongate quartz-crystals which surround significantly finer-grained selvages consisting primarily of hornblende + minor grunerite, chlorite, garnet, microcline, pyrrhotite, and magnetite.
4b-PM05-001	X		•	•	•													•	Meta-chert sample consisting of: 98% relatively equigranular quartz surrounding 2% medium-grained grunerite agglomerates which themselves contain minor carbonate. Interesting feature of this t.s. is finer grained qtz-crystal agglomerates which may represent original crystal size (meta-chert).
4b-PM05-006	X		•	•	•						•								Folded meta-BIF, consisting of: 80% quartz-bands (~1cm thick) and 20% grunerite-rich relict magnetite bands. Qtz-band consist of: 99% fgr equigranular polygonal qtz crystals and ~1% coarser-grained radiating bt-agglomerates. Relict mag-band consist of: 20% mag, 75% grun, 5% qtz.
4b-PM05-012	X		•	•	•														Thin-section of meta-chert consisting of: 100% fine-grained, equigranular, polygonal quartz-crystals. Relatively undeformed sample. Contains <1% very-fine grained disseminated grunerite crystals.
4b-PM05-015	X		•	•	•														Thin-section of meta-BIF, consisting of: 55% 0.4-0.8 cm thick qtz-bands and 45% 0.4-0.8cm thick relict mag-bands. Mag-bands consist of 95% grunerite, 5% magnetite, and <1% biotite porphyroblasts. Quartz-bands consist of 98% fgrd qtz, 1% mag, and <1% bt bowties.
4b-PM05-016	X		•	•	•													•	Metasomatic BIF consisting of: 70% meta-chert and 30% grun-rich (relict magnetite) bands. Qtz-bands consist of 90% fgr, equigranular, polygonal qtz, 7% fgr mag, and 3% mgr biotite-aggregates. Relict magnetite (gru) bands: 93% fgr gru, 7% fgr disseminated mag.
4b-PM05-018	X		•																Thin-section of meta-chert consisting of: 100% fine-grained, equigranular, polygonal quartz-crystals. Relatively undeformed sample
4b-PM05-020	X		•	•	•														Relatively 'Well preserved' laminated meta-BIF consisting of ~50% mag- and ~50% qtz-bands (0.1-0.3cm thick). Qtz-bands consist of: 90% fgr, equigranular qtz, 3% mag, 7% cgr-bladdered grun. Mag-bands consist of: 60% euhedral mag, 3% qtz, and 5% gru.
4b-PM05-021	X		•	•	•														Thin-section of magnetite band from meta-BIF consisting of: 95% fine-grained magnetite with 5% mostly disseminated grunerite (also found as concentrated 2mm thick tightly folded band, presumably pseudomorphed meta-chert band).
4b-PM05-028	X		•	•	•													•	T.s. of meta-BIF: 60% relict mag-band (1.5cm thick) consisting of: 40% mag, 45% gru, 5% carbonate. Mag is disseminated (save for 2 mm thick mag- bands in the otherwise grunerite-rich matrix). Roughly 40% of t.s. is qtz-band: 99% fgr qtz, 1% grunerite. Good example of polygonal qtz.
4b-PM05-030	X		•	•	•														Thinly-banded meta-BIF band cross-cut by qtz-vein: 60% BIF and 40% qtz-vein. Meta-BIF is thinly-banded on mm-scale and contains roughly 60% grunerite, 40% magnetite, and negligible quartz content.
4b-PM05-031	X		•	•	•														Meta-BIF consisting of: 90% qtz-bands, 10% mag-bands. Qtz-bands: 85% fgr qtz, 15% vgr gru, 1% mag. Mag-bands: 98% mag, and 2% qtz+gru. Gru-bands : 98% grun and 2% qtz+mag (long axis of gru is perp to mag band). Unique sample due to gru bands and abundant gru in qtz-band.
4b-PM05-035	X		•	•	•														Meta-BIF: Inequigranular fgr to cgr sample. Consists of 85% grunerite-rich matrix surrounding 15% boudinaged and coarse-grained magnetite-bands (0.1-0.4cm thick). Magnetite and grunerite are coarser-grained than average oxide-dominant meta-BIF sample.

NIF ASSEMBLAGE OXIDE-DOMINANT BIF

Sample ID	Section	Mineralogy													Description					
		Disk	T.S.	Qtz	Mag	Gru	Hbl	Grt	Chl	Po	Ccp	Bt	Ms	Plag		Kfs	Act	Stauf	Cpx	Cal
NIF ASSEMBLAGE OXIDE-DOMINANT BIF	4b-PM05-041	X		•	•	•														Meta-BIF sample consisting of 60% (0.7-1.0cm thick) qtz-bands and 40% (0.3-0.9cm thick) mag-bands. Mag-bands: 90% mag, 8% gru, and 2% qtz. Qtz-bands are finer grained and consist of: 95% qtz, 4% needle-like gru, and 1% vfg mag. 1mm thick gru-bands between mag- and qtz-bands.
	4b-PM05-042	X		•	•	•														Thin-section of meta-BIF consisting of: roughly 50% qtz-bands and 50% mag-bands. Mag bands consist of: 55% mag, 25% qtz, and 20% gru, the crystals in these bands are coarser-grained than their equivalents in the meta-chert band. Qtz bands: 80% qtz, 15% mag, 5% gru.
	4b-PM05-044	X		•	•	•					•									Meta-BIF consisting of: 50% 0.1-0.5cm thick qtz-bands, 15% 0.1-0.4cm thick mag-bands, and 35% diffuse gru-rich bands. Magnetite-bands consist of: 97% mag, 2% qtz, 1% gru. Qtz-bands consist of: 98% qtz, 1% mag, 1% gru, and <1% bt. Gru bands: 98% gru and 2% bt porphyroblasts.
	4b-PM05-045	X		•	•	•														Meta-BIF consisting of: 80% inequigranular grunerite-rich matrix surrounding 20% diffuse fine-grained relict magnetite-bands. Moderately to strongly sheared. Folded nature is weakly evident but bands have diffused margins so it is difficult to see.
	4b-PM05-046	X		•	•	•														Thinly-banded meta-BIF consisting of: ~55% qtz-bands (~1.2 cm thick) and 45% (0.1-0.4cm) mag-bands. Mag-bands: 90% mag, 9% gru, and ~1% qtz. Qtz-bands consist of: 96% fgr qtz, 3% needle like gru, and 2% mag. Qtz-bands are much finer-grained than mag bands.
	4ea-PM06-002	X		•	•	•						•								
NIF ASSEMBLAGE SILICATE-DOMINANT BIF	4ea-0720-044	X		•	•	•														Relatively fine-grained equigranular sample with 0.5cm thick alternating bands of qtz-rich and aluminosilicate mineral material. Consists of: 25% mgr cpx, 30% qtz, 2% mgr garnet porphyroblasts, 1% po, 30% grunerite, 10% carb. Sample cross-cut by calc-silicate+carb vein.
	4ea-0720-063	X		•	•	•														Consists of: 70% aluminosilicate mineral bands and 30% qtz-carb bands. Bands are deformed. Aluminosilicate-bands consist of: 45% cgr anhedral porphyroblastic garn, 3% po, 2% mag, 1% chlrt, 1% carb, 3% bt, 2% hbl, 4% gru. Qtz-carb: 80% qtz, 20% coarser carb.
	4ea-0720-065	X		•	•	•														Consists of: 70% qtz, 15% bt, 10% garn, 2% mag, 2% gru, 1% po, and <1% chl. The majority of the aluminosilicate minerals are confined to a ~1cm thick band in the middle of t.s. Gru is associated with mag. Chl found in garnet fractures. This sample contains abundant quartz-veins.
	4ea-0720-067	X		•	•	•														Sample consists of: 65% gru, 18% qtz, 10% garn, 3% po, 2% hbl, and 2% mag. This sample contains abundant grunerite. Qtz is mostly confined to 0.7cm thick qtz-band. Garn-porphyroblasts are xenomorphic, very deformed, and contain inclusions of magnetite and grunerite.
	4ea-PM05-058	X		•	•	•														Bt-rich silicate-dominant BIF sample consisting of: 90% aluminosilicate mineral bands encompassing one (0.7cm thick) qtz-band (15% of sample total), 25% bt, 30% gru (bt and gru form separate bands). Sample contains minor disseminated hbl (3%), <1% po, and <1% mag.
	4ea-PM05-061	X		•	•	•														Horblende-rich silicate-dominant BIF sample consisting of: 70% aluminosilicate mineral bands and 30% mono-mineralic qtz-bands. Aluminosilicate-bands consist of: 80% hbl, 15% cgr subhedral garnet porphyroblasts. Interesting Cpx+carbonate+chlorite band (~5% of sample).
	4ea-PM05-062	X		•	•	•														Uncomplicated sample of silicate-dominant BIF consisting of 35% qtz bands and 65% aluminosilicate mineral bands (80% gru, 15% garn, 2% hornblende, 2% magnetite, <1% pyrrhotite). Hornblende is minor and found in small cluster near margin of aluminosilicate band.

Sample ID	Section		Mineralogy													Description			
	Disk	T.S.	Qtz	Mag	Gru	Hbl	Grt	Chl	Po	Ccp	Bt	Ms	Plag	Kfs	Act		Staur	Cpx	Cal
NIF ASSEMBLAGE SILICATE-DOMINANT BIF	4ea-PM06-007	X	•	•	•	•	•	•	•										This sample consists of: 75% grunerite, 15% garnet, 3% magnetite, ~5% quartz, ~2% chlorite, and ~1% carbonate. This sample is very grunerite-rich, and contains relatively abundant chlorite. Most garnet-porphyroblasts are anhedral, deformed, and contain magnetite inclusions.
	4ea-PM06-018	X	•	•	•	•	•	•	•		•								Silicate-dominant BIF consisting of: 85% aluminosilicate mineral bands and 15% qtz-bands on either side (nil-qtz in aluminosilicate-mineral band). Consists of: 15% cgr subhedral gam, 10% mag, 2% po, 5% hornblende, 2% biotite, 1% chlorite, 50% inequigranular grunerite.
	4ea-PM06-043	X	•	•	•	•	•	•	•		•							•	Hornblende-rich silicate-dominant BIF consisting of: 45% hornblende, 20% grunerite, 20% cgr porphyroblastic gam, 5% carb, 1% bt, <1% chl, 1% chalcocopyrite, 2% po, ~1% mag, 3% qtz, and 2% cgr cpx porphyroblasts.
	4ea-0830-001	X	•	•	•	•	•	•	•		•								Inequigranular porphyroblastic sample consisting of: 90% aluminosilicate mineral bands and 10% qtz-bands (0.7cm thick). Aluminosilicate-bands consist of: 45% grunerite, 40% cgr anhedral gam, 10% bt (confined to one band), 5% chl (associated with fractures in gam) + accessory zircon.
	4ea-0830-002	X	•	•	•	•	•	•	•		•	•							T.s. of aluminosilicate mineral band, high biotite and sulfide content. Consists of 45% bt, 20% gru, 5% qtz, 15% mgr sub-euhedral gam, 10% po, 1% mag, 2% ccp, <1% zircon, and <1% muscovite. Interesting sample due to lack of hornblende as well. Garnets are unusually inclusion rich.
	4ea-UG004	X	•	•	•	•	•	•	•		•		•						Inequigranular cgr porphyroblastic sample consisting of: 20% for disseminated qtz (+0.5cm thick cgr qtz-vein), 60% relatively cgr hbl, 2% bt (with accessory zircon), 12% anhedral cgr gam porph, 5% kfs (high percentage for this lithology, +sericite), 2% chlorite associated with garnets.
	4e-0720-019	X	•	•	•	•	•	•	•	•		•		•					Inequigranular porph-hbl-garnet schist consisting of 90% for matrix surrounding 10% mgr euhedral gam porphyroblasts. Consists of: 70% hbl, 10% gam, 5% qtz, 2% chalcocopyrite, 3% po, 5% mag, 5% gru. Mag confined to thin laminations. Accessory muscovite and zircon
	4e-0720-022	X	•	•	•	•	•	•	•	•		•							Inequigranular porphyroblastic hbl-garnet schist consisting of: 75% hbl, 15% anhedral to xenomorphic deformed garnet porphyroblasts, 5% disseminated quartz, 2% disseminated grunerite, 2% po, 1% chalcocopyrite, +unidentified opaque mineral.
	4e-0720-034a	X	•	•	•	•	•	•	•	•		•							Hornblende-garnet schist consisting of: 68% fine-grained hornblende-matrix (contains 2% quartz) which surrounds 20% coarse-grained anhedral to xenomorphic garnet porphyroblasts. Garnet porphyroblasts are surrounded by 10% gru and 1% carb. 1% disseminated po.
	4e-0720-034b	X	•	•	•	•	•	•	•	•		•							Banded hornblende-garnet schist consisting of: 25% cgr subhedral garnet porphyroblasts, 3% bt (confined to bt-garn band), 60% for hbl +10% for qtz matrix (surrounding gam), 5% gru+2% po (disseminated). Interesting contrast between garns in hbl and bt rich bands.
HORNBLLENDE-GARNET SCHIST	4e-0720-047	X	•	•	•	•	•	•	•		•								T.s. consisting of: 60% hornblende, (matrix contains qtz and k-feldspar), 20% chorite (confined to band), 5% bt (found at garnet cores and associated pressure shadows), 5% cgr subhedral gam (associated with chl-band), 3% kfs, 3% qtz, 2% mag, 2% carb, 1% po.
	4f-PM05-060	X	•								•								Biotite-garnet schist sample consisting of: 70% biotite, 15% vgr distorted euhedral garnet porphyroblasts, 10% unidentified pseudomorphed porphyroblasts, 5% for qtz, + accessory zircon and ~1% zoisite (?)
BIOTITE-GARNET SCHIST	4f-0720-002	X	•	•	•	•	•	•	•		•		•						Sample consists of 90% for matrix surrounding 10% sub-to-euhedral cgr garnet porphyroblasts containing staurolite porphyroblast inclusions. For equigranular matrix consists of: 3% qtz, 35% bt, 5% staurolite, 5% ms, 6% kfs, 2% microcline, and 2% plag. Accessory zircon.

Sample ID	Section		Mineralogy													Description			
	Disk	T.S.	Qtz	Mag	Gru	Hbl	Grt	Chl	Po	Ccp	Bt	Ms	Plag	Kfs	Act		Staur	Cpx	Cal
BIOTITE-GARNET SCHIST	4f-0720-008	X	•				•				•								Mineralogically simple biotite-garnet schist sample consisting of: 10% mgr euhedral garnet porphyroblasts surrounded by an equigranular matrix composed of 50% biotite and 40% quartz. Biotite exhibits parallel extinction. Sample contains accessory zircon.
	4f-0720-009	X	•				•				•								Sample composed of simple mineral assemblage consisting of: 60% garnet, 30% biotite, and 10% quartz, as well as very minor zircon. Note the abundant garnet content in this sample. The garnet porphyroblasts are quite euhedral. Inclusions within the garnet are very fine-grained.
	4f-0720-027	X	•	•			•				•					•			Consists of: 48% bt, 30% staurolite, 15% Qtz, 5% garn porphyroblasts, ~1% magnetite, and <1% zircon. Sample is interesting due to abundant staurolite content. Staurolite occurs as inclusions within garnets as well as matrix (interesting intergrowth textures). Bt is pleochroic light- to dark-honey brown.
	4f-PM05-050	X	•	•			•				•			•					A-typical looking biotite-garnet schist thin-section (not sure if its biotite-garnet schist, check h.s.) Consists of 40% fgr mag, 64% poikioblastic gr, 15% fgr biotite, ~5% vfgd Qtz, 5% garnet porphyroblasts, <1% carbonate.
	4f-PM05-052	X	•	•			•				•			•					Bt.garn schist consisting of: 40% biotite, 30% quartz, 25% plagioclase (form fgr matrix), 5% coarser-grained euhedral garnet porphyroblasts, 5% of sample consists of mm-scale hornblende confined to monomineralic band. Accessory zircon and possible minor potassium feldspar.
ULTRA MAFIC	1-PM05-064	X	•	•			•			•				•				•	Strange and grotty looking sample. hand sample looks ultramafic, consists of: 45% serpentine, 25% gr, 8% kfs, 7% mag, 3% po, 2% carbonate, and 10% talc. Talc and carbonate are coarser-grained and appear to be related to veining.
SCHIST	bt.grt-0720-007	X	•	•			•				•								Consists of: 65% hbl, 15% Qtz, 15% bt, 3% gr, 2% garn, and <1% carb. Sample contains diffuse Qtz-rich bands containing fine-grained hbl. Hbl crystals in hbl-rich bands are equigranular. Garn in bt bands are more euhedral than garn in the hbl-rich bands.
	bt.grt-0720-016	X	•	•			•				•			•					Consists of: 80% hbl, 10% Qtz, 5% bt, 2% carb, 2% garn, and <1% plag. Unique sample as it is very hbl-rich (possible 4e?). Minor bt confined to thin band. Matrix mostly consists of equigranular hbl. Qtz is finer-grained than hornblende.
	bt.grt-0720-020	X	•	•			•				•								Consist of: 65% bt, 20% garn, 10% Qtz, and <1% of each of the following chl, carb, gr, zircon, and mag. Note garn are zoned, very-euhedral, and inclusion free, fractures in garn are filled with bt. Clr are distinct crystals. Crenulation in bt is well developed. Zircon are very rare compared to 4f.
	bt.grt-0720-049	X	•	•			•				•								Consist of: 80% bt, 5% garn, 5% gr, 5% Qtz, 2% hbl, and 2% carb. Gru, Qtz, mag, and hbl form relict ~1cm thick band. Bt. Has well developed crenulation. Garn are less euhedral, and contain more inclusions in this t.s relative to others. Sample is somewhat similar to bt.gan-07-20-020.
	Alt-PM05-048	X	•	•			•				•				•				Sample contains quartz-rich mylonitic bands. Grotty looking sample consisting of: 45% quartz, 40% hornblende, 10% actinolite, 2% pyrrhotite, 1% chalcopyrite, and <1% magnetite. Amphiboles are weak to moderately pleochroic in xpl.
METASOMATIC OXIDE DOMINANT BIF	Alt-PM05-049	X	•	•			•								•				Sheared mafic metavolcanic sample consisting of: 30% fine-grained anhedral quartz, 50% medium-grained bladed actinolite, 15% medium-grained hornblende porphyroblasts, 4% potassium feldspar, and <1% magnetite.
	Alt-PM05-005	X	•	•			•												Sample consisting of inequigranular grunerite-rich matrix surrounding relict (mm scale) magnetite bands. Sample consists of: 70% grunerite and 30% magnetite. The most interesting feature is total lack of quartz in this sample. Good example to take photographs of.

Sample ID	Section	Mineralogy													Description					
		Disk	T.S.	Qtz	Mag	Gru	Hbl	Grt	Chl	Po	Ccp	Bt	Ms	Plag		Kfs	Act	Stauf	Cpx	Cal
METASOMATIC OXIDE DOMINANT BIF	Alt-PM05-009	X		•	•	•														This sample consists of: 60% fine-grained meta-chert bands (80% quartz and 20% magnetite) and 40% fgr gr-bands (60% gru, 30% qtz, 10% mgr mag). Good example of meta-chert band cross-cut by medium-grained dismembered quartz-vein.
	Alt-PM05-010	X		•	•	•		•												Folded sample consisting of: 40% quartz and 60% grunerite-rich bands. Grunerite-bands consist of 85% fgr subhedral grunerite, 10% fgr magnetite, 3% carbonate-porph, 2% mgr euhedral mag porph, <1% vfr po. Quartz-rich bands are 97% fgr quartz and 3% vfr disseminated grunerite.
	Alt-PM05-011	X		•		•														Sample of metasomatic BIF. Consists of 60% gru and 40% qtz-vein material. Gru ranges from fgr to mgr. Qtz appears to be vein material because it is coarser-grained. Particularly impressive cgr gru band in this sample. Remaining grunerite material is typical in appearance.
	Alt-PM05-013	X			•	•														Sample consisting of inequigranular grunerite-matrix surrounding disseminated fgr magnetite. Sample consists of 85% gru, 10% hematite, and 5% magnetite. Most interesting feature is total lack of quartz crystals in this sample. Sample does not transmit light very well (dark).
	Alt-PM05-019	X		•	•	•			•											Sample of metasomatic BIF consisting of: 80% relict mag bands (~1% bt porph, 5% fgr mag, 94% inequigranular gru), 20% qtz-vein (<1% fgr po, 2% fgr gru, 2% mgr bt, 92% mgr equigranular qtz-crystals. Interesting feature is bladed bt and gru penetrating qtz-vein.
	Alt-PM05-036	X		•	•	•														Impressive and important t.s. Dr. Falick needs to take a look at this thin-section. Mgr to cgr grunerite and greenalite (?) with fgr quartz-bands (relict meta-chert). Sample consists of: 60% mgr grun, 30% cgr an-to-subhedral pleochroic greenalite, 10% fgr quartz, and ~1% fgrd magnetite.
	Alt-PM05-032	X		•	•	•						•								Fgrd grunerite-rich matrix surrounding relict mag-bands and cross-cut by mm scale bt-bands. Sample consists of 75% fgr-grun + 5% carb + 2% qtz rich matrix, surrounding 15% coarser-grained magnetite crystals. Two ~1mm thick bands of bladed, porphyroblastic bt.
	Alt-PM05-047	X		•	•	•			•											Groty appearance. This thin-section has a rather a-typical appearance for this lithology. Consists of altered porphyroblasts. Probably a metavolcanic. Consists of: 60% mgr hornblende, 20% fgr potassium feldspar, 10% fgr quartz, 10% mgr actinolite, ~1% chlorite, <1% fgr pyrrhotite.
	Alt-PM05-027	X				•						•								Fine-grained sample consisting of: 85% fgr grunerite surrounding, 20% fgr magnetite, 2% euhedral biotite porphyroblasts, <1% mgr hematite, <1% chalcopyrite associated with magnetite. The most interesting feature of this thin section is the total lack of quartz crystals.
	GARNET QUARTZITE	6-0720-024		X	•	•	•													
6-0720-058b			X	•	•	•														Equigranular fine-grained matrix consisting of 45% quartz, 40% biotite, 8% plagioclase, 5% k-feldspar, and 1% muscovite surrounding ~2% disperse medium-grained subhedral garnet porphyroblasts. Also contains accessory zircon.
PORPHYRY	QP-PM05-025	X		•				•												Vfr sample, consisting of: 70% quartz, 15% biotite, 10% muscovite, ~1% of each of the following: pyrrhotite, k-feldspar, and carbonate, as well as 5% epidote (?). Very minor opaques, euhedral muscovite porphyroblasts, fine-grained sub-to euhedral biotite. Possible relict siliciclastic grains.
	QP-PM05-023	X		•	•	•														Strange sample. Consists of aggregates of radiating needle like mineral (looks like musc or talc); consists of 85% muscovite, 10% quartz, 1% plagioclase, <1% magnetite, <1% unidentified brown porphyroblastic mineral. Probably minor kfs. Check sample!

Sample ID	Section	Mineralogy													Description				
		Disk T.S.	Qtz	Mag	Gru	Hbl	Grt	Chl	Po	Cop	Bt	Ms	Plag	Kfs		Act	Staur	Cpx	Cal
PORPH YRY	QP-PM05-014	X	•	•				•			•			•					Inequigranular sample with grotty appearance, consists of: 60% fgr anhedral quartz, 15% mgr sub-to euhedral muscovite porphyroblasts, 10% fine-grained an-to subhedral biotite, 3% carbonate (veins + disseminated), 5% epidote, 5% K-feldspar, and <1% anhedral pyrrhotite.
	tb-PM05-007	X			•														This sample exhibits very interesting metamorphic textures with pseudomorphed very coarse-grained porphyroblasts surrounded by crenulated chlorite. Sample consists of 95% chlorite and 5% grunerite.
	tb-PM05-024	X				•					•								Chlorite-schist consisting of: 57% mgr chlorite with 40% biotite (postdates chlorite as biotite needles radiated into chlorite crystals), ~1% garnet (fgr anhedral relict garn + cgr euhedral dark blue-grey pleochroic hexagonal crystal, contains both chlorite and biotite inclusions).
MAFIC METAVOLCANIC	2-PM05-017	X	•	•			•						•					Possible volcaniclastic sample. Inequigranular porphyroblastic sample composed of pseudomorphed porphyroblasts of crenulated chlorite. Sample consists of 55% mgr hornblende, 20% fgr qtz, 15% clorite porphyroblasts, 10% fgr-to mgr actinolite, <1% magnetite, and <1% pyrrhotite.	
	2-PM05-026	X	•				•				•							Possibly intermediate metavolcanic or metasediment lithology. Consists of 55% fine-grained biotite, 30% fgr potassium feldspar, 5% medium-grained chlorite porphyroblasts, 10% fgr quartz, ~1% po, and <1% zircon.	
	2-PM05-055	X	•				•						•					Fine-grained equigranular matrix composed of 65% hornblende, 25% kfs, 10% quartz, and ~5% of sample is biotite, found mainly in 'miniature shear-zone' in middle of thin-section. Hornblende on edge of this structure is coarser-grained.	
	2-PM05-056	X	•				•				•							Mafic-metavolcanic sample consisting of: 55% mgr carbonate vein material separating less abundant matrix composed of: 20% bt, 15% potassium feldspar, 5% quartz, 1% hornblende, 2% po, and 1% chalcopyrite. The lack of hbl and the abundance of biotite indicates intermediate to felsic.	
	2-PM05-057	X	•	•	•			•						•					Inequigranular deformed sample which contains abundant qtz veins. Sample consists of: 55% mgr-qtz, 30% mgr hbl, 5% gru, 4% mag, 2% euhedral gam (contains titanomagnetite inclusions), 2% bt (contains zircons), 1% plag (plag associated with cgr hbl selvages).
FELSIC METAVOLCANIC	AVoI-PM05-053	X	•				•				•						•	Felsic metavolcanic, consisting of: 40% quartz, 30% potassium feldspar, 5% hornblende, 3% garnet, 1% pyrrhotite, 10% biotite, 1% carbonate, 10% plag, 4% cpx and accessory zircon+titanite. Sample is fgr equigranular except where cut by carbonate-vein (cgr bt, carbonate, sulfide, and cpx).	
	AVoI-PM05-054	X	•				•				•						•	Partially mylonitized felsic metavolcanic: consists of 35% qtz, 20% ms, 20% kfs, 3% po, 1% pyrite (euhedral cubic), <1% microcline, 1% bt, and <1% staurolite. Sample contains several coarser-grained qtz-veins and muscovite-rich bands (contains one staurolite porphyroblast).	
QUARTZ-VEINS	QV-PM05-029	X	•				•											Thin-section of quartz vein. Consists of: 70% medium-grained quartz crystals, 26% kfs, and 4% pyrrhotite. Sample is unremarkable save for unique kfs component (low birefringence, rare sericite and simple twins. Feldspar-rich selvage has grotty appearance.	
	QV-PM05-033	X	•				•											Thin-section of inequigranular quartz-vein: consists of 90% anhedral quartz crystals, 5% fine-grained to medium-grained sub- to euhedral grunerite, 3% hornblende, ~1% medium-grained sub-to euhedral pyrrhotite, and ~1% fine-grained anhedral chlorite	
	QV-PM05-034	X	•	•	•													Inequigranular mgr-cgr quartz vein with associated grunerite-rich magnetite band selvage. Sample consists of: 90% quartz vein (97% quartz, 3% magnetite), and 10% relict magnetite band (40% fgr-mgr mag and 60% medium-grained grunerite).	

# **Appendix C**

## **Mineral Chemistry**

(Abbreviations used in this section are explained on pg. XIII of Appendix A)



MAJOR Elements														Total		
Mineral	Sample ID	%	Na2O	MgO	Al2O3	SiO2	P2O5	K2O	CaO	TiO2	MnO	FeO	Fe2O3	O	Total	Cation sum
Carbonate	Point 1	%	0.31	0.8	0.12*	0.3	N.M.	0.03*	51.11	-0.11*	0.22*	1.79	N.M.	N.M.	54.57	6
Carbonate	Point 2	%	0.32	0.77	0.26	0.35	N.M.	0.13*	50.62	-0.20*	0.36	1.89	N.M.	N.M.	54.5	6
Carbonate	Point 3	%	0.15*	0.76	-0.09*	0.27	N.M.	0.12*	49.93	0.04*	0.04*	1.98	N.M.	N.M.	53.2	6
Carbonate	Point 9	%	0.31	0.83	0.03*	0.36	N.M.	-0.07*	50.37	0.15*	0.13*	1.82	N.M.	N.M.	53.93	5.98
Carbonate	Point 11	%	0.26	0.77	0.11*	0.28	N.M.	0.04*	49.42	0.08*	0.26	3.44	N.M.	N.M.	54.58	5.98
Carbonate	Point 14	%	0.31	0.83	0.04*	0.22	N.M.	0.08*	49.72	-0.05*	0.29	3.43	N.M.	N.M.	54.88	6.02
Carbonate	Point 18	%	0.15*	0.74	0.00*	0.21*	N.M.	0.09*	49.85	-0.01*	0.26	3.42	N.M.	N.M.	54.71	6
Carbonate	Point 21	%	0.02*	1.03	-0.09*	0.29	N.M.	-0.02*	49.66	0.00*	0.73	3.8	N.M.	N.M.	55.42	5.98
Carbonate	Point 24	%	0.17*	1.11	0.09*	0.16*	N.M.	0.00*	48.77	-0.05*	1.13	5.09	N.M.	N.M.	56.48	6
Carbonate	Point 27	%	0.08*	6.99	-0.03*	0.3	N.M.	-0.02*	29.95	-0.10*	1.4	19.32	N.M.	N.M.	57.88	5.99
Carbonate	Point 28	%	0.22*	9.63	0.20*	52.96	N.M.	0.05*	0.33	0.05*	0.75	36.1	N.M.	N.M.	100.29	3.91
Carbonate	Point 29	%	0.21*	9.23	0.26*	52.5	N.M.	0.02*	0.3	0.07*	0.69	36.33	N.M.	N.M.	99.6	3.91
Carbonate	Point 37	%	-0.06*	0.66	0.04*	0.3	N.M.	0.04*	34.28	-0.03*	0.74	3.75	N.M.	N.M.	55.46	5.93
Carbonate	Point 31	%	0.17*	0.87	0.04*	0.18*	N.M.	-0.03*	49.74	-0.16*	0.92	4.53	N.M.	N.M.	56.26	6.01
Gruerite	Point 4	%	0.89	12.77	0.10*	52.08	N.M.	-0.09*	0.46	-0.03*	0.34	30.3	N.M.	N.M.	96.82	3.95
Gruerite	Point 6	%	0.82	12.85	0.26*	52.81	N.M.	-0.04*	0.47	-0.02*	0.14*	30.1	N.M.	N.M.	97.38	3.94
Gruerite	Point 7	%	0.84	13.22	0.29*	53.58	N.M.	0.00*	0.8	-0.02*	0.32	29.55	N.M.	N.M.	98.58	3.94
Gruerite	Point 10	%	0.68	9.1	0.23*	51.88	N.M.	-0.08*	0.59	-0.18*	0.21*	34.58	N.M.	N.M.	97.02	3.92
Gruerite	Point 12	%	0.72	9.9	0.34	51.99	N.M.	-0.02*	0.52	0.09*	0.26*	34.65	N.M.	N.M.	98.45	3.94
Gruerite	Point 13	%	0.73	9.8	0.23*	52.18	N.M.	0.00*	0.21	0.13*	0.21*	35.71	N.M.	N.M.	99.18	3.94
Gruerite	Point 15	%	0.81	9.43	0.42	51.62	N.M.	0.04*	0.15*	-0.06*	0.32	35.02	N.M.	N.M.	97.75	3.94
Gruerite	Point 16	%	0.65	9.35	0.04*	50.87	N.M.	-0.12*	0.31	-0.12*	0.13*	35.64	N.M.	N.M.	96.75	3.94
Gruerite	Point 17	%	0.57	9.61	0.39	51.54	N.M.	-0.11*	0.26	0.08*	0.34	34.11	N.M.	N.M.	96.78	3.92
Gruerite	Point 19	%	0.62	9.6	0.07*	51.62	N.M.	0.09*	0.61	0.14*	0.05*	35.04	N.M.	N.M.	97.84	3.94
Gruerite	Point 20	%	0.02*	9.46	0.06*	52.5	N.M.	-0.11*	0.42	-0.01*	0.49	36.25	N.M.	N.M.	99.07	3.9
Gruerite	Point 22	%	0.14*	9.24	0.29*	52.06	N.M.	0.00*	0.38	0.09*	0.65	36.39	N.M.	N.M.	99.25	3.91
Gruerite	Point 23	%	-0.04*	9.17	0.03*	51.86	N.M.	-0.02*	0.33	-0.01*	0.57	36.27	N.M.	N.M.	98.16	3.9
Gruerite	Point 25	%	0.17*	9.38	0.13*	52.99	N.M.	-0.07*	0.22	0.04*	0.42	36.29	N.M.	N.M.	99.57	3.9
Gruerite	Point 26	%	0.31*	9.73	0.22*	52.26	N.M.	0.07*	0.49	0.01*	0.55	35.81	N.M.	N.M.	99.46	3.93
Gruerite	Point 30	%	-0.06*	9.56	0.10*	51.76	N.M.	-0.07*	0.18	0.12*	0.54	36.16	N.M.	N.M.	98.29	3.9
Gruerite	Point 32	%	0.06*	9.12	0.18*	52.97	N.M.	0.00*	0.2	0.05*	0.49	37.03	N.M.	N.M.	100.11	3.9
Gruerite	Point 33	%	0.13*	9.11	0.19*	53.03	N.M.	0.02*	0.25	-0.12*	0.35	36.48	N.M.	N.M.	99.43	3.9
Gruerite	Point 35	%	0.16*	5.59	0.12*	24.07	N.M.	-0.01*	0.15	-0.03*	0.54	26.9	N.M.	N.M.	96.67	3.9
Gruerite	Point 36	%	0.17*	5.71	0.06*	24.42	N.M.	-0.11*	0.2	0.02*	0.41	28.1	N.M.	N.M.	98.9	3.91
Gruerite	Point 38	%	0.03*	5.36	0.09*	24.39	N.M.	0.04*	0.14	0.09*	0.38	28.07	N.M.	N.M.	98.28	3.89
Gruerite	Point 39	%	0.12*	5.37	0.07*	24.43	N.M.	0.03*	0.23	-0.02*	0.4	28.05	N.M.	N.M.	98.39	3.9
Hornblende	Point 5	%	0.61	14.39	0.29*	55.13	N.M.	-0.05*	12.23	-0.08*	0.21*	17.14	N.M.	N.M.	99.87	3.95
Hornblende	Point 8	%	0.69	14.44	0.46	55.08	N.M.	0.07*	12.19	0.08*	0.06*	16.47	N.M.	N.M.	99.53	3.95
Hornblende	Point 34	%	0.10*	7.03	0.02*	0.20*	N.M.	-0.05*	30.06	-0.06*	1.28	18.82	N.M.	N.M.	57.41	5.99

Southern Banded Iron Formation

Mineral	Sample ID	MAJOR ELEMENTS														Total	Cation sum
		Na2O	MgO	Al2O3	SiO2	P2O5	K2O	CaO	TiO2	MnO	FeO	Fe2O3	O				
Apatite	Point 6	%	-0.02*	0.06*	0.25	0.05*	42.93	0.02*	57.6	-0.02*	0.02*	0.57	N.M.	N.M.	101.46	3.86	
Biotite	Point 17	%	0.13*	0.17*	17.34	61.37	-0.08*	15.63	0.12*	-0.03*	0.19*	2.08	N.M.	N.M.	96.91	3.78	
Biotite	Point 22	%	0.79	6.46	16.36	34.52	N.M.	9.68	-0.01*	1.6	0.13*	27.77	N.M.	N.M.	97.31	4.36	
Biotite	Point 24	%	0.68	6.17	15.92	34.4	N.M.	9.7	-0.11*	1.53	0.13*	27.24	N.M.	N.M.	95.66	4.34	
Biotite	Point32	%	0.67	5.93	16.39	33.54	N.M.	9.37	0.22	1.1	0.05*	27.77	N.M.	N.M.	95.03	4.36	
Biotite	Point37	%	0.71	5.89	15.73	33.52	N.M.	9.45	0.01*	0.96	0.18*	28.23	N.M.	N.M.	94.68	4.37	
Carbonate	Point36	%	0.27	0.55	-0.03*	0.06*	N.M.	0.03*	49.09	-0.11*	0.66	3.19	N.M.	N.M.	53.71	6.03	
Carbonate	Point 3	%	0.04*	0.37	0.15*	0.23	N.M.	0.00*	52.22	-0.03*	0.51	1.62	N.M.	N.M.	55.13	5.97	
Chlorite	Point 16	%	0.44	8.42	23.55	22.74	0.19*	0.10*	0.05*	0.11*	0.16*	32.09	N.M.	N.M.	87.84	4.29	
Garnet	Point 4	%	0.11*	0.86	20.52	38.01	N.M.	0.01*	9.84	0.07*	4.11	27.29	N.M.	N.M.	100.82	4.01	
Garnet	Point 10	%	0.18*	1.18	20.52	37.37	-0.22*	0.01*	5.93	0.16*	4.73	30.82	N.M.	N.M.	100.69	4.02	
Garnet	Point 11	%	0.02*	1.08	20.27	36.84	-0.11*	-0.05*	5.1	0.19*	4.32	31.83	N.M.	N.M.	99.49	4.01	
Garnet	Point 13	%	0.26*	0.99	20.42	37.2	-0.12*	0.11*	6.49	0.27	4.01	30.88	N.M.	N.M.	100.5	4.02	
Garnet	Point 14	%	0.09*	0.96	20.55	37.8	0.03*	0.05*	11.11	0.15*	3.55	26.86	N.M.	N.M.	101.15	4.02	
Garnet	Point 20	%	-0.01*	0.88	20.89	37.19	-0.25*	-0.04*	7.99	-0.03*	4.78	28.74	N.M.	N.M.	100.16	4.01	
Grunerite	Point 19	%	0.20*	10.01	0.46	52.78	-0.17*	-0.07*	0.81	0.09*	0.76	34.4	N.M.	N.M.	99.27	3.91	
Grunerite	Point 21	%	0.84	8.74	0.24*	51.1	N.M.	0.07*	0.39	0.04*	1.15	35.21	N.M.	N.M.	97.76	3.95	
Grunerite	Point31	%	0.85	8.72	0.34	51.3	N.M.	0.00*	0.39	-0.01*	1.06	34.83	N.M.	N.M.	97.47	3.94	
Hornblende	Point 1	%	0.6	8.36	6.5	48.6	N.M.	0.22	11.81	0.27	0.4	23.11	N.M.	N.M.	99.88	3.99	
Hornblende	Point 5	%	0.65	5.47	11.05	42.76	N.M.	0.81	12.17	0.3	0.09*	23.41	N.M.	N.M.	96.67	4.03	
Hornblende	Point 7	%	0.6	7.12	7.75	46.52	-0.07*	0.37	12.25	0.57	0.06*	23.08	N.M.	N.M.	98.24	3.99	
Hornblende	Point 8	%	0.74	7.17	7.76	46.81	-0.14*	0.6	11.71	0.62	0.3	24.48	N.M.	N.M.	100.04	4.02	
Hornblende	Point 15	%	0.67	6.62	9.29	44.97	0.14*	0.56	12.13	0.64	0.09*	23.27	N.M.	N.M.	98.36	4.01	
Hornblende	Point 18	%	0.63	6.37	9.27	45.51	-0.07*	0.35	11.91	0.28	0.25*	23.4	N.M.	N.M.	97.9	4	
Hornblende	Point33	%	1.44	6.66	7.11	46.72	N.M.	0.47	9.14	0.15*	0.47	27.45	N.M.	N.M.	99.6	4.04	
Hornblende	Point34	%	0.84	8.78	0.65	51.73	N.M.	0.02*	0.54	0.18*	1.21	35.09	N.M.	N.M.	99.03	3.94	
Hornblende	Point35	%	1.83	4.37	12.74	41.23	N.M.	0.79	11.16	0.06*	0.35	24.92	N.M.	N.M.	97.44	4.1	
Ilmenite	Point 9	%	-0.10*	0.09*	0.26	0.28	-0.06*	0.06*	0.19	49.49	2.27	45.94	N.M.	N.M.	98.42	4.05	
Ilmenite	Point 12	%	0.22*	-0.07*	0.21*	0.19*	0.03*	-0.01*	0.17*	49.99	1.02	46.34	N.M.	N.M.	98.09	4.05	
Ilmenite	Point29	%	0.79	0.5	1.7	2.12	N.M.	0.00*	0.08*	45.89	1.3	43.74	N.M.	N.M.	96.12	4.09	
Quartz	Point 2	%	0.07*	-0.01*	0.13*	101.11	N.M.	-0.07*	-0.05*	0.01*	0.05*	0.18*	N.M.	N.M.	101.42	3	
Tourmaline	Point 23	%	2.52	5.78	30.88	36.05	N.M.	-0.01*	0.33	0.89	0.13*	9.71	N.M.	N.M.	86.28	3.87	
Tourmaline	Point 25	%	2.1	5.86	28.36	34.83	N.M.	0.12*	2.66	0.21*	0.06*	13.82	N.M.	N.M.	88.01	3.95	
Tourmaline	Point 26	%	1.91	5.71	28.4	34.92	N.M.	0.18	2.45	0.33	-0.06*	13.63	N.M.	N.M.	87.47	3.93	
Tourmaline	Point27	%	3.04	6.4	32.07	35.91	N.M.	0.02*	0.28	0.95	0.16*	8.96	N.M.	N.M.	87.8	3.9	
Tourmaline	Point28	%	3.23	6.94	30.53	36.19	N.M.	0.06*	0.43	1.02	0.09*	8.64	N.M.	N.M.	87.14	3.92	
Tourmaline	Point30	%	2.98	5.95	33.06	36.99	N.M.	-0.07*	0.06*	0.2	0.18	8.97	N.M.	N.M.	88.31	3.88	
Tourmaline	Point38	%	1.97	5.62	27.91	34.56	N.M.	0.11*	2.58	0.43	0.03*	13.73	N.M.	N.M.	86.92	3.94	
Tourmaline	Point39	%	1.96	5.9	26.96	34.28	N.M.	-0.01*	2.95	0.4	0.07*	13.99	N.M.	N.M.	86.51	3.95	

META-ARGILLITE

MAJOR Elements															
Mineral	Sample ID	Na2O	MgO	Al2O3	SiO2	P2O5	K2O	CaO	TiO2	MnO	FeO	Fe2O3	O	Total	Cation sum
Biotite	Point34	%	6.91	0.36*	50.55	N.M.	0.05*	0.72	0.16*	N.M.	38.97	N.M.	N.M.	97.71	1.95
Biotite	Point38	%	2.87	6.05	44.85	N.M.	1.13	0.51	-0.08*	N.M.	32.4	N.M.	N.M.	87.73	1.92
Calcite	Point 6	%	0.14*	0.17*	0.36	0.14*	N.M.	51.47	0.00*	2.53	N.M.	N.M.	N.M.	54.81	2.98
Calcite	Point 13	%	0.33	0.17*	0.20*	N.M.	N.M.	48.62	0.01*	N.M.	2.15	N.M.	N.M.	51.54	2.99
Fe-Calcite	Point 15	%	0.12*	0.01*	0.10*	N.M.	0.15*	51.19	0.17*	N.M.	2.93	N.M.	N.M.	54.66	2.99
Fe-Calcite	Point 21	%	0.49	0.01*	1.79	N.M.	0.07*	48.67	0.05*	N.M.	3.66	N.M.	N.M.	54.75	2.91
Fe-Calcite	Point 22	%	0.22*	-0.08*	0.22*	N.M.	0.05*	50.85	0.09*	N.M.	2.47	N.M.	N.M.	53.82	2.99
Fe-Calcite	Point29	%	0.26*	0.03*	0.21*	N.M.	0.21	49.14	-0.13*	N.M.	2.15	N.M.	N.M.	51.88	3
Fe-Calcite	Point30	%	0.27	-0.02*	0.11*	N.M.	0.10*	51.08	0.05*	N.M.	2.23	N.M.	N.M.	53.82	3
Fe-Calcite	Point31	%	0.36	0.02*	1.83	N.M.	0.10*	47.96	0.18*	N.M.	2.27	N.M.	N.M.	52.72	2.9
Fe-Calcite	Point33	%	0.33	0.14*	0.13*	N.M.	0.07*	50.66	0.08*	N.M.	2.25	N.M.	N.M.	53.65	2.99
Fe-Calcite	Point 8	%	0.22*	0.07*	0.19*	N.M.	N.M.	50.6	0.20*	N.M.	2.44	N.M.	N.M.	53.75	2.98
Chlorite	Point 17	%	5.31	0.41*	43.32	N.M.	0.10*	0.25	0.08*	N.M.	40.39	N.M.	N.M.	89.86	1.99
Grunerite	Point 2	%	8.76	0.27*	51.88	N.M.	N.M.	0.29	N.M.	N.M.	N.M.	36.04	N.M.	97.13	1.94
Grunerite	Point 3	%	8.5	0.53	51.37	N.M.	N.M.	0.48	N.M.	N.M.	36.1	N.M.	N.M.	97.07	1.95
Grunerite	Point 5	%	6.73	0.15*	50.98	N.M.	N.M.	0.25	-0.07*	N.M.	39.68	N.M.	N.M.	97.71	1.95
Grunerite	Point 7	%	6.89	0.34*	50.53	N.M.	N.M.	0.49	-0.10*	N.M.	38.49	N.M.	N.M.	96.55	1.95
Grunerite	Point 9	%	6.77	0.38*	51.46	N.M.	N.M.	0.47	-0.08*	N.M.	38.9	N.M.	N.M.	97.85	1.94
Grunerite	Point 10	%	6.55	0.34*	49.86	N.M.	N.M.	0.17*	0.14*	N.M.	39.33	N.M.	N.M.	96.45	1.95
Grunerite	Point 11	%	6.59	0.31*	50.3	N.M.	N.M.	0.49	-0.13*	N.M.	38.88	N.M.	N.M.	96.39	1.95
Grunerite	Point 12	%	6.53	0.38*	50.08	N.M.	N.M.	0.36	-0.01*	N.M.	38.24	N.M.	N.M.	95.55	1.94
Grunerite	Point 14	%	6.9	0.35*	50.73	N.M.	-0.14*	0.5	0.17*	N.M.	39.2	N.M.	N.M.	97.7	1.95
Grunerite	Point 16	%	6.8	0.11*	50.75	N.M.	0.11*	0.52	0.06*	N.M.	39.41	N.M.	N.M.	97.78	1.95
Grunerite	Point 18	%	6.91	0.36*	50.55	N.M.	0.05*	0.72	0.16*	N.M.	38.97	N.M.	N.M.	97.71	1.95
Grunerite	Point 19	%	6.59	0.33*	50.6	N.M.	-0.09*	0.29	-0.11*	N.M.	38.85	N.M.	N.M.	96.46	1.94
Grunerite	Point 20	%	6.7	0.13*	49.74	N.M.	0.03*	0.25	-0.09*	N.M.	39.19	N.M.	N.M.	95.95	1.95
Grunerite	Point 23	%	6.3	0.31*	51.04	N.M.	0.03*	0.51	-0.06*	N.M.	39.89	N.M.	N.M.	98.01	1.95
Grunerite	Point 24	%	6.46	0.38*	50.88	N.M.	-0.09*	0.42	-0.20*	N.M.	38.73	N.M.	N.M.	96.57	1.94
Grunerite	Point 25	%	6.75	0.52	50.09	N.M.	-0.05*	0.42	-0.01*	N.M.	38.7	N.M.	N.M.	96.41	1.95
Grunerite	Point 26	%	6.25	0.06*	50.87	N.M.	0.18	0.49	0.15*	N.M.	39.62	N.M.	N.M.	97.62	1.95
Grunerite	Point27	%	5.96	0.07*	50.11	N.M.	0.01*	0.51	0.13*	N.M.	38.85	N.M.	N.M.	95.64	1.94
Grunerite	Point28	%	6.55	0.27*	50.19	N.M.	-0.05*	0.53	0.06*	N.M.	38.46	N.M.	N.M.	96.01	1.95
Grunerite	Point36	%	5.44	0.33*	50.34	N.M.	0.06*	0.16*	0.00*	N.M.	40.67	N.M.	N.M.	96.99	1.95
Grunerite	Point37	%	4.97	0.22*	50.12	N.M.	0.02*	0.26	0.13*	N.M.	40.17	N.M.	N.M.	95.9	1.94
Magnetite	Point32	%	-0.04*	0.05*	0.15*	N.M.	0.00*	-0.07*	0.01*	N.M.	94.63	N.M.	N.M.	94.73	2.4
Magnetite	Point35	%	4.99	49.55	N.M.	N.M.	N.M.	N.M.	N.M.	N.M.	41.06	N.M.	N.M.	96.17	N.M.
Magnetite	Point 1	%	-0.14*	0.11*	1.75	N.M.	N.M.	0.05*	-0.06*	N.M.	N.M.	92.91	N.M.	94.62	2.37
Magnetite	Point 4	%	0.10*	0.24*	0.29*	N.M.	N.M.	0.07*	N.M.	N.M.	N.M.	94.2	N.M.	94.97	2.4

NIF ASSEMBLAGE OXIDE-DOMINANT BIF

MAJOR ELEMENTS																
Mineral	Sample ID	%	Na2O	MgO	Al2O3	SiO2	P2O5	K2O	CaO	TiO2	MnO	FeO	Fe2O3	O	Total	Cation sum
Apatite	Point 29	%	N.M.	N.M.	N.M.	N.M.	N.M.	18.71	39.97	N.M.	N.M.	N.M.	0.84	40.35	99.87	5.13
Apatite	Point 31	%	-0.01*	0.13	0.64	N.M.	-0.01*	18.63	39.87	N.M.	0.04*	0.04*	0.69	41.09	101.24	5.11
Apatite	Point 32	%	-0.11*	0.10*	0.24	N.M.	0.06*	19.05	40.16	N.M.	-0.05*	-0.11*	0.19*	40.99	100.76	5.09
Apatite	Point 34	%	-0.02*	0.07*	0.31	N.M.	0.06*	18.86	40.34	N.M.	0.00*	-0.10*	0.07*	40.88	100.53	5.1
Calcite	Point 33	%	0.04*	0.03*	0.08*	N.M.	0.05*	0.00*	37.5	N.M.	0.05*	0.31	0.7	15.4	54.02	7.98
Garnet	Point 1	%	N.M.	0.76	11.08	17.26	N.M.	N.M.	4.17	N.M.	N.M.	0.52	26.88	39.54	100.21	5.35
Garnet	Point 39	%	N.M.	1.24	N.M.	23.02	N.M.	N.M.	15.69	N.M.	N.M.	0.63	20.09	39.25	99.92	5.33
Garnet	Point 35	%	1.75	0.32	23.6	N.M.	-0.01*	-0.08*	8.27	N.M.	-0.01*	0.29	25	38.76	97.85	5.22
Garnet	Point 36	%	1.23	0.31	22.68	N.M.	0.01*	-0.14*	15.39	N.M.	-0.03*	0.65	20.21	38.91	99.45	5.35
Garnet	Point 27	%	0.51	0.46	10.86	17.12	0.00*	N.M.	2.74	N.M.	0.02*	0.64	28.72	39.17	100.24	5.38
Garnet	Point 28	%	0.94	4.77	0.17	23.46	-0.01*	N.M.	0.24	N.M.	0.05*	0.02*	29.08	38.81	97.52	5.3
Garnet	Point 24	%	N.M.	0.59	10.96	17.19	N.M.	N.M.	2.75	N.M.	0.08*	0.58	28.41	39.17	99.71	5.33
Garnet	Point 5	%	1.74	2.09	8.38	18.39	N.M.	N.M.	7.77	N.M.	N.M.	0.03*	19.37	39.05	96.82	5.47
Garnet	Point 6	%	1.85	2.38	7.77	18.27	N.M.	N.M.	7.63	N.M.	N.M.	0.06*	19.26	38.52	95.74	5.49
Garnet	Point 7	%	1.49	2.13	8.42	18.55	N.M.	N.M.	8.02	N.M.	N.M.	0.01*	19.71	39.39	97.72	5.45
Garnet	Point 8	%	0.92	5.5	0.38	23.68	N.M.	N.M.	0.4	N.M.	N.M.	0.15*	28.17	39.52	98.7	5.31
Garnet	Point 12	%	N.M.	3.93	0.65	23.33	N.M.	N.M.	0.76	N.M.	N.M.	0.36	30.04	38.76	97.83	5.22
Garnet	Point 13	%	N.M.	4.03	0.48	23.88	N.M.	N.M.	0.41	N.M.	N.M.	0.32	30.26	39.22	98.61	5.2
Grunerite	Point 4	%	5.11	0.44	23.75	0.48	N.M.	N.M.	0.07*	N.M.	N.M.	0.22	39.1	97.16	5.21	5.21
Grunerite	Point 9	%	0.71	5.07	0.33	23.68	N.M.	N.M.	0.36	N.M.	N.M.	0.03*	27.84	38.98	97	5.26
Grunerite	Point 14	%	N.M.	3.87	0.38	23.54	N.M.	N.M.	0.35	N.M.	N.M.	0.26	29.89	38.48	96.77	5.19
Grunerite	Point 17	%	0.7	3.95	0.32	23.67	0.06*	N.M.	0.29	N.M.	N.M.	0.31	30.34	39	98.64	5.27
Grunerite	Point 21	%	0.59	4	0.33	23.43	0.06*	N.M.	0.4	N.M.	N.M.	0.18*	29.5	38.49	96.98	5.25
Grunerite	Point 22	%	0.71	3.86	0.4	22.46	0.02*	N.M.	0.22	N.M.	N.M.	0.29	29.59	37.38	94.93	5.29
Grunerite	Point 26	%	0.6	4.64	0.26	23.65	0.01*	N.M.	0.28	N.M.	-0.05*	0.02*	29.4	38.95	97.76	5.26
Hornblende	Point 2	%	N.M.	0.64	10.94	16.97	N.M.	N.M.	3.83	N.M.	N.M.	0.56	27.1	38.94	98.99	5.35
Hornblende	Point 3	%	N.M.	0.51	10.85	17.05	N.M.	N.M.	3.96	N.M.	N.M.	0.4	26.71	38.77	98.26	5.33
Hornblende	Point 15	%	N.M.	1.76	1.89	7.4	18.71	N.M.	8.08	N.M.	N.M.	0.07*	20.87	38.98	97.77	5.49
Hornblende	Point 16	%	1.63	1.68	8.24	18.59	0.36	N.M.	8.19	N.M.	N.M.	-0.02*	20.63	39.43	98.73	5.49
Hornblende	Point 18	%	1.56	1.8	6.94	19.14	0.45	N.M.	7.96	N.M.	N.M.	0.11*	21.26	39.1	98.31	5.48
Hornblende	Point 19	%	1.8	1.7	7.39	18.4	0.46	N.M.	8.01	N.M.	N.M.	0.18*	20.27	38.43	96.65	5.51
Hornblende	Point 20	%	1.73	1.89	8.16	18.68	0.48	N.M.	8.05	N.M.	N.M.	0.05*	19.92	39.42	98.38	5.49
Hornblende	Point 23	%	1.66	1.91	7.32	18.73	0.52	N.M.	7.98	N.M.	N.M.	0.2	20.71	38.97	98.01	5.5
Hornblende	Point 25	%	1.47	1.61	8.55	18.08	0.45	N.M.	7.87	N.M.	0.15	-0.03*	20.3	38.91	97.36	5.48
Hornblende	Point 30	%	0.55	10.79	16.97	-0.12*	0.01*	N.M.	2.74	N.M.	0.07*	0.45	28.87	38.68	99.01	5.35
Ilmenite	Point 10	%	0.34	0.13*	0.00*	0.17	N.M.	N.M.	0.10*	N.M.	30.04	0.12*	36.1	30.88	97.89	5.41
Ilmenite	Point 11	%	0.19*	0.10*	0.12	0.18	N.M.	N.M.	0.2	N.M.	29.94	0.18*	36.68	31.09	98.69	5.41
Scheelite	Point 37	%	N.M.	N.M.	N.M.	0.18	N.M.	-0.37*	14.17	67.94	N.M.	N.M.	N.M.	22.91	104.65	3.97
Scheelite	Point 38	%	N.M.	N.M.	N.M.	0.18	N.M.	-0.49*	14.05	67.96	N.M.	N.M.	N.M.	22.72	104.24	3.97

NIF ASSEMBLAGE SILICATE-DOMINANT BIF

MAJOR ELEMENTS																
Mineral	Sample ID	%	Na2O	MgO	Al2O3	SiO2	P2O5	K2O	CaO	TiO2	MnO	FeO	Fe2O3	O	Total	Cation sum
Fe Calcite	Point 5	%	0.34	0.42	0.01*	0.2	N.M.	-0.01*	52.19	0.01*	0.66	1.95	N.M.	N.M.	55.77	6.01
Fe Calcite	Point 9	%	-0.02*	0.24	0.13*	0.26	N.M.	0.06*	52.62	-0.14*	0.8	1.89	N.M.	N.M.	55.83	5.98
Fe Calcite	Point 17	%	0.10*	0.27	-0.02*	0.18*	N.M.	-0.02*	52.47	0.22*	0.43	1.78	N.M.	N.M.	55.42	5.98
Fe Calcite	Point33	%	0.25	0.54	-0.04*	0.17*	N.M.	-0.02*	51.03	0.01*	0.62	2.27	N.M.	N.M.	54.85	6.01
Chlorite	Point 6	%	0.13*	7.6	18.78	24.05	N.M.	0.02*	0.08*	-0.03*	0.22*	35.92	N.M.	N.M.	86.78	4.3
Garnet	Point 1	%	0.77	1.09	20.44	37.55	N.M.	0.00*	7.91	0.03*	5.39	28.75	N.M.	N.M.	101.93	4.05
Garnet	Point 2	%	0.43	0.95	20.81	37.72	N.M.	0.09*	8.34	0.07*	5.37	27.75	N.M.	N.M.	101.53	4.03
Garnet	Point 3	%	0.48	1.17	21.05	38.29	N.M.	-0.05*	9.29	0.02*	4.66	27.4	N.M.	N.M.	102.32	4.03
Garnet	Point 14	%	0.15*	1.04	20.72	37.41	N.M.	-0.02*	6.13	0.07*	4.68	30.29	N.M.	N.M.	100.45	4.01
Garnet	Point 15	%	0.16*	1.1	20.73	37.68	N.M.	-0.03*	8.42	0.20*	4.38	29.35	N.M.	N.M.	101.97	4.02
Garnet	Point 18	%	0.07*	1.09	20.33	37.34	N.M.	-0.03*	8.75	0.07*	4.82	28.06	N.M.	N.M.	100.5	4.02
Garnet	Point 21	%	0.65	1.37	20.93	38.47	N.M.	-0.04*	7.25	0.20*	3.21	30.27	N.M.	N.M.	102.3	4.02
Garnet	Point 22	%	0.5	1.07	20.41	37.39	N.M.	-0.03*	7.62	0.20*	2.78	30.07	N.M.	N.M.	100.02	4.02
Garnet	Point 23	%	0.76	1.21	20.74	37.13	N.M.	0.06*	8.37	0.22*	2.64	29.57	N.M.	N.M.	100.7	4.05
Garnet	Point 24	%	0.49	1.34	20.88	37.65	N.M.	0.01*	8.35	0.24*	2.35	29.78	N.M.	N.M.	101.09	4.03
Garnet	Point29	%	0.49	1.11	21.15	37.55	N.M.	-0.04*	9.14	0.11*	2.52	28.85	N.M.	N.M.	100.88	4.02
Garnet	Point37	%	0.5	1.13	20.52	37.48	N.M.	-0.06*	8	0.33	2.35	30.18	N.M.	N.M.	100.43	4.02
Garnet	Point38	%	0.45	1.19	20.29	37.86	N.M.	-0.03*	9.91	0.25	2.49	27.89	N.M.	N.M.	100.31	4.02
Garnet	Point32	%	0.48	0.97	20.51	38.32	N.M.	0.02*	9.26	0.22*	2.58	29.58	N.M.	N.M.	101.95	4.02
Garnet	Point 7	%	0.14*	0.79	20.41	38.08	N.M.	-0.03*	9.18	0.19*	4.77	27.65	N.M.	N.M.	101.18	4.01
Garnet	Point 8	%	0.11*	1.12	20.7	37.73	N.M.	0.03*	7.65	0.05*	5.13	28.62	N.M.	N.M.	101.15	4.01
Garnet	Point 12	%	-0.07*	0.83	20.62	37.3	N.M.	-0.03*	8.6	-0.07*	5.1	27.77	N.M.	N.M.	100.05	4.01
Grunerite	Point 25	%	0.84	9.29	0.5	52.14	N.M.	-0.02*	0.71	0.02*	0.33	35.46	N.M.	N.M.	99.27	3.94
Grunerite	Point30	%	0.79	9.38	0.49	52.51	N.M.	-0.02*	0.66	0.06*	0.58	34.83	N.M.	N.M.	99.28	3.93
Grunerite	Point39	%	0.91	9.44	0.28*	52.49	N.M.	0.05*	0.46	-0.02*	0.56	34.94	N.M.	N.M.	99.11	3.94
Grunerite	Point35	%	0.78	9.26	0.22*	52.48	N.M.	-0.03*	0.51	0.06*	0.51	33.29	N.M.	N.M.	97.09	3.91
Hornblende	Point 4	%	1.13	8.8	5.02	49.15	N.M.	0.2	11.97	0.27	0.36	22.82	N.M.	N.M.	99.71	4.01
Hornblende	Point 10	%	0.7	8.78	5.42	49.37	N.M.	0.18	12.2	0.41	0.32	22.47	N.M.	N.M.	99.86	3.98
Hornblende	Point 13	%	0.4	8.73	5.6	49.26	N.M.	0.12*	10.82	0.42	0.36	23.19	N.M.	N.M.	98.9	3.96
Hornblende	Point 16	%	0.67	6.53	9.06	45.69	N.M.	0.53	11.94	0.47	0.3	25.04	N.M.	N.M.	100.24	4.02
Hornblende	Point 19	%	0.72	7.71	7.37	47.17	N.M.	0.38	11.96	0.29	0.17*	23.29	N.M.	N.M.	99.06	4
Hornblende	Point 20	%	0.96	7.17	8.09	46.86	N.M.	0.38	12.38	0.33	0.21*	24.56	N.M.	N.M.	100.95	4.03
Hornblende	Point27	%	1.5	6.37	9.52	45.18	N.M.	0.18	11.61	0.6	0.10*	22.79	N.M.	N.M.	97.86	4.02
Hornblende	Point28	%	1.66	6.06	11.02	44.02	N.M.	0.23	11.43	0.4	0.35	23.12	N.M.	N.M.	98.28	4.05
Hornblende	Point 26	%	1.59	6.21	11	44.06	N.M.	0.22	11.77	0.41	0.03*	23.69	N.M.	N.M.	98.99	4.05
Hornblende	Point36	%	1.3	5.61	10.41	43.85	N.M.	0.26	11.61	0.61	0.31	23.32	N.M.	N.M.	97.3	4.03
Ilmenite	Point34	%	0.31*	0.14*	0.17*	0.21*	N.M.	0.08*	0.25	47.24	0.41	46.21	N.M.	N.M.	95.04	4.09
Quartz	Point 11	%	0.21	-0.06*	0.19*	102.73	N.M.	0.00*	-0.06*	-0.05*	-0.03*	0.25*	N.M.	N.M.	103.17	3.01
Quartz	Point31	%	0.3	0.02*	0.35	102.13	N.M.	-0.03*	0.04*	0.19*	0.02*	0.52	N.M.	N.M.	103.54	3.02

HORNBLENDE-GARNET SCHIST

MAJOR ELEMENTS															
Mineral	Sample ID	Na2O	MgO	Al2O3	SiO2	P2O5	K2O	CaO	TiO2	MnO	FeO	Fe2O3	O	Total	Cation sum
Hornblende	Point 22	% 0.34	10.01	24.31	31.5	N.M.	1.48	0.83	0.64	0.25	27.12	N.M.	N.M.	96.35	15.96
Apatite	Point31	% -0.16*	0.03*	0.17*	0.77	42.11	0.12*	54.74	-0.05*	-0.20*	0.02*	N.M.	N.M.	97.56	14.62
Apatite	Point32	% 0.24*	0.07*	0.22	0.66	42.48	0.06*	54.8	0.06*	-0.15*	0.31	N.M.	N.M.	98.74	14.69
Biotite	Point 5	% 0.08*	9.66	19.39	34.72	-0.11*	8.44	-0.01*	1.93	0.13*	22.05	N.M.	N.M.	96.28	16.33
Biotite	Point 6	% 0.35	10.53	18.42	33.92	0.13*	6.26	1.1	2.73	-0.04*	22.62	N.M.	N.M.	96.02	16.23
Biotite	Point 7	% 0.16*	8.92	17.12	33.75	-0.01*	5.33	5.3	7.24	-0.06*	17.96	N.M.	N.M.	95.69	15.81
Biotite	Point 9	% 0.34	11.12	17.83	35.3	-0.07*	9.62	0.02*	2.44	0.02*	19.06	N.M.	N.M.	95.68	16.47
Biotite	Point 19	% 0.33	9.54	18.55	35.66	N.M.	9	0.01*	2.6	0.13*	21.32	N.M.	N.M.	97.14	16.32
Biotite	Point 20	% 0.14*	9.54	17.82	34.85	N.M.	9.46	-0.08*	2.68	0.10*	20.61	N.M.	N.M.	95.12	16.37
Biotite	Point38	% 0.32	9.71	18.24	33.81	0.06*	7.99	0.05*	2.08	0.13*	21.86	N.M.	N.M.	94.25	16.37
Calcite	Point 24	% 0.05*	-0.06*	0.04*	0.16*	N.M.	0.10*	53.36	0.01*	0.13*	0.52	N.M.	N.M.	54.29	22.98
Chlorite	Point 10	% 0.08*	12.05	20.48	24.88	-0.09*	0.02*	0.19	0.04*	0.19*	28.62	N.M.	N.M.	86.46	16.4
Gamet	Point 1	% 0.37	3.3	21.02	36.59	-0.25*	0.04*	2.14	0.20*	0.10*	36.28	N.M.	N.M.	99.79	15.48
Gamet	Point 2	% 0.24*	3.37	21.31	38.08	-0.04*	0.04*	2.32	-0.11*	0.19*	37.69	N.M.	N.M.	103.1	15.45
Gamet	Point 3	% 0.39	2.49	20.93	36.17	0.07*	-0.02*	2.33	0.14*	0.16*	37.13	N.M.	N.M.	99.79	15.46
Gamet	Point 4	% 0.08*	0.48	24.08	43.22	0.03*	0.16	26.66	0.62	0.01*	0.9	N.M.	N.M.	96.26	14.71
Gamet	Point 8	% 0.28*	3.04	21.71	38.46	0.09*	-0.05*	2.26	-0.18*	0.09*	38.1	N.M.	N.M.	103.82	15.4
Gamet	Point 11	% 0.07*	0.49	30.11	39.23	-0.21*	0.01*	22.17	0.17*	0.09*	5.49	N.M.	N.M.	97.61	14.88
Gamet	Point 12	% 0.35	2.82	22.35	38.32	N.M.	0.05*	2.45	-0.14*	0.13*	38.66	N.M.	N.M.	104.98	15.46
Gamet	Point 13	% 0.07*	2.88	21.27	37.3	N.M.	-0.07*	2.48	0.01*	0.08*	39.08	N.M.	N.M.	103.08	15.46
Gamet	Point 14	% 0.26*	2.8	21.17	37.56	N.M.	-0.12*	2.49	-0.03*	0.02*	38.61	N.M.	N.M.	102.76	15.45
Gamet	Point 15	% 0.22*	3.09	20.38	36.91	N.M.	0.07*	2.35	0.02*	0.12*	36.98	N.M.	N.M.	100.13	15.45
Gamet	Point 16	% 0.02*	2.46	21.01	37.27	N.M.	0.10*	2.49	0.00*	-0.01*	36.96	N.M.	N.M.	100.29	15.35
Gamet	Point 17	% 0.30*	2.58	20.84	36.85	N.M.	-0.07*	2.31	0.10*	0.33	36.93	N.M.	N.M.	100.17	15.41
Gamet	Point 18	% 0.14*	2.61	21.2	36.72	N.M.	-0.01*	2.18	0.16*	0.25*	37.91	N.M.	N.M.	101.17	15.43
Gamet	Point 23	% 0.01*	0.09*	0.36	0.95	N.M.	0.06*	55.05	0.06*	-0.10*	0.8	N.M.	N.M.	100.02	14.65
Gamet	Point 25	% -0.07*	3.1	20.69	36.77	N.M.	-0.02*	2.28	0.05*	0.09*	37.01	N.M.	N.M.	99.9	15.38
Gamet	Point 26	% 0.22*	3.13	22.35	38.27	N.M.	-0.01*	2.2	-0.01*	0.12*	38.16	N.M.	N.M.	104.23	15.43
Gamet	Point27	% 0.10*	2.94	21.18	37.93	-0.08*	0.03*	2.4	0.07*	0.14*	38.37	N.M.	N.M.	103.09	15.42
Gamet	Point28	% 0.15*	2.7	21.07	37.95	-0.14*	-0.01*	2.2	0.02*	0.14*	39.18	N.M.	N.M.	103.25	15.44
Gamet	Point29	% 0.07*	3.04	20.81	36.16	0.01*	-0.01*	2.18	-0.01*	0.10*	36.56	N.M.	N.M.	98.91	15.42
Gamet	Point30	% 0.22*	3.22	20.82	36.51	0.08*	0.03*	2.32	-0.04*	0.01*	36.78	N.M.	N.M.	99.95	15.46
Gamet	Point33	% 0.16*	3.01	20.38	35.88	-0.19*	-0.04*	2.22	0.06*	0.42	35.81	N.M.	N.M.	97.72	15.44
Gamet	Point34	% 0.19*	3.08	21.23	37.1	-0.04*	0.03*	1.89	0.04*	0.18*	37.05	N.M.	N.M.	100.75	15.41
Gamet	Point35	% 0.36	2.88	21.04	37.54	-0.08*	0.09*	2.41	0.07*	0.00*	37.47	N.M.	N.M.	101.79	15.45
Gamet	Point36	% 0.20*	2.89	21.25	38.01	0.14*	-0.11*	2.35	0.10*	0.13*	37.39	N.M.	N.M.	102.36	15.35
Gamet	Point37	% 0.31	3.32	20.95	37.05	0.27*	0.04*	2.24	0.08*	0.02*	36.39	N.M.	N.M.	100.66	15.41
limerite	Point39	% 0.33	-0.02*	0.12*	0.29	0.05*	-0.05*	0.14*	50.4	4.65	43.64	N.M.	N.M.	99.55	15.56
limerite	Point 21	% 0.25*	0.13*	0.14*	0.23*	N.M.	0.02*	0.08*	50.32	4.57	45.51	N.M.	N.M.	101.23	15.67

BIOTITE-GARNET SCHIST

# **Appendix D**

## **Whole Rock Geochemistry**

(Abbreviations used in this section are explained on pg. XIII of Appendix A)

		MAJOR Elements										
Sample ID		SiO <sub>2</sub>	Al <sub>2</sub> O <sub>3</sub>	TiO <sub>2</sub>	Fe <sub>2</sub> O <sub>3</sub>	FeO	MgO	CaO	Na <sub>2</sub> O	K <sub>2</sub> O	MnO	P <sub>2</sub> O <sub>5</sub>
SIF ASSEMBLAGE OXIDE DOMINANT BIF	SIF-PM05-63c	45.63	0.08	0.01	0.59	17.46	4.28	1.14	0.04	N.D.	0.15	0.19
	SIF-0720-060c	78.82	0.05	0.02	N.D.	10.15	2.14	5.03	0.01	0.01	0.25	0.17
	SIF-0720-060M	23.81	0.05	0.01	39.82	29.71	2.74	1.57	0.07	0.01	0.24	0.05
	SIF-0720-062m	39.79	0.2	0.02	20.07	28.73	3.16	3.83	0.05	0.06	0.55	0.18
	SIF-0720-063c	66.93	0.11	0.03	0.59	17.46	5.73	4.59	0.02	0.02	1.11	0.2
	SIF-0720-063m	33.5	0.09	0.01	20.97	26.02	2.6	2.77	0.05	0.01	0.51	0.26
	SIF-0720-071m	19.09	0.09	0.01	33.63	24.65	2.43	3.41	0.06	0.01	0.38	0.22
	SIF-0720-072m	35.34	0.11	0.01	31.58	24.75	2.5	4.34	0.05	0.01	0.06	0.2
META-ARGILLET	4h-0720-042	31.56	4.32	0.15	1.51	42.58	3.94	4.22	0.17	0.4	1.15	0.33
	4h-0720-043	76.79	1.49	0.02	1.11	13	1.68	1.96	0.08	0.04	0.41	0.01
	4h-0720-046	43.31	4.89	0.19	0	34.69	2.84	3.81	0.15	0.38	1.08	0.1
	4h-0720-051	53.47	7.7	0.29	11.67	11.12	2.7	1.34	0.08	0.72	0.13	0.03
	4h-0720-053a	45.13	5.34	0.2	0	33.31	2.3	3.1	0.16	1.59	0.58	0.17
	4h-0720-053b	59.82	4.44	0.18	0	22.67	2.76	3.11	0.13	1.43	0.69	0.09
	4h-0720-056	54.57	1.32	0.07	0.05	24.85	3.7	8.09	0.16	0.22	0.72	0.14
	4h-0720-057	54.14	3.38	0.12	3.6	21.52	2.68	6.34	0.07	0.76	0.74	0.08
	4h-0720-070	47.52	14.95	0.88	10.42	0.2	9.06	12.46	1.62	0.02	0.17	0.02
	4h-0720-071	25.92	2.13	0.02	0.8	36.42	3.44	11.56	0.26	0.28	0.41	0.24
QUARTZ- GRUNERITE BIF	4a-0720-012	87.75	0.03	N.D.	0.15	7.38	1.07	1.25	N.D.	N.D.	0.23	0.01
	4a-0720-028	55.11	0.14	0.01	1.52	24.82	3.75	8.38	0.04	0.05	1.04	0.08
	4a-0720-039	53.45	0.99	0.03	1.18	26.37	4.19	6.69	0.04	0.15	1.26	0.14
	4a-0720-041	60.83	0.43	0.03	2.73	22.3	3.98	4.08	0.03	0.05	1.49	0.13
	4a-0720-044	60.58	0.78	0.05	0.83	24.73	3.39	4.29	0.03	0.05	0.91	0.14
	4a-0720-054c	83.89	0.13	0.03	N.D.	9.1	1.63	2.65	0.01	0.01	0.6	0.01
	4a-0720-054m	17.71	1.13	0.06	22.86	24.65	7.43	9.74	0.05	0.29	2.21	0.08
NIF ASSEMBLAGE OXIDE DOMINANT BIF (MAGNETITE)	4b-PM05-21b	28.93	0.18	0.02	25.45	66.49	4.06	0.78	0.02	0.02	0.17	0.15
	4b-PM05-21m	18.39	0.22	0.02	25.45	66.48	3.81	0.19	0.05	0.06	0.14	0.11
	4b-PM05-31m	17.78	0.13	0.02	26.7	78.55	2.34	1.69	0.06	N.D.	0.2	0.33
	4b-PM05-37	23.94	0.05	N.D.	24.73	75.64	1.38	0.14	0.05	N.D.	0.22	0.07
	4b-PM05-38m	25.26	0.05	N.D.	25.15	73.94	1.74	0.12	0.05	N.D.	0.19	0.02
	4b-PM05-39	9.75	0.05	0.01	27.29	89.28	1.65	0.13	0.05	N.D.	0.29	0.03
	4b-PM05-40m	14.16	0.04	N.D.	29.77	84.79	1.58	0.32	0.06	N.D.	0.27	0.16
	4b-PM06-042	45.72	14.93	1.1	13.06	1.79	5.08	13.84	2.52	0.19	0.25	0.1
	4b-PM05-101	20.96	0.11	0.02	30.53	77.28	3.28	0.2	0.03	0.01	0.22	0.05
	4b-PM06-28m	12.15	0.08	N.D.	24.97	53.53	1.67	0.56	0.05	N.D.	0.11	0.13
	4b-PM06-28m	30.65	2.77	0.15	24.97	53.54	4.57	4.06	0.08	0.73	1.34	0.16
	4b-0720-004m	22.6	0.84	0.06	28.26	60.74	5.46	5.59	0.08	0.22	1.1	0.22
	4b-0720-040m	16.49	0.87	0.03	28.74	68.9	5.26	5.17	0.07	0.16	0.48	0.29
	4b-0720-055m	40.39	3.4	0.18	22.43	51.78	1.98	0.57	0.72	1.44	0.63	0.13
	4b-0720-006	46.12	8.74	0.5	24.29	34	3	3.17	1.37	2.62	0.67	0.1
	4b-0720-067m	33.36	1.47	0.07	28.96	52.24	4.65	5.16	0.15	0.24	1.15	0.26
NIF ASSEMBLAGE OXIDE DOMINANT BIF (QUARTZ)	4b-PM05-006	84.41	0.05	0.02	6.61	13.05	1.13	0.14	0.03	N.D.	0.16	0.09
	4b-PM05-012	96.41	0.02	N.D.	1.15	1.71	0.28	0.03	0.03	N.D.	0.04	N.D.
	4b-PM05-018	97.26	0.03	N.D.	0.71	1.5	0.16	0.03	0.03	N.D.	0.02	N.D.
	4b-PM05-028b	90.8	0.03	0.03	4.1	5.09	0.71	1.57	0.03	N.D.	0.06	N.D.
	4b-PM05-031b	69.59	0.1	N.D.	20.42	25.45	3.56	1.12	0.04	N.D.	0.26	0.06
	4b-PM05-038b	88.73	0.03	N.D.	5.33	9.1	1.13	0.07	0.03	N.D.	0.12	N.D.
	4b-PM05-040b	55.76	0.04	N.D.	30.56	35.96	6.94	0.68	0.03	N.D.	1.07	0.22
	4b-PM05-043	85.42	0.05	0.03	5.32	13.69	0.46	0.31	N.D.	N.D.	0.08	0.02
	4b-PM05-065c	86.69	1.83	N.D.	4.66	6.91	0.53	0.29	0.22	0.88	0.08	0.02
	4b-PM05-067c	81.21	0.52	0.05	8.31	8.93	1.6	4.17	0.03	0.15	0.42	0.07
	4b-PM06-028c	91.52	0.47	0.05	3.27	3.52	0.58	2.15	0.1	0.06	0.16	0.11
	4b-0720-005c	78.28	1.07	0.04	10.9	12.66	2.05	3.78	0.06	0.33	0.46	0.08
	4b-0720-053c	85.12	0.2	N.D.	7.8	12.08	0.83	1.08	N.D.	0.04	0.29	0.05
	GARNET- QUARTZITE	6-0720-024	65.65	18.15	0.38	1.46	3.34	1.78	3.79	0.18	3.74	0.22
6-0720-025		64.84	17.52	0.38	0.15	4.16	1.8	3.48	1.94	4.36	0.11	0.08
6-0720-033		62.78	20.44	0.4	2.2	2.66	1.64	2.06	0.37	5.17	0.18	0.08
6-0720-038		65.3	17.22	0.36	0.18	4.24	1.7	2.36	1.82	5.78	0.07	0.07
6-0720-058		61.04	17.66	0.46	0.71	7.67	2.26	5.18	0.23	3.06	0.2	0.12
SILICATE- DOMINANT BIF	4ea-PM05-057	68.47	7	0.21	19.53	12.06	2.23	1.34	0.39	0.52	0.16	0.08
	4ea-PM05-066	47.65	6.78	0.23	N.D.	35.03	2.48	3.98	0.27	0.68	0.58	0.08
	4ea-PM06-002	37.37	7.41	0.33	49.47	N.D.	3.3	1.73	0.11	0.46	0.75	0.13
	4ea-PM06-007	43.45	5.59	0.26	46.05	N.D.	3.97	1.07	0.51	0.04	0.83	0.19
	4ea-PM06-018	48.52	6.7	0.44	5.8	31.09	3.35	1.42	0.05	0.01	0.3	0.15



			REE, LILE, HFSE									
	Sample ID	LOI	Ce	Cs	Dy	Er	Eu	Gd	Hf	Ho	La	Lu
SIF ASSEMBLAGE OXIDE DOMINANT BIF	SIF-PM05-63c	N.D.	6.32	0.126	1.37	1.09	0.689	1.19	N.D.	0.336	3.49	0.169
	SIF-0720-060c	2.6	6.51	0.029	1.222	0.909	0.843	1.12	0.2	0.295	3.58	0.137
	SIF-0720-060M	0.05	8.66	0.035	1.512	1.137	0.68	1.334	N.D.	0.367	4.98	0.174
	SIF-0720-062m	0.05	11.19	0.827	2.187	1.448	1.188	1.954	N.D.	0.483	5.08	0.225
	SIF-0720-063c	2.55	12.91	0.235	2.151	1.536	1.218	1.905	N.D.	0.503	6.52	0.264
	SIF-0720-063m	0.05	13.73	0.209	2.263	1.581	1.271	2.005	N.D.	0.513	6.92	0.241
	SIF-0720-071m	0.05	9.38	0.091	1.708	1.224	0.901	1.55	N.D.	0.406	4.99	0.175
SIF-0720-072m	0.05	3.99	0.128	1.12	0.876	0.249	0.961	N.D.	0.279	2.23	0.128	
META-ARGILLET	4h-0720-042	3.75	11.71	0.88	3.012	2.106	1.183	2.435	0.5	0.678	5.28	0.318
	4h-0720-043	1.73	3.5	0.135	0.495	0.333	0.332	0.48	0.1	0.109	1.78	0.058
	4h-0720-046	3.9	13.13	0.418	2.294	1.512	0.875	1.996	1.2	0.494	6.21	0.247
	4h-0720-051	9.2	6.9	2.531	1.101	0.803	0.214	0.969	1.4	0.244	3.21	0.169
	4h-0720-053a	5.4	24.76	0.849	2.489	1.615	1.191	2.508	1.1	0.535	12.79	0.292
	4h-0720-053b	2.28	24.3	0.883	2.95	2.013	1.375	2.805	1.1	0.645	12.41	0.339
	4h-0720-056	1.57	17.9	0.467	2.121	1.391	1.031	2.012	0.8	0.46	9.51	0.224
	4h-0720-057	2.66	11.57	0.163	1.799	1.196	0.612	1.665	0.5	0.398	5.97	0.181
	4h-0720-070	2.6	25.85	1.411	3.5	2.281	1.41	3.254	1.3	0.74	12.22	0.377
4h-0720-071	2.82	8.77	0.806	2.491	1.597	1.023	2.198	N.D.	0.544	4.31	0.213	
QUARTZ- GRUNERITE BIF	4a-0720-012	0.72	0.56	0.021	0.156	0.132	0.067	0.117	N.D.	0.039	0.33	0.022
	4a-0720-028	2.28	2.24	1.372	0.593	0.528	0.15	0.475	N.D.	0.151	1.13	0.089
	4a-0720-039	2.26	7.06	0.23	1.51	1.083	0.609	1.221	0.3	0.346	3.56	0.165
	4a-0720-041	1.3	4.52	1.868	1.284	0.931	0.55	1.064	0.2	0.294	2.1	0.151
	4a-0720-044	1.29	7.9	0.132	1.549	1.14	0.641	1.384	0.3	0.372	3.87	0.18
	4a-0720-054c	1.74	2.35	0.118	0.452	0.348	0.215	0.377	0.2	0.11	1.42	0.056
	4a-0720-054m	10.12	12.09	0.418	2.137	1.596	0.926	1.838	0.3	0.519	6.68	0.269
NIF ASSEMBLAGE OXIDE DOMINANT BIF (MAGNETITE)	4b-PM05-21b	N.D.	9.02	7.72	0.678	0.576	0.415	0.636	0.2	0.166	4.96	0.117
	4b-PM05-21m	N.D.	9.02	7.72	0.678	0.576	0.415	0.636	0.2	0.166	4.96	0.117
	4b-PM05-31m	N.D.	1.5	0.066	0.343	0.3	0.194	0.302	0.2	0.09	1.18	0.057
	4b-PM05-37	N.D.	4.11	0.091	0.361	0.285	0.187	0.326	N.D.	0.088	2.71	0.05
	4b-PM05-38m	N.D.	3.11	0.063	0.213	0.173	0.095	0.168	N.D.	0.054	2.46	0.034
	4b-PM05-39	N.D.	3.84	0.045	0.245	0.193	0.141	0.232	N.D.	0.062	2.84	0.029
	4b-PM05-40m	N.D.	5.53	0.051	0.526	0.389	0.271	0.484	N.D.	0.127	3.15	0.063
	altb-PM06-042	3.18	9.37	0.026	4.461	2.911	0.931	3.696	1.9	0.965	3.41	0.436
	4b-PM05-101	N.D.	6.3	0.497	0.37	0.315	0.195	0.347	N.D.	0.093	4.33	0.059
	4b-PM06-28m	N.D.	4.98	0.486	0.592	0.381	0.331	0.585	N.D.	0.129	2.46	0.059
	4b-PM06-28m	3.28	15.06	0.345	1.932	1.353	0.751	1.833	0.6	0.44	8.01	0.209
	4b-0720-004m	3.7	13.98	0.176	1.972	1.39	0.98	1.882	0.3	0.456	7.77	0.217
	4b-0720-040m	3.46	12.13	1.515	2.245	1.613	0.957	2.095	0.2	0.525	6.61	0.235
	4b-0720-055m	N.D.	8.95	6.427	1.363	0.965	0.398	1.284	0.6	0.322	5.65	0.147
	4b-0720-006	0.23	13.16	53.578	1.872	1.294	0.687	1.747	1.5	0.428	7.37	0.194
4b-0720-067m	1.99	8.43	0.214	1.378	0.973	0.674	1.323	0.3	0.315	5.05	0.15	
NIF ASSEMBLAGE OXIDE DOMINANT BIF (QUARTZ)	4b-PM05-006	N.D.	2.6	0.221	0.303	0.202	0.155	0.277	0.1	0.066	1.35	0.03
	4b-PM05-012	0.08	1.14	0.03	0.054	0.046	0.029	0.06	0.1	0.012	0.66	0.008
	4b-PM05-018	0.14	0.61	0.061	0.119	0.089	0.048	0.087	0.1	0.03	0.32	0.011
	4b-PM05-028b	1.14	1.69	0.079	0.331	0.255	0.168	0.267	0.1	0.08	0.9	0.04
	4b-PM05-031b	N.D.	1.01	0.034	0.113	0.106	0.058	0.087	N.D.	0.028	1.02	0.028
	4b-PM05-038b	N.D.	0.6	0.036	0.037	0.033	0.013	0.032	N.D.	0.01	0.46	0.007
	4b-PM05-040b	N.D.	5.94	0.062	0.822	0.612	0.416	0.743	N.D.	0.19	2.9	0.096
	4b-PM05-043	N.D.	7.46	0.087	0.249	0.177	0.138	0.241	N.D.	0.059	5.76	0.027
	4b-PM05-065c	0.63	0.32	1.483	0.09	0.053	0.05	0.113	0.2	0.019	0.16	0.009
	4b-PM05-067c	3.32	4.45	0.14	0.633	0.46	0.329	0.577	0.2	0.148	2.73	0.07
	4b-PM06-028c	1.81	2.72	0.046	0.578	0.325	0.31	0.619	0.2	0.119	1.33	0.04
	4b-0720-005c	2.21	5.96	0.249	0.943	0.7	0.495	0.839	0.3	0.221	3.3	0.112
	4b-0720-053c	0.35	3.57	0.664	0.339	0.253	0.187	0.347	0.1	0.083	2.42	0.041
GARNET- QUARTZITE	6-0720-024	1.21	32.93	1.777	1.935	1.025	0.928	2.175	3.8	0.368	17.71	0.138
	6-0720-025	0.69	34.55	2.605	1.811	0.975	0.779	2.151	3.7	0.35	19.02	0.13
	6-0720-033	1.68	40.68	2.51	1.88	1.033	0.95	2.202	4.8	0.366	22.55	0.143
	6-0720-038	0.4	34.41	3.043	1.47	0.802	0.695	1.816	4	0.282	19.35	0.118
	6-0720-058	0.53	29.46	2.237	1.963	1.122	0.881	2.243	3.4	0.398	14.47	0.155
SILICATE- DOMINANT BIF	4ea-PM05-057	0.06	10.07	1.215	1.41	0.922	0.458	1.335	0.8	0.309	5.28	0.131
	4ea-PM05-066	0.05	11.68	2.095	1.501	1.022	0.585	1.402	1.0	0.347	6.94	0.16
	4ea-PM06-002	0.05	16.57	1.179	2.111	1.447	0.742	1.993	1.2	0.485	9.24	0.213
	4ea-PM06-007	0.05	15.11	0.111	2.287	1.578	0.773	2.108	0.9	0.528	8.13	0.25
	4ea-PM06-018	0.05	14.72	0.072	2.71	1.956	0.73	2.452	1.2	0.639	8.25	0.303

		REE, LILE, HFSE												
		Sample ID	Nb	Nd	Pr	Rb	Sm	Sr	Ta	Tb	Th	Tm	U	
SIF ASSEMBLAGE OXIDE DOMINANT BIF	SIF-PM05-63c	N.D.	3.36	0.771	0.24	0.79	9.3	N.D.	0.197	N.D.	0.158	0.013		
	SIF-0720-060c	N.D.	3.28	0.781	0.39	0.76	57.1	N.D.	0.178	N.D.	0.131	0.013		
	SIF-0720-060M	N.D.	4.09	0.981	0.51	0.92	15.3	N.D.	0.213	N.D.	0.168	0.011		
	SIF-0720-062m	0.2	5.89	1.404	2.95	1.49	24.3	N.D.	0.323	N.D.	0.218	0.052		
	SIF-0720-063c	N.D.	6.31	1.575	0.68	1.45	16.1	N.D.	0.311	N.D.	0.236	0.018		
	SIF-0720-063m	N.D.	6.54	1.653	0.99	1.52	11.4	N.D.	0.327	N.D.	0.233	0.019		
	SIF-0720-071m	N.D.	4.72	1.102	0.34	1.06	22.2	N.D.	0.247	N.D.	0.176	0.025		
SIF-0720-072m	N.D.	2.3	0.492	0.42	0.55	12.3	N.D.	0.153	N.D.	0.125	0.011			
META-ARGILLET	4h-0720-042	1.4	6.55	1.501	15.36	1.73	19.7	N.D.	0.431	0.8	0.318	0.515		
	4h-0720-043	N.D.	1.67	0.41	1.33	0.4	14.4	N.D.	0.077	0.3	0.052	0.12		
	4h-0720-046	2.1	6.47	1.578	14.62	1.56	18.8	0.19	0.348	2.4	0.23	0.768		
	4h-0720-051	2.7	3.32	0.828	21.62	0.84	15.6	0.22	0.164	4.6	0.133	1.535		
	4h-0720-053a	2.7	10.93	2.812	89.81	2.41	23.6	0.23	0.391	3.74	0.246	1.163		
	4h-0720-053b	2.2	11.06	2.794	91.63	2.46	21.5	0.19	0.452	3.2	0.299	1.052		
	4h-0720-056	1.7	7.91	2.018	23.8	1.71	39.4	N.D.	0.317	1.9	0.212	0.629		
	4h-0720-057	1.5	5.8	1.399	4.99	1.34	75	N.D.	0.267	0.93	0.175	0.311		
	4h-0720-070	2.8	12.13	3.077	62.29	2.86	40.9	0.25	0.533	3.64	0.343	1.185		
4h-0720-071	N.D.	5.2	1.126	6.33	1.48	76.3	N.D.	0.371	0.06	0.226	0.04			
QUARTZ- GRUNERITE BIF	4a-0720-012	N.D.	0.29	0.067	0.11	0.07	8.9	N.D.	0.019	N.D.	0.02	0.011		
	4a-0720-028	N.D.	1.37	0.307	3.14	0.33	14.2	N.D.	0.082	N.D.	0.086	0.045		
	4a-0720-039	0.6	3.65	0.884	6.39	0.88	28.1	N.D.	0.214	0.44	0.157	0.172		
	4a-0720-041	0.4	2.57	0.574	3.29	0.7	16.1	N.D.	0.179	0.25	0.139	0.102		
	4a-0720-044	0.5	4.18	0.978	2.15	1	18.6	N.D.	0.225	0.54	0.169	0.148		
	4a-0720-054c	N.D.	1.16	0.278	0.6	0.26	22.1	N.D.	0.062	0.06	0.053	0.045		
	4a-0720-054m	0.5	5.96	1.429	8.48	1.33	72.4	N.D.	0.302	0.67	0.24	0.313		
NIF ASSEMBLAGE OXIDE DOMINANT BIF (MAGNETITE)	4b-PM05-21b	0.3	3.91	1.01	10.5	0.61	4.5	N.D.	0.096	0.55	0.095	0.087		
	4b-PM05-21m	0.3	3.91	1.01	10.5	0.61	4.5	N.D.	0.096	0.55	0.095	0.087		
	4b-PM05-31m	N.D.	0.75	0.168	0.18	0.19	5	N.D.	0.048	0.29	0.046	0.029		
	4b-PM05-37	N.D.	1.44	0.385	0.14	0.26	0.7	N.D.	0.05	N.D.	0.044	N.D.		
	4b-PM05-38m	N.D.	0.94	0.264	0.14	0.14	0.6	N.D.	0.029	N.D.	0.028	N.D.		
	4b-PM05-39	N.D.	1.15	0.333	0.14	0.18	0.7	N.D.	0.033	N.D.	0.028	N.D.		
	4b-PM05-40m	N.D.	1.97	0.508	0.1	0.36	1	N.D.	0.074	N.D.	0.06	N.D.		
	altb-PM06-042	2.8	7.83	1.498	1.58	2.59	144.7	0.19	0.655	0.33	0.426	N.D.		
	4b-PM05-101	N.D.	1.88	0.524	0.67	0.3	0.5	N.D.	0.056	N.D.	0.047	0.013		
	4b-PM06-28m	0.2	2.36	0.552	0.69	0.47	2	N.D.	0.091	N.D.	0.058	0.008		
	4b-PM06-28m	1	7.13	1.762	21.24	1.54	57.5	N.D.	0.284	1.09	0.201	0.329		
	4b-0720-004m	0.5	6.72	1.625	8.78	1.41	35.8	N.D.	0.296	0.42	0.206	0.131		
	4b-0720-040m	0.3	6.53	1.471	12.46	1.52	30.9	N.D.	0.328	0.28	0.232	0.091		
	4b-0720-055m	0.9	4.17	1.013	66.78	0.92	23	N.D.	0.201	0.63	0.138	0.195		
	4b-0720-006	2.4	6.04	1.487	150	1.4	88.7	N.D.	0.279	1.49	0.185	0.421		
	4b-0720-067m	0.6	4.22	0.987	7.99	0.94	28.7	N.D.	0.207	0.45	0.141	0.166		
	NIF ASSEMBLAGE OXIDE DOMINANT BIF (QUARTZ)	4b-PM05-006	N.D.	1.06	0.255	0.28	0.22	0.9	N.D.	0.045	N.D.	0.029	0.018	
4b-PM05-012		N.D.	0.47	0.127	0.09	0.07	0.5	N.D.	0.008	N.D.	0.007	0.018		
4b-PM05-018		N.D.	0.32	0.075	0.15	0.08	0.6	N.D.	0.015	N.D.	0.013	0.018		
4b-PM05-028b		N.D.	0.82	0.188	0.12	0.2	4.5	N.D.	0.047	N.D.	0.038	0.008		
4b-PM05-031b		N.D.	0.31	0.086	0.12	0.06	2	N.D.	0.014	N.D.	0.017	0.007		
4b-PM05-038b		N.D.	0.17	0.051	0.08	0.03	N.D.	N.D.	0.005	N.D.	0.005	N.D.		
4b-PM05-040b		N.D.	2.41	0.578	0.11	0.54	1.5	N.D.	0.118	N.D.	0.087	0.013		
4b-PM05-043		N.D.	1.82	0.613	0.13	0.21	1.1	N.D.	0.037	N.D.	0.027	N.D.		
4b-PM05-065c		N.D.	0.23	0.048	25.64	0.08	8.4	N.D.	0.017	N.D.	0.008	0.008		
4b-PM05-067c		0.2	2.04	0.514	5.23	0.45	23.3	N.D.	0.088	0.13	0.064	0.044		
4b-PM06-028c		N.D.	1.62	0.362	1.84	0.48	35.8	N.D.	0.093	0.1	0.043	0.033		
4b-0720-005c		0.5	2.84	0.705	11.34	0.64	21.1	N.D.	0.135	0.42	0.106	0.104		
4b-0720-053c		N.D.	1.54	0.382	2.71	0.27	14	N.D.	0.049	0.1	0.037	0.031		
GARNET- QUARTZITE		6-0720-024	6	12.24	3.447	50.8	2.3	60.1	0.58	0.323	5.18	0.144	1.68	
		6-0720-025	5.9	12.84	3.601	80.46	2.36	73.4	0.57	0.312	5.59	0.135	1.672	
	6-0720-033	7.6	14.22	4.15	102.6	2.54	40.6	0.74	0.316	7.28	0.148	2.329		
	6-0720-038	6.5	12.2	3.508	115.47	2.11	52.6	0.63	0.254	6.32	0.115	1.892		
	6-0720-058	5.6	12.12	3.263	46.2	2.35	83	0.51	0.323	4.18	0.159	1.474		
SILICATE- DOMINANT BIF	4ea-PM05-057	1.9	4.92	1.199	21.97	1.1	117.1	N.D.	0.215	1.07	0.129	0.326		
	4ea-PM05-066	1.1	5.24	1.313	26.43	1.12	66.8	N.D.	0.218	1.11	0.152	0.311		
	4ea-PM06-002	1.6	7.32	1.864	23.25	1.55	20.4	N.D.	0.319	1.26	0.205	0.366		
	4ea-PM06-007	1.4	7.4	1.774	2.16	1.64	20.3	N.D.	0.335	1.16	0.236	0.336		
	4ea-PM06-018	1.7	7.45	1.759	1.21	1.77	14.3	N.D.	0.391	0.97	0.284	0.276		

	Sample ID	REE, LILE, HFSE												
		Y	Yb	Zr	Au	Ag	As	Ba	Co	Cr	Cs	Cu	Ga	
SIF ASSEMBLAGE OXIDE DOMINANT BIF	SIF-PM05-63c	12.8	1.05	N.D.	N.M.	N.D.	1	N.D.	46	30	7	18	2	
	SIF-0720-060c	9.71	0.89	8.5	0.1	N.D.	7	N.D.	N.D.	5	N.D.	14	N.D.	
	SIF-0720-060M	12.36	1.08	N.D.	0.1	N.D.	8	N.D.	N.D.	N.D.	N.D.	20	N.D.	
	SIF-0720-062m	13.64	1.46	4.9	0.0438	N.D.	9	31	N.D.	5	N.D.	29	N.D.	
	SIF-0720-063c	14.16	1.59	N.D.	0.1509	N.D.	9	N.D.	N.D.	7	N.D.	13	N.D.	
	SIF-0720-063m	14.92	1.58	N.D.	0.1509	N.D.	2	N.D.	N.D.	16	N.D.	29	2	
	SIF-0720-071m	13.35	1.11	4	0.02	N.D.	1	40	N.D.	63	N.D.	187	N.D.	
	SIF-0720-072m	10.21	0.81	N.D.	0.02	5	1	N.D.	N.D.	N.D.	N.D.	19	N.D.	
META-ARGILLET	4h-0720-042	18.58	2.12	22	0.08	N.D.	39	49	16	1117	N.D.	140	10	
	4h-0720-043	3.24	0.37	5	0.4096	N.D.	2	62	21	14	N.D.	89	4	
	4h-0720-046	13.1	1.56	47.8	0.13	N.D.	21	89	29	225	N.D.	135	9	
	4h-0720-051	5.74	0.97	52.4	0.1	N.D.	64	164	17	100	N.D.	119	14	
	4h-0720-053a	14.46	1.74	43.1	0.11	N.D.	351	145	28	454	N.D.	195	8	
	4h-0720-053b	18.33	2.09	43.8	0.11	N.D.	68	104	16	80	N.D.	99	7	
	4h-0720-056	13.78	1.41	31.7	0.04	N.D.	37	72	25	103	N.D.	160	3	
	4h-0720-057	11.67	1.17	19.1	0.01	N.D.	3	77	N.D.	42	N.D.	31	3	
	4h-0720-070	19.21	2.39	51.7	0.02	N.D.	46	219	30	63	7	135	9	
4h-0720-071	15.85	1.44	N.D.	5.1	5	66	134	13	51	N.D.	254	9		
QUARTZ- GRUNERITE BIF	4a-0720-012	1.47	0.14	N.D.	0.47	N.D.	N.D.	N.D.	N.D.	N.D.	N.D.	1	N.D.	
	4a-0720-028	3.82	0.36	6.3	0.35	N.D.	36	108	N.D.	12	N.D.	10	N.D.	
	4a-0720-039	4.89	0.59	N.D.	0.11	N.D.	24	31	N.D.	N.D.	N.D.	35	N.D.	
	4a-0720-041	10.36	1.06	12.2	0.03	N.D.	85	68	16	8	10	25	2	
	4a-0720-044	8.54	0.94	9.2	0.23	N.D.	96	69	N.D.	N.D.	N.D.	15	N.D.	
	4a-0720-054c	10.86	1.11	10.8	0.23	N.D.	17	N.D.	N.D.	11	N.D.	15	N.D.	
	4a-0720-054m	16.35	1.63	14	N.M.	N.D.	65	52	N.D.	17	N.D.	46	N.D.	
	4b-PM05-21b	5.7	0.68	8.4	N.M.	N.D.	4	31	N.D.	N.D.	N.D.	17	N.D.	
4b-PM05-21m	5.7	0.68	8.4	N.M.	N.D.	3	N.D.	62	44	11	22	N.D.		
4b-PM05-31m	4.34	0.32	6.8	N.M.	N.D.	N.D.	N.D.	61	43	13	24	N.D.		
4b-PM05-37	2.81	0.3	N.D.	N.M.	N.D.	2	N.D.	82	42	19	17	N.D.		
4b-PM05-38m	1.96	0.19	N.D.	N.M.	N.D.	N.D.	N.D.	83	42	9	20	N.D.		
4b-PM05-39	2.34	0.19	N.D.	N.M.	N.D.	1	N.D.	87	44	18	22	N.D.		
4b-PM05-40m	4.26	0.4	N.D.	N.M.	N.D.	1	N.D.	76	41	8	23	N.D.		
4b-PM06-042	24.6	2.83	N.D.	0.057	55	0	0	43	183	N.D.	127	16		
4b-PM05-101	3.12	0.36	N.D.	N.M.	N.D.	N.M.	N.M.	N.M.	N.M.	N.M.	N.M.	N.M.		
4b-PM06-28m	3.57	0.39	N.D.	0.3593	N.D.	46	N.D.	81	58	N.D.	25	N.D.		
4b-PM06-28m	13.8	1.35	24.2	0.3593	N.D.	17	115	N.D.	48	N.D.	48	3		
4b-0720-004m	15.34	1.37	11.5	0.1661	N.D.	25	36	N.D.	8	N.D.	41	2		
4b-0720-040m	16.87	1.52	10.4	N.M.	N.D.	7	43	N.D.	9	20	25	2		
4b-0720-055m	12.38	0.92	21.7	0	N.D.	N.D.	101	N.D.	62	8	87	5		
4b-0720-006	14.2	1.22	54.3	N.M.	N.D.	12	227	16	110	91	58	10		
4b-0720-067m	11.68	0.93	13.5	0.0454	N.D.	20	N.D.	N.D.	17	N.D.	33	N.D.		
NIF ASSEMBLAGE OXIDE DOMINANT BIF (MAGNETITE)	4b-PM05-006	1.82	0.2	7	N.M.	N.D.	10	N.D.	13	35	9	6	N.D.	
	4b-PM05-012	0.48	0.05	5.5	N.M.	N.D.	1	84	N.D.	33	7	N.D.	N.D.	
	4b-PM05-018	0.84	0.08	6.9	N.M.	N.D.	N.D.	N.D.	N.D.	16	11	1	N.D.	
	4b-PM05-028b	2.58	0.25	5.4	N.M.	N.D.	5	N.D.	N.D.	14	15	N.D.	N.D.	
	4b-PM05-031b	1.36	0.14	N.D.	N.M.	N.D.	1	N.D.	20	24	9	8	N.D.	
	4b-PM05-038b	0.3	0.04	N.D.	N.M.	N.D.	N.D.	N.D.	N.D.	16	9	2	N.D.	
	4b-PM05-040b	6.34	0.6	N.D.	N.M.	N.D.	1	N.D.	32	25	N.D.	11	N.D.	
	4b-PM05-043	1.87	0.18	N.D.	N.M.	N.D.	N.D.	N.D.	N.D.	N.D.	N.D.	3	N.D.	
	4b-PM05-065c	0.63	0.06	6.4	5.5638	N.D.	6	74	15	4	N.D.	8	3	
	4b-PM05-067c	5.55	0.43	9.9	0.0454	N.D.	21	N.D.	14	7	N.D.	13	N.D.	
	4b-PM06-028c	3.64	0.26	6.4	0.3593	N.D.	5	N.D.	16	62	N.D.	5	N.D.	
	4b-0720-005c	7.03	0.69	12.4	0.039	N.D.	64	36	23	6	N.D.	24	2	
	4b-0720-053c	3.19	0.25	5.1	0.01	N.D.	1	N.D.	14	9	N.D.	8	N.D.	
	GARNET- QUARTZITE	6-0720-024	9.78	0.95	152.8	0.04	2	2	383	14	63	N.D.	18	17
		6-0720-025	9.25	0.9	142.5	0.01	2	2	306	13	61	N.D.	24	16
6-0720-033		9.68	0.98	190.5	NM	4	4	465	12	48	8	1	19	
6-0720-038		7.32	0.78	160.9	0.02	2	2	290	13	39	N.D.	7	15	
6-0720-058		10.18	1.04	136.7	NM	6	6	264	19	94	N.D.	3	17	
SILICATE- DOMINANT BIF	4ea-PM05-057	9.64	0.85	31.4	N.M.	N.D.	2	85	14	66	N.D.	70	11	
	4ea-PM05-066	11.85	1	37	13100	6	13	158	15	89	N.D.	132	12	
	4ea-PM06-002	16.09	1.33	44.3	917.5	N.D.	151	122	N.D.	97	N.D.	125	10	
	4ea-PM06-007	16.91	1.56	34.6	215.5	N.D.	23	31	N.D.	66	N.D.	31	5	
	4ea-PM06-018	21.05	1.9	42	8486.7	N.D.	1	N.D.	N.D.	79	N.D.	27	10	

	Sample ID	TRACE										
		K	Mn	Mo	Na	Nb	Ni	P	Pb	Rb	Sb	Sc
SIF ASSEMBLAGE OXIDE DOMINANT BIF	SIF-PM05-63c	N.D.	1693	N.D.	N.D.	2	14	1188	N.D.	N.D.	N.D.	13
	SIF-0720-060c	65	1994	N.D.	78	N.D.	5	890	14	N.D.	N.D.	N.D.
	SIF-0720-060M	34	2173	N.D.	59	N.D.	18	602	8	N.D.	N.D.	N.D.
	SIF-0720-062m	598	4607	N.D.	125	N.D.	19	1152	8	3	N.D.	6
	SIF-0720-063c	111	8689.00	N.D.	63	N.D.	10	1052	N.D.	N.D.	N.D.	N.D.
	SIF-0720-063m	106	4568	N.D.	N.D.	N.D.	26	1652	N.D.	2	N.D.	N.D.
	SIF-0720-071m	26	3711	N.D.	46	N.D.	44	1431	6	2	6	N.D.
SIF-0720-072m	28	550	N.D.	62	2	16	1393	5	N.D.	N.D.	6	
META-ARGILLET	4h-0720-042	3837	3837	4	735	2	89	1633	12	18	N.D.	15
	4h-0720-043	362	2977	N.D.	550	N.D.	48	60	5	N.D.	N.D.	N.D.
	4h-0720-046	3397	3397	2	723	2	103	450	11	17	N.D.	10
	4h-0720-051	6574	1003	3	344	4	53	155	20	24	5	15
	4h-0720-053a	15544	4364	4	987	4	127	776	33	100	6	12
	4h-0720-053b	13330	13330	N.D.	840	3	61	448	18	99	N.D.	7
	4h-0720-056	7370	7370	N.D.	424	3	84	414	12	26	N.D.	8
	4h-0720-057	2029	3397	N.D.	970	N.D.	28	705	N.D.	6	N.D.	7
	4h-0720-070	40766	2916	2	1310	3	96	632	18	61	N.D.	10
4h-0720-071	2769	3634	N.D.	1222	N.D.	66	972	10	7	N.D.	20	
QUARTZ- GRUNERTIE BIF	4a-0720-012	23	1811	N.D.	N.D.	N.D.	5	64	N.D.	N.D.	N.D.	N.D.
	4a-0720-028	128	4759	N.D.	110	N.D.	10	49	N.D.	N.D.	N.D.	N.D.
	4a-0720-039	486	8275	N.D.	216	N.D.	16	393	N.D.	3	N.D.	7
	4a-0720-041	1453	10547	N.D.	120	N.D.	27	820	N.D.	7	N.D.	N.D.
	4a-0720-044	418	5000	N.D.	67	N.D.	18	673	N.D.	4	N.D.	N.D.
	4a-0720-054c	438	7267	N.D.	144	N.D.	17	719	N.D.	2	N.D.	N.D.
	4a-0720-054m	3170	19385	N.D.	209	2	43	462	8	9	N.D.	11
NIF ASSEMBLAGE OXIDE DOMINANT BIF (MAGNETITE)	4b-PM05-21b	213	1529	N.D.	265	2	25	965	N.D.	3	N.D.	N.D.
	4b-PM05-21m	702	1750	N.D.	N.D.	N.D.	17	838	N.D.	13	N.D.	12
	4b-PM05-31m	25	2251	N.D.	N.D.	2	16	2333	5	N.D.	7	15
	4b-PM05-37	N.D.	3162	N.D.	N.D.	2	31	607	N.D.	N.D.	N.D.	14
	4b-PM05-38m	N.D.	2497	N.D.	N.D.	N.D.	17	105	N.D.	N.D.	N.D.	15
	4b-PM05-39	N.D.	3927	N.D.	N.D.	N.D.	13	146	N.D.	2	N.D.	18
	4b-PM05-40m	N.D.	3207	N.D.	N.D.	2	14	1207	N.D.	N.D.	N.D.	18
	allb-PM06-042	1406	2052	N.D.	14396	N.D.	119	492	0	N.D.	0	43
	4b-PM05-101	N.M.	N.M.	N.D.	N.M.	N.M.	N.M.	N.M.	N.M.	N.M.	N.M.	N.M.
	4b-PM06-28m	71	1350	N.D.	N.D.	2	25	1059	7	N.D.	N.D.	14
	4b-PM06-28m	7218	10856	N.D.	401	3	35	902	5	25	N.D.	11
	4b-0720-004m	2279	9513	N.D.	304	2	24	1313	6	11	N.D.	9
	4b-0720-040m	1629	4298	N.D.	248	N.D.	24	1778	N.D.	15	N.D.	8
	4b-0720-055m	14039	5308	N.D.	6537	2	47	769	7	76	N.D.	9
	4b-0720-006	23590	5271	N.D.	9849	3	61	520	9	230	N.D.	18
	4b-0720-067m	2183	9386	N.D.	895	2	24	1528	N.D.	8	N.D.	9
NIF ASSEMBLAGE OXIDE DOMINANT BIF (QUARTZ)	4b-PM05-006	30	1591	N.D.	N.D.	N.D.	9	594	N.D.	N.D.	N.D.	N.D.
	4b-PM05-012	34	1593	N.D.	N.D.	N.D.	18	587	N.D.	N.D.	N.D.	N.D.
	4b-PM05-018	N.D.	193	N.D.	N.D.	N.D.	13	N.D.	N.D.	N.D.	N.D.	N.D.
	4b-PM05-028b	N.D.	582	N.D.	N.D.	N.D.	3	16	N.D.	N.D.	N.D.	N.D.
	4b-PM05-031b	12	2278	N.D.	N.D.	N.D.	12	355	N.D.	N.D.	N.D.	7
	4b-PM05-038b	N.D.	1116	N.D.	N.D.	N.D.	10	N.D.	N.D.	N.D.	N.D.	N.D.
	4b-PM05-040b	N.D.	4298	N.D.	N.D.	N.D.	8	1344	N.D.	N.D.	N.D.	8
	4b-PM05-043	104	712	N.D.	N.D.	N.D.	14	128	N.D.	N.D.	N.D.	N.D.
	4b-PM05-065c	8004	634	N.D.	2064	N.D.	15	127	6	26	N.D.	N.D.
	4b-PM05-067c	1429	3391	N.D.	310	N.D.	9	422	5	5	N.D.	N.D.
	4b-PM06-028c	530	1240	N.D.	860	N.D.	16	566	N.D.	2	N.D.	N.D.
	4b-0720-005c	2931	3549	N.D.	413	N.D.	20	426	5	11	N.D.	N.D.
4b-0720-053c	435	2379	N.D.	105	N.D.	5	242	N.D.	2	N.D.	N.D.	
GARNET- QUARTZITE	6-0720-024	37212	1472	N.D.	1534	6	29	418	11	107	N.D.	14
	6-0720-025	39790	866	N.D.	14801	6	30	366	15	97	N.D.	13
	6-0720-033	51690	1237	N.D.	2938	7	28	422	9	134	N.D.	11
	6-0720-038	51074	575	N.D.	11982	6	25	345	13	113	N.D.	10
	6-0720-058	30983	1381	N.D.	1676	6	53	558	8	106	N.D.	17
SILICATE- DOMINANT BIF	4ea-PM05-057	4465	1152	N.D.	3214	2	44	454	8	21	N.D.	12
	4ea-PM05-066	6546	4233	N.D.	1530	N.D.	38	448	N.D.	30	N.D.	13
	4ea-PM06-002	4410	5797	N.D.	428	3	53	723	N.D.	27	N.D.	14
	4ea-PM06-007	333	6425	N.D.	3705	2	53	972	N.D.	2	N.D.	13
	4ea-PM06-018	138	2304	N.D.	163	2	41	785	6	2	N.D.	17

		TRACE													
		Sample ID	Se	Sn	Sr	Ta	Th	Ti	U	V	W	Y	Zn	Zr	TOTAL
SIF ASSEMBLAGE OXIDE DOMINANT BIF	SIF-PM05-63c	N.D.	5	9	N.D.	N.D.	20	N.D.	N.D.	26	15	34	N.D.	100.15	
	SIF-0720-060c	N.D.	N.D.	55	N.D.	N.D.	N.D.	N.D.	N.D.	55	10	34	4	100.36	
	SIF-0720-060M	N.D.	N.D.	17	N.D.	4	N.D.	N.D.	N.D.	6	61	16	58	3	99.91
	SIF-0720-062m	N.D.	N.D.	25	N.D.	6	40	N.D.	N.D.	9	36	17	57	6	99.19
	SIF-0720-063c	N.D.	N.D.	16	N.D.	4	N.D.	N.D.	N.D.	4	46	16	38	3	101.26
	SIF-0720-063m	N.D.	N.D.	12	N.D.	N.D.	N.D.	N.D.	N.D.	9	24	18	30	3	99.97
	SIF-0720-071m	N.D.	12	26	N.D.	4	N.D.	N.D.	N.D.	8	28	18	75	3	99.91
SIF-0720-072m	N.D.	8	14	10	N.D.	N.D.	N.D.	N.D.	7	50	12	15	3	100.84	
META-ARGILLET	4h-0720-042	2	8	22	N.D.	4	974	N.D.	N.D.	94	18	22	688	26	98.82
	4h-0720-043	2	N.D.	14	N.D.	4	86	N.D.	N.D.	21	48	3	143	4	99.77
	4h-0720-046	N.D.	8	20	N.D.	6	1090	N.D.	N.D.	51	34	15	138	55	99.16
	4h-0720-051	4	N.D.	17	N.D.	9	1948	N.D.	N.D.	108	24	7	97	61	99.69
	4h-0720-053a	11	8	26	N.D.	8	1302	N.D.	N.D.	73	17	15	237	46	100.71
	4h-0720-053b	2	N.D.	22	N.D.	6	1041	N.D.	N.D.	50	33	19	278	47	100.02
	4h-0720-056	3	N.D.	43	N.D.	6	780	N.D.	N.D.	36	26	15	138	33	98.23
	4h-0720-057	N.D.	N.D.	79	N.D.	4	392	N.D.	N.D.	21	25	12	70	11	98.49
	4h-0720-070	4	N.D.	40	N.D.	8	1245	N.D.	N.D.	64	22	19	299	53	99.94
4h-0720-071	27	6	82	N.D.	N.D.	140	N.D.	N.D.	130	24	20	72	N.D.	88.36	
QUARTZITE- GRUNERITE BIF	4a-0720-012	N.D.	N.D.	9	N.D.	N.D.	N.D.	N.D.	N.D.	43	1	13	N.D.	99.41	
	4a-0720-028	N.D.	N.D.	21	N.D.	4	N.D.	N.D.	N.D.	43	4	22	4	100.38	
	4a-0720-039	N.D.	N.D.	14	N.D.	4	13	N.D.	N.D.	5	24	6	54	N.D.	99.98
	4a-0720-041	N.D.	6	34	N.D.	6	191	N.D.	N.D.	13	22	12	75	6	99.69
	4a-0720-044	N.D.	N.D.	16	N.D.	5	70	N.D.	N.D.	9	26	10	38	5	99.86
	4a-0720-054c	N.D.	N.D.	19	N.D.	7	170	N.D.	N.D.	13	29	12	55	8	99.81
	4a-0720-054m	N.D.	6	78	N.D.	N.D.	377	N.D.	N.D.	25	26	20	87	14	99.09
NIF ASSEMBLAGE OXIDE DOMINANT BIF (MAGNETITE)	4b-PM05-21b	N.D.	10	10	17	6	13	N.D.	N.D.	10	17	12	26	12	99.22
	4b-PM05-21m	N.D.	12	4	N.D.	N.D.	135	N.D.	N.D.	6	16	6	23	7	99.33
	4b-PM05-31m	N.D.	13	6	N.D.	5	96	N.D.	N.D.	8	22	6	15	7	98.84
	4b-PM05-37	N.D.	5	N.D.	N.D.	N.D.	32	N.D.	N.D.	21	3	15	3	99	
	4b-PM05-38m	N.D.	11	N.D.	N.D.	4	34	N.D.	N.D.	N.D.	N.D.	2	17	N.D.	99.42
	4b-PM05-39	N.D.	12	N.D.	N.D.	N.D.	33	4	N.D.	N.D.	N.D.	2	25	N.D.	98.62
	4b-PM05-40m	N.D.	15	N.D.	11	8	20	N.D.	N.D.	20	6	18	N.D.	N.D.	98.77
	altb-PM06-042	N.D.	N.D.	N.D.	N.D.	N.D.	6464	0.085	286	13	N.D.	N.D.	108	68.8	99.97
	4b-PM05-101	N.M.	N.M.	N.M.	N.M.	N.M.	N.M.	N.M.	N.M.	N.M.	N.M.	N.M.	N.M.	N.M.	100
	4b-PM06-28m	N.D.	9	N.D.	11	5	36	N.D.	N.D.	6	15	5	25	3	99.11
	4b-PM06-28m	N.D.	11	63	N.D.	8	1019	N.D.	N.D.	38	21	17	78	25	101.34
	4b-0720-004m	N.D.	N.D.	39	11	5	372	N.D.	N.D.	16	14	18	47	9	100.62
	4b-0720-040m	N.D.	6	35	N.D.	5	214	N.D.	N.D.	16	13	20	40	9	101.18
	4b-0720-055m	N.D.	N.D.	25	N.D.	7	1204	N.D.	N.D.	75	47	15	50	19	100.27
	4b-0720-006	57	N.D.	97	N.D.	4	3439	N.D.	N.D.	136	23	17	70	59	100.51
	4b-0720-067m	N.D.	10	29	11	7	434	N.D.	N.D.	23	67	12	41	11	100.74
NIF ASSEMBLAGE OXIDE DOMINANT BIF (QUARTZ)	4b-PM05-006	N.D.	N.D.	N.D.	N.D.	N.D.	18	N.D.	N.D.	17	2	17	N.D.	98.82	
	4b-PM05-012	N.D.	N.D.	N.D.	N.D.	N.D.	12	N.D.	N.D.	12	N.D.	13	N.D.	98.6	
	4b-PM05-018	N.D.	N.D.	N.D.	N.D.	N.D.	10	N.D.	N.D.	18	1	9	3	99.18	
	4b-PM05-028b	N.D.	N.D.	4	N.D.	N.D.	N.D.	N.D.	N.D.	18	3	11	N.D.	99.49	
	4b-PM05-031b	N.D.	N.D.	2	N.D.	N.D.	N.D.	N.D.	N.D.	13	1	17	N.D.	99.34	
	4b-PM05-038b	N.D.	N.D.	N.D.	N.D.	N.D.	10	N.D.	N.D.	26	N.D.	12	N.D.	98.96	
	4b-PM05-040b	N.D.	N.D.	N.D.	N.D.	5	14	N.D.	N.D.	18	7	34	N.D.	99.62	
	4b-PM05-043	N.D.	N.D.	N.D.	N.D.	N.D.	10	N.D.	N.D.	4	33	1	9	9	100
	4b-PM05-065c	N.D.	N.D.	8	N.D.	N.D.	35	N.D.	N.D.	23	59	1	20	3	101.08
	4b-PM05-067c	N.D.	N.D.	22	N.D.	N.D.	103	N.D.	N.D.	4	54	6	18	5	100.48
	4b-PM06-028c	N.D.	N.D.	33	N.D.	N.D.	45	N.D.	N.D.	5	61	4	17	4	100.53
	4b-0720-005c	N.D.	N.D.	21	N.D.	5	229	N.D.	N.D.	8	95	7	42	9	101.01
	4b-0720-053c	N.D.	N.D.	13	N.D.	5	23	N.D.	N.D.	5	57	3	18	4	100.06
	GARNET- QUARTZITE	6-0720-024	N.D.	N.D.	68	N.D.	6	2813	N.D.	N.D.	79	17	8	53	160
6-0720-025		N.D.	N.D.	71	N.D.	8	2741	N.D.	N.D.	74	16	8	64	152	99.96
6-0720-033		N.D.	N.D.	44	N.D.	8	2882	N.D.	N.D.	62	13	7	60	201	99.96
6-0720-038		N.D.	N.D.	50	N.D.	8	2580	N.D.	N.D.	54	16	7	60	168	99.97
6-0720-058	N.D.	N.D.	84	N.D.	8	3267	N.D.	N.D.	104	15	8	77	143	99.97	
SILICATE DOMINANT BIF	4ea-PM05-057	5	N.D.	118	N.D.	5	1246	N.D.	N.D.	103	26	10	70	21	99.99
	4ea-PM05-066	11	6	72	N.D.	10	1498	N.D.	N.D.	82	42	13	64	32	99.12
	4ea-PM06-002	7	N.D.	22	10	8	2129	N.D.	N.D.	99	25	20	103	39	99.84
	4ea-PM06-007	N.D.	8	21	N.D.	5	1551	N.D.	N.D.	82	22	20	85	31	99.88
4ea-PM06-018	N.D.	N.D.	15	N.D.	N.D.	2586	N.D.	N.D.	124	23	23	80	41	99.47	

		MAJOR Elements										
Sample ID		SiO <sub>2</sub>	Al <sub>2</sub> O <sub>3</sub>	TiO <sub>2</sub>	Fe <sub>2</sub> O <sub>3</sub>	FeO	MgO	CaO	Na <sub>2</sub> O	K <sub>2</sub> O	MnO	P <sub>2</sub> O <sub>5</sub>
SILICATE-DOMINANT BIF	4ea-PM06-043	46.62	7.65	0.36	2.6	26.81	4.46	7.72	0.23	0.1	0.97	0.09
	4ea-0620-UG04	61.12	4.73	0.19	N.D.	24.19	1.86	2.34	0.42	0.59	0.6	0.13
	4ea-0720-044	46.07	6.51	0.32	11.9	27.65	3.06	1.6	0.5	0.59	0.35	0.1
	4ea-0720-061	46.57	6.86	0.35	7.91	30.94	3.62	1.19	0.12	0.03	0.5	0.15
	4ea-0720-065	46.14	9.43	0.56	7.36	27.55	4.06	2.4	0.09	0.5	0.54	0.15
	4ea-0720-067	41.82	9.58	0.61	8.84	30.7	3.85	1.58	0.06	0.12	0.67	0.14
	4ea-0720-068	46.84	7.67	0.35	2.99	30.36	3	3.77	0.31	0.62	0.85	0.1
	4ea-0720-069	43.05	13.97	1.55	6.8	20.98	4.12	4.25	3.27	0.12	0.26	0.18
	4ea-0830-001	43.53	10.47	0.54	4.42	30.49	3.97	3.37	0.09	0.08	0.52	0.17
	4ea-0830-002	39.91	8.01	0.39	6.63	34.48	3.81	2.24	0.16	1.26	0.46	0.18
4ea-0830-004	36.96	10.58	0.69	16.05	28.13	3.02	1.53	0.07	0.04	0.55	0.05	
HORNBLende-GARNET SCHIST	4e-0720-018	47.01	12.15	0.54	3.5	19.65	4.08	7.87	0.37	1.23	0.6	0.08
	4e-0720-019	40.64	8.22	0.38	18.64	22.47	2.5	0.86	N.D.	1.74	0.61	0.17
	4e-0720-022	50.02	13.19	0.54	8.32	15.51	3.18	6.34	0.18	0.39	0.78	0.07
	4e-0720-023	50.99	13.5	0.63	5.25	15.59	3.48	6.31	0.33	0.74	0.65	0.09
	4e-0720-034a	46.77	10.86	0.44	4.86	21.66	4.05	7.57	0.4	0.13	0.76	0.1
	4e-0720-034b	48.56	11.74	0.56	7.47	17.81	3.78	5.89	0.17	0.79	1.26	0.14
	4e-0720-047	45.31	16.04	1.02	2.05	14.77	4.99	7.57	2.82	1.76	0.25	0.09
	4e-0720-048	49.64	14.78	0.57	2.23	19.07	2.54	1.38	1.47	5.08	0.17	0.03
BIOTITE-GARNET SCHIST	4f-0720-001	52.04	18.1	0.96	N.D.	20.67	2.72	3.8	0.28	3.19	0.43	0.11
	4f-0720-002	51.56	20.05	0.96	5.44	9.92	2.52	2.71	0.52	4.22	0.27	0.06
	4f-0720-008	46.77	19.74	1.04	1.83	15.06	2.25	5.13	0.28	4.46	0.36	0.06
	4f-0720-009	45.2	16.29	0.96	12.52	15.34	2.51	1.85	0.04	3.64	0.66	0.06
	4f-0720-011	53.09	21.44	1.12	3.18	11.03	2.08	1.5	0.35	4.27	0.45	0.07
	4f-0720-027a	52.55	21.59	1.08	7.77	7.52	3.69	0.34	0.23	3.64	0.08	0.07
	4f-PM05-050	38.74	6.19	0.29	20.12	24.36	3.04	1.59	0.19	2.64	0.5	0.18
METASOMATIC BIOTITE-GARNET SCHIST	bt.garn-0720-001	39.39	15.23	1.73	3.22	20.67	5.47	5.95	0.77	3.73	0.26	0.09
	bt.garn-0720-007	35.09	15.48	1.52	7.97	22.68	5.01	4.19	0.46	4.31	0.18	0.19
	bt.garn-0720-017	37.7	21.84	1.02	27.03	0.3	4.41	2.3	0.62	4.28	0.15	0.05
	bt.garn-0720-020	34.7	19.15	0.8	32.89	0.33	4.7	1.45	0.44	4.6	0.18	0.02
	bt.garn-0720-049	31.89	13.48	0.45	41.86	0.24	3.8	1.93	0.13	4.8	0.21	0.09
	bt.garn-0720-054	26.87	11.2	0.63	19.83	26.87	4.27	2.45	0.28	4.19	0.22	0.14
TRENCH METASOMATIC BIF	alt-PM05-005	39.08	0.08	0.02	51.89	20.54	4.99	1.32	0.02	0	0.91	0.96
	alt-PM05-009	48.33	0.12	0.03	46.37	14.75	4.84	0.22	0	0.01	1.11	0.07
	alt-PM05-010	46.26	0.14	0.01	45.77	7.51	4.69	1.84	0.02	0.02	1.2	0.13
	alt-PM05-013	41.9	0.26	0.02	50.19	12.53	5.71	0.72	0.02	0.04	1.31	0.27
	alt-PM05-019	47.38	0.15	0.03	45.3	8.88	4.82	1.18	0.25	0.03	1.24	0.09
	alt-PM05-027	45.46	0.12	0.04	46	13.29	4.95	1.68	0.02	0.01	0.98	0.26
	alt-PM05-032	39.78	0.34	0.03	50.82	15.18	4.35	2.66	0.03	0.06	0.76	0.13
	alt-PM05-045	47.33	0.16	0.02	44.41	11.07	7.17	0.62	0.02	0.03	0.63	0.08
	alt-PM05-048	62.55	11.12	0.62	8.45	4.25	4.36	7.74	1.52	0.31	0.12	0.06
alt-PM05-049	63.83	7.81	0.88	8.62	4.33	5.7	7.12	1.04	0.41	0.15	0.03	
CHL-SCHIST	tb-PM05-007	29.94	15.69	0.66	39.78	3.45	7.88	0.11	0.04	0.1	0.07	0.03
	tb-PM05-024	28.53	16.91	0.82	40.91	11.33	4.5	0.15	0.11	0.82	0.1	0.05
	tb-PM05-100	27.75	16.31	0.83	42.51	10.86	4.61	0.14	0.04	0.39	0.12	0.04

		REE, LILE, HFSE											
		Sample ID	LOI	Ce	Cs	Dy	Er	Eu	Gd	Hf	Ho	La	Lu
SILICATE-DOMINANT BIF	4ea-PM06-043	0.05	15.25	0.012	2.124	1.436	0.728	1.959	1.2	0.472	8.1	0.221	
	4ea-0620-UG04	2.85	9.88	1.624	1.313	0.886	0.48	1.31	0.6	0.298	5.74	0.126	
	4ea-0720-044	0.05	8.95	2.017	1.571	1.11	0.51	1.417	1	0.362	5.01	0.183	
	4ea-0720-061	0.05	13.68	0.873	2.178	1.494	0.662	2.097	1	0.494	7.35	0.233	
	4ea-0720-065	0.05	11.02	1.44	3.293	2.271	0.724	2.725	1.5	0.75	5.2	0.342	
	4ea-0720-067	0.05	13.23	1.045	2.756	1.918	0.74	2.451	1.5	0.628	7.04	0.305	
	4ea-0720-068	0.05	15.62	11.09	1.831	1.291	0.66	1.757	1.4	0.424	8.89	0.2	
	4ea-0720-069	0.05	18.53	0.768	5.989	3.684	1.247	5.256	3	1.281	7.71	0.507	
	4ea-0830-001	0.05	22.29	0.201	3.303	2.165	0.912	3.12	1.9	0.729	11.51	0.308	
	4ea-0830-002	0.05	12.51	4.328	1.96	1.456	0.877	1.819	1.3	0.469	7.1	0.229	
4ea-0830-004	0.05	23.48	0.095	2.914	2.145	0.897	2.553	2.6	0.681	13.29	0.337		
HORNBLENDE-GARNET SCHIST	4e-0720-018	N.D.	18.04	0.859	2.976	1.921	0.81	2.674	1.6	0.632	9.14	0.296	
	4e-0720-019	1.16	17.42	6.944	2.593	1.735	0.683	2.502	1.2	0.574	10.65	0.222	
	4e-0720-022	N.D.	12.3	0.454	3.242	2.204	0.744	2.676	1.5	0.719	5.54	0.362	
	4e-0720-023	0.37	15.04	0.666	3.051	1.998	0.818	2.758	2	0.652	6.89	0.308	
	4e-0720-034a	N.D.	19.79	0.045	2.78	1.857	0.869	2.593	1.6	0.606	10.15	0.284	
	4e-0720-034b	N.D.	16.12	0.758	3.404	2.245	1.019	3.144	1.4	0.74	7.96	0.321	
	4e-0720-047	1.61	10.42	20.89	3.823	2.482	0.839	3.151	1.9	0.828	4.38	0.366	
	4e-0720-048	0.66	15.04	4.932	1.499	1.139	0.484	1.375	2.5	0.349	8.55	0.192	
BIOTITE-GARNET SCHIST	4f-0720-001	0.05	20	13.065	5.512	3.445	1.197	4.833	3.6	1.174	8.98	0.463	
	4f-0720-002	0.61	14.16	3.734	2.637	1.79	0.699	2.183	2.5	0.584	6.45	0.285	
	4f-0720-008	0.56	8.92	3.589	2.929	1.982	0.734	2.277	2.2	0.655	3.38	0.319	
	4f-0720-009	N.D.	8.15	2.957	2.919	2.152	0.627	2.172	2.2	0.665	3.71	0.363	
	4f-0720-011	1.09	14.94	2.625	3.082	2.133	0.736	2.468	2.7	0.673	6.7	0.334	
	4f-0720-027a	0.54	8.46	1.463	1.877	1.253	0.381	1.871	2.7	0.405	3.03	0.202	
	4f-PM05-050	N.D.	16.36	5.619	2.051	1.374	0.749	2.03	1	0.469	10.97	0.189	
	4f-PM05-050	N.D.	16.36	5.619	2.051	1.374	0.749	2.03	1	0.469	10.97	0.189	
METASOMATIC BIOTITE-GARNET SCHIST	bt.gam-0720-001	0.86	18.33	2.635	3.274	2.042	0.933	2.877	2.6	0.692	8.45	0.3	
	bt.gam-0720-007	0.32	22.74	11.018	7.101	4.371	1.411	6.397	3.1	1.494	10.1	0.587	
	bt.gam-0720-017	0.2	14.83	2.607	2.564	2.022	0.534	1.886	3.6	0.611	6.71	0.354	
	bt.gam-0720-020	0.48	5.48	12.618	2.108	1.479	0.455	1.586	1.4	0.474	2.37	0.224	
	bt.gam-0720-049	0.82	23.66	15.265	1.422	1.056	0.603	1.558	2.9	0.329	13.74	0.169	
	bt.gam-0720-054	N.D.	16.68	19.764	2.34	1.622	0.771	2.294	1.5	0.526	9.65	0.245	
	bt.gam-0720-054	N.D.	16.68	19.764	2.34	1.622	0.771	2.294	1.5	0.526	9.65	0.245	
TRENCH METASOMATIC BIF	alt-PM05-005	0.71	18.91	0.148	2.238	1.464	1.628	2.36	N.D.	0.499	11.44	0.183	
	alt-PM05-009	0	2.47	0.392	0.554	0.438	0.259	0.421	N.D.	0.133	1.23	0.077	
	alt-PM05-010	0	4.84	0.274	1.064	0.815	0.473	0.863	N.D.	0.25	2.54	0.14	
	alt-PM05-013	0	9.23	0.721	1.551	1.072	0.793	1.428	N.D.	0.353	4.8	0.179	
	alt-PM05-019	0	4.24	0.256	0.868	0.647	0.437	0.718	N.D.	0.203	2.1	0.119	
	alt-PM05-027	0	9.91	0.447	1.802	1.214	0.829	1.683	N.D.	0.41	5.04	0.172	
	alt-PM05-032	1.04	5.53	2.802	1.025	0.795	0.502	0.899	0.2	0.246	3.44	0.125	
	altb-PM05-045	0	3.21	0.516	0.25	0.215	0.168	0.216	0	0.061	1.84	0.06	
	alt-PM05-048	3.09	22.06	3.098	3.336	1.921	1.309	3.062	3.4	0.669	9.16	0.31	
alt-PM05-049	4.23	10.93	3.146	2.502	1.512	0.959	2.195	2.3	0.517	4.32	0.234		
CHL-SCHIST	tb-PM05-007	5.58	4.3	1.473	1.675	1.167	0.366	1.231	1	0.364	1.63	0.204	
	tb-PM05-024	7.04	2.5	194.623	0.521	0.318	0.21	0.466	1.3	0.105	0.88	0.048	
	altb-PM05-100	7.21	1.17	76.598	0.225	0.157	0.063	0.199	1.4	0.047	0.38	0.035	

		REE, LILE, HFSE										
Sample ID		Nb	Nd	Pr	Rb	Sm	Sr	Ta	Tb	Th	Tm	U
SILICATE-DOMINANT BIF	4ea-PM06-043	2.1	6.99	1.737	0.56	1.6	20.7	N.D.	0.319	1.5	0.21	0.464
	4ea-0620-UG04	0.5	4.6	1.1	22.15	1.01	78.5	N.D.	0.2	0.64	0.123	0.215
	4ea-0720-044	1.6	4.41	1.038	48.37	1.06	127.9	N.D.	0.228	1.2	0.166	0.358
	4ea-0720-061	1.6	6.61	1.611	2.83	1.58	29.9	N.D.	0.323	1.1	0.221	0.333
	4ea-0720-065	2.6	5.71	1.358	24.01	1.7	21.5	N.D.	0.474	2.09	0.331	0.658
	4ea-0720-067	2.4	6.85	1.613	7.04	1.74	14.3	N.D.	0.408	1.45	0.286	0.452
	4ea-0720-068	2	6.97	1.75	30.85	1.46	57.1	N.D.	0.274	1.73	0.189	0.47
	4ea-0720-069	4.8	13.03	2.68	8.45	3.93	83.7	0.3	0.907	0.83	0.524	0.22
	4ea-0830-001	2.9	10.95	2.625	3.68	2.44	41.1	0.23	0.509	2.05	0.307	0.592
	4ea-0830-002	1.9	5.86	1.423	82.44	1.35	32.6	N.D.	0.289	1.44	0.218	0.309
4ea-0830-004	2.5	10.46	2.614	1.75	2.12	10.3	0.24	0.418	2.86	0.321	0.745	
HORNBLENDE-GARNET SCHIST	4e-0720-018	2.8	8.93	2.161	24.38	2.15	15.8	0.21	0.446	1.88	0.284	0.615
	4e-0720-019	2.1	8.3	2.016	94.91	1.86	14	N.D.	0.392	1.56	0.237	0.462
	4e-0720-022	2.4	7.27	1.633	7.32	2.04	38.6	N.D.	0.471	1.05	0.336	0.322
	4e-0720-023	3.4	8.35	1.948	20.48	2.17	27.1	0.26	0.453	2.05	0.289	0.658
	4e-0720-034a	2.7	9.51	2.35	0.48	2.16	19.4	0.22	0.419	2.11	0.273	0.662
	4e-0720-034b	2.5	8.89	2.058	26.54	2.31	14.5	0.18	0.511	1.34	0.318	0.423
	4e-0720-047	3	7.12	1.523	72.33	2.26	133.4	0.2	0.551	0.74	0.362	0.21
	4e-0720-048	3.9	6.05	1.64	146.65	1.3	40.5	0.3	0.224	3.12	0.176	0.928
BIOTITE-GARNET SCHIST	4f-0720-001	4.6	13.09	2.771	150	3.68	57.1	0.38	0.819	1.42	0.481	0.452
	4f-0720-002	4.4	7.6	1.772	38.41	1.9	39.5	0.32	0.376	1.94	0.27	0.683
	4f-0720-008	4	5.49	1.219	116.39	1.69	117.9	0.26	0.418	1.47	0.306	0.477
	4f-0720-009	4.2	4.96	1.089	67.85	1.53	1.9	0.29	0.4	1.21	0.328	0.559
	4f-0720-011	4.5	8.3	1.896	42.4	2.15	16	0.28	0.441	1.71	0.323	0.601
	4f-0720-027a	4.8	6.02	1.239	9.89	1.77	13.1	0.34	0.29	1.12	0.189	0.607
	4f-PM05-050	1.7	7.3	1.81	90.69	1.52	30.9	N.D.	0.305	1.3	0.189	0.401
METASOMATIC BIOTITE-GARNET SCHIST	bt.garn-0720-001	4.3	9.72	2.264	20.05	2.44	35	0.3	0.493	2.07	0.293	0.588
	bt.garn-0720-007	4.6	15.53	3.184	150	4.52	40.2	0.34	1.077	1	0.616	0.317
	bt.garn-0720-017	6.8	7.6	1.841	23.99	1.7	114.3	0.5	0.343	2.85	0.325	1.487
	bt.garn-0720-020	1.8	3.77	0.775	76.33	1.06	20.5	N.D.	0.294	0.26	0.22	0.277
	bt.garn-0720-049	2.9	9.46	2.555	150	1.65	33.9	0.32	0.216	4.08	0.156	0.872
	bt.garn-0720-054	2.9	8.64	2.007	150	1.91	29.4	0.2	0.346	1.4	0.229	0.446
TRENCH METASOMATIC BIF	alt-PM05-005	0	8.66	2.056	0.38	1.7	5.3	N.D.	0.34	0	0.196	N.D.
	alt-PM05-009	0	1.17	0.269	1.11	0.3	1.2	N.D.	0.075	0.07	0.068	N.D.
	alt-PM05-010	0	2.45	0.565	0.76	0.59	5.6	N.D.	0.146	0.09	0.126	N.D.
	alt-PM05-013	0.2	4.66	1.087	1.74	1.08	3.9	N.D.	0.227	0.18	0.16	N.D.
	alt-PM05-019	0	2.06	0.484	0.74	0.52	3.8	N.D.	0.121	0.07	0.1	N.D.
	alt-PM05-027	0	5.44	1.238	0.82	1.24	4.3	N.D.	0.26	0.08	0.171	N.D.
	alt-PM05-032	0.3	2.68	0.619	4.05	0.61	8	N.D.	0.145	0.2	0.114	N.D.
	altb-PM05-045	0	1.22	0.337	1.36	0.21	2.5	N.D.	0.034	0.07	0.038	N.D.
	alt-PM05-048	7.4	11.02	2.757	9.57	2.9	92.5	0.61	0.516	10.86	0.285	N.D.
alt-PM05-049	7.2	6.51	1.482	11.7	1.82	46.9	0.51	0.381	3.97	0.218	N.D.	
CHL-SCHIST	tb-PM05-007	1.7	2.96	0.606	3.73	0.92	1	N.D.	0.234	0.26	0.191	N.D.
	tb-PM05-024	2.2	1.45	0.301	150	0.42	21.4	N.D.	0.077	0.6	0.046	N.D.
	altb-PM05-100	2	0.57	0.128	62.66	0.18	12.7	N.D.	0.033	0.44	0.025	N.D.



		REE, LILE, HFSE												
		Sample ID	Y	Yb	Zr	Au	Ag	As	Ba	Co	Cr	Cs	Cu	Ga
SILICATE-DOMINANT BIF	4ea-PM06-043	14.56	1.4	43.4	57	N.D.	8	N.D.	18	100	N.D.	219	8	
	4ea-0620-UG04	10.38	0.79	22	N.M.	N.D.	2	N.D.	35	58	N.D.	445	12	
	4ea-0720-044	11.54	1.13	34.8	30	N.D.	N.D.	486	18	92	8	48	8	
	4ea-0720-061	16.61	1.46	38.4	N.M.	N.D.	6	N.D.	13	97	N.D.	83	7	
	4ea-0720-065	23.76	2.18	54.4	2150	N.D.	99	159	19	119	N.D.	57	13	
	4ea-0720-067	20.48	1.92	55.1	1560	5	390	37	N.D.	158	N.D.	58	12	
	4ea-0720-068	14.66	1.27	53.6	1383.8	N.D.	10	92	N.D.	89	12	58	9	
	4ea-0720-069	33.12	3.37	106.9	40	N.D.	38	49	51	146	N.D.	144	20	
	4ea-0830-001	22.76	1.98	70.6	1296.1	N.D.	120	99	15	119	N.D.	53	12	
	4ea-0830-002	16.56	1.45	48.6	8350	N.D.	4	1021	12	119	9	41	10	
4ea-0830-004	22.33	2.1	95.1	10000	N.D.	1	29	N.D.	220	N.D.	198	13		
HORNBLENDE-GARNET SCHIST	4e-0720-018	17.13	1.91	60.8	20	N.D.	3	39	41	163	N.D.	208	11	
	4e-0720-019	20.92	1.46	46.2	210	N.D.	6	209	14	107	N.D.	69	10	
	4e-0720-022	18.3	2.3	61.5	10	N.D.	18	60	34	203	N.D.	103	12	
	4e-0720-023	17.8	1.96	72.9	1720	N.D.	33	81	41	214	N.D.	171	13	
	4e-0720-034a	16.7	1.84	59.9	410	N.D.	1	N.D.	32	154	N.D.	255	11	
	4e-0720-034b	21.13	2.09	51.7	1000	N.D.	55	82	29	198	N.D.	240	10	
	4e-0720-047	20.92	2.43	68.4	10	N.D.	6	286	60	360	N.D.	170	19	
	4e-0720-048	9.57	1.23	94.4	20	5	12	617	27	151	N.D.	34	15	
BIOTITE-GARNET SCHIST	4f-0720-001	30.86	3.15	132.8	0.07	N.D.	25	285	43	317	N.D.	142	21	
	4f-0720-002	14.33	1.84	91.9	0.0354	N.D.	8	307	49	347	N.D.	83	18	
	4f-0720-008	16.87	2.07	82.3	0.02	N.D.	45	471	53	410	7	35	22	
	4f-0720-009	17.13	2.31	80.1	0.02	5	23	369	49	398	N.D.	54	17	
	4f-0720-011	17.89	2.19	96.8	0.02	N.D.	50	290	60	417	N.D.	211	23	
	4f-0720-027a	7.91	1.32	98.9	0.02	N.D.	6	286	60	360	N.D.	170	19	
	4f-PM05-050	19.23	1.19	39.4	N.M.	N.D.	3	347	N.D.	62	N.D.	54	6	
METASOMATIC BIOTITE-GARNET SCHIST	bt.garn-0720-001	18.19	1.98	97.5	N.M.	N.D.	9	261	52	122	18	14	22	
	bt.garn-0720-007	39.05	3.9	113.6	0.37	N.D.	31	452	40	161	15	185	19	
	bt.garn-0720-017	15.02	2.3	129.6	N.M.	N.D.	5	541	50	337	N.D.	8	24	
	bt.garn-0720-020	12.65	1.47	51.6	7.54	N.D.	11	1290	28	199	28	38	24	
	bt.garn-0720-049	11.23	1.07	109	0.08	N.D.	29	647	16	131	19	24	18	
	bt.garn-0720-054	16.57	1.54	56.3	0.16	N.D.	41	763	20	176	20	135	15	
TRENCH METASOMATIC BIF	alt-PM05-005	16.48	1.2	N.D.	N.M.	21	N.D.	30	N.D.	N.D.	N.D.	14	N.D.	
	alt-PM05-009	4.44	0.48	N.D.	N.M.	35	N.D.	N.D.	N.D.	N.D.	N.D.	18	N.D.	
	alt-PM05-010	8.37	0.86	N.D.	N.M.	14	N.D.	N.D.	N.D.	N.D.	N.D.	15	3	
	alt-PM05-013	11.04	1.08	N.D.	N.M.	71	N.D.	N.D.	N.D.	N.D.	N.D.	26	N.D.	
	alt-PM05-019	6.28	0.72	N.D.	N.M.	42	N.D.	N.D.	N.D.	N.D.	N.D.	19	N.D.	
	alt-PM05-027	12.24	1.1	N.D.	N.M.	40	N.D.	N.D.	N.D.	N.D.	N.D.	22	N.D.	
	alt-PM05-032	9.2	0.76	N.D.	N.M.	47	N.D.	N.D.	N.D.	N.D.	N.D.	22	N.D.	
	altb-PM05-045	1.99	0.32	N.D.	N.M.	7	0	55	0	15	N.D.	23	16	
	alt-PM05-048	16.3	1.96	N.D.	N.M.	104	N.D.	198	112	489	N.D.	355	21	
alt-PM05-049	13.27	1.47	N.D.	N.M.	8	N.D.	138	47	1429	N.D.	325	14		
CHL. SCHIST	tb-PM05-007	8.24	1.31	N.D.	N.M.	177	N.D.	28	39	877	N.D.	39	15	
	tb-PM05-024	2.31	0.33	N.D.	N.M.	262	N.D.	64	19	440	N.D.	9	13	
	altb-PM05-100	1.15	0.2	N.D.	N.M.	N.D.	N.D.	53	N.D.	N.D.	N.D.	N.D.	N.D.	

	Sample ID	TRACE										
		K	Mn	Mo	Na	Nb	Ni	P	Pb	Rb	Sb	Sc
SILICATE-DOMINANT BIF	4ea-PM06-043	848	7332	N.D.	1141	3	74	466	N.D.	N.D.	N.D.	19
	4ea-0620-UG04	5006	1141	N.D.	2689	2	70	678	5	23	N.D.	11
	4ea-0720-044	5491	2681	N.D.	3558	3	66	523	N.D.	53	N.D.	16
	4ea-0720-061	283	3878	N.D.	744	2	63	767	N.D.	3	N.D.	14
	4ea-0720-065	4690	4063	N.D.	381	3	72	823	N.D.	26	N.D.	18
	4ea-0720-067	979	5141	N.D.	173	3	44	787	6	7	7	23
	4ea-0720-068	5471	6572	N.D.	1780	3	50	555	6	33	N.D.	14
	4ea-0720-069	1035	2059	N.D.	25955	5	110	905	7	9	N.D.	43
	4ea-0830-001	734	3922	N.D.	346	3	72	985	N.D.	4	N.D.	18
	4ea-0830-002	11949	3537	N.D.	648	3	76	913	N.D.	95	N.D.	16
4ea-0830-004	392	4261	N.D.	191	3	56	243	N.D.	2	N.D.	22	
HORNBLENDE-GARNET SCHIST	4e-0720-018	11383	4390	N.D.	2100	4	120	469	5	23	N.D.	27
	4e-0720-019	17734	4521	N.D.	162	3	79	932	N.D.	97	N.D.	17
	4e-0720-022	3774	5475	N.D.	1132	3	116	445	7	7	N.D.	32
	4e-0720-023	7042	4363	N.D.	2045	3	107	475	6	20	N.D.	29
	4e-0720-034a	1110	5217	N.D.	2212	3	102	589	N.D.	N.D.	N.D.	24
	4e-0720-034b	7664	8671	N.D.	1096	3	114	830	N.D.	26	N.D.	28
	4e-0720-047	16109	518	N.D.	1848	5	155	334	N.D.	86	N.D.	50
4e-0720-048	44585	1222	N.D.	9512	4	83	146	6	187	N.D.	19	
BIOTITE-GARNET SCHIST	4f-0720-001	28753	3143	N.D.	2191	5	173	578	N.D.	81	N.D.	34
	4f-0720-002	42131	1615	N.D.	3721	5	139	278	7	102	N.D.	37
	4f-0720-008	38158	2593	N.D.	1954	5	153	289	10	187	N.D.	52
	4f-0720-009	41029	4069	N.D.	406	5	202	344	N.D.	154	N.D.	34
	4f-0720-011	38734	3211	N.D.	2946	5	158	343	N.D.	97	N.D.	46
	4f-0720-027a	38645	518	N.D.	1848	5	155	334	N.D.	86	N.D.	50
	4f-PM05-050	13500	3733	N.D.	1578	3	50	973	6	101	N.D.	12
METASOMATIC BIOTITE-GARNET SCHIST	bt.garn-0720-001	34415	1891	N.D.	3807	4	104	487	7	150	N.D.	39
	bt.garn-0720-007	39841	1278	N.D.	2402	3	137	1034	11	175	N.D.	39
	bt.garn-0720-017	40901	1100	N.D.	4582	6	179	278	19	155	N.D.	40
	bt.garn-0720-020	46623	1255	N.D.	3418	2	99	101	9	207	N.D.	28
	bt.garn-0720-049	44007	1570	N.D.	797	3	106	422	6	207	N.D.	13
	bt.garn-0720-054	40766	1757	N.D.	1511	3	128	710	13	188	N.D.	28
TRENCH METASOMATIC BIF	alt-PM05-005	124	7535	N.D.	78	N.D.	17	5881	N.D.	N.D.	N.D.	N.D.
	alt-PM05-009	165	8852	N.D.	73	N.D.	18	419	7	N.D.	N.D.	N.D.
	alt-PM05-010	168	9538	N.D.	60	N.D.	15	766	N.D.	N.D.	N.D.	N.D.
	alt-PM05-013	317	10440	N.D.	84	N.D.	24	1619	N.D.	N.D.	N.D.	N.D.
	alt-PM05-019	193	10016	N.D.	186	N.D.	16	513	6	N.D.	N.D.	N.D.
	alt-PM05-027	159	7894	N.D.	120	N.D.	24	1419	N.D.	N.D.	N.D.	N.D.
	alt-PM05-032	436	6363	N.D.	69	N.D.	23	743	8	N.D.	7	N.D.
	altb-PM05-045	4258	101	N.D.	20622	N.D.	18	26	11	N.D.	0	0
	alt-PM05-048	2674	899	7	11673	N.D.	179	322	27	N.D.	N.D.	23
	alt-PM05-049	3801	1177	3	8568	N.D.	162	169	19	N.D.	N.D.	29
CHI-SCHIST	tb-PM05-007	697	660	N.D.	108	N.D.	250	121	N.D.	N.D.	18	45
	tb-PM05-024	7206	945	N.D.	219	N.D.	127	202	9	N.D.	N.D.	17
	altb-PM05-100	N.D.	N.D.	N.D.	N.D.	N.D.	N.D.	N.D.	N.D.	N.D.	N.D.	N.D.

	Sample ID	TRACE												TOTAL
		Se	Sn	Sr	Ta	Th	Ti	U	V	W	Y	Zn	Zr	
SILICATE-DOMINANT BIF	4ea-PM06-043	N.D.	N.D.	22	N.D.	6	2218	N.D.	108	22	16	112	40	99.51
	4ea-0620-UG04	18	N.D.	80	N.D.	6	1074	N.D.	80	56	11	55	20	100.52
	4ea-0720-044	N.D.	7	140	N.D.	4	2153	N.D.	101	42	13	61	37	100.55
	4ea-0720-061	N.D.	N.D.	32	N.D.	5	2107	N.D.	99	35	18	63	34	99.74
	4ea-0720-065	N.D.	N.D.	22	N.D.	6	3384	N.D.	159	30	26	101	53	100.19
	4ea-0720-067	3	N.D.	15	N.D.	5	3777	N.D.	185	34	24	98	54	99.62
	4ea-0720-068	N.D.	6	61	N.D.	5	2123	N.D.	87	26	17	71	50	100.39
	4ea-0720-069	N.D.	7	89	N.D.	N.D.	9782	N.D.	392	33	35	171	116	100.92
	4ea-0830-001	N.D.	N.D.	42	N.D.	7	3355	N.D.	153	22	26	142	75	99.55
	4ea-0830-002	N.D.	6	35	N.D.	4	2609	N.D.	112	30	20	78	44	99.82
4ea-0830-004	12	5	12	N.D.	7	4277	N.D.	151	31	26	104	103	99.93	
HORNBLENDE-GARNET SCHIST	4e-0720-018	N.D.	N.D.	14	N.D.	5	3361	N.D.	170	N.D.	17	319	69	99.23
	4e-0720-019	N.D.	7	14	N.D.	7	2631	N.D.	119	14	20	76	54	99.92
	4e-0720-022	N.D.	N.D.	36	N.D.	N.D.	3463	N.D.	200	17	19	157	67	99.89
	4e-0720-023	N.D.	N.D.	25	N.D.	6	3963	N.D.	205	20	17	274	79	99.67
	4e-0720-034a	2	N.D.	16	N.D.	5	2736	N.D.	138	18	17	331	65	99.88
	4e-0720-034b	2	N.D.	13	N.D.	4	3550	N.D.	202	19	21	143	58	99.91
	4e-0720-047	N.D.	N.D.	19	N.D.	6	7427	N.D.	377	18	16	208	111	99.93
	4e-0720-048	N.D.	N.D.	39	N.D.	7	3763	N.D.	168	N.D.	9	135	106	99.76
BIOTITE-GARNET SCHIST	4f-0720-001	N.D.	N.D.	47	N.D.	6	6016	N.D.	302	28	20	205	101	100.86
	4f-0720-002	N.D.	N.D.	47	N.D.	4	6705	N.D.	332	18	13	134	102	99.94
	4f-0720-008	N.D.	N.D.	148	N.D.	6	6635	N.D.	380	17	16	141	78	99.22
	4f-0720-009	N.D.	N.D.	3	N.D.	4	7184	N.D.	393	21	15	218	87	99.92
	4f-0720-011	N.D.	N.D.	27	N.D.	6	7076	N.D.	371	20	19	152	104	100.9
	4f-0720-027a	N.D.	N.D.	19	N.D.	6	7427	N.D.	377	18	16	208	111	99.93
	4f-PM05-050	N.D.	N.D.	35	N.D.	8	2047	N.D.	77	20	20	53	42	99.61
	bt.garn-0720-001	N.D.	N.D.	52	N.D.	4	11143	0.588	389	18	30	180	146	99.65
METASOMATIC BIOTITE-GARNET SCHIST	bt.garn-0720-007	N.D.	N.D.	38	N.D.	N.D.	9657	0.317	389	N.D.	37	186	129	99.93
	bt.garn-0720-017	N.D.	N.D.	141	N.D.	8	6781	1.487	328	13	19	263	141	99.92
	bt.garn-0720-020	2	7	22	N.D.	N.D.	5498	0.277	277	16	14	181	55	99.79
	bt.garn-0720-049	N.D.	8	35	N.D.	4	2940	0.872	137	14	9	107	128	99.74
	bt.garn-0720-054	N.D.	N.D.	31	N.D.	N.D.	4490	0.446	175	22	16	149	65	99.91
	alt-PM05-005	N.D.	N.D.	N.D.	N.D.	N.D.	0	0.038	7	19	N.D.	26	10	100
TRENCH METASOMATIC BIF	alt-PM05-009	N.D.	9	N.D.	N.D.	N.D.	0	0.06	8	20	N.D.	63	12	100
	alt-PM05-010	N.D.	N.D.	N.D.	N.D.	N.D.	25	0.101	9	17	N.D.	64	11	100
	alt-PM05-013	N.D.	N.D.	N.D.	N.D.	N.D.	17	0.132	15	18	N.D.	40	13	100
	alt-PM05-019	N.D.	11	N.D.	N.D.	N.D.	0	0.056	5	15	N.D.	66	11	100
	alt-PM05-027	N.D.	5	N.D.	N.D.	N.D.	21	0.053	8	13	N.D.	32	10	98.77
	alt-PM05-032	N.D.	N.D.	N.D.	N.D.	N.D.	74	0.075	9	13	N.D.	31	14	100
	altb-PM05-045	N.D.	N.D.	N.D.	N.D.	N.D.	236	0.048	14	24	N.D.	18	0	99.27
	alt-PM05-048	2	N.D.	N.D.	N.D.	N.D.	3408	2.527	154	N.D.	N.D.	1734	127	99.93
	alt-PM05-049	3	N.D.	N.D.	N.D.	N.D.	5118	1.33	191	N.D.	N.D.	341	87	99.82
CHL-SCHIST	tb-PM05-007	N.D.	7	N.D.	N.D.	N.D.	3439	0.066	268	13	N.D.	109	35.3	99.89
	tb-PM05-024	N.D.	N.D.	N.D.	N.D.	N.D.	4491	0.076	297	12	N.D.	90	44.9	99.94
	altb-PM05-100	N.D.	N.D.	N.D.	N.D.	N.D.	N.D.	0.09	N.D.	N.D.	N.D.	N.D.	54.8	99.94